Max-Planck-Institut für Festkörperforschung
Stuttgart

Optical properties of metallic photonic crystal structures

André Christ

Dissertation an der
Philipps-Universität Marburg

August 2005

Optical properties of metallic photonic crystal structures

Dissertation

zur

Erlangung des Doktorgrades

der Naturwissenschaften

(Dr. rer. nat.)

dem

Fachbereich Physik

der

Philipps-Universität Marburg

vorgelegt von

André Christ

aus Marburg

Marburg/Lahn 2005

Bei Beobachtung sind selbst die Irrtümer nützlich,
indem sie aufmerksam machen
und dem Scharfsichtigen Gelegenheit geben,
sich zu üben.

J. W. von Goethe, 1784

Zusammenfassung

Im Rahmen dieser Arbeit werden resonante Kopplungsphänomene in periodisch angeordneten Metallstrukturen mit Hilfe spektroskopischer Verfahren untersucht. Das Verständnis dieser grundlegenden Phänomene ist besonders im Hinblick auf zukünftige technologische Anwendungen vergleichbarer Nanostrukturen von besonderer Bedeutung. Generell sind metallische Nanostrukturen heute sowohl von großem wissenschaftlichem als auch technischem Interesse, da sie die Realisierung neuartiger optischer Materialien, so genannter Metamaterialien, ermöglichen. Als Metamaterialien werden unter anderem solche Verbundmaterialien bezeichnet, die ungewöhnliche - in der Natur nicht vorhandene - elektromagnetische Eigenschaften aufweisen. Die außergewöhnlichen optischen Eigenschaften nanostrukturierter Metalle sind generell auf die mögliche Anregung von Partikel- oder Oberflächenplasmonen zurückzuführen. So genannte Oberflächenplasmon-Polaritonen entstehen im Allgemeinen durch die kohärente Wechselwirkung der Leitungsbandelektronen mit elektromagnetischen Feldern an der Grenzfläche zwischen dielektrischen und metallischen Materialien. Es handelt sich dabei im Prinzip um eine kollektive Anregung des Elektronensystems, die sich an der Oberfläche gemeinsam mit einer elektromagnetischen Welle ausbreitet. Die Anregung von Plasmonenmoden führt generell zur räumlichen Konzentration elektromagnetischer Felder an der Metalloberfläche und kann so zum Beispiel zur Verstärkung unterschiedlicher Prozesse genutzt werden (z.B. Ramanstreuung oder Photolumineszenz).

Gegenstand dieser Arbeit ist die Untersuchung der linearen optischen Eigenschaften von periodisch angeordneten Metall-Nanodrähten, die auf dielektrischen oder metallischen Substraten aufgebracht sind. Die verwendeten Nanostrukturen können dabei der neuen Materialklasse der sogenannten polaritonischen photonischen Kristalle zugeordnet werden. Im Gegensatz zu rein dielektrischen Nanostrukturen, deren Transmissionsspektren durch die Anregung geometrischer Resonanzen gekennzeichnet sind, können die Spektren der verwendeten metallischen photonischen Kristalle zusätzliche elektronische Resonanzen im sichtbaren Spektralbe-

reich aufweisen. Diese als Partikelplasmon bezeichneten Resonanzen sind auf die Kollektivschwingung der Leitungsbandelektronen in den einzelnen Nanodrähten zurückzuführen. Eine sehr wichtige Fragestellung ist in diesem Zusammenhang, in wie weit mögliche elektromagnetische Kopplungsphänomene die optischen Eigenschaften der untersuchten metallischen Nanostrukturen zusätzlich beinflussen können. Sowohl die direkte elektromagnetische Wechselwirkung zwischen den einzelnen Nanodrähten, als auch die mögliche Wechselwirkung mit verschiedenen Oberflächenmoden sollen im Rahmen dieser Arbeit eingehender betrachtet werden. Neben der Verwendung verschiedener dielektrischer Substrate wird vor allem der Einfluss metallischer Substratschichten demonstriert. Ziel der Untersuchungen ist es dabei, generell ein besseres und genaueres Verständnis der physikalischen Ursachen der beobachteten Kopplungsphänomene zu erhalten. Im Rahmen dieser Arbeit kommen sowohl experimentelle Methoden als auch theoretische Simulationen zur Anwendung, um einen tieferen Einblick in die komplexen Zusammenhänge zu ermöglichen. Die Arbeit belegt eindeutig, dass sowohl die Entstehung von Polaritonmoden als auch so genannte Hybridisierungseffekte die optischen Transmissionseigenschaften sehr stark beeinflussen. Die beobachteten grundlegenden Kopplungsphänomene können möglicherweise zur Entwicklung oder Optimierung neuartiger optischer Bauelemente genutzt werden.

Die vorgelegte Arbeit ist in mehrere voneinander unabhängige Kapitel unterteilt. Zusätzlich zur ausführlichen Einleitung kann die Arbeit im Wesentlichen in drei Abschnitte gegliedert werden:

Im ersten Teil der Arbeit werden die optischen Eigenschaften von periodisch angeordneten Metall-Nanodrähten vorgestellt, die mittels Elektronenstrahllithographie auf dielektrischen Substraten aufgebracht wurden. Die beobachteten optischen Phänomene zeigen dabei eine sehr starke Abhängigkeit von der geometrischen Dicke der verwendeten dielektrischen Substratschichten. Während die Spektren bei der Verwendung sehr dünner dielektrischer Substrate durch so genannte Rayleigh-Anomalien dominiert werden, führen wellenleitende Substrate zur Bildung gekoppelter Polaritonmoden. Wie bereits durch Linden *et al.* in früheren Untersuchungen an regelmäßig angeordneten Gold-Nanopartikel-Feldern demonstriert werden konnte, sind die Spektren der verwendeten metallischen photonischen Kristalle durch eine charakteristische Linienform der Plasmonresonanzen gekennzeichnet. Ihm Rahmen der vorliegenden Arbeit wurde erstmals der Nachweis erbracht, dass der als selektive Unterdrückung der Extinktion bezeichnete Effekt durch die starke Kopplung zwischen elektronischen und optischen Resonanzen und die daraus resultierende Polaritonbildung zu erklären ist. Neben linea-

ren Transmissionsexperimenten kommen theoretische Simulationen zur Anwendung, um eine detaillierte theoretische Beschreibung zu ermöglichen. Die auf einer Streumatrix-Methode basierenden numerischen Rechnungen weisen eine sehr gute Übereinstimmung mit den experimentellen Resultaten auf. Es zeigt sich, dass besonders die Möglichkeit zur genauen Simulation der elektromagnetischen Feldverteilung innerhalb der verwendeten Nanostrukturen bei der Interpretation der optischen Eigenschaften eine große Hilfe ist.

Im zweiten Teil der Arbeit werden Modifikationen der optischen Eigenschaften, die durch die Verwendung metallischer Substrate entstehen, ausführlich diskutiert. Die periodisch angeordneten Metall-Nanodrähte werden für diese Untersuchungen auf speziell präparierten Metallfilmen aufgebracht. So kann zum Beispiel der Abstand zwischen Nanodraht-Feld und Metallfilm durch vorheriges Aufdampfen einer dielektrischen Barrierenschicht sehr präzise kontrolliert werden. Neben der Anregung von lokalisierten Partikelplasmonen ermöglichen diese Strukturen ebenfalls die Ausbildung ausgedehnter Oberflächenplasmonmoden. Die Untersuchung der Kopplung zwischen diesen lokalisierten und ausgedehnten Plasmonmoden in metallischen photonischen Kristallen ist von besonderem Interesse. Die experimentellen und theoretischen Ergebnisse zeigen eindeutig, dass die optischen Transmissionsspektren dieser Strukturen sowohl Hybridisierungsphänomene als auch polaritonische Effekte aufweisen. Während die Hybridisierung eine Rotverschiebung der Plasmonresonanz zur Folge hat, führt die starke elektromagnetische Wechselwirkung zwischen lokalisierten und ausgedehnten Plasmonen zur Bildung neuartiger Polaritonmoden. Die detaillierte Untersuchung umfasst eine Analyse der optischen Phänomene in Abhängigkeit der dielektrischen Barrierendicke. Alle numerischen Rechnungen zeigen wiederum eine sehr gute Übereinstimmung mit den experimentellen Resultaten.

Der letzte Abschnitt der Arbeit beschäftigt sich schließlich mit der detaillierten theoretischen Untersuchung der optischen Eigenschaften dreidimensionaler Nanodrahtstrukturen, die als so genannte plasmonische Kristalle bezeichnet werden können. Streumatrix-basierende Rechnungen zeigen eindeutig, dass sowohl Nahfeld- als auch Fernfeldkopplung eine starke Modifikation der Transmissionseigenschaften der untersuchten metallischen photonischen Kristalle zur Folge haben. Die dipolare Nahfeldwechselwirkung zwischen benachbarten Nanodrähten führt so zum Beispiel zu ausgeprägten Hybridisierungseffekten, die sich durch eine deutliche spektrale Aufspaltung der Plasmonresonanzen bemerkbar machen. Es wird gezeigt, dass die energetische Aufspaltung der entstehenden Normal-Moden dabei direkt durch den vertikalen Abstand der Nanodrähte bestimmt wird. Die ebenfalls

vorhandene strahlende Kopplung führt hingegen zur Modifikation der Dephasierungszeiten der Plasmonoszillationen, ein Phänomen, das allgemein unter dem Begriff der Superradianz bekannt ist. Strahlungskopplung in Bragg-Strukturen führt generell zu einer beschleunigten Dephasierung und somit zur spektralen Verbreiterung der theoretisch berechneten Plasmonresonanzen. Die Untersuchung der photonischen Bandlücke in metallischen Bragg-Strukturen bildet den Abschluss der Arbeit. Die numerischen Simulationen zeigen, dass die untersuchten dreidimensionalen Nanodrahtstrukturen durch eine deutliche Bandlücke im sichtbaren Spektralbereich gekennzeichnet sind.

Abstract

This work presents a comprehensive study of the linear optical properties of metallo-dielectric photonic crystals. These artificially structured materials generally belong to the new material class of so-called polaritonic photonic crystals. They provide simultaneous electronic and photonic resonances in the same energy range. In this work, we investigate one-dimensional periodic gold nanowire arrays deposited on top of different substrate materials as an ideally suited model system. The influence of both dielectric and metallic substrates is studied. In particular, it is shown that the optical response of these metallo-dielectric nanostructures is generally modified due to the appearance of various electromagnetic coupling phenomena. Polariton formation as well as plasmon hybridization are reported.

The first part of this thesis is devoted to the study of metallic nanowire arrays deposited on top of purely dielectric substrates. The appearance of grating anomalies, which critically depend on the substrate thickness, provides evidence that the optical response of these planar metallic photonic crystal structures can be strongly modified. While only Rayleigh-type anomalies are observed for thin dielectric substrates, thicker waveguiding substrates can induce strong coupling phenomena. The observed strong coupling between plasmon and waveguide modes results in the formation of waveguide-plasmon polaritons with a large Rabi splitting up to 250 meV. It is shown that the coupling phenomena vary with the nanowire grating period, the angle of incidence, and also the waveguide layer thickness. A scattering-matrix based numerical method is used to calculate the transmission properties and the near-field spatial distributions of such metallic photonic crystal structures. All experimental results are well confirmed by theoretical calculations.

The influence of metallic substrates is analyzed in the second part of the thesis. The metal nanowire arrays are now placed in front of a thin metal film, supporting short- and long-range surface plasmon modes. It is demonstrated both

experimentally and theoretically that the optical response of these photonic crystal structures critically depends on the specific grating-film separation, which is artificially controlled by the deposition of a thin dielectric spacer layer. In addition to dipole-dipole coupling between the individual nanowires and their mirror dipoles, especially the interaction between localized particle plasmons and extended surface plasmon modes induces interesting optical effects. The investigations indicate that the simultaneous excitation of particle plasmons of the metal nanowires and surface plasmon resonances on the nearby thin metal film gives rise to strong coupling phenomena. Similar to metallo-dielectric structures, the observed anticrossing behavior can be interpreted in terms of polariton formation. We show that the resonant coupling phenomena vary with the nanowire grating period, with the nanowire cross-section, and with the metal- as well as the spacer layer thickness.

As third part of the thesis, we present a theoretical study of particle plasmon excitation in so-called plasmonic crystal structures. It is shown by using the scattering-matrix based formalism that the collective optical response of a periodic metal nanowire ensemble strongly differs from the single nanowire case. In addition to more complex plasmonic Bragg structures, especially electromagnetic coupling between metal nanowire pairs is analyzed. Our numerical results give clear evidence for near- as well as far-field coupling effects. While near-field coupling leads to hybridization-like phenomena, radiative coupling on the other hand gives rise to a superradiant behavior and results in the formation of cavity-polariton-like modes. Additionally, also polaritonic bandgap structures are briefly addressed. It is shown that a stacking of metal nanowire arrays results in the formation of a large one-dimensional polaritonic stopband at optical wavelengths.

Publications

Parts of this work have already been published:

In scientific journals and books:

- S. Linden, A. Christ, J. Kuhl, and H. Giessen, *Selective suppression of extinction within the plasmon resonance of gold nanoparticles*, Appl. Phys. B. **73**, 311 (2001)

- A. Christ, S.G. Tikhodeev, N.A. Gippius, J. Kuhl, and H. Giessen, *Plasmon polaritons in a metallic photonic crystal slab*, phys. stat. sol (c) **0**, 1393 (2003)

- A. Christ, S.G. Tikhodeev, N.A. Gippius, J. Kuhl, and H. Giessen, *Waveguide-plasmon polaritons: Strong coupling of photonic and electronic resonances in a metallic photonic crystal slab*, Phys. Rev. Lett. **91**, 183901 (2003)

- A. Christ, S. Linden, T. Zentgraf, K. Schubert, D. Nau, S.G. Tikhodeev, N.A. Gippius, J. Kuhl, F. Schindler, A.W. Holleitner, J. Stehr, J. Crewett, J. Lupton, T. Klar, U. Scherf, J. Feldmann, C. Dahmen, G. von Plessen, and H. Giessen, *Optical properties of planar metallo-dielectric photonic crystals*, in Photonic Crystals: Advances in Design, Fabrication, and Characterization, (ed. by K. Busch, S. Lölkes, R.B. Wehrspohn, and H. Föll, Wiley, 2004)

- A. Christ, T. Zentgraf, S.G. Tikhodeev, N.A. Gippius, J. Kuhl, and H. Giessen, *Optical properties of planar metallic photonic crystal structures: Experiment and theory*, Phys. Rev. B **70**, 125113 (2004)

- S.G. Tikhodeev, N.A. Gippius, A. Christ, J. Kuhl, and H. Giessen, *Waveguide-plasmon polaritons in metal-dielectric photonic crystal slabs*, Physics of the Solid State **47**, 145 (2005)

- S.G. Tikhodeev, N.A. Gippius, A. Christ, T. Zentgraf, J. Kuhl, and H. Giessen, *Waveguide-plasmon polaritons in photonic crystal slabs with metal nanowires*, phys. stat. sol. (c) **2**, 795 (2005)

- T. Zentgraf, A. Christ, J. Kuhl, N.A. Gippius, S.G. Tikhodeev, and H. Giessen, *One-dimensional metallo-dielectric photonic crystal superlattices*, submitted (2005)

At international conferences and workshops:

- A. Christ, S.G. Tikhodeev, N.A. Gippius, J. Kuhl, and H. Giessen, *Plasmon polaritons in a metallic photonic crystal slab*, 7th International Workshop on Nonlinear Optics and Excitation Kinetics in Semiconductors (NOEKS 7), poster I.26, Karlsruhe, Germany (2003)

- A. Christ, S.G. Tikhodeev, N.A. Gippius, J. Kuhl, and H. Giessen, *Strong plasmon-polariton mode splitting in a metallic grating-waveguide structure*, talk J2.4, Materials Research Society (MRS) spring meeting, San Francisco, USA (2003)

- A. Christ, S.G. Tikhodeev, N.A. Gippius, J. Kuhl, and H. Giessen, *Waveguide-plasmon polaritons in a 1D metallic photonic crystal slab*, Quantum Electronics and Laser Science Conference (QELS), talk QTuL5, Baltimore, USA (2003)

- A. Christ, S.G. Tikhodeev, N.A. Gippius, J. Kuhl, and H. Giessen, *Far-field interaction in planar metallic photonic crystals*, poster presentation, International Symposium on Photonic and Electromagnetic Crystal Structures V (PECS), Kyoto, Japan (2004)

- A. Christ, T. Zentgraf, J. Kuhl, S.G. Tikhodeev, N.A. Gippius, and H. Giessen, *Optical properties of planar metallo-dielectric photonic crystal superlattices*, accepted for oral presentation, talk QMK4, Quantum Electronics and Laser Science Conference (QELS), Baltimore, USA (2005)

- A. Christ, T. Zentgraf, J. Kuhl, N.A. Gippius, S.G. Tikhodeev, and H. Giessen, *One-dimensional metallo-dielectric photonic crystal superlattices*, Surface Plasmon Photonics 2, Graz, Austria (2005)

Additional scientific publications which are not presented in this thesis:

- Y.M. Manz, A. Christ, O.G. Schmidt, T. Riedl, and A. Hangleiter, *Optical and structural anisotropy of InP/GaInP quantum dots for laser applications*, Appl. Phys. Lett. **83**, 887 (2003)

- K. Schubert, A. Christ, J. Kuhl, and H. Giessen, *Extremely slow coherent polarization decay of waveguide-plasmon-polaritons in metallic photonic crystal slabs*, Technical Digest Series of the Optical Society of America (Washington DC): Trends in Optics and Photonics TOPS 90, paper QTuH1 (2003)

- D. Nau, A. Christ, S. Linden, J. Kuhl, and H. Giessen, *The influence of disorder in metallic photonic crystal slabs*, CLEO/IQEC and PhAST Technical Digest on CDROM (The Optical Society of America, Washington, DC, 2004), IThB6

- H. Giessen, S. Linden, A. Christ, J. Kuhl, D. Nau, T. Meier, P. Thomas, and S. W. Koch, *Fano resonances in metallic photonic crystals*, CLEO/IQEC and PhAST Technical Digest on CDROM (The Optical Society of America, Washington, DC, 2004), IFC5

- U. Neuberth, N. Rau, M. Wegener, S. Linden, S. Pereira, K. Busch, A. Christ, and J. Kuhl, *Near-field transmission spectroscopy of one-dimensional metallic photonic crystal slabs* , CLEO/IQEC and PhAST Technical Digest on CDROM (The Optical Society of America, Washington, DC, 2004), IThB2

- T. Zentgraf, A. Christ, J. Kuhl, and H. Giessen, *Tailoring ultrafast dephasing of quasiparticles in metallic photonic crystals*, Phys. Rev. Lett. **93**, 243901 (2004)

- S. Linden, U. Neuberth, N. Rau, A. Naber, M. Wegener, S. Pereira, K. Busch, A. Christ, and J. Kuhl ,*Near-field optical microscopy and spectroscopy of one-dimensional metallic photonic crystals*, Phys. Rev. B **71**, 245119 (2005)

- T. Zentgraf, A. Christ, J. Kuhl, S.G. Tikhodeev, N.A. Gippius, and H. Giessen, *Ultrafast Particle Plasmon Dynamics of Waveguide-Plasmon Polaritons*, International Symposium on Photonic and Electromagnetic Crystal Structures VI (PECS), Crete, Greece (2005)

- D. Nau, A. Schönhardt, A. Christ, J. Kuhl, and H. Giessen, *Disorder in metallic photonic crystals*, International Symposium on Photonic and Electromagnetic Crystal Structures VI (PECS), Crete, Greece (2005)

- T. Ishihara, A. Christ, A.S. Vengurlekar, X. Luo, C. Kamaga, M. Iwanaga, N.A. Gippius, T.G. Tikhodeev, *Origin of Photovoltaic Effect in Metallic Photonic Crystal Slabs*, International Symposium on Photonic and Electromagnetic Crystal Structures VI (PECS), Crete, Greece (2005)

- D. Nau, A. Schönhardt, H. Giessen, A. Christ, and J. Kuhl, *The influence of the disorder type on the optical properties of metallic photonic crystals*, IQEC and CLEO PR, Tokyo, Japan (2005)

- T. Ishihara, C. Kamaga, A. Christ, X. Luo, A.S.Vengurlekar, N.A. Gippius, and S.G. Tikhodeev, *Does the momentum conservation explain photo-induced current in metallic photonic crystal slabs?*, IQEC and CLEO PR, Tokyo, Japan (2005)

Contents

Chapter 1

Introduction

1.1 Metal optics at the nanoscale

The investigation of nanostructured materials is currently one of the most fascinating research fields in modern science. The growing interest in these materials generally relies on the fact that the well-known bulk properties of common materials can be strongly modified when considering an artificial structuring on a nanometer scale. It is very remarkable that the emerging field of so-called nanoscience does not derive from a single scientific discipline. Nanoscience is generally characterized by its interdisciplinary nature, which attracts a wide spectrum of scientists, including physicists, chemists, and biologists. For example, nanostructured materials, nanocrystals, or nanoparticles have potential applications in electronics and optics as well as in the promising fields of biotechnology and biomedicine. The rapid progress in nanoscience is closely related to the continuous development of novel fabrication and structuring techniques. In addition to well-developed top-down lithographical processes (e.g., electron beam lithography), especially bottom-up processes like self-assembling and self-organization offer further fascinating possibilities for generating spatial patterns on the nanometer scale. Based on the recent progress in nanotechnology and the exponentially increasing number of related scientific publications, it is strongly believed that the use of nanostructured materials will be one of the key building blocks for the development of new technological applications in the 21st century.

In addition to a possible modification of the electronic properties, for example due to the utilization of quantum size effects (e.g., semiconductor quantum dots), especially the interaction between external radiation fields and nanostructured

matter is subject to strong changes. A prominent example are the so-called photonic crystal or photonic bandgap structures [1–4], which have become popular very recently. It has been demonstrated that the light-matter interaction can be artificially controlled by introducing a periodic structuring on a length scale comparable to the wavelength of light. Similar to the description of electronic states in solid state material, also the propagation of photons in periodically modulated dielectric structures can be described by the introduction of a bandstructure. Especially the discovery of the possibility to create photonic bandgaps by appropriate structuring has stimulated the increasing interest in these fascinating photonic structures. A full photonic bandgap is generally characterized as the specific energy region of the band diagram for which the propagation of electromagnetic radiation inside the periodically patterned structure is forbidden for all spatial directions. The formation of a complex bandstructure in photonic crystals and the investigation of the related physical effects already led to many fundamental discoveries and inspired various scientists. Well-known examples are the proposal of inhibited spontaneous emission in periodically patterned solid state material [3], the demonstration of negative refraction in the optical regime [5], the realization of optical microcavities with large quality factors and small mode volumes [6, 7], or the verification of vacuum Rabi splitting with a single quantum dot in a photonic crystal nanocavity [8]. Although full photonic bandgaps can only be achieved by three-dimensional structuring of the bulk material, especially the investigation of two-dimensional photonic crystal slab structures has become very popular. This fact is closely related to easier handling of a planar design, which is more or less compatible with the common lithographical fabrication techniques. Two-dimensional photonic crystal slabs generally benefit from their waveguide-based design. The periodically patterned dielectric waveguide structures provide the missing confinement in the third dimension due to utilization of total internal reflection at the slab interfaces. The further optimization of these two-dimensional photonic structures is still a very important research goal. In the field of cavity quantum electrodynamics, for example, structural tuning can be used to suppress out-of-slab photon leakage and therefore obtain photonic crystal nanocavities with ultra-high quality factors. Nanocavities with a quality factor of 600,000 have been demonstrated recently [9].

From a fundamental point of view, the use of nanostructured materials and the utilization of their surprising optical properties have renewed the interest in classical optics, a scientific discipline which so far was believed to be more or less completely understood. In course of the renaissance of so-called nanoscale pho-

tonics especially the prominent subfield of surface plasmon optics [10] (sometimes also referred to as plasmonics) has attracted a significant amount of attention. As extension to the investigations on purely non-absorptive dielectric structures, the research in this arising subfield is based on the realization of metal nanostructures and the analysis of their fundamental optical properties. The use of metals is of increasing interest due to their possibility to support surface plasmon polaritons [11, 12]. Surface plasmons are generally characterized as hybrid surface-bound waves that can propagate at the interface between a metal and a dielectric half space. These polaritonic excitations consist of electromagnetic fields which are bound to the surface due to their resonant interaction with the conduction band electrons of the metal. The nonradiative electromagnetic fields, which decay exponentially into the metal and the dielectric media, are directly connected to longitudinal density fluctuations of the surface electrons. The exceptional and unique properties of materials supporting surface plasmons have been widely investigated since publication of the first pioneering works in the middle of the last century [13–16]. In general, surface plasmons can be excited by the absorption of fast electrons or electromagnetic radiation respectively. Due to the fact that the momentum of a surface plasmon mode on a flat metal surface is greater than that of a free-space photon of the same energy, especially optical excitation can only be accomplished by providing additional momentum. One possible way to achieve momentum matching is to use periodically patterned metal substrates. First experimental investigations of such structures can be dated back to the beginning of the last century. Some of the well-known Wood´s anomalies [17], which have been observed experimentally during optical measurements on metallic diffraction gratings, are now known to arise due to surface plasmon excitation [13]. Particularly with regard to possible optical applications, especially surface plasmon damping has to be considered. A notable fraction of the surface plasmon related electromagnetic fields is located inside the metal in case of plasmon excitation at the interface of a semi-infinite metal half space. The propagation length of surface plasmons is therefore strongly determined by absorption losses. One possibility to overcome this problem is the use of very thin metal layers which are bound between identical dielectric half spaces. Resonant surface plasmon coupling, i.e., the interaction between the surface modes on both interfaces, leads to the formation of so-called long- and short-range plasmon modes [18]. The two modes can be viewed as the symmetric and antisymmetric coupled modes of the thin film geometry. Due to the fact that the emerging long-range mode is characterized by decreased electric field intensities within the metal

layer (symmetric distribution of the transverse magnetic field), the propagation length of this mode can be drastically enhanced.

The wide technological application of surface plasmons on planar surfaces and thin films is generally closely related to the generation of enhanced electromagnetic fields at the metal-dielectric interfaces. For example, surface plasmon resonant sensors have been realized and are already commercially available [19]. Additionally, also surface-enhanced Raman scattering (SERS) has become a very useful spectroscopic tool [20]. From a more fundamental point of view, especially the possibility to enhance nonlinear optical phenomena like higher-harmonic generation [21, 22] or optical bistability [23, 24] is of potential interest. Another important surface plasmon related phenomenon is the possibility to modify the decay characteristics of dipolar light emitters. It is well-known that the lifetime of oscillating dipoles (e.g., excited molecules) near reflecting interfaces can be altered by changing the emitter-surface separation and hence modifying the photonic mode density [25]. In addition to the possibility of, e.g., applying dielectric Bragg mirrors, especially noble metal interfaces have been used in related experimental studies. In a classical picture, an oscillating dipole placed in front of a metal surface can be generally considered as a damped classical oscillator, which is forced by its own reflected field (coupling with the induced mirror dipole). As a result, the spontaneous emission rate generally shows an oscillatory dependence on the metal-dipole separation. While radiative decay processes may dominate in case of larger separations, non-radiative decay channels on the other hand are opened when the dipole is brought into close proximity to the metal interface. Thus, the lifetime of the emitter is additionally modified due to resonant coupling with surface plasmons. Many experimental and theoretical studies can be found for systems considering molecular fluorescence near interfaces [26]. More recent experiments have demonstrated that also the decay of optically generated electron-hole pairs in quantum-wells [27, 28] or quantum-dots [29] can be modified due to resonant coupling with surface plasmons on nearby noble metal interfaces. Note that the increased non-radiative coupling to surface plasmons is generally considered to be an important loss channel which lowers the optical efficiency of light emitting devices. In case of electrical pumping, such devices therefore suffer from the fact that the metal contacts have to be placed in close proximity of the semiconductor layer [30]. One possibility to overcome these limitations is the use of modulated metal contacts [31]. They enable the coupling between the excited surface plasmons and the radiation field and thus increase the emission efficiency. Another interesting alternative approach has been presented very re-

cently. Although only surface roughness is used to recover radiation from the surface plasmon modes, it has been shown that enhanced light emission can be realized by simply increasing the amount of energy that is coupled to the surface plasmon modes [32]. In contrast to previous works, the authors make use of the asymptotic limit of the surface plasmon dispersion to enhance the surface plasmon mode density in their counterintuitive approach. Note that also surface plasmon mediated energy transfer across thin metal films is an important issue which has to be mentioned in this context [33]. Energy transfer between molecules on opposite sides of a metal film [34] as well as surface-plasmon-mediated single-molecule fluorescence through a thin metal layer [35] have been demonstrated recently.

In addition to planar or modulated metal surfaces, also metal nanoparticles offer interesting optical properties. Especially small gold or silver particles are currently the subject of significant scientific research activities. In contrast to extended metal surfaces supporting propagating surface plasmons, the optical response of noble metal nanoparticles is characterized by the excitation of so-called particle plasmons. Particle plasmons are related to coherent oscillations of the conduction band electrons within the individual particles. Their excitation results in strongly enhanced dipolar near-fields and characteristic light scattering properties [36]. One interesting aspect of metal nanostructures supporting particle plasmon excitations is that their optical response strongly depends on the size and the shape of the used particle geometry. These additional design parameters allow to control the supported resonances and to tailor the optical response for various applications. It is very interesting to point out that the application of colloidal metal particles for optical purposes can be traced back to the time of the Romans. Although the discovery that glass could be colored red by adding a small amount of gold powder is often credited to Johann Kunckel, a German glassmaker in the late seventeenth century, the first application of this technique can be found even earlier. A very prominent example is the Lycurgus Cup that was manufactured by Roman artists in the 4th century A.D. This famous cup is well-known for its particular optical properties. One of the very unusual features is the color of the used glass. Due to the inclusion of small metal crystals with distinct light scattering properties, the color of the cup changes between green and red for different illumination conditions. Although the technique of coloring glasses by adding metal nanoparticles was widely used, the origin of the phenomenon was not understood unless the beginning of the 20th century. It is the merit of Gustav Mie to have shown that spherical metal particles with a diameter smaller than the wavelength of light can support resonant modes which lead

to increased scattering and absorption cross sections for certain frequencies [37]. However, due to the fact that the material properties enter as a phenomenological dielectric constant, his famous theoretical approach cannot provide any deeper microscopic insight in the origin of the optical resonances. That the observed and theoretically predicted extinction resonances have to be intrinsically attributed to coherent particle plasmon oscillations was discovered only later on while investigating noble metal nanoparticles by electron energy loss spectroscopy [38].

Generally, metal nanoparticles can be applied for many important scientific and technological purposes. In addition to chemical and biological applications [39], especially the utilization of their specific electromagnetic properties are of increasing interest. For example, gold and silver nanocrystals are still used in optics for coloring glasses. Depending on the sizes of the embedded particles, wavelength selective optical filters can be fabricated. The use of elongated particles on the other hand enables the realization of polarization filters [40]. It has been shown that polarizing glasses can be fabricated by stretching glass substrates containing colloidal metal nanoparticles [41]. Based on the fact that high efficient polarizers can be realized by using very thin substrate layers, these optical elements are especially interesting for possible application in ultrafast optics. Similar to planar metal surfaces, also the electromagnetic field enhancement due to particle plasmon excitation can be utilized. A very prominent example are surface-enhanced Raman scattering (SERS) experiments which make use of the exciting optical properties of metallic nanoparticles [42]. It has been shown that Raman signals can be strongly increased when molecules are attached to gold and silver nanoparticles. The method utilizes the confined local fields of metallic nanoparticles or particle ensembles to detect single molecules with a high spatial resolution below the diffraction limit [43]. Another very interesting proposal makes use of dipolar plasmon coupling in linear metal nanoparticle chains [44–46]. Plasmon waves can propagate along these nanoparticle chains, due to near-field interaction between the successive particles. Although the lossy character of the metal particles may restrict the achievable propagation length, a possible application as a miniature optical waveguide has been discussed very recently.

The research field of nanoscale photonics also includes the investigation of so-called metallo-dielectric photonic crystal structures. In extension to the more common dielectric photonic crystals, which are fabricated by using purely non-absorptive materials, these structures can be characterized by the inclusion of metallic constituents. In the simplest realization, a metallo-dielectric photonic crystal is thought of as a periodic lattice of metallic spheres embedded in a

uniform dielectric background. Metallo-dielectric photonic crystals have already been explored since many years [47, 48]. For example, large omni-directional bandgaps [49–51], well-defined defect modes [52, 53], and negative refraction [54] have been demonstrated. Among the class of metallo-dielectric photonic crystals, especially two-dimensional planar geometries have been intensively investigated. Different implementations of such structures can be found in literature.

Planar metallo-dielectric photonic crystals can be realized, e.g, in the form of modulated metal films which exhibit a periodicity comparable to the wavelength of light. The implemented surface corrugations can be either of one- or two-dimensional character. It has already been demonstrated that Bragg scattering of surface plasmons may lead to standing waves and to the formation of surface plasmon stopbands in these modulated nanostructures [55–58]. Although significant propagation losses have to be considered, the use of periodically modulated metal films generally may open up the way to the realization of various surface plasmon based subwavelength photonic devices. For example, guiding along line defects [59] and the implementation of basic optical elements [60] have been shown very recently. As already mentioned, other important studies on periodically modulated metal surfaces include the extensive investigation of surface plasmon cross-coupling [61–63] or the optimization of light emitting devices [64–66]. A very fundamental study on planar metallo-dielectric structures is the recent demonstration of enhanced photoinduced currents due to surface plasmon excitation. It has been shown that voltage signals can be detected across modulated metal surfaces which are exposed to intense laser radiation [67]. We have to mention that, in extension to the application of simple corrugated metal interfaces or modulated metal films, also the combination of two closely spaced metal layers may be of general technological importance. Metal nanocavities which incorporate one or two modulated metal interfaces have been realized. Consequently, these so-called textured metallic microcavities [68] also have to be assigned to the class of planar metallo-dielectric photonic crystals. For example, a complete band gap for all propagation directions has been demonstrated for the supported guided modes by using a suitable two-dimensional texture profile [69]. Similar nanoscale geometries might be especially interesting for the realization of highly efficient light-emitting devices [70].

Another very prominent realization of planar metallo-dielectric photonic crystals are regular arrays of subwavelength apertures drilled into a metallic film. Well-known examples are based on two-dimensional hole- or one-dimensional slit-arrays. These structures have recently gained a lot of interest due to their sur-

prisingly large light transmission [71]. Depending on the exact geometry of the investigated structure (e.g., metal thickness, period, aperture design), different physical effects have to be taken into account to explain the observed optical phenomena. Both the influence of localized Fabry-Perot-like resonances as well as the excitation of coupled surface plasmon modes have been discussed extensively (e.g., see Refs. [72–78]). Beside their extraordinary transmission, such structures may offer new ways to explore fundamental physical phenomena. For example, the related strong electromagnetic field enhancement within the individual nanoapertures can be utilized in nonlinear experiments. The use of perforated metal films whose holes or slits are filled by some nonlinear material generally results in much stronger nonlinear optical response due to the enhanced local-field strength. Optical bistability in subwavelength slit apertures [79] as well as optically gated transmission [80] have been investigated. Other interesting recent studies are devoted to the implementation of strong coupling phenomena [81], the utilization of coherent coupling and control of radiative surface plasmon damping [82], the exploration of beaming and focusing phenomena [83, 84], or the investigation of plasmon-assisted transmission of entangled photons [85, 86]. In addition to the more common hole- and slit-based realizations, also the discussion of structures with more complex unit cells can be found in the literature [87]. For example, gammadion-like apertures arranged in regular two-dimensional square gratings are applied in studies on planar chirality [88].

Additionally, also the metal nanoparticle based designs can be attributed to the new class of metallic photonic crystals [89–91]. In particular, these planar structures do not incorporate a continuous metal film. They consist of perfectly ordered noble metal nanoparticle arrays deposited on top of plain dielectric or waveguiding substrates. In contrast to planar geometries supporting surface plasmons, their characteristic optical properties are strongly determined by the excitation of localized particle plasmons. As will be shown later on in more details (e.g., see Chap. 4), these structures are characterized by their ability to independently tune the supported electronic and optical resonances by changing the nanoparticle sizes or the nanoparticle periods respectively. From a fundamental point of view, the planar metal nanoparticle based photonic crystal structures are therefore ideally suited polaritonic model systems and allow for studying of new light-matter interaction phenomena. It is further important to remark that the nanoparticle based planar photonic structures do not only make use of simple spherical or disk-like metal nanoparticles. Depending on the specific application, different more complex particle geometries can be found. For example,

non-centrosymmetric heart- or L-shaped particles have been applied in experiments concerning second-harmonic generation [92, 93]. Regular arrays of metal nanoparticles deposited on top of dielectric substrates might be very useful for surface enhanced Raman scattering applications [94]. For example, the localized particle plasmons and the related field enhancement (origin of the SERS effect) can be tuned to almost any desirable optical wavelength by varying the particle shape, size, and spacing, thus optimizing the Raman amplification. Due to a waveguide based geometry, especially resonant coupling phenomena can be utilized as an additional design parameter. Lengthening of the particle plasmon dephasing time [95], which is directly proportional to the electric-field enhancement, might result in further enhancement of the Raman signals. It is worth mentioning that also possible applications of similar metallo-dielectric photonic crystal structures in light-emitting devices have been discussed quite recently [96].

In particular, the presented short review on nanoscale metal optics shows that the attractiveness of nasnostructures supporting surface plasmons is strongly related to their possible application in subwavelength optics. However, the achievable advantages, e.g., the size reduction of plasmon based optical devices come at a prize: The lossy character of metals generally has to be taken into account when future technological applications are discussed. Due to the fact that many new ideas are directly adopted from the microwave regime (e.g., split-ring resonators to realize negative refraction [97]), where a metal behaves as an almost perfect conductor and absorption losses can be nearly neglected, larger dissipative losses have to be considered at optical frequencies. One of the important goals in the field of applied research will be the implementation of new methods to overcome these severely limiting restrictions in the optical regime.

1.2   Main objectives of the thesis

Concerning the recent developments in surface plasmon optics (e.g., realization of metallo-dielectric photonic crystals), it seems that especially arising resonant coupling phenomena have to be studied in more details. The related effects generally result in strong modifications of the optical properties and may lead to the exploration of new fundamental phenomena. For example, it is well-known that the optical response of interacting metal nanoparticles strongly differs from the single particle case [36]. Generally, the optical properties are no longer determined by the geometry of the individual metallic scatterers alone. Due to the appearance

of near- as well as far-field coupling effects, a strong dependence on the specific nanoparticle arrangement can be observed. Although such coupling phenomena have been investigated for many years (e.g., see Ref. [98]), the restricted sample fabrication possibilities made comparison with theory very complicated. Surprisingly, the first systematic experimental studies of interacting nanoparticles have emerged only very recently. Today, due to application of optimized fabrication methods, the use of electron beam lithography allows to generate metal particle arrays with precise geometric properties on top of transparent substrates in a controlled way [99]. In the course of progress in recent nanoscale photonics, especially the investigation of such periodic metal nanoparticles arrays has become very popular both from a basic as well as from an applied point of view. In addition to the regular hole and slit arrays [71], also periodically arranged two-dimensional metal nanoparticle arrays deposited on top of dielectric substrates belong to the material class of metallo-dielectric photonic crystals. Compared to more common dielectric photonic crystals, especially their possibility to support localized surface plasmons is a very important property and gives rise to many interesting optical phenomena.

The present thesis is generally devoted to the study of metallo-dielectric photonic crystals by means of linear spectroscopic methods. In extension to previous investigations, the work tries to give a more comprehensive picture of various resonant coupling phenomena. Similar to Ref. [100], we use metal nanowire gratings as an ideally suited model system. It is explicitly shown that near- as well as far-field coupling effects can induce impressive modifications of the optical response. The work includes both experimental as well as theoretical investigations of three important sample geometries. In particular, the following main objectives will be addressed:

(i) *Coupling phenomena in metallo-dielectric photonic crystals*

Depending on the particle separation, both near- as well as far-field interaction can be observed. The coupling phenomena generally result in strong modifications of the dipolar plasmon resonances. For example, it has been shown very recently that near-field coupling between closely spaced metal nanoparticles can induce shifts of the particle plasmon resonance [101] or may result in the formation of extended plasmon modes in case of particle chains [102]. Far-field interaction on the other hand dominates the optical properties of contiguous particles with a separation on a length scale comparable to the wavelength of light. Especially the appearance of diffraction phenomena in periodically arranged par-

ticle arrays has been reported [89, 103]. Additionally, also substrate-enhanced dipole-dipole coupling effects have been observed [104]. While these experimental studies were based on random silver nanoparticle arrays on top of waveguiding substrates, a very important further step was the investigation of similar effects in perfectly ordered gold nanoparticle structures. It was demonstrated by Linden *et al.* that the lineshape of the plasmon resonances of ordered arrays deposited on top of waveguiding substrates can be additionally modified due to the appearance of waveguide modes [90, 91]. In this work, we show that the optical phenomenon referred to as *selective supression of extinction* can be explained by a simple polariton model. The resonant interaction between electronic and photonic resonances induces strong coupling and results in the formation of a so-called waveguide-plasmon polariton. In addition to the nanowire period and the angle of light incidence, also the influence of the waveguide thickness is investigated. The presented results therefore allow a detailed comparison of diffractive and waveguide-induced phenomena. The observed resonant coupling phenomena essentially rely on the regular nanowire arrangement. This fact is further proven by introducing artificial disorder within the nanowire arrays.

(ii) *Interaction between localized and extended plasmon modes*

In extension to noble metal nanowire arrays on top of dielectric slab waveguides, the influence of thin metal substrates is reviewed. The experimentally realized photonic crystal structure consists of regular nanowire gratings which are deposited on top of thin metal layers. As an important parameter, especially the nanowire-film separation can be controlled by introducing an additional dielectric spacer layer. It is important to remark that the metal-film-based structures simultaneously support localized particle and extended surface plasmons in the same energy range. Due to the periodic arrangement, the nanowire array acts as a grating coupler and therefore allows the excitation of surface modes. As already discussed theoretically in a recent publication by Nordlander *et al.* [105], two important phenomena may arise. First, the nanoparticle plasmons can interact with their images dipoles in the metal film. Second, also plasmon hybridization effects due to strong interaction between the different plasmon modes have to be considered. Similar to the prior investigations of Holland *et al.* [106, 107], all recent studies are based on the interaction of single or random metal nanoscatterers placed in front of a metallic surface [108]. In contrast to these publications, our new approach of using *ordered* metal nanowire arrays offers various advantages in comparison to the single particle case. For example, the modification of the nanowire period allows for direct controlling of the surface plasmon resonances.

The spectral overlap between particle and grating induced surface plasmons can be artificially adjusted. This additional parameter simplifies the investigations and allows to separate both interaction effects. In general, shifts of the particle plasmon resonances in dependence on the spacer layer thickness as well as strong coupling phenomena are demonstrated within this work. Especially the observed modifications due to the resonant interaction of the two supported plasmon modes are discussed because of their similarity with coupling phenomena in metallo-dielectric structures. The observed effects can again be explained by polariton formation. Additionally, also the appearance of Fabry-Perot-type phenomena is investigated.

(iii) *Resonant coupling in plasmonic crystal structures*

Another nanowire based photonic crystal structure can be realized by stacking several identical metal grating layers. The linear optical response of these metallic photonic crystals, sometimes also called plasmonic crystals, is characterized by the appearance of very fundamental interaction phenomena which may lead to dramatic modifications of the plasmon resonances. In particular, the dependence of the optical response on the vertical separation between the individual metal nanowires is investigated theoretically. Two important optical regimes have to be distinguished. While near-field interaction dominates for smaller interparticle distances, also radiative coupling of the dipolar plasmon resonances has to be considered. As shown by a recent theoretical publication, resonant near-field interaction between identical metal scatterers may lead to hybridization-like effects [109]. In contrast to planar structures [101], our proposed multilayer geometry allows the detailed study of such interaction phenomena. The presented theoretical studies especially focus on the specific properties of the appearing normal modes of the coupled system. The specific symmetry as well as the lifetime of the normal modes are discussed on the base of scattering-matrix calculations. Additionally, the influence of radiative coupling is of potential interest. In case of Bragg-spaced nanowire structures, a superradiant-like behavior is found. Similar to multiple-quantum-well-based photonic crystals [110], the resonant interaction might be interpreted in terms of an increased radiative dephasing of the collective plasmon modes. Particularly with regard to possible applications of these structures, the formation of a one-dimensional photonic stopband has to be investigated. For these purposes, especially the dependence on the number of used grating layers is analyzed.

1.3 Outline

In the following chapters, the optical properties of various metallic photonic crystal structures are analyzed. The investigations include experimental studies as well as theoretical modeling of the observed resonant coupling phenomena. It is important to remark that the individual chapters are organized as independent research reports. In particular, the thesis is composed of more or less self-containing chapters, which can be read selectively.

The first three chapters are of introductory character. After a general motivation of the thesis in Chapter 1, fundamental properties of metal nanostructures are summarized in Chapter 2. The linear optical response of noble metals (gold and silver) is theoretically analyzed in dependence on the dimensionality of the considered sample geometry. In addition to the concept of surface plasmon polaritons on metal films, especially the excitation of particle plasmons in lower dimensional structures is reviewed. Individual metal particles as well as nanowires are considered within the discussion.

The physical essentials of two-dimensional photonic crystal slab structures are studied in Chapter 3. Especially the line shape of the supported eigenstates and the arising stopbands are analyzed in dependence on the specific design of the considered photonic crystal structure. The observed narrow spectral bandwidths of the photonic resonances are discussed in terms of possible filter applications. In addition to more common regular structures, also photonic crystal superlattice structures are investigated. The observed linear optical phenomena are generally analyzed both theoretically and experimentally.

A characterization of metallo-dielectric photonic crystal slabs is presented in Chapter 4 of the thesis. The appearance of grating anomalies, which critically depend on the substrate thickness, provides evidence that the optical response of these planar metallic photonic crystal structures can be strongly modified. While only Rayleigh-type anomalies are observed for thin dielectric substrates, thicker waveguiding substrates can induce strong coupling phenomena. The resulting anticrossing phenomena can be explained in terms of waveguide-plasmon polariton formation. All experimental results are well confirmed by theoretical calculations.

The optical properties of regular metal nanowire arrays placed in front of a thin metal film are reviewed in Chapter 5. It is demonstrated that extinction measurements allow for direct probing of the interaction between localized and extended plasmon modes. In addition to near-field interaction with mirror dipoles, espe-

cially the simultaneous excitation of particle and surface plasmons gives rise to interesting optical phenomena. Similar to the metallo-dielectric photonic crystal slabs, the observed anticrossing effects can be explained by polariton formation. The chapter contains clear experimental verifications of the theoretical predictions.

Plasmonic crystal structures are discussed in Chapter 6. Starting from the investigations of nanowire pair structures, the theoretical simulations give clear evidence for the appearance of near- as well as far-field coupling effects. Hybridization like phenomena lead to a large normal mode splitting in case of closely spaced nanowires. Radiative coupling between Bragg spaced nanowires on the other hand results in strongly modified plasmon dephasing times and the formation of cavity-polariton-like modes. The last part of the chapter is devoted to the investigation of so-called plasmonic Bragg structures. The formation of a large spectral stopband is analyzed.

Chapter 7 summarizes important results of the work and gives a short outlook on future projects concerning metallo-dielectric nanostructures.

Chapter 2

Optical properties of metal nanostructures

This chapter will give an extended survey on the linear optical properties of metal nanostructures, especially of the noble metals silver and gold. The precise knowledge of these properties will be fundamentally important when dealing with more complex optical phenomena in the later chapters of this work. After the dielectric function and the bulk properties of gold and silver are discussed in the first part by means of a plasma-model, lower dimensional metal systems will be covered in the second part. It will be shown that, like semiconductor nanostructures, also metal nanostructures exhibit a linear optical response which depends strongly on the dimensionality of the considered systems. Therefore, in addition to the bulk properties, the concept of surface plasmon polaritons on metal surfaces and on thin films will be presented, followed by a detailed discussion of particle plasmon excitations in single dot and single wire systems.

2.1 General properties of bulk metals

Noble metals like silver and gold are characterized by a high electrical and thermal conductivity as well as a high reflectivity in the visible part of the electromagnetic spectrum. As we will see in greater details for the case of optical reflectivity within this chapter, all of these distinct properties can be directly related to the electron configuration and the special band structure of metals (see, e.g., Ref. [111]). The linear optical response of metals can be described in general by a material and frequency dependent dielectric function $\varepsilon(\omega)$ which can be decomposed into real
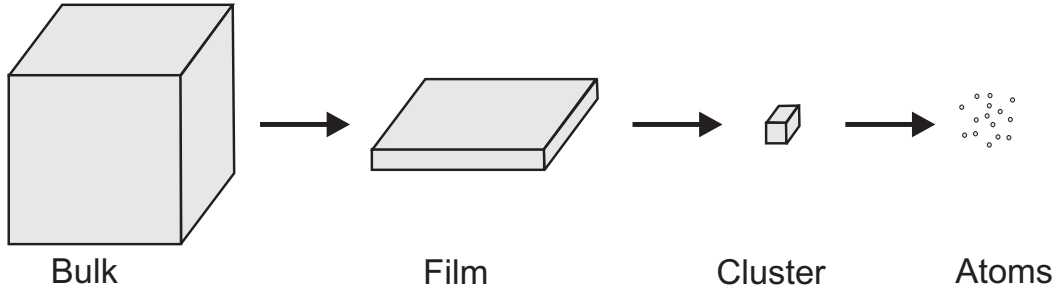
Figure 2.1: From bulk to single atoms: The optical properties of metals depend strongly on the dimensionality of the considered structure.

and imaginary parts by

$$\varepsilon(\omega) = \varepsilon_1(\omega) + i\varepsilon_2(\omega). \tag{2.1}$$

Assuming that an external electromagnetic field is acting on a homogeneous, isotropic, and nonmagnetic metal, then the linear relationship between the material polarization $\vec{P}$ and the electric field strength $\vec{E}$ is given by the equation

$$\vec{P} = \varepsilon_0 \chi^{(1)} \vec{E} \quad \text{with} \quad \chi^{(1)} = (\varepsilon - 1). \tag{2.2}$$

The quantities ε_0 and $\chi^{(1)}$ are called the permittivity of vacuum and the linear susceptibility, respectively. In principle, this equation can be considered as an expansion of $\vec{P}(\vec{E})$ in a power series in $\vec{E}$. Here however, the power series can be truncated after the linear term, because all presented discussions will be limited to linear optical effects only. It is important to note that the dielectric functions vary as a function of particle size. If we reduce an infinite bulk system stepwise to the limit of small metal clusters of only few atoms (see Fig. 2.1), $\varepsilon(\omega)$ becomes size dependent. Therefore intrinsic size effects have to be considered for metal nanoclusters with a radius below a critical value of ~ 10 nm. All of the nanostructures presented in this work exceed this small-cluster limit. Therefore, only the dielectric functions of the bulk metals will be of further interest and considered in the following discussions.

In Fig. 2.2, the experimentally measured dielectric functions obtained by Johnson et al. are depicted in dependence on the photon energy for the noble metals silver and gold [112]. In this figure, real and imaginary parts of $\varepsilon(\omega)$ are plotted separately. One of the remarkable optical properties of metals is the negative ε_1, which is caused by their unique electron configuration. Noble metal atoms like silver and gold have completely filled $4d$ and $5d$ shells and just one single electron
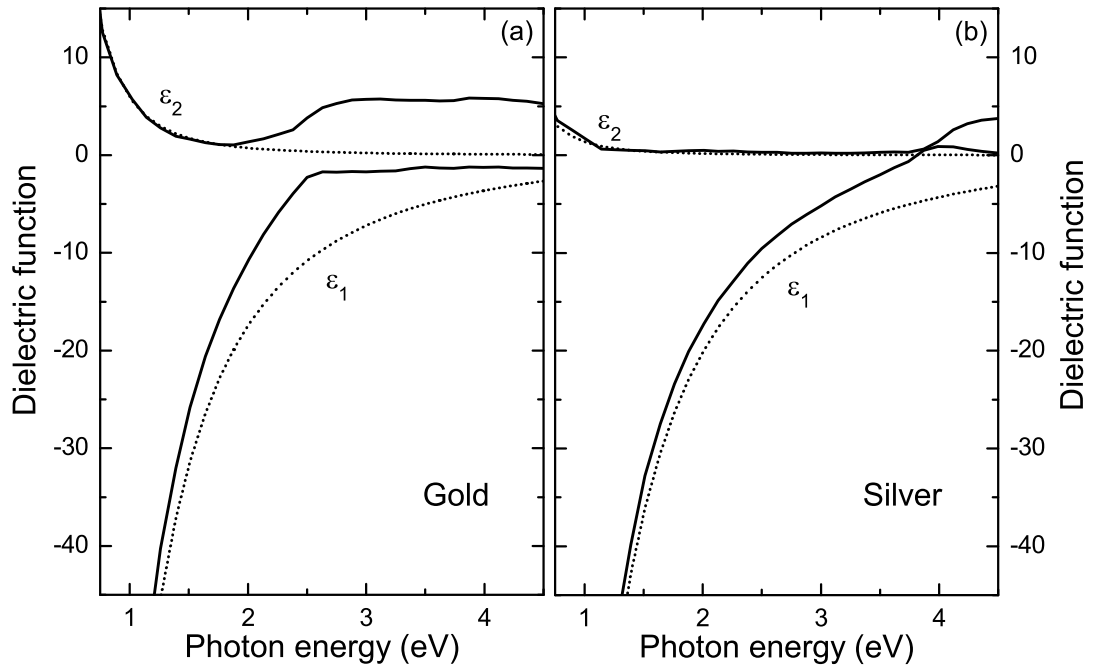
Figure 2.2: Dielectric function of gold (a) and silver (b) as a function of photon energy. Experimentally measured values [112] (solid lines) and theoretical fits (dotted lines), using the Drude-Sommerfeld model, are shown.

in the $5s$ and $6s$ shells, respectively. Unambiguously, the metallic properties of the bulk crystal can be related to these s electrons which fill the conduction band up to the Fermi energy. Gold, for example, possesses a partly filled conduction band (hybridized $6sp$ band) with a Fermi energy of approximately $E_F = 5.5$ eV. Due to the metallic binding between the atoms that form the bulk structure and the resulting free electron density of $n_f \approx 5.85 \cdot 10^{22} \mathrm{cm}^{-3}$ for noble metals, the Fermi energy can be approximated by the formula [111]

$$E_F = \frac{\hbar^2}{2m_e} \cdot k_F^2 \quad \text{with} \quad k_F = (3\pi^2 n_f)^{\frac{1}{3}}. \qquad (2.3)$$

Within the hybridized sp conduction bands, the gold electrons of mass m_e can move quasi-freely due to the nearly parabolic dispersion of the bands. Especially for the infrared and visible part of the electromagnetic spectrum, the dielectric functions of silver and gold are governed by these quasi-free conduction electrons. For higher energies, possible interband transitions between the lower lying d bands and the conduction band have to be considered additionally. The influences of interband transitions have to be included for any analysis at energies above ≈ 3.87 eV for silver and ≈ 2.38 eV for gold, respectively. Exemplary, a schematic drawing of the band diagram and the possible electron-hole pair ex-

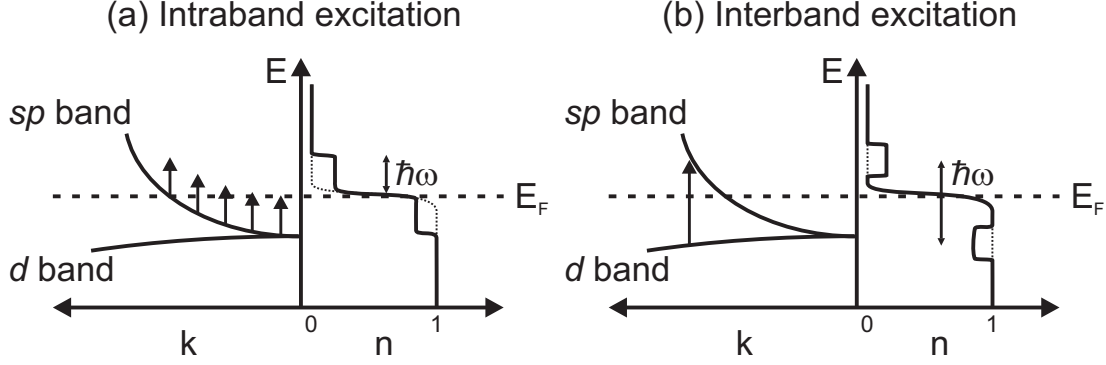## (a) Intraband excitation   (b) Interband excitation

Figure 2.3:   Schematic drawing of the dispersion of the d and sp bands for gold. Electron-hole pair excitations within the conduction band (intraband excitation) or between the d band and the conduction band (interband excitation) are possible. The corresponding non-thermalized electron distributions are depicted in both panels, respectively.

citations are shown in Fig. 2.3. Both intraband (a) as well as interband (b) excitations have to be considered.

The dielectric function is directly linked to the complex index of refraction by

$$\tilde{n}(\omega) = n(\omega) + i\kappa(\omega) = \sqrt{\varepsilon(\omega)}, \tag{2.4}$$

whose real and imaginary parts n and κ obey the two relations

$$n^2 = \frac{1}{2}\left(\sqrt{(\varepsilon_1^2 + \varepsilon_2^2)} + \varepsilon_1\right) \quad \text{and} \quad \kappa^2 = \frac{1}{2}\left(\sqrt{(\varepsilon_1^2 + \varepsilon_2^2)} - \varepsilon_1\right). \tag{2.5}$$

Regarding Snells law of refraction [113], the refractive index $n(\omega)$ describes the oscillatory spatial propagation of light in matter. The wavelength λ of a propagating electromagnetic wave in a medium is directly connected with the wavelength λ_v in vacuum by the relation $\lambda = \lambda_v n^{-1}(\omega)$. The imaginary part $\kappa(\omega)$ on the other hand specifies the damping of an electromagnetic wave in the direction of propagation. By using the Fresnel formulas for example, the precise knowledge of the material and frequency dependent dielectric function allows to calculate the reflectivity R of a planar metal surface. For a plane wave impinging at normal incidence, the reflectivity of the light intensity from an unstructured surface follows the relation

$$R(\omega) = \frac{(n(\omega) - 1)^2 + \kappa^2(\omega)}{(n(\omega) + 1)^2 + \kappa^2(\omega)}. \tag{2.6}$$

Exemplarily, calculations of the reflectivity using the measured dielectric functions obtained by Johnson et al. [112] are presented in Fig. 2.4 (b) for the two

noble metals silver and gold. As will be discussed in more details later on, the depicted reflectivity values show clear evidence for strong interband transitions.

Also the small skin depth δ of metals can be simply explained by their dielectric functions. If a parallel light beam of a certain intensity is propagating normal to a metal surface, part of the impinging intensity I_0 is absorbed by the metal. Due to the energy dissipation, the electromagnetic wave has only a certain penetration depth δ which can be estimated from the absorption index κ. Considering Beer's law of absorption, the damping of the beam inside the metal is described by the formula

$$I(z) = I_0 \mathrm{e}^{-\alpha z} \quad \text{with} \quad I_0 \propto \vec{E}^2. \tag{2.7}$$

The absorption coefficient $\alpha(\omega)$ is directly related to κ and can be calculated by

$$\alpha(\omega) = \frac{2}{\delta} = \frac{2\omega}{c_0}\kappa(\omega). \tag{2.8}$$

Metals are generally characterized by large values of κ in the optical regime. Calculations show that electromagnetic waves are strongly damped within the first few nanometers inside the metal structures. At a photon energy of 2 eV, typical values for the calculated skin depths are approximately $\delta_{Ag} = 24$ nm for silver and $\delta_{Au} = 31$ nm for gold [36].

2.1.1 Dielectric function of a free electron gas

The optical properties of nearly-free-electron metals can be successfully described by introducing a simple electron plasma concept. Such metals are characterized by an optical response which is mainly dominated by the quasi-free conduction electrons alone. Examples of such materials are the alkali metals and to some extent, as already mentioned earlier, also the noble metals silver and gold. Especially at optical wavelengths, the electromagnetic properties of silver and gold closely resemble those of an electron gas. Neglecting any influences due to interband transitions, the dielectric function $\varepsilon_{(f)}$ of a free-electron metal can be obtained with the Drude-Sommerfeld susceptibility χ_{DS} [36] by means of

$$\varepsilon_{(f)}(\omega) = 1 + \chi_{DS}(\omega). \tag{2.9}$$

In this simple model, the response of a free electron of mass m_e and charge e to an external electric field $\vec{E}$ is described by the equation of drift motion superimposed on the motion of the electrons in the field-free case by the equation

$$m_e\frac{\partial^2 \vec{r}}{\partial t^2} + m_e\Gamma_0\frac{\partial \vec{r}}{\partial t} = e\vec{E} \quad \text{with} \quad \vec{E} = \vec{E}_0\mathrm{e}^{-i\omega t}. \tag{2.10}$$

The phenomenological relaxation or damping constant Γ_0 describes the damping of the electron motion due to scattering events and is inversely related to the electron mean free path. Note that in contrast to ionic crystals (considering bound electrons), Eq. 2.10 does not include linear terms taking care of any restoring forces. This assumption corresponds to an eigenfrequency of $\omega_0 = 0$ for the free electron motion [114]. Using the material polarization

$$\vec{P} = en_f\vec{r} = \varepsilon_0\chi_{DS}\vec{E}, \tag{2.11}$$

the Drude-Sommerfeld susceptibility follows the relation

$$\chi_{DS}(\omega) = -\frac{\omega_p^2}{\omega^2 + \Gamma_0^2} + i\frac{\omega_p^2\Gamma_0}{\omega(\omega^2 + \Gamma_0^2)} \quad \text{with} \quad \omega_p = \sqrt{\frac{n_fe^2}{\varepsilon_0m_e}}. \tag{2.12}$$

The important parameter ω_p is generally called plasma frequency and is directly related to a longitudinal collective excitation of the electron gas in the bulk metal. If the influence of damping is neglected (e.g., $\Gamma_0 \ll 1$), ω_p is the eigenfrequency of the ideal volume plasmon obtained from the condition that ε_1 equals zero [111]. The density fluctuations around the normal bulk density n_0 of the nearly-free electron plasma with frequency ω_v may be considered to have the form

$$n(\vec{r}, t) \sim n_0\mathrm{e}^{i(\vec{k}\vec{r}-\omega_v t)}. \tag{2.13}$$

Due to the restriction to the free-electron-model and therefore missing shear forces, no transversal plasma modes are possible.

The Drude-Sommerfeld model has been used to calculate the real and imaginary parts of $\varepsilon(\omega)$ for gold and silver. A comparison between experimentally measured and theoretically predicted values is given in Fig. 2.2. Acceptable fits to the measured values are obtained by using the free parameters $\hbar\omega_p = 8.6$ eV and $\hbar\Gamma_0 = 0.08$ eV for gold. For silver, the parameters have been adjusted to $\hbar\omega_p = 9.2$ eV and $\hbar\Gamma_0 = 0.016$ eV, respectively. Qualitatively, the Drude-Sommerfeld model seems to work quite well for both metals, although, especially for gold, some significant deviations are clearly observable. These deviations are caused by the interband transitions which have been neglected in this simple approach for obtaining the dielectric function of the metal. The influence of these interband transitions will be shortly discussed in the following section.

2.1.2   Influence of interband transitions

Silver can be almost treated as a free-electron-metal at optical frequencies. This assumption does not apply to gold in the same way due to the lower threshold
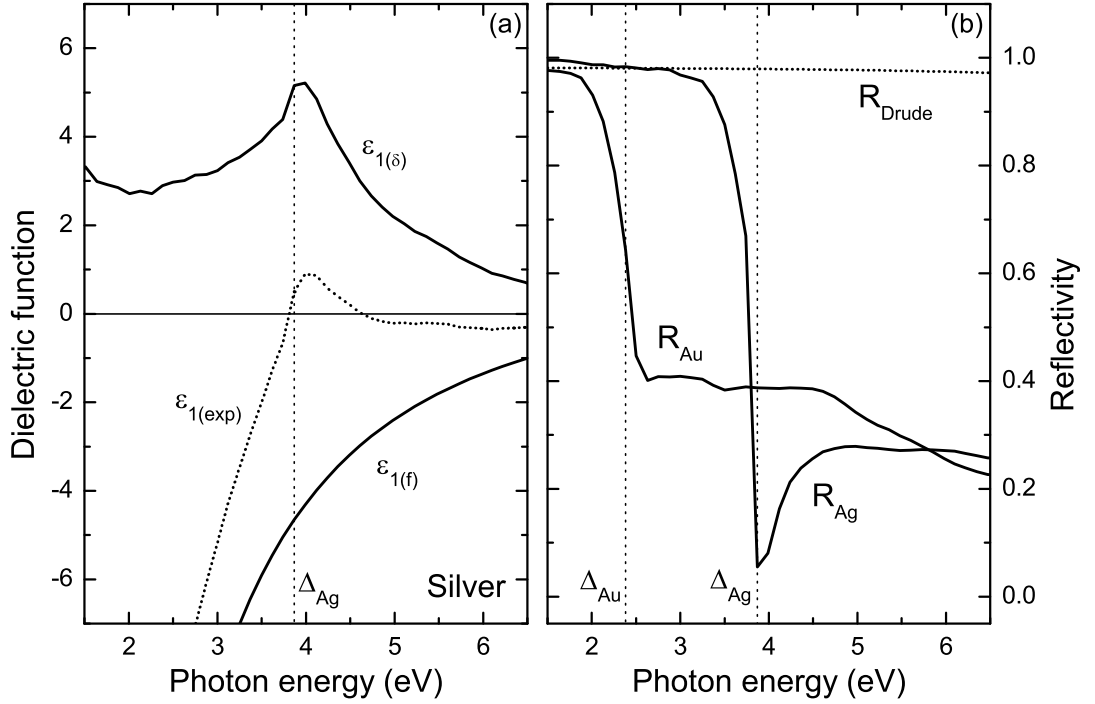
Figure 2.4:   The decomposition of the experimental values of $\varepsilon_{1(\text{exp})}$ for Ag into free $\varepsilon_{1(\text{f})}$ and interband contributions $\varepsilon_{1(\delta)}$ is depicted in panel (a). Panel (b) displays the calculated reflectivity values for an air-metal interface (R_{Au}, R_{Ag}, and R_{Drude}) at normal incidence using the experimentally obtained complex dielectric functions and the Drude model. The threshold energies of the interband transitions are indicated by Δ_{Au} and Δ_{Ag}.

energy Δ_{Au}, describing the onset of interband transitions. In Fig. 2.2 for example, the complex part of the dielectric function of gold deviates from the Drude values, starting at energies slightly above approximately 2 eV. Therefore, in extension to the treatment of just quasi-free conduction electrons, the complex dielectric function $\varepsilon(\omega)$ incorporating all other electrons in deeper levels is given by

$$\epsilon(\omega) = \varepsilon_{(f)}(\omega) + \chi_{IB}(\omega) = 1 + \chi_{DS}(\omega) + \chi_{IB}(\omega). \qquad (2.14)$$

The influence of the interband transitions is introduced as an additive contribution $\chi_{IB}(\omega)$ to the Drude-Sommerfeld susceptibility $\chi_{DS}(\omega)$ within this approach. Therefore, taking care of all electronic transitions, the linear optical response is traced back to the band structure model of the solid state [36, 115].

Referring to Fig. 2.4, some important consequences due to the appearance of interband transitions for gold and silver will be shortly discussed in the following. Panel (a) displays the decomposition of the measured dielectric function $\varepsilon_{1(\text{exp})}$

for silver into free $\varepsilon_{1(f)}$ and bound $\varepsilon_{1(\delta)}$ electron contributions. In this simple approach, the bound contributions $\varepsilon_{1(\delta)}$ are obtained by subtraction of the calculated free electron contributions from the experimentally obtained values. The vertical dotted line at approximately 3.87 eV indicates the interband transition threshold Δ_{Ag} of silver. The onset of interband transitions is generally associated with transitions from a lower lying filled band to the Fermi level or from the excitation of electrons at the Fermi energy to the lowest empty conduction band. In the case of silver, this threshold energy corresponds to the energy difference between the Fermi energy and the highest d band. As can be seen in Fig. 2.4(a), the large redshift of the bulk plasmon energy $\hbar\omega_p$ from the free-electron value of 9.2 eV to 3.81 eV (at the position where $\varepsilon_{1(\exp)}(\omega)$ equals zero) is a clear consequence of the interband transitions [36, 116]. A similar shift in energy holds for gold, where $\hbar\omega_p$ is decreased to approximately 6 eV [117]. Panel (b) of Fig. 2.4 on the other hand displays the calculated reflectivity values (R_{Au} and R_{Ag}) for an air-metal interface at normal incidence (see Eq. 2.6) using the experimentally obtained complex dielectric functions of gold and silver. Additionally, also the results of calculations based on the Drude-Sommerfeld model for gold (R_{Drude}) are presented. The threshold energies of the interband transitions are again indicated by Δ_{Au} and Δ_{Ag}. Due to the strong interband transitions for energies above the threshold, gold as well as silver show a rapid decrease of their reflection values. If we compare the calculated reflectance data R_{Au} and R_{Drude} for gold directly, this important observation can not be explained within the simple Drude-Sommerfeld model. As depicted in Fig. 2.4 (b), the free-electron-model wrongly predicts a high and nearly constant reflectivity R_{Drude} for the whole spectral range shown in this figure.

2.2   Surface plasmon polaritons

Collective excitations in metals give rise to various phenomena observable in different physical situations. Bulk metals, metal surfaces, and especially metal slabs for example can support an interesting variety of collective electron density oscillations [12, 118, 119]. As already discussed, one possible effect is the excitation of the longitudinal bulk or volume plasmon. The situation gets more complex when an interface (e.g., metal-air interface) is introduced. Now bound surface modes can exist for energies below the bulk plasma energy due to the broken symmetry of the system.
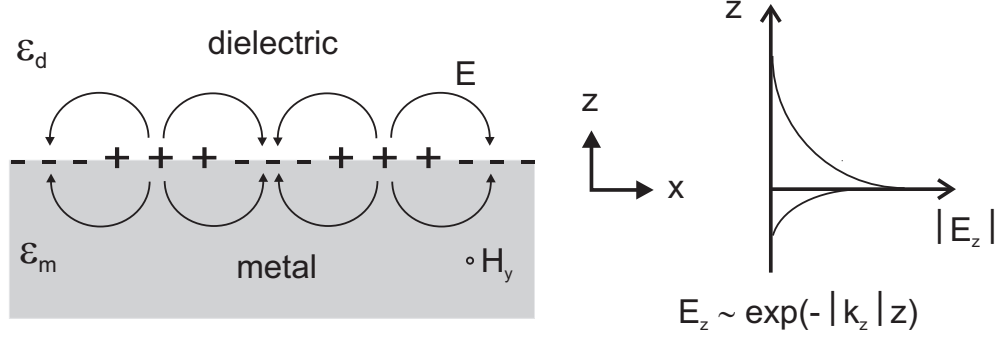
Figure 2.5: Schematic view of surface plasmon polaritons bound to the interface between a metal and a dielectric half space. Charge and electromagnetic field distributions (E, H_y) are shown. The right panel displays the exponential decay of the field E_z on both sides of the interface.

2.2.1   Surface plasmon polaritons supported at a single interface

Since the first early works on surface plasmon polaritons (SPP) (e.g., see Refs. [14, 15]), it is a well established fact that an electron gas can support electron density oscillations at its surface. In contrast to propagating solutions, these oscillations can be interpreted as bound or evanescent solutions of Maxwell's equations. A schematic view of such an oscillation is shown in the left part of Fig. 2.5. The periodic displacement of the electrons at the metal surface leads to a charge density modulation and therefore electromagnetic fields with components parallel and perpendicular to the boundary. Such oscillations (fields and charges) can be considered as being nonradiative surface waves at the metal interface. The wave is bound to the surface due to the evanescent character of the fields. As schematically shown in the right part of Fig. 2.5, the field distribution along the surface can be described by the expression

$$E = E_0^{\pm} \mathrm{e}^{i(k_x x \pm k_z z - \omega t)} \tag{2.15}$$

with + for $z \geq 0$ and - for $z \leq 0$. Here, the evanescent decay of the fields in the z direction is caused by an imaginary wave vector k_z. The eigenfrequency ω of these surface plasmon polaritons is directly connected with a complex wave vector $k_x = k_x' + ik_x''$ in x direction. Theoretical calculations starting from Maxwell's equations with the assumption $\varepsilon_m'' \ll |\varepsilon_m'|$ predict that the dispersion relation of the p-polarized surface plasmon polariton is then given by the equations [12]

$$k_x' = \frac{\omega}{c_0} \left(\frac{\varepsilon_m' \varepsilon_d}{\varepsilon_m' + \varepsilon_d} \right)^{1/2} \quad \text{and} \tag{2.16}$$
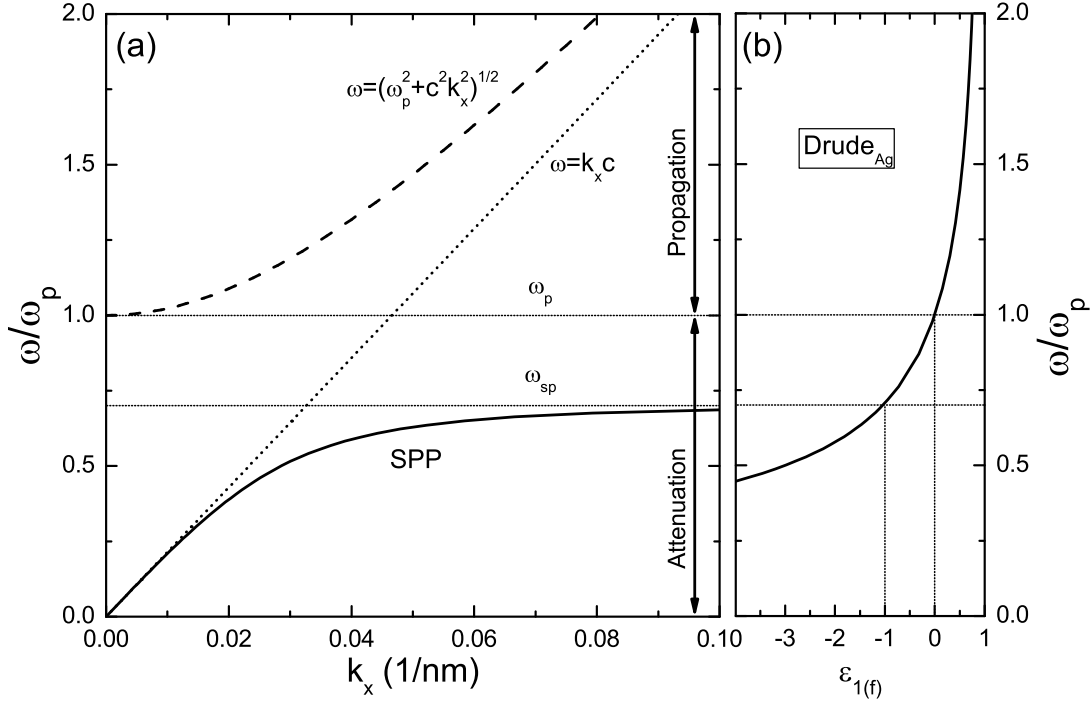
Figure 2.6:   Panel (a) displays the dispersion relation of a nonradiative surface plasmon polariton at a silver-air interface calculated with the Drude-Sommerfeld model. The dotted line represents the air light cone (dispersion of light in air, $\omega = ck_x$). The dispersion of light in a free electron metal can be described by the relation $\omega = \sqrt{\omega_p^2 + c^2 k_x^2}$ and is plotted left to the light cone (dashed line). The arrows mark the regions of attenuation and propagation. Additionally, the real part of the dielectric function of silver, calculated with the Drude-Sommerfeld model, is shown in panel (b).

$$k_x'' = \frac{\omega}{c_0} \left(\frac{\varepsilon_m' \varepsilon_d}{\varepsilon_m' + \varepsilon_d} \right)^{3/2} \frac{\varepsilon_m''}{2(\varepsilon_m')^2} \ . \tag{2.17}$$

Therefore, assuming a semi-infinite metal half space, the complex wave vector k_x can be simply obtained only with the knowledge of the complex dielectric function $\varepsilon_m = \varepsilon_m' + i\varepsilon_m''$ of the metal and the dielectric function ε_d of the adjacent dielectric material. Note that ε_d is assumed to be real within this approach, neglecting any absorption effects in the dielectric material. To get more insight into the exact derivation of Eq. 2.16 and Eq. 2.17, the interested reader will find an extended analysis in Ref. [12].

Exemplarily, the calculated surface plasmon polariton dispersion at the interface between air and silver half spaces is depicted in panel (a) of Fig. 2.6. The dielectric

function obtained with the Drude-Sommerfeld model (see, e.g., panel (b)) has been used for these calculations assuming a nearly-free-electron metal. Like in Sec. 2.1.1, the free parameters $\hbar\omega_p = 9.2$ eV and $\hbar\Gamma_0 = 0.016$ eV have been retained unchanged. The plotted dispersion relation reflects the nonradiative character of the surface plasmon polaritons. The surface plasmons can not couple to light because the wave vector k_x always remains larger than $\sqrt{2}\omega/c$. The dispersion is therefore located below the light line which is only approached for small values of k_x. For larger k_x values and in case of a Drude like electron gas, the frequency of the surface plasmon increases monotonically to the asymptotic value

$$\omega_{sp} = \frac{\omega_p}{\sqrt{1 + \varepsilon_{\mathrm{d}}}}. \tag{2.18}$$

For example, as can be seen in Fig. 2.6(a) for the Drude-Sommerfeld model of the silver-air interface with $\varepsilon_{\mathrm{d}} = 1$, the surface plasmon frequeny approaches $\omega_p/\sqrt{2}$ for larger values of k_x. It is important to remark that the existence of a bound or nonradiative surface plasmon mode requires a negative $\varepsilon_{\mathrm{m}}'$ and a positive ε_{d} which simultaneously have to fulfill the additional relation $|\varepsilon_{\mathrm{m}}'| > \varepsilon_{\mathrm{d}}$.

Generally, Fig. 2.6(a) can be separated into two spectral regions. A free-electron metal supports propagating modes for frequencies above the plasma frequency ω_p. Only for positive values of $\varepsilon_{1(\mathrm{f})}'$ and therefore real wave vectors, light can propagate as transverse electromagnetic wave in the electron gas, following the dispersion relation [111]

$$\omega^2 = \omega_p^2 + c^2 k_x^2. \tag{2.19}$$

The wave vector is purely imaginary for frequencies below ω_p and the wave is therefore damped rapidly inside the metal. As already addressed in Sec. 2.1 of this work, this conclusion clearly explains the small skin depth δ of silver and gold at optical wavelengths.

In comparison to the situation of Fig. 2.6 when assuming a free-electron metal, the dispersion has to be modified in the case of a real metal including interband transitions. Fig. 2.7 for example shows two dispersion relations of nonradiative surface plasmon polaritons at a silver-air interface calculated with different assumptions. The theoretical surface plasmon polariton dispersion relation of silver (Drude-Sommerfeld model) is compared with a calculated dispersion relation (SPP$_{(\mathrm{exp})}$) based on the measured dielectric function of silver [112]. Additionally, the real parts $\varepsilon_{1(\mathrm{f})}$ and $\varepsilon_{1(\mathrm{exp})}$ are depicted in panel (b) of this figure. The surface
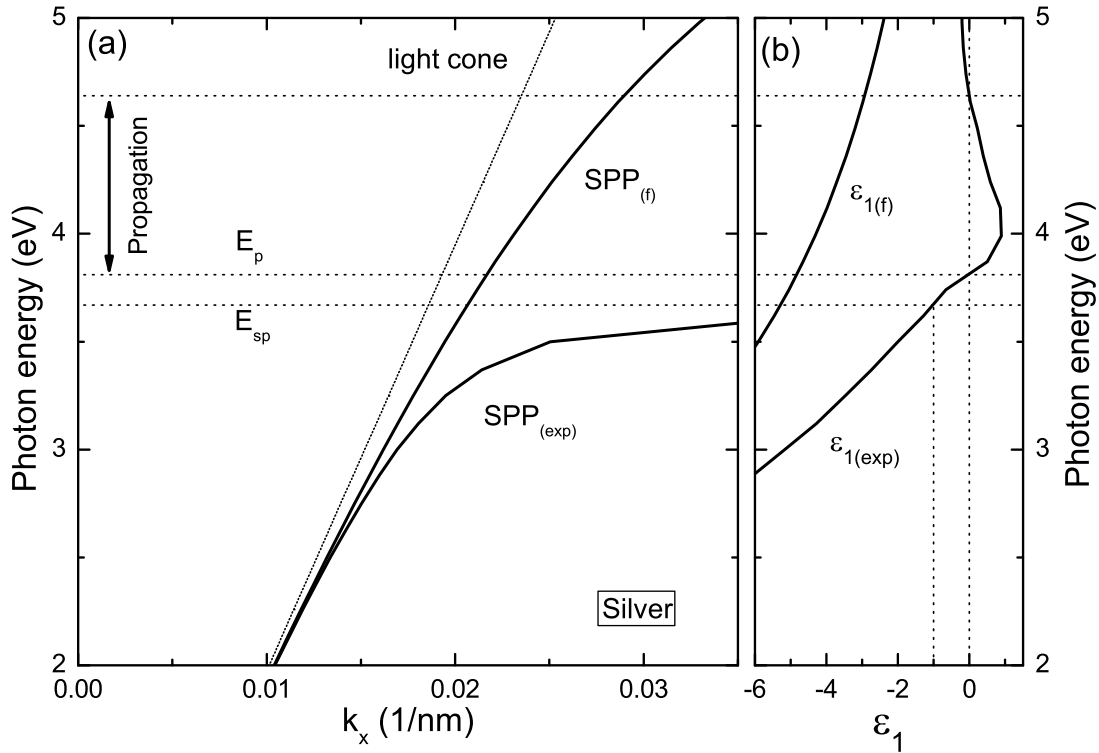
Figure 2.7:   Panel (a) shows calculated dispersion relations of nonradiative surface plasmon polaritons on a silver-air interface. The dispersion curve calculated with the Drude-Sommerfeld model (SPP$_{(f)}$) is compared with theoretical results (SPP$_{(exp)}$) based on the measured dielectric function [112]. Panel (b) displays the corresponding real parts of the dielectric functions. Thin silver films exhibit a small window of transmission in the region marked by the single vertical arrow.

plasmon polariton dispersion of the real metal is clearly modified due to the onset of interband transitions. The drastic reduction of the plasma energy $E_p = \hbar\omega_p$ to 3.81 eV is accompanied by a simultaneous redshift of the asymptotic surface plasmon polariton energy $E_{sp} = \hbar\omega_{sp}$ to approximately 3.67 eV. In the case of real silver, also the energy difference between E_p and E_{sp} appears to be much smaller than in the simple Drude-Sommerfeld model. Additionally, the region of propagating transverse electromagnetic waves is now reduced to a restricted energy interval where the real part of the dielectric function ε_1 is positive (marked by the vertical arrow in this figure).

Up to now, the complex character of the wave vector k_x has been completely neglected during all considerations. The propagation length of surface plasmon polaritons at a metal surface and therefore their lifetime depends on the imag-
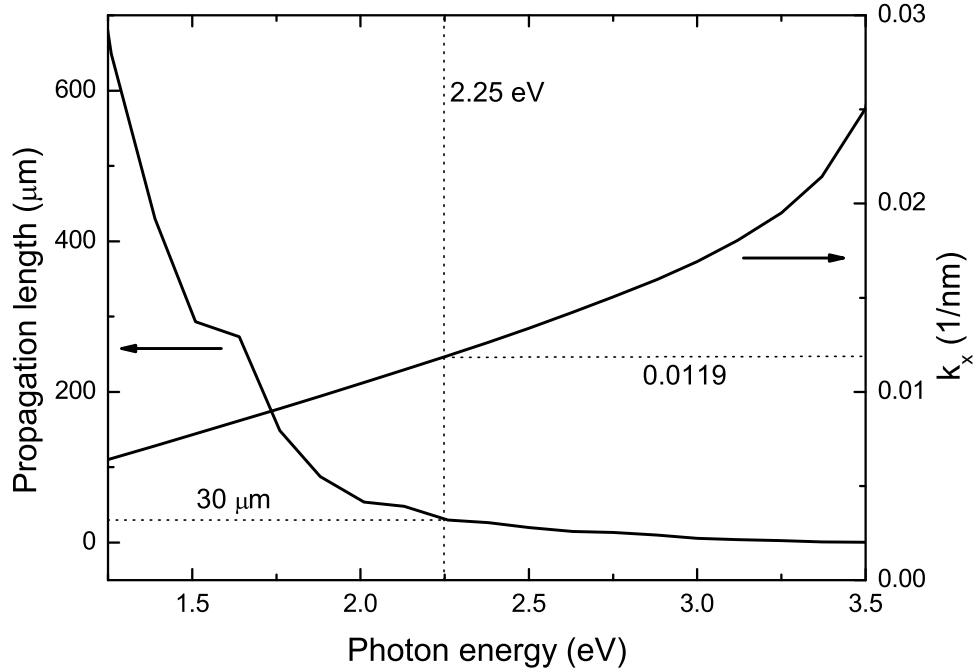
Figure 2.8: Calculated surface plasmon polariton propagation length at a silver-air interface in dependence on the photon energy. The real part of the wave vector k_x is plotted for comparison.

inary part k_x'' of the wave vector. The intensity of the surface mode is damped exponentially according to $e^{-x/L_{sp}}$. Then the length L_{sp} after which the intensity decreases to $1/e$ is given by the equation

$$L_{sp} = \frac{1}{2k_x''}. \tag{2.20}$$

The surface plasmon polariton propagation length and the real part of the wave vector are displayed in Fig. 2.8 in dependence on the photon energy. These calculations are based on the measured dielectric function of silver [112]. The propagation length of the nonradiative surface mode on a silver-air interface increases for decreasing photon energies. At a photon energy of 2.25 eV ($\lambda = 528$ nm) for example, the propagation length reaches approximately 30 μm. The propagation length will be a very crucial factor for further technical applications of surface plasmons in the active field of nanooptics. As will be discussed in the next section, especially surface modes on thin metal films offer great potential. The propagation length can be highly enhanced by the use of a thin film configuration, giving rise to a long-range surface mode.
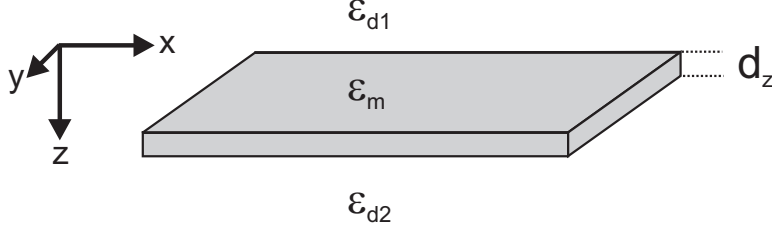
Figure 2.9:   Schematic view of a thin metal slab between two dielectric half spaces. The situations $\varepsilon_{d1} = \varepsilon_{d2}$ and $\varepsilon_{d1} \neq \varepsilon_{d2}$ have to be considered.

2.2.2   Surface plasmon polaritons supported by thin metal films

In addition to the well-known dielectric slab waveguides [120], also thin metal films of a certain thickness bounded by dielectrics above and below can act as waveguiding slab structures [18]. Surface plasmon modes can propagate on both sides of the metal core, leading to a thickness-dependent dispersion relation. It has been shown that the properties of surface plasmon modes can be dramatically changed as the thickness of the slab decreases. A schematic view of such a thin metal slab with a complex ε_m between two dielectric half spaces is shown in Fig. 2.9. When such a film is thin enough, the surface plasmon polariton modes guided by the two interfaces become coupled due to overlap of their fields inside the metal. As will be shown in the following, the field tunnelling through the metal leads to the creation of normal modes that exhibit dispersion with metal thickness.

Again, starting from Maxwell's equations and taking into account all boundary conditions, the following dispersion relation [119, 121]

$$\tanh(S_2 d_z) = -\frac{S_2 \varepsilon_m (\varepsilon_{d1} S_3 + \varepsilon_{d2} S_1)}{\varepsilon_{d1} \varepsilon_{d2} S_2^2 + \varepsilon_m^2 S_1 S_3} \tag{2.21}$$

has to be satisfied for a solution to exist. Within this approach, the values S_1, S_2, and S_3 are defined by the relations

$$S_1^2 = k_x^2 - \varepsilon_{d1} k_0^2, \quad S_2^2 = k_x^2 - \varepsilon_m k_0^2, \quad S_3^2 = k_x^2 - \varepsilon_{d2} k_0^2. \tag{2.22}$$

Note that the wave vector k_x is again assumed to be complex. In principle, the situations $\varepsilon_{d1} = \varepsilon_{d2}$ and $\varepsilon_{d1} \neq \varepsilon_{d2}$ have to be considered separately. Although interesting phenomena may appear in an asymmetric geometry as well (bound, leaky, and growing surface modes), the presented discussions will be limited to the nonradiative modes of the symmetric geometry ($\varepsilon_{d1} = \varepsilon_{d2}$).
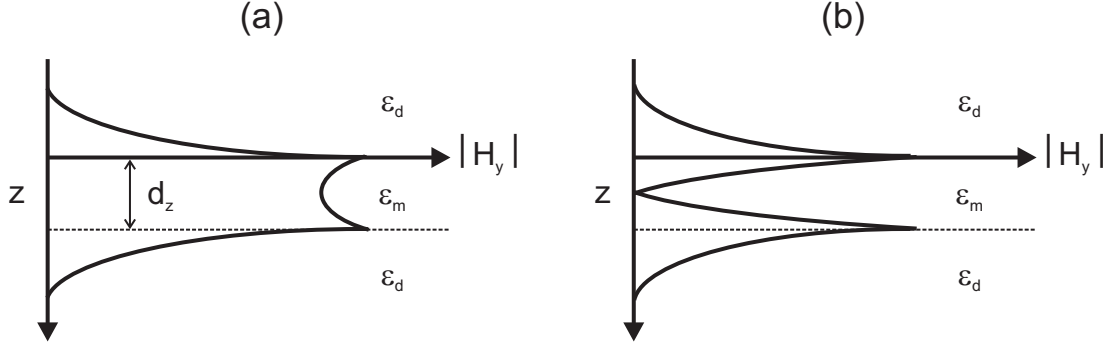
Figure 2.10: Field distribution of $|H_y|$ associated with the bound modes guided by a thin metal slab. The symmetric (a) and antisymmetric (b) normal modes are shown schematically.

When a metal film is covered on both sides by the same dielectric material, then Eq. 2.21 can be further simplified. Now the single transcendental equation splits into two equations

$$\tanh\left(\frac{S_2 d_z}{2}\right) = -\frac{\varepsilon_{d1} S_2}{\varepsilon_m S_1} \quad \text{and} \quad \tanh\left(\frac{S_2 d_z}{2}\right) = -\frac{\varepsilon_m S_1}{\varepsilon_{d1} S_2}, \qquad (2.23)$$

which describe separate branches of the surface plasmon dispersion relation. In the limit of an infinitely thick metal layer ($\tanh(S_2 d_z) \rightarrow 1$), the solutions of Eq. 2.23 specify two uncoupled surface plasmon modes propagating along each surface of the thick metal film. The situation gets more complex when the thickness of the film is reduced ($d_z \rightarrow 0$). Due to strong coupling of the surface modes on both sides of the thin metal layer, a clear splitting of the dispersion branches will be observable. Now the fields of the two surface modes are no longer localized on one interface but rather spread over the entire slab structure. Due to the large overlap of their fields, the two established modes can be considered as being the normal modes of the system. The two normal modes will have either symmetric or antisymmetric profiles with respect to the field component H_y. These modes correspond to the so-called short- and long-range surface plasmon modes of a thin film configuration. A schematic view of the corresponding magnetic field profiles (absolute values of H_y) is shown in Fig. 2.10.

To demonstrate the strong influence of the metal layer thickness, the dispersion relation of the surface plasmon polaritons has been calculated numerically for various silver films sandwiched between quartz half spaces ($n = 1.46$). The results of these calculations using the measured dielectric function of silver [112] are depicted in Fig. 2.11 for films with a thickness d_z of 30 nm (1), 20 nm (2), 10 nm (3), and 5 nm (4) in dependence on the real part of the wave vector k_x.
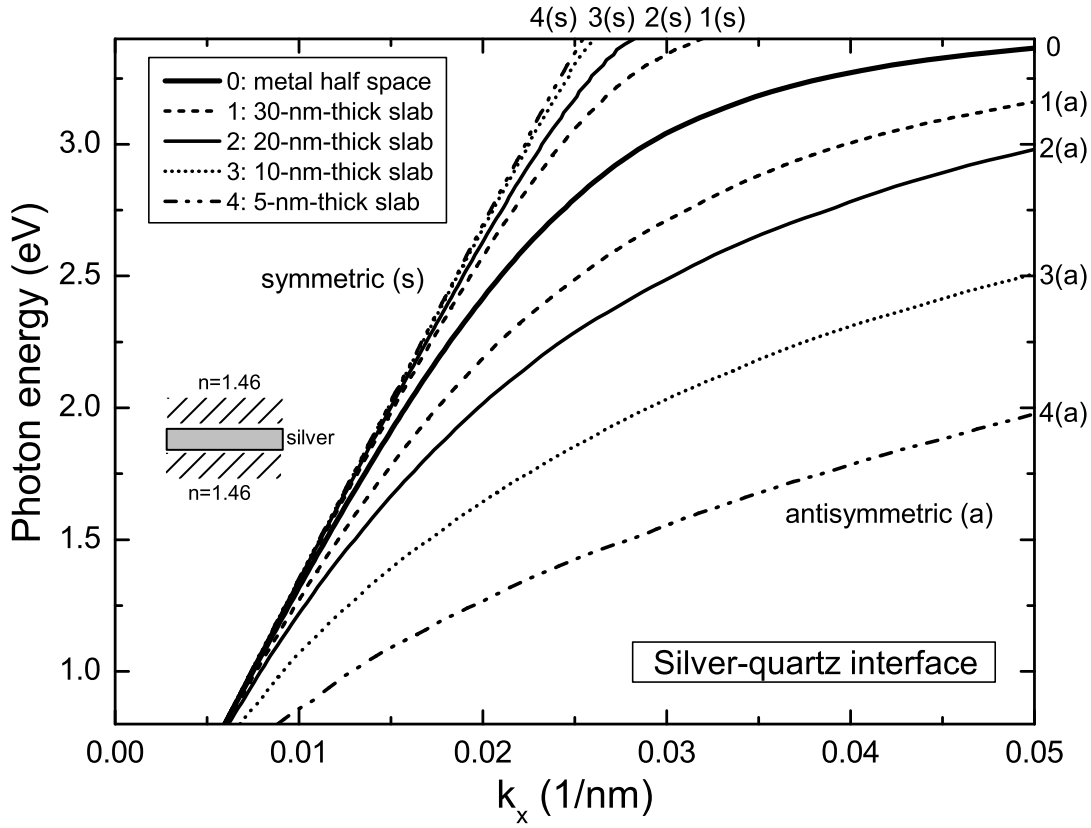
Figure 2.11:   Calculated dispersion relations of nonradiative surface plasmons. The symmetric (s) and antisymmetric modes (a) are shown for thin silver films of different thickness d_z bounded by quartz above and below ($\varepsilon_{d1} = \varepsilon_{d2}$). The dispersion relation of a single interface mode is displayed for comparison.

Additionally, the dispersion relation of a single interface mode on a silver half space (0) is displayed for comparison. The figure clearly shows that the symmetric (antisymmetric) surface plasmon dispersion is shifted to higher (lower) energies in respect to the single interface mode. As already mentioned, the splitting between the two normal modes is increased with decreasing thickness of the silver slab. For $d_z \rightarrow 0$ the dispersion relation of the symmetric or long-range surface plasmon will approach the quartz light line asymptotically. Like in the case of a metal half space (see Eq. 2.20), the imaginary part of the complex wave vector k_x (not shown) also determines the damping or propagation length of the surface plasmon polaritons supported by thin metal films. Here, especially the classification into short- and long-rang modes already describes the observations very precisely. Due to the opposite symmetries of the two plasmon modes, the achievable propagation lengths differ strongly. Considering Maxwell's equations, the short-range or antisymmetric surface plasmon exhibits a symmetric distrib-
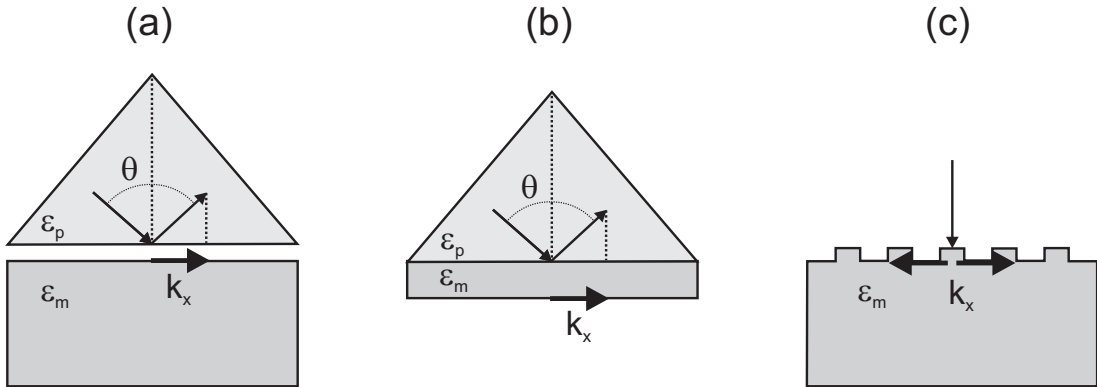
Figure 2.12:   Excitation of surface plasmon polaritons. Otto configuration (a), Kretschmann-Raether configuration (b), and grating coupler(c) are shown.

ution of the electric field components. This fact leads to relatively large electric fields inside the metals slab and therefore to a strong damping of the mode. This is in contrast to the long-range or symmetric surface plasmon where the damping is strongly reduced due to the antisymmetric distribution of the electric field components and therefore only weak electric fields inside the metal slab.

In case of a single silver-quartz interface and a photon energy of 1.5 eV, a surface plasmon propagation length of about 90μm has been calculated numerically using Eq. 2.20. This value can be changed dramatically when assuming a 30-nm-thick silver slab covered with quartz on both interfaces instead. The propagation length for photon energies of 1.5 eV will be reduced to 20 μm for the short-range mode and enhanced to approximately 660 μm for the long-range mode. Therefore, particularly with regard to further applications, especially the use of the symmetric long-range mode seems to offer great potential.

Up to now only the influence of the finite width of the metal slab along the z direction was discussed. An interesting situation may arise when also the slab extension along the y direction is additionally assumed to be finite. Depending on the cross-section, bound modes will exist as solutions of Maxwell's equations on the surface of such nanowires [122–125].

2.2.3   Excitation of surface plasmon polaritons

Surface plasmon polaritons can be excited by fast electrons [11] and by electromagnetic radiation. Although experiments using fast electrons to excite surface plasmons have been performed extensively, we will restrict ourself to the discus-

sion of the optical excitation processes in the following. Generally, the generation of a surface plasmon polariton at a metal-dielectric interface requires matching of the parallel wave vector component of the incident radiation field to that of the surface polariton. Due to the fact that the momentum of a surface plasmon mode on a flat metal surface is greater than that of a free-space photon of the same energy, the wave vector matching condition cannot be fulfilled directly. Mainly three well-known methods can be applied to overcome this technical problem. Two methods are based on attenuated total reflection (ATR), while the third uses a periodic modulation of the metal-dielectric interface. A schematic view of the possible techniques can be found in Fig. 2.12.

The Otto configuration [126] is displayed in Fig. 2.12(a). This method makes use of a dielectric prism (ε_{p}) which is separated from a metal half space by a narrow air slit. When incoming light is reflected at the boundary of the prism, the evanescent fields will couple to the surface plasmons at the metal interface. Thus, the efficiency of the surface plasmon excitation depends crucially on the slit width.

In contrast to the Otto configuration, the well known Kretschmann-Raether configuration [127] can only be applied for the excitation of surface plasmons on thin metal films. The thin metal layer is directly attached to the prism, as Fig. 2.12(b) shows. Incoming light is totally reflected and the evanescent fields can couple with the surface plasmon at the second boundary of the metal film. We have to remark that this configuration resembles the asymmetric metal slab situation (thin metal film bounded by two different dielectric materials). In contrast to the symmetric geometry, the nonradiative surface mode exhibits a certain cutoff energy in the antisymmetric case. Therefore, the mode becomes radiative or leaky below the cutoff frequency and an external excitation by light will be possible within this energy range.

Another important method to excite surface plasmons is the use of grating couplers similar to that shown in Fig. 2.12(c). Although any structural features which break translational invariance in the direction parallel to the surface may give rise to coupling, especially the periodic structuring seems to be highly efficient. Coupling from free space to the surface plasmon requires momentum conservation which may be achieved due to grating-induced Bragg scattering. Therefore the momentum matching condition can be described by the relation

$$k_{sp} = k_x + g\frac{2\pi}{d_x} \quad \text{with} \quad g = \pm 1, \pm 2, ... \tag{2.24}$$

Here k_{sp} is the wave vector of the surface plasmon, k_x is the component of the
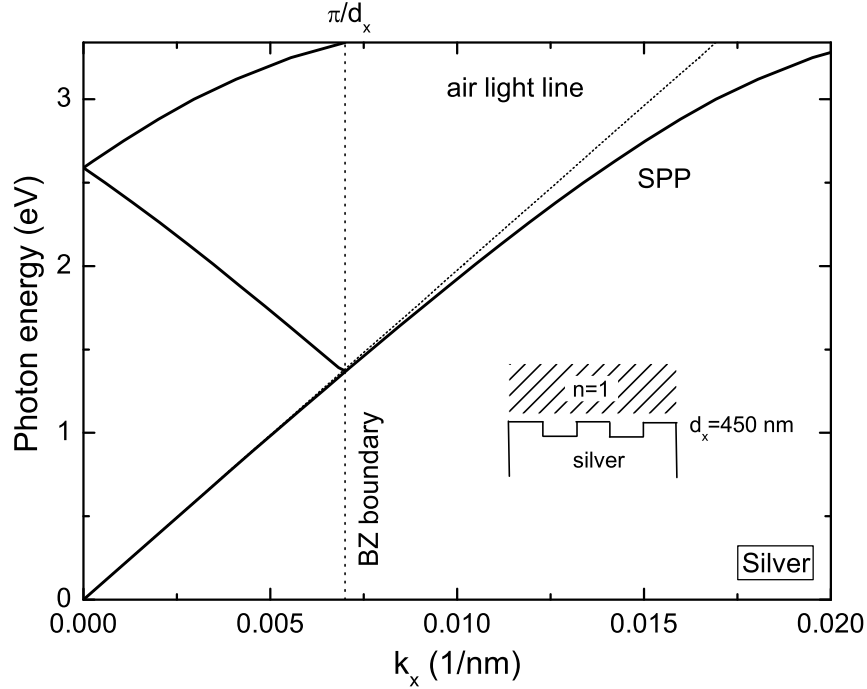
Figure 2.13:   Calculated dispersion relation of surface plasmon polaritons at a silver-air interface. Due to a periodic surface modulation with a period of $d_x = 450$ nm, the nonradiative modes have to be folded into the first BZ within this simple empty-lattice approximation. The boundary of the BZ is marked by a dotted vertical line.

wave vector of the incident light parallel to the metal interface, and d_x is the periodicity of the surface corrugation. Note that within this method surface plasmons propagating along the x and -x direction will be excited simultaneously. Therefore, assuming an excitation under normal light incidence, this fact leads to a standing wave pattern at the metal-dielectric interface (interference of surface modes with $k_{sp} = \frac{2\pi}{d_x}$ and $k_{sp} = -\frac{2\pi}{d_x}$). Within the empty lattice approximation, the periodic modulation of the metal interface can be interpreted as a folding of the surface plasmon dispersion relation[1]. Exemplarily, Fig. 2.13 shows the calculated dispersion relation of a surface plasmon at a planar metal-air interface. When a periodic corrugation is introduced, the calculated dispersion relation has to be folded into the first Brillouin zone (BZ). As shown in the left part of the same figure for a period of $d_x = 450$ nm, the previously nonradiative mode of the uncorrugated interface is now located above the air light line. Therefore, the

---

[1]In the empty lattice approximation the modulated metal surface is replaced by an homogeneous interface; then the resulting dispersion curves are folded into the first Brillouin zone of the original periodic structure.
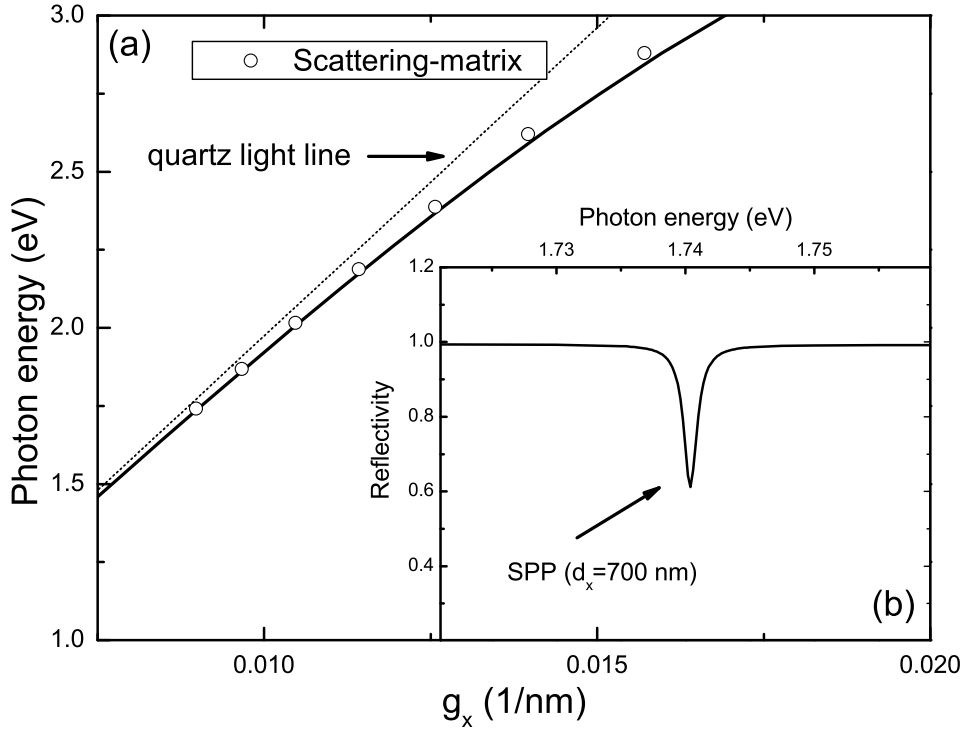
Figure 2.14: Calculated dispersion relations of surface plasmons at a silver-air interface. In panel (a), the results of a scattering-matrix-based formalism for a corrugated metal surface (circles) are compared with calculations for a plane interface using Eq. 2.16 (solid line). Exemplarily, panel (b) displays the calculated reflection spectrum of a modulated silver half space (period $d_x = 700$ nm) at normal incidence. The excitation of a surface plasmon is seen as a sharp dip in the reflection spectrum.

folded modes of the corrugated interface can couple to the photon continuum in air and become leaky in character (quasiguided surface modes). Note that the degeneracy of the surface plasmon dispersion may be lifted in the center and at the borders of the first BZ if the real geometry of the surface modulation is taken into account. It has been shown recently that a periodic texturing of the metal surface may lead to the formation of a plasmonic bandgap [55].

A very powerful method to calculate optical properties of metal nanostructures is the scattering-matrix-based numerical formalism [128–130]. As we will see later on, this formalism can be adapted to various problems and is therefore extensively used within this work. A more detailed description of the method will be given in Section 4.3. Generally, the scattering-matrix formalism allows the

determination of reflection, transmission, and absorption spectra based solely on the exact geometrical parameters and the dielectric functions of the considered materials. Beside the far-field properties, also near-field distributions can be calculated without the need for any fitting parameters. Theoretical results based on the scattering-matrix formalism are presented in Fig. 2.14 for surface plasmons at a corrugated silver-air interface. The surface modulation has been introduced by assuming a silver nanowire grating on top of the silver half space. While the grating period has been increased from 400 nm to 700 nm, the nanowire cross section of 100×10 nm^2 has been retained unchanged within all calculations. Again, the measured dielectric function of silver has been used within this approach [112]. Fig. 2.14(a) clearly shows that the scattering-matrix-based results for the weakly modulated silver surface are well confirmed by calculations based on Eq. 2.16 assuming a planar silver-air interface. In contrast to the dispersion relation of panel (a), panel (b) displays a single calculated reflection spectrum of a modulated silver half space for a period of $d_x = 700$ nm and normal incidence. The excitation of a surface plasmon is clearly seen due to the sharp dip in the reflection spectrum. With respect to the early works of Wood [17], such surface plasmon resonances are also known as resonant Wood anomalies. It has been realized that some features of the anomalous behavior of light observed by Wood for the first time are due to the excitation of surface plasmons on metallic diffraction gratings.

Finally, another possibility to excite surface plasmons by electromagnetic radiation has to be mentioned for the sake of completeness. In addition to the use of prisms or grating couplers, also the so-called end-fire coupling technique can be applied. Within this method the wave vector matching condition is achieved by focusing light onto the end face of the sample [131].

2.3   Particle plasmons

It is well-known that the optical response of a metal depends strongly on the dimensionality and therefore the confinement of the electron plasma. While surface plasmon polaritons at metal interfaces and on thin metal films have been discussed in the last section, the unique optical properties of single metal nanoparticles will be presented in the following. It will be shown that the enhanced spatial confinement gives rise to localized plasmon modes which modify both near- and far-field properties simultaneously.
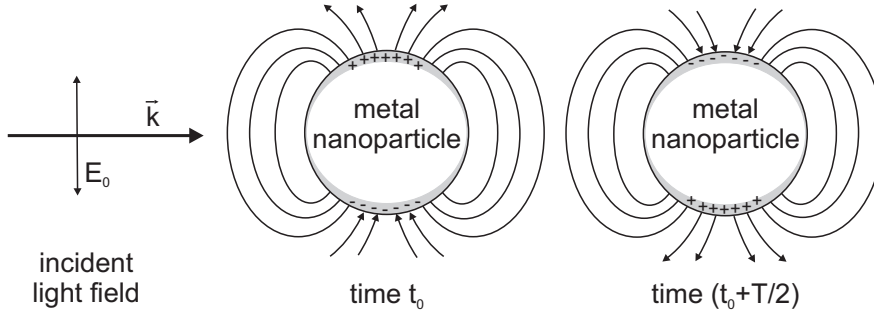
Figure 2.15: Particle plasmon: Excitation of a coherent oscillation of the conduction band electrons by the electric field of an incident light wave of frequency $\frac{1}{T}$.

In contrast to the electron density oscillations at a continuous metal-dielectric interface, especially small metal nanoparticles support a different type of plasma oscillation. Considering the three-dimensional confinement of the electron plasma, the resonant behavior of the metal nanoparticles is caused by an oscillatory movement of the conduction band electrons within the finite particle. When the conduction band electrons of a metal particle are collectively displaced against the positive background of the lattice by an external electromagnetic field, the resulting surface polarization charges give rise to an effective linear restoring force. Thus, neglecting any retardation effects for larger particles, the arising restoring force leads to a coherent dipole-like plasma oscillation [36, 114]. In contrast to extended surface plasmon polaritons at metal interfaces, these localized plasmon resonances of small metal nanoparticles are often referred to as particle plasmons. Note that particle plasmon resonances couple to the photon continuum and can be directly excited by propagating light waves. Their size should be smaller than half the wavelength of the exciting light.

The particle plasmon resonance of a sphere can be treated in a first approximation within classical electrostatic theory. When a metal sphere is placed in a constant electric field, polarization charges will be induced which modify the electric field $\vec{E}_{int}$ inside the metal particle. Taking into account the correct boundary conditions, the magnitude of the electric field inside the metal particle can be written as [36, 132]

$$\vec{E}_{int} = \vec{E}_0 \frac{3\varepsilon_{\mathrm{d}}}{\varepsilon_{\mathrm{m}} + 2\varepsilon_{\mathrm{d}}}, \qquad (2.25)$$

where ε_{d} is the dielectric constant of the surrounding medium. Assuming an instantaneous response to the external electric field (spatially constant phase, almost fulfilled by small particles), this solution will also apply to small metal

spheres under the influence of an oscillating electromagnetic field. Thus, important consequences for the optical properties of small metal particles can already be obtained within this approximation. A strong resonance will occur due to the frequency dependent complex dielectric function of the metal $\varepsilon_{\mathrm{m}} = \varepsilon_{\mathrm{m}}' + i\varepsilon_{\mathrm{m}}''$ which introduces the material response as a phenomenological parameter. The resonance position is therefore determined by the denominator in Eq. 2.25. Assuming a negligible imaginary part of the dielectric function ($\varepsilon_{\mathrm{m}}'' \ll 1$), the resonance frequency ω_s of the sphere can be found from the common relation

$$\varepsilon_{\mathrm{m}}'(\omega_s) = -2\varepsilon_{\mathrm{d}}. \tag{2.26}$$

A negative $\varepsilon_{\mathrm{m}}'$ is necessarily required to observe a strong plasmon resonance. Like in the case of a harmonic oscillator, the conduction band electrons will coherently oscillate at the frequency ω_{ex} of the external driving force (see Fig. 2.15). While the internal field is only weakly influenced far from resonance, the fields will be resonantly enhanced at the eigenfrequency ($\omega_{ex} = \omega_s$) of the confined electron plasma. As will be shown later in this work, the resonant behavior does not only lead to increased fields inside the metal nanoparticle but also induces an enhanced electromagnetic near-field. The evanescent near-field is strongly confined around the single metal nanoparticle and gives rise to many important physical phenomena such as surface-enhanced Raman scattering (SERS) [43, 133] or enhanced nonlinear optical effects [92, 134, 135].

The optical properties of small metal particles have been investigated extensively for many years. Even long before the modern concept of coherent particle plasmon oscillations was established after electron loss measurements [38], various scientists worked on exploring the observed optical scattering phenomena [136–138]. The most famous theoretical approach for example can be led back to the work of Mie [37]. Starting from Maxwell's equations, Mie developed a full solution to the scattering problem of a single spherical particle. Although the proposed formalism turned out to be a very powerful tool which can be adapted to various material systems, the description remains phenomenological. The material properties are introduced as parameters and therefore the theory could not give any deeper physical insight into the electronic properties.

In the next three sections, numerical results of the scattering problem will be presented for three different important geometries. Although the used numerical methods are more or less phenomenological in character, the main optical phenomena can already be described within these approaches. It will be shown that especially the geometry, the size, and the used host material strongly in-

fluence the optical response (e.g., transmission and reflection spectra) of small noble metal nanostructures. The optical properties of noble metal spheres will be discussed using the established exact Mie theory. Due to the fact that the Mie theory only applies for spherical geometries, the important case of spheroids will be treated within a quasistatic approximation. In addition to the results on metal particles, also the optical properties of noble metal nanowires will be presented and modelled by an efficient numerical scattering-matrix formalism [128–130].

2.3.1   Metal spheres

The optical scattering and absorption properties of spherical particles can be calculated using the theoretical approach of Gustav Mie [37], dating back to 1908. Starting from Maxwell's equations, the Mie theory allows for the theoretical determination of the extinction and scattering cross-sections with the knowledge of the particle radius and the dielectric functions of the used materials $(\varepsilon_{\mathrm{m}}, \varepsilon_{\mathrm{d}})$ only. The description of the scattering problem is based on the linear interaction of a monochromatic electromagnetic wave with a small homogeneous particle inside a dielectric host material. Within the Mie theory, the electromagnetic fields are expanded in a series of partial waves. The consideration of the appropriate boundary conditions then leads to a set of scattering coefficients a_n, b_n, c_n, and d_n which determine the exact field distributions inside and outside the spherical particle. The scattered field for example appears as a superposition of normal modes which are weighted by the appropriate coefficients a_n and b_n. With the knowledge of the incident and scattered fields, the extinction (σ_{ext}) and scattering cross-sections (σ_{sca}) can be obtained by the following equations

$$\sigma_{\mathrm{ext}} = \frac{2\pi}{|k|^2} \sum_{n=1}^{\infty} (2n+1) \cdot \mathrm{Re}(a_n + b_n), \qquad (2.27)$$

$$\sigma_{\mathrm{sca}} = \frac{2\pi}{|k|^2} \sum_{n=1}^{\infty} (2n+1) \cdot (|a_n|^2 + |b_n|^2), \qquad (2.28)$$

where k is the wave vector in the ambient dielectric medium. Note that the summation index n is related to the order of the spherical multipole excited in the particle. In the case of small particles, satisfactory results can be already obtained in a dipolar approximation ($n = 1$). Additionally, with the knowledge of the extinction and scattering cross-sections, the absorption cross-section is simply obtained by the relation

$$\sigma_{\mathrm{abs}} = \sigma_{\mathrm{ext}} - \sigma_{\mathrm{sca}}. \qquad (2.29)$$

Figure 2.16:   Extinction (E, solid), scattering (S, dashed), and absorption (A, dotted) efficiencies of single spherical gold nanoparticles in dependence on the particle radius r_p. Calculations are based on Mie-theory. The individual metal nanoparticles are embedded in a matrix with a dielectric constant of $\varepsilon_\mathrm{d} = 2.13$.

Although the approach of Mie is only valid for spherical particles (radius r_p), it can provide us with a first-order approximation for nonspherical particles. A more detailed analysis of the scattering problem can be found in Ref. [114].

It is important to remark that instead of specifying the calculated cross-sections, it makes sense to use efficiency factors which are normalized to the geometrical cross-section of the spheres. In the case of extinction and scattering, the so-called efficiencies are calculated by

$$Q_\mathrm{ext} = \frac{\sigma_\mathrm{ext}}{\pi r_p^2} \quad \text{and} \quad Q_\mathrm{sca} = \frac{\sigma_\mathrm{sca}}{\pi r_p^2}. \tag{2.30}$$

Exemplarily, some important optical properties of spherical metal particles will be discussed within the framework of the Mie theory in the following. Note that

all calculations are based on the measured dielectric functions ε_m of gold and silver listed in Ref. [112]. Fig. 2.16 presents numerically obtained extinction, scattering, and absorption efficiencies of single spherical gold nanoparticles in dependence on the particle radius r_p. The single nanoparticles are embedded into a quartz host material with an assumed dielectric constant of $\varepsilon_d = 2.13$. From panel (a) to panel (d), the particle radius is increased from $r_p = 20$ nm to $r_p = 100$ nm. The efficiency spectra of panel (a) show a clear resonance at approximately 2.3 eV. Obviously, the extinction efficiency Q_{ext} is dominated by absorption while the scattering efficiency Q_{sca} is nearly negligible. The strong peak at 2.3 eV is due to the spherical geometry and can be interpreted as the dipolar particle plasmon resonance of the gold nanoparticle. The large absorption above this resonance on the other hand is related to the onset of the interband transitions. As already discussed in Sec. 2.1.2, single particle excitations such as transitions from the $5d$ bands into the $6sp$ conduction band in the case of gold are referred to as interband transitions. A distinct shift of the particle plasmon resonances to lower energies can be observed when the radius of the gold spheres is further increased. While the spectra for particles with a radius of 20 nm, 30 nm, and 50 nm exhibit only a single resonance, the efficiency spectra of the particle with a radius of 100 nm show an additional second peak. The redshift of the particle plasmon resonance is caused by retardation effects. The external light field (driving force of the oscillator) is no longer homogeneous across the particle. Changes of the phase and the amplitude of the light field within the particle have to be taken into account. Therefore, a weakening of the surface charge induced restoring forces causes the observed shift of the particle plasmon resonances. Note that retardation effects are only observed under optical excitation. Assuming an excitation by electrons, the energies of the particle plasmon modes remain independent of particle size [38]. The second extinction peak in panel (d) is due to the excitation of the quadrupolar particle plasmon. While spectra of smaller particles are only characterized by a single dipolar resonance, gold particles with a radius of 100 nm feature spectrally well separated dipolar and quadrupolar plasmon resonances [114]. A very important additional phenomenon can be observed when the scattering and absorption efficiencies are compared for different particles sizes. The spectra of smaller particles are dominated by absorption, while the particle plasmon resonance of larger particles is predominantly related to scattering effects. For particles with a radius of 50 nm for example, the extinction efficiency Q_{ext} can be attributed to the light scattering efficiency. The still remaining absorption efficiency Q_{abs} is exclusively caused by single particle
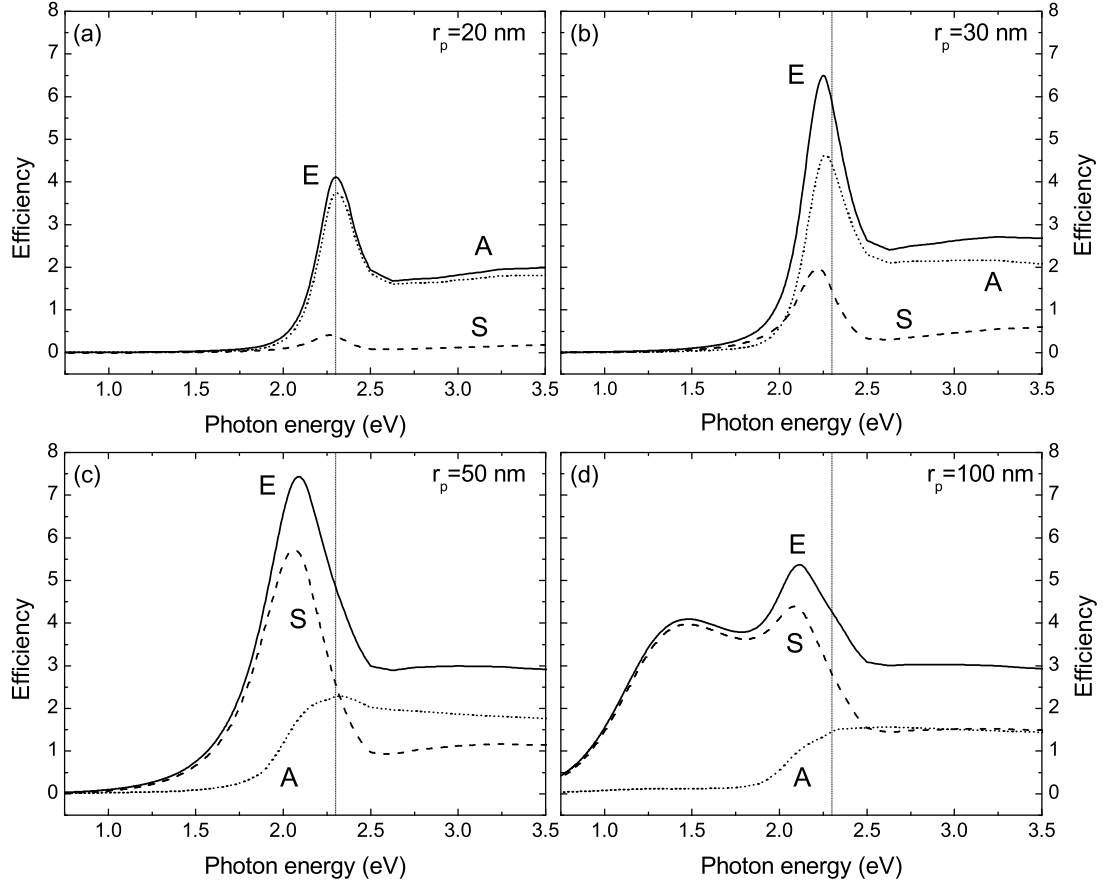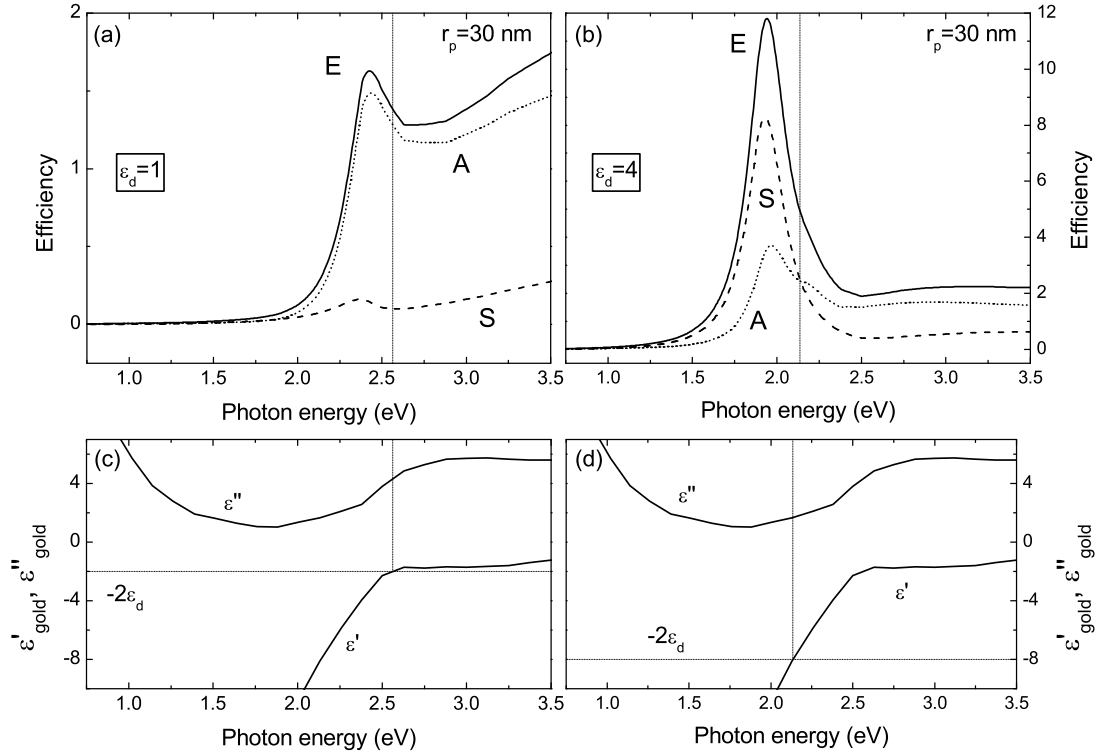
Figure 2.17:   Extinction (E, solid), scattering (S, dashed), and absorption (A, dotted) efficiencies of single spherical gold nanoparticles in dependence on the dielectric constant ε_d of the surrounding matrix. Calculations are based on Mie-theory. Spectra for single metal nanoparticles with $r_p = 30$ nm are shown for $\varepsilon_d = 1$ (a) and $\varepsilon_d = 4$ (b). Panel (c) and (d) display the real and imaginary parts of the dielectric function for gold.

excitations (interband transitions). Note that all extinction efficiencies displayed in panel (a)-(b) exceed unity. This important fact means that metal particles can scatter or absorb more light than is geometrically incident upon them.

The quality (spectral width and maximum efficiency) of the particle plasmon resonance of gold spheres also depends strongly on the dielectric constant ε_d of the ambient dielectric material. This effect is clearly demonstrated by the calculations shown in Fig. 2.17 where extinction, scattering, and absorption efficiencies of single spherical gold nanoparticles are depicted for $\varepsilon_d = 1$ (a) and $\varepsilon_d = 4$ (b). Both the extinction efficiency and the position of the particle plasmon resonance are strongly influenced. For a particle with a radius of 30 nm embedded into a host material with $\varepsilon_d = 1$, the particle plasmon resonance is only weakly pronounced and disappears nearly completely within a strong absorption band. As displayed in panel (b), stronger depolarization fields due to an increased refractive index of
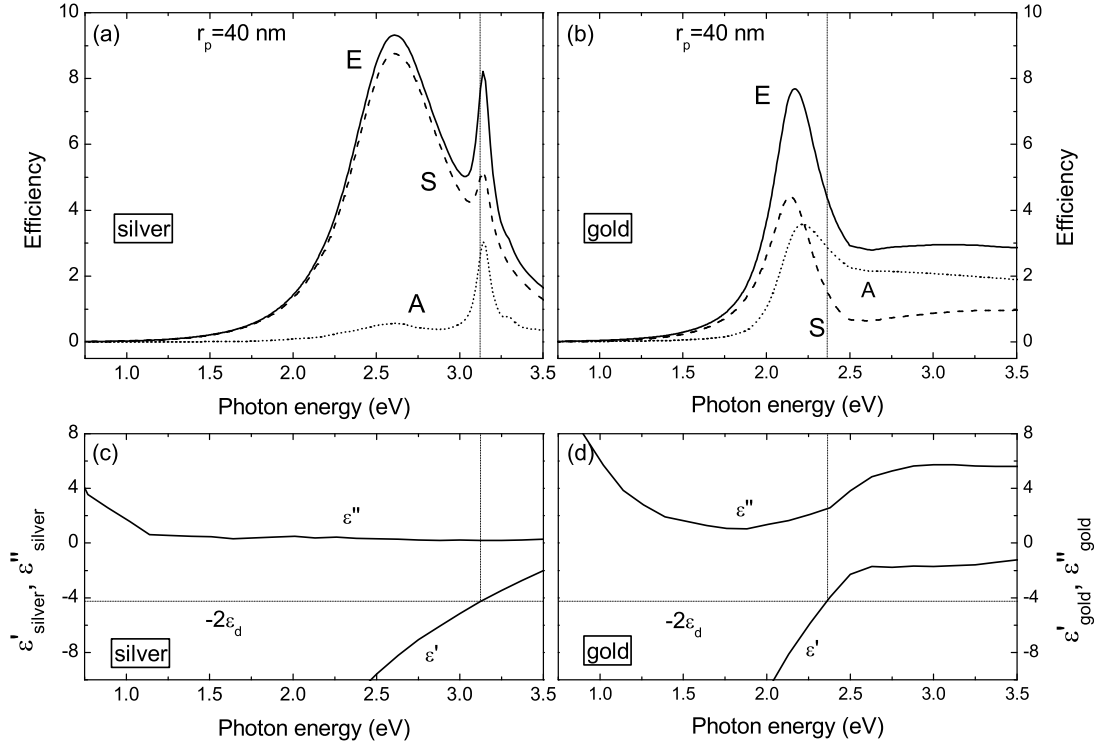
Figure 2.18:   Extinction (E, solid), scattering (S, dashed), and absorption (A, dotted) efficiencies of single spherical silver (a) and gold (b) nanoparticles. Calculations are based on Mie-theory. The single metal nanoparticles are embedded in a matrix with a dielectric constant of $\varepsilon_d = 2.13$. Panel (c) and (d) display the real and imaginary parts of the dielectric functions for silver and gold.

the host material will attenuate the restoring forces and therefore shift the particle plasmon resonance to lower energies. Simultaneously, the extinction efficiency and especially the scattering efficiency are both strongly enhanced, leading to a spectrally pronounced resonance. Panel (c) and (d) of this figure demonstrate that this behavior can be directly related to the complex dielectric function of gold. The observation of a pronounced particle plasmon resonance implies a small imaginary part of the dielectric function of the metal. Interband transitions and therefore larger imaginary parts ε''_{gold} lead to a strong damping of the resonance. Note that the spectral positions of the particle plasmon resonances differ slightly from their expected values (see Eq. 2.26) due to the retardation effects.

The smaller values of the imaginary parts of the dielectric function lead to the fact that the particle plasmon resonances of silver spheres are much more strongly pronounced within the considered spectral region. This can be seen in Fig. 2.18, where the particle plasmon resonances and the dielectric functions of silver and

gold are compared. Particles with a radius of 40 nm, embedded into a quartz host material, have been assumed for these calculations. The silver sphere shows a pronounced dipolar particle plasmon resonance at approximately 2.6 eV which is well separated from the spectrally narrow quadrupole resonance at 3.1 eV. The absorption efficiency can be neglected for the dipolar resonance which is basically caused by the high scattering efficiency. Assuming an identical particle radius, the dipolar particle plasmon resonance of gold spheres includes a much larger absorptive part due to the lower lying interband transitions. Therefore, scattering and absorption efficiencies are nearly comparable.

2.3.2 Metal ellipsoids

Due to the fact that Mie theory only provides an exact solution for scattering and absorption phenomena of particles with a spherical geometry, the scattering problem of elliptically shaped particles has to be solved within an electrostatic approach. Similar to the case of the already discussed quasistatic approach of spherical particles which results in the important Eq. 2.26, the formalism is restricted to very small ellipsoids. Therefore any retardation effects will be neglected within this electrostatic approximation. As shown in the books of Bohren [114] or van de Hulst [139], the extinction cross-section can be obtained by calculating the polarizability of the elliptically shaped particles. When the single particle is approximated as a dipole, the polarizability determines the dipole moment

$$\vec{p} = \varepsilon_{\mathrm{d}} \alpha \vec{E}_0, \tag{2.31}$$

which is induced by an applied external field $\vec{E}_0$. The polarizabilities α_j along the three main axes are defined by the relation

$$\alpha_{x,y,z} = \frac{4\pi}{3} r_x r_y r_z \frac{\varepsilon_{\mathrm{m}} - \varepsilon_{\mathrm{d}}}{\varepsilon_{\mathrm{d}} + L_{x,y,z}(\varepsilon_{\mathrm{m}} - \varepsilon_{\mathrm{d}})} \quad \text{with} \quad L_x + L_y + L_z = 1. \tag{2.32}$$

Within this formula, the exact geometry of the ellipsoidal particle is taken into account by the form factors $L_{x,y,z}$. They are directly related to the aspect ratio between the main axes and can be calculated using the equation

$$L_j = \frac{1}{2} \int_0^\infty \frac{r_x r_y r_z ds}{(s + r_j^2)[(s + r_x^2)(s + r_y^2)(s + r_z^2)]^{1/2}}, \quad j \in \{x, y, z\}. \tag{2.33}$$

Then, with the knowledge of the polarizability α_j, the extinction cross-sections for light which is polarized along one of the three main axes can simply be obtained by the relation

$$\sigma_{ext,j} = k \cdot \mathrm{Im}\{\alpha_j\} \quad \text{with} \quad j \in \{x, y, z\}. \tag{2.34}$$
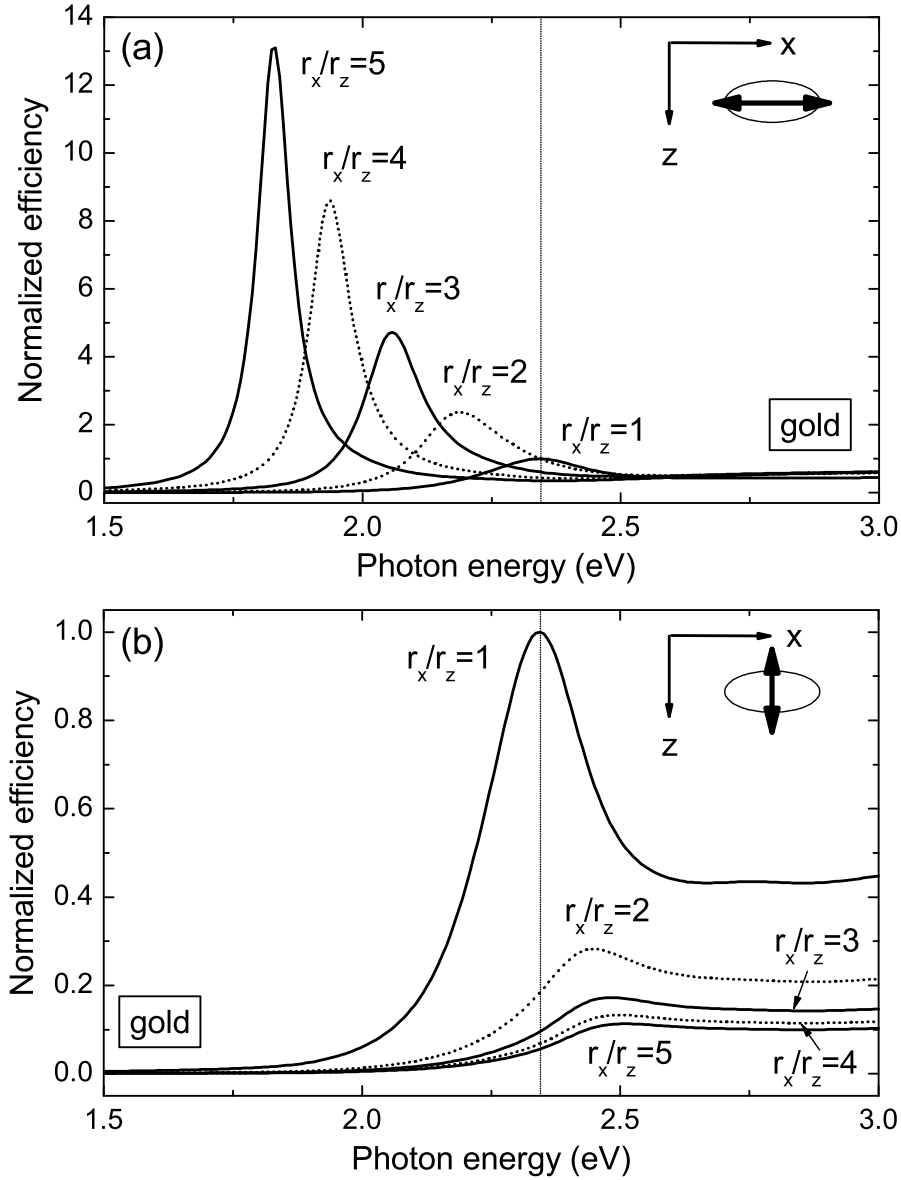
Figure 2.19: Calculated normalized extinction efficiencies of single gold spheroids $(r_x = r_y \geq r_z)$ using the quasistatic theory. The influence on the aspect ratio r_x/r_z is depicted. The spectra are shown for a polarization along r_x (a) and r_z (b), respectively. The single metal nanoparticles are embedded in a matrix with a dielectric constant of $\varepsilon_{\mathrm{d}} = 2.13$. The spectra are normalized with respect to the condition $r_x = r_z$.

To demonstrate the modifications which will be introduced by a nonspherical shape, Fig. 2.19 displays calculated extinction efficiencies of single gold spheroids embedded in a quartz host material. Spheroids are a special class of ellipsoids which have two axes of equal length ($r_x = r_y \geq r_z$). Therefore, depending on the chosen excitation geometry, two different particle plasmon resonances may appear. With respect to the fact that the scattering efficiency can be neglected for the assumed small nanoparticles (see, e.g., Sec. 2.3.1), the discussion will be restricted to the extinction efficiencies which approximately equal the absorption efficiencies. The calculations are again based on the measured dielectric function of gold taken from Ref. [112]. The influence on the aspect ratio r_x/r_z is depicted for two polarizations, each oriented along a different main axis of the spheroidal particle. Note that the geometrical cross-section of the particles in the xz-plane is assumed to be constant. Additionally, all spectra are normalized with respect to the special case of a metal sphere where $r_x/r_z = 1$. Panel (a) shows the extinction efficiencies for light polarized along the x-axis of the spheroid. When the aspect ratio r_x/r_z is increased, the particle plasmon is shifted to lower energies while the efficiency is increased simultaneously. Contrary, the particle plasmon is strongly damped and shifted to larger energies for a polarization along the z-axis. The observed shift of the resonance can be understood when considering the denominator of Eq. 2.32. For a small imaginary part of the metal dielectric function, the resonance condition can be simply found from the relation

$$\varepsilon_\mathrm{m} = \varepsilon_\mathrm{d} \left(1 - \frac{1}{L_{x,y,z}} \right). \tag{2.35}$$

Changing of the aspect ratio between r_x and r_z results in new form factors $L_{x,y,z}$, leading to a modified resonance condition. Note that for the case of a perfect sphere with $L_{x,y,z} = \frac{1}{3}$, the same relation as in Eq. 2.26 is derived. The extinction efficiencies are again strongly altered by the onset of the interband transitions. Considering the case of z-polarization depicted in panel (b), the particle plasmon is therefore strongly damped when shifted to higher energies by increasing the aspect ratio.

2.3.3   Metal nanowires

All discussions in the later chapters of this work will be restricted to the case of noble metal nanowires. In some respects, metal nanowires represent a very special geometry. They can be considered as an intermediate phase between a metal particle and a metal film. It might be possible to excite both localized
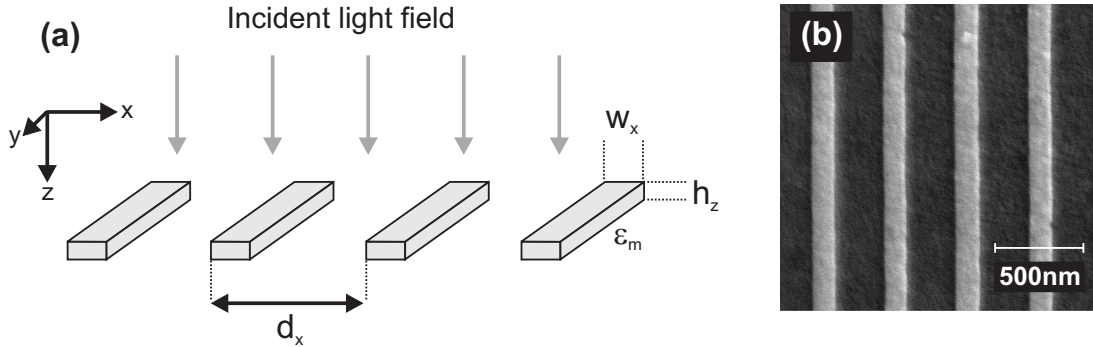
Figure 2.20: A schematic view of the nanowire arrangement is shown in panel (a). Important parameters are the height (h_z), the width (w_x) and the period (d_x) of the metal nanowires. Panel (b) displays a SEM image of a nanowire grating structure.

particle plasmons and extended surface plasmon polaritons within these structures simultaneously. Although the excitation of surface plasmons propagating along a metal nanowire would be possible [140] (e.g., by prism coupling or adding an additional surface modulation along the wire), this phenomenon will not be treated within this work. The presented results will focus only on the particle plasmon aspects of the metal nanowires. A schematic view of the considered nanowire arrangement and a scanning electron microscope (SEM) image of the experimentally realized structure are shown in panels (a) and (b) of Fig. 2.20. The two important geometrical parameters are the height h_z and the width w_x which determine the nanowire cross-section and therefore the optical response. Note that, although the properties of single nanowires will be discussed in this section, a periodic arrangement of nanowires has to be assumed for our calculations. All theoretical modelling is based on the scattering-matrix formalism [128–130], taking into account the measured dielectric functions [112]. This formalism is especially applicable to periodic systems such as the so-called photonic crystal slab structures. To reduce the influence of the well-known near- and far-field coupling effects [89, 100, 101], which induce modifications to the single nanowire extinction spectrum, special care has to be taken when choosing the grating period d_x.

Measured and calculated extinction [-ln(T), T: transmission] spectra of gold nanowire arrays with a period of $d_x = 275$ nm deposited on top of a quartz substrate ($n_{quartz} = 1.46$) are shown in Fig. 2.21. Near- and far-field effects can be neglected for the selected nanowire period. Panels (a) and (b) contain polarization dependent spectra for normal light incidence (along the z-direction). Electron beam lithography was used to prepare the nanowire array of panel (a)
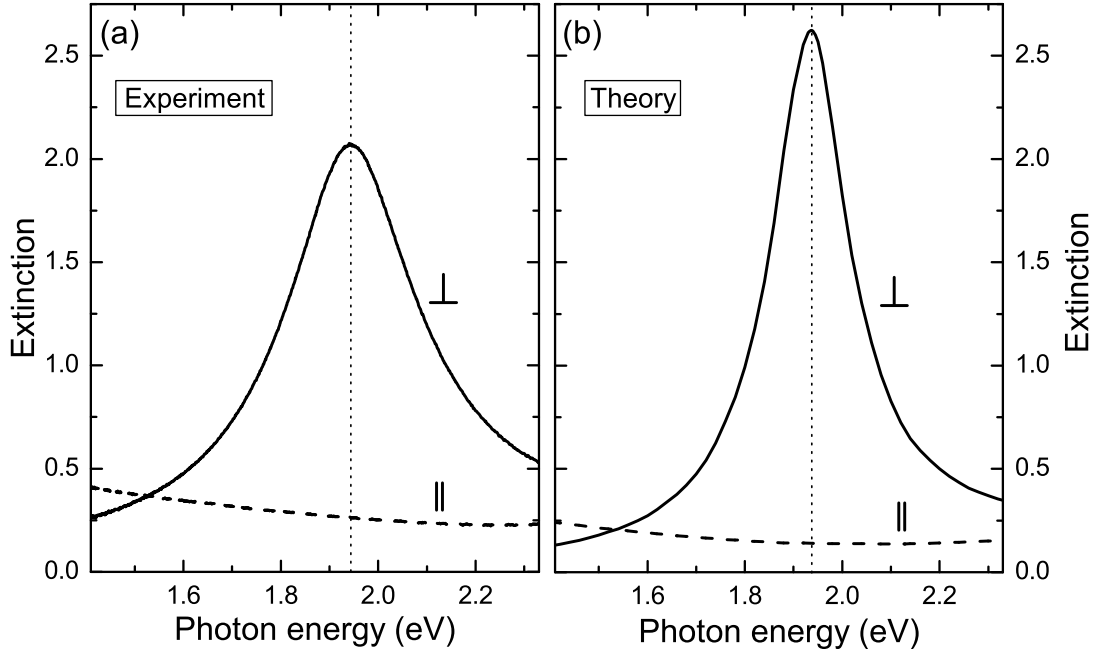
Figure 2.21: Measured (a) and calculated (b) extinction spectra of gold nanowire arrays ($d_x = 275$ nm) on top of a quartz substrate. Spectra are shown for light (normal incidence) which is linearly polarized parallel ($\parallel$, dashed lines) or perpendicular ($\perp$, solid lines) with respect to the nanowires. A wire cross-section of 100×20 nm^2 (100×15 nm^2) has been assumed within the measurements (calculations).

with a spatial extension of 100×100 μm^2 on top of the quartz substrate (see Appendix A for a precise description of the preparation process). To obtain acceptable accordance between measurements and calculations, the nanowire height has been adjusted. Instead of the assumed nanowire cross-section of 100×20 nm^2 (experiment), the calculations were performed for nanowires with a cross-section of 100×15 nm^2. Note that this deviation in height of approximately 5 nm can be due to uncertainties during the metal evaporation process.

In contrast to the case of a metal sphere or an ellipsoidal particle, the particle plasmon resonance of an uncoupled gold nanowire can be only excited when the incident light field is polarized perpendicular ($\perp$) to the nanowires. Due to missing restoring forces, no particle plasmon resonance can be found for a polarization parallel ($\parallel$) to the gold nanowires. Generally, the experimental spectra of panel (a) are well confirmed by the theoretical simulations in (b), although slight deviations are observable. Inhomogeneous broadening due to an always present size

distribution of the nanowires was not taken into account within these calculations.

The influence of the gold nanowire cross-section on the extinction spectra is demonstrated theoretically in Fig. 2.22 for normal light incidence and polarization perpendicular to the nanowires. Calculated extinction spectra of free-standing gold nanowire arrays in air (no substrate) are depicted for different nanowire heights (a) and widths (b), assuming a constant nanowire period of $d_x = 350$ nm. When the height h_z of the gold nanowires is increased from 10 nm to 50 nm while the width $w_x = 100$ nm retains unchanged, a clear shift of the particle plasmon to higher energies can be observed in panel (a). Although the amount of gold is increased by a factor of five, the shift of the plasmon resonance is accompanied by a decrease in extinction. This observation can be directly related to the onset of gold interband transitions which lead to a strong damping of the particle plasmon oscillations for energies above approximately 2.4 eV. Panel (b) displays a reversed situation where the width of the gold nanowires is increased while keeping a constant height of $h_z = 20$ nm. The already discussed retardation effects and therefore reduced restoring forces cause a shift of the plasmon resonance to smaller energies. Note that also near-field effects may become important for larger particles, although the period is not changed. An increased near-field coupling between adjacent nanowires would result in an additional lowering of the resonance energy.

Fig. 2.23 shows that the dielectric constant of the surrounding medium also has a very strong influence on the nanowire plasmon resonance. In this figure the calculated transmission, reflection and absorption spectra for gold nanowire arrays with a cross-section of 100×20 nm^2 are displayed for normal light incidence and polarization perpendicular to the nanowires. Whereas the nanowires are supported by a quartz substrate with $n = 1.46$ in panel (a), their free-standing counterparts are depicted in panel (b). The particle plasmon resonance energy is lowered due to consideration of the substrate. Again, the reason for the shift in energy can be found in the attenuated restoring forces. Stronger depolarization fields due to an increased refractive index will lower the resonance energy. Simultaneously, the influence of the interband transitions is reduced, leading to an enhanced reflection and a lowered transmission of the nanowire sample. Therefore, in addition to the nanowire cross-section, the adjustment of the refractive index of the surrounding media demonstrates a second opportunity to tune the optical response of the metal nanowire system in a proper way.
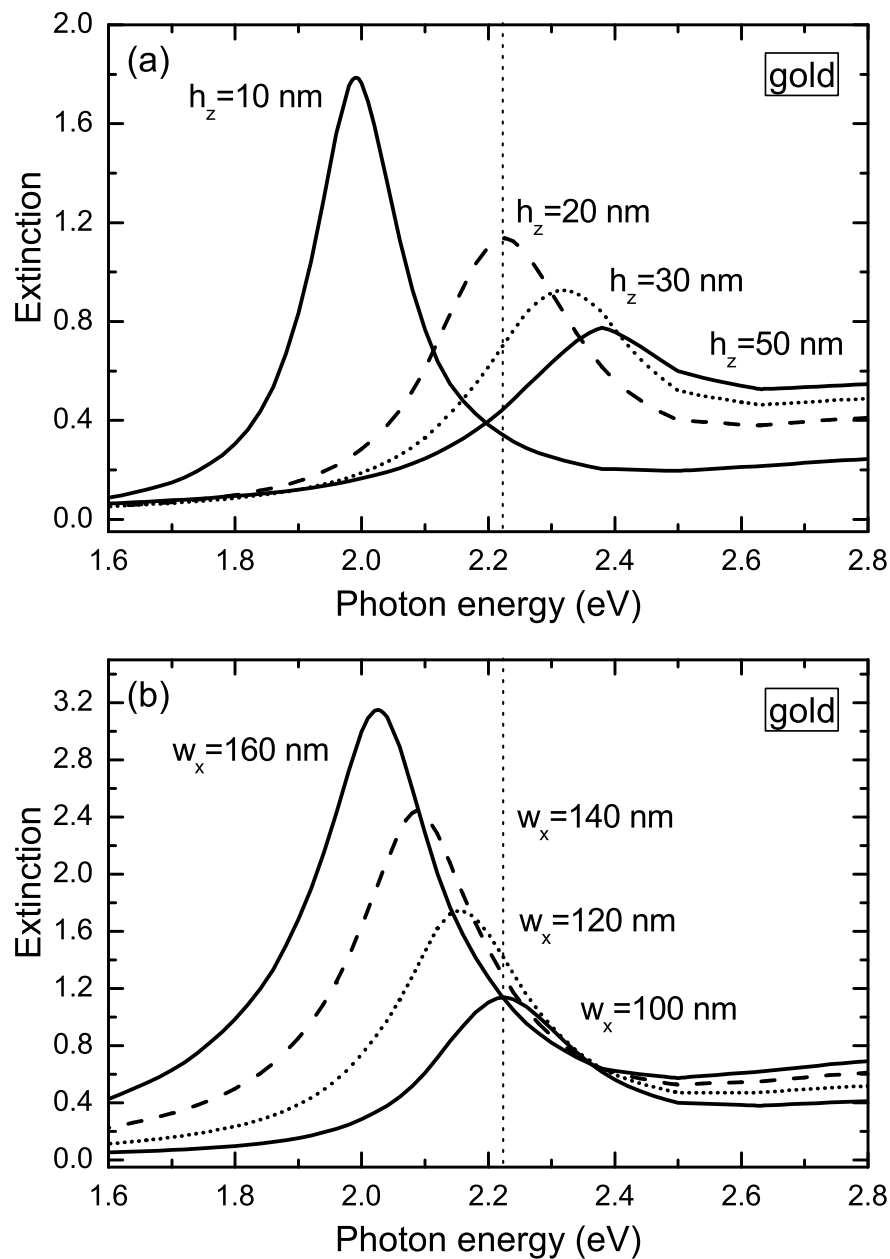
Figure 2.22:   Calculated extinction spectra (polarization $\perp$ to the nanowires, normal incidence, $d_x = 350$ nm) for free-standing gold nanowire arrays in air. In panel (a), the nanowire cross-section is increased from 100×10 nm^2 to 100×50 nm^2. The influence of the nanowire width is shown in panel (b), where the cross-section is changed from 100×20 nm^2 to 160×20 nm^2. The vertical dotted lines denote the position of the extinction maximum for a nanowire cross-section of 100×20 nm^2.
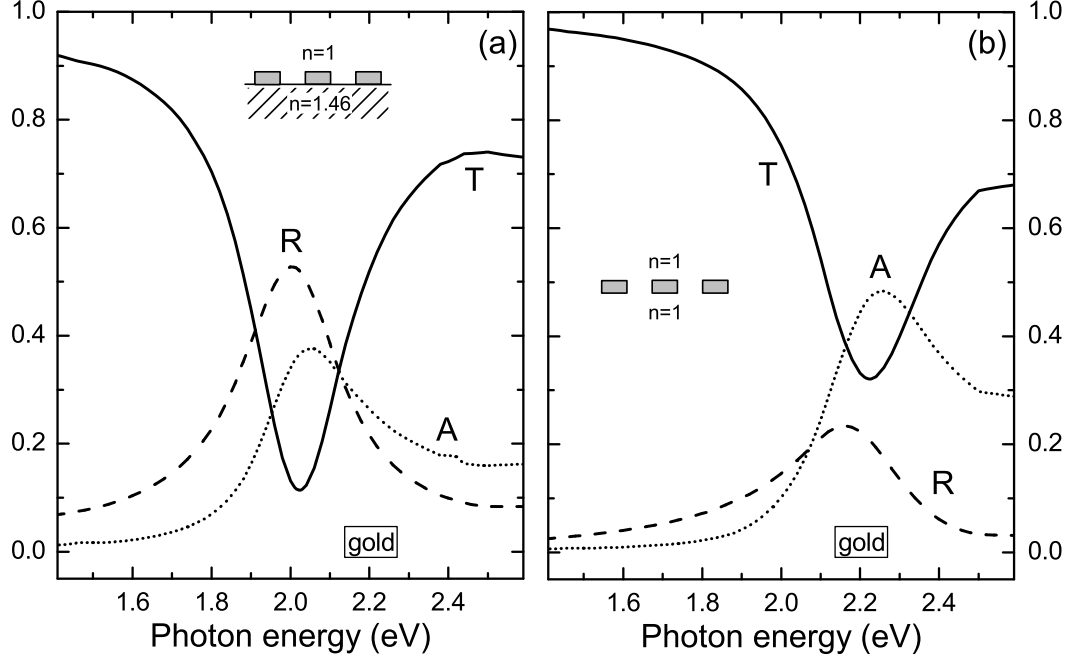
Figure 2.23: Calculated transmission (T, solid), reflection (R, dashed) and absorption (A, dotted) spectra of gold nanowire arrays at normal incidence (polarization $\perp$ to the nanowires, $d_x = 350$ nm). The nanowire array of panel (a) is supported by a thick quartz substrate while panel (b) displays spectra for a freestanding structure in air. The nanowire cross-section of 100×20 nm^2 is constant for spectra in both panels.

2.3.4   Dephasing of particle plasmons

The homogeneous spectral linewidth Γ_{hom} of the particle plasmon resonance is directly related to the dephasing time of the optical polarization [141, 142]. When the collective oscillations of the conduction band electrons of a metal nanoparticle (particle plasmons) are considered as a nearly perfect realization of a harmonic oscillator, the homogeneous linewidth and the dephasing time, which is characterized by the time constant T_2, are connected via

$$\Gamma_{hom} = \frac{2\hbar}{T_2} \quad \text{with} \quad \frac{1}{T_2} = \frac{1}{2T_1} + \frac{1}{T_2^*}. \tag{2.36}$$

As shown by the second relation, the plasmon dephasing time can be separated into two parts. T_1 includes all inelastic and T_2^* all elastic phase-loss processes.

The elastic phase-loss processes lead to a pure dephasing of the coherent electron motion. Scattering effects may destroy the collective phase coherence of the

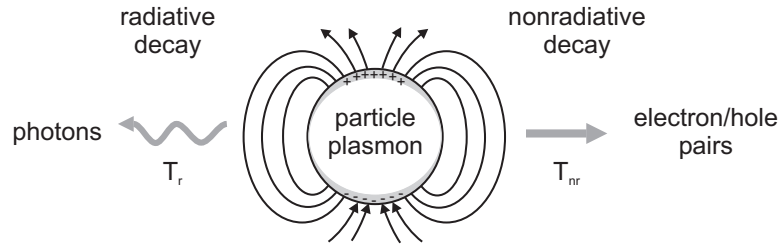Figure 2.24: Schematic view of possible population decay channels: The lifetime of particle plasmons is determined by radiative and nonradiative decay channels.

electrons without changing their energies. Although such processes should be possible, it has been shown recently that they give only negligible contributions to the total dephasing rates [143].

The possible population decay channels due to inelastic processes are shown schematically in Fig. 2.24. The particle plasmon energy will be either transformed into photons (radiative) or into electron-hole excitations (nonradiative). Note that the inelastic scattering of oscillating electrons into single electron excitations (electron-hole pairs) is also known as Landau damping. Taking care of the radiative and nonradiative fractions, the time constant T_1 can be further split-up and is simply obtained by the relation

$$\frac{1}{T_1} = \frac{1}{T_r} + \frac{1}{T_{nr}}. \tag{2.37}$$

The time constants T_r and T_{nr} describe the radiative and nonradiative dephasing channels, respectively. The nonradiative channel includes both the decay into interband as well as into intraband excitations.

The exact decay mechanisms of particle plasmons are still an important subject of ongoing research, even though intensive investigations of the dynamical properties were carried out during the last decades. One problem concerning the measurement of the dephasing times of particle ensemble is the inhomogeneous broadening of the particle plasmon resonance. In principle, it should be possible to extract the T_2 time directly from the spectral bandwidth of the plasmon resonance when measuring the optical extinction in the far-field regime. However, the always present size and shape distributions of the nanoparticles prevent an exact determination of the homogeneous linewidth. Different methods have been proposed to overcome these circumstances. For example, one method to measure the plasmon dephasing times is based on persistent spectral hole burning [144]. Dephasing times of 4.8 fs were found for silver nanoparticles with a radius of only 7.5 nm. Instead of using an ensemble of individual particles, also the direct

extraction of the dephasing times from the near-field spectra of single particles
has been presented [142]. Plasmon dephasing times of around 8 fs have been re-
ported for single gold particles in a dielectric TiO_2 matrix. Another method based
on single-particle light-scattering spectroscopy has been discussed in Ref. [143].
The proposed experimental technique was used to systematically study the de-
phasing of particle plasmons in gold nanoparticles as a function of particle size
and shape. Also the determination of the dephasing times in the time domain
by directly measuring the second- or third-order interferometric autocorrelation
functions of the particle plasmons has been proposed [92, 145, 146]. However,
it was shown quite recently that these time-resolved second- or third-harmonic
generation experiments do not allow to distinguish between homogeneous and
inhomogeneous contributions in case of particle ensembles [147]. In contrast to
the claim of previous publications and similar to extinction measurements, only
a lower limit of the dephasing times may be extracted from these experiments.
Indeed, four-wave mixing experiments would allow for such a differentiation.

Although small metal particles show typical plasmon dephasing times of ap-
proximately 10 fs, the subsequent relaxation of the electron-hole pairs happens
on a much larger time scale. The excited electrons (nonthermal distribution)
thermalize by scattering proccesses (e.g., electron-electron and electron-phonon
scattering) within approximately 500 fs. After a thermal electron distribution
is achieved, the hot electrons lose their thermal energy due to electron-phonon
scattering on a ps time scale until the lattice temperature is reached.

Note that the coherent motion of electrons in a small metal nanoparticle under
the influence of an external light field can be modelled by a driven damped
harmonic oscillator. Following the simple model presented in Ref. [146], the
particle plasmon field $E_{pl}(t)$ will be proportional to

$$E_{pl}(t) \propto \int_{-\infty}^{t} \frac{1}{\omega_0} K(t') \mathrm{e}^{-\gamma(t-t')} sin[\omega_0(t-t')]dt', \qquad (2.38)$$

where $K(t)$ denotes the external driving force (electromagnetic wave) and ω_0 the
resonance frequency of the particle plasmon. Within this model all dephasing
processes are described by the phenomenological damping constant γ which is
related to the dephasing time by $\gamma = 1/T_2$. Originally, referring to the work
of Lamprecht [146], this oscillator model was used to simulate the plasmon field
oscillations and calculate the nonlinear optical response of metal nanoparticles.

Exemplarily, calculated plasmon field oscillations under resonant excitation are
shown in Fig. 2.25 for two different dephasing times T_2. For the presented cal-
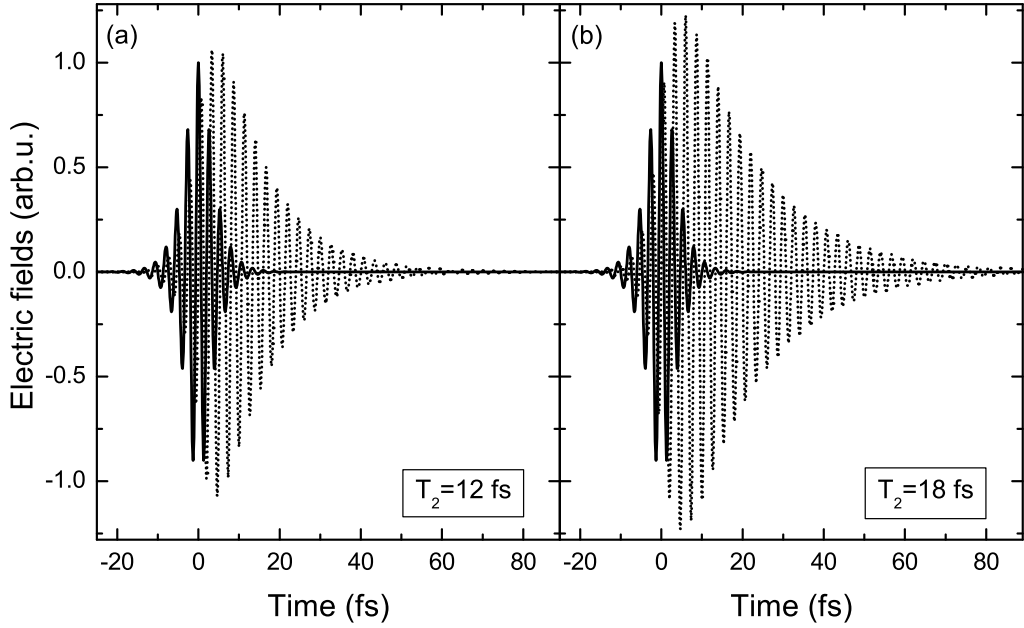
Figure 2.25: Calculated plasmon field oscillations (dotted line) under resonant excitation. A laser pulse at 1.55 eV ($\lambda = 800$ nm) with a pulse length of 5 fs has been assumed as external driving force (solid line). Results for particle plasmon dephasing times of $T_2 = 12$ fs (a) and $T_2 = 18$ fs (b) are shown.

culations, a short laser pulse with a length of 5 fs and a center wavelength of $\lambda_{ex} = 800$ nm (1.55 eV) has been assumed as the external driving force $K(t)$. The resulting laser pulse field is depicted in both panels in addition to the resonant plasmon fields. The displayed oscillations (particle plasmons) with a resonance energy of 1.55 eV exhibit a dephasing time of $T_2 = 12$ fs in panel (a) and $T_2 = 18$ fs in panel (b). As expected, the lifetime and the amplitude of the plasmon oscillations are increased due to a longer dephasing time in panel (b). Note that the plasmon dephasing time is directly related to the electric-field enhancement factor f by the relation $|f| \propto T_2$ [142]. This fact is particularly important for the observation of nonlinear effects or SERS applications, where relatively long dephasing times are favorable.

Chapter 3

Photonic crystal slabs

The optical response of planar one-dimensional grating structures can be strongly modified if a waveguiding layer is brought into close proximity. Such multilayer structures, so-called photonic crystal slabs, are characterized by a strong resonant behavior. Under certain conditions waveguiding anomalies will appear as sharp spectral features in the measured transmission or reflection spectra. After reviewing the basic properties of planar dielectric slab structures in the beginning of the chapter, a more detailed description of one-dimensional photonic crystal slab structures will be presented in a second part. Especially the specific line shapes and the narrow spectral bandwidth of the supported eigenstates will be analyzed in dependence on the explicit geometry of the considered structure. It will be shown by numerical simulations that the optical response can be controlled by a proper sample design. One-dimensional superlattice structures will be discussed in the last section. In addition to more common geometries, the proposed superlattice structures allow for further modification of the observed optical phenomena.

3.1   Introduction

Photonic materials with a structuring on a length scale comparable to the wavelength of light are currently the subject of intensive studies. In addition to optical microcavities [148], so-called photonic crystal structures [1, 3, 4] have become a very prominent material system. Important fundamental optical effects like the control of spontaneous emission [149] or low-threshold defect mode lasing [7] have been demonstrated recently. Although some of the related optical phenomena

have been proposed theoretically even earlier, especially the improved fabrication possibilities and the application of new optical materials have stimulated the current rapid progress in photonic crystal research. The use of modern optical lithography and electron-beam techniques for example now allows for structuring on a very small length scale and therefore manufacturing of the required high quality samples.

In addition to more complex three-dimensional structures (3D), especially two-dimensional (2D) photonic crystal slab structures have attracted widespread interest. Although a full three-dimensional photonic bandgap cannot be obtained, these structures are much easier to handle with the standard lithographical fabrication techniques. In its simplest form, planar photonic crystal structures are based upon optical waveguide slabs which exhibit a periodic one-dimensional spatial modulation along the guiding direction. These perturbations can be either due to a surface corrugation or due to a periodic modification of the dielectric function of the waveguide itself. Naturally, more sophisticated structures make use of two-dimensional structuring of the waveguide slab (e.g., air holes) to exploit their full capabilities. High-quality nanocavities [6], negative refraction in the optical regime [5, 150], and defect mode guiding with negligible losses [151] have been realized for example.

Planar photonic crystal slab structures can be characterized by their corresponding electromagnetic eigenstates within the first Brillouin zone. Two types of supported eigenstates or modes can be identified. The bound or guided modes are completely confined by the waveguide slab and can not couple to external light fields. Leaky or quasiguided modes on the other hand possess finite lifetimes due to their coupling with the photon continua and leakage into the cladding layers [130, 152]. Only these quasiguided modes appear as well-pronounced features in transmission or reflection spectra of photonic crystal slab structures. Note that the appearance of these leaky modes is a very fundamental optical effect. First observations can be traced back to the early investigations on waveguiding diffraction gratings. These optical elements are often referred to as grating-waveguide structures in the literature. These leaky modes were previously discussed in terms of so-called grating anomalies since the photonic crystal perspective was not yet established.

The optical properties of diffraction gratings have already been studied for almost one century. Starting with the observations of Wood in the beginning of the last century [17], grating anomalies have become a well-known optical phenomenon.
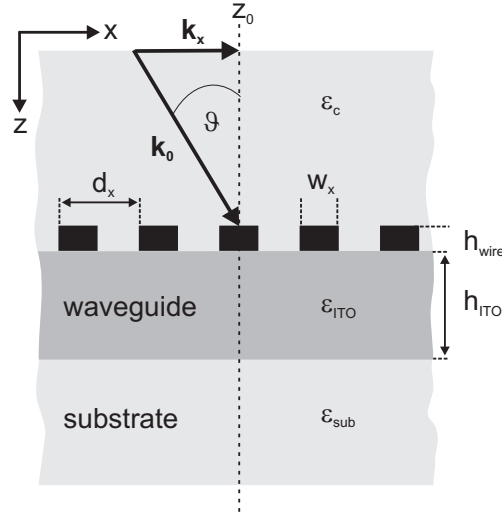
Figure 3.1:   Schematic view of the grating-waveguide structure. A periodic one-dimensional nanowire array is prepared on top of a dielectric waveguiding layer. Samples with specific geometrical parameters have been investigated. Angle as well as polarization dependent transmission and reflection measurements are possible.

In the grating perspective, the appearance of these spectral features can be related to two different mechanisms. In extension of diffractive anomalies (known as Rayleigh anomalies [153]), also resonant anomalies (waveguiding anomalies) have been observed [154, 155]. Diffractive anomalies are associated with the abrupt redistribution of energy caused by the opening of new diffraction orders. Resonant anomalies on the other hand are related to the resonant interaction between an incoming light field and surface or waveguide modes supported by the grating structure itself.

With respect to the coupling phenomena which will be analyzed in the next chapter (waveguide-plasmon coupling), the discussion will be restricted to optical transmission experiments in the direction perpendicular to the waveguiding slab. Note that therefore only modes near the second-order stop band at the center of the Brillouin zone will be accessible within the considered excitation geometry. The still existent guided modes below the light cone and first-order stopbands will not be treated within this introductory chapter.

The basic one-dimensional design of the used photonic crystal geometry is displayed in Fig. 3.1. In its most simple form, the structures consist of a periodic arrangement of dielectric or metallic nanowires on top of a waveguiding layer deposited on a quartz substrate ($\varepsilon_{\mathrm{sub}} = 2.1$). If not stated otherwise, a vacuum half

space has been assumed as upper cladding layer ($\varepsilon_\mathrm{c} = 1$). Indium-tin-oxide (ITO) is used as dielectric waveguide material for simplicity reasons in our investigations. Electron beam lithography was used for the preparation of the one-dimensional nanowire grating structures. The small conductivity of the ITO film is essential and allows for discharging of the electrons during the writing process. As it will be shown in the following, the optical response depends on various geometrical parameters. In addition to the grating (h_wire) and waveguide (h_ITO) thicknesses, especially the nanowire period (d_x) and width (w_x) have major influence on the detected optical response. A conventional white light transmission setup was used to record all spectra shown in this chapter (see Appendix). It is important to re-mark that the experiments have to ensure a high angular selectivity to detect the existing small stopbands and especially to suppress the appearance of optically inactive modes at normal incidence.

3.2   Eigenmodes of planar dielectric waveguides

We will start with a brief introduction to guided modes of planar dielectric slab waveguides within this section. The presentation is therefore based on a simple slab structure similar to Fig. 3.1 but without taking into account the periodic nanowire array in the first step. The discussion will focus on the main points only. The reader is referred to the literature for more detailed reviews (see, e.g., Refs. [120, 156]).

3.2.1   Dispersion relation

Generally, a slab geometry requires a three-layer arrangement in its simplest form, where the upper and lower dielectric half spaces (cladding layers) are assumed to be infinitely thick in the z-direction. Due to the fact that waveguiding phenomena imply total internal reflection at the slab boundaries, the specific waveguide design is based on a dielectric core region with an averaged effective index which is higher than for the surrounding regions. Our presentations will be restricted to asymmetric slab designs only. Therefore one-dimensional confinement within the structure can be achieved by the explicit assumption

$$\varepsilon_\mathrm{ITO} > \varepsilon_\mathrm{sub} > \varepsilon_\mathrm{c}. \tag{3.1}$$

The dispersion relation of guided modes in the case of dielectric slab waveguides can be obtained starting from Maxwell's equations and taking into account the

correct boundary conditions. In planar layered structures, the propagating waves separate into transverse electric (TE polarization, $E_x = E_z = H_y = 0$) and transverse magnetic (TM polarization, $H_x = H_z = E_y = 0$) modes, which will be treated independently in the following. The field components of each of these modes can be expressed in terms of the remaining transverse component, respectively. Due to the continuity requirement at the slab interfaces, these transverse field components (TE: $\vec{E}_{\mathrm{TE}} = E_y \vec{e}_y$, TM: $\vec{H}_{\mathrm{TM}} = H_y \vec{e}_y$) have to satisfy the corresponding Helmholtz equations

$$\nabla^2 \vec{E} + k_0^2 \varepsilon_n \vec{E} = 0 \text{ (TE)}, \quad \nabla^2 \vec{H} + k_0^2 \varepsilon_n \vec{H} = 0 \text{ (TM)} \tag{3.2}$$

in all three media of the waveguide structure. Here, $k_0 = \omega \sqrt{\mu_0 \varepsilon_0}$ is the absolute value of the free space wave vector and ε_n is the dielectric function of the considered material. In TE polarization for example, assuming plane waves which decay exponentially with increasing distance from the waveguide, the fields can be described by solutions (implying a time dependence $\mathrm{e}^{i\omega t}$) of the following form:

$$\begin{aligned}
E_{y(c)} &= E_1 \, e^{pz} \, e^{i(k_x x - \omega t)}, \quad (z < 0) & (3.3) \\
E_{y(ITO)} &= (E_2 \, e^{ik_z z} + E_3 \, e^{-ik_z z}) \, e^{i(k_x x - \omega t)}, \quad (0 \le z \le h_{\mathrm{ITO}}) & (3.4) \\
E_{y(sub)} &= E_4 \, e^{-qz} \, e^{i(k_x x - \omega t)}, \quad (z > h_{\mathrm{ITO}}). & (3.5)
\end{aligned}$$

Similar equations will appear for TM polarization when replacing E_y by H_y (not shown). It follows from the wave equation that the propagation constants in the different materials (k_z, q, and p) are related to the free space constant k_0 by the equations

$$\begin{aligned}
p^2 - k_x^2 &= -k_0^2 \varepsilon_{\mathrm{c}} & (3.6) \\
-k_z^2 - k_x^2 &= -k_0^2 \varepsilon_{\mathrm{ITO}} & (3.7) \\
q^2 - k_x^2 &= -k_0^2 \varepsilon_{\mathrm{sub}}. & (3.8)
\end{aligned}$$

Now the coefficients E_j ($j = 1, 2, 3, 4$) and therefore also the guided modes can be found by requiring continuity of the tangential components of the electric and magnetic fields at the two slab interfaces. For the two modes, this requirement can be expressed by the relations

$$E_{y(ITO)} = E_{y(n)} \quad \text{and} \quad \frac{\partial}{\partial z} E_{y(ITO)} = \frac{\partial}{\partial z} E_{y(n)} \tag{3.9}$$

for TE polarization and by

$$H_{y(ITO)} = H_{y(n)} \quad \text{and} \quad \frac{\partial}{\partial z} H_{y(ITO)} = \left(\frac{\varepsilon_{\mathrm{ITO}}}{\varepsilon_n} \right) \frac{\partial}{\partial z} H_{y(n)} \tag{3.10}$$

for TM polarization. Both interfaces have to be considered ($n = c$ or $n = sub$) to obtain the full set of linear equations. We can directly derive the two dispersion relations with the knowledge of these four equations for each polarization. TE polarization yields the characteristic equation

$$h_{\mathrm{ITO}}\sqrt{k_0^2\varepsilon_{\mathrm{ITO}} - k_x^2} = \arctan\left(\sqrt{\frac{k_0^2(\varepsilon_{\mathrm{ITO}} - \varepsilon_{\mathrm{c}})}{k_0^2\varepsilon_{\mathrm{ITO}} - k_x^2} - 1}\right) +$$

$$\arctan\left(\sqrt{\frac{k_0^2(\varepsilon_{\mathrm{ITO}} - \varepsilon_{\mathrm{sub}})}{k_0^2\varepsilon_{\mathrm{ITO}} - k_x^2} - 1}\right) + m\pi. \qquad (3.11)$$

The corresponding solution for TM polarization results in

$$h_{\mathrm{ITO}}\sqrt{k_0^2\varepsilon_{\mathrm{ITO}} - k_x^2} = \arctan\left(\frac{\varepsilon_{\mathrm{ITO}}}{\varepsilon_{\mathrm{c}}}\sqrt{\frac{k_0^2(\varepsilon_{\mathrm{ITO}} - \varepsilon_{\mathrm{c}})}{k_0^2\varepsilon_{\mathrm{ITO}} - k_x^2} - 1}\right) +$$

$$\arctan\left(\frac{\varepsilon_{\mathrm{ITO}}}{\varepsilon_{\mathrm{sub}}}\sqrt{\frac{k_0^2(\varepsilon_{\mathrm{ITO}} - \varepsilon_{\mathrm{sub}})}{k_0^2\varepsilon_{\mathrm{ITO}} - k_x^2} - 1}\right) + m\pi. \qquad (3.12)$$

Comparing Eqs. 3.11 and 3.12, one discovers that both characteristic equations only differ in the consideration of the ratio of the dielectric functions of adjacent media. The order of the corresponding modes is taken into account and will be labeled by the number m ($m = 0, 1, 2, ...$). The dispersion relations are described by so-called transcendental equations, which have to be solved numerically in the following.

It is important to note that the two dispersion relations 3.11 and 3.12 may have no full solution in the case of antisymmetric waveguide geometries ($\varepsilon_{\mathrm{sub}} \neq \varepsilon_{\mathrm{c}}$). Only symmetric structures support at least one guided mode in TE and TM polarization for the whole energy range independent on the waveguide layer thickness. Therefore, due to the fact that the wavevector component q has to be real inside the quartz substrate, the possible photon energies are limited by a lower cut-off energy E_{cut}. In TE polarization for example (assuming all materials as being non-absorptive), no guided modes will be supported by asymmetric structures for photon energies below

$$E_{\mathrm{cut,TE,m}} = \frac{\hbar c_0}{h_{\mathrm{ITO}}\sqrt{\varepsilon_{\mathrm{ITO}} - \varepsilon_{\mathrm{sub}}}}\left(\arctan\left(\sqrt{\frac{\varepsilon_{\mathrm{sub}} - \varepsilon_{\mathrm{c}}}{\varepsilon_{\mathrm{ITO}} - \varepsilon_{\mathrm{sub}}}}\right) + m\pi\right). \qquad (3.13)$$

The cut-off energy for the mth TM modes is slightly shifted to higher energies and can be calculated by the analog relation

$$E_{\mathrm{cut,TM,m}} = \frac{\hbar c_0}{h_{\mathrm{ITO}}\sqrt{\varepsilon_{\mathrm{ITO}} - \varepsilon_{\mathrm{sub}}}}\left(\arctan\left(\frac{\varepsilon_{\mathrm{sub}}}{\varepsilon_{\mathrm{c}}}\sqrt{\frac{\varepsilon_{\mathrm{sub}} - \varepsilon_{\mathrm{c}}}{\varepsilon_{\mathrm{ITO}} - \varepsilon_{\mathrm{sub}}}}\right) + m\pi\right). \qquad (3.14)$$

The equations clearly show that E_{cut} equals zero when the condition $\varepsilon_{sub} = \varepsilon_c$ is fulfilled for the lowest order modes ($m = 0$). We have to remark that the existence of a lower cut-off energy will be very important when dealing with more complex metallic photonic crystal structures in the next chapter. The optical response will be altered dramatically when shifting the cut-off energy by varying the slab layer thickness.

3.2.2   Numerical results

The two equations 3.11 and 3.12 have been solved numerically to demonstrate the influence of the waveguide slab design. Both the dielectric surrounding as well as the core thickness have to be considered. Selected examples will be presented in the following section.

Fig. 3.2 (a) displays the calculated dispersion relation of guided modes of a planar indium-tin oxide slab structure (ε_{ITO}=3.61) bounded between quartz (ε_{sub}=2.1) and vacuum (ε_c=1) half spaces. A slab thickness of $h_{ITO} = 140$ nm has been used for these calculations. Only the lowest order modes ($m = 0$), the so-called TE_0 and TM_0 modes, are shown in this figure. Note that the frequency dependencies of the dielectric functions have been neglected for all calculations presented within this section.

The dispersion relation of the guided modes is located below the quartz and vacuum light cones. As expected, these modes of the waveguide slab will therefore not couple to external light fields when assuming a perfect dielectric core layer without surface roughness. The wave vector k_x of the confined electromagnetic modes will always be larger than for waves propagating in the surrounding media (free space propagation). The dispersion relation only approaches the quartz light cone asymptotically for decreasing photon energies. The optical confinement of the modes is finally lost when the dispersion relation starts crossing the quartz light cone ($q^2 < 0$). This characteristic point of the dispersion relation is labelled as cut-off energy. The cut-off energies of the zero order modes ($E_{cut,TE} = 0.81$ eV and $E_{cut,TM} = 1.44$ eV) are depicted in the figure. Note that no higher order modes appear within the considered spectral range. The cut-off of these modes is shifted to much higher energies. In the case of first order modes ($m = 1$), the cut-off is found at 4.41 eV for TE polarization and 5.05 eV for TM polarization.

The cut-off energies of the lowest order modes are shown in Figs. 3.2 in dependence on the dielectric function of the cladding layer (b) and in dependence on the slab
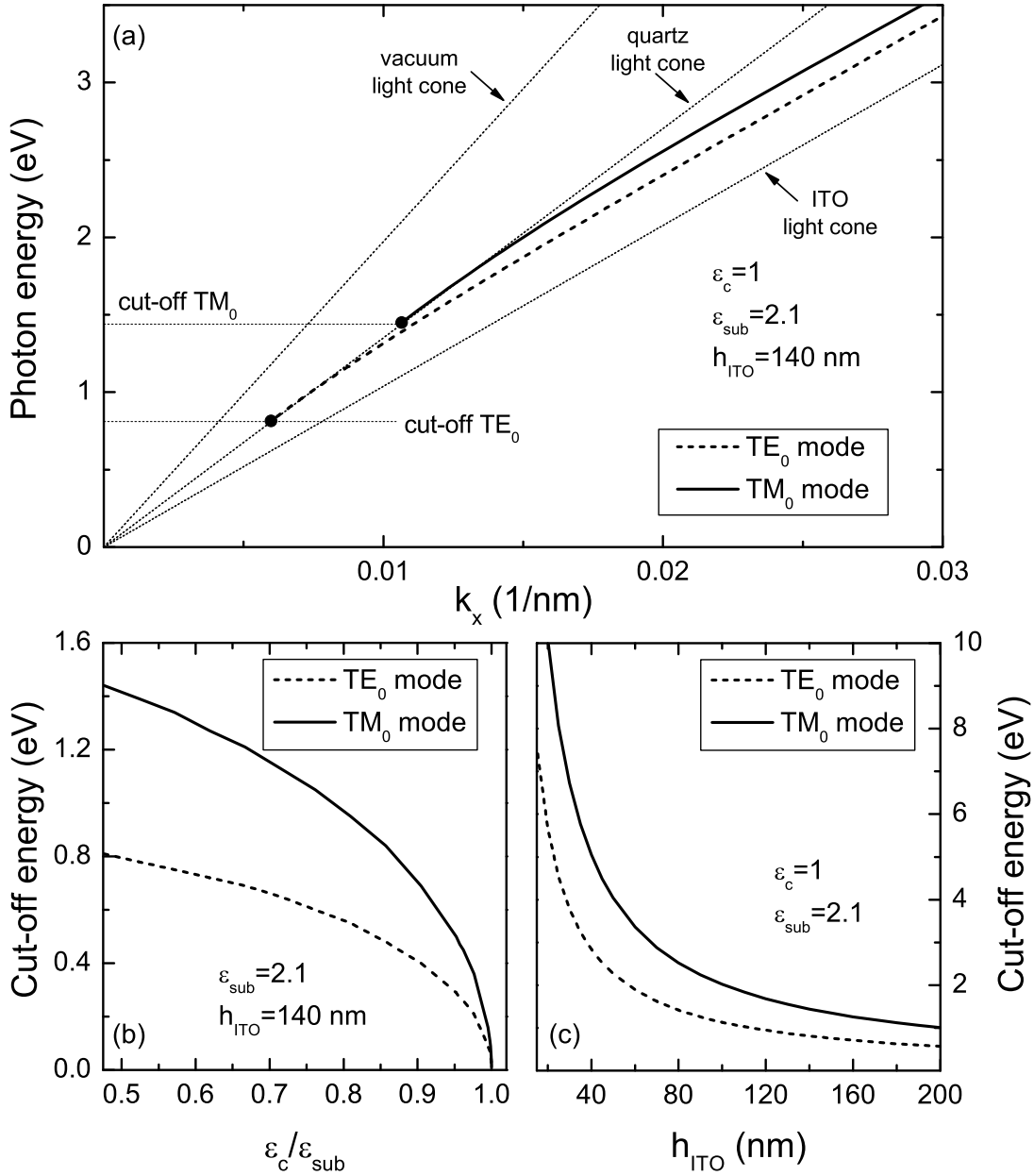
Figure 3.2:   The dispersion relation of the TE_0 and TM_0 modes are shown in panel (a). A slab thickness of 140 nm has been assumed for these calculations (ε_{sub}=2.1, ε_{ITO}=3.61, and ε_c=1). The dependence of the cut-off energies on the ratio of the dielectric functions ($\varepsilon_c/\varepsilon_{sub}$) is depicted in panel (b). The influence of the waveguide layer thickness is shown in panel (c).

layer thickness (c). As already mentioned in the last section, the mode cut-off vanishes for structures with symmetrical cladding layers ($\varepsilon_{sub} = \varepsilon_c$). The

Figure 3.3:   Normalized spatial distribution of the electric field amplitudes in dependence on the propagation constant. A 140-nm-thick slab waveguide has been assumed for these calculations. The spatial position of the waveguide slab is marked by the two horizontal lines.

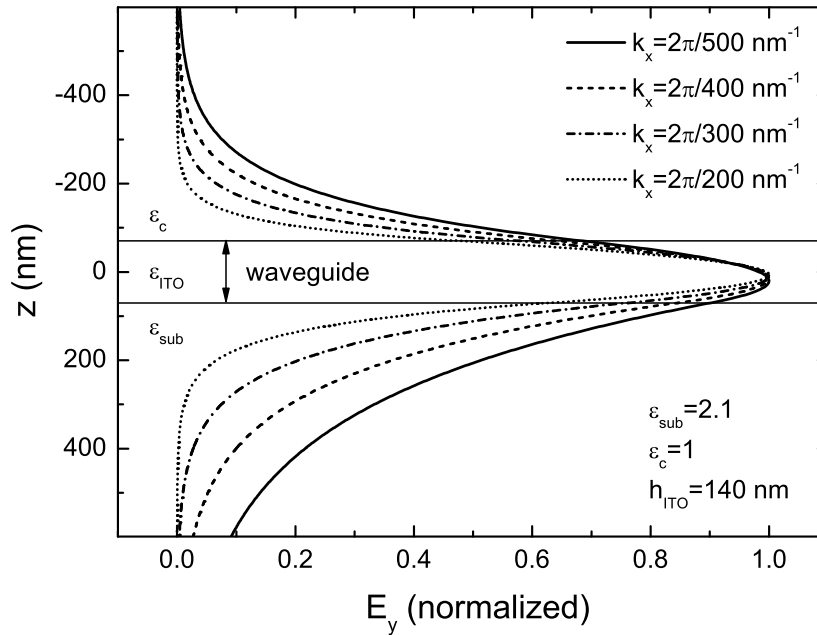first order mode of asymmetric structures on the other hand shows a strong thickness dependence. While the variation of the cut-off energy is only marginal for structures with thicknesses exceeding 140 nm, the cut-off energy increases rapidly for thinner slab geometries.

It is quite revealing to take a closer look at the field distribution of the guided modes. Fig. 3.3 displays the normalized spatial distribution of the electric field amplitudes of the TE_0 mode along the z-axis in dependence on the propagation constant k_x. Similar to Fig. 3.2 (a), a 140-nm-thick asymmetric slab structure ($\varepsilon_{sub}=2.1$, $\varepsilon_{ITO}=3.61$, and $\varepsilon_c=1$) has been assumed for the depicted calculations. In contrast to uniform slab geometries ($\varepsilon_{sub} = \varepsilon_c$), where a classification into symmetric and antisymmetric modes is possible e.g., see Ref. [1]), the field distribution of the guided modes possesses no mirror symmetry with respect to the waveguide plane. The figure shows that the spatial confinement of the TE_0 mode is continuously reduced when approaching the cut-off condition. While a more symmetrical spatial field distribution can be found for larger values of k_x (the field is concentrated within the core of the waveguide), the extension of the evanescent tail into the quartz substrate is strongly enhanced for smaller propagation
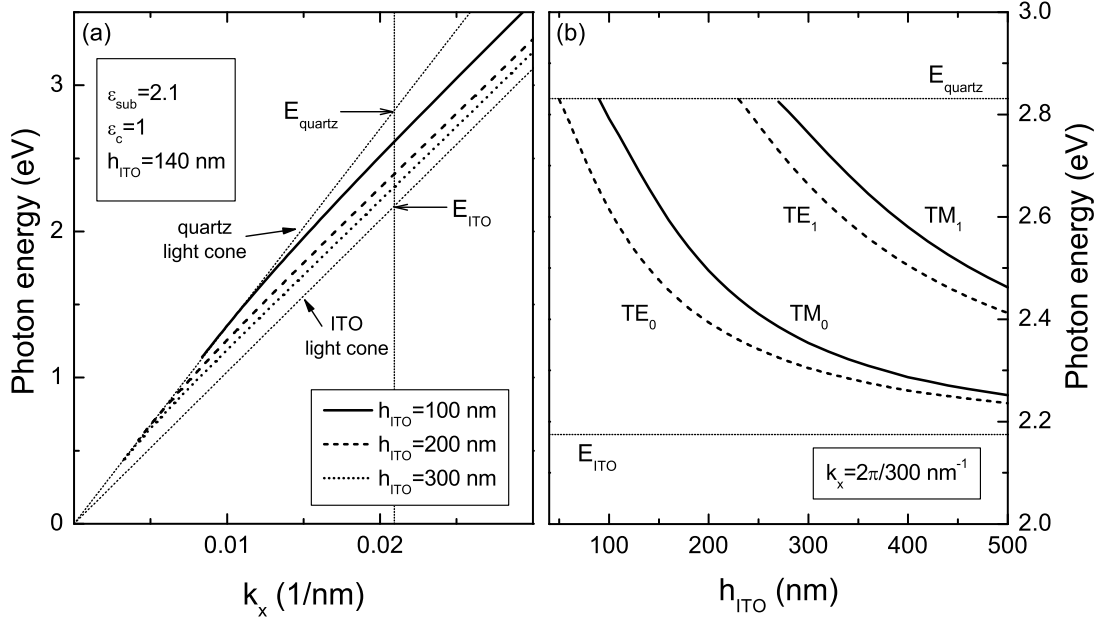
Figure 3.4:   The dispersion relation of the TE_0 mode is shown in panel (a) for various waveguide layer thicknesses h_{ITO}. Panel (b) displays the mode energies for constant $k_x = 2\pi/300$ nm^{-1} in dependence on the waveguide thickness for TE and TM polarization. The assumed propagation constant is marked by a vertical line in panel (a).

constants. Naturally, the spatial field distribution directly reflects the calculated dispersion relation. Due to the enhanced field concentration within the ITO waveguide, the dispersion relation is asymptotically approaching the ITO light cone for larger values of the propagation constant k_x. Contrary, the increased spreading of the field into the quartz substrate near the cut-off energy explains that the dispersion can be approximated by the substrate light cone for smaller in-plane momentum. Similar results can be obtained for TM polarization when plotting the H_y field component (not shown).

The dispersion relation of the TE_0 mode is depicted in Fig. 3.4 (a) in dependence on the waveguide layer thickness. While the dielectric functions remain unchanged (ε_{sub}=2.1, ε_{ITO}=3.61, and ε_c=1), the slab thickness is increased from $h_{ITO} = 100$ nm to $h_{ITO} = 300$ nm. An increased thickness h_{ITO} leads to a lowering of the cut-off energy (see also Fig. 3.2 (c)) and a shift of the dispersion relation. This behavior is elucidated in Fig. 3.4 (b), where the mode energies are plotted for a constant in-plane momentum of $k_x = 2\pi/300$ nm^{-1} and core thicknesses ranging from 40 nm up to 500 nm. The dependencies for TE and TM polar-

ized modes are shown, respectively. For an increased waveguide layer thickness, the mode energies for a given propagation constant asymptotically approach the corresponding value for propagation in bulk ITO. Note that this observation is equivalent to an enhanced spatial confinement of the guided modes inside the waveguide slab.

3.3 Eigenmodes of photonic crystal slab structures

Now that some of the basic properties of homogeneous waveguide slabs have been presented, we will extend the discussion to photonic crystal slabs in the next section. The confined modes of a dielectric waveguide become leaky in character when an additional surface modulation is introduced. Due to Bragg-scattering and therefore coupling of the guided modes with the photon continua in vacuum and substrate, so-called quasiguided modes appear as sharp spectral features in the transmission and reflection spectra. Especially the optical properties near the second-order stopband will be reviewed shortly. The considered photonic crystal slab geometry has already been depicted in Fig. 3.1. In contrast to more common two-dimensional structures, a simpler one-dimensional geometry will be used to highlight the underlying fundamental optical phenomena. Note that the presented discussion is limited to the lowest modes in TE polarization only. TM polarization and higher order modes have been neglected for simplicity reasons.

3.3.1 Band structure: Empty-lattice approximation

Generally, if a corrugation with period d_x is introduced along the guiding direction, the remaining electric field component in TE polarization can be expressed in a Bloch-Floquet form

$$E_y(x, z) = \sum_{g=-\infty}^{\infty} E_g(z) e^{i(k_x + gK_x)x} \tag{3.15}$$

with $K_x = 2\pi/d_x$. Again, this transverse field component has to satisfy the corresponding wave equation (see Eq. 3.2). In contrast to homogeneous waveguides, now a dielectric function of the form $\varepsilon(x, z) = \varepsilon(x + d_x, z)$ has to be considered, which actually contains all of the structural information of the periodic photonic crystal slab. The dispersion relation of the formerly guided modes then evolves
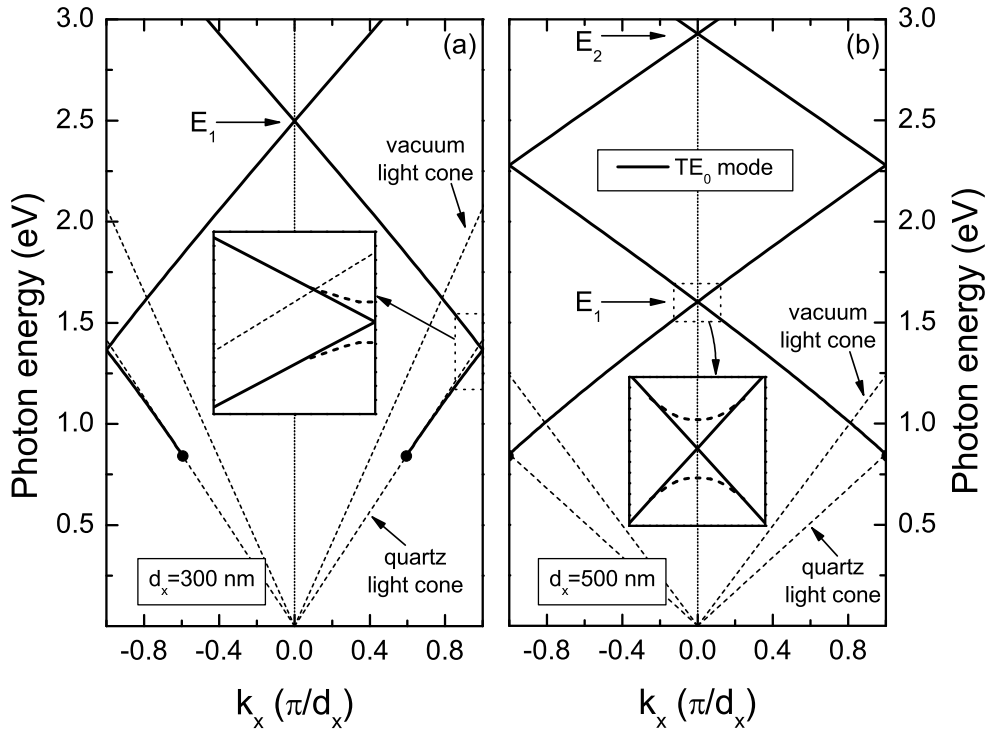
Figure 3.5: Dispersion relation for a corrugated 140-nm-thick ITO slab waveguide in empty-lattice approximation. The folding of the dispersion lines is depicted for two different periods (a: $d_x = 300$ nm and b: $d_x = 500$ nm). The insets allow a magnified view on the crossing regions. The expected repulsion of the modes and the formation of stop-bands is indicated schematically by the dotted lines.

into various branches of a more complex band diagram. In empty-lattice approximation, this band diagram can simply be obtained by folding of the dispersion relation of the unmodulated structure (assuming a slab with effective dielectric index) into the first Brillouin zone of the modulated structure.

Exemplary, the folding of the guided modes is depicted in Fig. 3.5. The two panels display the band structures for identical slab geometries but assuming different modulation periods. First, the dispersion of the lowest order guided mode (TE_0 mode) of a homogeneous and 140-nm-thick ITO waveguide deposited on top of a quartz substrate has been calculated. Second, this dispersion relation of the homogeneous slab has been folded into the first Brillouin zone of the corrugated structure. While a period of $d_x = 300$ nm has been taken into account for the folding in panel (a), an increased period of $d_x = 500$ nm has been considered in panel (b). The dispersion relation of the photonic crystal slab is now characterized

by degenerated Bragg resonances at the center ($k_x = 0$) and the border ($k_x = \pm\pi/d_x$) of the first Brillouin zone. Furthermore, the band diagram of the photonic crystal slab shows two types of eigenstates. In addition to the still existing guided modes with infinite lifetimes, especially the appearance of quasiguided modes with finite lifetimes well above the quartz and vacuum light cones is one of the most striking features. Note that the obtained band diagrams depend strongly on the exact geometrical parameters of the assumed structure. For example, only the photonic crystal slab structure with a periodicity of $d_x = 300$ nm exhibits a guided band below the quartz light cone. This observation can be clearly related to the asymmetry of the considered slab design. Only symmetric structures ($\varepsilon_c = \varepsilon_{sub}$) support at least one guided band below the substrate light cone due to the vanishing cut-off for the zero-order modes.

As already mentioned earlier, resonant anomalies appear in the transmission and reflection spectra of planar photonic crystal slab structures due to excitation of quasiguided modes well above the substrate and vacuum light cones. Diffraction orders of the incident plane wave [$\propto \exp(i\mathbf{kr} - i\omega t)$] are phase matched to spatial harmonics of a leaky wave propagating along the modulated waveguide slab (x-direction). More precisely, the one-dimensional surface corrugation couples an incoming wave with frequency ω and wave vector

$$\mathbf{k} = (k_x, k_y, k_z) = \frac{\omega}{c}(\sin\vartheta, 0, \cos\vartheta) \tag{3.16}$$

with all Bragg harmonics of the same frequency. The corresponding Bragg harmonics reflected into the upper cladding layer ($\varepsilon_n = \varepsilon_c$) and transmitted into the substrate ($\varepsilon_n = \varepsilon_{sub}$) can be described by

$$\mathbf{k}^{\pm}_{\mathbf{G},n} = (k_{x,\mathbf{G}}, k_{y,\mathbf{G}}, \pm k_{z,\mathbf{G},n}) = \left(k_x + G_x, \; 0, \pm\sqrt{\frac{\omega^2}{c^2}\varepsilon_n - (k_x + G_x)^2}\right) \tag{3.17}$$

where the reciprocal lattice vector is given by

$$G_x = \frac{2\pi}{d_x}g, \quad g = 0, \pm 1, \pm 2, \pm 3, \dots . \tag{3.18}$$

These Bragg harmonics can be either propagating ($k^2_{z,\mathbf{G},n} > 0$) or evanescent ($k^2_{z,\mathbf{G},n} < 0$) in character [130]. At the lowest band in the center of the first Brillouin zone (E_1 in Fig. 3.5) for example, three different waves are coupled by the photonic crystal slab at normal incidence. While the zeroth diffraction order ($g = 0$) is propagating perpendicularly to the slab, the first diffraction orders ($g = \pm 1$) are phase matched with leaky modes of the photonic crystal slab. The two excited counter-propagating waves with momentum $k_{x,\mathbf{G}} = \pm 2\pi/d_x$ form a

standing wave, which is again scattered by the surface corrugation. Interference between the directly transmitted and the diffracted components then lead to sharp variations in the reflected and transmitted field intensities. The second band at the center of the Brillouin zone (E_2 in Fig. 3.5) on the other hand originates from the excitation of a standing wave with $k_{x,\mathbf{G}} = \pm 4\pi/d_x$. Now the zeroth and the first diffraction orders into vacuum and substrate are opened.

As we will show later on in more detail, the real band structure of a one-dimensional photonic crystal slab will differ from the shown approximative solution. Especially at the high symmetry points of the first Brillouin zone, modifications of the dispersion relation have to be considered. When two dispersion branches cross, they repel each other (degeneracy is lifted) and small photonic stopbands are formed. This fact, i.e. the flattening of the bands near the appearing gaps, is schematically shown by the two insets of Fig. 3.5.

3.3.2   Excitation of leaky modes

More precise results can be obtained by applying rigorous calculation techniques. We used a scattering-matrix based method [130] to determine the exact positions and the specific line shapes of the leaky modes of photonic crystal slab structures. Generally, this formalism allows for the calculation of transmission, reflection and absorption spectra of periodically modulated multilayer structures without using any fit parameters. Only the assumed geometrical design of the structure and the known dielectric functions of the materials were taken into account to determine the optical response.

To illustrate the accuracy of the applied theoretical method, Fig. 3.6 shows measured (a) and calculated (b) transmission spectra of a metallo-dielectric photonic crystal slab structure for normal light incidence ($\vartheta = 0°$, see Fig. 3.1) and TE polarization. The sample structure was fabricated by electron beam lithography and consists of a metal nanowire grating on top of a 140-nm-thick ITO waveguide deposited on a quartz substrate. A nanowire cross-section of 100×20 nm^2 and a grating period of $d_x = 501$ nm has been used for the theoretical simulation in panel (b). While the dielectric function of gold was taken from Ref. [112], the corresponding ITO values have been approximated by the relation $\varepsilon_{\mathrm{ITO}}(\lambda) \approx 1 + 1.81302\lambda^2/(\lambda^2 - 0.07597)$ [157].

Both spectra are characterized by a narrow transmission dip at approximately 1.69 eV. This spectral feature can be directly related to the resonant excitation
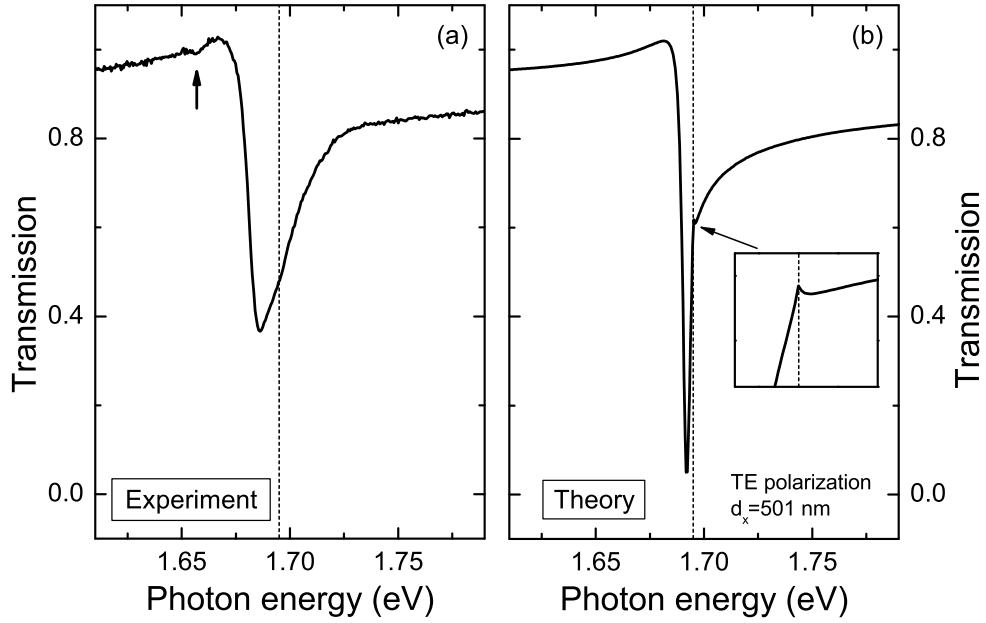
Figure 3.6: Measured (a) and calculated (b) transmission spectra of a metallo-dielectric photonic crystal slab structure ($h_{\mathrm{ITO}} = 140$ nm) for normal light incidence. Only spectra for TE polarization are shown. A gold nanowire period of 501 nm has been assumed for the calculated spectra in panel (b). The position of the Rayleigh anomalies is marked by vertical dotted lines. The arrow in panel (a) denotes the position of the antisymmetric mode.

of the lowest order leaky mode of the grating-waveguide structure. The narrow spectral bandwidth (high quality factors) implies a relatively long lifetime of these quasiguided modes. Note that the resonance exhibits a non-Lorentzian line shape. This spectrally asymmetric response can be related to the Fano-type nature of the resonance [158], which originates from interference between a direct and a resonance-assisted indirect pathway [152, 159]. While the qualitative agreement between both spectra is quite good, especially the comparison of the spectral bandwidths shows large differences. First, sample imperfections (e.g., fluctuations of the grating period, surface roughness) lead to an inhomogeneous broadening of the measured resonance. These effects were not taken into account during the theoretical simulations. Second and perhaps more important, also the finite number of nanowires and the finite diameter of the incident beam have to be considered in more realistic calculations. In contrast to the assumed theoretical conditions, the incident beam is not a plane wave and also the achievable grating size is strictly limited. Due to restrictions of the used electron beam system, the

grating extension for example was restricted to 100×100 μm^2. Therefore only 200 grating lines have been illuminated by the incident light wave, reducing the spectral resolution and the efficiency (energy will leak out laterally at the edges of the grating) dramatically. In contrast to electron beam lithography, especially optical interference lithography allows for structuring of larger regions. Therefore better experimental results, i.e., sharper resonances are expected to appear. The possible influence of Gaussian beams and the finite number of illuminated nanowires have already been investigated in connection with guided-mode resonance filters (see, e.g. Ref. [160] and Ref. [161]).

Although the formation of a second order stopband at the center of the first Brillouin zone is expected, the anticrossing behavior (e.g., appearance of two modes at the Γ point) is generally not observable in measurements at normal incidence. Symmetry considerations clearly point out that only one of the appearing modes is of leaky nature (symmetric mode) [1]. The additional antisymmetric mode is optically inactive (dark mode) and is not accessible at normal incidence [163]. We have to point out that, in contrast to the calculations (assumption of plane waves), the finite aperture of the experimentally used light beam has to be considered. It can lead to a weak excitation of the antisymmetric mode even under normal incidence. This fact is also observable in Fig. 3.6 (a), where the antisymmetric mode (indicated by the arrow) shows up as a weakly pronounced transmission dip. The related optical effects (e.g., dispersion properties) will be discussed in more details later on.

A very remarkable point is the appearance of the so-called Rayleigh anomaly near the transmission minima. The position of this feature is marked by a dotted vertical line in both panels. While the anomaly shows up as a cusp-like feature in the calculated spectra (see inset of Fig. 3.6), the sharp anomaly can not be observed in the presented experimental data (only a weak asymmetry can be anticipated at the position of the expected Rayleigh anomaly). This fact might be explained by inhomogeneous broadening or insufficient angular resolution of the experimental setup. The appearance of Rayleigh anomalies is directly related to the opening of new diffraction orders into the substrate or cladding layers [154]. Here the visibility of this anomaly is strongly enhanced due to the overlap with the resonant mode of finite linewidth.

As has already been shown in chapter 2, the considered metal nanowire gratings

---

[1]Note that this implication generally does not apply for photonic crystal slab structures with asymmetric unit cells (e.g., see Ref. [162])
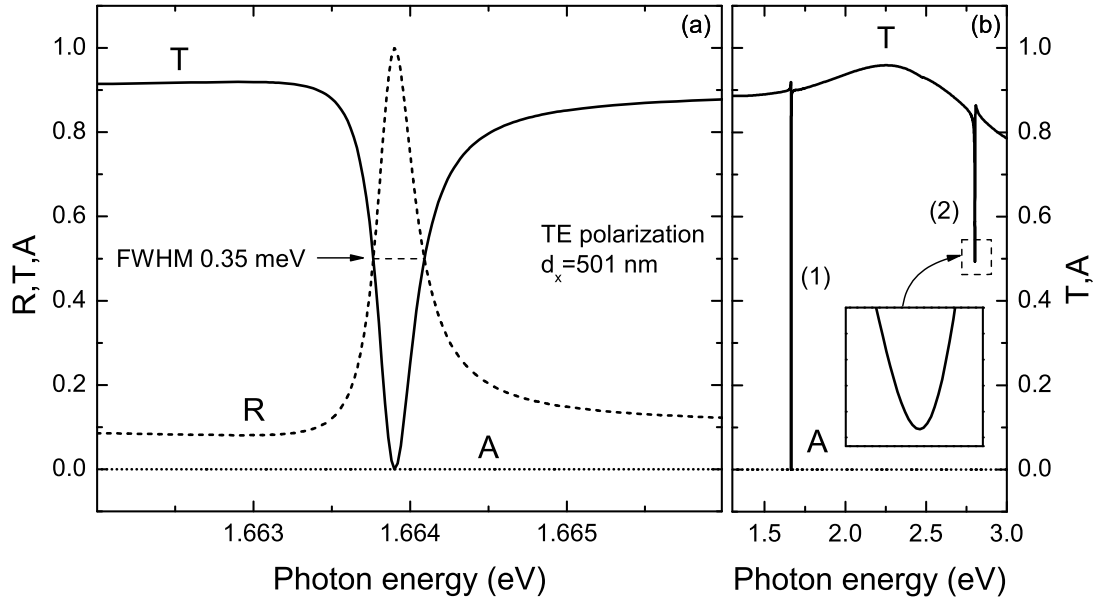
Figure 3.7:   Calculated transmission (T: solid line), reflection (R: dashed line), and absorption (A: dotted line) spectra of a dielectric photonic crystal slab structure (h_{ITO} = 140 nm) for normal light incidence and TE polarization. ITO nanowires (100×20 nm^2) with a period of 501 nm have been assumed for the shown simulations. Only the first (1) Bragg resonance at the Γ point is shown in panel (a). Panel (b) displays the same spectra (T,A) on a larger scale. The inset of panel (b) allows a magnified view on the transmission minimum of the second order Bragg resonance (2).

can support particle plasmon resonances in case of TM polarization. Therefore a simultaneous excitation of quasiguided modes and plasmon resonances of metallo-dielectric structures will be possible under certain conditions. The appearing interaction phenomena, e.g., the formation of a waveguide-plasmon polariton, will be presented in chapter 4 of this work.

The optical response of a dielectric photonic crystal slab structure is shown in Fig. 3.7. The gold grating on top of the 140-nm-thick ITO waveguide is replaced by an ITO grating with a periodicity of $d_x = 501$ nm. The individual nanowires possess a cross-section of 100×20 nm^2. Calculated transmission (T), reflection (R), and absorption (A) spectra of the lowest order Bragg resonance are shown in panel (a) for TE polarization and normal light incidence. Panel (b) displays the calculated transmission and absorption spectra on a larger scale.

Sharp resonant features appear in the shown transmission and reflection spectra

due to excitation of quasiguided modes of the waveguide slab. Note that the idealized dielectric ITO structures exhibit no absorption. Therefore, in contrast to the gold nanowire case, the specular reflectivity equals unity in the vicinity of phase-matched excitation of the lowest order leaky TE_0 slab mode (1). Only the zeroth forward- and backward- diffracted waves propagate with all higher-order waves cut off. This high reflectivity and especially the narrow spectral bandwidth lead to their application as efficient filter devices. For example, a linewidth of only 0.35 meV has been calculated for the assumed ITO-based grating structure. Further on, it is intriguing to compare the two lowest Bragg resonances of the TE_0 mode at the center of the Brillouin zone. Therefore the region of interest is shown on a larger scale in panel (b). The spectrum consists of two sharp resonances, superimposed upon a smoothly varying background (Fabry-Perot oscillations due to the multilayer geometry). While the lowest order resonance (1) is characterized by a sharp dip with zero transmissivity, the second Bragg resonance (2) allows for resonant transmission. This fact can be related to opening of the first diffraction orders into vacuum and substrate which results in a weakening of the zeroth order diffraction efficiency.

3.3.3   Lineshape analysis: Fano resonances

As well-known from solid-state and atomic physics, the interference of a discrete state with a continuum gives rise to characteristically asymmetric peaks in the related spectra. Such interference effects are commonly referred to as Fano resonance phenomena [158]. Generally, also the discussed quasiguided photonic crystal slab modes are characterized by a Fano-type line shape in the optical transmission and reflection spectra. Considering the one-dimensional grating-waveguide structures, the line shape of the supported waveguide resonances in the transmission spectra can be explained by the interference of direct and indirect transmission pathways. More precisely, the directly transmitted fraction of the incident radiation interferes with the light field components which are resonantly scattered in the forward direction. The observable asymmetric line shapes are generally very sensitive to the the exact geometry of the considered structure. Depending on the specific slab design and the induced phase differences between both transmission pathways, strong modifications can be detected.

Exemplarily, the theoretical transmission spectra of two different grating-waveguide structures are displayed in Fig. 3.8 to highlight the induced line shape changes. The considered sample structures are each based on a 140-nm-thick ITO slab
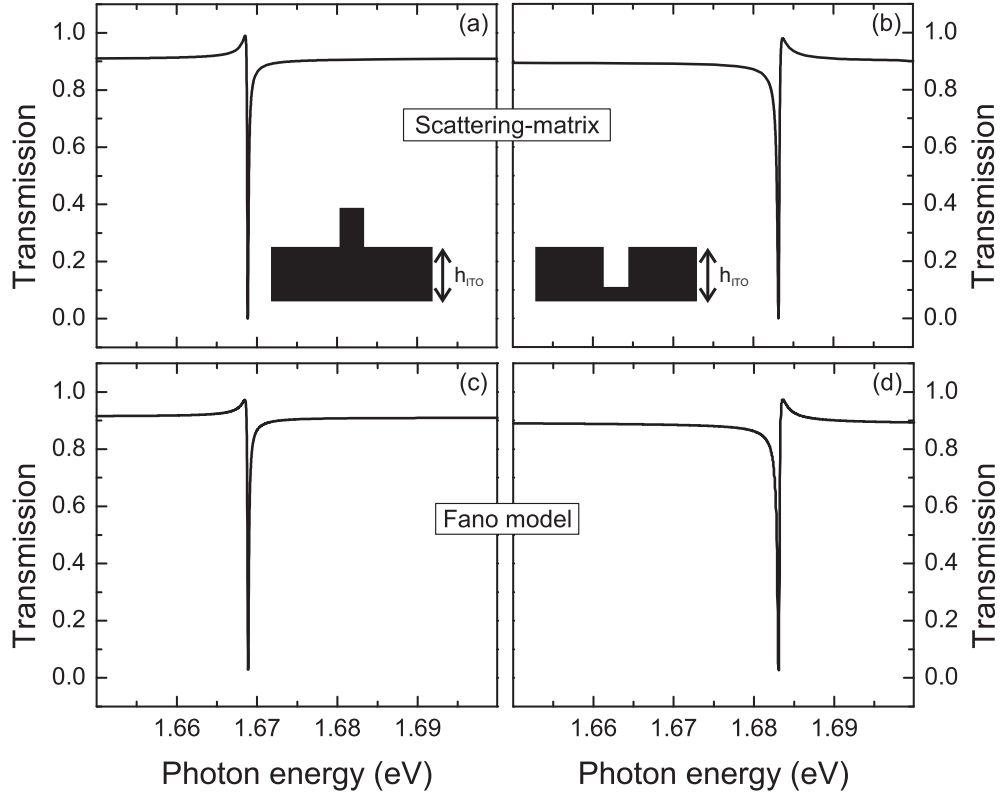
Figure 3.8: Comparison between scattering-matrix based calculations (a,b) and simulations using a simple Fano-type model (c,d). Transmission spectra for two different grating-waveguide geometries are shown. The structures consist of 140-nm-thick ITO waveguide slabs with a periodic surface corrugation ($d_x = 500$ nm). Either wires or slits with an identical cross-section of 20×100 nm^2 have been used for the rigorous calculations in the two upper panels.

waveguide deposited on top of a quartz substrate. Only the assumed surface corrugation is introduced in two different ways. A periodic arrangement of ITO nanowires with a cross-section of 20×100 nm^2 has been used for the scattering-matrix calculation in panel (a). For the calculation of the spectrum in panel (b), the individual nanowires have been replaced by slits with an identical cross-section. Both the nanowire as well as the slit structure exhibit a period of $d_x = 500$ nm. The theoretical transmission spectra are shown for normal light incidence and TM polarization, respectively.

Fig. 3.8 clearly demonstrates the strong influence of the specific slab design and the induced line shape modifications. In the course of the inversion of the surface modulation (i.e., slits instead of wires), also the symmetry of the single dispersive transmission anomaly is reversed. The observed anomalies in panels (a) and (b)

can be identified as being caused by the excitation of the lowest order leaky TM_0 slab mode. Due to the Fano-type nature of the resonance and the use of non-absorbing slab material (i.e., absorption of ITO is neglected) the transmission varies from 0 to 1 over a very narrow energy range. Neither the transmission maximum nor the transmission minimum specify the exact resonance position.

The Fano resonance line shape in the optical transmission spectra can be easily explained by a very intuitive model which has originally been proposed in Ref. [152]. Within this model, the transmittance t and the reflectance amplitude r are expressed as a sum of two coefficients:

$$t = t_d + f \frac{\gamma}{i(\omega - \omega_0) + \gamma}, \qquad (3.19)$$

$$r = r_d \pm f \frac{\gamma}{i(\omega - \omega_0) + \gamma}. \qquad (3.20)$$

Away from the resonance, the optical properties are simply determined by the direct transmission t_d and reflection coefficients r_d. The parameters generally describe the slowly varying background of the spectra. Approaching the resonance, indirect transmission has to be taken into account. The second term in the equations therefore describes the resonance-assisted pathway. Here ω_0 and γ are the center frequency and the homogeneous linewidth of the Lorentzian resonance. The parameter f, which has to satisfy the condition

$$f = -(t_d \pm r_d), \qquad (3.21)$$

specifies the complex amplitude of the resonance mode [152].

To explore the capability of the intuitive approach, simulation results thus obtained are presented in panels (c) and (d) of Fig. 3.8. The displayed spectra allow a direct comparison between the rigorous calculations (upper panels) and the Fano model (lower panels). The coefficients t_d and r_d have been obtained by fitting the background to the optical response of a uniform slab with an adjusted effective dielectric permittivity (e.g., see Ref. [113]). A good agreement with the numerically results in panel (a) can be achieved when assuming a Lorentzian with a resonance energy of 1.669 eV and a linewidth of 0.1 meV. For a matching with the results in panel (b), the resonance energy has to be slightly shifted to 1.683 eV. Simultaneously, the homogeneous width of the resonance has to be increased to 0.15 meV. The modified symmetry of the lineshape is taken into account by using the minus sign in Eq. 3.21.

In Fig. 3.8, it is clearly demonstrated that the calculated spectra in panels (a) and (b) can be modeled with the intuitive Fano approach. The corresponding spectra agree more or less completely. Thus, in addition to the qualitative explanation of the observed lineshape asymmetries, the Fano model allows a more exact determination of the resonance frequency. For example, it might be possible to extract the position and the width of a resonance by fitting the measured data with the simulated spectra.

3.3.4   Narrow spectral bandwidth: Filter applications

Before resuming the discussion of the photonic crystal band diagram near the second-order stop band in the next section, especially focusing on measurements at inclined incidence, we will present some important geometrical aspects first. It will be shown that the optical response can be altered by the specific design of the considered photonic crystal slab structures. Theoretical calculations reveal that the lifetime of the quasiguided modes (and hence their linewidth) is strongly influenced by the geometry of the grating structure. Our observations confirm the well-known requirements for the development of narrow-band reflection filters.

Both experimentally and theoretically, a lot of scientific effort has been devoted to the investigation of possible technological applications of periodically corrugated waveguide structures. While a substantial number of papers have focused on integrated optics using first-order gratings (e.g., distributed-feedback lasers [164]), also second-order gratings ($\lambda \simeq d_x$) are of potential interest. In contrast to classical multilayer structures (e.g., thin-film Fabry-Perot stacks), especially grating-waveguide structures represent an alternative solution of realizing narrow-band reflection filters or modulators in the optical regime. As we have already shown in the last section, it is not surprising that in the case of absence of any absorption the usage of the resonant grating anomalies would theoretically yield polarization-sensitive narrow-band reflection filters with 100% peak reflectance. After first theoretical investigations (e.g., Ref. [165–169]), highly efficient grating-waveguide filters with a bandwidth below 1 nm and above 90% peak (resonant) reflectance have been demonstrated experimentally. Both dielectric [170–172] as well as metal-based [173] structures have shown their capability recently.

Although the optical properties of grating-waveguide filters have been investigated intensively in recent years, we will demonstrate some of the important geometrical requirements in the following. Basically, two important geometrical

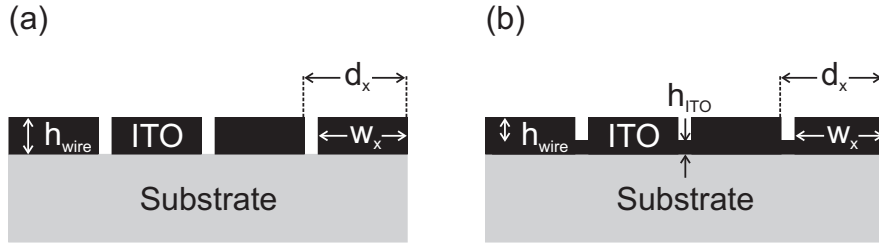(a)   (b)

Figure 3.9: Schematic view of possible grating-waveguide filter geometries. Both structures consist of corrugated 140-nm-thick ITO slab waveguides. Panel (a) displays a slab structure with etched slits. The design of panel (b) exhibits a weaker surface modulation. The influence of the parameters w_x and h_{ITO} on the calculated spectral bandwidth will be investigated.

parameters affect the spectral bandwidth of the observed quasiguided modes [170, 174]. First, an extremely narrow linewidth can be obtained by using photonic crystal slab structures that exhibit only a weak modulation of the dielectric constant along the guiding layer. Second, also the thickness of the surface modulation (h_{wire}) has to be minimized to cause reasonably sharp resonances. Exemplary, two different slab geometries have been investigated theoretically to illustrate the important dependencies. One possible design is displayed in Fig. 3.9 (a). Instead of directly probing the influence of different dielectric materials, only the effective permittivity of the waveguide slab is modified. The structure consists of a nanowire grating on top of a quartz substrate. The individual ITO nanowires are arranged with a period of $d_x = 500$ nm and exhibit a thickness of $h_{\mathrm{wire}} = 140$ nm. A vacuum half space is assumed as upper cladding layer. While all other parameters have been kept unchanged, only the nanowire width w_x has been modified in the theoretical simulations. Note that no additional waveguide layer was introduced, so the grating structure itself has to provide the required optical confinement. Due to the specific geometry, the effective permittivity of the considered slab structure is given by $\varepsilon_{eff} = [\varepsilon_{\mathrm{ITO}}w_x + \varepsilon_{air}(d_x - w_x)]/d_x$. In a second structure, as displayed in Fig. 3.9 (b), the influence of the geometrical modulation strength is probed. Therefore an ITO waveguide slab of thickness h_{ITO} on top of a quartz substrate has been assumed. Now the additional ITO nanowire grating acts as surface corrugation. While the period of $d_x = 500$ nm, the width $w_x = 480$ nm, and the overall thickness of 140 nm ($h_{\mathrm{ITO}} + h_{\mathrm{wire}}$) have been retained unchanged, only the aspect ratio between h_{wire} and h_{ITO} has been modified.

The numerical results for both geometries are depicted in Fig. 3.10 (a) and (b),
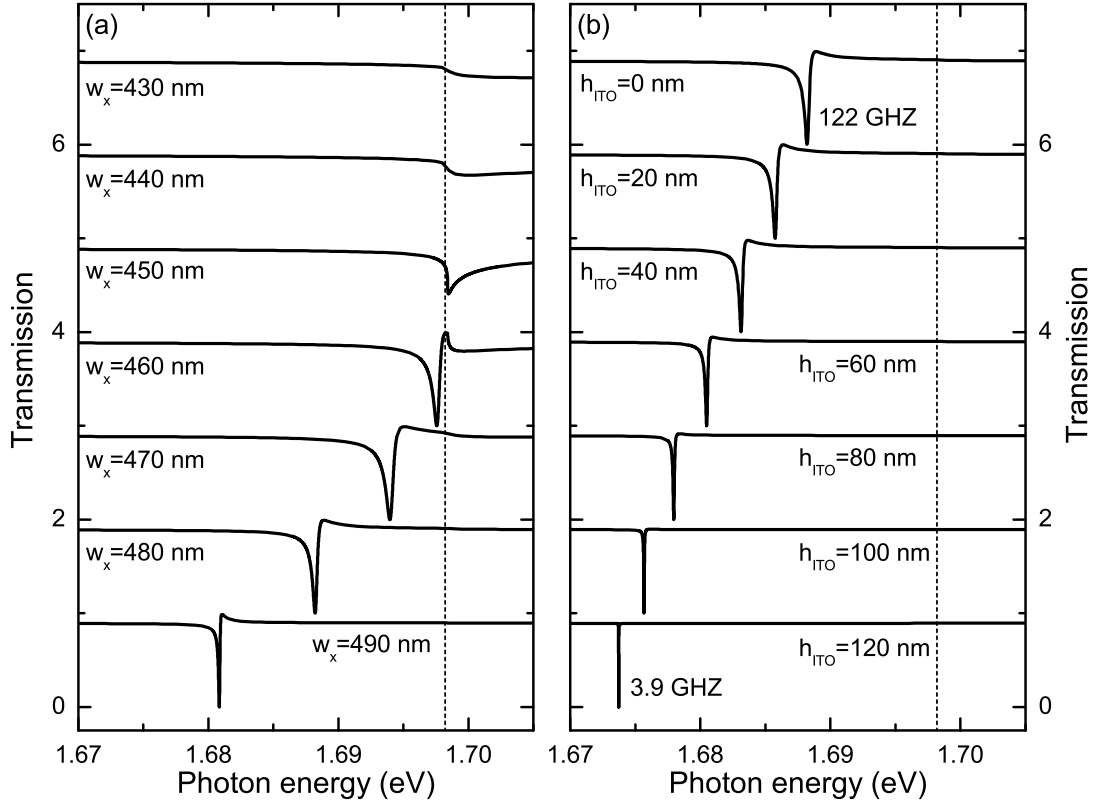
Figure 3.10:   Calculated transmission spectra of dielectric grating-waveguide structures are shown for normal light incidence and TE polarization. The structures of panel (a) consist of ITO nanowire gratings on top of a quartz substrate. No additional waveguide layer was used. While the nanowire thickness of $h_{\mathrm{wire}} = 140$ nm and the period of $d_x = 500$ nm have been retained unchanged, the nanowire width w_x was increased from 430 nm to 490 nm. Additionally, the spectra of ITO nanowire arrays deposited on top of an ITO waveguide layer are depicted in panel (b). A constant period of $d_x = 500$ nm and a nanowire width of $w_{\mathrm{wire}} = 480$ nm have been assumed for these calculations. From top to bottom, the waveguide layer thickness h_{ITO} was increased from 0 nm to 120 nm. The nanowire height was determined by the relation $h_{\mathrm{wire}} + h_{\mathrm{ITO}} = 140$ nm. Vertical lines mark the spectral position of the Rayleigh anomaly.

respectively. Again the scattering matrix formalism has been used to calculate the shown transmission spectra assuming TE polarization and normal light incidence. From top to bottom, the individual nanowire width w_x of the first structure has been increased from 430 nm to 490 nm in panel (a). The second possibility, namely the variation of the aspect ration, is realized in panel (b). Here the
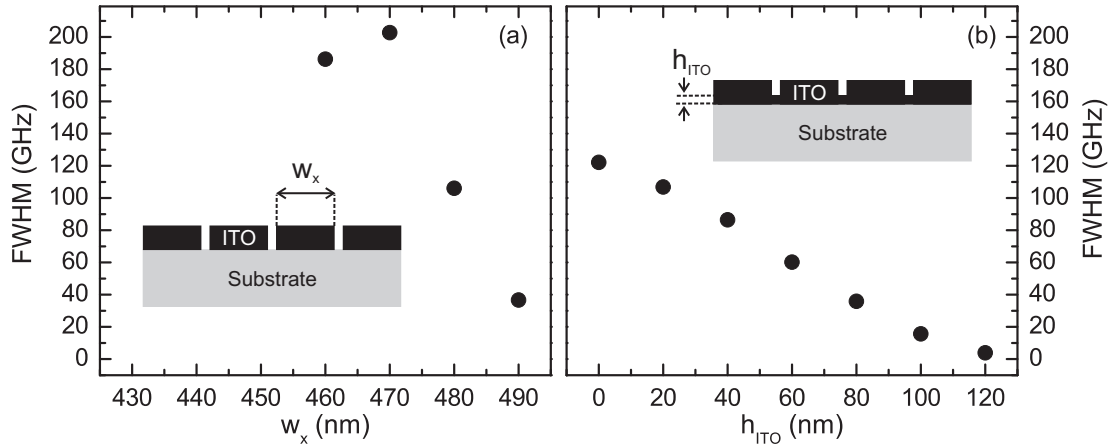
Figure 3.11:   Spectral bandwidth (FWHM) of the grating-waveguide resonances in dependence of the parameters w_x and h_{ITO}. The depicted values have been extracted from the numerical calculations shown in panels (a) and (b) of Fig. 3.10.

thickness of the homogeneous part of the waveguide h_{ITO} has been increased from 0 nm to 120 nm in steps of 10 nm. A strong modification of the optical response can be observed in panel (a). Note that the sharp resonance due to excitation of the lowest quasiguided mode (TE_0) does not show up in the transmission spectra until the nanowire width exceeds $w_x = 460$ nm. Simultaneously, while shifting to smaller energies, also the linewidth of the resonant anomaly is decreased. All resonant features are again characterized by a strongly asymmetric line shape due to their Fano-type nature. When the aspect ratio is minimized (reduction of the modulation depth) in panel (b), the spectral linewidth can be further reduced. Starting from a bandwidth of 122 GHz for structures with $h_{ITO} = 0$ nm, a spectral width of 3.9 GHz can be extracted for $h_{ITO} = 120$ nm. Simultaneously, also the line shape of the resonant features is getting more symmetric, i.e., the appearing sidebands are less pronounced. For the sake of completeness, the full width at half maximum (FWHM) of the individual transmission resonances (extracted form Fig. 3.10) is depicted in panels (a) and (b) of Fig. 3.11 in dependence on the parameters w_x and h_{ITO}.

The displayed theoretical transmission spectra and the extracted bandwidths of the waveguide anomalies clearly reveal that the optical response is directly related to the specific design of the assumed slab structure. For dielectric structures without absorption, the most narrow transmission dips, i.e., the longest lifetimes can be obtained by assuming only weakly modulated structures. As the modulation amplitudes vanish, the corrugated structure generally approximates a more or less homogeneous slab structure. The guided modes of planar structures are

characterized by its zero linewidth. Therefore, as $\varepsilon_{eff} \rightarrow \varepsilon_{\text{ITO}}$ (a) or $h_{\text{wire}} \rightarrow 0$ (b), also the bandwidth of the leaky modes tends to zero. In other words, the physical reason for this long lifetime is the reduced coupling to the external radiation fields.

It is further important to note that the considered resonant filter structures are characterized by an asymmetric slab design, i.e., the permittivity of the upper cladding layer (vacuum) differs from the substrate (quartz) value. As shown in panel (a) of Fig. 3.10, this fact has major influence on the optical response. If the effective permittivity of the waveguide layer is continuously reduced (e.g., decreasing the width of the individual nanowires), the appearing leaky modes are shifted to higher energies and finally cross the quartz light cone (marked as dotted vertical line). As a result, the mode confinement is lost because the first diffraction orders are now opened into the substrate (propagating Bragg harmonics). The sharp resonances disappear in the transmission spectra, and only the weakly pronounced cusp-like Rayleigh anomaly remains visible.

Although the presented theoretical calculation in principle predicts the possibility to obtain extremely narrow spectral bandwidths, especially the angular tolerance (e.g., see next section) of the proposed filter design is a limiting factor. As the incidence angle deviates from normal, the dispersion relation of the specific modes has to be taken into account (e.g., see next sections). The neglected divergence of an incident beam for example leads to a broadening of the theoretically observed transmission dips.

3.3.5   Second-order stopbands

It has been shown in the previous sections that the excitation of quasiguided modes results in sharp spectral features in the reflection and transmission spectra. Additional information on the band structure can be obtained when the investigation of photonic crystal slab structures is extended to measurements under oblique incidence. Generally, angular-dependent measurements can be used to map out the band structure of the leaky modes of periodically patterned slab waveguides [175]. We will use this experimental method to analyze the dispersion relation of the quasiguided modes near the lowest Bragg resonance at the center of the Brillouin zone (Γ-point) in the following. As already denoted in Fig. 3.5, clear evidence for the formation of a small stopband can be found.

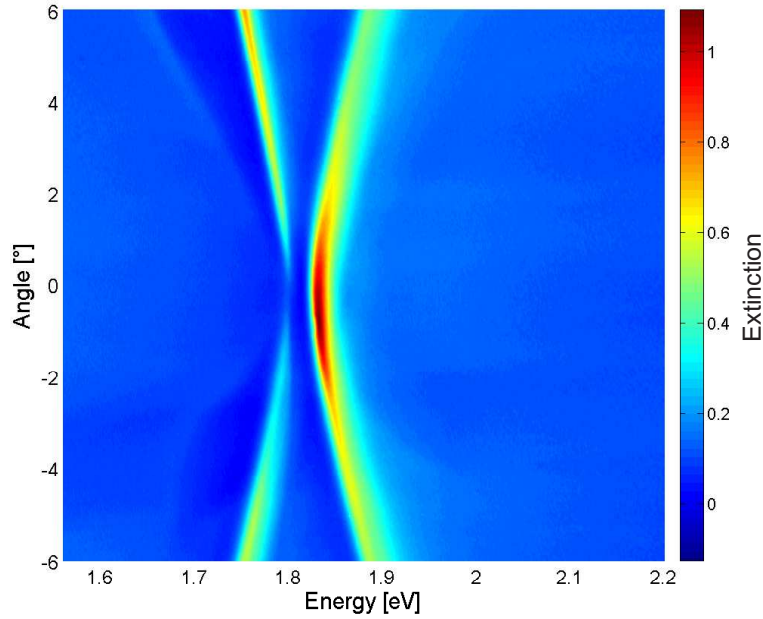The angular dependence of the resonant modes is depicted in Fig. 3.12. The

Figure 3.12:   Measured extinction spectrum of a gold nanowire array deposited on top of a 140-nm-thick ITO layer. The dependence on the angle of incidence ($-6° \leq \vartheta \leq 6°$) is shown for a fixed nanowire period of $d_x = 450$ nm and TE polarization.

contour plot displays the experimentally measured extinction data for a metallo-dielectric photonic crystal structure in dependence on the energy and the angle of incidence. A gold nanowire grating ($d_x = 450$ nm) on top of a 140-nm-thick ITO waveguide has been used for the plotted experimental results. Again, the individual nanowires of the grating exhibit a cross-section of approximately 100×20 nm^2. Only the results for TE polarization are shown. Note that the two-dimensional contour plot was derived from a single measurement. Instead of using pinholes to reduce the aperture of the light beam (see Appendix A) and turning the sample stepwise, the transmitted intensities of the focused beam were directly imaged onto the CCD detector array. The angular information ($-6° \leq \vartheta \leq 6°$) could be extracted by using a cylindrical lens (f=70 mm) in front of the entrance slit of the monochromator.

The experimentally measured dispersion diagram reveals two fundamental optical phenomena. First, as already depicted schematically in the last section, the displayed contour plot gives clear evidence for the formation of a small stop-band at the center of the Brillouin zone. The extinction contours follow the shape of the dispersion curves and a small anticrossing between the two branches

can be observed. Second and equally important, the figure additionally shows that only one of the existent eigenstates is optically active in transmission measurements at normal incidence. For this special excitation condition ($\vartheta = 0°$), the low-energy resonance vanishes in the extinction spectrum (bound mode with zero linewidth) while the upper mode can still be excited. Although the general form of the depicted dispersion diagram can be understood in terms of zone folding (e.g., empty-lattice approximation), especially the specific behavior at the zone center needs further explanation. In general, the second-order stopband at the center of the Brillouin zone originates from grating-induced coupling of two counter-propagating modes with momenta $\pm 2\pi/d_x$, respectively. As a result, the degeneracy of the modes is split at the crossing point and the formation of two eigenstates with inverse symmetry can be observed. For a structure with symmetric unit cell and on the basis of the resulting electric field distributions, the two eigenstates (standing waves) at the zone center can be classified into either symmetric or antisymmetric modes [130, 163, 176].

Symmetry considerations lead to the surprising result that the considered photonic crystal structure supports a truly bound mode above the vacuum light cone. In Fig. 3.12, the upper band-edge eigenstate corresponds to a symmetric mode with respect to the z_0 axis (see Fig. 3.1), and the lower one to an antisymmetric mode. Generally, antisymmetric modes cannot be excited by a symmetric illumination such as normal incidence. As important consequence, the lower band-edge eigenstate (antisymmetric mode) is a dark state. Only the upper eigenstate is optically active and possesses a leaky character. Note that the apperance of a bound mode has already been investigated in connection with second-order distributed feedback lasers [177]. It has been shown that scattering losses can be suppressed when the antisymmetric mode becomes a lasing mode. It is further important to remark that only the antisymmetric band-edge state at the second-order stopband is characterized by an infinite lifetime (zero linewidth). All antisymmetric modes due to higher Bragg resonances of the TE_0 mode are indeed optically inactive at normal incidence, but their linewidth on the other hand is nonzero (finite lifetime of the mode). This surprising fact can be related to the opening of higher diffraction orders. Starting from the second resonance at the zone center, also the antisymmetric modes can radiate Bragg harmonics into the vacuum and into the substrate [130].

In addition to the experimental measurements, scattering-matrix based calculations have been performed to highlight some of the related fundamental optical phenomena. The numerical simulations clearly demonstrate that both the width
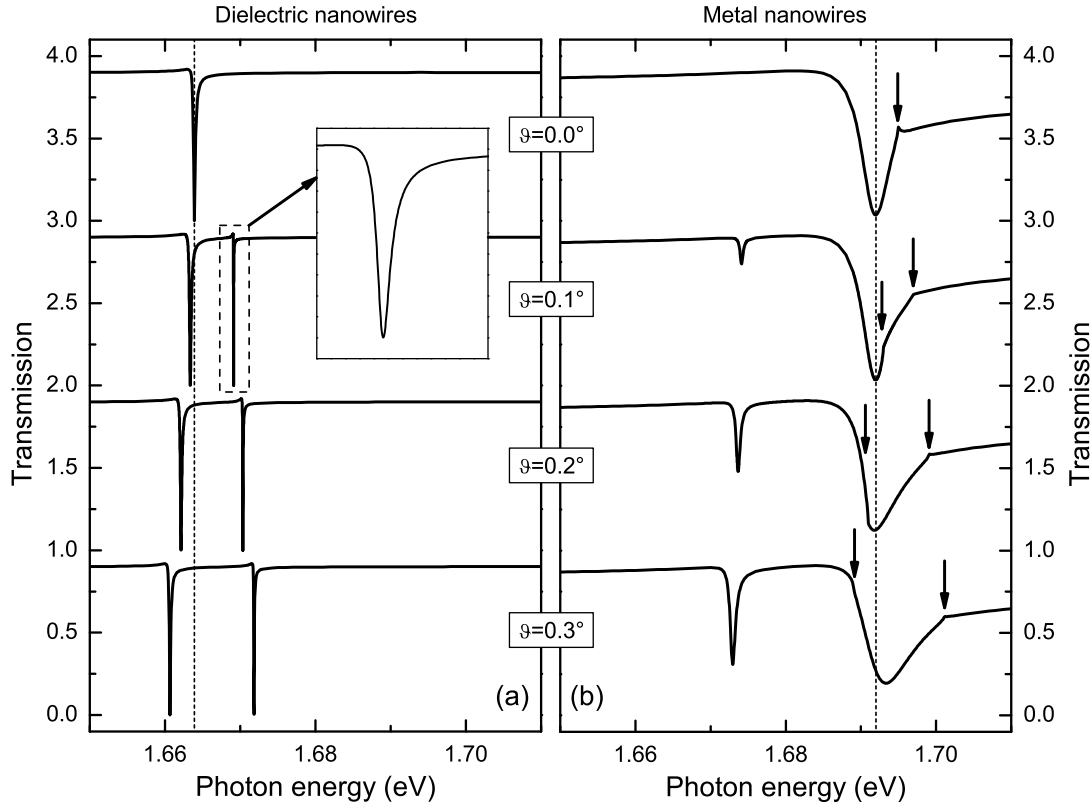
Figure 3.13:   Calculated transmission spectra for nanowire gratings on top of a 140-nm-thick ITO waveguide layer are shown in dependence on the angle of incidence (TE polarization). A nanowire period of 501 nm and a cross-section of 100×20 nm^2 have been assumed. While dielectric (ITO) gratings were used for the calculations of panel (a), results for metal based structures (gold) are depicted in panel (b). The arrows in panel (b)denote the spectral positions of the diffractive anomalies. The individual spectra are shifted upwards for clarity in each panel.

of the stopband as well as the symmetry of the band-edge eigenstates can be strongly influenced by the specific design of the photonic crystal slab. Fig. 3.13 for example displays angular dependent transmission spectra (only TE polarization) for two different sample designs. While nanowire gratings deposited on top of a 140-nm-thick ITO waveguide slab have been assumed for all numerical calculations, different nanowire materials have been considered. Spectra for metallo-dielectric structures (gold nanowires) are displayed in panel (b). Additionally, the corresponding results for a similar dielectric structure (ITO nanowires) are depicted in panel (a). The individual nanowire cross-sections of 100×20 nm^2 and the periodicity of 501 nm have been kept constant. From top to bottom, the

angle of incidence is increased from $\vartheta = 0°$ to $\vartheta = 0.3°$.

Although the angular dependent transmission spectra of the metallo-dielectric structure in panel (b) confirm our experimental observations (formation of a small stopband, disappearance of the lower band-edge eigenstate at normal incidence), the shown theoretical results of the metallic structure strongly differ from the purely dielectric case in panel (a). The observed differences are very remarkable, especially with the knowledge that only the nanowire material has been changed in the numerical calculations. In contrast to the metallo-dielectric structure, the spectral width of the resonances is strongly decreased in the dielectric case due to the absence of any absorption. Simultaneously, also the resonant transmission is strongly reduced. All resonant features of the dielectric structure show zero transmissivity at their transmission minima. Another conspicuous phenomenon is directly related to the symmetry of the observed band-edge states at the center of the Brillouin zone. While the low-energy eigenstate is antisymmetric in the metallo-dielectric structures, the situation is inverted for the purely dielectric case. Now the high-energy eigenstate at the zone center is antisymmetric and therefore optically inactive in measurements at normal light incidence. Before analyzing the symmetry of the band-edge eigenstates in more details, it is important to remark that a strong modification of the optical response due to appearance of the nearby Rayleigh anomaly has to be considered in the metallo-dielectric slab structures. Similar to the resonant modes, also the Rayleigh anomaly shows a angular dependent dispersion (folding of the light cones). The single cusp-like anomaly splits for oblique incidence [marked by small vertical arrows in panel (b) of Fig. 3.13] and leads to spectral modifications of the upper resonant mode. Strongly asymmetric lineshapes and a simultaneous broadening of the resonance can be observed in the calculated spectra of panel (b).

To further elucidate the influence of the assumed photonic crystal slab design on the symmetry of the band-edge eigenstates, the angle-dependent transmission spectra of a slightly modified dielectric slab structure have been calculated. In extension to the results of Fig. 3.13, the considered dielectric slab structure can be considered as an inverted design. Instead of using a nanowire grating on top of the ITO waveguide, a periodic arrangement of shallow trenches has been assumed. While Fig. 3.14 (a) displays the theoretical spectra of the previously discussed ITO nanowire structure [identical with the spectra of Fig. 3.13 (a)], angle-dependent transmission spectra of the inverted grating structure are displayed in panel (b). It is important to remark that the individual nanowires (grating structure) and the assumed shallow trenches (inverted structure) exhibit
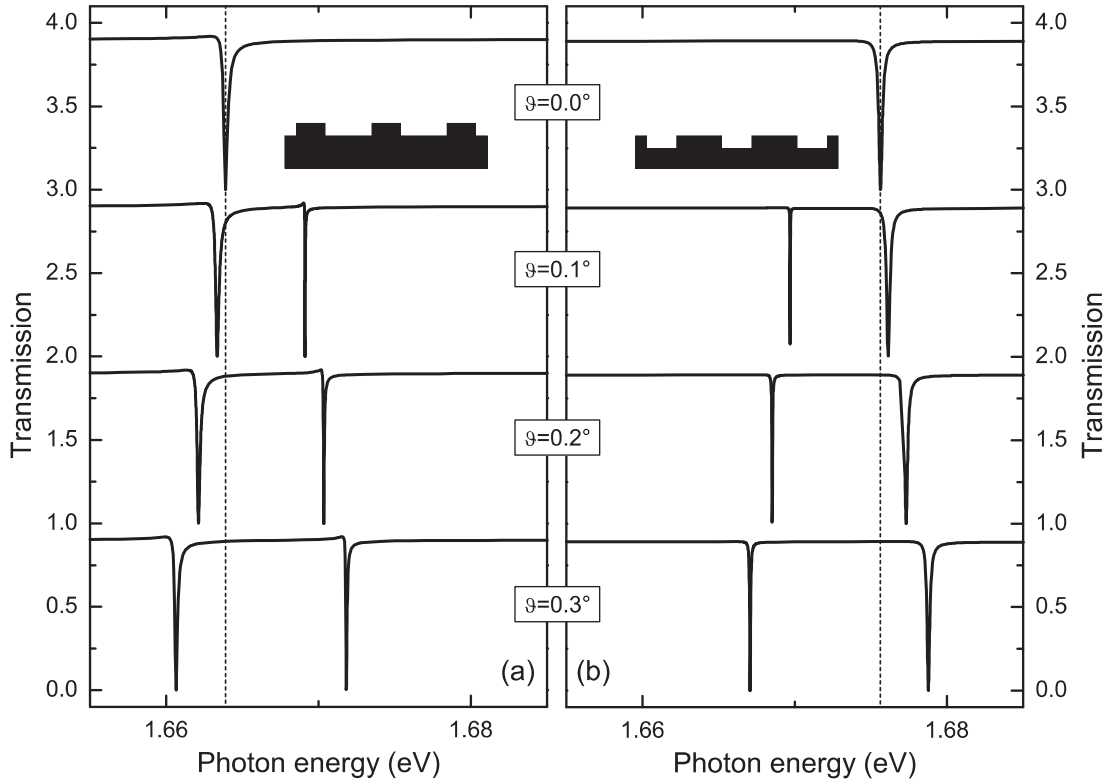
Figure 3.14: Calculated transmission spectra for two dielectric grating-waveguide geometries are shown in dependence on the angle of incidence (TE polarization). While ITO nanowires ($d_x = 501$ nm) with a cross-section of 100×20 nm^2 on top of a 140-nm-thick ITO waveguide have been assumed for the simulations of panel (a), an inverted structure (120-nm-thick ITO waveguide layer, nanowire cross-section of 401×20 nm^2) was taken into account for the calculations of panel (b). The individual spectra are shifted upwards for clarity in each panel.

an identical cross-section of 100×20 nm^2, respectively. Note that the inverted structure is based on a 120-nm-thick ITO slab waveguide on top of a quartz substrate in the numerical calculations. The trenches are modelled by assuming a periodic nanowire grating ($d_x = 501$ nm) with a nanowire cross-section of 401×20 nm^2 on top of the waveguide slab. The schematic view of the corresponding photonic crystal geometry is shown as an inset in both panels. The depicted angle-dependent transmission spectra again exhibit an inverse behavior at the center of the Brillouin zone. While the resonant transmissivity and the spectral width of the modes are more ore less comparable, the symmetry of the band-edge states is changed. Similar to the metallo-dielectric case, also the inverse dielectric structure is characterized by an optically inactive low-energy band-edge eigenstate.
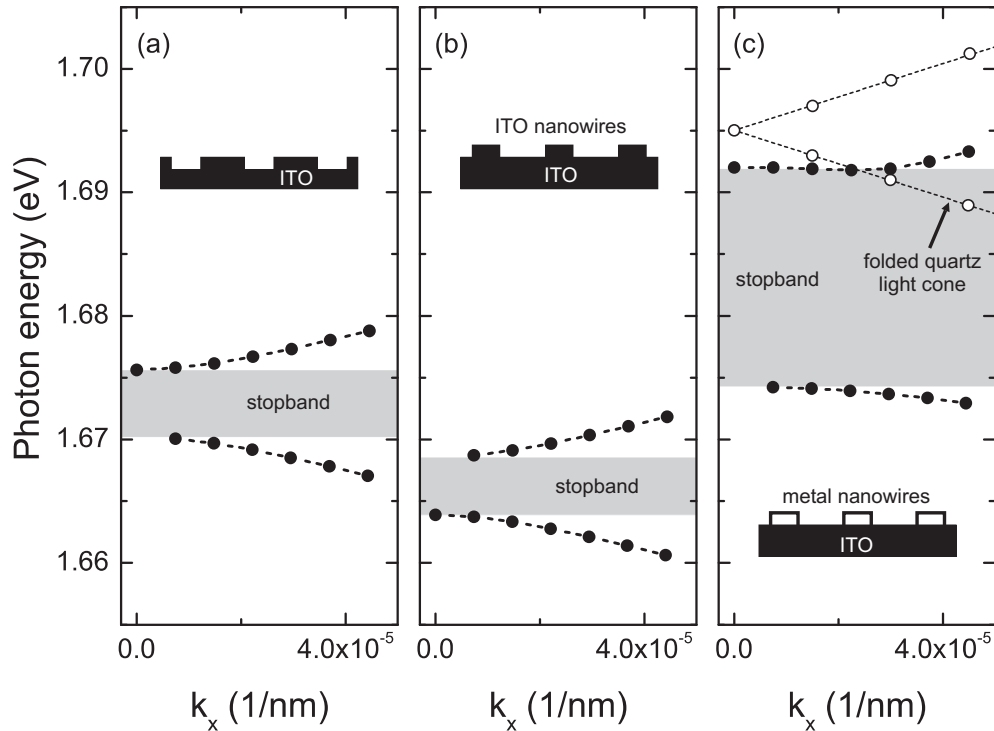
Figure 3.15:   Calculated dispersion diagrams of the investigated grating-waveguide structures (see Fig. 3.13 and Fig. 3.14). The transmission minima are plotted in dependence on the in-plane propagation constant k_x. An identical nanowire period of $d_x = 501$ nm has been used for all shown geometries. Additionally, the folded quartz light cone is shown in panel (c).

All important observations are summarized in Fig. 3.15 to further explore the wave vector dependencies of the extinction resonances. The depicted diagrams allow for direct comparison of the calculated band structures near the second-order stopband. The angle-dependent positions of the modes (approximately indicated by the extinction maxima of the Fano type resonances) have been extracted from the calculated spectra of the considered photonic crystal slab structures. While panels (a) and (b) display the dispersion relations of the purely dielectric structures, the results for the metallo-dielectric photonic crystal slab are shown in panel (c). First of all, the three panels again clearly point out the formation of a small second-order stopband at the center of the Brillouin zone. While the spectral width of the stopband is quite small for the purely dielectric structures (≈ 5 meV), the width is strongly increased for the metallo-dielectric case in panel (c). Due to the usage of gold nanowires, the spectral width of the gap approaches approximately 20 meV. Additionally, the antisymmetric eigenstates are clearly observable. Some of the bands do not continue to the zone center, in-

dicating the existence of optically inactive states (bound modes). It is important to remark that especially the metallo-dielectric (c) and the inverted structure (a) are characterized by a similar symmetry of their band-edge eigenstates. The high-energy band-edge state is antisymmetric in panel (b) and symmetric in panels (a) and (c). Note that also the extracted positions of the Rayleigh anomalies are shown in panel (c) of Fig. 3.15. The folded quartz light cone crosses the high-energy branch of the quasiguided mode for increased in-plane momentum.

The different widths of the stopbands as well as the inverted symmetry of the band-edge eigenstates at the zone center can be understood by taking into account the spatial field distribution of the eigenstates. Generally, there exist two ways to position a standing wave within the waveguide with respect to the periodic surface modulation (e.g., nanowire grating). In case of a second-order grating, the symmetric eigenstate with momentum $\pm 2\pi/d_x$ has its intensity maxima (electric field) at the position of the nanowires and exactly at the center between two neighboring nanowires. The antisymmetric mode on the other hand is spatially shifted ($d_x/4$) with respect to the symmetric mode and has its intensity maxima directly between adjacent maxima of the symmetric mode. Intuitively, the gap at the center of the Brillouin zone therefore arises due to the fact that the field maxima of the two standing waves are concentrated in regions of different effective permittivity ε_{eff}. Note that especially the symmetric band-edge eigenstates are influenced by the specific surface corrugation. These modes have their electric field maxima at the position of the nanowires, which implies a significant modification of the effective permittivity due to the changed nanowire material. The energy of the symmetric band-edge eigenstate for example is strongly increased, when the dielectric nanowire array [panel (b)] is replaced by a gold grating [panel (c)]. The antisymmetric modes on the other hand are only weakly affected. Especially in the case of the two dielectric structures [panels (a) and (b)], the optically inactive antisymmetric band-edge eigenstates exhibit nearly identical energies (≈ 1.67 eV).

3.4   One-dimensional metallo-dielectric superlattice structures

Although photonic crystal slab structures have been investigated for quite a long time (both one- and two-dimensional periodic structures), only little effort has been devoted to the analysis of more complex geometries. In addition
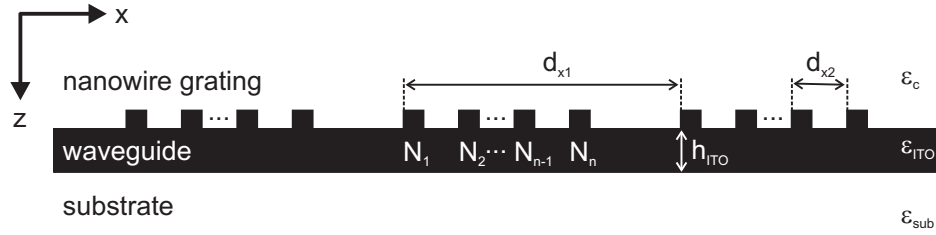
Figure 3.16:   Schematic view of the investigated one-dimensional superlattice structure. The photonic crystal slab structure is characterized by the grating period d_{x2}, by the superperiod d_{x1}, and by the parameter n which specifies the number of nanowires within each supercell.

to work on planar structures with asymmetrical unit cell [162, 163, 178] or artificial disorder [179], especially doubly periodic structures have been investigated [180]. These structures are composed of conventional grating-waveguide structures which are modified by adding a second grating component parallel to the first one. It has been suggested that these doubly periodic structures might be capable to increase the angular tolerance of resonant grating filters without modifying the spectral bandwidth [181, 182]. In extension to the work on double periodic structures, we will present a detailed discussion of so-called photonic crystal superlattice structures within this section. The analysis will be based upon optical transmission measurements as well as numerical simulations using the scattering-matrix formalism. It will be shown that the specific superlattice geometry leads to dramatic modifications of the band structure at the center of the first Brillouin zone. Generally, superlattice geometries have already been applied in a wide variety of different physical fields and many interesting fundamental effects have been demonstrated. In the optical regime for example, dielectric superlattice structures have been shown to support photonic Bloch oscillations [183] very recently.

3.4.1   Experimental and theoretical results

The schematic view of the considered superlattice design is shown in Fig. 3.16. Electron beam lithography was used to prepare gold nanowire arrays on top of ITO waveguide layers deposited on a quartz substrate. Note that the ITO layer thickness of 140 nm and the gold nanowire cross-section of 100×20 nm^2 have been retained unchanged for all investigated sample structures. In contrast to grating structures with a single periodicity d_x (e.g., see previous sections), the introduced

superlattice design is now characterized by three essential parameters. Generally, the assumed surface grating can be separated into individual supercells, which are composed out of n gold nanowires (N_1, N_2,...,N_n) grouped with periodicity d_{x2}. The individual supercells in turn are arranged with a larger superperiod of d_{x1}. Three different sample series will be discussed to demonstrate the influence of various superlattice configurations. Again, a white light transmission setup was used to determine the experimental extinction spectra. All spectra are recorded at normal incidence and TE polarization. Note that possible interaction phenomena due to particle plasmon excitations (TM polarization, e.g., see Chap. 4) will not be treated within the presented discussion.

Fig. 3.17 displays measured (a) and calculated (b) extinction spectra of the first sample series. The specific geometry of the individual superlattice structures is schematically depicted in panel (c). The first sample structure (0) for example is characterized by a perfect periodicity of 440 nm. Note that also this perfect grating structure can be interpreted as a superlattice in some respects. When assuming a superperiod of $d_{x1} = 2640$ nm and a period of $d_{x2} = 440$ nm within each supercell, then the structure exhibits six nanowires within the individual supercell. From top to bottom, defects have been introduced by removing single nanowires of the grating structure. Starting from a supercell with six nanowires and $d_{x2} = 440$ nm, the procedure finally results in a photonic crystal structure which has only one nanowire left within the individual supercells. Similar to the first structure, also the lowest grating structure (5) is characterized by a regular periodicity.

The displayed measured and calculated extinction spectra are characterized by various sharp spectral features, which can be related to the excitation of leaky modes of the photonic crystal slab structure. We have to point out that all experimental spectra of panel (a) are well confirmed by our numerical calculations depicted in panel (b). The overall agreement is quite excellent and especially the spectral position of the individual resonances can be calculated with high accuracy. As expected for structures with a perfect periodicity of 440 nm, the upper extinction spectra (0) are characterized by a single resonance at ≈ 1.9 eV within the considered spectral range. The observed extinction resonance can be simply explained by the excitation of the symmetric band-edge eigenstate at the second-order stopband. As shown in panel (d), the position of the observed resonance can be approximated by folding of the dispersion relation of the TE_0 mode of the homogeneous waveguide into the first Brillouin zone of a corrugated structure (dotted line). Additional peaks immediately arise below and above this
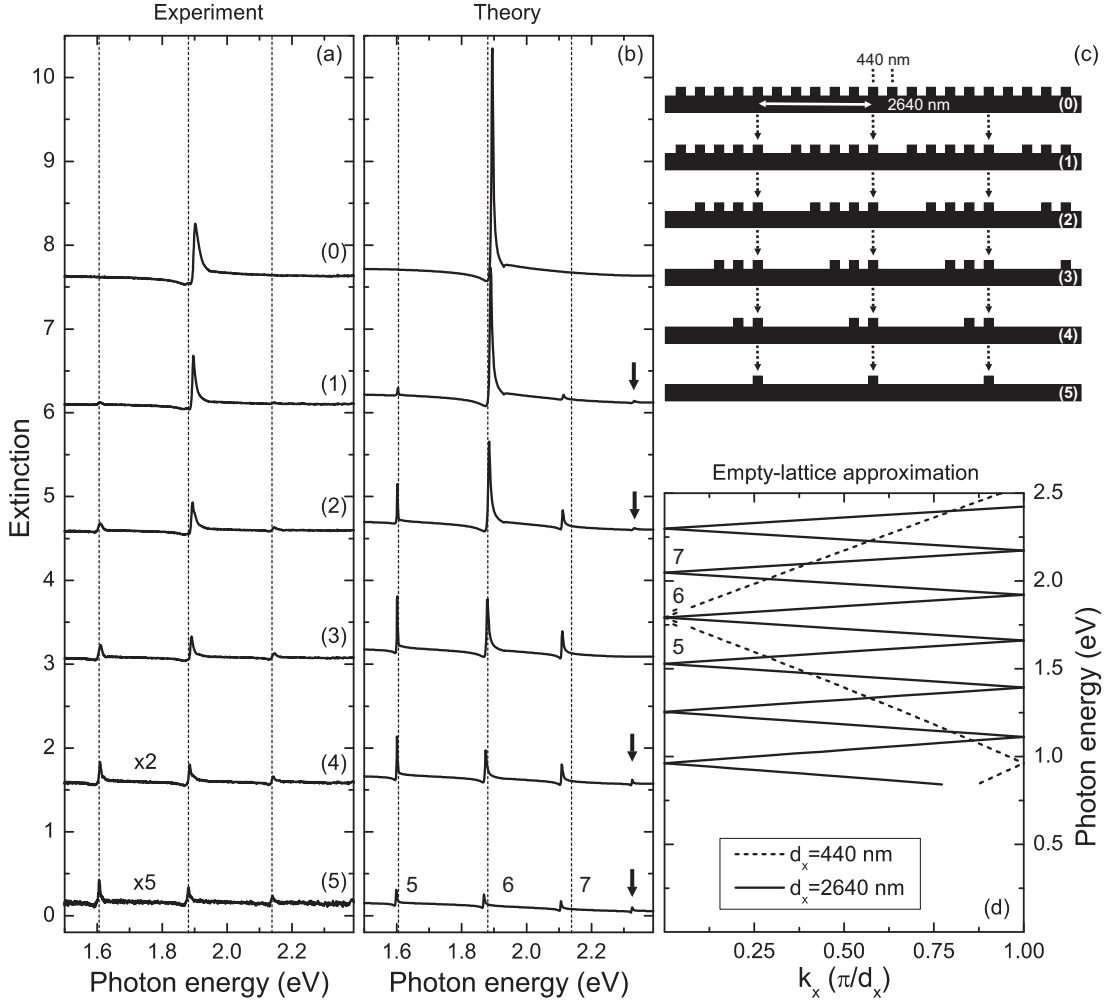
Figure 3.17: Measured (a) and calculated (b) extinction spectra of metallo-dielectric superlattice structures are shown for normal light incidence and TE polarization. A schematic view of the considered sample geometries is displayed in panel (c). While the periods $d_{x1} = 2640$ nm and $d_{x2} = 440$ nm have been retained unchanged, the number of missing nanowires per supercell is increased stepwise from (0) to (5). The individual spectra are shifted upwards for clarity in each panel. Note that the experimental spectra (4) and (5) are drawn on an expanded scale. A simple empty-lattice approximation for waveguide structures with a period of $d_x = 440$ nm and $d_x = 2640$ nm is depicted in panel (d).

single extinction maximum, when the number of nanowires is decreased stepwise, and defects (missing nanowires) are introduced periodically [(1)-(5)]. The spectral positions of the resonant features are only weakly influenced and generally do not depend on the number of nanowires. While the extinction of the central resonance at ≈ 1.9 eV is constantly reduced, the appearing additional resonances show a

rather complex behavior. Finally, the lowest spectra (5) can be characterized by four extinction maxima which are more or less barely pronounced.

In a first step, the empty-lattice approximation can be used to clarify the origin of the appearing additional resonances. The folding demonstrates that the spectral position of the individual resonances is unambiguously determined by the superperiod $d_{x1} = 2640$ nm. As shown in panel (d), the folding of the TE_0 mode of the homogeneous waveguide results in a strongly modified band diagram. Now the higher order Bragg resonances at the zone center are lowered in energy due to the considered larger period of 2640 nm (solid line). The increased period generally corresponds to a size reduction of the Brillouin zone. According to the obtained band diagram, the observed resonant features of the superlattice structure can be related to higher order Bragg resonances. While the lowest resonance at ≈ 1.6 eV corresponds to the fifth Bragg resonance, the strongest extinction peak at ≈ 1.9 eV for example can be interpreted as the sixth Bragg resonance of a corrugated waveguide structure with a period of 2640 nm. Note that, due to the specific geometry, the spectral position of the sixth Bragg resonance in the superlattice framework corresponds to the first Bragg resonance of a grating with regular period of 440 nm. Although the simple empty-lattice picture can be used to calculate the approximate positions of the possible superlattice resonances, the model fails to make any predictions about the excitation efficiencies of the individual modes.

A more precise interpretation of the superlattice results can be obtained by Fourier decomposition of the used grating geometry. According to the theory of mode coupling in planar photonic crystal structures (e.g., Ref. [164]), the coupling strength is brought about by the amplitudes of the corresponding Fourier harmonics of the considered spatial perturbation. In case of measurements at normal incidence, the coupling strength between an incoming wave and a pair of counter-propagating TE_0 modes with momenta $\pm l\, 2\pi/d_x$ ($l = 1, 2, ...$) is therefore directly proportional to the amplitude of the lth Fourier harmonic of the considered spatial perturbation.

A series of simulations has been performed to directly determine the amplitudes of the individual Fourier components of the assumed superlattice grating. For the theoretical calculations, the specific nanowire arrangement has been modelled by a one-dimensional series of Dirac delta functions, neglecting the specific cross-section of the individual nanowires completely. While all other points in space are zero, only the amplitudes at the center of the nanowires have been set to one
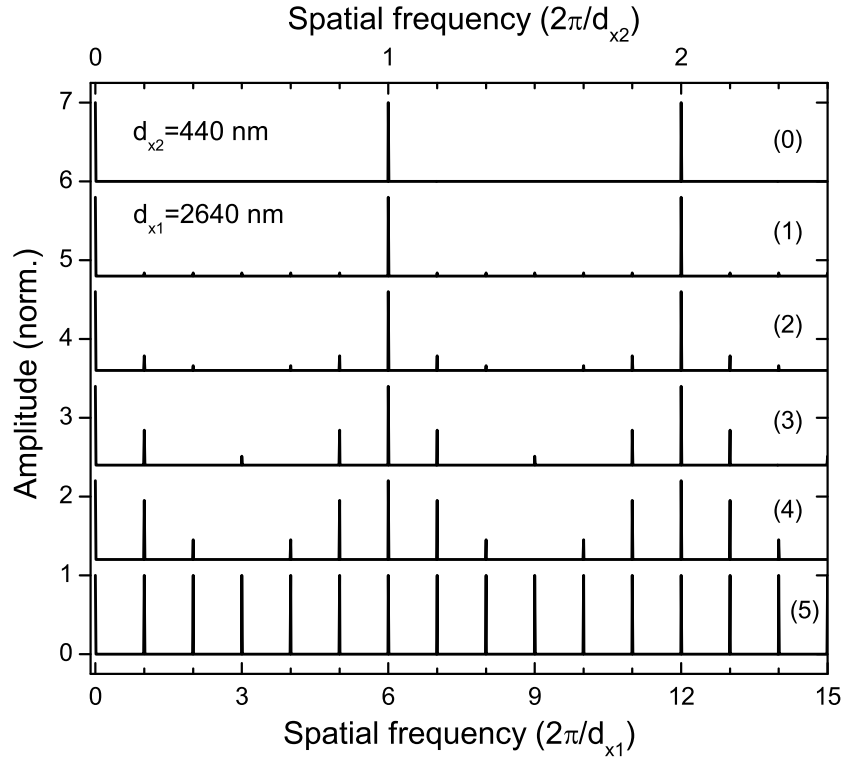
Figure 3.18:   Fourier decompositions of the grating structures (approximated by a series of Dirac delta functions) shown in Fig. 3.17. The normalized amplitudes are depicted in dependence on the spatial frequency.

within this approximation. Generally, 500 supercells with a spatial discretization of 1 nm have been assumed for the calculations.

The obtained theoretical results are shown in Fig. 3.18. The figure displays the normalized amplitudes of the Fourier harmonics in dependence on the spatial frequency (Fourier transformation of the modeled grating structures). The Fourier decomposition generally contains both, positive and negative frequencies. Due to mirror symmetry, only the amplitudes of spatial harmonics with positive frequencies are depicted. As expected, the Fourier decomposition of the two perfect grating structures (0) and (5) results in regular gratings in reciprocal space, too. Only the amplitudes for multiples of the reciprocal lattice vector are nonzero. It is again important to note that the considered superlattice series is somehow special. The reciprocal lattice vector $(2\pi/d_{x2})$ of grating structure (0) is a direct multiple of the reciprocal vector $(2\pi/d_{x1})$ of structure (5). Therefore the first Fourier harmonic of structure (0) can alternatively be interpreted as the sixth spatial harmonic in the superlattice view. If the number of nanowires is modified without changing the superperiod, the amplitudes of the spatial harmonics

show a rather complex behavior in dependence on the specific supercell geometry. Note that only the amplitudes of the sixth Fourier harmonic (and its multiples) are not subject to changes. A more precise comparison between Fig. 3.17 and Fig. 3.18 reveals that the excitation efficiencies of the different Bragg resonances are directly correlated with the spatial Fourier harmonics of the superlattice. A larger amplitude of a particular spatial harmonic results in a stronger extinction of the corresponding Bragg resonance. Due to the fact that only the normalized amplitudes are displayed in Fig. 3.18, the specific intensity distributions of the extinction maxima have to be interpreted with respect to the efficiency of the sixth Bragg resonance. Note that even small details of the extinction spectra can be found in the related Fourier decompositions. The eighth Bragg resonance of the TE_0 mode (marked by arrows in Fig. 3.17) for example is suppressed in the spectra of the superlattice structure (3). This observation is clearly confirmed by the corresponding Fourier decomposition. As expected, the amplitude of the eighth spatial harmonic is zero in the shown decomposition.

The obtained results can be summarized in the following way. Generally, the position of the supported fundamental modes is determined by the superperiod d_{x1}. If the individual supercells are unstructured, i.e., contain only one single nanowire, then all Bragg resonances at the zone center show up as weakly pronounced extinction maxima in the according transmission measurements. The situation is modified if the supercells get a more complex structure. Now the excitation efficiencies of the individual modes directly depend on the explicit nanowire arrangement within the supercells. The specific design of the individual supercells (e.g., number of nanowires) can be interpreted in a sense of a geometrical form factor which allows for artificial control over the optical response. The period d_{x2} within the individual supercells for example can be used to accentuate some of the resonances, while others are suppressed simultaneously. The number of nanowire n on the other hand directly affects the optical strength of the favored modes.

The specific influence of the period d_{x2} is further demonstrated by a second sample series. The schematic view of the considered sample structures is displayed in panel (c) of Fig. 3.19. All sample structures are again based on gold nanowire arrays deposited on top of 140-nm-thick ITO waveguide layers. While the period of 475 nm within the individual supercells and the number of nanowires (n=10) have been kept constant for all samples, only the superperiod d_{x1} is increased from 4750 nm (0) to 5550 nm (8) in steps of 100 nm. Apart from structure (0), the superperiod d_{x1} is no longer an exact multiple of the period d_{x2}. The experimental and theoretical extinction spectra (scattering matrix) are shown in
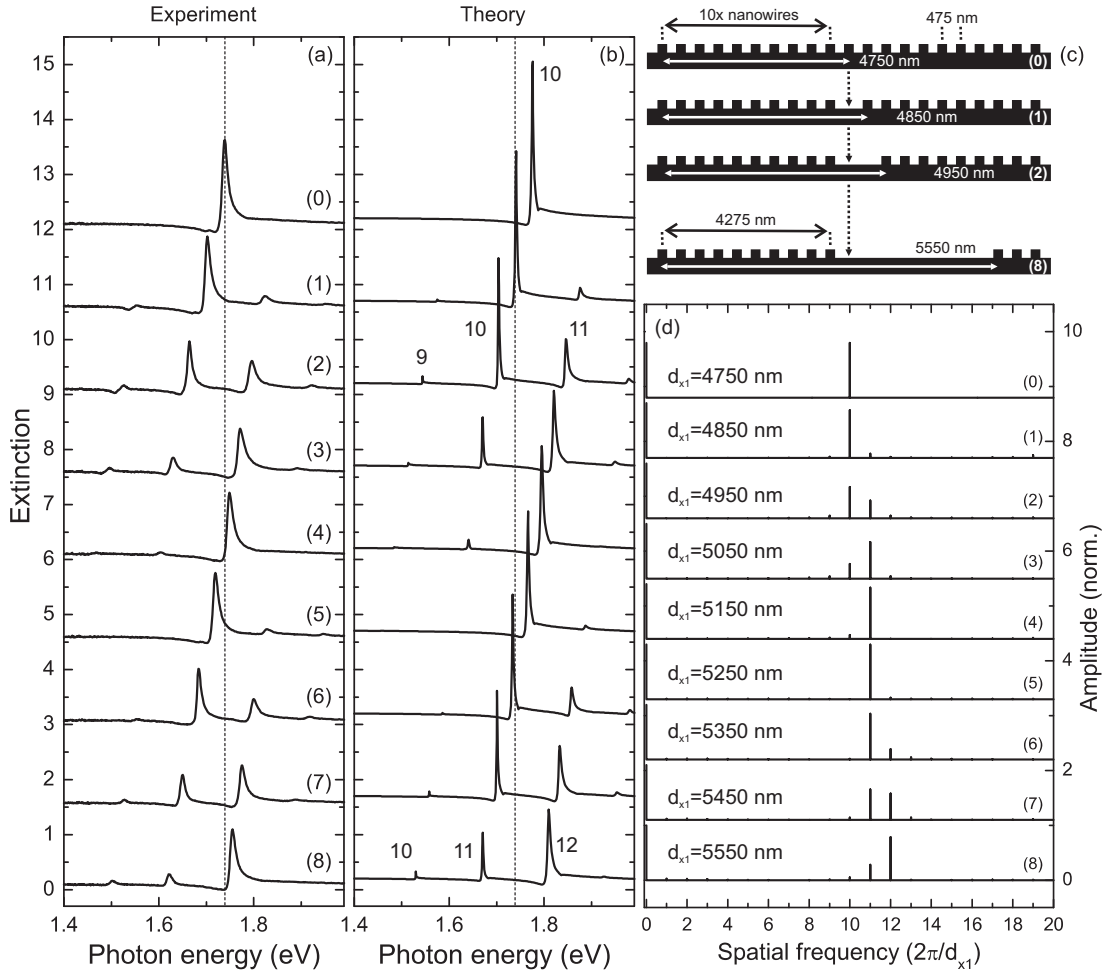
Figure 3.19:   Measured (a) and calculated (b) extinction spectra of metallo-dielectric superlattice structures are shown for normal light incidence and TE polarization. A schematic view of the considered sample geometries is displayed in panel (c). While the period of 475 nm within the supercells and the number of nanowires ($n=10$) have been kept constant for all samples, the superperiod d_{x1} is increased from 4750 nm (0) to 5550 nm (8) in steps of 100 nm. The individual spectra are shifted upwards for clarity in each panel. The Fourier decompositions of the grating structures are shown in panel (d) in dependence on the spacial frequency.

panels (a) and (b) of Fig. 3.19. Note that the qualitative agreement is again quite excellent and only small deviations are observable. In comparison to the experimentally detected resonances, the corresponding theoretical peaks are slightly blue-shifted. This fact can be related to uncertainties in the exact determination of the nanowire periods. A better agreement might be achievable by adjusting the theoretically assumed periods. Additionally, the measured linewidths of the

Figure 3.20:   Bandstructure of a photonic crystal slab in empty-lattice approximation and TE polarization. Periods of 475 nm and 4950 nm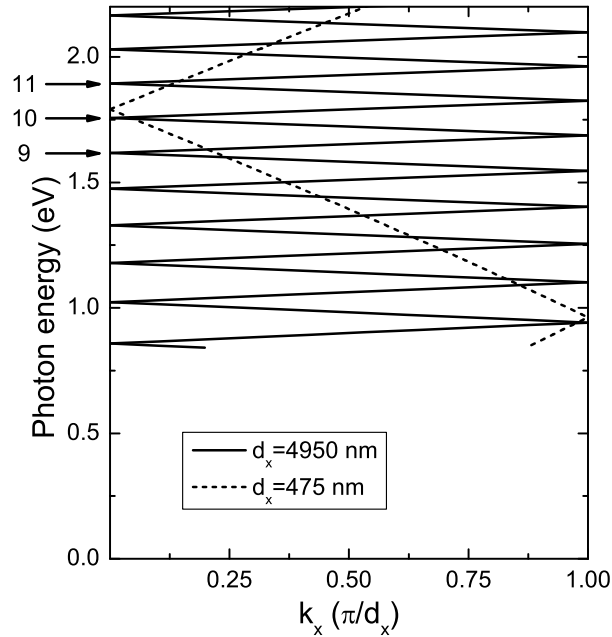 have been assumed. The positions of the ninth, tenth, and eleventh Bragg resonances of the TE_0 mode at the zone center are marked by arrows ($d_x = 4950$ nm).

individual modes deviate from the theoretical values. Although the observed broadening can be partially explained by fabrication tolerances (e.g., variation of the exact periods), especially the limited number of illuminated supercells has to be taken into account.

The appearing extinction maxima show a rather complex behavior in dependence on the superperiod d_{x1}. In contrast to the results of Fig. 3.17, the extinction efficiencies as well as the spectral position of the modes are now strongly influenced. All observed extinction maxima are caused by the excitation of higher order Bragg resonances. For example, considering the corresponding empty-lattice approximation in Fig. 3.20, the three resonant features of structure (2) [$d_{x1} = 4950$ nm] can be attributed to the ninth, tenth, and eleventh Bragg resonances of the TE_0 mode at the zone center. Generally, all superlattice spectra [except for structure (0)] are characterized by at least two more or less pronounced maxima, while all others being suppressed simultaneously. The relative amplitudes of the extinction maxima are again well described by the amplitudes of the corresponding Fourier decomposition of the spatial structure. The theoretically obtained

results are shown in panel (d) of Fig. 3.19.

The depicted dependencies are well confirmed by our proposed intuitive model. While the superlattice period d_{x1} only determines the spectral position of the supported modes (higher order Bragg resonances), their individual excitation efficiencies on the other hand are directly related to the specific period d_{x2} within the supercells. The stepwise reduction of the size of the Brillouin zone, i.e., an increased superlattice period leads to a lowering of the individual Bragg resonances. The eleventh Bragg resonances for example is shifted from 1.87 eV in structure (1) to approximately 1.66 eV in structure (8). Simultaneously, also the extinction efficiencies are strongly modulated. After a first enhancement (increased extinction), the mode is again attenuated for larger periods. Generally, the lth Bragg resonance reaches its extinction maximum when the lth multiple of the reciprocal lattice vector $2\pi/d_{x1}$ coincides with the reciprocal lattice vector $2\pi/d_{x2}$ of the supercell. This important fact is clearly visible in the measured and calculated extinction spectra. Only higher order Bragg resonances, whose spectral positions are close to the first Bragg resonance of a regular grating with exact period of 475 nm [structure (0)], show up in the obtained extinction spectra.

The results of the third investigated sample series are shown in Fig. 3.21. In contrast to the previously analyzed series, now both the superlattice period d_{x1} as well as the number of nanowires n are modified simultaneously. The schematic view of the superlattice structures is shown in panel (c) of the figure. Starting from structure (1), the number of nanowires per supercell is stepwise increased from one to ten, while the superperiod d_{x1} is enlarged from 2150 nm to 6425 nm at the same time. Again a constant period of $d_{x2} = 475$ nm has been chosen within the supercells. Note that the distance of 2150 nm between the individual supercells retains unchanged for all sample structures. The grating structure (0) with a regular period of 475 nm is used as a reference sample. The structure with a reciprocal lattice vector $2\pi/d_{x2}$ allows for exact determination of the spectral position of the first Bragg resonance. All experimentally measured and theoretically calculated extinction spectra are presented in panels (a) and (b) of Fig. 3.21. With respect to the already mentioned structural uncertainties, the achieved correspondence is again very excellent. Especially the extracted spectral positions of the measured and calculated extinction maxima, which are separately shown in panel (d), coincide very precisely.

A straightforward explanation of the observed spectral behavior can be given with the knowledge of the previous results. The optical response of the regular
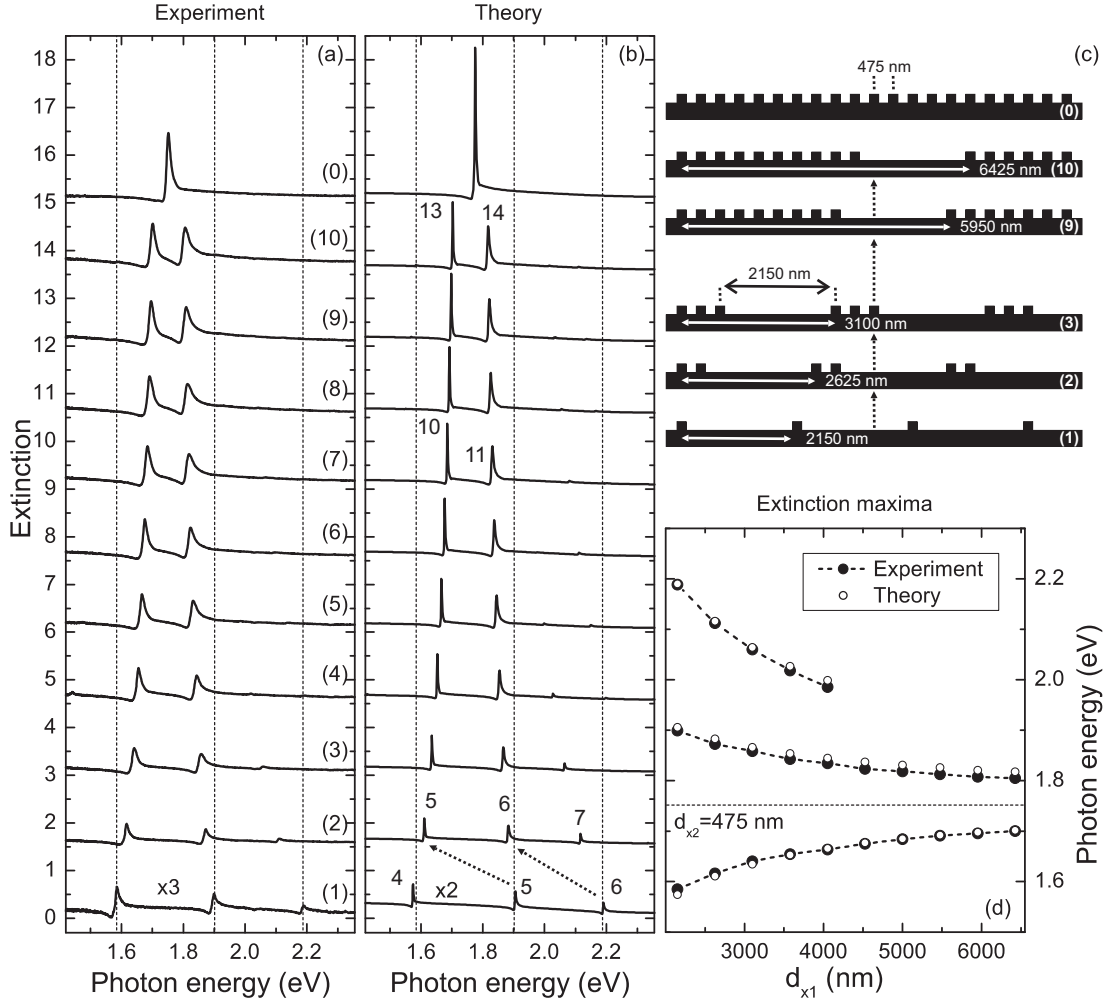
Figure 3.21:   Measured (a) and calculated (b) extinction spectra of metallo-dielectric superlattice structures are shown for normal light incidence and TE polarization. A schematic view of the considered sample geometries is displayed in panel (c). Starting from a grating with a period of 2150 nm (1), the number of nanowires (+1) and the period d_{x1} (+475 nm) are increased simultaneously. The period $d_{x2} = 475$ nm and the supercell distance of 2150 nm have been kept constant for all samples. The individual spectra are shifted upwards for clarity in each panel. Note that the lowest spectra (1) are drawn to an expanded scale. The extracted extinction spectra maxima (experiment and theory) are plotted in panel (d) in dependence on the superperiod d_{x1}.

grating structure (1) with a nanowire period of $d_{x1} = 2150$ nm is characterized by the excitation of the full set of corresponding Bragg harmonics. The fourth, fifth, and sixth Bragg resonances of the TE_0 mode are located within the considered spectral range. If the influence of the supercells is accentuated by increasing

Figure 3.22: Fourier decompositions of the grating structures (approximated by a series of Dirac delta functions) shown in Fig. 3.21. The normalized amplitudes are depicted in dependence on the spatial frequency. All superlattice structures are analyzed in terms of their individual superperiod d_{x1} (see panel (c) of Fig. 3.21).
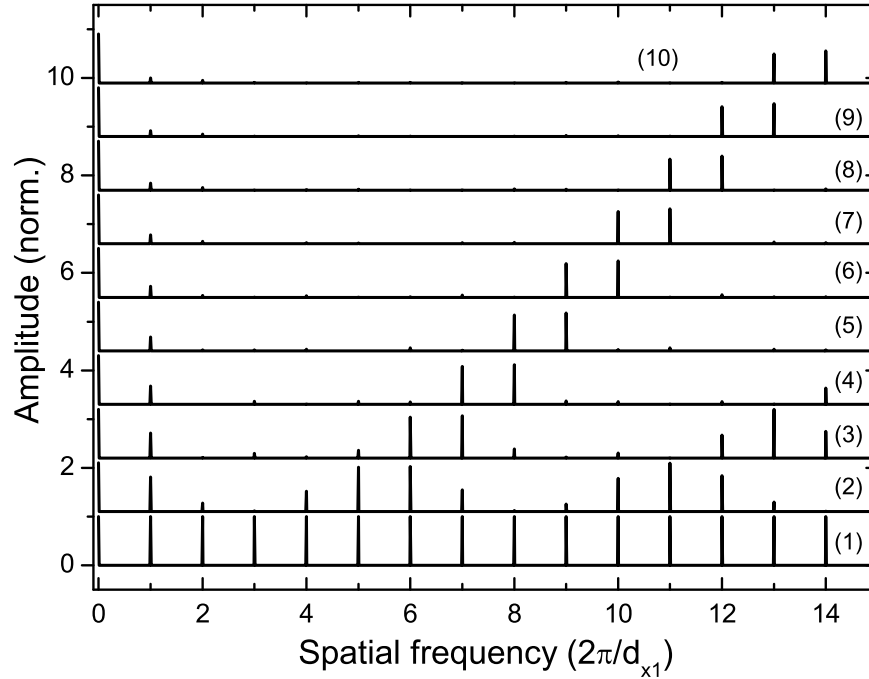
the number of assigned nanowires continuously, only the extinction maxima of two remaining modes are strongly amplified. The position of the resonances is determined by the exact superlattice period d_{x1}, while their individual excitation efficiencies are only influenced by the inner structure of the supercells. Due to the relatively large stepsize of 475 nm, the size of the Brillouin zone is decreased very rapidly. The fifth Bragg resonance at ≈ 1.9 eV of structure (1) is already shifted to ≈ 1.6 eV for the modified structure (2). The spectral position of the sixth resonance is simultaneously decreased form ≈ 2.2 eV to ≈ 1.9 eV. The procedure finally results in the two pronounced adjacent extinction maxima of structure (10), which arise due to excitation of the thirteenth and the fourteenth Bragg orders. Due to the fact that the order of the excited modes is increased continuously from bottom to top, also the effective distance between the two remaining modes is reduced. Asymptotically, both modes are approaching the spectral position of the first Bragg resonance of a grating with reciprocal lattice vector $2\pi/d_{x2}$, indicating the enhanced influence of the supercell geometry.
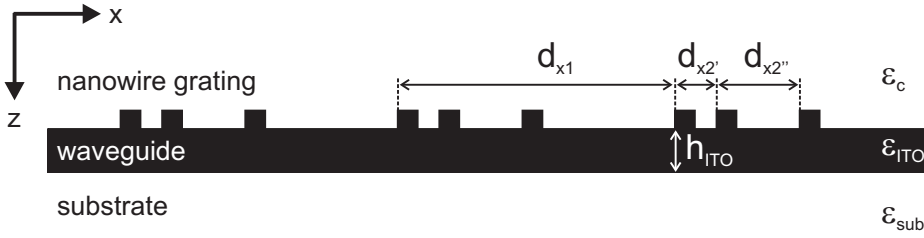
Figure 3.23:   Schematic view of the proposed one-dimensional superlattice structure. The photonic crystal slab is now characterized by a asymmetrical unit cell.

For the sake of completeness, also the corresponding Fourier decompositions of the assumed superlattice structures are shown in Fig. 3.22. The spectral response of the superlattice structures can again be deduced from the depicted amplitudes of the spatial harmonics. Starting from the third structure, also the displayed Fourier decompositions are dominated by only two strong components.

In conclusion, the presented experimental and theoretical result have clearly shown that the optical response of planar photonic crystal slab structures can be strongly modified by introducing periodic defects, i.e., by applying superlattice geometries. Three different metallo-dielectric sample series have been analyzed. The investigations reveal that especially the geometrical design of the individual supercells allows for additional control. Further experiments, especially focusing on purely dielectric structures, have to be performed to demonstrate possible technical applications of these photonic crystal superlattice structures. It has to be analyzed, for example, whether such structures may be applicable as efficient multimode reflection filters. Particularly, the possible angular dependencies as well as the influence of possible diffraction losses have to be investigated in more detail.

3.4.2   Future experiments

Only photonic crystal slab structures with a symmetric unit cell (rotation invariant grating geometry) have been addressed within this thesis work. It should be possible to extend the analysis to structures with asymmetric unit cells in a second step. Such structures allow for further modification of the optical response. A possible geometry is displayed schematically in Fig. 3.23. Again, the assumed design is based on a waveguide slab deposited on top of a quartz substrate. In contrast to the possible usage of blazed gratings, a superlattice structure with

an asymmetric arrangement of the individual nanowires within each supercell is proposed. The individual supercells contain three identical nanowires which are arranged considering the assumption $d_{x2'} \neq d_{x2''}$. This specific geometry does not exhibit a 180° rotational invariance. Therefore, additional optical phenomena are expected to occur. For example, it would be interesting to analyze the angle-dependent transmission and reflection properties near the second-order stopband. Note that both a removal of individual nanowires within each supercell as well as a selective size variation of single nanowires will be possible by using electron beam lithography as the fabrication method.

Another important aspect, which has not been addressed so far, is related to the influence of possible disorder. In contrast of using a regular arrangement of nanowires, one can think of introducing artificial disorder within the individual supercells. While the period of the supercells d_{x1} and the number of nanowires n are not affected, only the regular periodicity d_{x2} will be lost. Note that two fundamentally different realizations might be possible. First, the individual supercells of the superlattice will keep their far-field correlation, i.e., all disordered supercells exhibit an identical nanowire arrangement. Second, the individual supercells can be artificially modelled in such a way that all cells are characterized by a unique nanowire distribution. The influence of both modifications has to be analyzed in future experiments.

Chapter 4

Far-field interaction in planar metallic photonic crystals

This chapter will report on results of transmission measurements of metallic nanowire arrays deposited on top of different dielectric substrates. The appearance of grating anomalies, which critically depend on the substrate thickness, provides evidence that the optical response of these planar metallic photonic crystal structures can be strongly modified. While only Rayleigh-type anomalies are observed for thin dielectric substrates, thicker waveguiding substrates can induce strong coupling phenomena. This strong coupling results in the formation of waveguide-plasmon polaritons with a large Rabi splitting up to 250 meV. It will be shown that the coupling phenomena vary with the nanowire grating period, the angle of incidence, and also the waveguide layer thickness. A scattering-matrix-based numerical method is used to calculate the transmission properties and the near-field spatial distributions of such metallic photonic crystal structures. All experimental results are well confirmed by theoretical calculations.

4.1 Introduction

The exceptional optical properties of nanostructured materials have been the subject of extensive research activities in recent years. It has been shown that spatial structuring on a sub-micrometer scale can strongly change the light-matter interaction if compared with the properties of a macroscopically homogeneous material. Especially the well-known photonic crystal structures [3, 4, 184] exhibit a rich variety of important optical phenomena which already have inspired the

development of various nanooptical devices for future technical applications. Initially, such photonic crystal structures were mainly built of transparent dielectric materials with a distinct difference of their refractive indices. However, nowadays considerable effort is devoted to the investigation of *polaritonic* photonic crystal structures with complex unit cells, containing nanostructured semiconducting or metallic materials [110, 185–188]. Such polaritonic crystals are particularly attractive because of their ability to control electronic and photonic resonances simultaneously. Therefore, such structures may open up further impressive possibilities for tailoring the light-matter interaction.

Various photonic crystal structures with nanostructured metals have been realized so far. In addition to periodically modulated metal surfaces, including surface corrugation [55, 59] and hole arrays [71], especially regular arrangements of individual metal nanoparticles on dielectric substrates [90] are prominent examples of such polaritonic crystal structures. Large photonic band gaps [48], extraordinary light transmission properties [71], negative refraction [54], and strong coupling effects between electronic and photonic resonances [157] have been demonstrated. The particular optical properties of these metallic nanostructures can be attributed to the excitation of so-called particle or surface plasmons [12]. These electronic excitations are a consequence of the collective oscillation of the conduction band electrons in the metal. They manifest themselves in strong field enhancement near the metal surface.

Like more complex two- or three-dimensionally periodic structures [51], also planar metal gratings which are based on a periodic one-dimensional (1D) arrangement of individual metallic nanowires can be interpreted as 1D metallic photonic crystal slabs (PCS). It is obvious that different interaction phenomena have to be taken into account for a detailed analysis of such PCS. The investigation of these interaction phenomena seems to be quite important, especially with regard to the nature of inter-particle-plasmon interaction in future plasmonic nanodevices (e.g., three-dimensional metallic photonic crystals or surface plasmon polariton grating couplers). In contrast to isolated metal nanoparticles [36, 142, 143] or nanowires, the optical response of a periodic arrangement of individual metal nanostructures (dots or wires) will be influenced by near- and far-field coupling effects. While shifts of the particle plasmon resonance [101] and extended plasmon modes have been found for contiguous particles [102] with $d \sim a$ (where d is the distance between the nanostructures and a is their characteristic size, e.g., the nanowire width), far-field coupling effects will dominate the optical properties of planar photonic crystals with a periodicity on a length scale $d > a$ and

comparable to the wavelength of light [89]. In addition to works on randomly distributed metallic nanoparticles [104], it has been recently shown that the interaction between photonic and electronic resonances of ordered structures can lead to very pronounced modifications of their optical response [90, 157]. Another similar example of such interaction phenomena is the interplay between localized and extended surface plasmon resonances of periodic hole arrays in metallic films.

This chapter presents an extended analysis of the far-field effects observed in periodic gold nanowire arrays with periods $d > a$, exceeding the near-field coupling regime. The described phenomena can be related to the appearance of so-called Wood anomalies [155] which are intrinsic properties of photonic crystal slabs. The signatures of two types of Wood anomalies can be found in the transmission spectra of PCS, both types associated with waves exited by the incoming light and propagating along the periodic structure. Metal nanowire gratings on dielectric substrates show diffractive Wood anomalies (also called Rayleigh anomalies) which are associated with the opening of new diffraction orders either into air or into the substrate with the increase of the incoming photon energy [154]. If a waveguiding layer is added below the grating structure, additional resonance effects (waveguiding anomalies, see, e.g., Ref. [130] and references therein) will appear. By changing the geometrical properties of the metallic photonic crystal and therefore influencing for instance the spectral overlap of the particle plasmon resonance and the grating anomaly, it will be shown that both effects can lead to dramatic changes of the individual particle plasmon resonances[1]. It is worth mentioning that, in principle, all phenomena reported in this chapter also occur for two-dimensional gold nanocluster arrays deposited on top of dielectric substrates. However, the nanowire structure is advantageous for highlighting the observed phenomena. Besides a larger oscillator strength of the nanowire plasmons, the possibility to turn off the nanowire plasmon resonance is quite instructive. For light polarization parallel to the nanowires, no particle plasmons can be excited, and we can clearly identify the pure uncoupled grating anomalies.

The structure of the chapter is as follows. In Sec. 4.2, the metal nanowire structures and the experimental setup are described. Sec. 4.3 gives an extensive overview of the scattering-matrix-based numerical method which is used for

---

[1]Another historically first example of the resonant Wood anomaly are the surface plasmons anomalies in periodically corrugated metallic layers [189]. A lot of research is connected with these anomalies, see, e.g., in Ref. [10]. The discussions in the current chapter, however, are restricted to structures with isolated metal nanowires, where such plasmons do not manifest themselves, unless a periodic modulation along the wires is included.
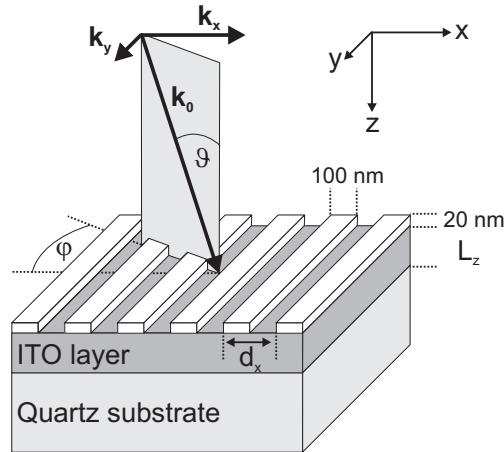
Figure 4.1:   Schematic view of the gold nanowire array on top of an ITO layer. Samples with different ITO thicknesses are investigated ($L_z = 15$ nm or $L_z = 140$ nm). Angle and polarization dependent transmission measurements are possible.

modelling of the experimental results. In Sec. 4.4, the optical properties of metal nanowire gratings deposited on top of a non-waveguiding substrate are discussed. The results show clear evidence of Rayleigh-type anomalies in accordance with the theoretical predictions. In contrast, Sec. 4.5 concentrates on nanowire structures deposited on top of thicker dielectric waveguiding layers. Strong coupling between optical modes and plasmon resonances is observed for these structures, and the experimental data are well reproduced by the theory. The calculated near-field spatial distributions will be discussed in this section. Finally, a summary of all findings is given in Sec. 4.8.

4.2   Samples and experimental techniques

Fig. 4.1 displays a schematic view of the sample structure. One-dimensional gold nanowire gratings were prepared by electron beam lithography on top of indium tin oxide (ITO) layers deposited on a quartz substrate. For all experimental investigations, the nanowire width of 100 nm and the nanowire height of 20 nm were kept fixed, while the nanowire periods were varied between d_x=350 nm and 600 nm. The possible grating extensions were restricted to 100×100 μm^2 due to limitations of the electron beam writing system. Two slightly modified sample geometries have to be taken into account for the comprehensive analysis of the fundamental optical properties of these metallic photonic crystal structures. While samples with an ITO layer thickness of L_z=15 nm were used for experi-

ments concerning Rayleigh-type phenomena, resonant coupling effects were only observed for thicker ITO films, supporting guided modes. Therefore samples with a 140-nm-thick ITO waveguiding layer were produced.

A conventional white light (halogen lamp) transmission setup was used for recording all extinction spectra. The samples were mounted on a rotation stage so that angle dependent measurements were possible. Besides the angle of incidence, also a distinct light polarization could be selected. Experiments with polarization parallel or perpendicular to the nanowires have been performed. It is important to remark that precise measurements of these fine spectral features require a careful adjustment of the setup. Special care has to be taken on the light aperture angle which has turned out to be a sensitive parameter. It has been shown that an aperture below $0.2°$ is necessary for reasonably exact measurements. Within all experiments this requirement was achieved by placing a 100 μm pinhole into the transmitted and recollimated white light beam.

4.3   Scattering-matrix based theoretical description

For the theoretical description of the optical properties of the photonic crystal slab, the scattering matrix method [128–130] was employed. This section will focus on the main points as the method itself has been extensively described in Ref. [130]. The incoming light with frequency ω and wavevector

$$\mathbf{k} = (k_x, k_y, k_z) = k_0(\sin\vartheta\cos\varphi, \sin\vartheta\sin\varphi, \cos\vartheta), \tag{4.1}$$

(where $k_0 = \omega/c$, and ϑ and φ are the polar and azimuthal angles of incidence, respectively, see Fig. 4.1) is treated as a planar incoming wave with electric and magnetic fields $(\mathbf{E}, \mathbf{H}) \propto \exp(i\mathbf{k}\mathbf{r} - i\omega t)$ far away from the structure on the vacuum side, $z < 0$.

The 1D periodic structure couples this incoming wave, the main harmonic, with all Bragg harmonics outgoing into vacuum and substrate. The reflected main harmonic ($g = 0$) and the diffracted and evanescent harmonics ($g = \pm 1, \pm 2, \ldots, \pm G$) into the vacuum are

$$
\begin{aligned}
\mathbf{k}_g^{\text{out,vac}} &= \left(k_{g,x}, k_y, -k_{g,z}^{\text{vac}}\right) \\
&= \left(k_x + \frac{2\pi g}{d_x}, k_y, -\sqrt{k_0^2 - \left(k_x + \frac{2\pi g}{d_x}\right)^2 - k_y^2}\right).
\end{aligned} \tag{4.2}
$$

The transmitted main harmonic and the diffracted and evanescent harmonics into the substrate are

$$
\begin{aligned}
\mathbf{k}_g^{\text{out,sub}} &= \left(k_{g,x}, k_y, k_{g,z}^{\text{sub}}\right) \\
&= \left(k_x + \frac{2\pi g}{d_x}, k_y, \sqrt{\frac{k_0^2}{\varepsilon_{\text{sub}}} - \left(k_x + \frac{2\pi g}{d_x}\right)^2 - k_y^2}\right),
\end{aligned}
\tag{4.3}
$$

where ε_{sub} is the substrate dielectric constant.

The method allows to calculate, via the full scattering matrix of the system $\mathbb{S}$, all $4N_G$ (where $N_G = 2G + 1$) amplitudes of the full set of outgoing harmonics [Eqs. (4.2) and (4.3)], if the amplitudes of all $4N_G$ incoming Bragg harmonics $\mathbf{k}_g^{\text{in,vac}} = \left(k_{g,x}, k_y, k_{g,z}^{\text{vac}}\right)$ and $\mathbf{k}_g^{\text{in,sub}} = \left(k_{g,x}, k_y, -k_{g,z}^{\text{sub}}\right)$ are known.

In the limit $G \to \infty$, the $\mathbb{S}$-matrix represents the asymptotically exact solution of Maxwell's equations for the PCS. In the numerical calculations, however, the expansion was truncated $\mathbb{S}$ at some finite $4N_G \times 4N_G$ matrix. The scattering matrix is used instead of the more familiar transfer matrix formalism, in order to avoid the otherwise inevitable numerical instabilities due to evanescent waves for higher reciprocal lattice vectors.

The method allows to calculate the frequency dependencies of the reflectivity, transmissivity, diffraction and absorption coefficients, and also the spatial distribution of the electromagnetic fields inside the structure.

The input parameters of the method are the geometrical sizes of the structure and the dielectric susceptibilities of the constituent materials. The latter are treated as spatially local and frequency dependent, which is especially important in case of metals. The dielectric function of gold was taken from Ref. [112]. The ITO dielectric susceptibility dispersion was taken into account as well[2].

The convergence of the truncated scattering matrix with N_G is an important problem in case of metals and depends, as is well known, on the polarization of the incoming light. If the light is polarized along the wires (TE polarization), calculations of the transmission spectra with $N_G = 49$ provide an estimated relative error smaller than 0.01%. The convergence in TM polarization (electric field components perpendicular to the wires) is much slower, although the idea of Ref. [190] has been employed, thus significantly improving the convergence. The

---

[2]Experimental values of the ITO dielectric constant [R. Parmentier et al., private communication] were fitted by $\varepsilon_{\text{ITO}}(\lambda) \approx 1 + 1.81302\lambda^2/(\lambda^2 - 0.07597)$ for λ between 0.3 μm and 0.6 μm.

TM spectra were usually calculated with $N_G = 301$, and several checks with N_G up to 1000 allow to estimate the relative error as $\approx 1\%$. The real problem here is that the computing time of this method is proportional to N_G^3, which means that, with the increase of the number of harmonics used, it quickly becomes impractical even on a supercomputer.

The physical reason for the slow convergence of the Fourier-series-based methods in the case of PCS with nanostructured metals is the very strong change of the electric field near the metal surface, especially if the latter has sharp features. However, a comparison of theoretical and experimental results shows that this method produces a very good qualitative agreement with the measured results in all cases, without using additional fitting parameters. In Sec. 4.4, a slightly smaller gold nanowire thickness was used in the calculations if compared with the experimental value in order to obtain a better agreement with the measured nanowire plasmon energy. All cases of such differences which are most likely due to uncertainties in the experimentally measured dimensions or the dielectric susceptibilities are especially emphasized.

4.4   Rayleigh anomalies in metallo-dielectric nano-structures

This section starts from the investigation of systems with a thinner ITO layer, not supporting any guided modes in the spectral range of the nanowire plasmon resonances. As already mentioned, the optical response of a periodic arrangement of metallic scatterers can differ substantially from that of noninteracting individual metallic particles. It turns out that the period of the grating structure is the crucial parameter for the modification of the isolated nanowire plasmon response. This can be interpreted as a manifestation of the nanowire-nanowire interaction in the far-field regime.

In Fig. 4.2, a collection of measured [(a),(c)] and calculated [(b),(d)] extinction spectra [-ln(T), T: transmission] for gold nanowire arrays on top of a 15-nm-thick ITO layer are depicted. Panels (a) and (b) contain period-dependent spectra recorded at normal incidence ($\varphi = \vartheta = 0°$). From top to bottom, the grating period d_x is increased from 350 nm to 500 nm in steps of 50 nm. In panels (c) and (d), an overview of the angular dependence for a fixed nanowire period of $d_x = 450$ nm is given. The azimuthal angle $\varphi = 0°$ remains unchanged, and the
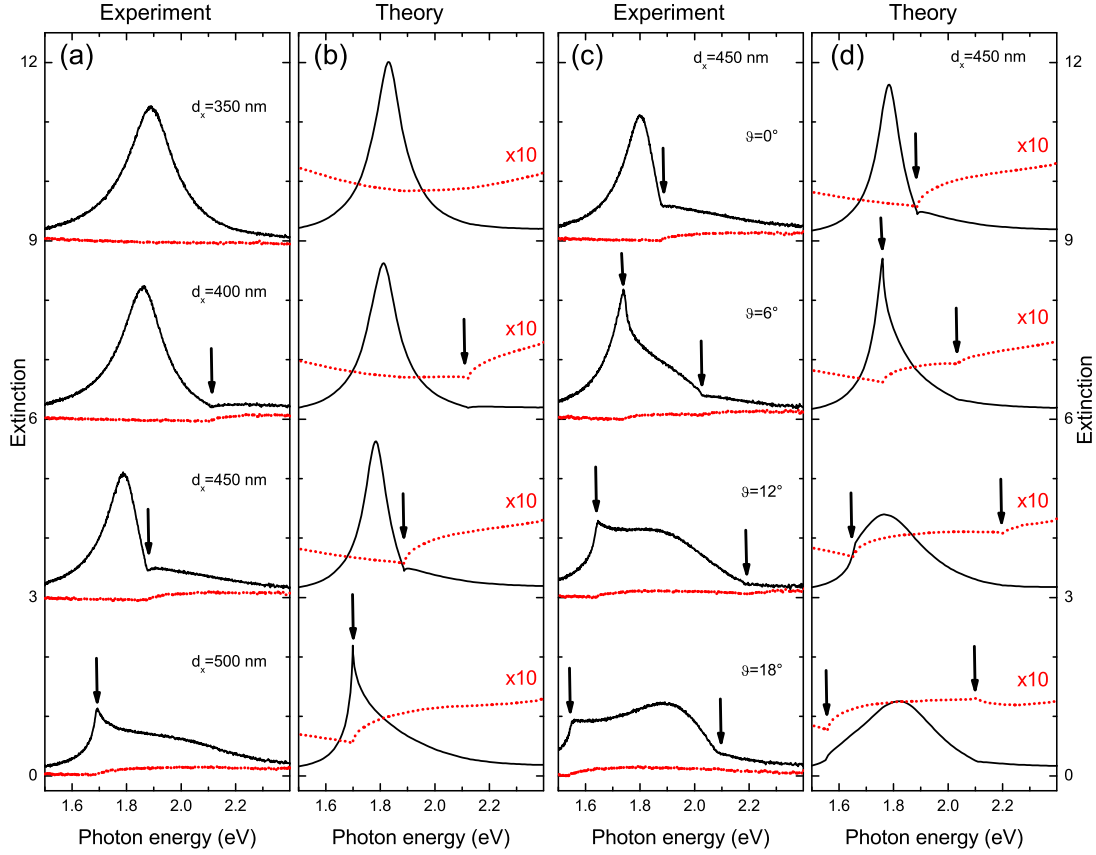
Figure 4.2: A collection of measured (a) and calculated (b) extinction spectra for nanowire gratings on top of 15-nm-thick ITO layers at normal incidence. From top to bottom, the nanowire period d_x is changed from 350 nm to 500 nm in steps of 50 nm. In addition, measured (c) and calculated (d) extinction spectra for different angles of incidence and a fixed nanowire period of 450 nm are depicted. Spectra are shown for TE- (dotted lines) and TM-polarization (solid lines)(Electric and magnetic field parallel to the nanowires, respectively). TE-polarized spectra in (b) and (d) are drawn to a larger scale (x10). The individual spectra are shifted upwards for clarity in each panel. Vertical arrows mark the positions of the diffractive anomalies.

polar angle ϑ is varied between 0° and 18° in steps of 6°. Beside the more relevant case of TM-polarization (the magnetic field parallel to the nanowires), also the corresponding spectra for TE-polarization (electric field parallel to the nanowires) are displayed. All extinction spectra exhibit pronounced spectral features with distinct dependencies on the grating period as well as on the angle of incidence.

Note that, instead of the assumed 20 nm (experiment), all calculations of Sec. 4.4 were performed for gold nanowires with a height of 15 nm, while the wire width

of 100 nm has been retained unchanged. This minor modification, causing a red shift of the calculated nanowire plasmon peak, leads to a better quantitative agreement between experiment and theory. Otherwise, assuming the height of 20 nm, the calculated nanowire plasmon peak energy is about 100 meV higher than that seen experimentally. This deviation can be due to uncertainties in the exact experimental determination of the nanowire geometry or the ITO dielectric function.

A detailed analysis of the displayed period-dependent results [Fig. 4.2(a) and 4.2(b)] shows that the undisturbed plasmon resonance of the quasi noninteracting nanowires can only be seen for a period of $d_x = 350$ nm and TM-polarization (oscillation of the conduction band electrons of the metal nanowires perpendicular to the nanowire axis). Neither near- nor far-field effects influence the isolated broad resonance, centered at approximately 1.9 eV, which can be attributed to the excitation of the particle plasmons of the individual gold nanowires. The spectral shape of this strong plasmon resonance is clearly modified by increasing the nanowire period. As indicated by the arrows, an additional cusp-like anomaly occurs for nanowire periods exceeding $d_x = 350$ nm. With increasing d_x this anomaly shifts to lower energies.

The variation of the angle of incidence for a fixed nanowire period shows strong spectral modifications, too. In Fig. 4.2(c) and 4.2(d), the anomaly splits for oblique incidence, and two dips or kinks, shifting in opposite directions with increasing ϑ, become visible. It is important to notice that all anomalies show up at an identical spectral position for TE- and TM-polarizations, although they are less pronounced for TE-polarization (see the dotted lines).

Rayleigh-type anomalies have to be considered as the physical origin of the spectral features reported here. The Rayleigh anomalies are due to the opening of new diffraction orders. Or, more precisely, they appear when the light field of some Bragg harmonics [see Eqs. (4.2) and (4.3)] changes from evanescent to radiative in ambient air or substrate layers at a given frequency. This happens when the term under the square root in Eqs. (4.2) and (4.3) changes the sign from negative to positive,

$$\omega_{\text{Rayleigh}} = \frac{c}{\sqrt{\varepsilon}} \sqrt{k_{g,x}^2 + k_y^2}, \tag{4.4}$$

where $\varepsilon = \varepsilon_{\text{sub}} = 2.14$ for the quartz substrate or $\varepsilon = \varepsilon_{\text{vac}} = 1$ for air ambience. Since these anomalies are connected with the asymptotic far-field behavior (radiating conditions), they depend only on the dielectric constants of the substrate and the ambient layer. In agreement with the experiment, there is no dependence
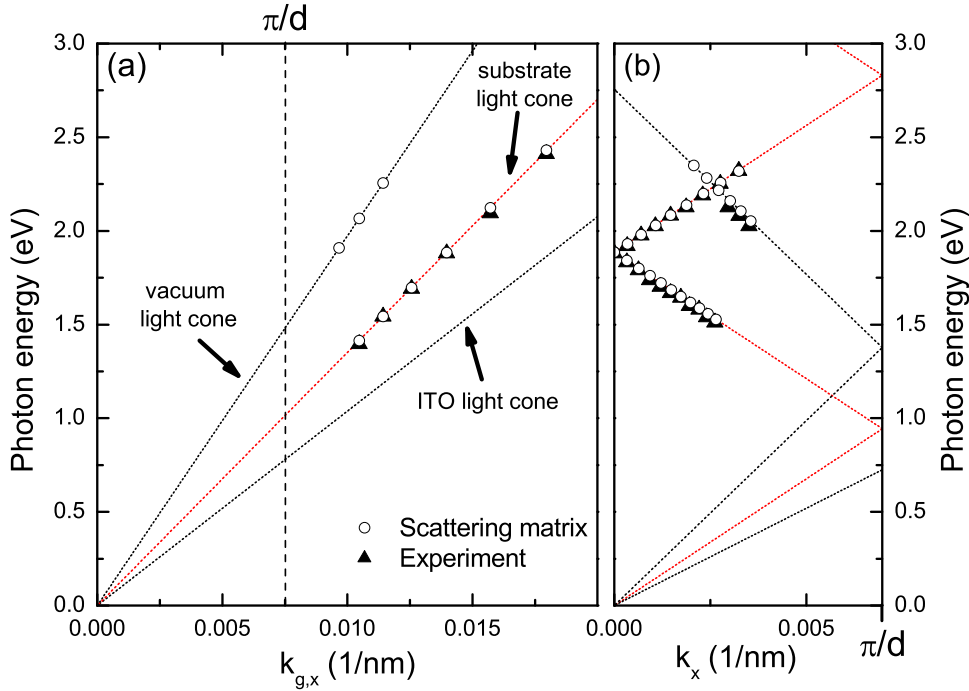
Figure 4.3:   Measured and calculated spectral positions of the observed grating anomalies.   The dependency on the grating period (normal incidence: $k_{g,x} = 2\pi/d_x$) is shown in panel (a). A period of $d_x = 450$ nm was chosen for the angle resolved experiments (Variation of k_x) in panel (b). Light cones for air, quartz and ITO are depicted as dotted lines. Additionally, the dispersion of the light cones folded into the first BZ are displayed in panel (b).

on the near-field and, thus, on the polarization state of the incoming light or the dielectric susceptibilities of the PCS itself. It is important to remark that several recent publications which refer to dipolar particle interaction have already addressed similar optical phenomena of periodic gold nanostructures [89, 100, 191]. Although no sharp spectral features were found in these measurements (presumably due to poor angular resolution in the measurement setup), it has already been shown that scattering effects can lead to strong modifications of the particle plasmon resonance.

For an exact interpretation of the spectra displayed in Fig. 4.2, the peak positions of all spectral features have been determined for the whole sample series. Fig. 4.3 shows the period- and angle-dependent dispersions of the measured anomalies, in comparison with the light cones of the air environment and the quartz substrate. At normal incidence where $\vartheta = \varphi = 0°$ with $k_x = 0$, following Eq. (4.4), the dependence of the anomalies on $k_{g,x} = 2\pi/d_x$ can be probed by changing the

nanowire grating period, as displayed in panel (a). The dependence on $k_x = k_0 \sin \vartheta$ is depicted in panel (b), extracted from angle of incidence dependent measurements at a fixed period of $d_x = 450$ nm. The light cones of air and quartz, folded into the 1st Brillouin zone (BZ) in (b), are shown as lines in both panels. As anticipated, all the measured (and calculated) anomalies lie exactly on these light cones. Based on these excellent polarization-independent fits, the interpretation as Rayleigh anomalies is appropriate. Note that the Rayleigh anomalies are weak when detuned far from the particle plasmon resonance. They become resonantly increased when approaching the nanowire plasmon extinction peak. Note also an inversion of the cusp-like Rayleigh anomaly while crossing the isolated nanowire plasmon band (see Fig. 4.2).

Another important experimental confirmation is the direct observation of the Bragg-diffracted light field components in x-direction. Dependent on the grating period, they appear as visible bright spots at the edges of the quartz substrate during our the measurements (not shown here).

To support the conclusion further, additional calculations for a free-standing structure without any quartz substrate below the ITO layers have been performed. Such structures have not been realized experimentally, but they present an instructive model. The ITO layer thickness is taken as 15 nm, and the gold nanowire cross section (100×15 nm^2) has been retained unchanged. The calculated extinction spectra are shown in Fig. 4.4(a). For a direct comparison, the same calculations for an identical structure with a quartz substrate below the 15-nm-thick ITO are additionally depicted in panel (b) (the same calculations as in Fig. 4.2). From top to bottom, the nanowire period is increased from 150 nm to 800 nm in steps of 50 nm in both panels. In comparison with the free-standing structures, all spectra of panel (b) are slightly shifted to lower energies due to the changed dielectric surroundings of the gold nanowires. Although identical periods have been assumed for the calculation of both structures, the sharp spectral features visible in panel (b) for nanowire periods ranging from 350 nm to 500 nm disappear for the spectra in panel (a). Due to the missing quartz substrate, the substrate-induced Rayleigh anomalies are absent. Only for $d_x \approx 650$ nm, the far-field interaction phenomena can be seen for both structures, connected with the vacuum-induced Rayleigh anomaly (cusp-like structure). In contrast to the pure Rayleigh-type anomalies in panel (b), the narrow structures in Fig. 4.4(a) for periods larger than $d_x = 550$ are actually resonance anomalies. The inset of Fig. 4.4(a) clearly demonstrates the Fano-type nature of these sharp resonances. They appear due to the excitation of quasiguided modes in this free-standing
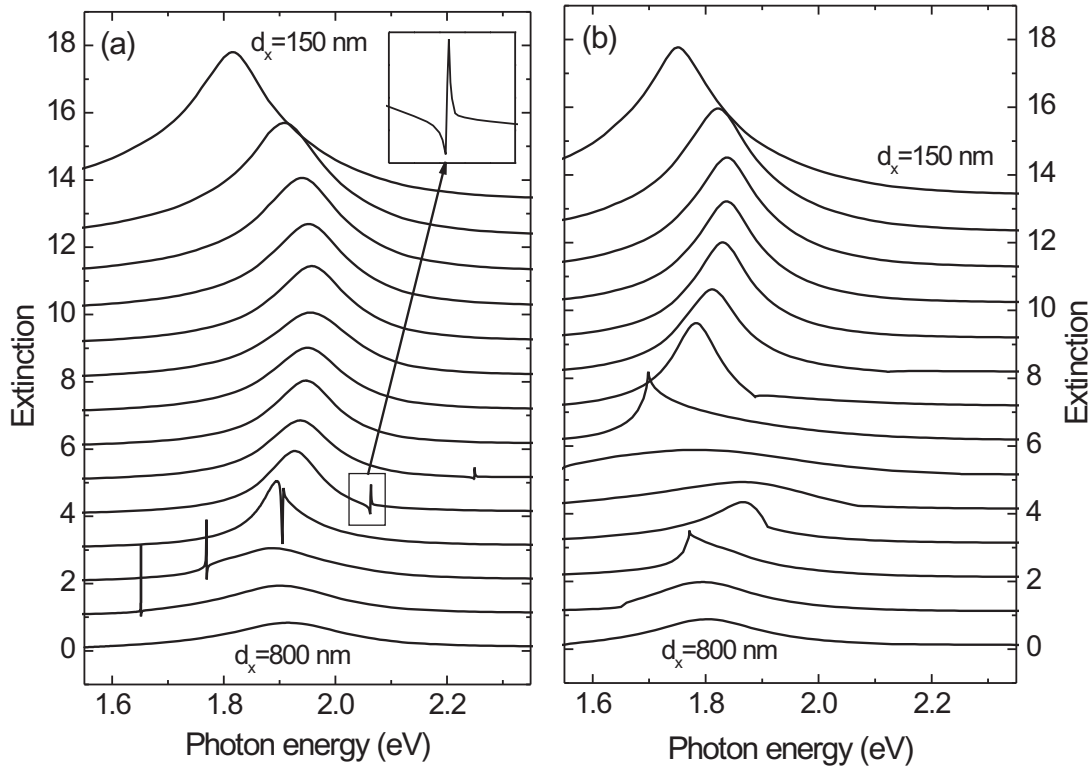
Figure 4.4: Calculated spectra (TM-polarization, normal incidence) for gold nanowire gratings on top of a free-standing 15-nm-thick ITO film are shown in panel (a). Panel (b) displays the calculated spectra for an identical structure, but without removing the quartz substrate below the ITO layer (same structure as assumed for the calculations in Fig. 4.2). From top to bottom, the nanowire period d_x is changed from 150 nm to 800 nm in steps of 50 nm. The individual spectra are shifted upwards for clarity. Inset: Fano-type resonance for a nanowire period of 600 nm.

structure (see the discussion in Sec. 4.5 for more details).

To conclude, the presented results show clearly that the observed interaction phenomena rely on a collective scattering effect of the whole nanowire ensemble. In contrast to near-field phenomena ($d_x < 300$ nm), which are based on the nanowire-nanowire interaction via evanescent fields, such grating effects only appear for nanowire samples with larger periods ($d_x > 350$ nm). For this special regime, the optical near-fields (acting on the individual metal nanowires) are strongly modified due to the opening of new diffraction orders. As a result, the characteristic nanowire far-field distribution and therefore the shape of the nanowire plasmon resonances are changed, as has been shown in Fig. 4.2.

Although the discussion of near-field coupling phenomena at smaller periods exceeds the scope of the current work, it is important to mention that the calculated spectra in Figs. 4.4(a) and 4.4(b) give clear evidence for them. The enhanced near-field coupling for a decreased nanowire period ($d_x < 300$ nm) induces a red shift and broadening of the nanowire plasmon resonances. Similar effects have already been demonstrated for two-dimensional gold nanoparticle arrays [101]. These near-field coupling phenomena can be explained by the dipole-dipole interaction between the individual gold nanowires and have to show a $(a/d_x)^{-2}$ dependence (a is the nanowire width).

4.5   Polaritonic photonic crystal slab

In Sec. 4.4, it has been shown that the observed far-field interaction phenomena for gold nanowire gratings deposited on top of 15-nm-thick ITO layers are based on a collective substrate-induced scattering effect at the Rayleigh wavelength. In addition to these results, another interaction effect due to waveguiding anomalies (resonant anomalies) of thicker ITO layers will be discussed in the following. It will be shown that the optical properties of similar gold grating structures on top of 140-nm-thick ITO layers are primarily dominated by an additional strong coupling phenomenon. In particular, this section will give evidence that the interaction of electronic and photonic resonances of metallic photonic crystal slabs can lead to the formation of a waveguide-plasmon polariton [157].

4.5.1   Empty-lattice approximation

In contrast to a 15-nm-thick ITO layer, a 140-nm-thick ITO slab deposited on a quartz substrate supports guided modes in the spectral range of the considered nanowire plasmon resonances. Therefore the metallic photonic crystal slab provides electronic and optical resonances simultaneously. The resulting spectral modifications can be clearly observed. For example, Fig. 4.5 shows the measured spectra of gold nanowire arrays with an identical period of $d_x = 450$ nm with 15 (a) and 140-nm-thick (b) ITO layers. The shape of the nanowire plasmon resonance for samples with a thicker guiding ITO layer differs substantially from that discussed previously. The spectra for TE- and TM-polarization in panel (b) are now characterized by an additional extinction maximum. It will be shown that this maximum arises due to the interaction with the lowest TE or TM guided
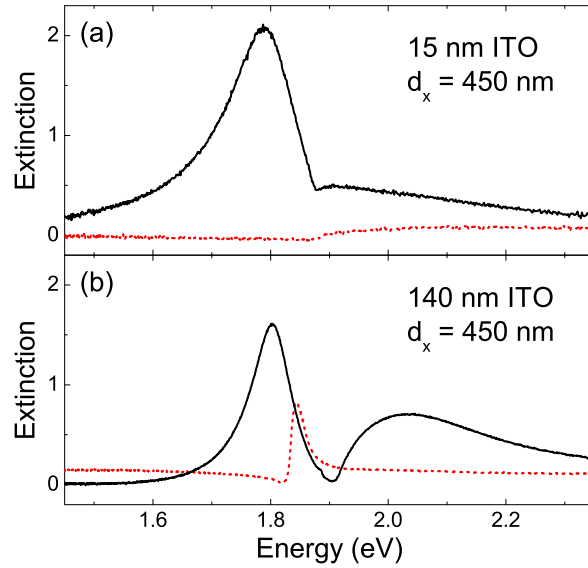
Figure 4.5:   Measured extinction spectra of gold nanowire arrays (Period $d_x = 450$ nm) for normal light incidence. Spectra of samples with 15-nm-thick (a) and 140-nm-thick (b) ITO layers are shown for comparison in TE (dotted lines) and TM (solid lines) polarization.

modes. Here, the strongly asymmetric shape of the resonances can be attributed to the Fano-type nature of the excited waveguide resonance. Although diffractive Rayleigh anomalies can still be seen for such structures, waveguiding anomalies dominate the spectral response of the interacting waveguide-nanowire-system.

To understand the energy dispersions of the different resonances in the modified structure, the discussion starts from a simple empty-lattice approximation. As a first step of this approximation for a metallic grating-waveguide structure, the structure has to be replaced by a homogeneous ITO layer. The energy dispersions of the lowest transverse electric (TE_0) and transverse magnetic (TM_0) guided modes can then be found from the solution of the transcendent equations for the waveguide slab (see, e.g., in Ref. [120]).

When assuming a surface corrugation with periodicity d_x in a second step, the guided modes have to be folded back into the first Brillouin zone of the 1D photonic crystal slab. These folded (due to the periodic surface corrugation) modes are now located above the air light cone and can couple to the photon continua of the air environment and the quartz substrate. Therefore, the formerly guided modes of the uncorrugated structure become leaky (quasiguided). Such modes are characterized by relatively long lifetimes and large quality factors and may lead
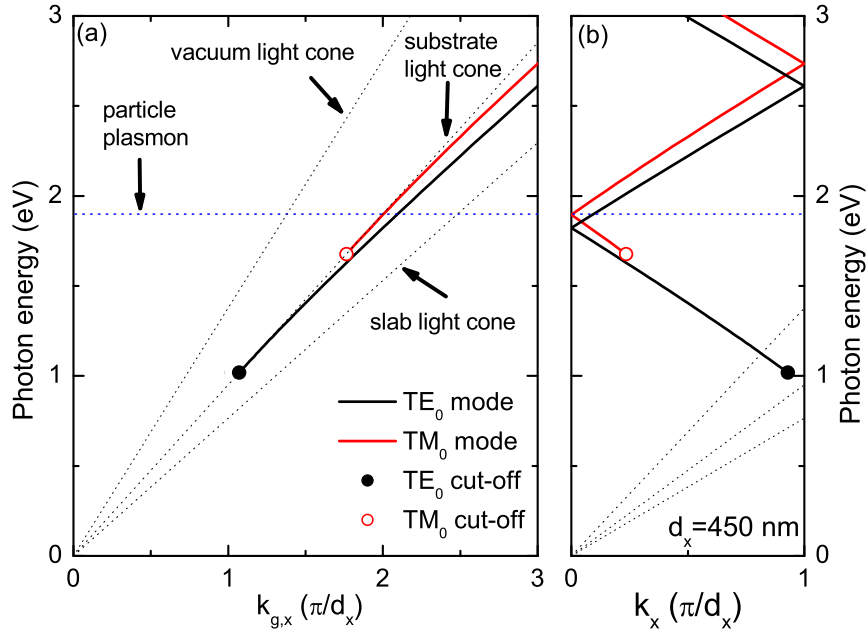
Figure 4.6:   Empty-lattice approximation: The lowest TE and TM polarized guided modes of an homogeneous and 140-nm-thick ITO waveguide. Their dependencies on $k_{g,x}$ are shown in panel (a). Panel (b) displays these guided modes folded into the first BZ for an assumed grating period of $d_x = 450$ nm. The particle plasmon dispersion of noninteracting gold nanowires (dotted horizontal line) is shown too.

to resonantly enhanced fields inside the planar photonic crystal structures. As a result, the dispersion of these quasiguided modes can be probed by period- and angle-dependent transmission measurements, where they will show up as sharp spectral resonances in the transmission or extinction (see, e.g., in Ref. [130] and references therein).

The results of this empty-lattice approximation are shown in Fig. 4.6 for a sample structure with an ITO layer thickness of $L_z = 140$ nm. Panel (a) displays the lowest TE_0 and TM_0 guided modes of the homogeneous ITO waveguide on top of a quartz substrate. For simplicity, the frequency dispersion of the ITO dielectric susceptibility has been neglected within this qualitative discussion assuming $\varepsilon_{ITO} = 3.61$. It is important that in the asymmetric guiding structure on the quartz substrate, TE_0 and TM_0 modes do not exist for energies below their cut-off frequencies. For example, structures with a 15-nm-thick ITO layer on top of a quartz substrate do not support quasiguided modes in the visible part of the spectrum, because their cut-off is shifted to much higher energies. The folded

guided modes, as explained above, are displayed in panel (b) for an assumed grating period of $d_x = 450$ nm. Note that for the degenerate Bragg resonances in the center and borders of the first BZ, the degeneracy is lifted if the neglected corrugation is taken into account.

Up to now the metallic properties of the corrugated structure were not taken into account. If the electromagnetic coupling between the individual metal nanowires is neglected, the resulting flat dispersion of the nanowire particle plasmon can be depicted as a horizontal line at approximately 1.9 eV (the dotted line in Fig. 4.6).

For an assumed period of $d_x = 450$ nm and TM polarization, especially the band located at 1.9 eV in the center of the first BZ is quite important [see Fig. 4.6(b)]. It is a degenerate triplet in this simple noninteracting picture, originating from the Bragg resonance of the lowest TM_0 guided modes with $k_{g,x} = \pm 2\pi/d_x$ and the uncoupled nanowire plasmon resonance.

According to the observations in Fig. 4.5(b), where two resonances have been detected for TM polarization at normal incidence, this degenerated triplet is actually split off. The reason for that is the periodic corrugation and the strong coupling between the electronic and optical modes. Similar interaction phenomena have already been discussed for excitonic systems [188, 192]. This behavior will be considered in Sec. 4.5.2.

4.5.2   Waveguide-plasmon polaritons

The experimental and theoretical verification of strong coupling in metallic photonic crystals is depicted in Fig. 4.7. In this figure, the measured and calculated extinction spectra of gold nanowire arrays deposited on top of 140-nm-thick ITO layers are shown for normal light incidence and different grating periods d_x. Here, a nanowire width of 100 nm and a nanowire height of 20 nm have been assumed for the scattering-matrix based calculations. For TE polarization, only one sharp spectral feature appears in each spectrum, because no nanowire plasmons can be excited for this special polarization. The existing narrow peaks can be related to the excitation of TE quasiguided modes, which are characteristic features of waveguiding photonic crystal structures. Thus, these spectrally asymmetrically shaped Fano-type resonances are not found in spectra for thinner ITO layers which do not support quasiguided modes for this spectral range. In the measurement geometry, these spectral features arise due to the grating-induced Bragg resonance of the TE_0 waveguide modes with $k_{x,g} = \pm 2\pi/d_x$. The figure clearly
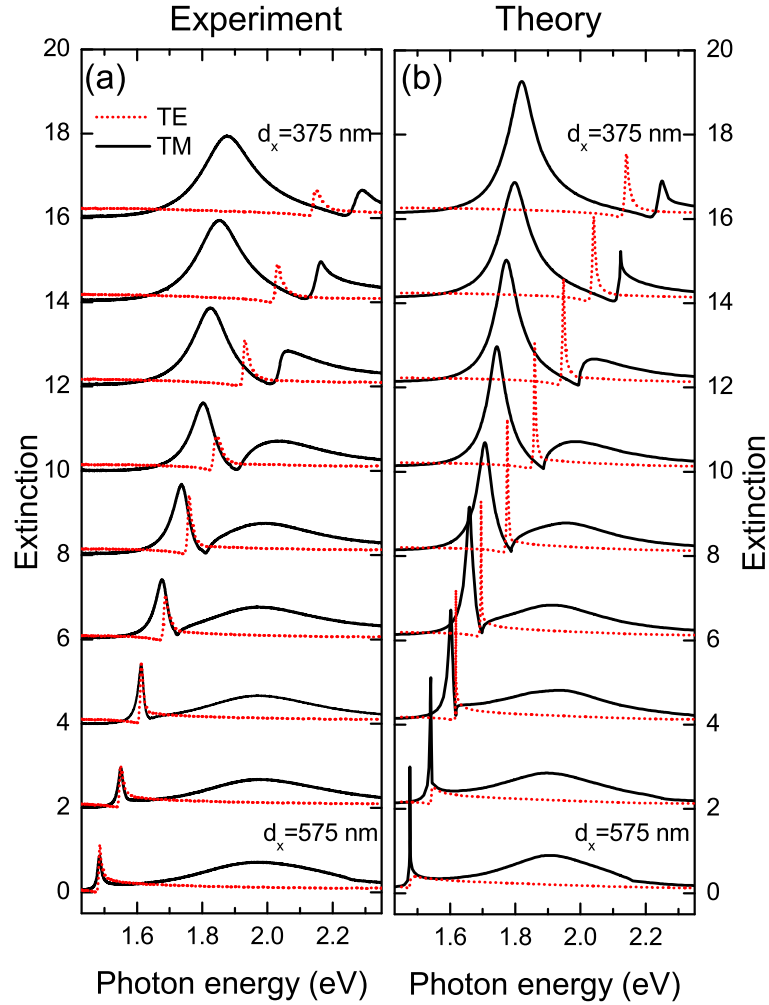
Figure 4.7: Measured (a) and calculated (b) extinction spectra of gold nanowire arrays deposited on top of 140-nm-thick ITO layers for normal light incidence and nanowire periods ranging from 375 nm to 575 nm in steps of 25 nm. Spectra for TE (dotted line) and TM (solid line) polarization are shown. The individual spectra are shifted upwards for clarity in each panel.

demonstrates that a change of the Bragg condition, caused by increasing the grating period d_x shifts the TE_0 quasiguided mode to lower energies. In principle, as already discussed earlier in this chapter, two quasiguided modes should exist at normal incidence, leading to a small stopband at the center of the first BZ. However, due to the mirror symmetry of the structure, only the upper symmetric quasiguided mode can be excited at normal incidence [193]. As is common for such structures, the lower antisymmetric mode is optically inactive and can only be observed for transmission measurements under inclined incidence.

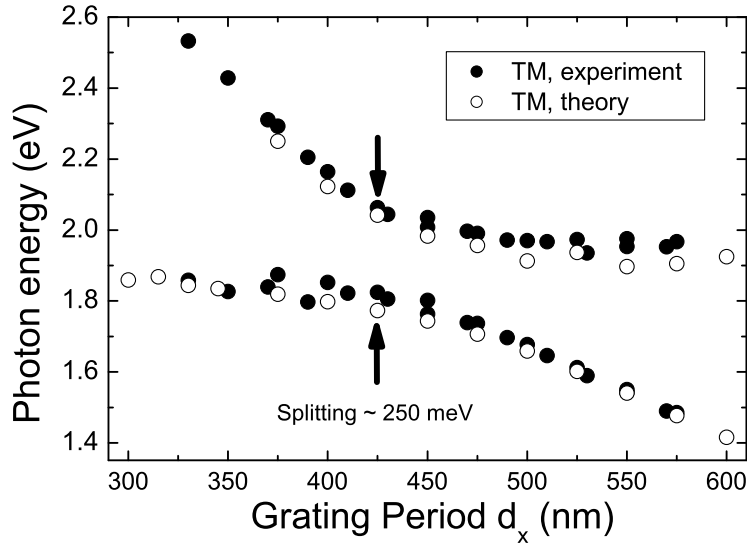Figure 4.8:   Measured (hollow circles) and calculated (solid circles) energies of the extinction spectra maxima for gold nanowire arrays deposited on top of 140-nm-thick ITO layers. The dependence on d_x for normal light incidence and TM polarization is shown.

Again, the attention has to be focused on the more significant case of TM polarization. In contrast to TE polarization, all TM polarized spectra of Fig. 4.7 exhibit two extinction maxima. For example, the extinction spectra for a period of d_x=575 nm are characterized by a narrow peak at 1.5 eV and an additional broader peak centered at 2 eV. The broader peak can be attributed to the particle plasmon of the individual gold nanowires. Like in TE polarization, the narrower extinction resonance is due to the excitation of the TM_0 quasiguided mode. Reducing the nanowire period shifts the TM_0 quasiguided mode spectrally closer to the nanowire plasmon resonance. Due to strong coupling between the waveguide and nanowire plasmon resonances, a strong anticrossing of the modes can be observed instead of their spectral overlap. This situation is comparable to the normal mode coupling in semiconductor microcavities [194], where the splitting can be interpreted as the formation of a new polaritonic state. The dispersions of the polariton branches are depicted in Fig. 4.8, nicely demonstrating the strong coupling phenomena. In this figure, the position of the maxima extracted from all measured and calculated extinction spectra are plotted for comparison. Besides the excellent agreement between the experimental and calculated values, especially the large Rabi splitting of 250 meV between the upper and lower polariton branches is very conspicuous.

The strong coupling effects lead to a more dramatic modification of the interacting systems compared to the diffractive interaction phenomena of gold nanowire structures on thin ITO layers. The key for understanding this spectacular behavior is to realize that we no longer investigate the properties of an individual metal nanowire, but rather the extinction of a new compound system, namely a strongly coupled *waveguide-plasmon polariton* system. As already discussed in a previous publication [157], the anticrossing behavior and thus the formation of a new polariton can be easily modeled in a simple resonance approximation, accounting for coupling between the isolated wire plasmon and a pair of counter-propagating guided TM_0 modes with momenta $k_x \pm 2\pi/d_x$.

Returning to the model calculations for the free-standing nanowire structure on top of a 15-nm-thick ITO layer with removed quartz substrate [see Fig. 4.4(a)], the analysis of the sharp spectral features for nanowire periods larger than $d_x = 550$ nm can now be further improved. Although assuming a very thin (only 15-nm-thick) ITO substrate in these calculations, this symmetric structure supports quasiguided modes. The frequency cut-offs for TE_0 and TM_0 modes are zero for any guiding layer thickness in case of symmetric waveguide structures (the same materials below and above the waveguide). Thus, when removing the substrate, the TM_0 mode exists in the symmetric 15-nm-thick ITO structure as well. These spectrally narrow resonances cannot be found for identical structures with an additional quartz substrate, as can be seen in the calculations for the asymmetric structures [see Fig. 4.4(b)]. Here, instead of sharp resonances, only the cusp-like Rayleigh anomalies are visible. It is important to remark that the small thickness of the ITO waveguide has a large influence on the observed coupling phenomena in the case of symmetric structures. As a consequence of the ITO thickness, the energy distance between the TM_0 mode and the vacuum light cone is very small, ~ 3 meV only. Additionally, the integrated polarization of the TM_0 guided mode is reduced, and, as a result, its coupling with the plasmon resonance is weakened. The first point explains the existence of the waveguiding anomalies in TM polarization in Fig. 4.4 notwithstanding the small ITO thickness. The second point explains why the Rayleigh anomalies are not seen: they are very close to the waveguiding anomalies.

4.5.3   Dispersion properties

The dispersion properties of the different resonances have been measured via transmission experiments by changing the angles of incidence ϑ and φ. Only two
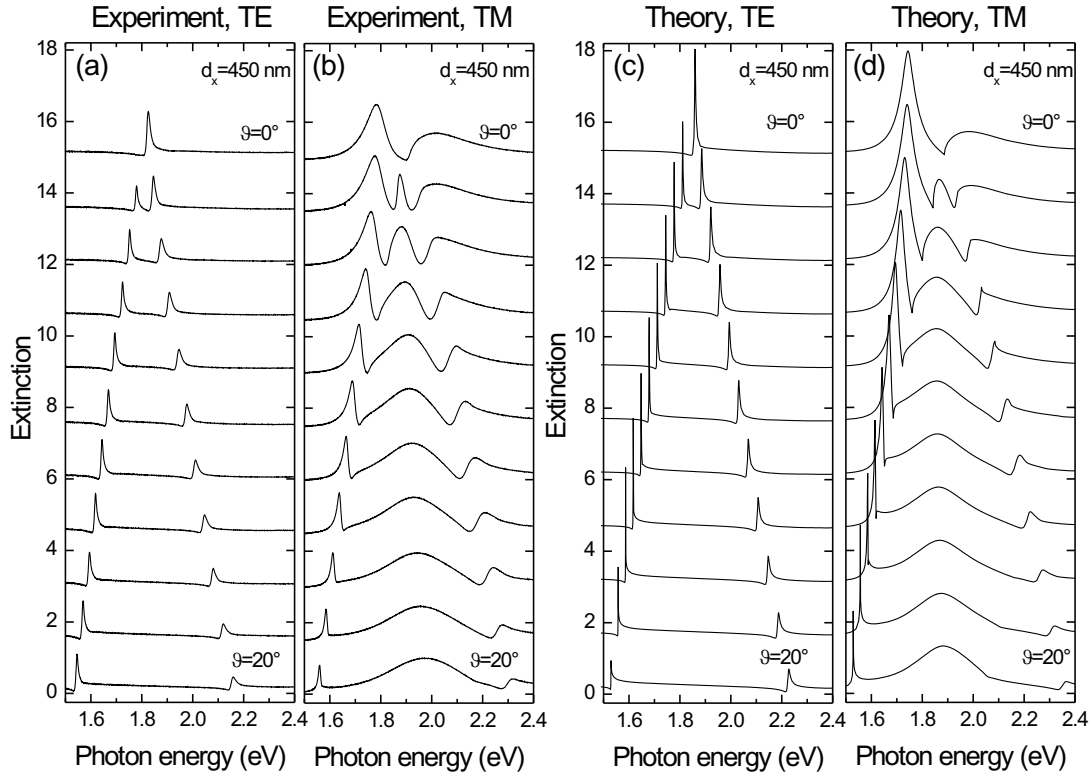
Figure 4.9:   Measured (a,b) and calculated (c, d) extinction spectra of gold nanowire arrays deposited on top of 140-nm-thick ITO layers for a fixed nanowire period of $d_x = 450$ nm. From top to bottom, the angle ϑ is increased from $0°$ to $20°$ in steps of $2°$ while $\varphi = 0°$ remains unchanged. Spectra for TE (a,c) and TM (b,d) polarization are depicted. The different spectra are shifted upwards for clarity in each panel.

cases of azimuthal angle, $\varphi = 0°$ and $90°$, will be discussed. In these cases the plane of incidence is orientated either perpendicular or along the nanowires, respectively. The results of the first set of measurements on a gold nanowire sample with fixed period $d_x = 450$ nm are displayed in Fig. 4.9 for TE (a) and TM (b) polarization. For these transmission measurements, the angle ϑ was increased from $0°$ to $20°$ in steps of $2°$ while $\varphi = 0°$ remained unchanged. Additionally, the theoretically obtained spectra are shown in Fig. 4.9 for TE (c) and TM (d) polarization. Again, gold nanowires with a width of 100 nm and a height of 20 nm on top of a 140-nm-thick ITO layer have been assumed for these calculations. It is clearly visible that the single resonance at normal incidence splits up for inclined incidence in TE polarization [(a),(c)]. The narrow peaks are due to the excitation of quasiguided TE modes of the PCS with momenta $k_{g,x} = k_x \pm 2\pi/d_x$. Now
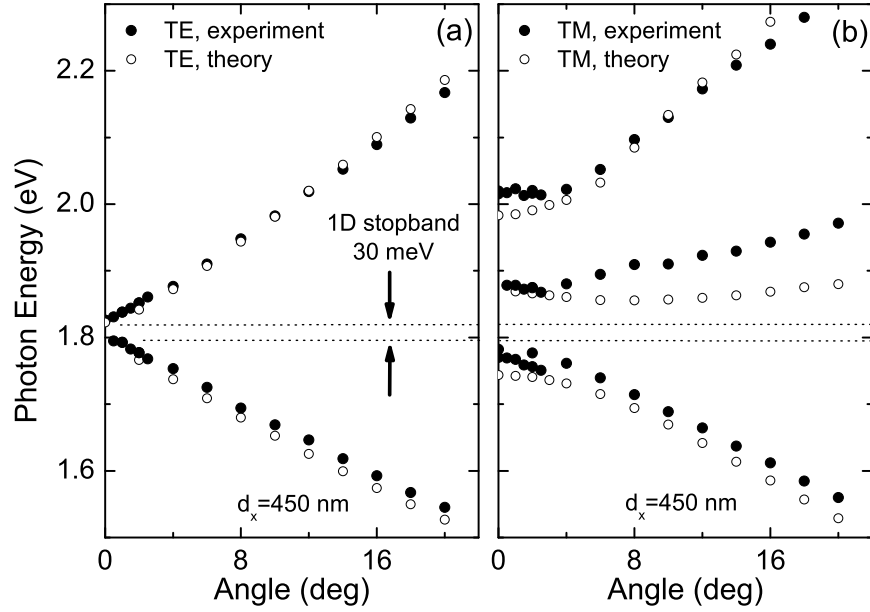
Figure 4.10: Measured (solid circles) and calculated (open circles) positions of the extinction spectra maxima in TE and TM polarization for nanowire arrays on top of 140-nm-thick ITO layers. The angle ϑ is increased from 0° to 20° while $\varphi = 0°$ and $d_x = 450$ nm remain unchanged. The arrows show the 1D stopbands in TE and TM polarizations.

the formerly not visible antisymmetric TE mode can be excited in transmission measurements for angles of incidence $\vartheta \neq 0°$. Also in TM polarization [(b),(d)] an additional peak appears between the two polariton branches for inclined incidence with $\vartheta \neq 0°$. With the change of ϑ, the plasmon resonance exhibits an anticrossing behavior with the narrower symmetric and antisymmetric TM polarized waveguide modes. All experimental results are reproduced by theory with excellent qualitative correspondence.

The energy positions of the measured and calculated extinction maxima are shown in Fig. 4.10 as solid and open symbols. It will be shown in the next section that the near-field is enhanced at the energies of such extinction maxima. In other words, the extinction maxima correspond to the energy positions of the resonant in-plane excitations of the PCS. It is interesting that in the resonant structure with $d_x = 450$ nm, the stopbands of these excitations in TE and TM polarization overlap. Therefore, the structure reveals a full (i.e., for all polarizations) 1D stopband for transmission in the x-direction.

In addition, similar measurements and calculations for another fixed azimuthal
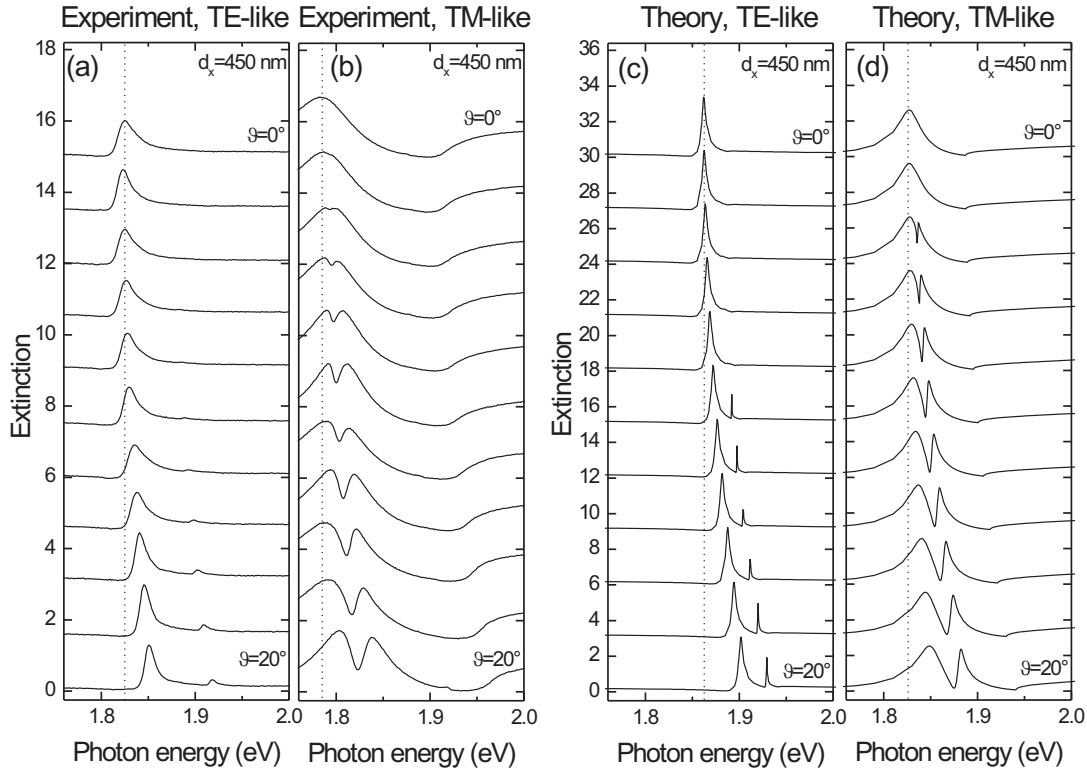
Figure 4.11: Measured (a,b) and calculated (c, d) extinction spectra of gold nanowire arrays deposited on top of 140-nm-thick ITO layers for a fixed nanowire period of $d_x = 450$ nm. From top to bottom the angle ϑ is increased from 0 to 20° in steps of 2° while $\varphi = 90°$ remains unchanged. Spectra for TE-like (a,c) and TM-like (b,d) polarization are depicted. For the calculations a wire cross-section of 85×30 nm^2 has been assumed to bring the calculated wire plasmon resonance to better agreement with the measured one. The individual spectra are shifted upwards for clarity in each panel.

angle of $\varphi = 90°$ have been performed. The polar angle ϑ was again increased from 0° to 20° in steps of 2°. Thus, the plane of light incidence is perpendicular to the slab plane, as before, but now parallel to the wires. In this geometry, the electric field is oriented perpendicular to the wires in case of s-polarization. Thus, s-polarization becomes TM-like, and a coupling with the wire plasmon is anticipated. For p-polarization, the electric field has components along the nanowires, and perpendicular to the nanowires along the z-direction. This means that no particle plasmon resonances of the gold nanowires exist in the range of light frequencies investigated in the latter case.

In Fig. 4.11, the measured and calculated spectra for p-polarized (a,c) and s-

Figure 4.12:   Calculated extinction spectra for a fixed nanowire period of $d_x =$ 450 nm and a fixed angle of $\vartheta = 20°$. Calculations for $\varphi = 90°$ (panel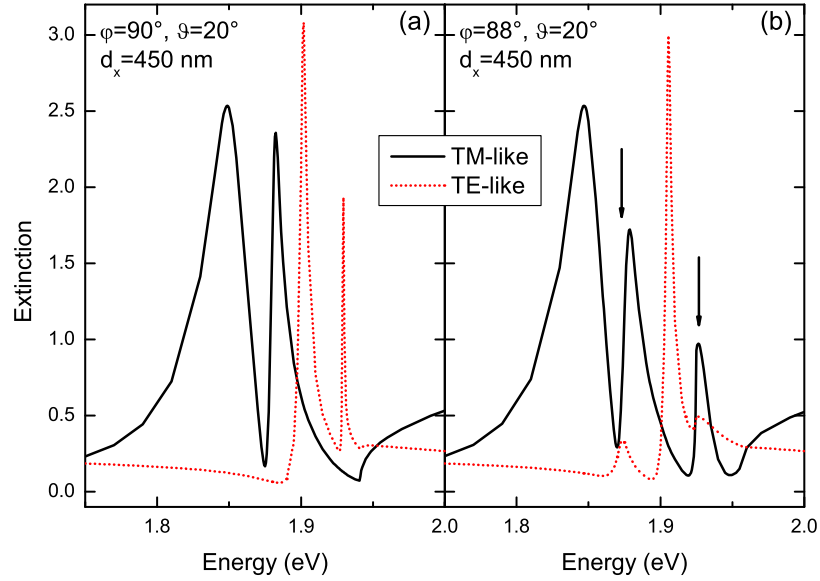 (a)) and $\varphi = 88°$ (panel (b)) are compared. Spectra for TE-like (dotted lines, p-polarization) and TM-like polarization (solid lines, s-polarization) are depicted. Again, a wire cross-section of 85×30 nm^2 has been assumed. The arrows in (b) correspond to the spectral positions of the extra modes.

polarized (b,d) light are depicted for different angles of incidence. From top to bottom, the angle ϑ is increased from 0 to 20° in steps of 2° while $\varphi = 90°$ remains unchanged. Again, the theory reproduces the measured behavior quite well. It is important to mention that the theoretically assumed nanowire dimensions have been modified slightly. The observed phenomena depend critically on the nanowire plasmon position. Therefore, a wire cross-section of 85×30 nm^2 has been employed within the calculations to get a better qualitative agreement with the experimentally measured spectra. As anticipated, the strong extinction peaks seen at normal incidence remain the dominant features at $\vartheta \neq 0°$, too. However, a new narrow mode becomes visible for each polarization with the increase of ϑ at fixed $\varphi = 90°$. Note that, according to Eq. (4.1), this geometry corresponds to the incoming light momentum $\mathbf{k} = (0, k_0 \sin\vartheta, k_0 \cos\vartheta)$. Thus, increasing the angle of incidence in this geometry, we actually measure the dispersion of the resonant modes along the nanowires.

In order to identify the additional modes, it is instructive to compare the calculated spectra (at $\vartheta = 20°$) between a symmetric situation (plane of incidence

along the wires, $\varphi = 90°$) and a slightly distorted case with $\varphi = 88°$. The results of such a calculation are shown in Fig. 4.12 for TE-like and TM-like polarization simultaneously. Important information can be deduced by comparing the spectra of panel (a) and panel (b). Additional modes become visible at $\varphi = 88°$, because this situation corresponds to a small $k_x = k_0 \sin \vartheta \sin 2° \approx 0.035 \, k_y$. The strongest extinction peak in p-polarization near the Γ-point is the symmetric TE_s mode, following the analysis above. The extra mode appearing at $k_x \neq 0$ in p-polarization at lower energies is the antisymmetric (in Γ) counterpart TE_a. Because this mode coincides exactly with the extra mode seen in the s-polarization at $\varphi = 88°$ (see the arrows in Fig. 4.12), this extra mode can be attributed to the TE_a one. Thus, the incoming s-polarized light (predominantly TM-like) can excite the TE_a mode in this geometry. The physical reason for coupling of TM- and TE-like modes is the following. Although for $\vartheta \neq 0°$ and $\phi \neq 0°$ the main harmonic is propagating along the wires ($k_x = 0$, $k_y \neq 0$), the higher Bragg harmonics are inclined, $k_{g,x} \neq 0$, $k_y \neq 0$, and therefore provide the observed polarization coupling. Repeating the same procedure with the extra mode appearing in p-polarization (predominantly TE-like), we see that the extra mode is of the TM_a type, i.e., becomes antisymmetric at the Γ-point.

It is interesting that this coupling with modes in another polarization is resonantly increased near the wire plasmon resonance. Therefore the additional modes are very weak for larger or smaller periods of d_x, although the extra modes are nominally present in the measured and calculated spectra.

The blue shift of all the modes with the increase of ϑ (that is, of k_y) is apparently quadratic in k_y due to the free light propagation in the y-direction (with no modulation), as anticipated.

4.5.4 Electromagnetic near-field distribution

In order to extend the spectral analysis of Sec. 4.5.2 and to investigate the underlying strong coupling phenomena in greater detail, it is very instructive to take a closer look at the near-field distribution of the coupled nanowire-waveguide system. The knowledge of such near-field distributions is not only important for understanding the physical mechanisms of the observed coupling phenomena, but can also help to control the nonlinear optical response in possible future applications. In this chapter, the discussion is restricted to the calculated near-field distributions, although experimental measurements with a scanning near-field

microscope should be possible at least near the sample surface [195]. All presented calculations were done within the scattering-matrix formalism. Because of very good qualitative agreement down to minor details between all calculated and measured extinction spectra, it has been assumed that the calculations of the electromagnetic field distributions give a qualitatively correct picture. All deduced information support the previous conclusions exactly.

To understand the main features of the complex near-field distributions, the discussion will be limited to structures with a period of $d_x = 450$ nm, TM-polarization, and normal light incidence ($\vartheta = \varphi = 0°$). Additionally, the field distributions are only shown for two characteristic photon energies at the waveguide-plasmon resonance. Figures 4.13 and 4.14 display the field distributions at the position of the lower polariton branch and at the extinction minimum between the two polariton branches. Due to a small spectral shift between theoretical and experimental results, the corresponding energies have to be assumed as 1.74 eV for the extinction maximum of the lower polariton branch (see Fig. 4.13) and 1.9 eV for the extinction minimum between the two polariton branches (see Fig. 4.14) in the theoretical considerations. The electric [(a),(b)] and magnetic [(c),(d)] field vectors are shown as a two-dimensional array of colored cones in the figures. The length of the cones is proportional to the field strength at the central point of each cone, and they specify the respective field direction by their orientation. However, such vector distributions are oscillating with time and cannot be displayed in a static picture. Thus, the near-field distributions are shown at the most characteristic moments of time, when the integrated intensity of the corresponding fields reaches its maximum value (see below).

Like in the beginning of this section, 100-nm-wide and 20-nm-thick gold nanowires on top of a 140-nm-thick ITO waveguide have been assumed. The schematic cross-section of the PCS is displayed by solid lines in each figure. In panels (a) and (c), the positions of the gold nanowires are indicated by rectangular regions above the 140-nm-thick ITO layer. In addition, the field distributions near the gold nanowires are drawn to a larger scale in panels (b) and (d). Note that the incoming light field propagates from the top ($z < 0$) to the bottom ($z > 0$) of the figure in all calculations.

To understand the basis of the coupling phenomena, all fields are depicted in Figs. 4.13 and 4.14 at the moments of time t (measured in units of light period $T = 2\pi/\omega$ and shown in the title of each panel) when the field intensities that are integrated over the displayed cross sections $\int_A \mathbf{E}^2 dA$ and $\int_A \mathbf{H}^2 dA$ reach maxima.
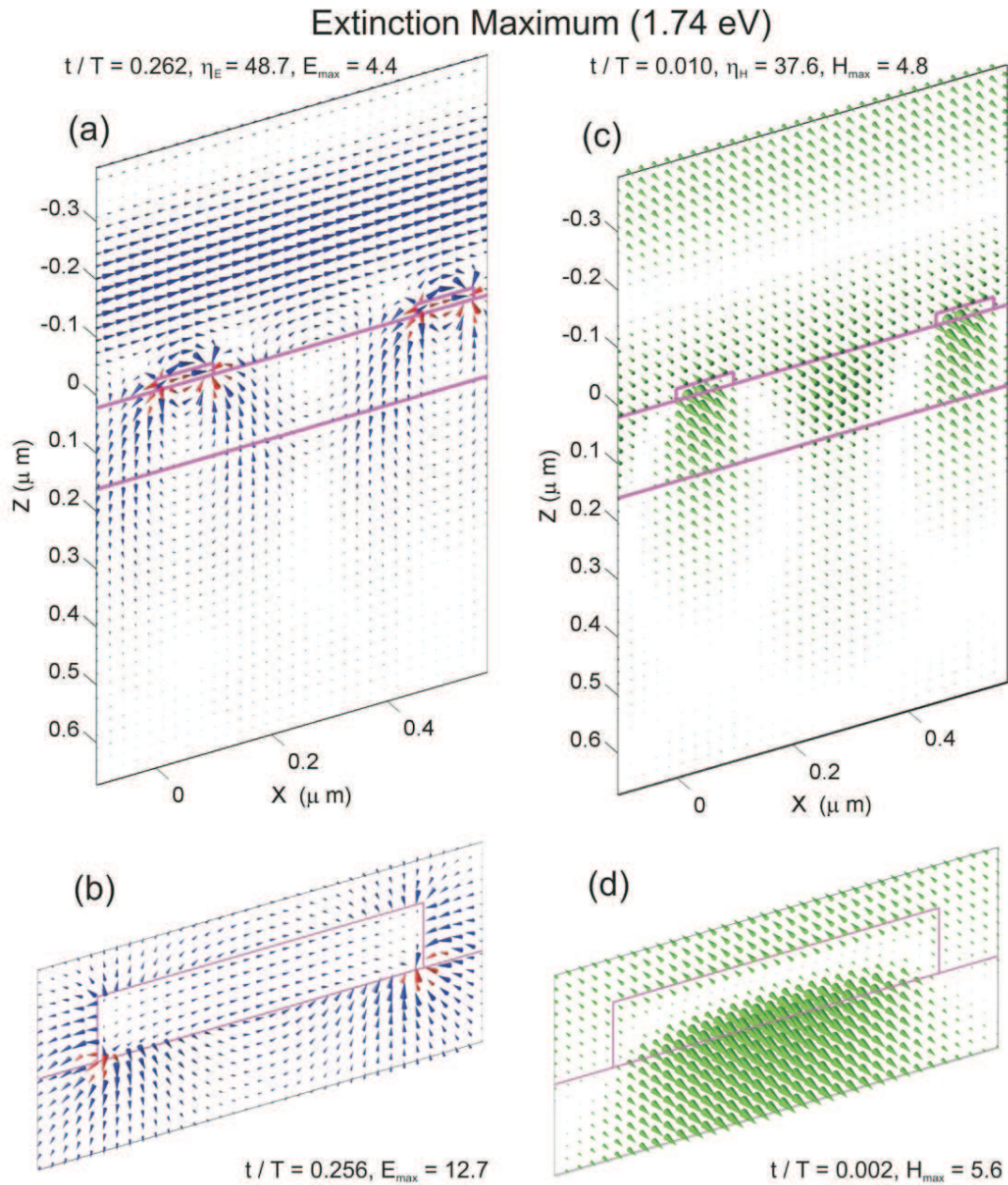
Figure 4.13: The calculated spatial distributions of the electric (panel (a) and (b)) and magnetic (panel (c) and (d)) fields in a structure with period $d_x = 450$ nm, for normal incidence ($\vartheta = \varphi = 0°$) and TM-polarization. The fields are shown for an photon energy of $\hbar\omega = 1.74$ eV. Panels (b,d) show the fields in a magnified region around the gold nanowire. Red cones in panels (a,c) are scaled by a multiplier of 0.5 in order to exclude the cones overlap.

Additional important information is provided by the calculated quantities t/T, η, and $E_{\max}$ (H_{max} for magnetic fields), shown on top of each panel, allowing an
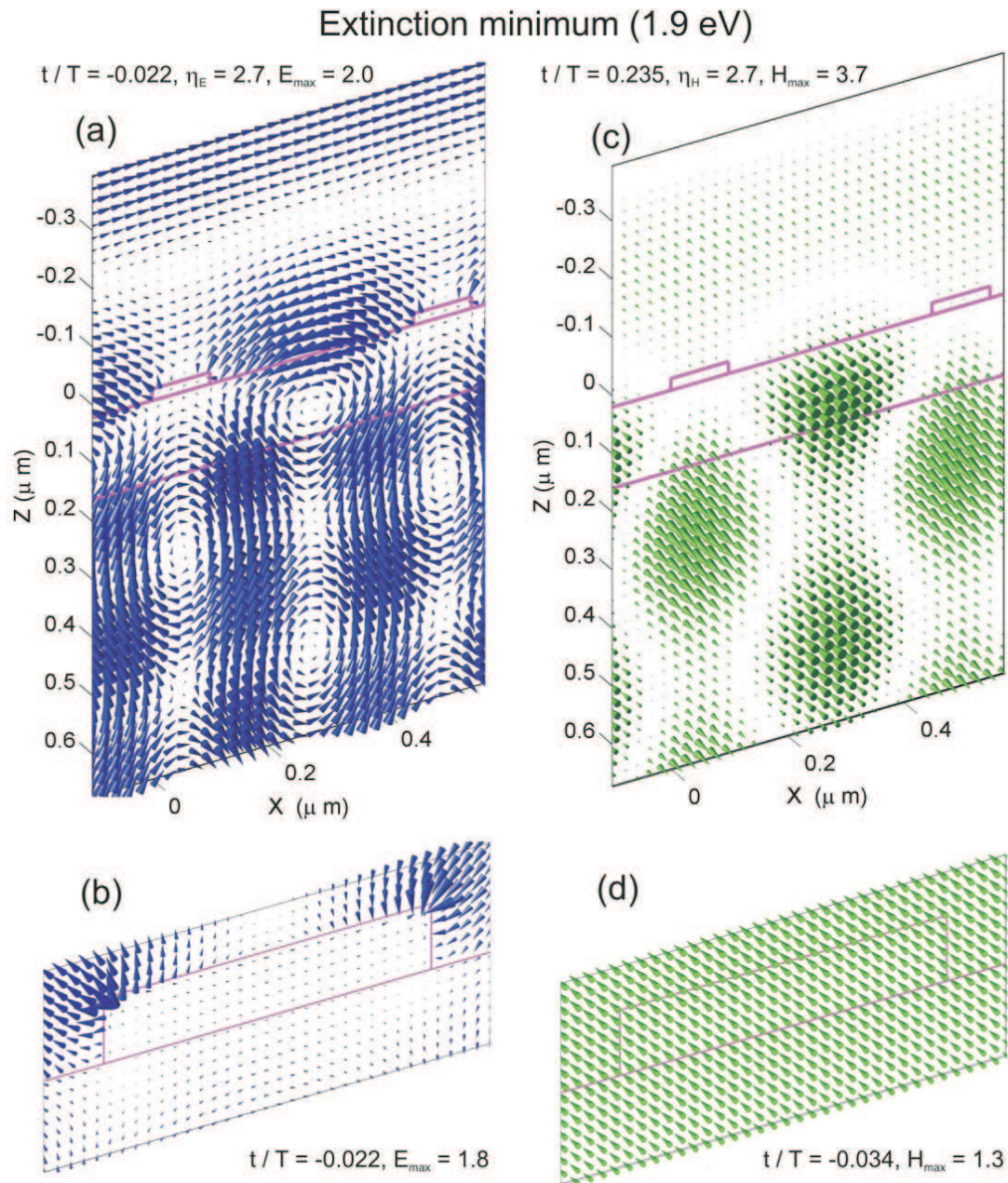
Figure 4.14: . The calculated spatial distributions of the electric (blue and red cones in panel (a) and (b)) and magnetic (green cones in panel (c) and (d)) fields in a waveguiding structure with period $d_x = 450$ nm, for normal incidence $(\vartheta = \varphi = 0)$ and TM-polarized (across the wires) light. The fields are shown for photon energy $\hbar\omega = 1.9$ eV, corresponding to the extinction minimum. All other rules for drawing this figure are the same as in Fig. 4.13.

improved interpretation of the static illustration of the oscillating fields.

The first parameter t/T enables a direct derivation of temporal information. For example, the electric field is $\mathbf{E}(\mathbf{r}, t) = \mathrm{Re}\left[\vec{\mathcal{E}}(\mathbf{r})\exp(-i\omega t)\right]$, where $\vec{\mathcal{E}}(\mathbf{r}) = \vec{\mathcal{R}}(\mathbf{r}) + i\vec{\mathcal{I}}(\mathbf{r})$. Then the electric field intensity integrated over the display area A is

$$W_E(t) = \int_A \mathbf{E}^2(\mathbf{r}, t) dA \tag{4.5}$$
$$= \overline{R_E^2}\cos^2(\omega t) + \overline{I_E^2}\sin^2(\omega t) + 2\overline{R_E I_E}\sin(\omega t)\cos(\omega t),$$

where

$$\overline{R_E^2} = \int_A \vec{\mathcal{R}}^2(\mathbf{r}) dA, \tag{4.6}$$
$$\overline{I_E^2} = \int_A \vec{\mathcal{I}}^2(\mathbf{r}) dA,$$
$$\overline{R_E I_E} = \int_A \vec{\mathcal{R}}(\mathbf{r})\vec{\mathcal{I}}(\mathbf{r}) dA.$$

Thus, $W_E(t)$ oscillates with frequency 2ω as

$$W_E(t) = \frac{1}{2}\left(\overline{R_E^2} + \overline{I_E^2}\right) \tag{4.7}$$
$$+ \frac{1}{2}\left[\left(\overline{R_E^2} - \overline{I_E^2}\right)^2 + 4\overline{R_E I_E}^2\right]^{1/2}\cos(2\omega t - \beta_E),$$
$$\beta_E = \arctan\frac{2\overline{R_E I_E}}{\overline{R_E^2} - \overline{I_E^2}}, \tag{4.8}$$

reaching its maximum value at $\omega t = \beta_E/2$ or $t/T = \beta_E/4\pi$, where $T = 2\pi/\omega$ is the light period. For the magnetic field, the maximum of $W_H(t)$ is reached at $t/T = \beta_H/4\pi$, with respective changes in Eqs. (6.2)-(6.5). Note that the minima of W_E and W_H are reached a time span $T/4$ later. The corresponding calculated values of t/T are shown for each panel.

By comparing the values of t/T for electric and magnetic fields, the character of the light propagation (standing or propagating) at a particular frequency can be estimated. In the case of purely running character, and without averaging over spatial area, both maxima are reached simultaneously. In the case of a purely standing wave, there should be a $T/4$ delay between both, because the light energy oscillates between the electric and magnetic fields.

An additional important characteristic of the EM-field distribution given in Figs. 4.13

and Figs. 4.14 [panels (a) and (c)] is the field modulation coefficient

$$\eta_E = \frac{W_{E,\mathrm{max}}}{W_{E,\mathrm{min}}} \tag{4.9}$$

$$= \frac{\overline{R_E^2} + \overline{I_E^2} + \left[\left(\overline{R_E^2} - \overline{I_E^2}\right)^2 + 4\overline{R_E I_E}^2\right]^{1/2}}{\overline{R_E^2} + \overline{I_E^2} - \left[\left(\overline{R_E^2} - \overline{I_E^2}\right)^2 + 4\overline{R_E I_E}^2\right]^{1/2}}$$

(and the corresponding quantity η_H for the magnetic field). For example, the modulation coefficient η is on the order of one for purely running waves and diverges for purely standing waves, provided that the displayed cross-section A extends over several wavelengths along the wavevector direction.

Note that the fields of Fig. 4.13 and Fig. 4.14 are scaled by different coefficients. In order to compare the absolute magnitudes of the fields, the maximum absolute value of each field, E_{max} and H_{max}, measured in units of the incoming field amplitudes is shown in each panel. Additionally, the largest cones in panels (a) and (b) of Fig. 4.13 (for the strongest electric fields near the gold nanowire edges) are shown in red and scaled by 0.5, to emphasize the regions of the largest field enhancement.

It is important to note that the averaged characteristics of the near-field distributions t/T, η, E_{max}, and H_{max} fluctuate with the mesh and cross-section A which is chosen to display the near-fields. However they provide an instructive qualitative information on the near-field distributions.

The case of the extinction maximum, which is depicted in Fig. 4.13, corresponds to a strongly standing character of the near-field. This follows from the high values of the field modulation ratios in panels (a),(c) of Fig. 4.13, $\eta_E \sim 50$ and $\eta_H \sim 40$. Compare these with the much smaller values in the case of extinction minimum, $\eta_E \sim \eta_H \sim 3$ in panels (a),(c) of Fig. 4.14.

The electric field is large and nearly homogeneous inside the wires and has a clearly dipolar character around the wires, see panel (b) in Fig. 4.13. These two features are characteristic for the dipolar plasmon resonance in subwavelength-size structures.

Another interesting feature can be noticed from a comparison between the electric and the magnetic field distributions inside the nanowires in panels (b),(d) of Fig. 4.13. Actually, it illustrates how the Maxwell equations work inside the metallic parts of the structure. First, the magnetic field is displayed approximately 1/4 of the period earlier than the electric field. Second, panel (d) shows

that the magnetic field changes its direction inside the wire, from negative to positive (i.e., along OY), approximately linearly with z. Thus,

$$\mathbf{H} \propto (0,\ z - z_0,\ 0)\, e^{-i\omega T/4} = (0,\ -i(z - z_0),\ 0),$$

where $0 < z_0 < L_z$ is inside the nanowire. From the Maxwell equation, rot $\mathbf{H} = (1/c)(\partial \mathrm{D}/\partial t)$, and for a harmonic wave $\propto e^{-i\omega t}$, this means that induction in panel (b), i.e., 1/4 of the period later than in panel (d), has to be

$$\mathbf{D} \propto (-1, 0, 0).$$

Therefore $\mathbf{D}$ has a direction opposite to OX and homogeneous along OZ. Because $\mathbf{D} = \varepsilon_{\mathrm{gold}}\mathbf{E}$, and $\varepsilon_{\mathrm{gold}} < 0$, this means that the electric field $\mathbf{E}$ has to be homogeneous across the wire and directed along OX. It is exactly what we see in panel (b).

Another exciting feature of the near-field distribution at the extinction maximum is a clearly visible horizontal standing wave inside the ITO layer. The important point is that this standing wave is pinned to the wires at the position of the anti-nodes (the field is maximum near the wire). The formation of this localized wave is due to the Bragg resonance of the two counter-propagating TM_0 guided modes with $k_{g,x} = \pm 2\pi/d_x$ as discussed above. This manifests itself by the predominant polarizations of the electric (perpendicular to the wire) and magnetic (along the wire) fields inside the ITO layer.

We can also see in Fig. 4.13 that the light does not propagate far into the substrate, which reveals the high extinction (simultaneous maxima of reflection and absorption).

In contrast to this situation for the extinction maximum, the electric field avoids the wire nearly completely in the case of high transmissivity (extinction minimum). As visible in Fig. 4.14, the distribution of the field inside the wire is still the same as in case of an extinction maximum, typical for a dipolar resonance. However, the amplitude of this dipolar field is one order of magnitude smaller. This follows from the fact that now the standing quasiguided wave in the ITO layer is pinned to the wires in another possible way, namely by its nodes. This explains actually the high transmissivity of the structure.

The fact that the wave is well transmitted through the structure is also clearly seen in Figs. 4.14(a) and 4.14(c). The strong modulation of the fields below the ITO layer occurs because the energy of the incoming light is above the Rayleigh anomaly, and two diffraction channels into the substrate are already opened. The

interference between the transmitted and diffracted beams produces this clearly visible modulation.

The maximum values of the electric and magnetic fields, given in each panel in Figs. 4.13 and 4.14, allow to estimate the degree of field enhancement in case of the resonance, and to compare it with the resonance Q-factor ($Q = \Omega/\Delta\Omega$, where Ω and $\Delta\Omega$ are the resonance energy and linewidth). For example, the quality factor of the lower energy resonance in Fig. 4.5(b) is $Q \sim 2.0$ eV/0.1 eV ~ 20, which gives the field enhancement factor $\sqrt{Q} \sim 5$. The latter is in agreement with the values of E_{max} and H_{max} specified in Figs. 4.13(a) and 4.13(c).

In order to conclude the discussion of the near-field distributions, it is important to emphasize that the near-field distribution analysis shows unambiguously that the electromagnetic field is resonantly increased at frequencies near the extinction maxima. It brings a clear additional evidence for the formation of a new quasiparticle, a waveguide-plasmon polariton, with energy dispersion manifesting itself via the extinction maxima (or, equivalently, transmission dips).

4.5.5 Effective Hamiltonian

As has been shown within the discussions of Sec. 4.5.2, the anticrossing behavior can be easily explained in terms of the formation of a new quasiparticle: polariton-type coupled modes emerge from the bare modes near the center of the first Brillouin zone (BZ). The bare modes of the considered metallic photonic crystal structure have been identified as being the gold wire plasmons and the lowest TM_0 waveguide photons with momenta around $K_\pm = \pm 2\pi/d_x$. With the exact knowledge of the dispersion of the bare modes, the observed strong coupling effects can be modelled by using a simple phenomenological approach. An effective Hamiltonian can be introduced where the polariton-type coupled modes appear as the corresponding eigenenergies of the postulated matrix. Within this approach, the effective Hamiltonian near the center of the first BZ can then be written as

$$H_{\mathrm{eff}} = \begin{pmatrix} E(K_+ + k_x) & V_1 & V_2 \\ V_1 & E(K_- + k_x) & V_2 \\ V_2 & V_2 & E_{\mathrm{pl}} \end{pmatrix}, \qquad (4.10)$$

where $E(k)$ are the bare energies of TM_0 guided modes with momenta $K_\pm + k_x$, E_{pl} is the individual wire plasmon energy, V_1 is the PBG halfwidth in the 1D PCS, and V_2 is the waveguide photon - wire plasmon coupling energy. Because of
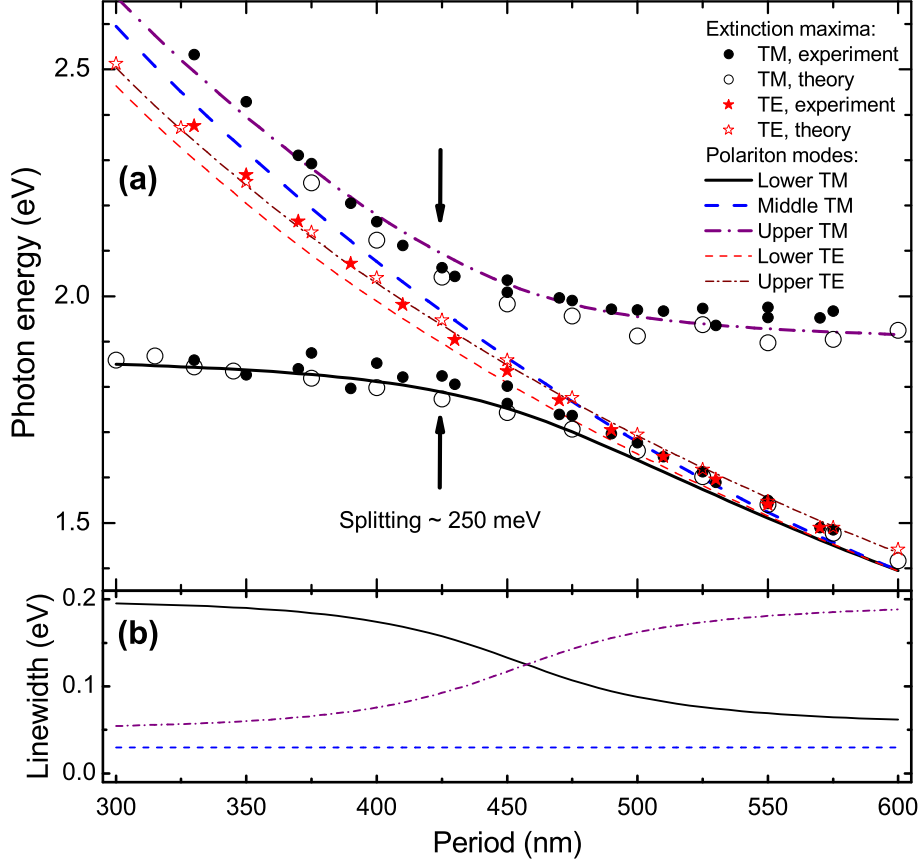
Figure 4.15: Measured and calculated positions of the extinction spectra maxima (solid and hollow) in TE (stars) and TM (circles) polarization for different grating periods. Thick lines present the dispersions of the three TM waveguide-plasmon polariton modes near the center of the 1st BZ: real and imaginary parts of the eigenenergies of Eq. (4.11) are shown in panel (a) and panel (b), respectively. Thin lines are the corresponding two quasiguided TE modes (top panel).

the mirror symmetry of the structure, $E(K_\pm + k_x) \approx E_0 \pm \tilde{c}k_x$, where E_0 and $\tilde{c}$ are the TM$_0$ mode energy and the group velocity, respectively, near momenta $\approx K_\pm$.

Due to absorption losses of light in the metal, all modes have finite linewidths. This can be accounted for using a non-Hermitian effective energy matrix instead of Eq. (4.10), substituting in Eq. (4.10) E and E_{pl} by $E - i\gamma$ and $E_{pl} - i\Gamma$, where γ and Γ are the halfwidths of the waveguide modes and wire plasmon.
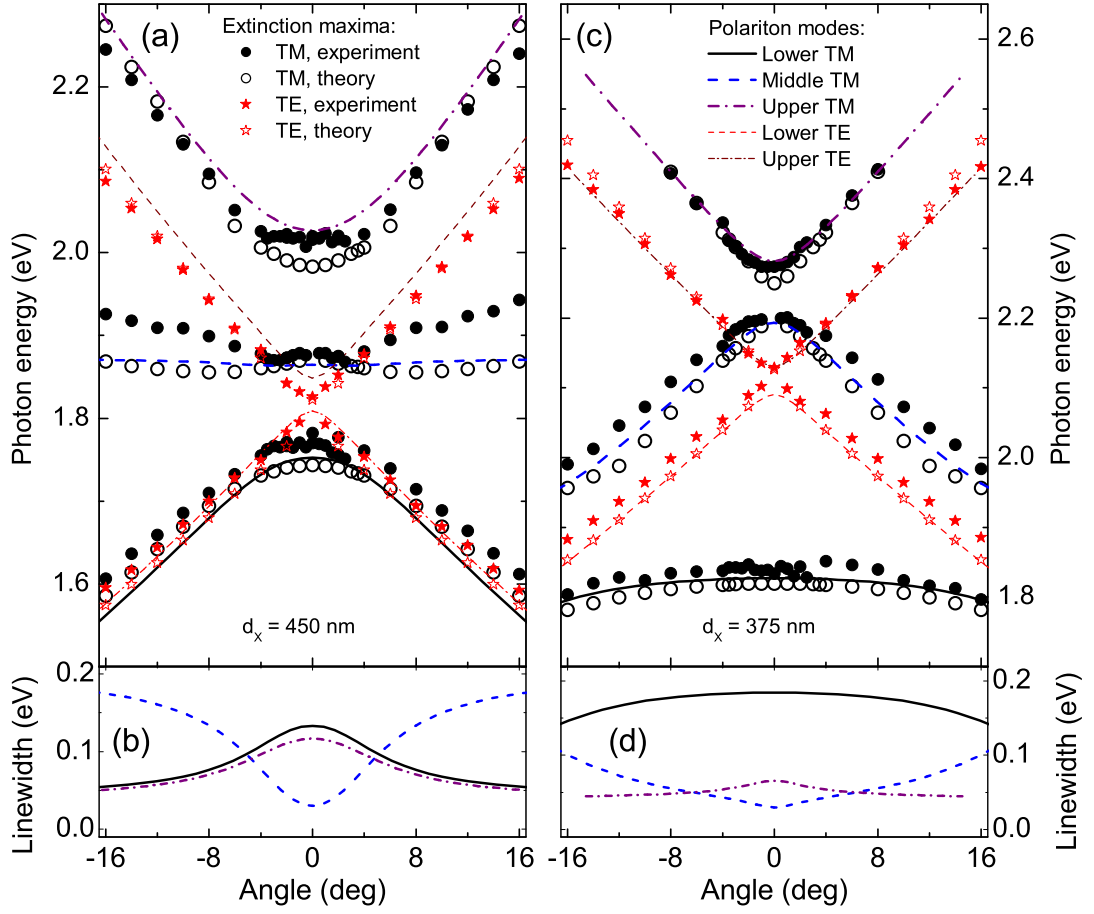
Figure 4.16: Measured and calculated positions of the extinction spectra maxima in dependence on the incidence angle ϑ. Results for periods of $d_x = 450$ nm and $d_x = 375$ nm are shown. Thick lines present the dispersions of the three TM waveguide-plasmon polariton modes near the center of the 1st BZ: real and imaginary parts of the eigenenergies of Eq. (4.11) are shown in panel (a,c) and panel (b,d), respectively. Thin lines are the corresponding two quasiguided TE modes (top panels).

The radiative losses of quasiguided modes [130] have to be included too. This can be accomplished assuming that the photonic bandgap in the PCS is complex, replacing V_1 by $V_1 - i\gamma_1$, where γ_1 is the radiative damping of the quasiguided modes. Symmetrizing and antisymmetrizing the first two rows in Eq. (4.10), we get the effective energy matrix

$$\begin{pmatrix} E_0 + V_1 - i(\gamma + \gamma_1) & \tilde{c}k_x & \sqrt{2}V_2 \\ \tilde{c}k_x & E_0 - V_1 - i(\gamma - \gamma_1) & 0 \\ \sqrt{2}V_2 & 0 & E_{\mathrm{pl}} - i\Gamma \end{pmatrix}, \qquad (4.11)$$

where the first (second) row represents the energy of the symmetrized (anti-symmetrized) photonic mode. It can be seen that the antisymmetrized mode is decoupled from the plasmon and from the symmetrized mode at $k_x = 0$, i.e., in the center of the first BZ. At $k_x \neq 0$ this mode is coupled with the particle plasmon only indirectly, via the coupling to the symmetrized mode.

The calculated eigenenergies of the matrix Eq. (4.11) reproduce the behavior of the maxima in the extinction spectra and of the linewidths surprisingly well. Fig. 4.15 displays measured and calculated (scattering-matrix formalism) positions of the extinction spectra maxima in TE and TM polarization as a function of the nanowire grating period. Again, a nanowire cross-section of $100 \times 20 \ \text{nm}^2$ has been assumed. The additionally plotted thick lines present the calculated dispersions of the three TM waveguide-plasmon polariton modes near the center of the 1st BZ. The real and imaginary parts of the eigenenergies of Eq. (4.11) are shown in panel (a) and panel (b), respectively. To draw the polariton-type coupled modes, the calculated dispersions of TE_0 and TM_0 waveguide modes in a 140-nm-thick ITO waveguide on quartz have been used. Additionally, the following fitted values were taken into account: $E_{\text{pl}}, \Gamma, \gamma, \gamma_1, V_1, V_2 = 1875, 100, 20, 5, 20, 100$ meV. The PBG halfwidth V_1 was taken from the results for the PBG from the exact scattering-matrix calculations. Presumably, these parameters (including their dependences on photon energy and horizontal components of the momentum) can be rigorously calculated within a resonance approximation to the scattering-matrix. Here, however, they are treated as adjustable parameters. In addition to the period dependent results of Fig. 4.15, the fitted angular dependencies are shown in Fig. 4.16 for nanowire periods of $d_x = 450$ nm and $d_x = 375$ nm, respectively. Note that the identical fit parameters as in the previous period dependent calculations were used. While $\varphi = 0°$ remained unchanged, the incidence angle ϑ was varied between $\pm16°$. Again, when comparing with the experimental results, the angular dependent spectral positions of the extinction maxima as well as the observed linewidths of the resonances can be modelled within this approach with high accuracy.

According to the measurements and the exact calculations, the splitting between the lower and upper polariton branches is ≈ 250 meV for normal light incidence ($\vartheta = 0°$). In the polariton model, this splitting is equal to $\sqrt{8V_2^2 - (\Gamma - \gamma - \gamma_1)^2}$. It allows to fit the value of V_2, using the measured bare plasmon mode linewidth far from the resonance. The modes in Fig. 4.15 and Fig. 4.16 weakly depend on γ and γ_1 because $\Gamma \gg \gamma, \gamma_1$.
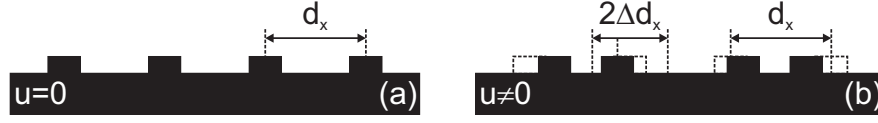
Figure 4.17: Schematic view of ordered ($u = 0$) and disordered ($u \neq 0$) nanowire arrays on top of a waveguiding substrate. In panel (b), the individual nanowires are shifted with respect to their original position (dashed squares). The individual nanowires are randomly distributed within the interval of width $2\Delta d_x$. The width of the interval is specified by the parameter u.

4.5.6   Disorder

The optical properties of metal nanowire gratings and especially the presented strong coupling between particle plasmons and quasiguided modes of the dielectric slab waveguide depend strongly on the quality of the used sample structures. Various effects like inhomogeneous broadening due to fluctuations of the nanowire geometries or a perturbation of the nanowire grating periodicity may appear. It will be shown in the following that especially the latter effect can lead to a strong modification of the observed coupling phenomena.

Although different ways of introducing an artificial disorder may be possible [179], the presented discussion is restricted to a frozen-phonon type model. In this model, the spatial position of the individual nanowire is randomly varied within a certain range around the original position (defined by the lattice constant d_x). Note that the so-called frozen-phonon model is directly derived from the phonon picture in solid state physics, where it is used for describing the lattice vibrations of a bulk crystal. An increased disorder within the nanowire array, for example, is equivalent to a higher lattice temperature in the solid state case.

A schematic view of the realized grating structures is depicted in panels (a) and (b) of Fig. 4.17. Electron beam lithography was used to prepare disordered metal nanowire arrays on top of a 140-nm-thick ITO waveguiding layer deposited on a quartz substrate. During the nanowire exposure, the effective nanowire positions were modified with respect to the perfectly ordered grating structure with a period d_x. The possible displacement was determined by the relation

$$\Delta d_x = \pm u \frac{d_x}{2} \quad \text{with} \quad u \in \{0, ..., 1\}, \tag{4.12}$$

where u is a predetermined form factor. For a given value of the parameter u, the nanowires were randomly distributed within the defined range Δd_x around their original position. All positions within the specified interval are selected with equal
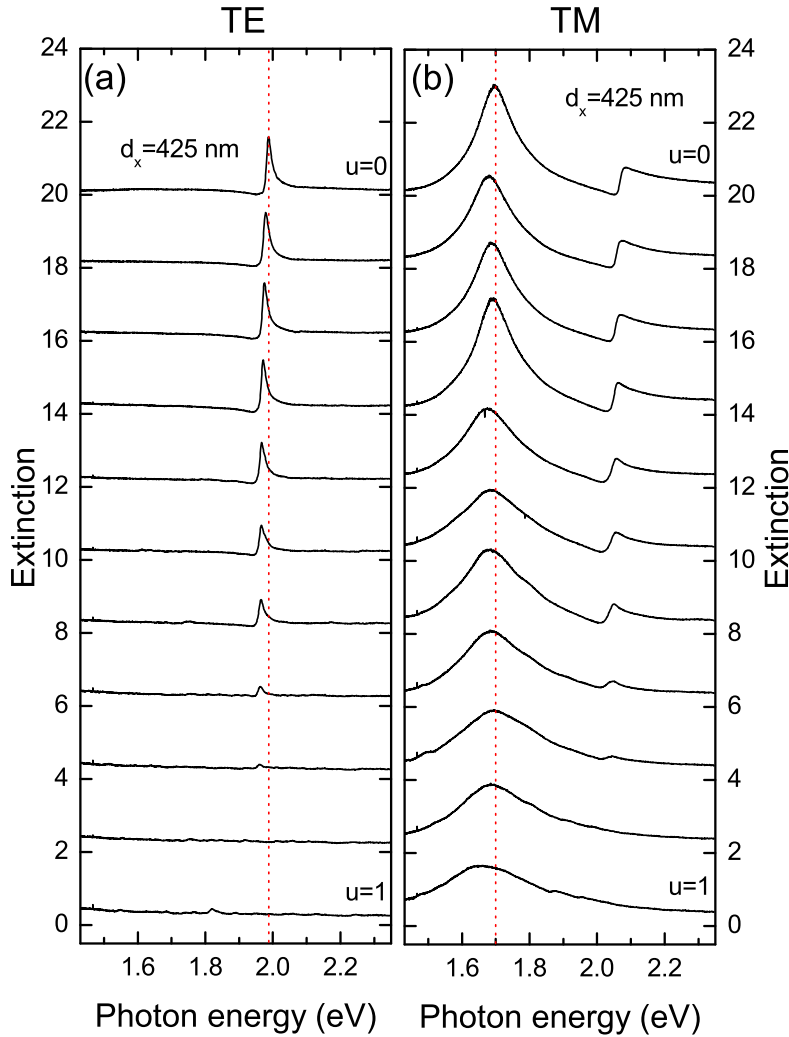
Figure 4.18: Measured extinction spectra of gold nanowire arrays with a period of $d_x = 425$ nm deposited on top of a 140-nm-thick ITO layer. The spectra are shown for TE (a) and TM polarization (b) and normal light incidence. The amount of disorder is increased from top to bottom. The width of the nanowire distribution is related to the form factor u, which is increased from 0 to 1 in steps of 0.1. The individual spectra are shifted upwards for clarity in each panel.

probability. The results of a typical extinction measurement are shown in Fig. 4.18 for a grating period of $d_x = 425$ nm and a nanowire cross-section of 100×20 nm^2. Spectra for TE and TM polarization at normal incidence are depicted in panel (a) and (b), respectively. Starting from the spectra of an ordered structure on top of the panels, the subsequent spectra are obtained by measurements on nanowire

arrays which are characterized by an increased form factor u (increased disorder).

Fig. 4.18 (a) clearly shows that the introduced disorder weakens the excitation efficiency of the lowest order TE_0 waveguide mode. While the form factor is increased from zero to one (step size: 0.1), the observed extinction is decreased simultaneously. A similar effect can be observed in panel (b) of this figure. The ordered structure (u=0) with $d_x = 425$ nm is characterized by two extinction maxima due to the arising strong coupling phenomena. If the efficient excitation of the TM_0 waveguide mode is suppressed, only the single particle plasmon resonance of the uncoupled nanowires remains visible ($u > 0.8$). Note that the suppression of the waveguide-plasmon polariton formation is accompanied by a broadening and a red shift of the nanowire plasmon resonance. This shift can be caused by two different phenomena. First, proximity effects during electron beam lithography cannot be neglected for structures with enhanced disorder. Therefore, the spatial width of certain nanowires may be increased within the fabricated array. The changed cross-section will lead to a lowering of the resonance energy, giving rise to an enhanced inhomogeneous broadening of the extinction of the nanowire ensemble. Second, also nanowire-nanowire coupling effects become more important. The effective distance between neighboring nanowires may be reduced, and near-field coupling will result in a red shift of the plasmon resonance. For larger disorder also an overlap between two single nanowires may be observable. It is important to note that in addition to the red shift of the particle plasmon, also the extinction maxima in TE polarization are slightly lowered in energy for the case $u \to 1$.

4.6   Polaritonic superlattice structures

In addition to regular and disordered metal nanowire arrays, different superlattice geometries have been investigated experimentally. As already demonstrated in Sec. 3.4 for the case of TE polarization, the proposed superlattice design strongly modifies the optical transmission properties of photonic crystal slab structures. Especially the influence of the superperiod (d_{x1}), the period within the individual supercells (d_{x2}), and the assumed number of nanowires per unit cell have been analyzed extensively (see Fig. 3.16). For example, it has been shown that the spectral positions of the supported quasiguided modes are directly determined by the chosen superperiod d_{x1}. The individual supercell geometry on the other hand can be interpreted as a geometrical form factor and can be used to suppress
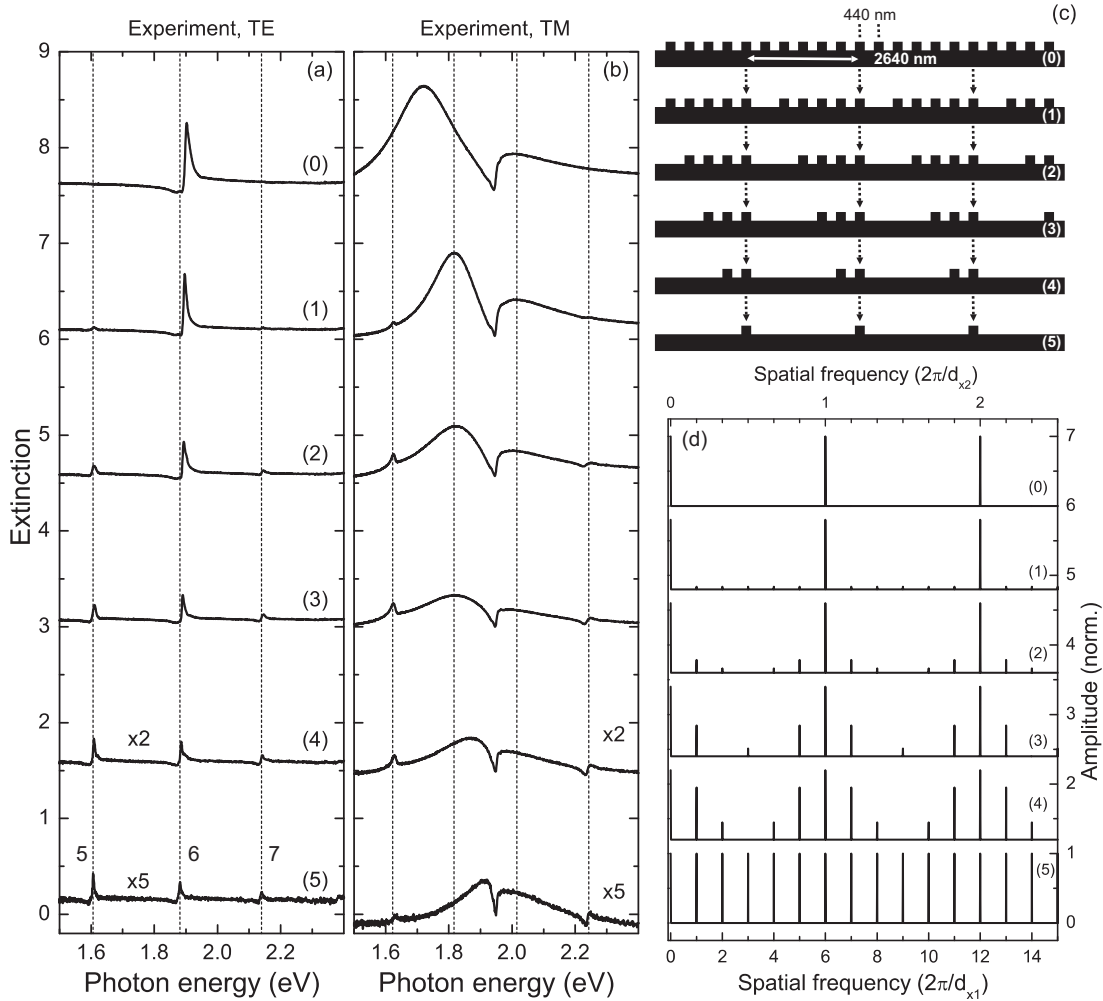
Figure 4.19: Measured extinction spectra of metallo-dielectric superlattice struc-tures at normal light incidence. Spectra for TE (a) and TM polarization are shown. A schematic view of the considered sample geometries is displayed in panel (c). The number of missing nanowires per supercell is increased stepwise from (0) to (5) while the periods $d_{x1} = 2640$ nm and $d_{x2} = 440$ nm have been retained unchanged. The individual spectra are shifted upwards for clarity in each panel. Note that the experimental spectra (4) and (5) are drawn to an ex-panded scale. The Fourier decompositions of the grating structures are shown in panel (d) in dependence on the spacial frequency. The dotted vertical lines are a guide to the eye.

or accentuate specific modes in the transmission spectra. While the studies in Sec. 3.4 were restricted to TE polarization only, the corresponding results using TM polarized light fields will be presented in the following section for the sake of completeness. It will be shown that the waveguide-plasmon polariton formation

in metallo-dielectric photonic crystal superlattice structures is strongly modified due to the appearing higher-order Bragg resonances.

Fig. 4.19 displays the experimentally measured extinction spectra of the first metallo-dielectric superlattice series for TE (a) and TM (b) polarization. All spectra were recorded at normal incidence. The specific geometries of the individual photonic crystal superlattice structures are schematically displayed in panel (c). The first sample structure (0) corresponds to a regular nanowire array deposited on top of a 140-nm-thick ITO layer. The grating exhibits a periodicity of 440 nm with an individual gold nanowire cross-section of 100×20 nm^2. The superlattice geometry is introduced by removing single nanowires of the regular grating structure. Starting from the top, structure (1) is now characterized by a supercell composed of five gold nanowires. All further structures [(2)-(5)] are characterized by the removal of additional nanowires. The superperiod $d_{x1} = 2640$ nm as well as the period within the supercells $d_{x2} = 440$ nm have been kept constant for the whole sample series. As expected, the extinction spectra in TM polarization are clearly affected by the introduction of the superlattice design. Similar to the results in TE polarization, the observed spectral modifications can be related to higher Bragg resonances of the TM$_0$ mode at the center of the first Brillouin zone.

The extinction spectrum of the regular grating structure (0) in Fig. 4.19 shows the typical waveguide-plasmon polariton signature for TM polarization (coupling between a single quasiguided mode and the nanowire particle plasmons). The depicted spectra (1)-(5) on the other hand are characterized by additional features due to the modified nanowire arrangement. More precisely, the observed interaction phenomena now incorporate three waveguide resonances and one plasmon mode. As already discussed in Sec. 3.4, the sharp spectral features in the depicted TE spectra can be related to the excitation of the fifth, sixth, and seventh Bragg resonances of the TE$_0$ mode [marked by the dotted lines in panel (a)]. Consequently, the corresponding TM modes appear in the measured extinction spectra when the light polarization is turned by 90°. Now the fifth, the sixth, and the seventh Bragg orders of the TM$_0$ mode interact with the particle plasmon resonance. While the position of these resonances can be obtained from a simple empty-lattice approximation, a Fourier decomposition of the grating structure allows the determination of the excitation efficiencies. The Fourier decomposition of the experimentally studied superlattice structures is again displayed in panel (d).

Thus, the interpretation of the phenomena observed in Fig. 4.19 is more or less

straightforward. All displayed superlattice structures are characterized by an identical superperiod of d_{x1}=2640 nm. The spectral position of the bare modes is therefore not modified and only the extinction as well as the coupling efficiencies (coupling between the particle plasmon resonance and the waveguide modes) are affected by the removal of individual nanowires (modification of the form factor). From top to bottom, the extinction is lowered due to the effectively reduced number of illuminated gold nanowires. However, it is worth emphasizing one important observation which is directly related to the altered coupling efficiencies. The pronounced lower extinction maximum in TM polarization is continuously shifted to higher energies when individual nanowires are successively removed from the perfect grating structure. While the extinction maximum coincides with the lower waveguide-plasmon polariton branch at approximately 1.72 eV for structure (0), the extinction maximum is shifted to 1.92 eV for the modified grating geometry (5). This experimental observation can be traced back to the reduced coupling strength between the particle plasmon mode and the sixth order Bragg resonance. Consequently, the removal of individual nanowires can be understood as an effective lowering of the field overlap between particle plasmon and waveguide resonance which generally results in a reduced polariton splitting. Note that the emerging fifth and seventh Bragg orders of the TM_0 mode [outer dotted lines in Fig. 4.19 (b)] are only weakly coupled to the particle plasmon due to their off resonant position with respect to the particle plasmon energy.

More pronounced modifications of the optical response can be observed in the measured spectra of the second sample series. The experimental results are displayed in Fig. 4.20. Measured extinction spectra (normal light incidence, $\vartheta = 0°$) are shown for TE (a) and TM (b) polarization, respectively. As schematically depicted in panel (c), the influence of the superperiod d_{x2} is probed. While the period d_{x2}=475 nm and the number of nanowires ($n = 10$) per supercell is kept constant, only the superperiod d_{x1} is increased from 4750 nm (0) to 5550 nm (8) in steps of 100 nm. This procedure corresponds to a continuous enlargement of the supercell separation. All fabricated superlattice structures again possess an individual nanowire cross-section of approximately 100×20 nm^2.

As shown in panel (a) for the case of TE polarization, the spectral positions as well as the excitation efficiencies of the individual waveguide resonances are strongly modified in dependence on the specific grating geometry. The plotted extinction spectra can be explained by the interplay of the chosen nanowire periods. The spectral position of the observed higher-order Bragg resonances of the TE_0 mode is directly determined by the superperiod d_{x1}. The extinction
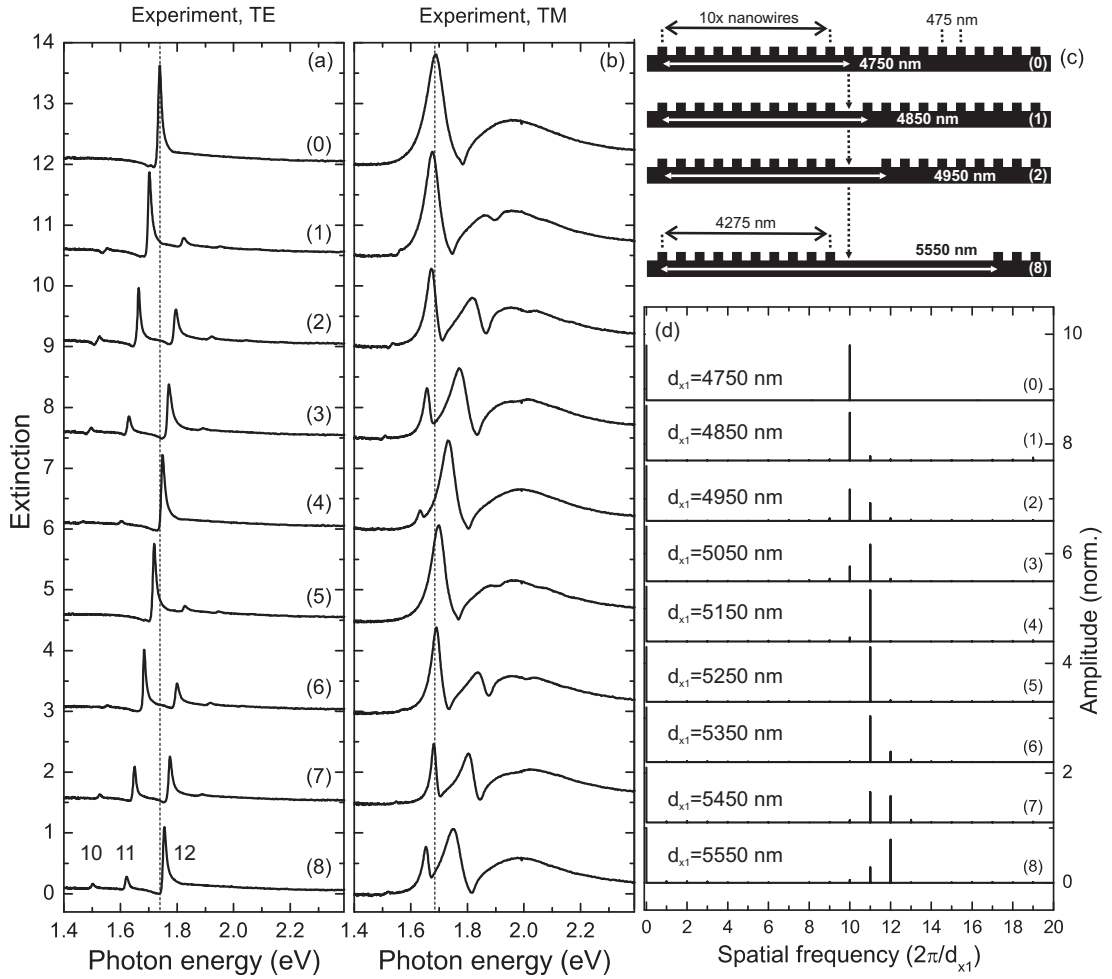
Figure 4.20: Measured extinction spectra of metallo-dielectric superlattice structures at normal light incidence. Spectra for TE (a) and TM polarization are shown. A schematic view of the considered sample geometries is displayed in panel (c). While the supercell period of 475 nm and the number of nanowires (n=10) have been kept constant for all samples, the superperiod d_{x1} is increased from 4750 nm (0) to 5550 nm (8) in steps of 100 nm. The individual spectra are shifted upwards for clarity in each panel. The Fourier decompositions of the grating structures are shown in panel (d) in dependence on the spacial frequency. The dotted vertical lines are a guide to the eye.

efficiencies of the individual Bragg orders on the other hand are controlled by the period d_{x2} and the number of nanowires per supercell. Hence, the specific supercell geometry can be interpreted as an artificial form factor (see also Sec. 3.4 for more details). As already discussed earlier, the Fourier decomposition of the grating in Fig. 4.20 (d) allows the extraction of the excitation efficiencies of the Bragg orders. For example, the extinction efficiencies of the tenth, eleventh, and

twelfth Bragg resonances of the superlatttice structure (8) are directly related to the corresponding amplitudes of the Fourier decomposition.

Compared to the results for the case of TM polarization in Fig. 4.19 (b), the displayed spectra in Fig. 4.20 (b) show a much stronger modification of the optical response with respect to the chosen geometrical parameters. One important difference can be related to the fact that the new sample series is generally characterized by the implementation of larger superperiods d_{x1}. While all superlattice structures in Fig. 4.19 possess a constant superperiod of d_{x1}=2640 nm, larger superperiods with $d_{x1} \geq 4750$ nm have been realized for the grating structures in Fig. 4.20. The energy spacing between the observed Bragg resonances of the lowest order waveguide modes is therefore clearly reduced. Hence, depending on the exact superlattice period d_{x1}, several more or less strongly pronounced Bragg orders show a spectral overlap with the broad particle palasmon resonance. For example, the experimental spectra of structure (2) in Fig. 4.20 (b) can be explained by the interaction between the particle plasmon and two higher-order Bragg resonances. Only the coupling with the tenth and eleventh Bragg order leads to significant spectral modifications. The Fourier amplitudes of the ninth and twelfth Bragg resonance are only weakly pronounced (compare with panel (d) of Fig. 4.20). Thus, there interaction strength with the particle plasmon resonance is nearly negligible for the specific grating geometry (2).

4.7   Investigation of the coupling strength

It has been shown in the previous sections that the interaction of optical waveguide modes and particle plasmon resonances in planar metallo-dielectric photonic crystals generally leads to the formation of a so-called waveguide-plasmon polariton. As a result, the dispersion of the strongly coupled system is characterized by an anticrossing between the emerging polariton branches. The coupling strength between the bare modes of the system is directly proportional to the observed polariton splitting. So far, all investigated periodic metal nanowire arrays were directly deposited on top of the used 140-nm-thick ITO waveguide slabs. For the further completion of the physical understanding, especially the question of whether the coupling strength can be controlled by introducing simple geometrical modifications has to be answered. In this section, we will therefore extend our analysis to the investigation of possible ways to alter the waveguide-plasmon coupling strength by changing the photonic crystal design. Two different approaches
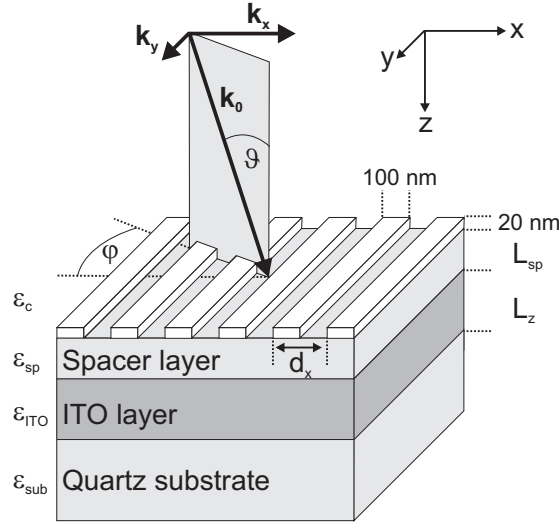
Figure 4.21: Schematic view of the modified sample geometry. The gold nanowire array is separated from the ITO waveguide slab by introducing a dielectric spacer layer. The thickness L_{sp} of the spacer layer can be used for controlling of the observed coupling phenomena.

will be addressed in the following. Both the introduction of an additional buffer layer as well as the modification of the waveguide thickness will be analyzed. The presented discussion is restricted to theoretical calculations only and should be considered as a motivation for further experimental investigations.

4.7.1   Influence of a dielectric spacer layer

One possible modification of the metallo-dielectric photonic crystal slab design is the introduction of an additional buffer layer. A schematic drawing of the proposed grating-waveguide geometry is shown in Fig. 4.21. As extension to the previously used slab structure (e.g., see Fig. 4.1), the one-dimensional metallo-dielectric photonic crystal is now characterized by the insertion of a dielectric spacer layer. The spacer layer of thickness L_{sp} leads to a spatial separation of the gold nanowire array and the underlying ITO waveguide slab. For simplicity reasons, quartz has been used as spacer as well as cladding layer material ($\varepsilon_{sp}=\varepsilon_c=\varepsilon_{sub}=2.13$) in all subsequent numerical calculations. The extinction efficiencies for the corresponding grating structures have been calculated for normal light incidence using the scattering-matrix formalism [130]. Period (d_x) as well as thickness dependent (L_{sp}) calculations have been accomplished for TE and TM polarization.

Figure 4.22:   Calculated extinction spectra of the modified grating waveguide structure. From top to bottom, the spacer layer thickness L_{sp} is decreased from 600 nm to 0 nm. The ITO waveguide thickness of 140 nm has been kept constant. Calculations for nanowire periods of $d_x = 300$ nm, $d_x = 400$ nm, and $d_x = 450$ nm are depicted. All spectra are shown for normal light incidence and TM polarization. The individual spectra are shifted upwards for clarity in each panel. The insets allow a magnified view of the arising spectral anomalies. Vertical arrows mark the position of the diffractive anomalies ($L_{sp} = 50$ nm).

Extinction spectra of the proposed grating waveguide structure are displayed in Fig. 4.22 in dependence on the spacer layer thickness. Numerical results for nanowire periods of 300 nm (a), 400 nm (b), and 450 nm (c) are shown at normal light incidence and TM polarization. From top to bottom, the thickness L_{sp}

is reduced from 600 nm to 0 nm in each panel, respectively. The theoretically obtained spectra are based on gold nanowire arrays with an individual nanowire cross-section of 100×20 nm^2. Additionally, a constant ITO waveguide thickness of 140 nm has been used for all shown calculations.

Only the bare particle plasmon resonances can be observed in panel (a) of Fig. 4.22. As a result of the chosen grating period of $d_x = 300$ nm, the extinction anomalies due to the excitation of the lowest quasiguided slab mode (TM$_0$ mode) are shifted to energies above 2.5 eV. The observed bare particle plasmon resonances are therefore only weakly modified when reducing the spacer layer thickness. Only a small shift of the particle plasmon resonance can be observed for small waveguide-grating separations ($L_{sp} < 50$ nm). This fact can be related to the modified effective dielectric constant of the nanowire surrounding. Thus, the nearby ITO waveguide layer alters the remaining restoring forces of the oscillating conduction band electrons and induces a redshift of the particle plasmon resonance energy. Alternatively, also a hybridisation-like picture might be possible. The nanowire plasmon resonance is redshifted due to the interaction with the own electromagnetic fields which are partially reflected at the quartz-ITO interface (interaction with a weak mirror dipole). The calculated extinction spectra become more complex when the nanowire periods are increased to $d_x = 400$ nm or $d_x = 450$ nm. Now the TM$_0$ waveguide mode is tuned to resonate with the particle plasmons of the individual gold nanowires. Especially panel (c) of Fig. 4.22 reveals some interesting physical phenomena. The lowest spectrum ($L_{sp} = 0$ nm) shows the characteristic line shape of the waveguide-plasmon polariton resonance. Hence, the two observed extinction maxima approximately correspond to the positions of the lower and upper branches of the formed polariton state. As shown in this panel, the energy spacing between the two maxima is strongly reduced when increasing the spacer layer thickness. In case of $L_{sp} = 600$ nm, only a very narrow dip at the center of the particle plasmon resonance remains visible. Note that a small additional feature appears at the high energy side of the depicted polariton resonances. As discussed earlier, these period dependent anomalies can be related to the opening of the first diffraction orders into the cladding layers (e.g., Rayleigh anomalies are marked by vertical arrows for $L_{sp} = 50$ nm). The distinct modification of the interaction phenomena can be related to the reduced coupling strength between the bare modes of the polariton. Both the achievable polariton splitting as well as the spectral width of the excited waveguide resonances are directly effected when increasing the buffer layer thickness. Phenomenologically, the spacer layer can be used to reduce the spatial overlap of the waveguide
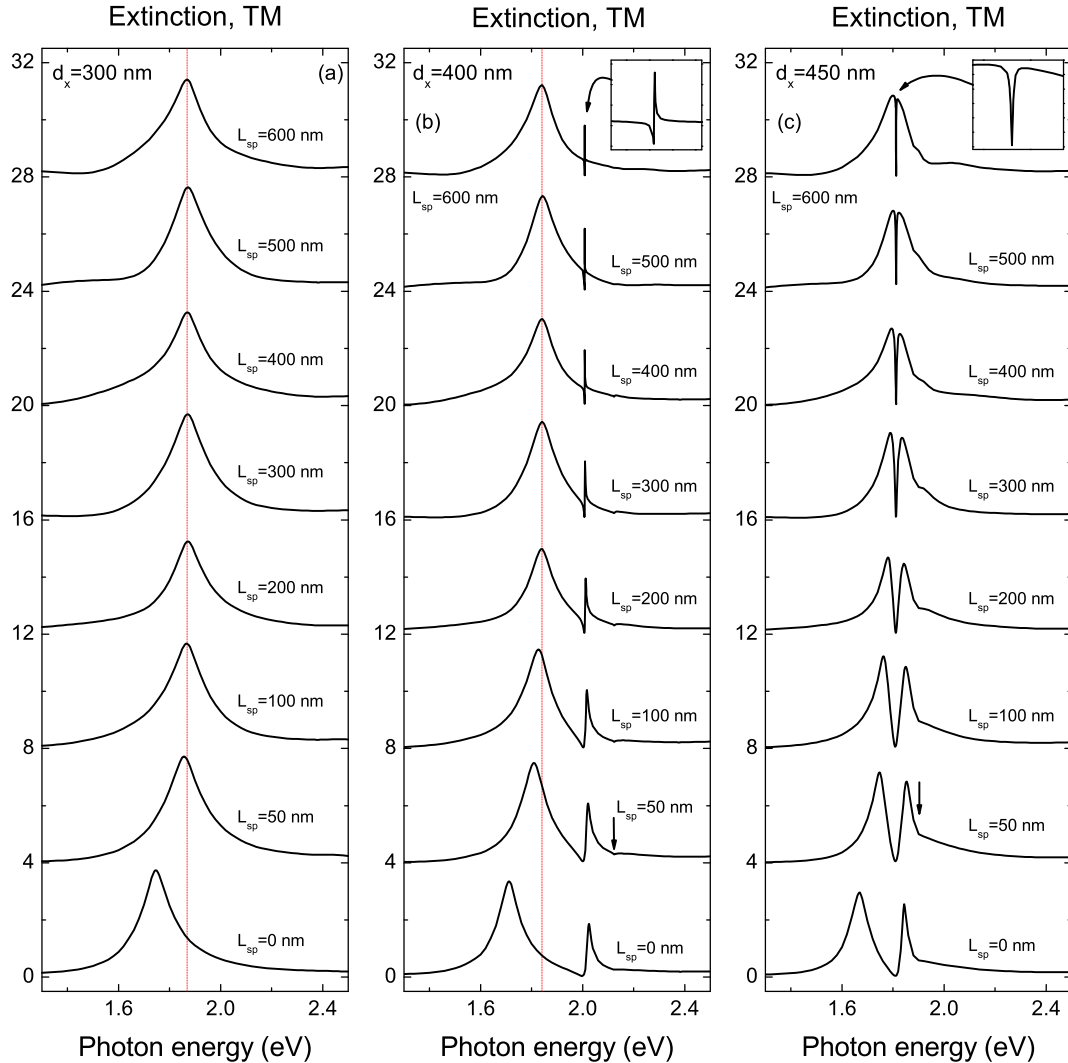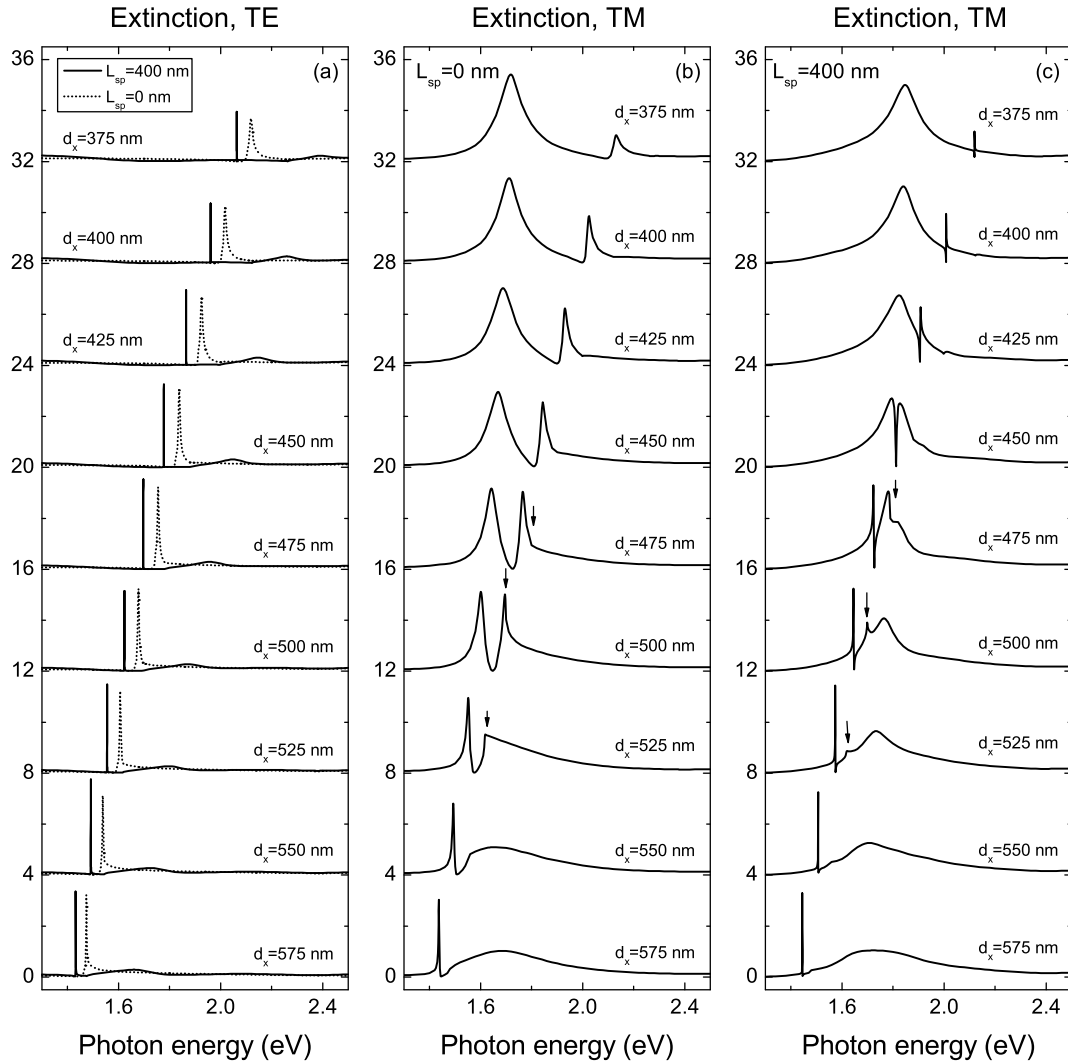
Figure 4.23: Calculated extinction spectra of the modified grating waveguide structure. From top to bottom, the nanowire period is increased from $d_x = 375$ nm to $d_x = 575$ nm in steps of 25 nm. Spectra for TE (a) and TM polarization (b,c) are displayed in dependence on the spacer layer thickness. The numerical results for structures with $L_{sp} = 0$ nm and $L_{sp} = 400$ nm are compared. The ITO waveguide thickness of 140 nm has been kept constant. All spectra are shown for normal light incidence. The individual spectra are shifted upwards for clarity in each panel. Vertical arrows mark the position of the diffractive anomalies.

and plasmon related electromagnetic fields and thus to weaken the interaction strength.

Important further details of the spacer layer induced phenomena can be extracted from Fig. 4.23. The extinction spectra are depicted in dependence on the nanowire

period d_x to highlight the exact anticrossing behavior in TM polarization. From top to bottom, the gold nanowire period is increased from $d_x = 375$ nm to $d_x = 575$ nm in steps of 25 nm. All calculations are based on gold nanowire arrays with an individual nanowire cross-section of 100×20 nm^2. Additionally, a constant ITO waveguide thickness of 140 nm has been used for all calculations. The numerical results for structures with $L_{sp} = 0$ nm and $L_{sp} = 400$ nm are compared in panel (a) of Fig. 4.23 for the case of TE polarization. The corresponding results for TM polarization are displayed in panel (b) and panel (c) of the figure, respectively.

The influence of the additional buffer layer on the optical response of the grating-waveguide structure is clearly seen in Fig. 4.23 for both light polarizations. While an increased spacer layer thickness leads to a redshift and to a prolonged lifetime (reduced linewidth) of the quasiguided TE$_0$ mode in panel (a), even more pronounced modifications can be found in panel (b) and (c) for the case of TM polarization. Generally, the reduction of the nanowire period shifts the waveguide resonance towards higher energies. Considering the quasiguided TM$_0$ mode only, the simultaneous excitation of the nanowire plasmons results in strong coupling and therefore the formation of a new polariton. Qualitatively, the theoretical spectra depicted in panels (b) and (c) of Fig. 4.23 show a similar behavior. The interaction between both resonances can be observed due to a clear mode splitting when changing the nanowire period. While the spectra for $d_x = 375$ nm and $d_x = 575$ nm look quite similar, stronger deviations can be found for intermediate periods. Especially the achievable mode splitting is drastically reduced due to the spacer layer induced weakening of the coupling efficiencies. Another interesting spectral feature is again related to the so-called Rayleigh anomalies. In addition to the two extinction maxima of the polariton modes in panel (c), a small spectral feature can be observed between these distinct maxima for the specific nanowire periods of $d_x = 525$ nm, $d_x = 500$ nm, and $d_x = 475$ nm (marked by vertical arrows).

It is important to remark that the modified sample design (incorporating an additional buffer layer) can also be used to optimize the discussed grating-waveguide based filter devices (e.g., see Chap. 3.3.4). As already shown by the numerical results in Fig. 4.23 (a), the combination of a dielectric spacer layer and a symmetric slab geometry ($\varepsilon_{sp}=\varepsilon_c=\varepsilon_{sub}=2.13$) leads to a reduced spectral width of the waveguide resonances. Thickness dependent calculations of the transmission spectra are plotted in Fig. 4.24 (a) assuming TE polarization and normal light incidence to illustrate the influence of the dielectric spacer layer more systemat-
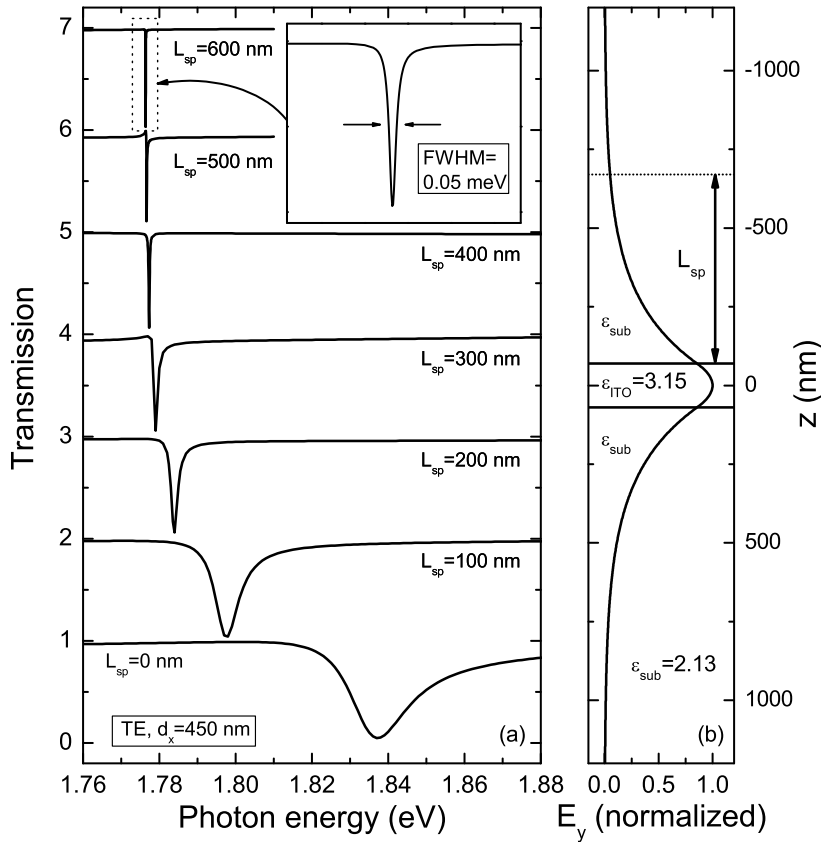
Figure 4.24:   Calculated extinction spectra of the modified grating waveguide structure for TE polarization and normal light incidence are shown in panel (a). A constant grating period of $d_x = 450$ nm, a nanowire cross-section of 100×20 nm^2, and a ITO slab thickness of 140 nm have been assumed. From top to bottom, the spacer layer thickness is decreased from $L_{sp} = 600$ nm to $L_{sp} = 0$ nm in steps of 100 nm. The individual spectra are shifted upwards for clarity in each panel. The spatial distribution of the electric field amplitudes (E_y) is displayed in panel (b) assuming $k_x = 2\pi/450$ nm^{-1}.

ically. A gold nanowire array with a nanowire cross-section of 100×20 nm^2, a grating period of $d_x = 450$ nm, and an ITO layer thickness of 140 nm have been used for the scattering-matrix calculations. From top to bottom, the spacer layer thickness is decreased form $L_{sp} = 600$ nm to $L_{sp} = 0$ nm in steps of 100 nm. Note that the depicted numerical calculations predict very narrow resonances, although metal nanowire gratings have been used. The influence of the dispersive metal wires is strongly seen in the reflection spectra (not shown). In contrast to filter geometries which are based on non-absorptive nanowire arrays (e.g., see
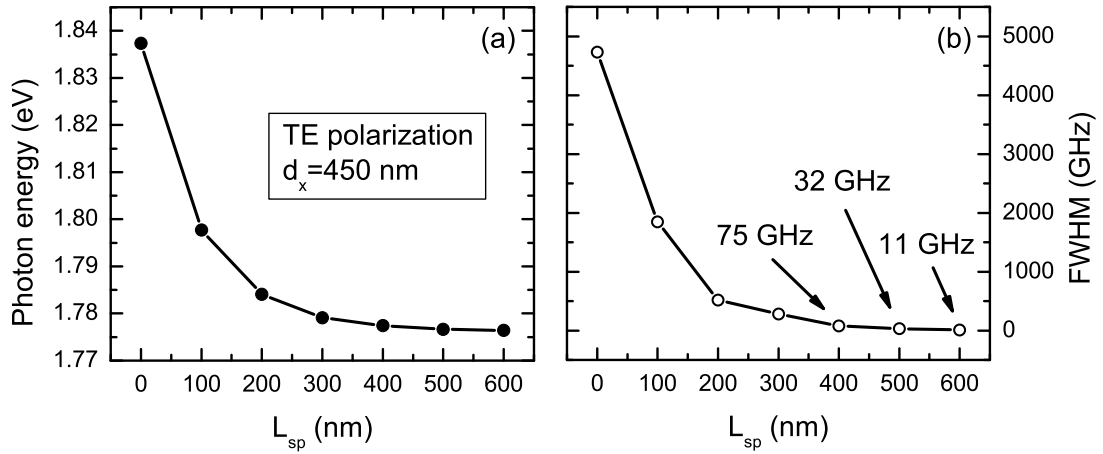
Figure 4.25:   Spectral position (a) and FWHM (b) of the TE_0 mode (symmetric slab mode) for normal light incidence and TE polarization in dependence on the spacer layer thickness.   A constant grating period of $d_x = 450$ nm, a nanowire cross-section of 100×20 nm^2, and an ITO slab thickness of 140 nm have been assumed. The shown data have been extracted from Fig. 4.24.

Chap. 3.3.4), the resonant reflectivity of the metallic structures does not reach 100 percent.

Two important observations can be extracted from the shown transmission spectra. Both the spectral position as well as the spectral bandwidth of the transmission resonances are clearly effected by the buffer layer. The extracted values (spectral position and FWHM) are shown in panels (a) and (b) of Fig. 4.25. The spectral shift of the quasiguided modes can be explained by the altered effective permittivity of the waveguide slab when changing the buffer layer thickness. The reduced spectral width of the transmission resonances on the other hand is caused by the weakened coupling between the TE_0 mode and the external light fields (reduced overlap of the fields). For example, the spatial distribution of the transverse component of the electric field is displayed in panel (b) of Fig. 4.25. For simplicity reasons, the calculation of the displayed field component is based on a homogeneous 140-nm-thick ITO waveguide neglecting the periodic nanowire array completely. In case of thicker spacer layers and due to the fact that the fields decay quickly within the cladding layers, the formerly guided modes of the slab structure (electromagnetic fields) are only weakly perturbed by the presence of the periodic grating array. The attenuated efficiency of the grating coupler (nanowire grating) therefore results in prolonged lifetimes of the quasiguided

modes and hence a higher quality of the obtained transmission resonances.

At first sight, it seems very surprising that the reduced coupling efficiency only affects the width of the calculated transmission resonances. Theoretically, the resonant transmissivity (absolute value) is not altered when changing the spacer layer thickness. Generally, waveguide anomalies as narrow as the numerically calculated modes cannot be seen in real experiments due to various reasons. For example, possible absorption of the slab material is neglected. Furthermore, all numerical calculations are based on structures with an infinitely large grating array. The grating size as well as the illuminated area have to be considered in all experimental investigations. Additionally, also the always present angular distribution of the incident light fields (non-normal light incidence) due to the use of imperfectly collimated beams acts as a limiting factor. Another important phenomenon is directly related to the non-perfect sample fabrication processes. Unintentionally, the introduction of disorder [see panel (a) of Fig. 4.18] leads to a reduction of the extinction efficiencies.

Note that a very similar behavior was found when discussing the filter properties of dielectric grating waveguide structures in Chap. 3. As already shown in Fig. 3.10, the linewidth of the quasiguided modes can be reduced by decreasing the height of the surface corrugation. In the limit of vanishing surface modulation, the linewidth approaches zero. The transmissivity, on the other hand, is theoretically not affected (zero transmission due to excitation of the waveguide mode).

4.7.2   Variation of the dielectric slab thickness

Finally, the influence of the ITO slab thickness will be discussed in the following subsection of the chapter for the sake of completeness. It is important to mention that the first evidence for such a modification of the optical response can already be found in Fig. 4.4 (a). In this figure, the plotted spectra of the grating-waveguide structure are characterized by very narrow spectral anomalies. In particular, the presented theoretical calculations are based on a 15-nm-thick ITO waveguide slab under the assumption of symmetric cladding layers (waveguide layer is sandwiched between air half spaces). The clearly visible anomalies show a strong dependence on the specific nanowire period. So far, an exact interpretation of the observed narrow features is still missing. Especially the conspicuous narrow dip at the center of the particle plasmon resonance ($d_x = 650$ nm) was not
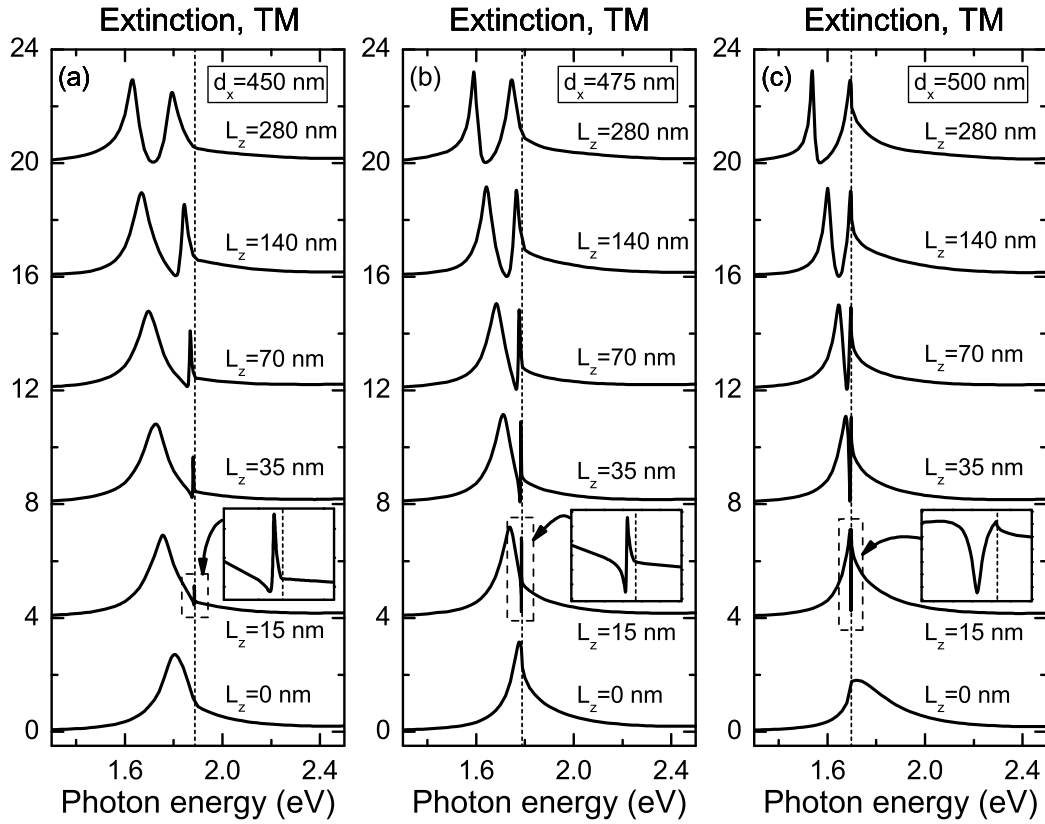
Figure 4.26:   Calculated extinction spectra of the grating waveguide structure without spacer layer (L_{sp}=0 nm) in dependence on the waveguide thickness. From top to bottom, the ITO slab thickness L_z is decreased from 280 nm to 0 nm. Calculations for nanowire periods of d_x = 450 nm, d_x = 475 nm, and d_x = 500 nm are depicted. All spectra are shown for normal light incidence and TM polarization. The individual spectra are shifted upwards for clarity in each panel. The insets allow a magnified view of the arising spectral anomalies. Vertical dotted lines mark the position of the diffractive anomalies.

addressed within the previous investigations. It will be shown in the following discussions, that the depicted spectra can be understood in terms of a reduced coupling strength between the single optical waveguide mode and the particle plasmon resonance.

New results of scattering-matrix based calculations are plotted in the three panels of Fig. 4.26. Similar to the schematic view in Fig. 4.21, gold nanowire arrays with a nanowire cross-section of 100×20 nm^2 have been used as a basis for these numerical calculations. All depicted spectra have been calculated for normal light incidence and TM polarization. Quartz has been chosen as spacer

as well as cladding layer material ($\varepsilon_{sp}=\varepsilon_{c}=\varepsilon_{sub}=2.13$). Note that no additional buffer layers have been introduced ($L_{sp}=0$ nm). The calculated extinction spectra are displayed in dependence on the ITO slab thickness for nanowire periods of $d_x=450$ nm (a), $d_x=475$ nm (b), and $d_x=500$ nm (c). From top to bottom, the slab thickness is decreased from $L_z=280$ nm to $L_z=0$ nm.

As expected, the depicted spectra show a clear dependence on the ITO slab thickness as well as on the nanowire period. Only the bare plasmon resonances can be observed in the specific case of $L_z=0$ nm (lowest spectra in the three panels). As marked by the vertical dotted lines, only the opening of the first-order diffraction channels (i.e., so-called Rayleigh anomalies) induces modifications of the particle plasmon line shape in this situation. The position of the Rayleigh anomaly is shifted to higher energies by increasing the nanowire period, thus altering the plasmon resonance. More pronounced modifications of the optical response can be observed when ITO layers with a thickness of $L_z \neq 0$ nm are taken into account. It is important to remark that the introduced ITO waveguide layers are characterized by zero cut-off frequencies due to the used symmetric slab design ($\varepsilon_{c}=\varepsilon_{sub}$) and the negligence of any material dispersion (ITO and quartz are assumed as being non-absorptive). The displayed extinction spectra are therefore characterized by two distinct maxima which can be related to the simultaneous excitation of quasiguided slab modes and particle plasmon resonances. As already discussed in more detail, strong-coupling between these two resonances generally leads to a polariton formation. The dispersion of the so-called waveguide-plasmon polariton is therefore characterized by an antcrossing of the arising polariton branches. The presented spectra in Fig. 4.26 show that the observed polariton splitting is clearly modified by changing the slab thickness and hence altering the waveguide-plasmon coupling strength. In panel (c) for example, the bare modes of the polariton are tuned in resonance, d.h., both modes possess identical resonance frequencies. While the spectra show a distinct splitting of the polariton branches in case of $L_z=280$ nm, the width of the observed polariton gap is strongly reduced when the slab thickness approaches $L_z=0$ nm. For $L_z=15$ nm, only a very narrow dip within the spectrally broad particle plasmon resonances can be found [e.g., see inset in panel (c)]. The calculated spectra can be understood by accounting for the spatial electromagnetic field distribution of the corresponding waveguide modes. Considering a homogeneous (no corrugation) and symmetric waveguide, the mode confinement is directly related to the assumed thickness of the slab. The mode is only weakly guided in case of thin slab layers due to the fact that a large part of the electromagnetic field is located outside of the waveguide [e.g., see panel (b)

of Fig. 4.24]. The dispersion of the guided modes therefore approaches the light cone of the cladding layer material. As a result, the effective overlap of the electromagnetic fields is strongly reduced if a periodic gold nanowire arrangement deposited on top of a very thin symmetric waveguide layer is considered. The reduced overlap of the fields is equivalent to a weakened interaction and hence an attenuated coupling efficiency between the two resonances. In other words, the grating array can be considered as being a weak perturbation in case of thin waveguide layers. Only the use of thicker waveguiding slab layers allow for optimization of the coupling efficiencies [3]. Another important fact seems to be quite interesting. Due to the large differences in the spectral width of the involved modes (waveguide and particle plasmon resonances), the displayed extinction spectra of the polaritonic system are characterized by strongly asymmetric line shapes. This observation is a clear indication of the Fano-type nature and is typically for systems where a narrow resonance (e.g., a waveguide mode) interacts with a spectrally broad continuum (e.g., a particle plasmon resonance).

A similar explanation (reduced coupling strength) holds for the observations in Fig. 4.4 (a), too. The spectrally narrow waveguide mode is tuned to lower energies by increasing the nanowire period. The interaction with the particle plasmon resonance results in a polariton splitting. However, due to the use of the thin ITO slab layer and therefore reduced coupling strength, only a small mode splitting can be observed. As shown by the inset of the figure, the arising polariton resonances are characterized by the typical Fano-type line shape (i.e., interaction between a narrow waveguide mode and a broad particle plasmon resonance).

4.8   Conclusions

In conclusion, it has been shown experimentally and theoretically that far-field coupling effects can strongly influence the optical properties of gold nanowire gratings deposited on top of dielectric ITO layers. The presented discussion clearly demonstrates that the transmission spectra of such photonic crystal structures can change substantially with the substrate thickness. While gold nanowire gratings on top of thinner ITO substrates, not supporting optical waveguide modes, only

---

[3]Note that also the use of very thick slab layers result in a weakening of the interaction (i.e., fields are strongly confined within the waveguide and the grating can be considered as a weak pertubation). Thus, the largest coupling efficiency may be achieved by using intermediate slab thicknesses. Further investigations have to clarify this point in more detail.

induce diffractive anomalies, structures on top of thicker waveguiding ITO layers can exhibit a much richer behavior. The transmission spectra of such structures are characterized by an additional sharp spectral feature due to the excitation of quasiguided modes of the corrugated waveguide. Strong coupling between these optical modes and the particle plasmon resonances of the nanowires results in the formation of a waveguide-plasmon polariton with a large Rabi splitting of nearly 250 meV. Scattering matrix theory gives an excellent agreement between all experimentally measured and theoretically modelled extinction spectra. Furthermore, it has been shown that the scattering matrix formalism can be used to model the spatial distribution of the electromagnetic near-fields of the photonic crystal structure. The calculations reveal the existence of a standing wave inside the ITO layer below the gold nanowire gratings. In the case of strong coupling, this standing wave has field maxima at the position of the gold nanowires, leading to a large field enhancement near the wires and therefore high extinction values. The extinction minimum between the two polariton branches in contrast is due to a standing wave with anti-nodes between the nanowires and therefore only weak fields at the position of the gold nanowires. Further experimental investigations have to clarify in more details how the observed coupling between the plasmon and the waveguide resonances can be influenced by introducing an additional dielectric spacer layer.

Chapter 5

Electric-dipole resonances near a metal surface

An experimental and theoretical analysis of the interaction between localized particle plasmons of metal nanowire gratings and surface plasmons on a nearby thin metal film will be presented. The appearance of grating-induced surface plasmon resonances, which critically depend on the dielectric spacer layer thickness, provides evidence that the optical response of these planar metal structures can be strongly modified. Numerical calculations indicate that especially the simultaneous excitation of particle plasmon and surface plasmon resonances gives rise to strong coupling phenomena. The predicted anticrossing behavior can be interpreted in terms of polariton formation. We show that the presented coupling phenomena vary with the nanowire grating period, with the nanowire cross-section, with the chosen angle of incidence, and also with the metal- as well as the spacer layer thickness.

5.1   Introduction

The investigation of the light-matter interaction is still a very important research field in modern physics. For example, it is well known from Fermi's golden rule [196] that the spontaneous emission and therefore the lifetime of an excited atom or molecule (oscillating dipole) can be altered by controlling the photonic density of states [197]. A modified photonic density of states (DOS) may be achieved by a proper sample design, changing the boundary conditions of the electromagnetic fields. Various approaches have been realized so far. In addition

to the use of microcavities as light confining structures [148, 194], especially the recent photonic crystal approach seems to be very promising [3, 4]. For example, photonic crystal microcavities with high quality factors and very small mode volumes have been presented quite recently [9]. A rather simple concept on the other hand is the modification of the photonic DOS due to an interaction with a single nearby reflecting surface [25]. It has been shown that the molecular fluorescence decay time strongly depends on the spatial separation between a molecule and a nearby metal interface [26]. Additionally, also frequency shifts of an electric dipole resonance near a conducting surface have been found experimentally [107] as was initially theoretically proposed [198]. Note that within these experiments metal island films were used as an optimized model system instead of using molecular dipoles. It is important to remark that not only the radiative decay and the spectral position of the electric dipole resonance may be influenced by the presence of the metal surface. Furthermore, a non-radiative energy transfer between the dipole and the surface may modify the lifetime of the dipolar excitation [25]. When the electric dipole is brought into close proximity to a planar metal surface, energy will be transferred due to resonant surface plasmon excitation. Although surface-plasmon induced effects have been investigated for quite a long time, the related phenomena have become popular again very recently. Significant research effort is especially devoted to the investigation of the interaction between lower-dimensional semiconductors (e.g., semiconductor quantum wells) and metal nanostructures. For example, one important current research goal is to enhance the efficiency of light-emitting devices. The modification of the photoluminescence efficiencies due to interaction with both corrugated as well as planar metal layers have been addressed quite recently [28, 32, 66, 70, 199].

Up to now, only the interaction between single or randomly distributed dipoles and metal surfaces has been investigated to our knowledge. Although the influence of periodically textured surfaces has been studied [200], an interesting alternative situation may arise when a periodic arrangement of dipoles (e.g., molecules, quantum dots, or metal particles) is placed in front of a planar metal film. As we will show in this section, the interaction between a regular array of electric dipoles and a thin metal film opens up new and interesting coupling phenomena. Similar to Ref. [106] and [107], we propose an entirely metallic model system. Noble metal nanowires have been used as elementary electronic dipoles within our experimental and theoretical considerations. The optical response of these metal nanowires is generally characterized by particle plasmon resonances which are a consequence of the coherent oscillation of their conduction band electrons [36].

As shown in the previous chapter, the optical response of metal nanowire arrays can already be strongly modified by a neighboring thin dielectric film. While Rayleigh-type anomalies were observed for metal gratings on top of dielectric substrates [201], waveguiding substrates can induce strong coupling phenomena [157]. Instead of an artificial control of electronic (plasmons) and geometrical resonances (waveguide modes), the new purely metallic structure investigated in this chapter enables the simultaneous control of localized nanowire particle plasmons and extended surface plasmons at the thin metal film.

The proposed grating structures are also interesting from another point of view. In some respects, the structures are very similar to the periodically modulated planar metal surfaces, including the well-known hole and slit arrays [71–73]. Besides their exceptional light transmission properties, these prominent structures are especially characterized by the simultaneous excitation of localized and extended modes. It has been shown that extended surface plasmons on both sides of the metal film as well as slit modes have to be considered to explain the observed extraordinary optical properties.

In this chapter, we present an extended theoretical and experimental analysis of the optical phenomena predicted for periodic metal nanowire arrays in front of a nearby thin metal film. We clearly demonstrate that near- as well as far-field effects strongly modify the optical response with respect to the single nanowire case. Particularly, it will be shown that the observed phenomena can be related to three main interaction mechanisms. First, an instantaneous (quasistatic) dipole-dipole coupling between the individual nanowire plasmons and their corresponding image dipoles induces spectral shifts of the particle plasmons. This near-field effect shows a strong distance dependence, i.e., the coupling strength decreases gradually with the grating-film separation. Second, also radiative coupling has major influence and has to be considered within the discussions. The particle plasmon oscillations are driven by their own radiation field which is reflected at the metal interface. Third, due to the periodic nanowire arrangement, the simultaneous excitation of particle and surface plasmons leads to additional interaction phenomena. Especially the modification of the nanowire periodicity and therefore the spectral tuning of the Bragg scattering-induced surface plasmon modes enables an artificial control of the coupling between both plasmon resonances. One of the most interesting related physical questions is how the interplay between these three interaction effects modifies the optical response of the proposed multilayer system.
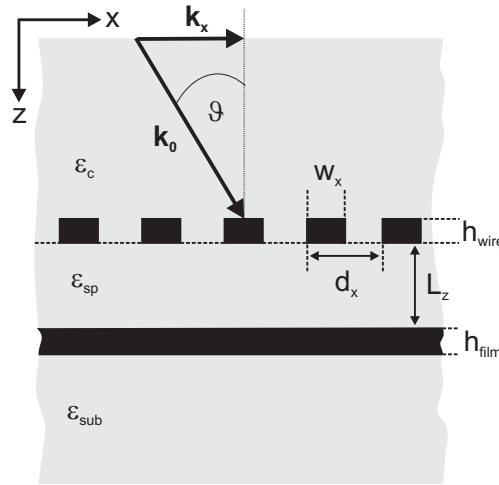
Figure 5.1:   Schematic view of the proposed metal structure. A periodic metal nanowire array is separated from a thin metal film by a dielectric spacer layer. Samples with different spacer- (L_z) and metal layer (h_{film}) thicknesses are investigated. Angle- as well as polarization-dependent transmission measurements are possible.

The structure of the chapter is as follows. In Sec. 5.2, we describe the proposed metal nanowire structure and the used experimental setup. The discussion of the related physical phenomena starts in Sec. 5.3 with a purely theoretical analysis of the optical response. The influence of near- and far-field coupling effects will be presented. The theoretical investigations are followed by first experimental verifications which will be analyzed in Sec. 5.4. Optical transmission measurements on gold nanowire gratings placed in front of thin silver films have been performed. Finally, a summary of all findings is given in Sec. 5.5.

5.2   Samples and experimental techniques

Fig. 5.1 displays a schematic view of the proposed sample geometry. The photonic crystal structure consists of a one-dimensional metal nanowire grating which is separated from a thin metal film by a dielectric spacer layer of thickness L_z. Although a combination of various dielectric materials might be possible ($\varepsilon_{\text{sub}}, \varepsilon_{\text{sp}}, \varepsilon_{\text{c}}$), the discussion is restricted to structures based on quartz as a substrate and spacer layer material ($\varepsilon_{\text{sub}} = \varepsilon_{\text{sp}} = \varepsilon_{\text{quartz}} = 2.13$), respectively. No dielectric cap layers (vacuum) have been considered, leading to the assumption $\varepsilon_{\text{c}} = 1$. Several of these nanowire structures have been fabricated. First, after

vapor deposition of a thin continuous metal layer on a quartz substrate, the metal film was covered (thermal evaporation) by a silicon dioxide (SiO_2) spacer layer. The metal films were thick enough to provide good reflectance while being thin enough to enable partial transmission through the sample. In a second step, electron beam lithography was used to prepare the periodic metal nanowire arrays on top of the dielectric spacer layer. While the theoretical investigations focus on a pure silver structure (silver nanowire grating in front of a silver film),samples with a gold grating in close proximity to a silver film have been investigated experimentally. Due to the limited nanofabrication facilities, we did not succeed in fabrication of silver nanowires with an acceptable optical quality so far. Typically, the individual gold nanowires exhibit a cross-section of 100×20 nm^2. In addition to the nanowire grating period d_x and the film-grating separation L_z, also the exact thickness h_{film} of the metal film has to be considered. While the thickness of the spacer layer was varied between 30 nm and 70 nm, metal films with a maximum thickness of 20 nm were used for all experimental investigations. Due to the limitations of the electron beam writing system, the possible grating extensions were restricted to 100×100 μm^2.

A conventional transmission setup including a white light halogen lamp was used for recording all extinction spectra. The samples were mounted on a rotating stage so that angle-dependent measurements were possible. Also a distinct light polarization could be selected. Especially measurements with light polarization parallel or perpendicular to the nanowires have to be considered. Special care has to be taken on the light aperture angle to obtain a nearly plane wave at the position of the nanowire array. Larger aperture angles will result in a splitting of the spectrally narrow resonances in the detected transmission spectra due to the strong angular-dependent dispersion of the optical modes (e.g., surface plasmon modes). Therefore, the aperture has been reduced below 0.2° for all measurements by placing a pinhole into the transmitted and recollimated white light beam.

5.3   Silver based nanostructures: A theoretical investigation

We will start with a purely theoretical analysis of the optical response of the proposed metal nanowire structures in the following section. The presented detailed theoretical description is based on numerical results which were obtained from the scattering-matrix formalism [128–130]. The method allows for calculation of the

transmission, reflection, and absorption spectra only with the knowledge of the exact sample geometry and of the frequency-dependent dielectric permittivities of the constituent materials. Additionally, also the spatial electromagnetic field distribution can be derived within this powerful method which works without the need for any fitting parameters.

The excellent correspondence between the experimental and theoretical results in Chap. 4 has already proven the capability of the used scattering-matrix formalism. Although the convergence of the algorithm is generally quite slow in the case of periodically nanostructured metals, it allows for determination of the optical response of the even more complex metallic grating-film structures with a very high accuracy. If not stated otherwise, all presented calculations will be restricted to the case of silver nanostructures with a nanowire cross-section of 100×10 nm^2 within this first section. In contrast to the restriction of the experimental investigation to gold nanowire based structures, the use of silver within the theoretical considerations seems to be very favorable for highlighting of the optical phenomena. In particular, the influence of interband transitions can be neglected in the considered spectral range, facilitating the interpretation of the accentuated resonances.

While calculations in TE polarization provide good results using a lower number of harmonics (e.g., see previous chapters), all spectra for TM polarization were calculated with $N_G = 301$ in order to obtain a reasonable agreement with the experimental results. The frequency dependent dielectric functions of silver (and gold) were taken from Ref. [112]. Good results have been obtained by assuming a constant dielectric permittivity $\varepsilon_{\mathrm{quartz}} = 2.13$ of the quartz substrate and the spacer layer material.

5.3.1   Excitation of localized and extended plasmon modes

It is very instructive to take a closer look at the two simplest nanowire configurations in the beginning of our theoretical investigation. Fig. 5.2 displays calculated period-dependent spectra for a silver nanowire grating on top of a pure quartz substrate ($L_z = 0$ nm, $h_{\mathrm{film}} = 0$ nm) and additionally spectra for an identical grating on top of a silver-coated substrate ($L_z = 0$ nm, $h_{\mathrm{film}} = 20$ nm). From top to bottom, the grating period is increased from $d_x = 200$ nm to $d_x = 400$ nm in steps of 100 nm in each panel. Extinction (a,d), reflection (b,e), and absorption (c,f) spectra are shown at normal incidence and TM polarization, respec-
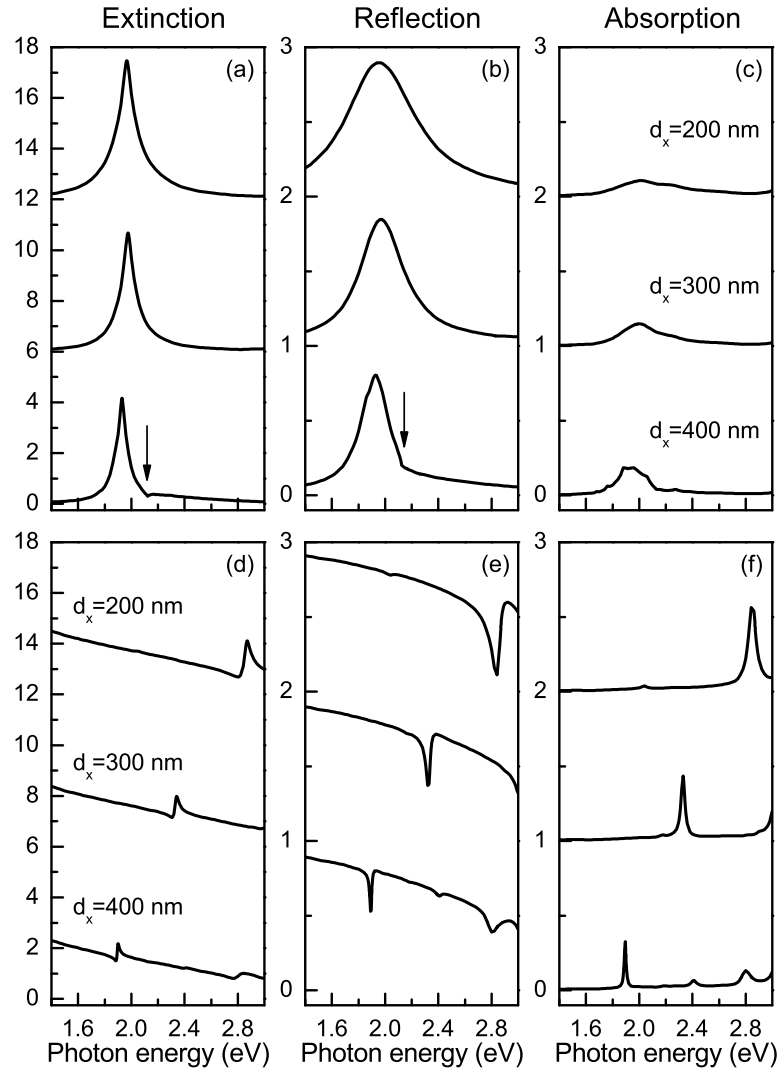
Figure 5.2: Calculated extinction (a,d), reflection (b,e), and absorption (c,f) spectra at normal incidence ($\vartheta = 0°$) and TM polarization for two different sample geometries. Spectra for silver nanowire gratings (cross-section 100×10 nm^2) on top of a 20-nm-thick silver film (d-f) and spectra for an identical nanowire grating without additional silver layer (a-c) are shown, respectively. From top to bottom, the grating periodicity is increased from $d_x = 200$ nm to $d_x = 400$ nm in each panel. Arrows mark the positions of the diffraction anomalies.

tively. As is well known from literature, uncoupled silver and gold nanowire gratings can support a strong particle plasmon resonance in the visible part of the electromagnetic spectrum [100, 146]. Such particle plasmon resonances, which are caused by oscillations of the conduction band electrons within the individual silver nanowires, can be clearly identified in the depicted spectra of
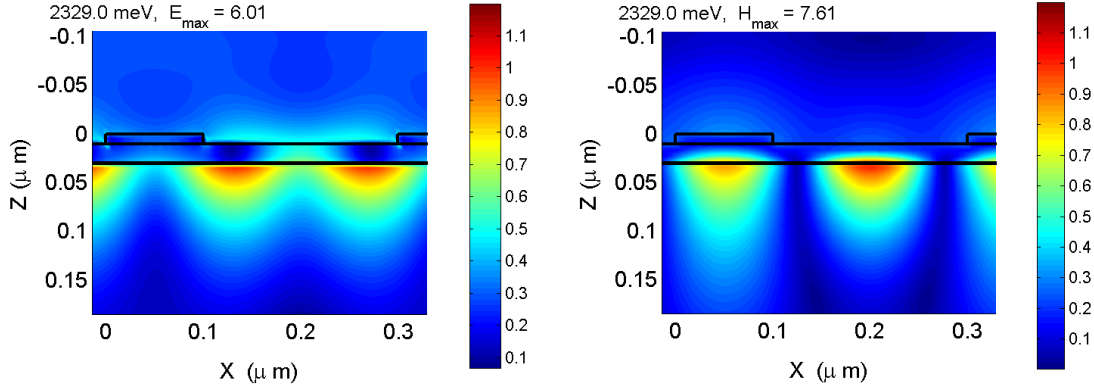
Figure 5.3: Calculated spatial field distributions of the electric (left panel) and magnetic fields (right panel) for normal light incidence and TM polarization. Shown are the normalized time-averaged field intensities for a nanowire grating with a periodicity of $d_x = 300$ nm on top of a 20-nm-thick silver film. The local fields are depicted for an incoming photon energy of $\hbar\omega = 2.329$ eV in a plane perpendicular to the nanowire extensions. The fields are normalized by the maximum electric ($|\vec{E}_{max}|^2$) and magnetic ($|\vec{H}_{max}|^2$) field intensities, respectively. Black lines denote the cross-section of the structure.

panels (a),(b), and (c) at approximately 1.97 eV. It is important to note that the plasmon resonances of the individual nanowires are modified due to near- as well as far-field effects. For example, the appearance of diffraction anomalies for structures with a nanowire period of $d_x = 400$ nm leads to a reduction of the spectral width of the particle plasmon resonance (e.g., see Chap. 4). On the other hand, clear evidence for an increased homogeneous broadening and a small red shift (≈ 10 meV) due to near-field coupling can be found for structures with a periodicity of $d_x = 200$ nm [101, 202].

The optical response changes dramatically when the silver grating is directly positioned on top of a thin silver film. In particular, no localized particle plasmon resonances can be found in Figs. 5.2 (d)-(f) within the considered spectral range. The appearance of narrow resonances, which show a strong period-dependent dispersion, can be attributed to the excitation of surface plasmon polaritons at the silver film. The periodic nanowire array acts as a surface corrugation and couples part of the external light field to the surface plasmon mode which is predominantly localized at the quartz-silver interface. The normalized time-averaged spatial field distribution for a structure with a period of $d_x = 300$ nm is displayed in Fig. 5.3 for normal light incidence and TM polarization. The calculated local electric ($|\vec{E}|^2$) and magnetic ($|\vec{H}|^2$) field intensities are depicted for an incoming photon
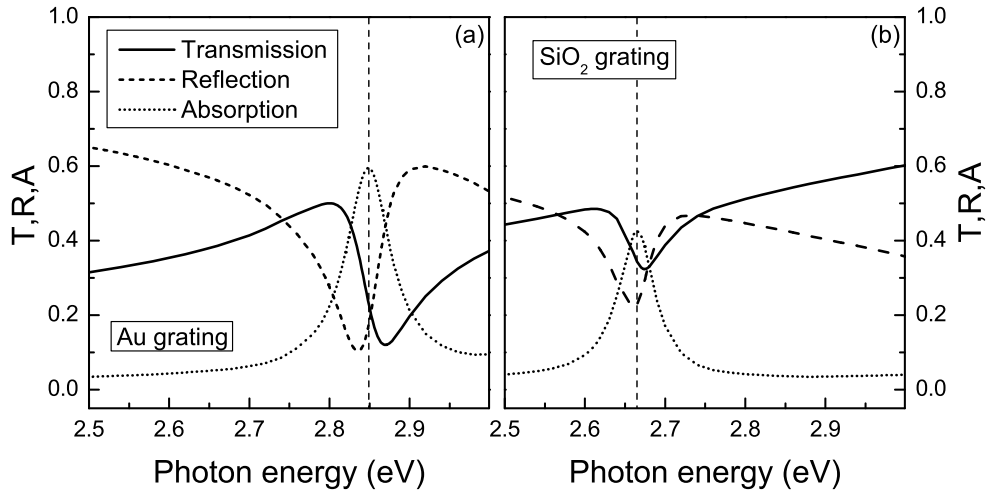
Figure 5.4: Calculated transmission (T), reflection (R), and absorption spectra (A) at normal incidence ($\vartheta = 0°$) and TM polarization. Panel (a) displays spectra for a silver nanowire array with a periodicity of 200 nm in front of a 20-nm-thick silver film for the situation $L_z = 0$ nm. Spectra for a dielectric quartz grating with a period of 200 nm on top of an identical silver film are shown in panel (b). A quartz nanowire cross-section of 100×40 nm^2 has been assumed for these calculations. The vertical lines indicate the position of the absorption maxima.

energy of $\hbar\omega = 2.329$ eV. The chosen energy corresponds to the spectral position of the pronounced absorption maximum in Fig. 5.2 (f). Two counter-propagating grating-induced plasmon modes with momenta $k_x = \pm 2\pi/d_x$ form a standing wave pattern. Similar to quasiguided modes of dielectric wavguide slabs, only the symmetric surface mode can be excited at normal light incidence. The field maxima are located at the silver-quartz interface and decay exponentially into both adjacent media. Due to the longitudinal nature of the coherent electron oscillations, the corresponding surface plasmon mode has only E_x, E_z, and H_y field components. Note that in principle also a surface plasmon mode at the silver-air interface should exist at higher photon energies. However, due to the asymmetric metal slab design (metal layer sandwiched between quartz and air half spaces), this additional quasiguided plasmon mode might be very lossy (i.e., light fields are diffracted into the quartz substrate). It is further important to remark that the chosen nanowire based design prevents excitation of particle as well as surface plasmon resonances under TE polarization (electric field parallel to the nanowires). For calculations assuming normal light incidence and TE polarization, no resonances can be found (spectra not shown).

An interesting fact is related to the specific line shape of the surface plasmon resonances. The observable nonsymmetric line shape in the extinction and reflection spectra clearly indicate the Fano-type nature of the modes [158]. Like quasiguided modes of photonic crystal slab structures [130, 152], also surface plasmon polaritons are a prominent example of the so-called Fano resonances (non-Lorentzian response due to interaction of a discrete mode with a continuum). Exemplary, the nonsymmetric optical response is highlighted in panel (a) of Fig. 5.4. Calculated transmission (T), reflection (R), and absorption spectra (A) of a silver nanowire array ($d_x = 200$ nm) deposited on top of a 20-nm-thick silver film ($L_z = 0$ nm) are shown for normal light incidence and TM polarization. The interference between the directly transmitted light fields and the scattered surface plasmon polariton fields induces the nonsymmetric transmission and reflection anomalies. It is further clearly visible that the transmission and reflection minima are shifted with respect to the surface plasmon absorption maximum. Note that only the absorption spectrum is characterized by a symmetric Lorentzian line shape. It is important to mention that the excitation of surface plasmon modes does not necessarily imply the use of a metal grating. Theoretical results for a similar structure with a dielectric (non-absorptive) grating are shown in panel (b) of Fig. 5.4 for the sake of completeness. The silver nanowires on top of the metal film have been replaced by SiO_2 nanowires with an individual cross-section of 100×40 nm^2. Qualitatively, the optical response is only weakly affected. In comparison to the pure metal structure in panel (a), mainly the mode energy has been slightly decreased due to the changed effective thickness of the metal layer. However, the nonsymmetric line shapes in the transmission and reflection spectra are still observable.

5.3.2 Variation of the dielectric spacer layer thickness

A number of interesting fundamental optical phenomena arise when an additional dielectric spacer layer ($L_z \neq 0$) is introduced. The resulting unique sample design (see Fig. 5.1) provides simultaneous excitation of particle and surface plasmon resonances due to the spatial separation of the silver nanowire grating and the metal-coated quartz substrate. In contrast to similar multilayer structures with a random distribution of metallic particles [106, 107], especially the artificial control of the coupling strength will be of fundamental physical interest. For example, the modification of the grating periodicity of the proposed nanowire structures allows for tuning of the interaction efficiency between particle- and
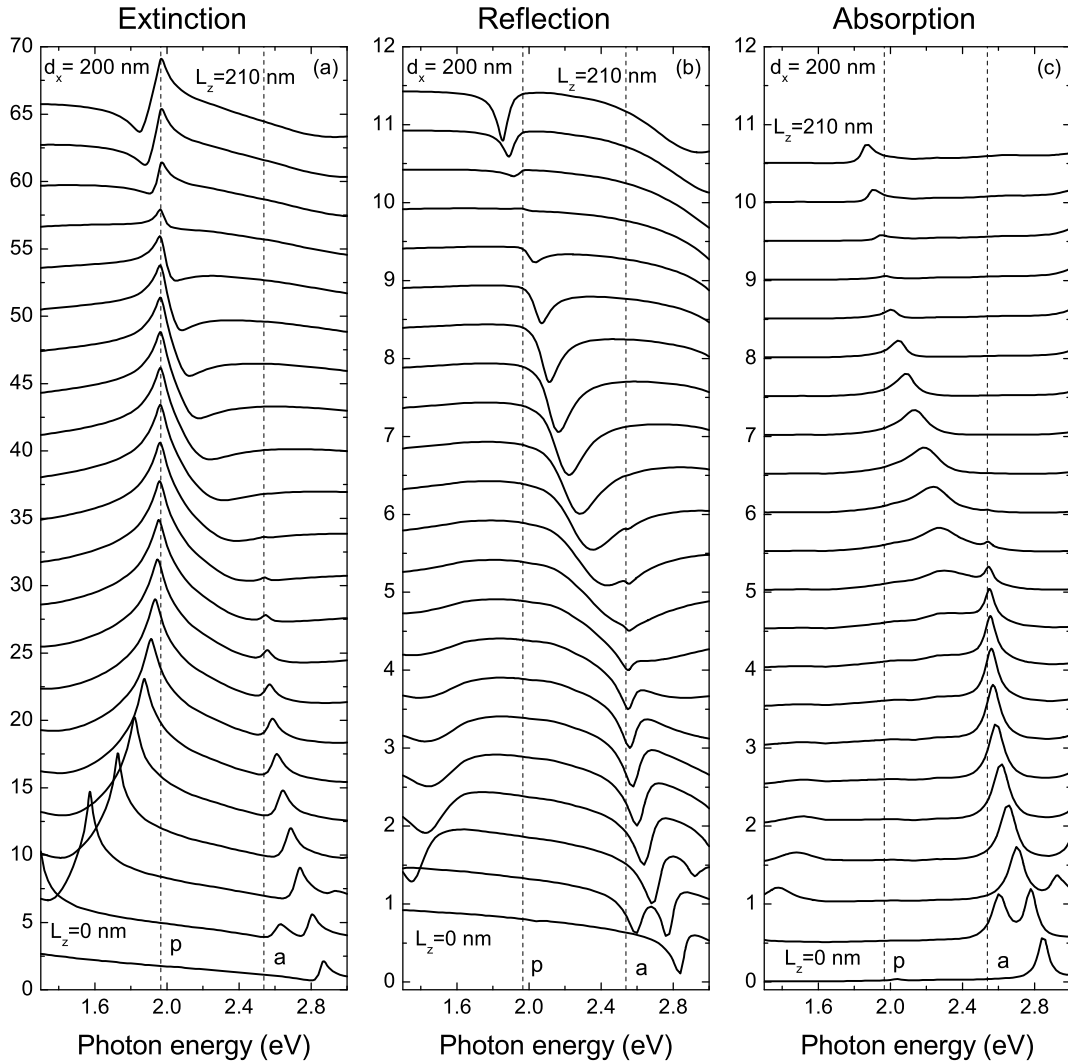
Figure 5.5: Calculated extinction (a), reflection (b), and absorption (c) spectra at normal incidence ($\vartheta = 0°$) and TM polarization. Spectra for nanowire arrays with a periodicity of 200 nm are shown. The underlying silver film exhibits a thickness of 20 nm. From top to bottom, the spacer layer thickness L_z is decreased from 210 nm to 0 nm in steps of 10 nm. The individual spectra are shifted upwards for clarity in each panel. The nanowire particle plasmon resonance of an identical grating without silver film is marked by a dashed vertical line [p, 1.966 eV]. Additionally, the position of the short-range surface plasmon mode of a homogeneous silver film is indicated by a second vertical line [a, 2.538 eV].

grating-induced surface plasmon resonances. Although the multilayer system gives rise to a very complex optical response, a clear separation and classification of various interaction phenomena will be presented.
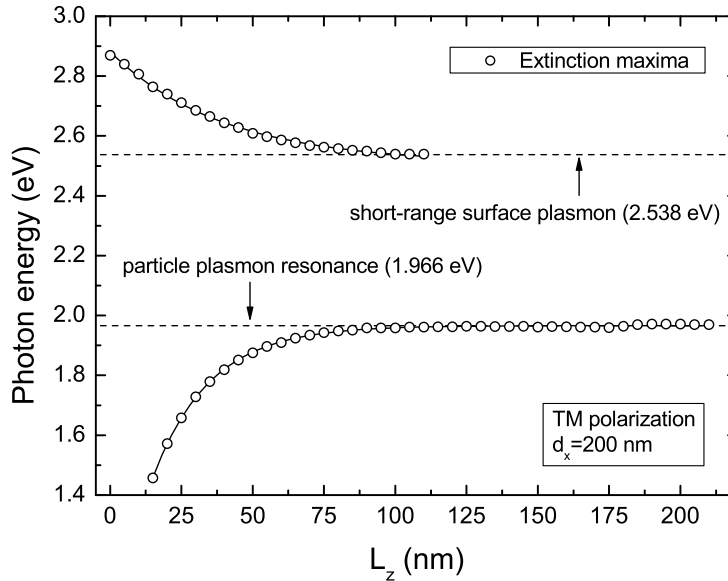
Figure 5.6:   Positions of the extinction spectra maxima extracted from Fig. 5.5 (a). The horizontal lines indicate the position of the particle plasmon resonance of a pure nanowire grating without an additional silver film and the position of the short-range surface plasmon resonance of a 20-nm-thick silver film bound between quartz half spaces.

The numerically obtained spectra for a silver nanowire grating in front of a 20-nm-thick silver film are shown in Fig. 5.5 for a nanowire period of $d_x = 200$ nm. Although the chosen period already induces some undesired particle-particle interaction phenomena between the adjacent nanowires (i.e., broadening and small red-shift of the nanowire particle plasmon resonance), the figure is quite essential and highlights several fundamental effects. It is especially important that the used small nanowire period allows the spectral separation of particle- and grating-induced phenomena. Calculated extinction (a), reflection (b), and absorption (c) spectra are displayed for normal light incidence ($\vartheta = 0°$) and TM polarization. A rather complex spectral behavior can be observed in all three panels when the spacer layer thickness L_z is increased from 0 nm to 210 nm.

The extinction spectra of panel (a) show two pronounced spectral features. A strong extinction peak at lower energies can be observed in all spectra, while the weaker upper maximum disappears for larger grating-film separations ($L_z >$ 110 nm). Especially the nonsymmetric line shape of the first spectral feature is quite striking. Note that the line shape strongly changes with spacer layer thickness. Simultaneously, a very large red-shift of the maximum appears for

smaller grating-film separations. The lower extinction maximum coincides with the position of the particle plasmon related extinction maximum of the pure silver nanowire grating without the nearby silver film (extracted from Fig. 5.2 (a) and marked by a vertical dotted line at approximately 1.966 eV in all three panels) for spacer layer thicknesses above $L_z = 90$ nm. The second extinction maximum at higher energies is less pronounced and shows a redshift for increased grating-film separations. A further important information can be deduced from the fact that this spectral feature is only visible until the spacer layer exceeds a thickness of 110 nm. Generally, the spectral position of the upper extinction maximum approaches the energy of the so-called short-range (or antisymmetric) surface plasmon mode of a symmetric silver film configuration ($\varepsilon_c = \varepsilon_{sub}$). Note that an additional extinction maximum can be found for the situation of $L_z = 10$ nm (slightly below the upper extinction maximum). This spectral feature has no counterpart in all other extinction spectra. For a better visibility of the induced spectral shifts, the spectral positions of both described extinction maxima have been extracted from Fig. 5.5 (a) and are depicted in Fig. 5.6 in dependence of the grating-film separation.

Further on, it is very instructive to compare the corresponding extinction, reflection, and absorption spectra. Although the positions of the pronounced spectral features do not necessarily coincide, the asymmetric extinction anomalies are in some way correlated with absorption maxima and dips in the reflection spectra, respectively. For example, the upper extinction maximum is directly related to a reflection dip and a relatively strong absorption peak. Note that their spectral signatures vanish for larger grating-film separations L_z. The situation looks more complex when considering the lower second extinction maximum. The spacer layer dependent modification of the pronounced extinction anomaly is accompanied by drastic changes of the shape (amplitude and linewidth) and the spectral position of the related absorption and reflection features. For example, a pronounced absorption maximum appears at 2.3 eV for structures with a spacer layer thickness of $L_z = 100$ nm. The maximum is clearly redshifted when increasing the grating-film separation. However, it seems that especially the grating-film separation of $L_z = 180$ nm specifies a very characteristic situation. The extinction, reflection, and absorption features at approximately 1.966 eV are nearly suppressed for this specific spacer layer thickness.

In Fig. 5.5, the complex spacer layer dependent optical response of the studied nanowire structures can be separated into grating (i.e., periodic nanowire ensemble) and single nanowire related phenomena. Additionally, also the appearing

near- as well as far-field interaction effects can be clearly distinguished. An interpretation and detailed discussion of the related effects will be presented in the following:

(i) *Grating induced phenomena*

The upper extinction maximum in Fig. 5.5 and Fig. 5.6, which is shifting to lower energies for increasing values of L_z, originates from the grating induced excitation of a surface plasmon mode at the silver film. More precisely, the periodic nanowire array acts as a grating coupler and couples the incoming radiation fields to the quasiguided surface plasmon modes of the nearby metal layer. As already shown in Sec. 5.3.1, the spectral anomaly for structures without additional spacer layer ($L_z = 0$ nm) is related to a quasiguided surface plasmon mode at the lower planar silver-quartz interface with momentum $k_x = \pm 2\pi/d_x$. The observed red-shift of this surface plasmon resonance when increasing the spacer layer thickness can be easily explained by the nonsymmetric sample design (metal film sandwiched between a quartz substrate and an air half space). It is well-known that metal films with symmetric dielectric cladding layers ($\varepsilon_c = \varepsilon_{\text{sub}}$) support degenerate surface plasmon modes at both of their interfaces. Coupling of these resonances results in the formation of two normal modes, namely the short- (antisymmetric in H_y) and the long-range (symmetric in H_y) surface plasmon mode, when considering sufficiently thin metal films [12]. While increasing the spacer layer thickness and thus changing the effective permittivity of the upper cladding layer, the considered slab geometry is continuously transferred from a non-symmetric to a symmetric slab design. The excited surface plasmon resonance of the metal interface is therefore modified and slowly converted into the short-range surface mode of the thin silver film. The energy of the short-range mode is reduced in comparison with the bare modes of the single interface. Simultaneously, the arising long-range mode is blue-shifted (not shown here). Note that the characteristic spacer layer dependent energy shift of the surface plasmon resonance is not visible in symmetric structures, where a quartz cladding layer with $\varepsilon_c = \varepsilon_{\text{quartz}} = 2.13$ is used (e.g., see calculations in Chap. 6). The depicted spectral position of the short-range surface plasmon mode (indicated by the dotted lines in Fig. 5.5 and Fig. 5.6) with $k_x = 2\pi/d_x$ of a 20-nm-thick symmetric silver film has been determined by calculating the dispersion relation similar to the approach of Ref. [119].

Another important phenomenon is the strong influence of the grating-film separation on the surface plasmon excitation efficiencies. While the resonance energy of the surface plasmon is red-shifted in Fig. 5.5 when increasing the spacer layer

thickness, the excitation efficiency is simultaneously reduced. The surface plasmon related spectral features disappear completely for grating-film separations above $L_z = 110$ nm. This behavior can be explained by the characteristic field distribution of the short-range surface plasmon mode. The electromagnetic field intensities of the short-range mode are strongly confined and decay exponentially into the dielectric surrounding. Bragg scattering and therefore an efficient excitation of the quasiguided modes implies an effective overlap between the surface plasmon fields and the nanowire grating structure (i.e., spatial perturbation of the homogeneous metal slab). The theoretical results show that this requirement is no longer fulfilled when the spacer layer thickness exceeds approximately 110 nm. However, as discussed in one of the following sections, the coupling efficiency can be strongly enhanced by changing the nanowire period and coupling to the particle plasmon resonance.

It is further important to emphasize one interesting observation. Calculations for similar structures with a non-absorptive dielectric slab layer (instead of a homogeneous metal film) show a slightly different behavior. When the coupling strength is reduced by increasing the waveguide-grating separation (e.g., see Sec. 4.7), only the width and the spectral position of the quasiguided modes are modified. However, the extinction efficiencies on the other hand are only weakly affected. This striking difference from the metal-based structures can be related to the non-absorptive character of the used dielectric slab layers.

(ii) *Single nanowire-related phenomena*

In addition to the grating-induced surface plasmon resonances, also the accentuated extinction maxima at lower photon energies (see Fig. 5.5 and Fig. 5.6) show a very conspicuous behavior at first sight. Large frequency shifts as well as modifications of the line shape can be observed when changing the spacer layer thickness. The origin of these pronounced spectral features can clearly be attributed to the localized particle plasmon resonances of the individual silver nanowires. Both near- as well as far-field interaction have to be considered for an exact interpretation of the theoretically predicted phenomena.

Neglecting the asymmetric line shape of the lower extinction anomalies in a first step, a clear redshift of the maxima can be observed in panel (a) of Fig. 5.5 when the grating approaches the underlying metal layer. This shift from the bare particle plasmon resonance position (denoted by a dashed vertical line) is a mirror effect and can be understood within a simple hybridization picture [105]. The lowering of the extinction maxima results from the interaction of the individual
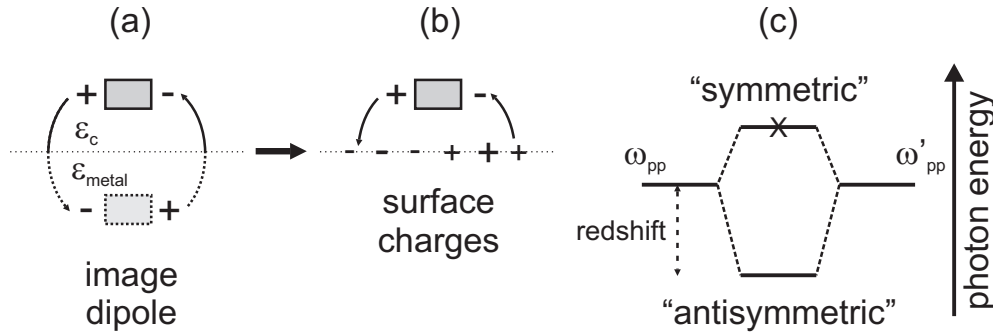
Figure 5.7:   Panel (a) illustrates the interaction of a metal nanowire (cross-section is indicated by the solid square) with a metal surface. The nanowire plasmon and its image are characterized by an antisymmetric polarization charge distribution. Charges (+,-) and electric fields (arrows) are schematically shown. As displayed in panel (b), the coupling leads to surface charges at the metal interface. The plasmon hybridization principle is drawn in panel (c). The interaction between a particle plasmon state (ω_{pp}) and its image (ω'_{pp}) results in a new hybridized state. Only the lower antiymmetric state exists. The expected redshift is indicated by the small dashed arrow.

nanowire plasmons with their images in the nearby metal layer. A schematic illustration of the hybridization is shown in Fig. 5.7. The considered process is similar to the formation of hybridized states due to electromagnetic near-field coupling between two individual metal particles [109]. When two degenerate states interact with each other, the coupling generally leads to a lifting of the degeneracy of the bare modes and hence results in the formation of so-called normal modes of the system. The arising antisymmetric mode is lowered in energy while the resonance energy of the symmetric mode is increased. Here, the symmetric (antisymmetric) normal mode is characterized by a parallel (antiparallel) oscillation of the interacting dipoles. However, in contrast to the interaction between two particle plasmon resonances with identical frequencies ω_{pp}, the hybridization principle has to be slightly modified when considering the coupling between a single particle plasmon resonance (ω_{pp}) and its own image state (ω'_{pp}). As shown in panel (a) of Fig. 5.7 for a specific moment in time, the polarization charge distribution of the dipolar particle plasmon (oscillation parallel to the surface) induces an image which is characterized by an inverted charge distribution. Note that therefore only the lower antisymmetric plasmon resonance can be excited. The upper symmetric state does not exist under these specific geometrical conditions. As shown in Fig. 5.5 and Fig. 5.6, the interaction strength directly scales with the spacer layer thickness. A stronger coupling (i.e., thinner spacer layer) results in a larger

normal mode splitting and hence an increased shift of the antisymmetric plasmon mode. The redshift of the particle plasmon resonance can easily be explained when considering the modified restoring forces. Generally, when the conduction band electrons of a metal nanowire are collectively displaced against the positive background of the lattice, the resulting surface polarization charges give rise to a linear restoring force. The arising restoring forces in the grating-film geometry are effectively weakened in comparison to the bare nanowires case. This fact is related to the attractive forces between the facing negative and positive surface charges of the nanowire and its image, respectively.

Alternatively, the introduced hybridization model can be understood in terms of a non-radiative energy transfer between the localized particle plasmons and the nearby metal interface. In a real system, as schematically shown for a quasistatic situation in panel (b) of Fig. 5.7, the image dipole is mimicked by arising surface charges. When an electric dipole (orientated parallel to the surface) is brought into close proximity of a metal interface, surface charges are induced by the dipolar near-fields. Taking into account an oscillating dipole and hence an oscillating polarization charge distribution (e.g., localized particle plasmon) in a next step, also the surface charges are forced to oscillate. The near-field induced surface charge oscillations are directly connected to a resonant energy transfer to the metal (e.g., silver surface) and hence the excitation of a surface plasmon mode. Referring to the silver nanowire system again, the non-radiative resonant surface plasmon excitation at the nearby silver layer leads to an enhanced damping of the particle plasmon compared to the bare plasmon mode. This additional damping and hence the resulting reduced restoring forces cause the redshift of the localized nanowire plasmon resonances when decreasing the spacer layer thickness. It is important to remark that the observed redshift of the lower extinction maximum is a single-nanowire effect and not related to the periodicity of the considered grating structure. Similar energy shifts have also been found in boundary-element-method-based calculations considering individual metal nanoparticles placed in front of a metal interface (not shown)[1].

In molecular systems, such non-radiative energy transfer processes generally result in a quenching of the arising fluorescence signals [25]. When excited molecules are brought into close proximity to a metal layer, a new non-radiative decay channel is opened and the energy can relax via direct surface plasmon excitation. The efficiency of this process is strongly distance-dependent similar to the discussed

---

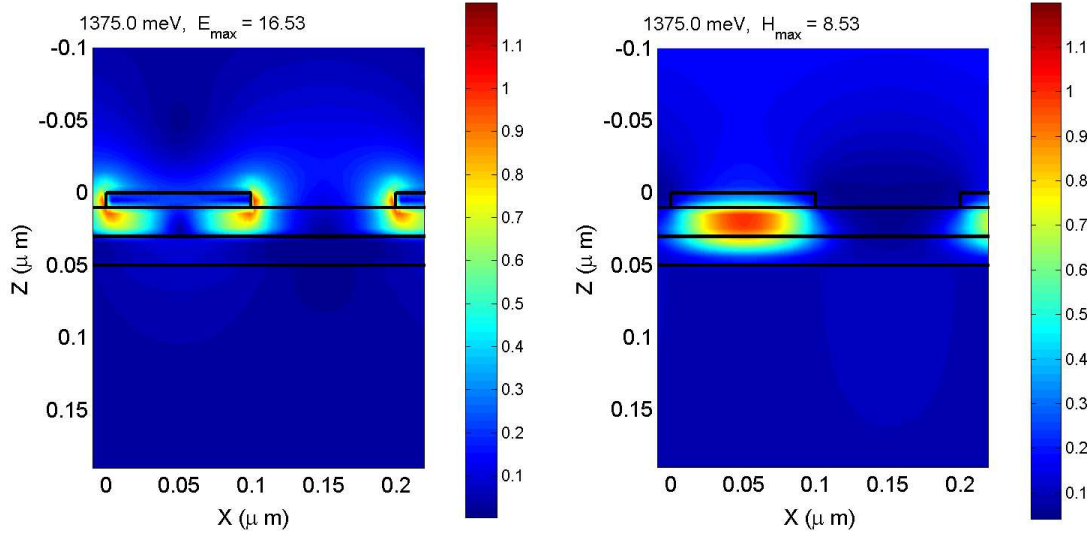[1]N. A. Gippius, private communication

Figure 5.8: Calculated spatial field distributions of the electric (left panel) and magnetic fields (right panel) for normal light incidence and TM polarization. Shown are the normalized time-averaged field intensities for a nanowire grating with a periodicity of $d_x = 200$ nm in front of a 20-nm-thick silver film and a spacer layer thickness of $L_z = 20$ nm. The local fields are depicted for an incoming photon energy of $\hbar\omega = 1.375$ eV in a plane perpendicular to the nanowire extensions. The fields are normalized by the maximum electric ($|\vec{E}_{\mathrm{max}}|^2$) and magnetic ($|\vec{H}_{\mathrm{max}}|^2$) field intensities, respectively. Black lines denote the cross-section of the structure.

metal nanowire structures. Note that the non-radiative energy transfer processes strongly depend on the exact dispersion of the surface plasmon modes. For example, an increased density of states and thus a very efficient energy transfer can be obtained by tuning the resonance position close to the asymptotic surface plasmon energy $\hbar\omega_{sp}$ [32].

Additional information on the nanowire-film interaction can be deduced from the electromagnetic field distribution. The calculated spatial field distributions of the electric (left panel) and magnetic fields (right panel) are displayed in Fig. 5.8, assuming normal light incidence and TM polarization. The normalized time-averaged field intensities are shown for a nanowire grating with a period of $d_x = 200$ nm positioned in front of a 20-nm-thick silver film. A spacer layer thickness of $L_z = 20$ nm has been used for the scattering-matrix based calculations. Note that the depicted field intensities are normalized by the maximum electric ($|\vec{E}_{\mathrm{max}}|^2$) and magnetic ($|\vec{H}_{\mathrm{max}}|^2$) field intensities, respectively. The arising maximum field
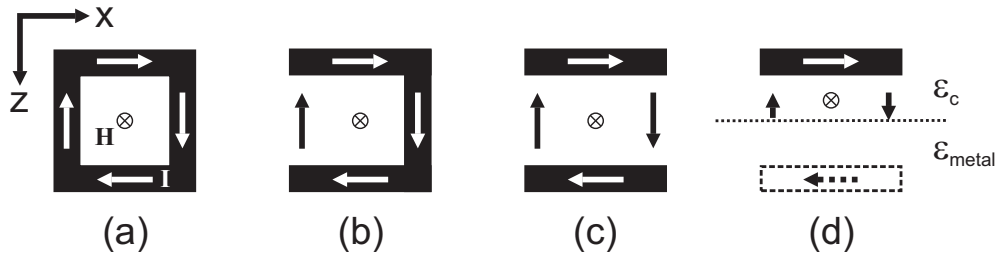
Figure 5.9:   Schematic view of circular currents in a metallic ring (a) and two different split-ring realizations [(b) and (c)]. The structure of panel (c) can be mimicked by the mirror based geometry of panel (d). The cross-section of the metallic components is illustrated by the colored black areas. Exemplary, the arrows indicate the direction of the currents (I). The current loop is closed by displacement currents (black arrows) when a capacitance is introduced (assuming oscillating currents). The induced magnetic field (H,$\otimes$) is orientated perpendicular to the xz-plane.

amplitudes E_{max} and H_{max} (in respect of the incident wave with amplitudes equal one) are specified on top of each panel. The local fields are shown for an incoming photon energy of $\hbar\omega = 1.375$ eV in a plane perpendicular to the long axis of the nanowires (i.e., xz-plane). This spectral position corresponds to the absorption maximum of the investigated resonance [e.g. see panel (c) of Fig. 5.5].

The calculated field distribution in Fig. 5.8 verifies our previous interpretations. Especially the asymmetric character of the hybridized state can be deduced. It is clearly shown that the time-averaged electric fields are concentrated at the edges of the nanowires, while large magnetic field intensities can be found below the individual nanowires of the array. The large electric fields at the edges of the nanowires are caused by the light-induced surface charges (oscillations of the conduction band electrons parallel to the metal surface). Considering the proposed hybridization model, the distribution of the magnetic field can be directly explained by the antisymmetric charge distribution of the nanowire plasmon and its own image. Generally, a circular current in a metal ring [e.g., see Fig. 5.9 (a)] generates large magnetic fields at the center of the current loop. The arising magnetic fields at the center of the loop are oriented perpendicular to the xz-plane. Assuming a periodically oscillating current, the ring structure can be further simplified stepwise by introducing one or even two capacitances [split-ring structures in panels (b) and (c) of Fig. 5.9]. Now, the current loop is closed by the appearing displacement currents between the opposing edges of the remaining metal parts. In a final step, the current loop can be mimicked by placing a single
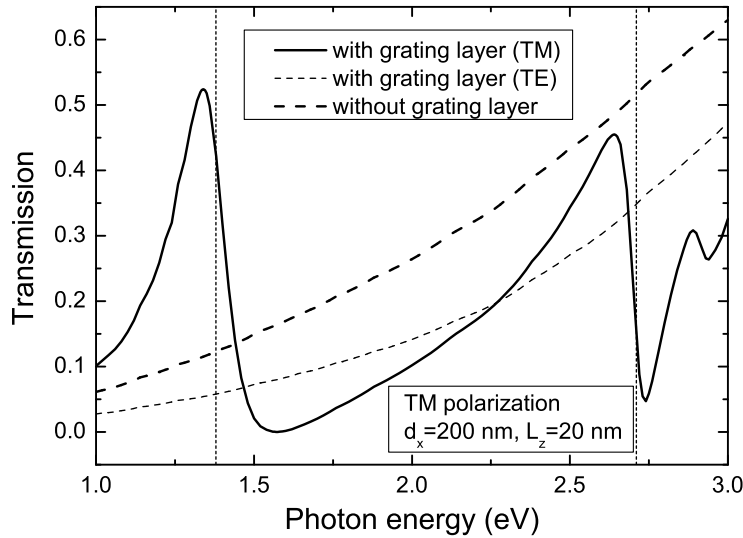
Figure 5.10: Calculated transmission spectra of a 20-nm-thick silver film. Spectra with (solid and thin dashed lines) and without (thick dashed line) additional grating layer are shown. A nanowire period of $d_x = 200$ nm and a spacer layer thickness of $L_z = 20$ nm have been used for the depicted numerical results. Spectra for TE and TM polarization are displayed. The dotted vertical lines indicate the position of the corresponding absorption maxima at 1.37 eV and 2.71 eV.

dipole oscillator (i.e., metal wire) in close proximity to a homogeneous metal interface. [Fig. 5.9 (d)]. Thus, the proposed grating-film design can be interpreted as a periodic arrangement of individual split-ring resonators. In a simple picture and for sufficiently small grating-film separations, the electron density oscillations across the wires induce oscillating magnetic fields which interfere with the fields of the image dipole (mimicked by the oscillating surface charges). Constructive interference therefore results in an enhanced magnetic field intensity below the individual nanowires, as clearly shown in Fig. 5.8 (b).

A further fundamental phenomenon is directly related to the Fano-type nature of the nanowire-based plasmon resonances. So far, the nonsymmetric line shape of the localized resonances has not been considered within our discussions. Fig. 5.5 clearly reveals that, similar to the grating induced surface plasmon resonance, also the localized particle plasmon related resonances are generally characterized by a Fano-type line shape. As a consequence, the extinction maxima do not necessarily coincide with the absorption maxima, that specify the resonance position. One optical phenomenon which arises from the Fano nature of the localized resonance

is quite surprising. As exemplary shown in Fig. 5.10, the nonsymmetric line shape is correlated with an enhanced off-resonant transmission through the thin metal layer. First, calculated transmission spectra of a silver nanowire grating placed in front of a 20-nm-thick silver film are depicted in the figure. Results for TE (thin dashed line) and TM polarization (solid line) are shown. A nanowire period of $d_x = 200$ nm and a spacer layer thickness of $L_z = 20$ nm have been used for the depicted numerical calculations. Second, the transmission spectrum of a homogeneous 20-nm-thick silver film (no grating layer) is additionally displayed (thick dashed line). All spectra are shown for normal light incidence.

The displayed transmission spectrum of the grating based structure is characterized by two pronounced spectral features in case of TM polarization. The lower peak can be attributed to the excitation of the nanowire plasmons while the upper maximum is related to the grating-induced surface plasmon mode. The related absorption maxima, which specify the spectral position of the resonances, are indicated by the dotted vertical lines. As expected, none of these anomalies can be found in the corresponding transmission spectrum in TE polarization nor in the calculated spectra of the homogeneous metal layer. The modified transmission properties are the striking features of the figure. In comparison to the spectrum for TE polarization, both plasmon modes induce an enhanced optical transmission in case of TM polarization. Compared to the spectrum of the homogeneous 20-nm-thick silver film, only the excitation of the localized wire plasmons results in an transmission enhancement (enhancement by a factor of 4.5 for photon energies of 1.33 eV). Note that although the observed effects are resonant in character, the transmission maximum is shifted to lower energies in comparison to the position of the indicated absorption maxima (dotted vertical lines).

The Fano-type line shape and thus the strongly enhanced transmission can be understood as a simple interference phenomenon (i.e., Fabry-Perot-like behavior). Electromagnetic fields which are directly transmitted through the structure interfere with the radiation fields originating from the radiative dephasing of the excited particle plasmons. The described interference effect generally corresponds to an interaction of a discrete state and a photon continuum. However, it is very surprising at first sight that especially the supported particle plasmon resonances can induce such dramatic modifications of the optical response. A very similar phenomenon is well known in literature. Subwavelength apertures in thicker metal films can also induce such unexpected phenomena. For example, individual slits in a thick metal layer (widths of the slits much smaller than the resonant wavelength) support resonant modes which can be used to enhance the optical
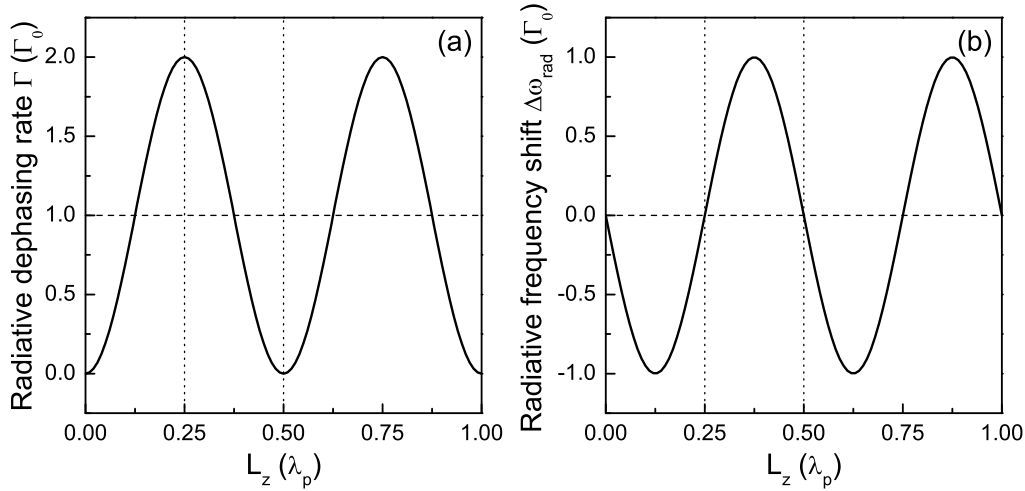
Figure 5.11:   Effective radiative dephasing rates (a) and induced radiative frequency shifts (b) for a dipole oscillator in front of a perfectly reflecting metal interface ($r_g = -1$). The dependence of the spacer layer thickness L_z is shown.

transmission through the metal structure (e.g., see Ref. [76, 203]).

(iii) *Radiative coupling*

In addition to the discussed near-field induced shifts of the localized plasmon resonance, also possible far-field interaction effects have to be considered for a full description of the complex optical response. While the near-field interaction is driven by an instantaneous dipole-dipole coupling (i.e., quasistatic dipole-dipole interaction), the far-field coupling proceeds via the coherent emission and reabsorption of a photon (i.e., dynamic dipole-dipole interaction). For example, it is well-known that the resonance frequency and the radiative dephasing time of a dipolar resonance are strongly modified due to the appearance of a radiative feedback [25, 198]. When a point dipole is placed in close proximity to a reflecting surface, the dipole oscillation is driven by its own radiation fields which are back-reflected from the metal surface (photon mediated coupling). Thus, especially the specific phase difference between the reflected radiation fields and the dipole polarization plays an important role and determines the optical response of the composite structure. It is important to mention that the interaction phenomena can alternatively be interpreted as a radiative coupling between the single dipole and its own image in the metal layer.

Similar interaction phenomena have also been discussed when studying the effect of dielectric cladding layers on the radiative dephasing time of quantum well

excitons [204]. As has been theoretically predicted [205, 206], the influence of a nearby reflecting interface on the radiative dephasing rates Γ and on the resonance frequency of an oscillating dipole (e.g., $1s$ exciton of a single quantum well) can be described by the two simple relations

$$\Gamma = \Gamma_0 \left(1 + r_g \cos \left(4\pi \frac{L_z}{\lambda_p} \right) \right), \tag{5.1}$$

$$\Delta\omega_{rad} = \Gamma_0 \, r_g \sin \left(4\pi \frac{L_z}{\lambda_p} \right). \tag{5.2}$$

Here, Γ_0 is the radiative dephasing rate of the bare (i.e., noninteracting) dipole resonance, neglecting any interface-induced feedback effects. The parameter λ_p specifies the bare dipole resonance wavelength. The properties of the interface are taken into account by specifying the reflection coefficient r_g. The parameter L_z, on the other hand, describes the effective dipole-interface separation.

The two equations clearly indicate that the influence of radiative coupling can be probed by either changing the dipole-film separation L_z or by altering the reflection coefficient r_g. In particular, it is important to highlight one further interesting aspect. Eq. 5.2 shows that the radiative frequency shift $\Delta\omega_{rad}$ is directly proportional to the radiative dephasing rate of the considered dipole oscillator. Therefore, especially a particle plasmon resonance seems to be a suitable dipolar model system. It should be possible to observe distinct frequency shifts due to the much larger radiative dephasing rates of the bare plasmons in comparison to molecular or quantum well based model systems [107].

Exemplary, the theoretically deduced influence of the dipole-film separation is displayed in Fig. 5.11. Noninteracting dipole oscillators placed in front of a perfectly reflecting metal interface ($r_g = -1$) have been assumed for the calculation of the depicted theoretical results. While the modified radiative dephasing rates are shown in panel (a), the simultaneously induced energy shifts can be found in panel (b). However, although the used model might be too simple to describe all features of a metal nanowire based realization (e.g., negligence of any near-field effects), first important results can be deduced from the displayed figure. It is clearly seen that the original resonance frequency of the bare dipole is only conserved for spacer layer thicknesses equal to $L_z = m(\lambda_p/4)$ and $m \in \{0, 1, 2, ...\}$. However, the radiative dephasing rates on the other hand are strongly modified for these characteristic dipole-interface separations. While a total suppression of the radiative dephasing is found for $L_z = m(\lambda_p/2)$, a spacing of $L_z = (2m+1)(\lambda_p/4)$ generally leads to strongly increased radiative dephasing rates. Note that the radiative coupling between two dipole oscillators generally
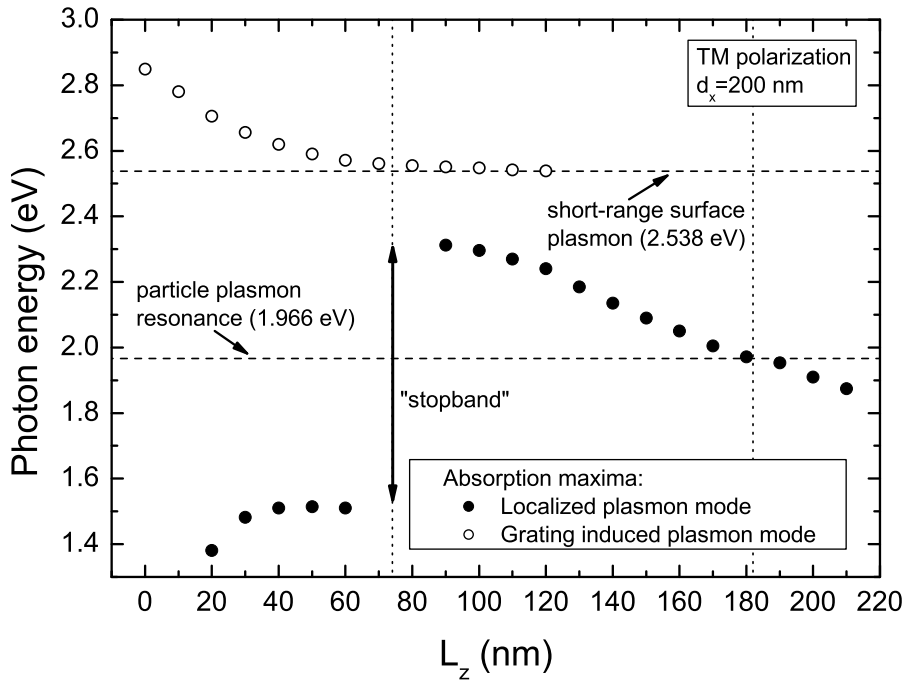
Figure 5.12: Positions of the absorption maxima extracted from Fig. 5.5 (c). The horizontal lines indicate the position of the particle plasmon resonance of a pure nanowire grating without additional silver film and the position of the short-range surface plasmon resonance of a 20-nm-thick silver film bound between quartz half spaces.

implies two normal modes of opposite symmetry. Similar to the discussed near-field interaction, symmetric and antisymmetric modes can be excited. However, only the antisymmetric solution exists in the discussed mirror geometry (i.e., the dipole and its image are characterized by an antiparallel orientation).

Guided by these results, it should be possible to extract similar spacer layer dependent phenomena from the theoretical spectra of the metal nanowire structure in Fig. 5.5. The presence of radiative coupling, mediated by the back-reflected light fields, should lead to both modifications of the particle plasmon dephasing rates as well as shifts of the resonance frequency. However, although some of the expected modifications can be observed, especially the extracted frequency shift requires a more careful investigation. Considering the already mentioned results of Ref. [107] (metal island film in front of a continuous Ag film), the observed frequency shifts of the dipole resonances have been discussed on the basis of the measured near-normal reflectance. More precisely, the exact resonance frequencies of the dipoles (i.e., metal islands) have been obtained by measuring the

spectral position of the reflection minima. Such minima can be as well extracted from the theoretical reflection spectra in panel (b) of Fig. 5.5 [2]. However, due to the Fano-type nature of the resonances, we will restrict the discussion to the related absorption maxima.

To investigate the spectral characteristics of the structure, the positions of the individual absorption maxima are displayed in Fig. 5.12 in dependence on the spacer layer thickness. All data points have been extracted from the theoretical spectra in Fig. 5.5 (c). In addition to the dashed horizontal lines which indicate the spectral positions of the bare particle and surface plasmon resonances, two characteristic spacer layer thicknesses are marked by dotted vertical lines. The lines indicate the specific spacer layer thicknesses which fulfill the Bragg ($L_z \approx 180$ nm) and anti-Bragg ($L_z \approx 75$ nm) conditions, respectively. Theoretically, the exact Bragg condition would imply a grating-film separation of approximately $L_z = 215$ nm [3]. The deviation from this value can be attributed to the finite skin depth of the 20-nm-thick silver layer which effectively reduces the required spacer layer thickness. Similar to the extracted extinction maxima in Fig. 5.6, the displayed dispersion is characterized by two pronounced features. The upper grating-induced plasmon mode (open circle in Fig. 5.12) shows the already discussed behavior. The related absorption maximum is redshifted and approaches the spectral position of the short-range surface plasmon mode (2.538 eV). The shift is caused by a more symmetrical geometry of the multilayer structure when increasing the spacer layer thicknesses (i.e., metal film with symmetric cladding layers). The continuously reduced excitation efficiencies of this mode result in a disappearance of the absorption maximum when L_z exceeds approximately 120 nm.

In contrast to the surface plasmon mode, the additional maxima (solid circles in Fig. 5.12) are related to the particle plasmon resonances of the individual silver nanowires. These resonances reveal a more complex dependence which deviates from the expected behavior (e.g., depicted in panel (b) of Fig. 5.11). One can see neither an absorption maximum in case of anti-Bragg spacing, nor does the oscillatory behavior for the frequency shift (as predicted by Fig. 5.11) occur.

---

[2]We would like to stress that the depicted reflection/extinction spectra in Fig. 5.5 highlight a very fundamental lineshape phenomenon. The symmetry of the appearing dispersive Fano-like feature is inverted when crossing the exact Bragg condition ($L_z \approx 180$ nm). Note that a similar line shape cycle has already been found when measuring the reflectance from GaAs/Ga$_{1-x}$Al$_x$As quantum well structures [207]. In these structures, the direct reflectance from the sample surface interferes with the light fields which are reflected from the buried quantum well.

[3]$L_{z,Bragg} \approx \lambda_p/(2\sqrt{\varepsilon_{sp}})$ with $\lambda_p \approx 630$ nm and $\varepsilon_{sp} = 2.13$
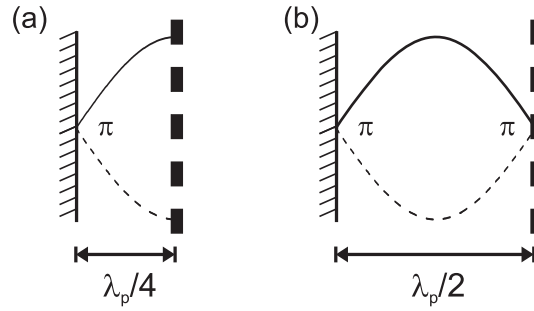
Figure 5.13:   Nanowire grating in front of a metal mirror. Two characteristic cavity geometries and the related cavity-fields are displayed schematically (electric field). The resonance position is determined by the length of the metal-clad microcavity ($\lambda_p/4$ or $\lambda_p/2$) and the phase shift on reflection.

It is remarkable that one instead observes a jump of the absorption maximum energy at just $L_z \approx 75$ nm. While the positions of the absorption maxima do not coincide with the expected values, the predicted linewidth changes due to lifetime modifications can be clearly observed when comparing with panel (c) of Fig. 5.5. In case of Bragg spacing, the subradiant character of the mode manifests itself in the disappearance of the absorption maximum at 1.966 eV. The subradiant character of the resonance can be deduced from the line narrowing and the decreased absorption efficiency when approaching Bragg distance. The shortest dephasing time on the other hand (superradiant character of the mode) is expected in case of anti-Bragg spacing. However, the exact interpretation of the spectra turns out to be extremely difficult for this specific sample geometry. Due to the fact that the related absorption maxima vanish in panel (c) of Fig. 5.5 ($L_z \approx 70$ nm), which indeed might be interpreted in terms of an accelerated radiative decay, especially the determination of the resonance frequency becomes ambiguous.

Since the considered sample design is more complex, distinct differences from the assumed idealized situation of Fig. 5.11 have to be considered. First, the used metal film is semitransparent and allows for light transmission (i.e., reduced reflection). Second, and maybe more important, the large oscillator strength of the particle plasmons and the assumed nanowire density have to be taken into account. In order to speculate about the origin of the spectral modifications, the proposed multilayer grating-film geometry might be alternatively interpreted in terms of a so-called metal-clad microcavity (e.g., see Ref. [70]).

As schematically shown in Fig. 5.13, the considered grating-film structure gener-

ally resembles a one-dimensional Fabry-Perot-like microcavity design. Instead of using two identical metal mirrors, the cavity is terminated by a dipole active layer (i.e., silver nanowire grating) at one of its boundaries. The optical properties are therefore not only determined by cavity length but also by the specific geometry of the grating layer (e.g., period and nanowire cross-section). Note that the excitation of cavity modes does not necessarily imply any particle plasmon resonances, as will be shown later on. Due to the nonresonant background reflectivity of the nanowire grating, a clear signature of cavity modes can even be found in spectra for TE polarization. However, in contrast to conventional Fabry-Perot resonators, the interaction of cavity and particle plasmon resonances has to be taken into account when analyzing the more fundamental case of TM polarization. Under specific conditions, mode coupling may be interpreted in terms of cavity-polariton-like resonances.

Further insight can be gained from the schematic drawings in Fig. 5.13. As shown in panel (b), Bragg spacing ($L_z = 0.5\lambda_p$) implies a stationary cavity mode such that the nodes of the standing wave (electric field) are located at both cavity interfaces. Assuming an ideal metal mirror without absorption losses opposite to the nanowire grating, phase jumps of π occur on reflection at both cavity interfaces. Thus, the schematic drawing of the mode profile provides a very simple explanation for the modification of the nanowire plasmon dephasing rates in TM polarization. Bragg spacing results in a nearly vanishing photonic mode density at the position of the metal nanowires (i.e., grating is located at the node of the arising standing wave), hence preventing an effective radiative decay of the particle plasmon polarization. On the other hand, as shown in panel (a), the cavity-field has to be modified when considering an anti-Bragg geometry ($L_z = 0.25\lambda_p$). Now the dipole active layer is located at the antinode of the cavity mode which is equivalent to a strongly enhanced photonic mode density at the grating layer. Thus, an increased radiative dephasing rate of the plasmon polarization can be expected. However, the formation of the considered cavity mode implies a zero phase change on reflection at the dipole active grating layer. Since this condition cannot be fulfilled at the exact particle plasmon resonance, strong coupling might result in a normal-mode splitting of the resonances [208]. Thus, the observed stopband in Fig. 5.12 ($L_z \approx 75$ nm) and the related mode splitting might likely be interpreted in terms of a cavity-polariton-like effect.

Returning to Fig. 5.10, also the already discussed enhanced transmissivity can be easily interpreted in terms of a Fabry-Perot-type resonance. However, due to the nearly vanishing spacer layer thickness of the considered metallic structure

Transmission   Transmission
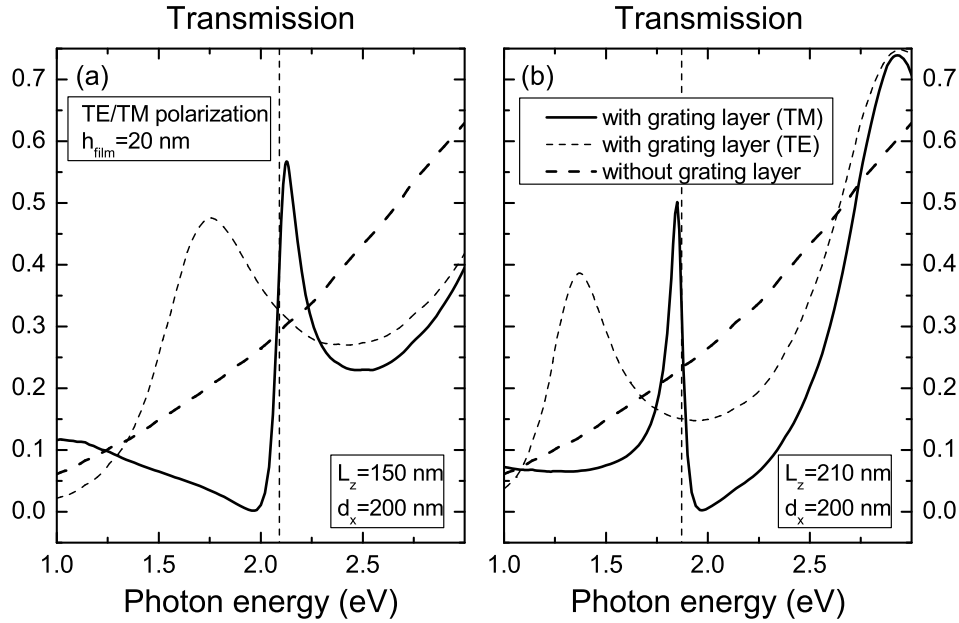
Figure 5.14: Calculated transmission spectra of a 20-nm-thick silver film. Spectra with (solid and thin dashed lines) and without (thick dashed line) additional grating layer are shown. A nanowire period of $d_x = 200$ nm has been used for the depicted numerical results. Calculations for spacer layer thicknesses of $L_z = 150$ nm (a) and $L_z = 210$ nm (b) are shown for TE and TM polarization. The vertical dashed lines in each panel indicate the position of the corresponding absorption maxima.

$(L_z = 20$ nm), the radiative interaction is superimposed by arising near-field phenomena. The near-field interaction generally results in a redshift of the bare particle plasmon resonance which directly influences the resonance condition of the metal-clad cavity (i.e., modification of λ_p). Obviously, the transmission enhancement is not restricted to structures with a specific spacer layer thickness. Except for the Bragg- and anti-Bragg-spaced multilayer structures, more or less pronounced transmission maxima can be extracted. Exemplary, calculated transmission spectra are displayed in Fig. 5.14 for two different sample structures. While panel (a) contains the results for structures with a grating-film separation of $L_z = 150$ nm, an increased spacer layer thickness of $L_z = 210$ has been used for the calculations in panel (b). Spectra for TE and TM polarization are shown, respectively. Note that the nanowire period of $d_x = 200$ nm has been kept constant. Additionally, the transmission spectra of a bare 20-nm-thick silver film are plotted in both panels as a reference.

The displayed spectra are again characterized by several interesting features.

First, the spectra in TM polarization clearly show the expected transmission enhancement in comparison to the bare silver layer. While the transmission maximum can be found at approximately 2.12 eV in panel (a), the energy is slightly reduced and approaches 1.85 eV in panel (b). Both panels indicate the Fano-type nature of the nanowire based resonances (i.e., transmission maximum is shifted in comparison to the marked absorption maximum). In contrast to Fig. 5.10, pronounced resonances can also be found in TE polarization. These Fabry-Perot-like modes are caused by the strong background reflectivity of the used metal gratings even in the absence of particle plasmon excitation. Similar to TM polarization, the resonances are redshifted when increasing the spacer layer thickness. However, clear differences between TE and TM polarization can be observed in the depicted theoretical spectra. The additional interaction with the particle plasmons in case of TM polarization modifies the spectral position of the arising polaritonic modes. Additionally, also the quality factor of the resonances is strongly increased (i.e., reduced linewidth). An important further information can be extracted from the spectra in panel (b) of Fig. 5.14. Due to the increased grating-film separation, a higher order cavity resonance emerges at approximately 2.9 eV. Surprisingly, the mode shows up in the spectra for TE and TM polarization, respectively. Due to the off-resonant position (far from the bare particle plasmon resonance), the resonance is simply caused by the background reflectivity of the used metal grating which acts as the upper mirror of the metal-clad microcavity. Distinct differences between the spectra in TE and TM polarization can only be observed when approaching the spectral region of the plasmon resonance.

In conclusion, the discussion of the radiative coupling phenomena reveals that further detailed investigations are still necessary. However, although the exact origin of the related absorption maxima might be more complex (i.e., plasmon-cavity interaction), we will refer to them as particle-plasmon-induced resonances in the subsequent subchapters.

5.3.3 Coupling between localized and extended surface plasmons

So far, all presented calculations have been restricted to nanowire-array-based structures with a period of $d_x = 200$ nm. This specific selection guarantees a large spectral separation of the particle plasmon related resonance and the grating-induced surface plasmon mode. As will be discussed in the following sec-
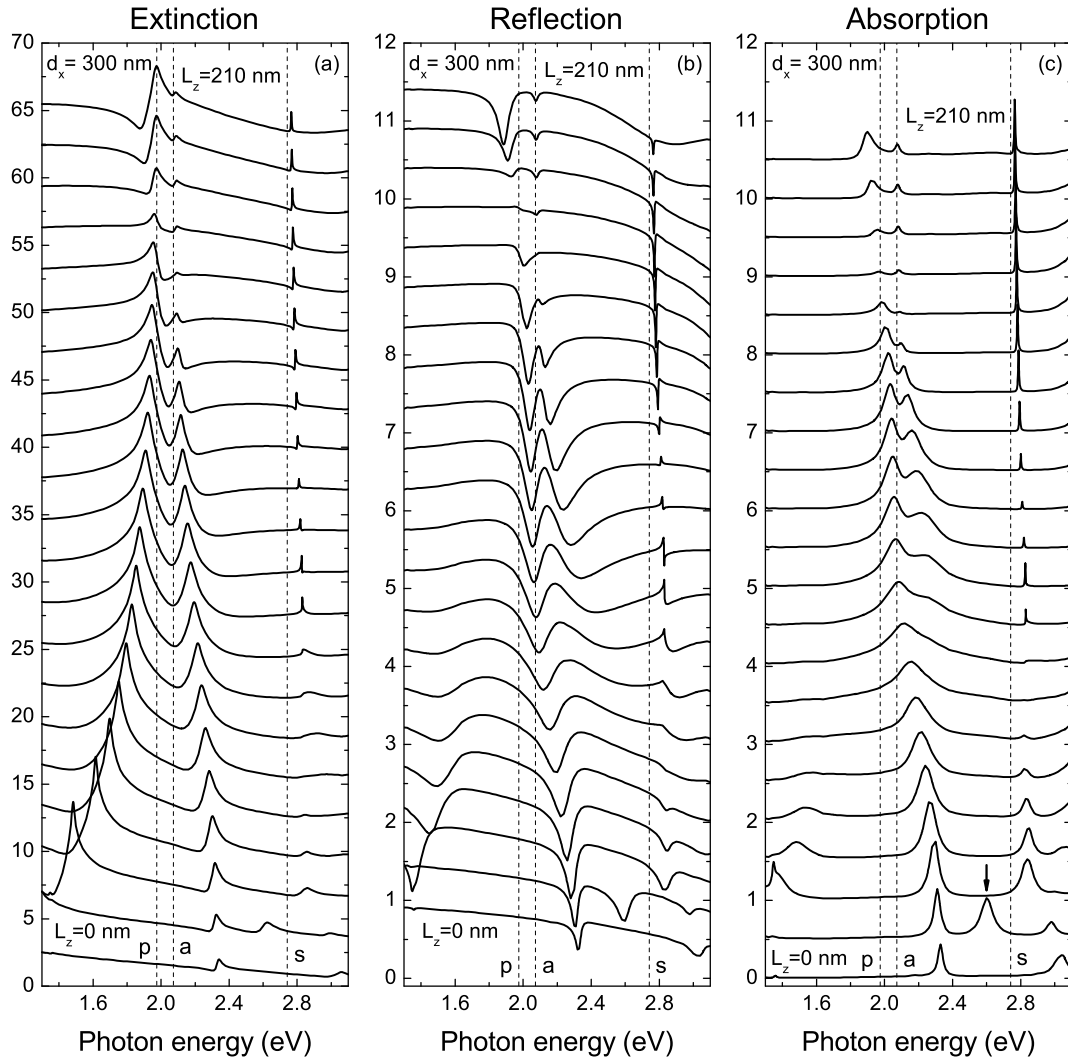
Figure 5.15: Calculated extinction (a), reflection (b), and absorption (c) spectra at normal incidence ($\vartheta = 0°$) and TM polarization. Spectra for nanowire gratings with a period of 300 nm are shown. From top to bottom, the spacer layer thickness L_z is decreased from 210 nm to 0 nm in steps of 10 nm. The individual spectra are shifted upwards for clarity in each panel. The nanowire particle plasmon extinction maximum of an identical grating without silver film is marked by a vertical dashed line [p, 1.97 eV]. Additionally, also the resonance energies of the short- [a, 2.07 eV] and long-range surface plasmon polaritons [s, 2.74 eV] are indicated, respectively. The single arrow at the bottom of panel (c) reveals the spectral position of a higher order particle plasmon resonance.

tion, important further phenomena can be observed when the nanowire period is increased. The modification of the nanowire period generally alters the spectral positions of the grating-induced surface plasmon resonances. Similar to the stud-

ied grating-waveguide structures (e.g., see Chap. 4), strong coupling phenomena are expected to appear. Exemplary, numerically obtained spectra for a silver nanowire grating in front of a 20-nm-thick silver film are shown in Fig. 5.15 for a nanowire period of $d_x = 300$ nm. Calculated extinction (a), reflection (b), and absorption (c) spectra are displayed for normal light incidence ($\vartheta = 0°$) and TM polarization. While all other parameters (e.g., nanowire cross-section and silver film thickness) have been kept constant, only the spacer layer thickness has been increased from $L_z = 0$ nm to $L_z = 210$ nm in steps of 10 nm. Compared to Fig. 5.5, the optical response changes significantly by increasing the nanowire period from $d_x = 200$ nm to $d_x = 300$ nm. Note that three characteristic energies are marked by dashed vertical lines. In addition to the position of the bare particle plasmon resonance of the nanowire array (neglecting the influence of the nearby surface), also the energies of the possible surface plasmon modes are indicated. A thin symmetric silver film (identical dielectric cladding layers above and below the metal film) generally supports so-called long- and short-range surface plasmon polariton modes. As already discussed, these modes arise due to the coupling between the surface plasmons on each interface [131]. The energies of quasiguided surface plasmon modes with $k_x = \pm 2\pi/d_x$ are denoted in all three panels of the figure. Both the antisymmetric short-range as well as the symmetric long-range surface plasmon mode of the symmetric film structure are now located within the displayed spectral region.

The depicted spectra for structures with an increased grating period of $d_x = 300$ nm reveal a more complex optical response in comparison to the already discussed results of Fig. 5.5. Now the extinction spectra in panel (a) of Fig. 5.15 show three pronounced features. From top to bottom, the positions as well as the line shapes of these spectral features strongly change when decreasing the spacer layer thickness. For larger nanowire-film separations ($L_z \geq 190$ nm), for example, the position of the lowest extinction maximum coincides with the position of the particle plasmon related extinction maximum of an identical grating structure without the additional metal film (e.g., see Sec. 5.3.1). The extinction maximum is continuously redshifted when decreasing the spacer layer thickness. A second extinction maximum can be found at slightly higher energies in all spectra. The observed maximum asymptotically approaches the position of the short-range surface plasmon mode (≈ 2.07 eV) of the 20-nm-thick silver film when increasing the spacer layer thickness. Simultaneously, also the extinction efficiencies are modified. The observed second maximum is most strongly pronounced in case of intermediate grating-film separations ($L_z \approx 80$ nm). While
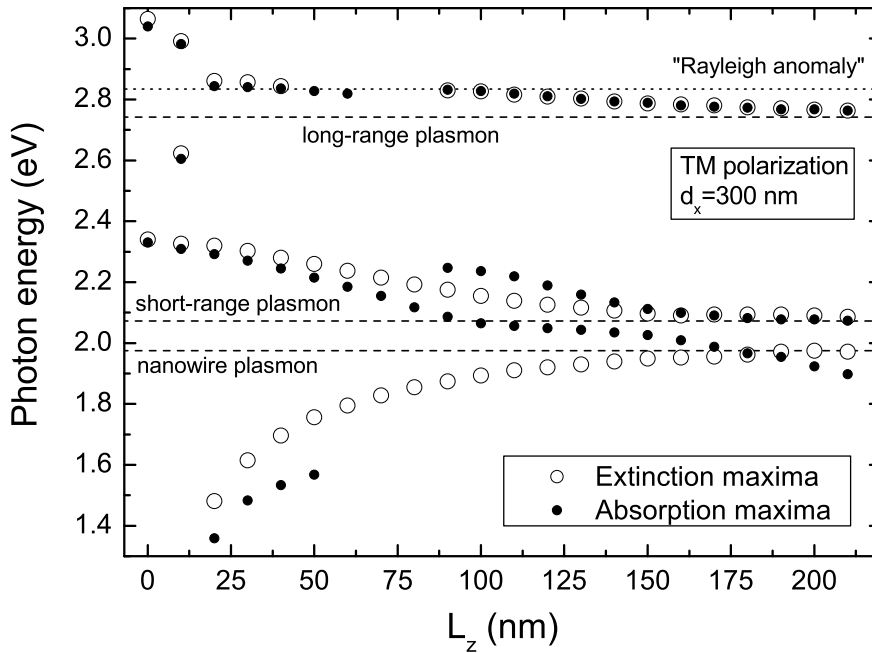
Figure 5.16:   Position of the extinction and absorption maxima extracted from Fig. 5.15. The position of the particle plasmon resonance of a pure nanowire grating without additional silver film is marked by the dashed horizontal line. Also the positions of the long- (symmetric) and short-range (antisymmetric) surface plasmon polariton modes are indicated by horizontal lines, respectively. The upper dotted line specifies the spectral position of the Rayleigh anomaly.

the two lower extinction peaks are spectrally broad, a rather narrow additional feature can be observed at higher energies. From top to bottom, starting from the spectral position of the long-range surface plasmon mode of the metal film (≈ 2.74 eV), the sharp extinction maximum is blueshifted. Note that this pronounced maximum disappears in the spectra for structures with a spacer layer thicknesses below approximately $L_z = 80$ nm. As already discussed in the previous sections, the extinction maxima are again slightly shifted in comparison to the related absorption maxima and the corresponding reflection minima. The exact thickness-dependent dispersion of the extinction and absorption maxima are displayed in Fig. 5.16 to highlight the induced changes. All depicted data points have been extracted from the numerically calculated spectra displayed in Fig. 5.15.

The observed complex spectral response can be understood when taking into account both near- as well as far-field coupling effects. Radiative coupling between

the individual dipole oscillators (silver nanowires) and their images in the metal film results in spectral shifts of their resonance frequencies and leads to a modification of the dephasing times. The induced radiative coupling effects (i.e., dynamic dipole-dipole interaction) are superimposed by the arising near-field phenomena (i.e., quasistatic dipole-dipole interaction) when considering small grating-film separations. Additional effects are introduced due to the use of a periodic nanowire arrangement and Bragg-coupling with the surface plasmon modes. In contrast to Fig. 5.5 (calculations for a similar sample structure with smaller grating period), the grating-induced short-range surface plasmon mode is now tuned near resonance with the localized nanowire related plasmon mode. Generally, the strong interaction of the supported plasmon modes is clearly observable in the theoretical spectra of Fig. 5.15.

The detailed analysis of Fig. 5.15 reveals that the expected influence of plasmon-plasmon coupling is largest for intermediate grating-film separations (i.e., $L_z \approx$ 120 nm). Starting from structures with smaller spacer layer thicknesses, both particle as well as surface plasmon mode are spectrally well separated thus preventing any interaction effects. For example, the single pronounced absorption maximum at approximately 2.3 eV ($L_z = 0$ nm) is caused by the grating-induced excitation of the lowest surface plasmon mode with momenta $k_x = \pm 2\pi/d_x$. Simultaneously, the particle plasmon related absorption peak is strongly redshifted due to the presence of strong near-field interaction (quasistatic dipole-dipole coupling). The interaction between both plasmon modes and hence a possible modification of the optical response can not be observed until the spacer layer thickness exceeds approximately $L_z = 40$ nm. All depicted subsequent spectra ($L_z > 40$ nm) are characterized by pronounced particularities which can be interpreted in terms of strong coupling and polariton formation. Generally, a possible interaction implies a spectral overlap of the bare particle and surface plasmon related resonances. This fundamental requirement is fulfilled due to a weakening of the quasistatic dipole-dipole interaction and the induced radiative plasmon shifts when increasing the spacer layer thickness (e.g., see Fig. 5.5). In particular, the interaction between the plasmon modes results in two fundamental phenomena. First, and maybe most surprisingly, the spectral signature of surface plasmon excitation does not vanish when increasing the spacer layer thickness. Even structures with a 210-nm-thick spacer layer are characterized by a weak absorption maximum at the spectral position of the short-range plasmon mode. This important observation constitutes a remarkable difference to the spectra of Fig. 5.5, where none of the grating-induced surface plasmon related features can be found

for structures with $L_z > 110$ nm. Second, a key phenomenon associated with the strong-coupling is the observable anticrossing of the localized and extended plasmon modes, wheras in the absence of a strong interaction they would have crossed. For example, the expected anticrossing behavior can be clearly extracted from the displayed reflection and absorption spectra. As already highlighted in Fig. 5.16, the spectral position of the grating-induced surface plasmon mode is redshifted when increasing the spacer layer thickness (i.e., surface plasmon mode becomes the short-range plasmon mode of the symmetric silver layer). The spectral shift of the resonance is simultaneously accompanied by a line broadening due to the slowly increasing interaction with the localized mode. For example, the largest linewidth is reached for structures with a spacer layer thickness of approximately 70 nm (absorption maximum at 2.15 eV). A further increase of L_z (starting from spacer layer thicknesses of approximately 100 nm) results in a splitting of the single absorption maximum. Similar to Fig. 5.16, the particle plasmon related resonance appears as peak (dip) in the absorption (reflection) spectra. The largest interaction is observed for structures with a spacer layer thickness of $L_z = 120$ nm where the absorption spectrum is characterized by two pronounced maxima. A further increase of the spacer layer thickness mainly affects the bare particle plasmon related mode (i.e., radiative coupling). Thus, the lower maximum is redshifted and transferred into the particle plasmon related resonance when approaching $L_z = 210$ nm. On the other hand, while its spectral signature is strongly reduced, the upper second absorption maximum asymptotically approaches the energy of the short-range surface plasmon mode. The described effects can be interpreted as a clear manifestation of the coupling between both plasmon modes.

Several additional spectral features of Fig. 5.15 have not been addressed so far. For example, the origin of the sharp absorption maximum at approximately 2.8 eV can be related to the grating-induced excitation of the so-called long-range surface plasmon mode at the homogeneous silver layer. For nearly symmetric structures, i.e., thick spacer layers, the energy of the resonance approaches 2.74 eV. This specific spectral position corresponds with the predicted long-range surface plasmon energy (modes with $k_x = \pm 2\pi/d_x$) which has been calculated by solving the dispersion relation of a homogeneous and 20-nm-thick silver layer. In comparison to a bare surface plasmon mode at a single quartz-silver interface, the narrow bandwidth of the resonance directly indicates its enhanced propagation length (i.e., prolonged lifetime), which arises due to coupling of the two interface modes. It is further shown in Fig. 5.15 that the resonance is strongly affected by decreas-

ing the dielectric spacer layer thickness. Generally, the symmetry of the structure is reduced (effective permittivities of the substrate and the upper cladding layer differ) and hence the degeneracy of the bare interface modes is lifted. In the limit of vanishing spacer-layer thicknesses, the long-range mode is therefore transferred into a surface plasmon mode which is predominantly localized at the upper air interface of the silver layer. However, the spectra in Fig. 5.15 reveal that the sharp plasmon resonance disappears for structures with a grating-film separation below $L_z = 80$ nm. This fact can be attributed to the opening of diffraction channels into the quartz substrate. If we plotted the dispersion relations of the considered modes (assuming $L_z < 80$ nm), it would be possible to see that their dispersion curves are located above the quartz light line within the considered spectral range. This fact can be interpreted as approaching the cut-off frequency.

Note that also the absorption spectra for structures with spacer layer thicknesses between $L_z \geq 20$ nm and $L_z \leq 60$ nm show a strong absorption maximum at photon energies of approximately 2.84 meV. The maximum is blueshifted when decreasing the grating-film separation below $L_z = 20$ nm. The origin of this resonance might be the grating-induced excitation of a quasiguided surface plasmon mode at the silver-quartz interface with momentum $k_x = \pm 4\pi/d_x$ (second Bragg order of the short-range mode).

One additional spectral feature can be observed in Fig. 5.15 for structures with a grating-film separation of $L_z = 10$ nm. Especially the related absorption maximum at approximately 2.6 eV in panel (c) of Fig. 5.15 is strongly pronounced (indicated by a small arrow). This maximum has no counterpart in all other spectra of the displayed sample series. Note that a similar anomaly has already been observed in the spectra of Fig. 5.5. Supplementary calculations clearly indicate that the anomaly is rapidly shifting to lower energies when decreasing the spacer layer thickness from 10 nm to 0 nm in steps of 1 nm (not shown). However, a calculation of the electromagnetic field distribution (not shown) allows a classification of the anomaly. The absorption maximum can be clearly attributed to the excitation of a higher order particle plasmon mode. As will be shown in Fig. 5.17, this localized plasmon mode can be found in the extinction spectra of structures with grating periods of $d_x = 200$, 300, and 400 nm, respectively.

Further important details on the coupling between particle and extended surface plasmon modes can be extracted from Fig. 5.17. The figure allows a direct comparison of the spacer layer dependent extinction spectra of grating-film structures which only differ in their nanowire periods, respectively. Numerical results for
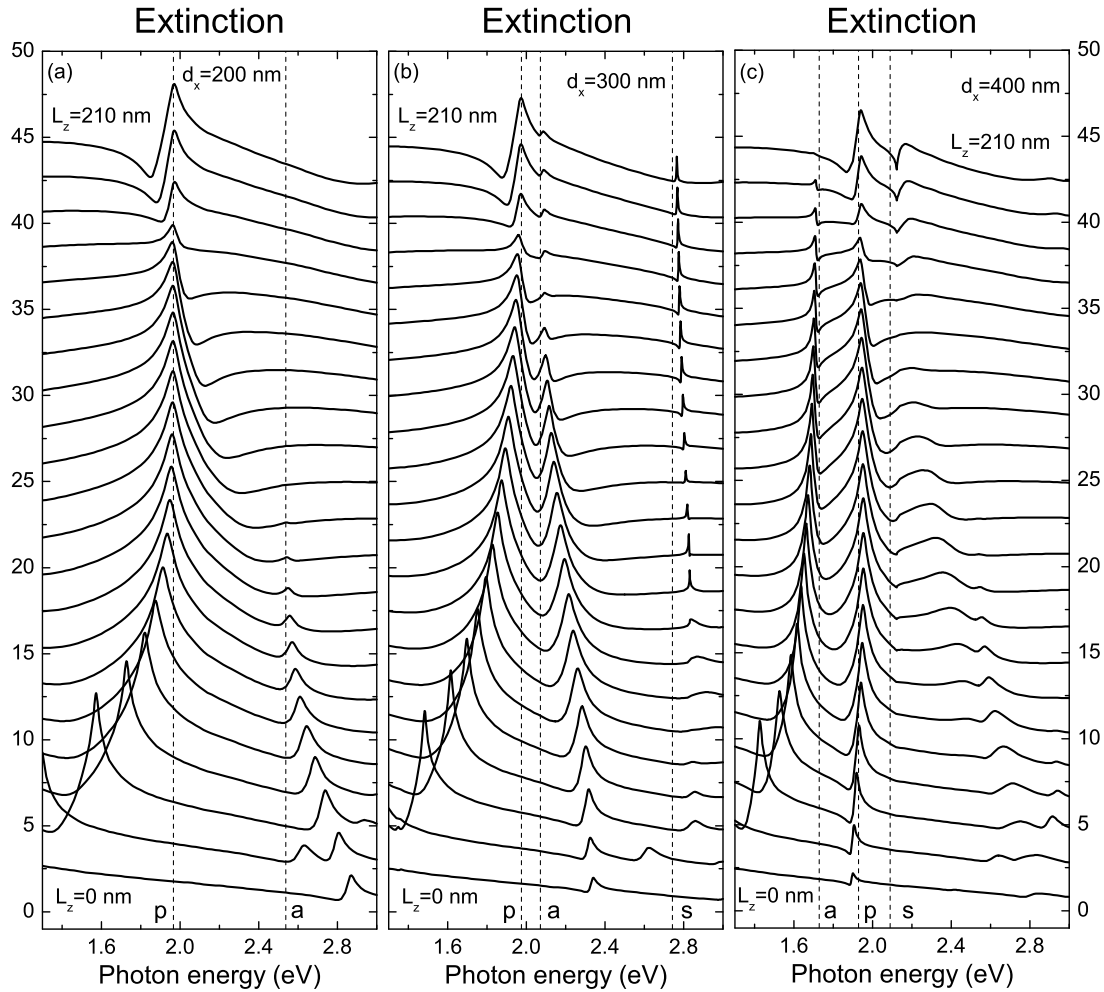
Figure 5.17: Calculated extinction spectra at normal incidence ($\vartheta = 0°$) and TM polarization. Spectra for nanowire grating periods of 200 nm (a), 300 nm (b), and 400 nm (c) are shown. From top to bottom, the spacer layer thickness L_z is decreased from 210 nm to 0 nm in steps of 10 nm while the metal film thickness of $h_{\mathrm{film}} = 20$ nm remains unchanged. Note that the individual spectra are shifted upwards for clarity in each panel. The position of the undisturbed nanowire particle plasmon resonance is marked by a vertical dashed line [p] in all panels. Additionally, also the positions of the symmetric [s] and antisymmetric [a] surface plasmons are indicated by vertical lines.

sample structures with grating periods of 200 nm, 300 nm, and 400 nm are shown for normal light incidence and TM polarization. From top to bottom, the spacer layer thickness L_z is decreased from 210 nm to 0 nm in steps of 10 nm, respectively. The metal film thickness of $h_{\mathrm{film}} = 20$ nm and the nanowire cross-section of 100×10 nm^2 are kept constant. Again, the characteristic energies of the bare

modes are indicated by dotted vertical lines in all three panels. In addition to the energy of the particle plasmon resonance of the pure metal grating without silver film, also the spectral positions of the short- and long-range surface plasmon modes of the silver film (sandwiched between quartz cladding layers) are marked.

The depicted spectra clearly reveal the influence of the nanowire period. Qualitatively, although the exact resonance positions can not be easily extracted from the shown extinction spectra (which displays a Fano-type line shape), the induced coupling effects can be highlighted. As already discussed, the particle and surface plasmon related features are spectrally well separated when considering structures with smaller grating periods. The main information which can be extracted from panel (a) of Fig. 5.17 is the spacer-layer dependent excitation efficiency of the short-range (antisymmetric) surface plasmon mode. Its spectral signature disappears in all extinction spectra for structures with $L_z \geq 110$ nm. However, the excitation efficiency and the thickness-dependent dispersion of the surface plasmon mode can be strongly modified by increasing the grating period. As displayed in panel (b), the surface plasmon related peak can still be observed in case of 210-nm-thick spacer layers due to the coupling between particle and surface plasmon modes (formation of polaritonic states). Note that especially the use of intermediate spacer layer thicknesses of approximately $L_z = 80$ nm induces two pronounced extinction maxima. Even stronger modifications of the optical response can be observed in panel (c) of the figure. Now the period is such that the short-range surface plasmon mode of the symmetric silver film is tuned to energies below the particle plasmon resonance. Furthermore, the chosen nanowire period of $d_x = 400$ nm is very special from another point of view. In case of vanishing spacer layer thickness ($L_z = 0$ nm), the extinction maximum of the surface plasmon resonance is found close to the energy of the particle plasmon resonance of the bare silver grating. As a consequence of the specific sample geometry and the induced strong coupling, interesting effects become visible when increasing the spacer layer thickness. It seems that, asymptotically, the red-shifted particle plasmon related extinction maximum is directly transferred into the short-range surface plasmon (1.73 eV). Contrary, the dispersive extinction maximum of the particle plasmon resonance (1.966 eV) emerges directly from the surface plasmon mode. This characteristic behavior is again a clear signature of strong coupling and polariton formation.

It is important to remark that the long-range surface plasmon mode does not show up as narrow extinction maximum in one single spectrum of Fig. 5.17 (c). Due to its interaction with the particle plasmon resonance, only a small dip appears

close to the expected resonance position (2.1 eV) in case of larger grating-film separations (e.g., $L_z = 210$ nm).

5.3.4   Influence of the metal layer thickness

It has been shown in the previous sections that the interaction between the localized nanowire plasmons and the grating-induced surface plasmons can be controlled by changing the spacer layer thickness or the grating period, respectively. So far, the additional dependence on the metal layer thickness has not been probed. First theoretical results are shown in Fig. 5.18. Calculated extinction (a), reflection (b), and absorption (c) spectra are displayed for normal light incidence ($\vartheta = 0°$) and TM polarization. While the spacer layer thickness of $L_z = 150$ nm and the grating period of 300 nm are kept constant, only the thickness of the nearby silver film is changed. From top to bottom, the thickness h_{film} is decreased from 30 nm to 0 nm in steps of 2 nm. Note that the displayed theoretical spectra must be analyzed with some caution. Especially structures including silver films with a thickness below 10 nm may cause several problems. In addition to the existent fabrication difficulties, especially the used bulk dielectric function of silver might be insufficient to describe the optical response of such thin metal layers. However, the calculations might help to get a better understanding of the fundamental optical dependencies when keeping in mind the mentioned restrictions.

The spectra are generally characterized by the appearance of three more or less pronounced features. Due to the use of a relatively thick spacer layer and the resulting symmetric metal slab geometry, both short- and long-range surface plasmon modes can be excited. Additionally, also the signature of the localized nanowire plasmon mode can be found in the shown spectra. The main feature of the figure is a pronounced anticrossing behavior between two of the observed resonances. The anticrossing is clearly observable in all three panels of the figure. To highlight the main effects, the spectral positions of the absorption maxima have been extracted. The derived mode positions are displayed in Fig 5.19 in dependence on the metal film thickness. Additionally, also the thickness-dependent dispersions of the short- (symmetric) and long-range (antisymmetric) surface plasmon modes are depicted[4].

---

[4]Obtained from a numerical solution of the dispersion relations, e.g., see Refs. [12, 119] for further details
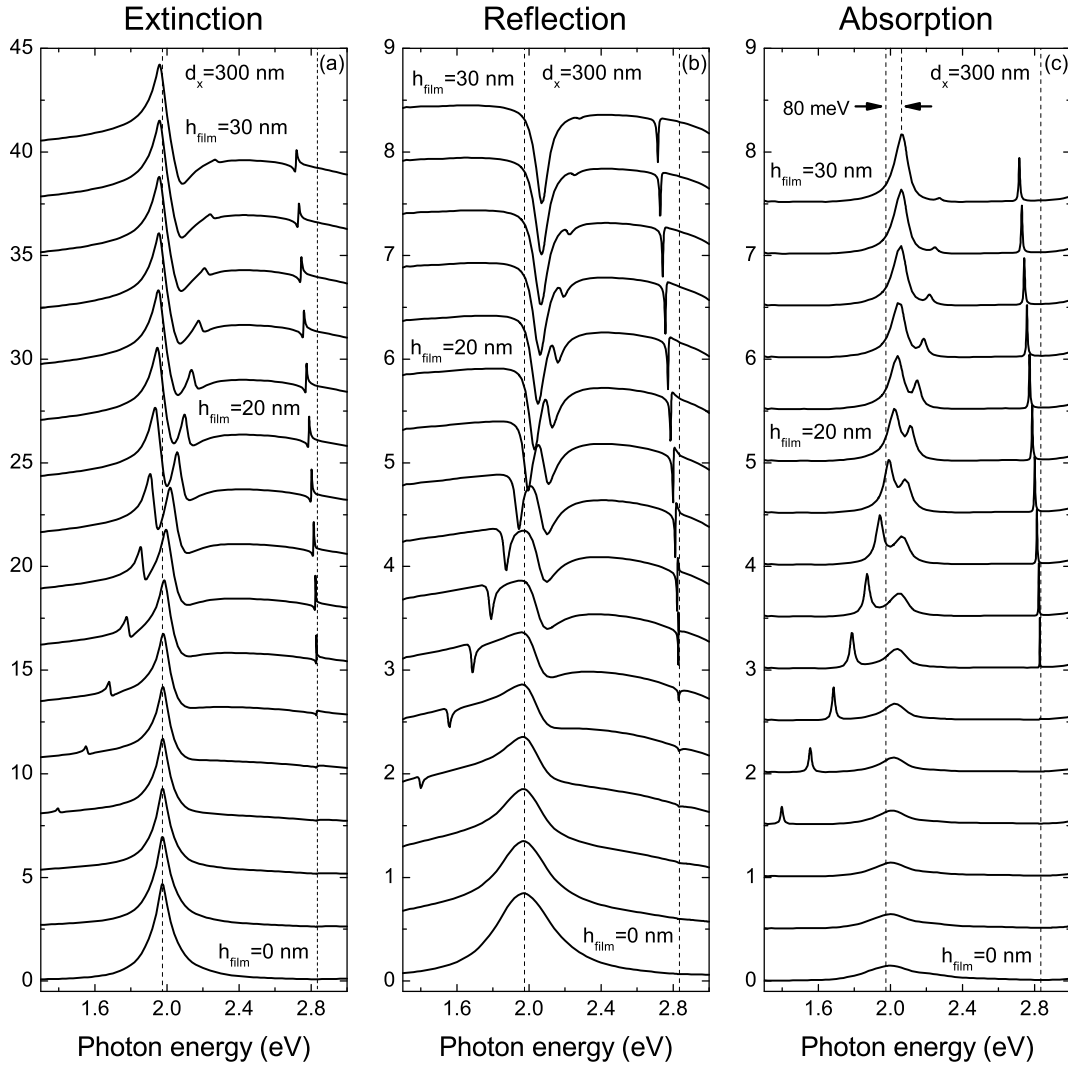
Figure 5.18: Calculated extinction (a), reflection (b), and absorption (c) spectra at normal incidence ($\vartheta = 0°$) and TM polarization. Spectra for nanowire grating periods of 300 nm are shown. From top to bottom, the metal film thickness h_{film} is decreased from 30 nm to 0 nm in steps of 2 nm while the spacer layer thickness of $L_z = 150$ nm remains unchanged. The individual spectra are shifted upwards for clarity in each panel. The undisturbed nanowire particle plasmon resonance (1.975 eV) as well as the spectral position of the Rayleigh anomaly (2.834 eV) are marked by vertical dotted lines.

As shown in Fig 5.19, the narrow absorption maximum close to photon energies of 2.8 eV can be identified as being the long-range (symmetric) surface plasmon mode of the thin silver film. As predicted, its photon energy is reduced when increasing the metal layer thickness. Note that the extracted maxima (hollow circles) are slightly shifted compared to the calculated dispersion (solid line).
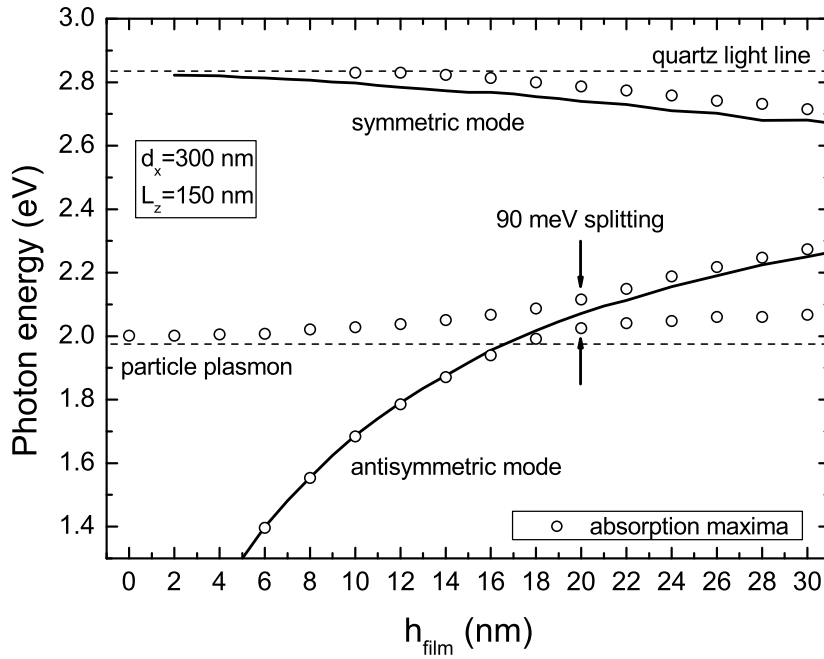
Figure 5.19: Calculated energies of the absorption maxima for a nanowire period of $d_x = 300$ nm (open circles). While the spacer layer thickness of $L_z = 150$ nm remains unchanged, the dependence on h_{film} is shown for normal light incidence and TM polarization. Additionally, the solid lines show the dispersion of the symmetric and antisymmetric surface plasmon modes at a planar metal slab with thickness h_{film}. The two dashed horizontal lines indicate the energy of the undisturbed nanowire plasmon resonance and the position of the Rayleigh anomaly (opening of diffraction channels into the quartz cladding), respectively.

This fact can be related to the still present nonsymmetric geometry of the considered system. While the displayed dispersion relation has been solved under the assumption of quartz cladding layers (metal film sandwiched between quartz half spaces), the scattering-matrix calculations are based on multilayer structures with an only 150-nm-thick spacer layer. On the other hand, the influence of the nonsymmetric cladding layers on the appearing short range mode can be neglected due to the much stronger confinement of the related fields. Until the nearby metal film reaches a thickness of approximately 14 nm, the extracted positions of the lower absorption maxima show a good agreement with the numerically obtained dispersion relation of the short-range surface plasmon mode. The arising deviations for larger metal film thicknesses can be explained by the strong coupling between the localized particle and the grating induced short-range plasmon

mode. The degeneracy of the modes is lifted at the crossing point of the two dispersion curves. A splitting of approximately 90 meV can be extracted from the scattering matrix based calculations.

Note that not only the dispersion of the bare surface plasmon modes is modified when changing the metal film thickness. The increased reflectivity of the thicker metal layers induces radiative coupling effects which influence the resonance frequency and the dephasing time of the particle plasmon (i.e., interaction with its own reflected fields). These modifications are clearly observable in panel (c) of Fig. 5.18. The lowest spectrum is characterized by a single broad absorption maximum due to excitation of the localized nanowire plasmons (grating without additional metal layer). Assuming a 30-nm-thick silver layer and a grating-film separation of $L_z = 150$ nm, the related absorption maximum of the localized mode is blueshifted by 80 meV from the original particle plasmon position [indicated by the horizontal arrows in Fig. 5.18 (c)]. Simultaneously, the metal film induced radiative coupling results in prolonged dephasing times, i.e., a reduced spectral width of the pronounced particle plasmon related absorption maximum.

Even stronger interaction phenomena can be observed when the spacer layer thickness is reduced to $L_z = 50$ nm. Exemplary, the corresponding theoretical extinction spectra are shown in Fig. 5.20 for normal light incidence ($\vartheta = 0°$) and TM polarization. Spectra for nanowire structures with a period of $d_x = 200$ nm and $d_x = 300$ nm are presented in panels (a) and (b), respectively. From top to bottom, the metal film thickness h_{film} is decreased from 20 nm to 0 nm in steps of 2 nm while the spacer layer thickness of $L_z = 50$ nm remains unchanged. Note that only the extinction spectra are displayed in Fig. 5.20. Due to the arising radiative coupling effects and hence the induced broadening of the localized plasmon absorption, the extraction of the exact resonance positions turns out to be rather complicated. However, the extinction maxima are suitable to highlight the fundamental effects, although the maxima do not exactly specify the mode positions (Fano-type line shape). Panel (a) of the figure indicates the strongly enhanced anticrossing behavior. While the localized plasmon mode is redshifted (i.e., radiative coupling), the surface plasmon mode energy is increased simultaneously. As result of the coupling, the degeneracy of the modes is lifted at the crossing point of the dispersion curves of the bare plasmon modes. The displayed extinction spectra become more complex in panel (b) of the figure. Due to the larger nanowire period, an additional third maximum can be observed. Now the the first and the second Bragg order of the surface plasmon mode with momenta $k_x = \pm 2\pi/d_x$ and $k_x = \pm 4\pi/d_x$ interact with the localized plasmon
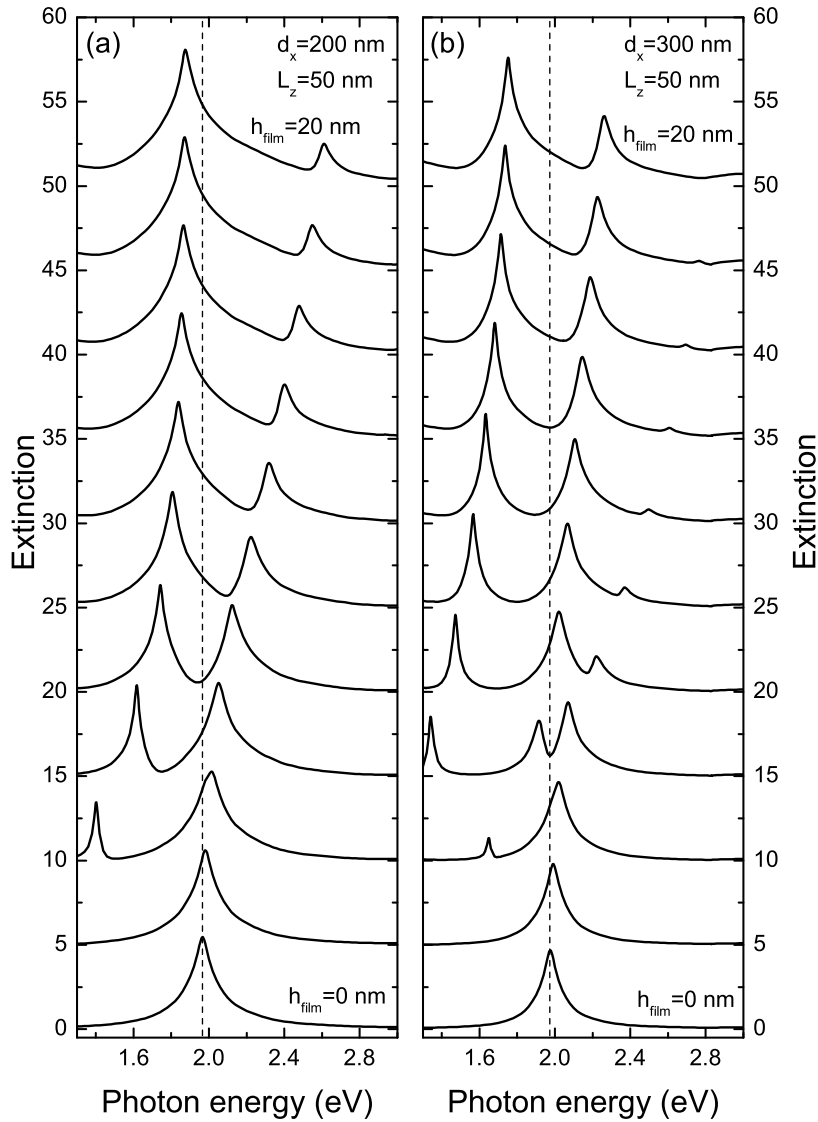
Figure 5.20: Calculated extinction spectra at normal incidence ($\vartheta = 0°$) and TM polarization. Spectra for nanowire grating periods of 200 nm (a) and 300 nm (b) are shown. From top to bottom, the metal film thickness h_{film} is decreased from 20 nm to 0 nm in steps of 2 nm while the spacer layer thickness of $L_z = 50$ nm remains unchanged. The individual spectra are shifted upwards for clarity in each panel. The undisturbed nanowire particle plasmon resonance is marked by a vertical dotted line.

mode.
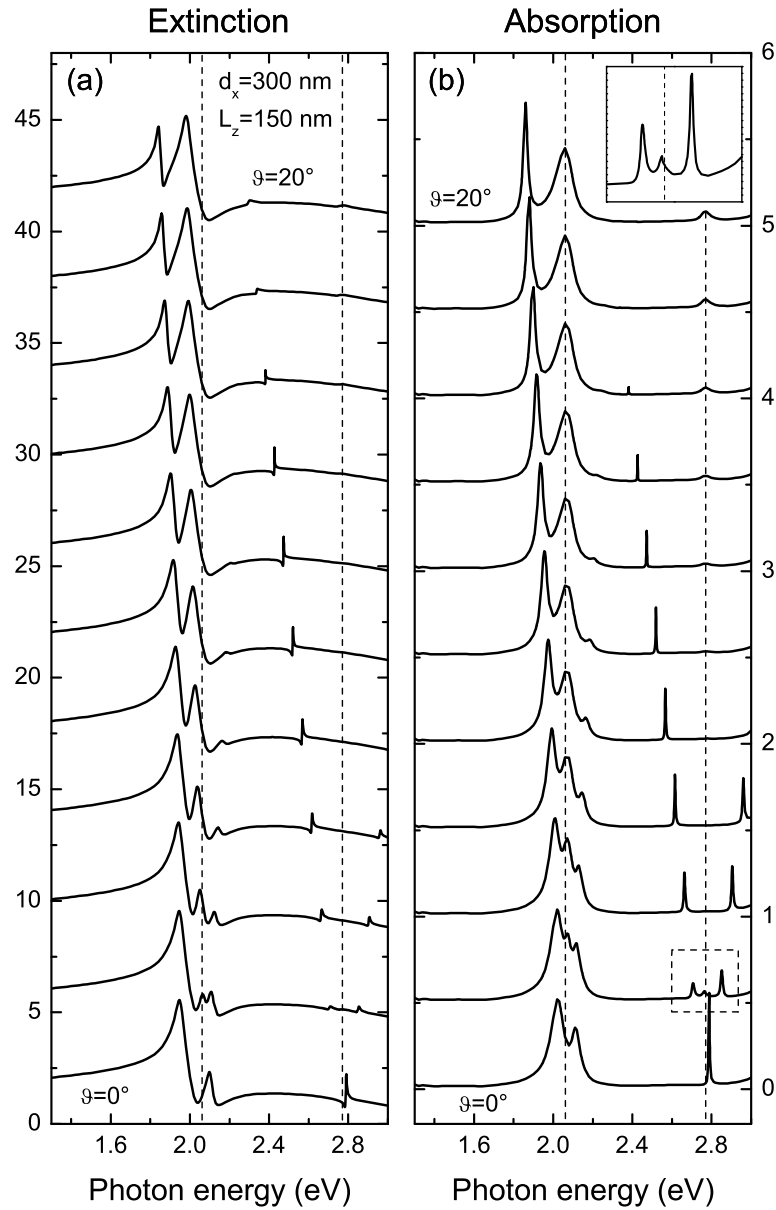
Figure 5.21: Calculated extinction (a) and absorption (b) spectra are depicted in dependence on the light incidence angle (p-polarization). Spectra for nanowire grating periods $d_x = 300$ nm are shown. From top to bottom, the angle of incidence is decreased from $\vartheta = 20°$ to $\vartheta = 0°$ in steps of $2°$ while the spacer layer thickness of $L_z = 150$ nm and the period of $d_x = 300$ nm remain unchanged. The individual spectra are shifted upwards for clarity in each panel. The particle plasmon resonance of the uncoupled silver nanowires is marked by a vertical dashed line at approximately 2.06 eV. The inset at the top of panel (b) presents an enlarged view of the area inside the dashed frame ($\vartheta = 2°$).
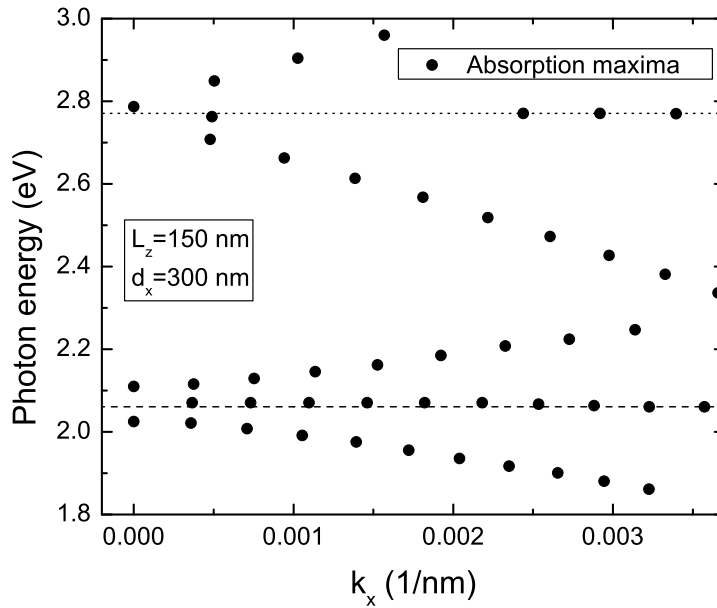
Figure 5.22: Position of the absorption maxima in dependence on the in-plane wave vector k_x. The depicted data points have been extracted from panel (b) of Fig. 5.21. The lower dashed horizontal line indicates the position of the bare particle plasmon resonance.

5.3.5   Angular dispersion

The interaction between localized particle and extended surface plasmon modes has been analyzed in dependence of various geometrical parameters in the previous sections. The nanowire period, the grating-film separation, and the thickness of the used metal layer have been varied to extract the related fundamental dependencies. However, all discussions were solely restricted to calculations assuming normal light incidence. Additional information might be deduced from angle-dependent studies of the optical response.

Exemplary, angle-dependent extinction and absorption spectra are shown in Fig. 5.21. All calculations are based on the proposed multilayer grating geometry (e.g., see Fig. 5.1). Again, a silver nanowire array positioned in close proximity to a 20-nm-thick silver film has been used. Numerical results for structures with a nanowire period of $d_x = 300$ nm and a constant spacer layer thickness of $L_z = 150$ nm are presented for p-plarization. Starting from the lowest spectra, the incidence angles are increased from $\vartheta = 0°$ to $\vartheta = 20°$ in steps of $2°$, respectively. Generally, the depicted spectra show strong modifications when changing the light incidence

angle. The main features of the figure are the emerging additional extinction and absorption peaks. The extracted spectral positions of the absorption maxima are shown in Fig. 5.22 to illustrate the angular dispersion of the individual modes.

The spectral modifications in Fig. 5.21 can be explained by the appearance of symmetric and antisymmetric surface plasmon modes. Considering a reduced zone scheme, the surface plasmon dispersion has to be folded into the first Brillouin zone. At the center of the Brillouin zone ($k_x = 0$), the degeneracy of the folded modes is generally lifted. Similar to the excitation of quasiguided slab modes (e.g., see Chap. 3), only one of the arising modes is optically active for normal light incidence (in case of periodic structuring with a symmetric unit cell). The antisymmetric normal mode is only visible for inclined incidence angles. Note that the modes at the center of the Brillouin zone correspond to standing surface plasmon modes. Here, the terms symmetric and antisymmetric are used for describing the symmetry of the electric fields with respect to the periodic grating structure. The appearance of the additional surface plasmon resonances can be clearly observed in the displayed absorption spectra. Therefore, especially the extracted absorption maxima in Fig. 5.22 allow a direct tracking of the dispersion curves. For example, the lowest absorption spectrum in Fig. 5.21 (b) is characterized by three maxima. The two lower maxima are caused by the interaction of the localized nanowire plasmons and the grating-induced short-range surface plasmon mode. Again, the very narrow additional maximum at ≈ 2.8 eV is attributed to the long-range surface plasmon mode. For inclined incidence, the antisymmetric surface plasmon modes can be excited and appear as additional maxima. At approximately 2.06 eV and $\vartheta = 2°$, two short-range plasmon modes interact with the localized mode. Due to the angular dispersion of the surface plasmon modes, the spectral overlap between the bare plasmon modes (and hence the interaction strength) is reduced when increasing the incidence angle. Finally, when the incidence angle reaches $\vartheta = 20°$, only two pronounced resonances can be found in the spectra. The maxima can be attributed to the redshifted short-range mode and the localized nanowire plasmon resonance (marked by a dashed vertical line at 2.06 eV).

An interesting additional effect can be extracted from the angle-dependent absorption spectra in Fig. 5.21. A new absorption maximum arises at approximately 2.77 eV for inclined illumination of the sample structure (starting from $\vartheta = 12°$). This additional maximum shows no angular dispersion (e.g., see Fig. 5.22). Only the absorption efficiency is modified when increasing the angle of incidence. Additional calculations (not shown) have proven that a similar maximum can be found

even for structures without additional silver film. Furthermore, considering the spectral position of the resonance, the supplementary calculations also predict a strong dependence on the chosen silver nanowire cross-section (i.e., thickness of the grating). Therefore, the origin of the absorption maximum has to be attributed to a nanowire related phenomenon. Taking into account all facts, it might be possible that the arising z-component of the incident light field causes the excitation of a mode which is connected with an electron oscillation along the z-axis of the nanowires. Surprisingly, the calculated absorption spectra in Fig. 5.21 (b) reveal the excitation of this mode due to the coupling with the narrow long-range surface plasmon mode. For an incidence angle of $\vartheta = 2°$, three absorption maxima can be observed instead of the expected two surface plasmon related peaks [see inset in Fig. 5.21 (b)]. However, further studies are necessary to clarify the exact origin of the resonance and to exclude possible errors due to numerically instabilities.

5.4   Experimental verification

It has been shown in the previous sections that the optical response of noble metal nanowire arrays is strongly modified by the presence of a nearby metal layer. Various interesting interaction phenomena have been presented. However, all discussions were solely based on numerical calculations so far. First experimental results will be presented in the following section to verify some of the theoretical predictions. As schematically depicted in Fig. 5.1, multilayer grating structures have been fabricated for the transmission measurements. The used sample structures are based on commercially available quartz substrates which have been covered by thin homogeneous metal films (thermal evaporation of silver layers). A thin silicon dioxide (SiO_2) buffer layer (thickness L_z) has been deposited in a second step. Finally, electron beam lithography was used to prepare the one-dimensional gold nanowire arrays on top of the spacer layers. Only experimental results for normal light incidence and TM polarization will be presented. For an exact interpretation of the observed phenomena, all experimentally obtained spectra are directly compared with the corresponding scattering-matrix based results.

We will start with the discussion of the plain grating structures neglecting the nearby metal films in the first step. Exemplary, measured (a) and calculated (b) extinction spectra of a gold nanowire array deposited on top of a pure quartz
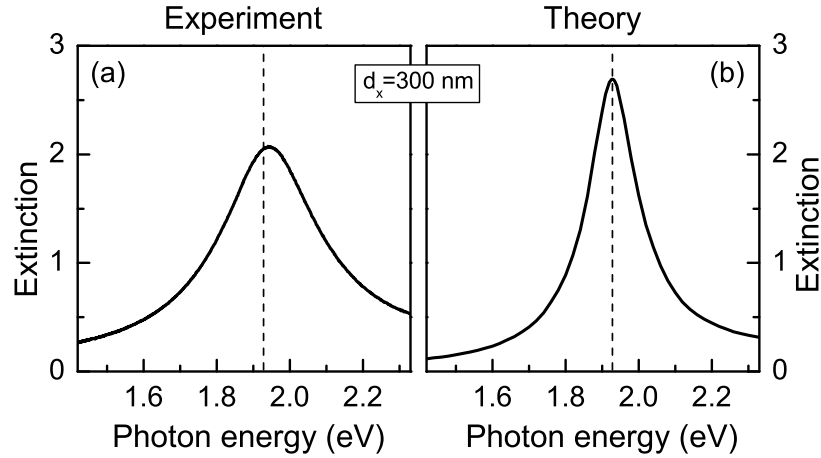
Figure 5.23: Measured (a) and calculated (b) extinction spectra for gold nanowire gratings on top of a quartz substrate. Spectra of nanowire gratings with a period of $d_x = 300$ nm are shown for TM polarization and normal light incidence. Instead of the experimentally assumed wire cross-section of 100×20 nm^2, the calculation was performed for nanowires with a cross-section of 100×15 nm^2.

substrate are depicted in Fig. 5.23. Spectra of nanowire gratings with a period of $d_x = 300$ nm are shown for TM polarization and normal light incidence. Both spectra are clearly characterized by a pronounced spectral feature, caused by the excitation of the nanowire particle plasmon resonance. Generally, the depicted extinction spectra show good agreement. As denoted by the dashed vertical lines, more or less identical resonance energies can be extracted. Small deviations, on the other hand, can be observed when comparing the spectral width of the extinction peaks. Especially sample imperfections may cause an inhomogeneous broadening and attenuation of the measured nanowire plasmon resonance. We have to remark that a gold nanowire cross-section of 100×15 nm^2 has been used for the depicted scattering-matrix based calculation. This value slightly deviates from the experimentally determined cross-section of approximately 100×20 nm^2. However, the fitted cross-section seems rather reasonable, especially when considering possible uncertainties during the exact determination of the geometrical parameters. Therefore, if not stated otherwise, all presented numerical calculations are based on gold nanowires with an optimized cross-section of 100×15 nm^2 in the following.

Figure 5.24:   Measured (left panels) and calculated (right panels) extinction spectra for gold nanowire gratings in front of a 20-nm-thick silver film. Spectra are shown for TM polarization and normal light incidence. While the grating period of $d_x = 300$ nm has been retained unchanged, the spacer layer thickness is increased from $L_z = 30$ nm to $L_z = 70$ nm. The dashed vertical lines mark the positions of the *measured* extinction spectra maxima.

5.4.1   Silver-gold nanostructures

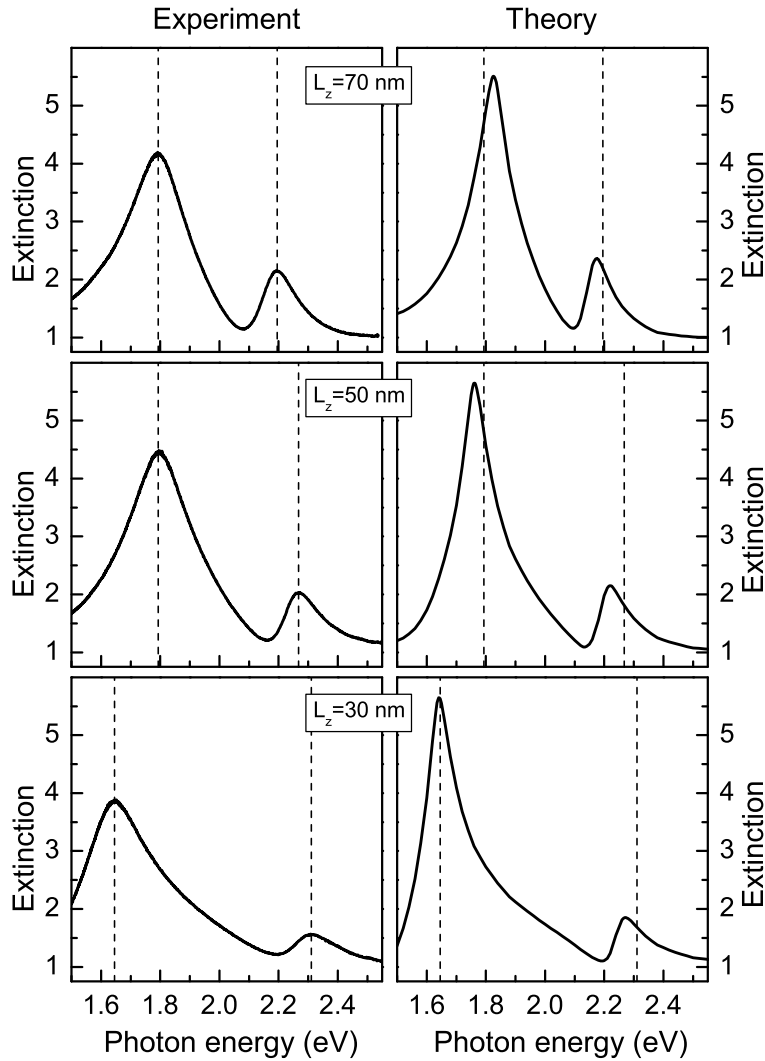The modification of the extinction spectra due to the presence of a nearby semi-transparent silver film is displayed in Fig. 5.24. Measured (left panels) and calculated (right panels) extinction spectra for gold nanowire gratings in front of a 20-nm-thick silver film are depicted, respectively. All spectra are shown for TM polarization and normal light incidence. While the grating period of

$d_x = 300$ nm has been kept constant, only the spacer layer thickness is increased from $L_z = 30$ nm to $L_z = 70$ nm in steps of 20 nm. Generally, the main features of the measured spectra are reproduced by the scattering-matrix based numerical calculations. Good agreement is found when comparing the spectral shapes or the positions of the extinction maxima. All spectra are characterized by two extinction maxima. The stronger feature is shifted to lower energies when compared with the spectral position of the bare particle plasmon resonance of Fig. 5.23. The weaker pronounced second maximum on the other hand is blueshifted. A reduction of the spacer layer thickness directly results in an increased spectral separation between the two observed maxima.

Now, based on the detailed knowledge obtained from the theoretical considerations, the interpretation is more or less straightforward. The observed modification of the optical response is clearly caused by the simultaneous excitation of localized nanowire and grating-induced surface plasmon resonances. The extinction maximum which is related to the localized plasmon resonance is shifted to lower energies when compared to the bare mode. The observed shift results from near-field interaction with the image in the nearby metal film (i.e., non-radiative energy transfer between the localized plasmons and surface plasmon polariton modes). The coupling strength shows a strong distance dependence. Thus, the redshift is increased when decreasing the grating-film separation. The second weaker extinction maximum in Fig. 5.24 originates from the grating-induced excitation of a surface plasmon mode with momentum $k_x = \pm 2\pi/d_x$ at the metal film. Depending on the spacer layer thickness, the spectral position of this surface plasmon mode is shifted, too. This fact is related to the modification of the asymmetric sample design (i.e., metal layer sandwiched between quartz and air half spaces). A thicker spacer layer means that the film geometry becomes more symmetric. Hence, the exited surface plasmon mode (localized at the quartz-silver interface for very thin spacer layers) is transferred into the short-range plasmon mode of the 20-nm-thick silver film (symmetric design).

However, it is generally impossible to extract the complex dependencies only from three individual extinction spectra. It might be reasonable to compare the obtained results with the theoretical spectra of the whole sample series. The calculated optical response is therefore presented in Fig. 5.25 in dependence on the grating-film separation for the sake of completeness. The calculated extinction (a), reflection (b), and absorption (c) spectra are displayed for normal light incidence ($\vartheta = 0°$) and TM polarization. Spectra of gold nanowire gratings with a period of 300 nm, placed in front of a 20-nm-thick silver film are shown. From
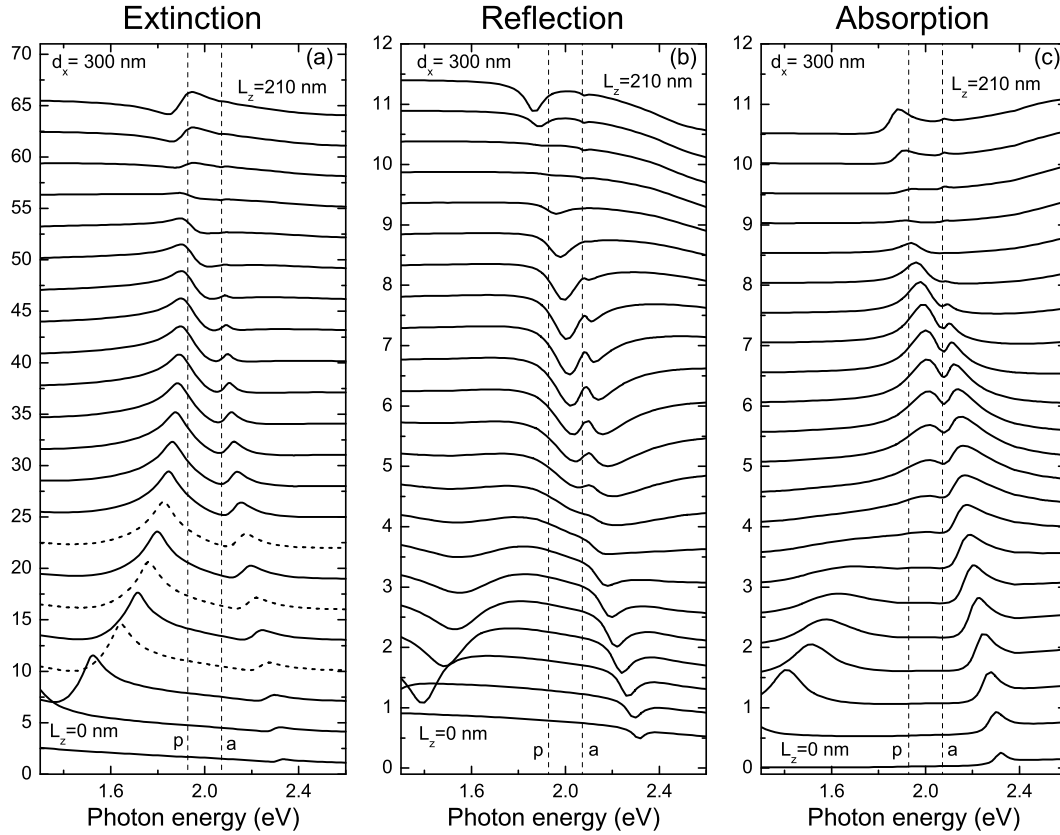
Figure 5.25: Calculated extinction (a), reflection (b), and absorption (c) spectra at normal incidence ($\vartheta = 0°$) and TM polarization. Spectra for gold nanowire gratings with a period of 300 nm are shown. From top to bottom, the spacer layer thickness L_z is decreased from 210 nm to 0 nm in steps of 10 nm. The individual spectra are shifted upwards for clarity in each panel. The undisturbed nanowire particle plasmon resonance [p] and the expected position of the antisymmetric surface plasmon [a] are marked by dashed vertical lines. The theoretical extinction spectra of Fig. 5.24 ($L_z = 30$ nm, $L_z = 50$ nm, and $L_z = 70$ nm) are included and indicated by dotted lines.

top to bottom, the spacer layer thickness L_z is decreased from 210 nm to 0 nm in steps of 10 nm. Note that the already presented theoretical extinction spectra of Fig. 5.24 are included and marked by dotted lines. Again, the displayed spectra clearly reveal the appearing interaction effects. Both the influence of near-field interaction as well as radiative coupling can be observed. Although the effects have already been discussed very extensively (e.g., see previous sections), it seems to be important to highlight one fundamental observation. Due to the coupling with the localized plasmon modes, the grating-induced surface plasmon excitation efficiency is maximum for small but finite separation of the grating and the
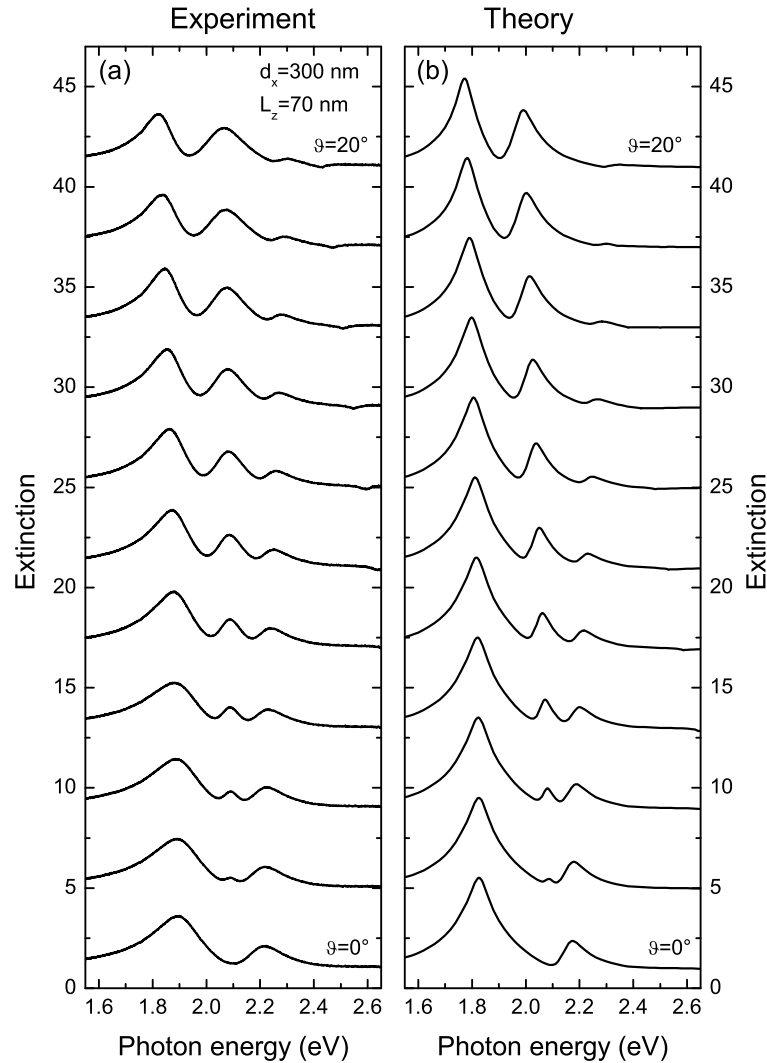
Figure 5.26: Measured (a) and calculated (b) extinction spectra are depicted in dependence on the light incidence angle (*p*-polarization). From top to bottom, the angle of incidence is decreased from $\vartheta = 20°$ to $\vartheta = 0°$ in steps of $2°$ while the spacer layer thickness of $L_z = 70$ nm and the period of $d_x = 300$ nm remain unchanged. The individual spectra are shifted upwards for clarity in each panel.

metal layer. More precisely, the absorption is strongly enhanced for a grating-film separation of $L_z = 90$ nm, i.e., when the bare plasmon modes are strongly coupled.

The dispersion of the polariton modes can be probed by either changing the angle of incidence or the nanowire period. Exemplarily, the angle-dependent extinction spectra for a structure with a 70-nm-thick spacer layer are shown in Fig. 5.26. Experimental as well as theoretical spectra are displayed for TM polarization, re-

spectively. From top to bottom, the angle of incidence is decreased from $\vartheta = 20°$ to $\vartheta = 0°$ in steps of $2°$ while the gold nanowire period of $d_x = 300$ nm remains unchanged. Qualitatively, the measured and calculated spectra show excellent agreement, indicating the effectiveness of our used scattering-matrix formalism. The existing deviations are mainly caused by inhomogeneous broadening (e.g., sample imperfections) which is neglected within the numerical approach. The depicted angular dependent spectra directly resemble the influence of the plasmon-plasmon interaction. While the lowest spectra are characterized by two extinction maxima, a third maximum appears for inclined incidence. The two extinction maxima for measurements at normal incidence are due to the interaction of the short-range surface plasmon mode at the 20-nm-thick silver film and the nanowire related particle plasmon resonance. However, the angular dependence can be understood by taking into account both symmetric as well as antisymmetric surface plasmon modes. Similarly to quasiguided modes of dielectric slab waveguides (e.g., see Chap. 3), the supported antisymmetric surface plasmon mode of the corrugated structure can only be excited for inclined incidence angles. In case of angular detuning ($\vartheta \neq 0°$), the spectral response is therefore determined by the interaction of three plasmon modes. A very fundamental effect is the disappearance of the upper blueshifted extinction maximum. Its spectral signature actually vanishes in case of $\vartheta = 20°$. On the other hand, the efficiency of the central extinction maximum is strongly increased. These observations again clearly indicate that the excitation efficiencies of the grating-induced surface plasmon modes can be strongly enhanced in the vicinity of the nanowire related particle plasmon resonance (i.e., formation of polariton modes).

An interesting additional question arises when considering the splitting between the bare grating-induced surface plasmon modes. Generally, although the antisymmetric mode is optically inactive at normal incidence, the dispersion diagram is characterized by a small stopband (i.e., anticrossing of the folded modes at the center of the Brillouin zone). Further investigations might be useful, especially to clarify to which extent the additional dielectric spacer layer influences the width of the surface plasmon stopband.

Period dependent measurements of the grating-film structures will be shortly discussed in the following. Exemplarily, the influence of the nanowire period is illustrated by the spectra in Fig. 5.27. Measured (left panels) and calculated (right panels) extinction spectra of gold nanowire gratings in front of a 20-nm-thick silver film are shown for normal light incidence and TM polarization. From top to bottom, the grating period is increased from $d_x = 300$ nm to $d_x = 385$ nm while
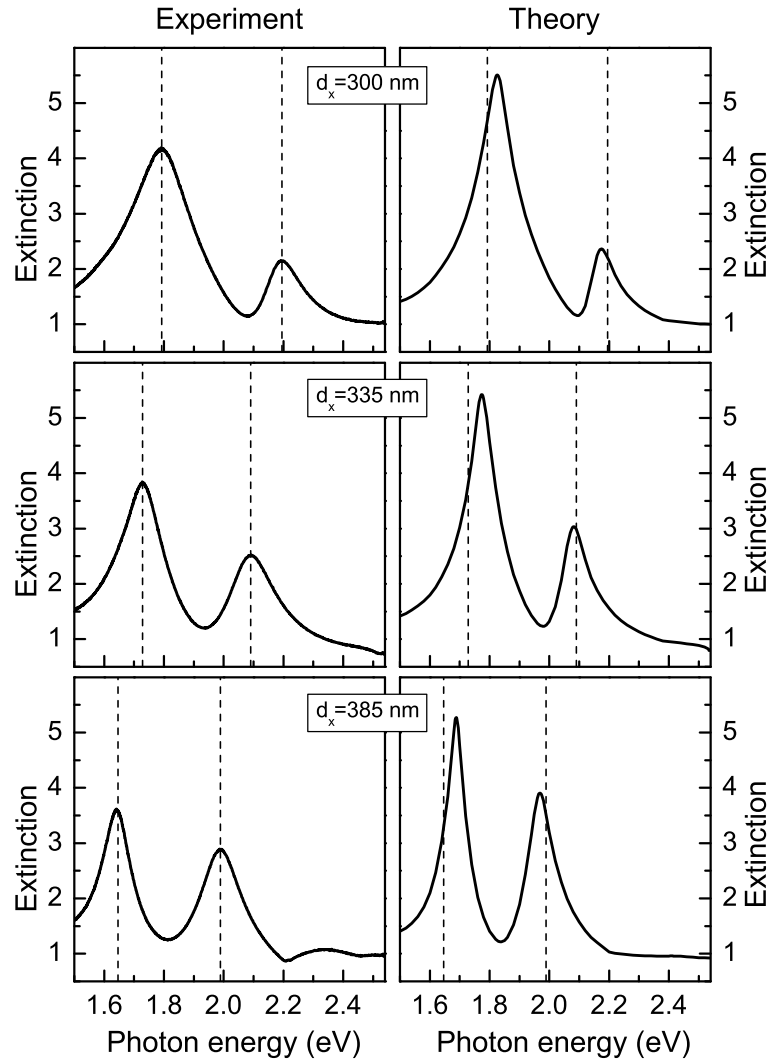
Figure 5.27:   Measured (left panels) and calculated (right panels) extinction spectra for gold nanowire gratings in front of a 20-nm-thick silver film. Spectra are shown for TM polarization and normal light incidence. While the spacer layer thickness of $L_z = 70$ nm has been retained unchanged, the grating period is increased from $d_x = 300$ nm to $d_x = 385$ nm. The dashed vertical lines mark the positions of the measured extinction spectra maxima.

the spacer layer thickness of $L_z = 70$ nm is kept constant. Qualitatively, the measured extinction spectra are well described by the theoretically obtained results. The increase of the nanowire period generally modifies the spectral position of the bare grating-induced surface plasmon mode. The surface plasmon mode is therefore redshifted, leading to a larger spectral overlap with the bare particle plasmon mode. Due to a strong coupling between the two plasmon modes and the formation of a collective polariton state, an anticrossing behavior is expected.

Such a behavior is clearly observable in Fig. 5.27. Both extinction maxima are redshifted when increasing the nanowire period (this behavior is characteristic for an anticrossing of the polariton modes). Simultaneously, the upper extinction maximum becomes more pronounced while the spectral width of the lower feature is decreased.

Finally, the influence of artificial disorder is analyzed experimentally. Electron beam lithography was used to prepare gold nanowire arrays on top of a silicon dioxide covered 20-nm-thick silver film. During the nanowire exposure, the spatial positions of the individual nanowires were modified with respect to a perfectly ordered grating structure with period d_x. The possible displacement was determined by the relation

$$\Delta d_x = \pm u \frac{d_x}{2} \quad \text{with} \quad u \in \{0, ..., 1\}, \tag{5.3}$$

where u is a predetermined form factor. For a given value of the parameter u, the nanowires were randomly distributed within the defined range Δd_x around their original position. All positions within the specified interval are selected with equal probability. The implemented spatial disorder corresponds to a so-called frozen-phonon type disorder. The spatial position of the individual nanowire is generally varied within a certain range around the original position (defined by the lattice constant d_x). The frozen-phonon model is directly derived from the phonon picture in solid state physics, where it is used for describing the lattice vibrations of a bulk crystal. An increased disorder within the nanowire array (i.e., enlargement of the parameter u), for example, is equivalent to a higher lattice temperature in the crystal.

The results of a typical measurement are shown in Fig. 5.28 for a gold nanowire structure with a grating period of $d_x = 400$ nm, a silver film thickness of $h_{\text{film}} = 20$ nm, and a spacer layer thickness of approximately $L_z = 50$ nm. All extinction spectra are displayed for normal light incidence and TM polarization. From top to bottom, the amount of disorder is continuously increased. Starting from the spectra of an ordered structure ($u = 0$), the subsequent spectra are obtained from transmission measurements on nanowire structures which are characterized by their increased form factors u. Additionally, also the result of a scattering-matrix based calculation is depicted (dotted line). A gold nanowire cross-section of 90×15 nm^2, a grating-film separation of $L_z = 50$ nm, a silver film thickness of $h_{\text{film}} = 20$ nm, and a period of $d_x = 400$ nm have been used for the numerical calculation. The perfectly ordered structure is characterized by the appearance of two pronounced extinction maxima. Generally, the figure reveals an excellent
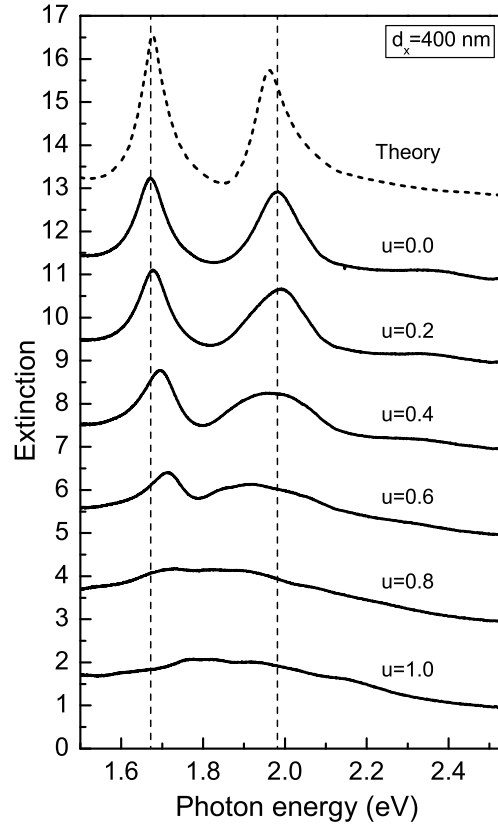
Figure 5.28:   Measured (solid lines) extinction spectra of gold nanowire arrays with a period of $d_x = 400$ nm in front of a 20-nm-thick silver film. Spectra are shown for TM polarization and normal light incidence. While the spacer layer thickness of $L_z = 50$ nm has been retained unchanged, the amount of disorder (u) is increased from top to bottom. Additionally, a calculated spectrum of an ordered grating structure is depicted (thick dashed line). The individual spectra are shifted upwards for clarity. The spectral positions of the extinction maxima $(u = 0)$ are indicated by dashed vertical lines.

agreement between the measured and theoretically obtained extinction spectra. Again, the coupling between the localized nanowire and the grating induced surface plasmon results in two pronounced spectral peaks which can be related to the branches of the new polariton (marked by vertical dashed lines). Note that the extinction maxima do not necessarily indicate the exact position of the polariton modes due to their Fano-type nature. The measured spectra of the structure are drastically modified when increasing the disorder within the grating layer. Shifts as well as an attenuation of the maxima can be observed. For the sample with the largest disorder $(u = 1)$, only a very broad, unstructured extinction maximum

remains visible.

The observations can be simply explained by the reduced excitation efficiency of the involved grating induced surface plasmon mode. It is well-known that the coupling between the incident light field and the bare surface plasmon mode is directly proportional to the absolute value of the Fourier component of the grating with spatial frequency $g_x = 2\pi/d_x$. An increased disorder generally results in an attenuation of the amplitude of the corresponding Fourier component and thus in a lowering of the excitation efficiencies. Naturally, also the polariton formation is suppressed by higher amounts of disorder. The reduced excitation efficiency leads to a weakening of the effective interaction strength between the localized and the grating induced surface plasmon modes (i.e., reduced overlap of the fields). In the limit $u \to 1$, the excitation efficiency of the grating-induced surface plasmon approaches zero. Therefore, only the bare particle plasmon resonance can be observed in the measured extinction spectra for structures with $u \geq 0.8$. However, it is important to mention one important fact which is directly related to the used sample fabrication method. An increased disorder may result in the formation of nanowire pairs that exhibit very small interparticle spacings. In such a case, near-field coupling will induce a redshift of the collective plasmon mode. In the worst case, even a direct spatial overlap of the nanowires might be possible. In addition to appearing proximity effects during electron beam writing, both effects generally lead to an increased inhomogeneous broadening of the detected nanowire plasmon resonance. In particular, such an inhomogeneous broadening of the plasmon resonance can be clearly observed in the extinction spectra of Fig. 5.28.

5.5   Conclusions

The discussed metal nanowire structure is a very fundamental model system that is characterized by the appearance of several important optical phenomena. For example, we have seen that the introduced metal film can have a significant effect on the optical properties of the nearby metal grating. More precisely, the appearance of both near- as well as far-field interaction effects can be verified in the detected linear optical response of the metallic nanowire system. The depicted theoretical and experimental results clearly reveal that the optical properties change substantially when modifying the geometrical parameters of the structure. Due to the specific geometry, the used nanowire-surface structure is

characterized by the simultaneous excitation of localized as well as extended surface plasmon modes. The individual metal nanowires support particle plasmon resonances in the optical regime. Hybridization, i.e., a near-field interaction between the individual nanowire plasmons and their images in the metal film results in a strong redshift when decreasing the spacer layer thickness. This effect is a single nanowire phenomenon and not related to the periodicity of the structure. Grating-induced scattering of the incoming light waves on the other hand is directly related to the periodic nanowire ensemble and results in surface plasmon excitation. A very important result is the verification of strong coupling between the localized and the extended surface plasmon modes. Similar to the formation of a waveguide-plasmon polariton, the interaction between the nanowire plasmons and the grating-induced surface plasmon modes can be understood within a simple polariton picture. The strong coupling between both resonances leads to the formation of polariton modes and thus can be observed due to the emerging mode splitting (anticrossing of the polariton branches). The dispersion of the polariton modes can be probed by changing the nanowire period, the spacer layer thickness, and the light incidence angle. Another interesting observation is connected to the Fano-type nature of the appearing resonances. The analyzed spectra reveal that the interference between direct and indirect pathways can lead to a significant transmission enhancement. For example, the optical excitation and subsequent radiative decay of a localized plasmon resonance represents such an indirect pathway. Although the presented discussions are mainly based on numerical results obtained from scattering-matrix calculations, first experimental verifications of the predicted phenomena are given. In conclusion, we have to remark that all discussions are solely restricted to the optical properties of the considered nanowire based system, so far. Further studies should be extended to the investigation of electric transport phenomena. For example, it might be interesting to analyze how the described interaction phenomena modify the generation of light-induced currents in similar multilayer metal structures [67].

Chapter 6

Plasmonic crystal structures

A theoretical study of particle plasmon excitation in so-called plasmonic crystal structures is presented. It is shown that the collective optical response of a periodic metal nanowire ensemble strongly differs from the single nanowire case. In addition to more complex plasmonic Bragg structures, coupling between metal nanowire pairs is analyzed. Our numerical results give clear evidence for near- as well as far-field coupling effects. The connection between the specific geometry of the considered nanowire system and its resonant behavior is studied. Additionally, polaritonic bandgap structures are addressed briefly. It is shown that a three-dimensional array of metal nanowires exhibits a large polaritonic stopband at optical frequencies.

6.1   Introduction

Noble metal nanoparticles have been studied extensively in recent years. Especially their remarkable optical properties as a resonantly polarizable element have attracted widespread interest. It is well known that the optical response of such metallic nanoparticles is characterized by the excitation of so-called particle plasmons [36]. Small metal nanostructures such as dots or individual nanowires strongly interact with an incident light field due to the resonant excitation of collective oscillations of their conduction band electrons. As a consequence of the large optical polarization associated with the resonant plasmon excitation, metal nanoparticles exhibit large scattering and absorption cross-sections and are characterized by strongly increased electromagnetic near-fields. The related local-field enhancement in the vicinity of small metal particles has already stimulated many

interesting applications. For example, metal nanoparticles are widely used in surface-enhanced Raman scattering (SERS) spectroscopy. Single molecule detection by using the specific near-field properties of silver nanoparticles has been demonstrated very recently [43, 209]. Generally, the optical response, i.e., the spectral position as well as the lifetime (bandwidth) of the particle plasmon resonances depend on the explicit geometry (shape and size of the particle) and the material properties (dielectric function) of the considered metal nanostructures.

In addition to the study of individual metal nanoparticles, especially particle-particle interaction phenomena are of increasing interest. Due to electromagnetic coupling between adjacent particles, the collective optical response of complex many-particle systems strongly deviates from the single particle case. When two or even more metal nanoparticles are arranged in close proximity, collective plasmon modes will be formed, leading to new characteristic spectral features. Depending on the particle spacing and the spatial arrangement of the individual particles, both near- as well as far-field interaction effects have to be considered.

Strong dipolar near-field interaction between closely spaced metal nanoparticles has been investigated both theoretically [210–212] and experimentally [101, 202, 213, 214]. Clear evidence of the formation of collective plasmon modes has been found in these studies. From the experimental point of view, especially the recent progress in nanofabrication techniques allows for systematic investigations of the coupling phenomena. Electron beam lithography for example can be used for artificial structuring on a nanometer scale. The interparticle distance can be controlled during sample fabrication, enabling precise measurement of the predicted distance dependencies. Frequency shifts of the plasmon resonance have been verified by optical transmission spectroscopy in pairs of identical gold nanoparticles [101, 202]. In dependence on the polarization of the incident electromagnetic field, either a red- or blue-shift of the collective plasmon resonances has been demonstrated. A very promising application of dipolar coupled metallic nanoparticles might be their use as a plasmonic waveguide for energy transport below the diffraction limit. In extension to studies on pair structures, coherent excitation transport in metal nanoparticle chains has been investigated theoretically [44, 45, 215, 216] and experimentally [46, 102, 217] quite recently. Energy shifts of the collective plasmon resonances as well as energy transport between adjacent particles have been found.

In contrast to near-field coupling effects between nearly touching metal nanoparticles, far-field interaction phenomena are responsible for pronounced modifica-

tions of the optical response in case of particle ensembles with a larger separation between the individual nanoscatterers. Especially ordered metal nanostructures (e.g., particle or wire arrays) with periods comparable to the wavelength of light have been investigated. Optical transmission measurements on planar metal nanowire arrays, for example, have shown that especially the spectral shape of the particle plasmon resonances will be altered due to the appearance of so-called Wood anomalies [89, 100, 201]. Depending on the substrate, diffractive or resonant Wood anomalies have been found. The study of these periodic metallic nanostructures, also known as metallic photonic crystals structures, is of growing interest from a fundamental as well as a technological point of view.

While more common passive photonic crystals are built of purely dielectric materials (e.g., see Refs. [1, 2]), resonant photonic crystals on the other hand can be characterized by their inclusion of dipole-active materials (i.e., frequency-dependent dielectric constants). As a result, radiative coupling effects have to be taken into account when the periodicity of the photonic crystal is comparable with the wavelength of light at the dipole resonance frequency. A very prominent class of resonant photonic bandgap materials are the so-called multiple-quantum-well Bragg structures. It has been shown by several recent publications that the optical response of these one-dimensional resonant photonic crystals is changed due to coherent radiative interaction between excitons in adjacent semiconductor quantum-wells [110, 185, 186, 205, 218, 219]. In addition to possible modifications of the radiative decay processes (superradiant emission of radiatively coupled excitons) and the formation of exciton polariton modes, especially the appearing photonic bandgaps in multiple-quantum well structures have been analyzed [220]. It is important to remark that the origin of the forbidden bands in optically active crystals is controlled by two mechanisms [221, 222]. In addition to coupling between light and internal excitations (optical lattice mechanism), also interface scattering due to a spatial mismatch of the dielectric functions (passive mechanism) is of major relevance.

Similar to the Bragg periodic multiple-quantum-well structures, also a three-dimensional periodic arrangement of metallic nanoparticles can be looked at as a resonant photonic crystal under certain conditions. Generally, the formation of photonic bandgaps in metallo-dielectric photonic crystal structures has already been investigated [48, 223, 224]. New phenomena may arise when, in addition to purely passive mechanisms, radiative effects are taken into account as well. For a realization of such a structure, the effective period d_{pc} of a photonic crystal consisting of small metal scatterers has to be chosen in such a way that the Bragg

condition $d_{pc} = \lambda_{pl}/2$ is fulfilled. Here λ_{pl} is the wavelength of light at the particle plasmon resonance frequency.

In this chapter, we present an extended theoretical study of coupling phenomena in so-called plasmonic nanostructures. Silver nanowire ensembles are used as an appropriate model system, similar to the previous chapters. The nanowire structures are chosen due to their favorable properties. For example, their one-dimensional character facilitates the numerical calculations drastically. Nevertheless, the obtained results hold for more complex three-dimensional structures (e.g., metal particles), too. The focus of the chapter is on coupling phenomena in nanowire pair structures. We clearly show that the linear optical properties of the proposed nanowire structures are strongly modified due to the appearance of near- as well as far-field interaction effects. In contrast to previous studies, especially the specific nanowire arrangement leads to the observation of new phenomena. We use stacked nanowire arrays, which allow for out-of-phase excitation of the coupled nanowires. Clear evidence of the formation of collective plasmon modes is found in the calculated transmission, reflection, and absorption spectra. For example, a normal mode splitting of approximately 840 meV is predicted for the dipolar plasmon resonances in case of closely spaced nanowires (i.e., vertical separation of 20 nm). A very interesting additional phenomenon is related to the specific symmetry of the collective polariton modes. While one of the normal modes is characterized by its strong electric moment (symmetric mode), the corresponding orthogonal mode exhibits a strong magnetic moment (antisymmetric mode). Additionally, far-field effects due to radiative coupling between the nanowires are shortly discussed. Our theoretical calculations clearly reveal a superradiant-like behavior. As extension to the nanowire pair structures, resonant metallo-dielectric Bragg structures are studied theoretically in the last section of the chapter. The considered geometry resembles the well-known design of Bragg periodic multiple-quantum-well structures. The formation of one-dimensional photonic bandgaps will be analyzed in dependence on the specific nanowire layer number. In contrast to passive photonic crystals built from Bragg-spaced silver films, the bandwidth of the appearing stopband can be nearly doubled by the use of nanowire arrays. Generally, the described phenomena may be of importance for the specific design and application of novel metallo-dielectric photonic crystal structures.

The structure of the chapter is as follows. In Sec. 6.2, the proposed metal nanowire structure is shortly described and all geometrical parameters are introduced. In Sec. 6.3, the optical properties of coupled silver nanowire arrays
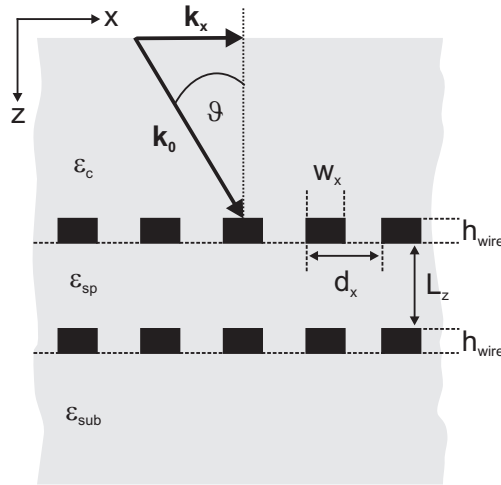
Figure 6.1: Schematic view of the proposed grating structure. A periodic metal nanowire array is separated from a second identical array by a dielectric spacer layer. The cross-sections of the individual silver nanowires are indicated by the solid rectangles. Structures with different spacer layer thicknesses L_z have been investigated theoretically. The electromagnetic wave is impinging from the top. The light polarization as well as the incidence angles can be controlled.

are discussed. The results of our numerical calculations show clear evidence for nanowire-nanowire interaction. The modifications due to near- as well as far-field coupling phenomena are analyzed theoretically. Plasmonic Bragg structures are studied in Sec. 6.4. The influence of radiative coupling and the formation of a large polaritonic bandgap are demonstrated. Finally, a summary of all findings is given in Sec. 6.5.

6.2   Sample geometry and theoretical method

Fig. 6.1 displays a schematic view of the proposed sample geometry. The considered structure consists of regular metal nanowire gratings with periodicity d_x which are separated by a thin dielectric spacer layer of thickness L_z. The coupling between two identical grating structures will be studied in the first part, while stacks with up to 10 grating layers will be treated in the second part of the chapter. The calculations are based on a scattering-matrix formalism [130]. This numerical method allows for calculating transmission, reflection, and absorption spectra (far-field) as well as the electromagnetic field distributions (near-field) of the photonic crystal structures. The theory works without the need of any fit

parameters. Only the exact geometry of the structure and the permittivities of the used materials are included as input parameters.

The presented theoretical results are restricted to the case of TM polarization and normal light incidence ($\vartheta = 0°$). While the spacer layer thickness and the number of grating layers are changed, the individual nanowire geometry is kept constant. All calculations are based on silver nanowires with a cross-section of 100×10 nm^2. The used dielectric function of silver is taken from Ref. [112]. Quartz with a constant permittivity of $\varepsilon_{quartz} = 2.13$ is chosen as substrate (ε_{sub}), spacer (ε_{sp}), and cap layer material (ε_c). Due to the slow convergence of the numerical method in TM polarization (particle plasmon excitation), all spectra of the silver grating structures are calculated with $N_G \geq 301$ harmonics (see also Sec. 4.3).

6.3　Interacting silver nanowire pairs

Before starting with a detailed discussion of coupling between adjacent silver nanowires in stacked metal gratings, we will briefly report on possible interaction phenomena in single layer structures for the sake of completeness. Up to now, all systematic studies on ordered particle ensembles were restricted to planar geometries, i.e., the particle pairs [101, 202] or particle chains [46, 102] were arranged in a plane perpendicular to the incident electromagnetic light fields. In order to theoretically confirm some of the reported phenomena related to this specific geometry (e.g., shifts of the particle plasmon resonance), we used a scattering-matrix formalism to calculate the optical response of an ordered linear array of closely spaced Ag nanowires [see panel (b) of Fig. 6.2]. While the individual nanowire cross-section of 100×10 nm^2 has been kept constant, the nanowire period d_x has been decreased from 300 nm to 140 nm in the numerical calculations. Quartz (n=1.46) has been assumed as substrate and cap layer material. The theoretical results of the scattering matrix calculations are shown in Fig. 6.2 (a) for the case of TM polarization. All depicted extinction spectra are characterized by a single resonance, which is caused by the particle plasmon excitation in the silver nanowire system. As expected, no such excitations were found in the corresponding spectra in case of TE polarization (not shown). The displayed extinction spectra clearly reveal the influence of the specific grating period. As already briefly discussed in Chap. 4, the depicted results give clear evidence of near-field interaction. From top to bottom, the collective particle plasmon resonance of the silver nanowire arrays is red-shifted when decreasing the nanowire
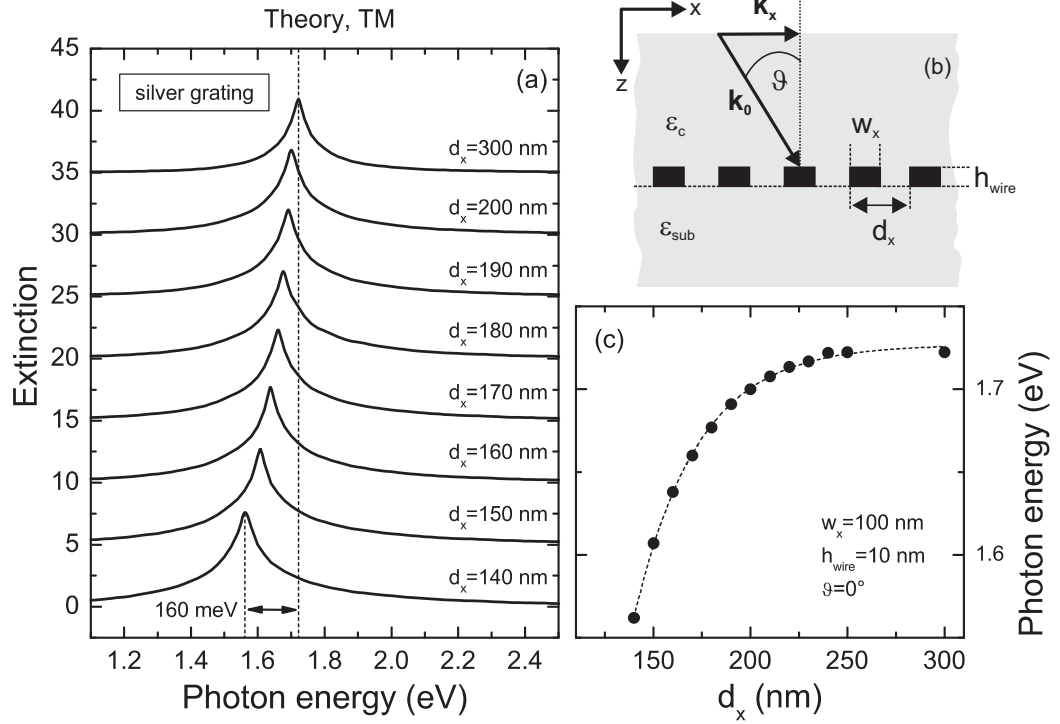
Figure 6.2:   Calculated extinction spectra of a regular silver nanowire array in dependence on the grating period d_x. Spectra are shown for normal light incidence ($\vartheta = 0°$) and TM polarization. From top to bottom, the nanowire period is decreased form 300 nm to 140 nm. The extracted extinction maxima are depicted in panel (c) in dependence of d_x. The dotted line is a guide to the eyes.

separation. The extracted spectral positions of the extinction maxima are displayed in panel (c) in dependence on the nanowire period d_x. For a nanowire period of 140 nm, for example, the plasmon resonance is shifted by 160 meV in comparison to structures with a larger periodicity of 300 nm. Note that all silver nanowires are excited in phase due to the far-field excitation geometry (normal incidence and TM polarization). The excitation of antisymmetric modes which are characterized by an out-of-phase oscillation of adjacent wires is forbidden within the considered excitation scheme. Generally, the number of supported modes is directly proportional to the number of coupled nanowires N. However, without violating the symmetry of the system, only a single symmetric mode can be excited. All other $N - 1$ modes are optically inactive and do not show up in the spectra (dark modes).

While far-field effects dominate the optical response of periodic nanowire en-

sembles with nanowire separations comparable to the wavelength of light [201], the observed red-shift of the plasmon resonance in Fig. 6.2 is caused by near-field interaction between the closely spaced nanowires. The resonant plasmon oscillations of the silver nanowires are coupled with each other by their strongly enhanced dipolar near-fields (i.e., quasistatic dipole-dipole interaction), leading to an efficient electromagnetic interaction. In a simple qualitative picture [101], the calculated red-shift of the collective plasmon resonance can be explained by a weakening of the repulsive forces for the induced surface charges. Generally, when the conduction band electrons of a single metal nanowire are displaced against the positively charged background by an incident electromagnetic field, the resulting surface polarization creates an effective linear restoring force, giving rise to a coherent plasmon oscillation. In a many-particle ensemble on the other hand, the appearing restoring forces are modified by electromagnetic interaction with the nearby particles. In case of silver grating structures, the resonance frequency of the collective plasmon oscillation is therefore significantly lowered in energy due to the arising attractive forces between negative and positive surface charges of the nearly touching nanowires.

In order to extend the investigations of planar systems to more complex geometries, we will present a detailed study of collective coupling phenomena in stacked silver nanowire arrays in the following. Note that the considered coupled grating structures will have a nanowire period of $d_x = 200$ nm in all subsequent studies of the chapter, if not stated otherwise. This specific selection prevents the appearance of Rayleigh type anomalies (far-field effects), which are related to the opening of diffraction orders. Simultaneously, direct near-field interaction between adjacent nanowires within the individual grating layers is still negligible.

6.3.1   Influence of the nanowire-nanowire separation

As already illustrated by the schematic view in Fig. 6.1, especially stacked grating structures represent an interesting alternative model system. Similar to more common planar structures, they allow the investigation of electromagnetic coupling between closely spaced silver nanowires in far-field experiments. While planar geometries are characterized by in-phase excitation of the involved particles, the serial arrangement of individual nanowires (stacking) enables an out-of-phase excitation of the coupled nanowire system. As an important result, the orthogonal normal modes of the nanowire pairs will appear in case of plane wave excitation. The calculated extinction (a), reflection (b), and absorption (c) spectra
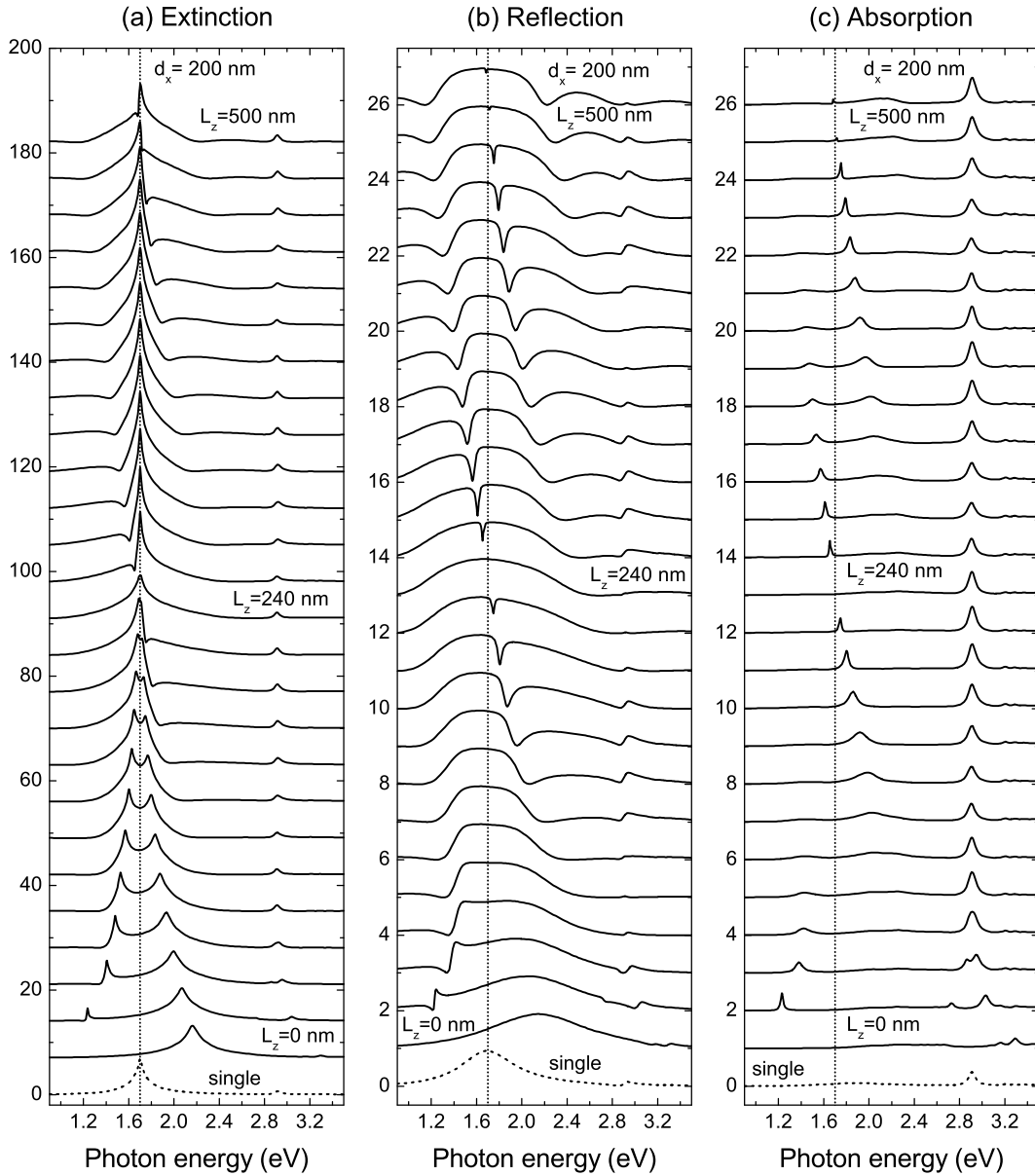
Figure 6.3:   Calculated extinction (a), reflection (b), and absorption (c) spectra of two coupled silver grating layers at normal incidence ($\vartheta = 0°$) and TM polarization. Spectra for nanowire arrays with a period of 200 nm are shown. The individual nanowires exhibit a cross-section of 100×10 nm^2. From top to bottom, the spacer layer thickness L_z is decreased from 500 nm to 0 nm in steps of 20 nm. The individual spectra are shifted upwards for clarity in each panel. The calculated spectra of a single grating layer are displayed as a reference (dotted lines at the bottom) in all three panels. The dotted vertical lines mark the position of the dipolar particle plasmon resonance of the single layer structure.

of a bilayer silver grating structure (see Fig. 6.1) are displayed in Fig. 6.3 in dependence on the vertical nanowire separation L_z. The individual silver nanowires exhibit a cross-section of 100×10 nm^2 and are arranged with a lateral period of $d_x = 200$ nm. From top to bottom, the vertical spacing of the grating structures is decreased from $L_z = 500$ nm to $L_z = 0$ nm in steps of 20 nm. Additionally, the calculated spectra of a single nanowire layer are displayed as a reference (dotted lines at the bottom) in all three panels, respectively. All spectra are shown for normal light incidence ($\vartheta = 0°$) and TM polarization.

The displayed theoretical spectra show a rather complex dependence on the specific nanowire separation. Starting from the simplest case, the calculated results of the single layer structure are characterized by two pronounced resonances [see dotted lines in Fig. 6.3]. Similar to the results of Fig. 6.2, the broad spectral feature centered at 1.7 eV is caused by excitation of the dipolar particle plasmon resonance of the uncoupled silver nanowires. The spectral position of the single layer plasmon resonance is marked by a dotted vertical line in all three panels of Fig. 6.3. Additionally, a pronounced second feature appears at approximately 2.9 eV. This resonance can be related to the excitation of a higher-order particle plasmon of the silver nanowires (e.g., see discussions of Fig. 6.13 and Fig. 6.14). Obviously, both plasmon resonances differ in their spectral bandwidth as well as in their absorptive behavior. While the dipolar plasmon resonance is associated with a broad reflection maximum and negligible absorption, the higher order resonance on the other hand is most strongly pronounced in the displayed absorption spectrum.

The optical response of the double layer structure strongly deviates from the single layer case. In particular, the calculated spectra show a clear dependence on the nanowire separation due to the arising dipole-dipole interaction. Especially the spectral region around the lower dipolar plasmon resonance (marked by dotted vertical lines at 1.7 eV) is subject to strong changes. For example, the extinction spectra are now characterized by a sharp maximum at 1.7 eV which splits into two maxima for closely spaced nanowire pair structures with $L_z < 220$ nm. Both distinct maxima show an opposite behavior in dependence on the spacer layer thickness. One of the maxima is shifting to lower energies when decreasing the vertical nanowire spacing. Simultaneously, also the extinction amplitude and the spectral bandwidth are reduced. In contrast, the second maximum is shifted to higher energies when decreasing the nanowire separation. The nanowire pair geometry has to be considered as a single layer structure with an enlarged silver nanowire cross-section of 100×20 nm^2 in the limit of a vanishing spacer layer

($L_z = 0$ nm). In this case, only one broad extinction maximum is found at approximately 2.17 eV. As expected for nanowires with increased thickness, the dipolar plasmon resonance is shifted to higher energies (e.g., shown in Fig. 2.22). The calculated extinction maximum is related to a broad peak in the reflection spectrum and exhibits negligible absorption.

Special attention has to be drawn to the situation where the two nanowire arrays are spaced at Bragg distance, i.e., the relation

$$m\frac{\lambda_{pl}}{2n_{quartz}} = L_z + h_{\text{wire}} \quad \text{with} \quad m = 1, 2, ... \tag{6.1}$$

is fulfilled[1]. Here λ_{pl} is the wavelength of light at the nanowire plasmon resonance frequency of the uncoupled single layer structure. The parameter m specifies the considered Bragg order. In case of the investigated coupled nanowire arrays with $\lambda_{pl} \approx 730$ nm, $h_{\text{wire}} = 10$ nm, and $n_{quartz} = 1.46$, the so-called Bragg condition implies a vertical layer separation of $L_z \approx 240$ nm (first Bragg order with $m{=}1$). Similar to the results of the single layer structure, the spectra in Fig. 6.3 show two pronounced features in case of Bragg spacing (see spectra for $L_z = 240$ nm). In addition to the higher-order plasmon resonance at 2.9 eV, the second lower resonance is again centered at 1.7 eV. The extinction maximum at 1.7 eV exhibits negligible absorption and is related to a broad peak in the corresponding reflection spectrum. Note that the spectral bandwidth of the reflection peak is increased in comparison to the single layer case (dotted lines at the bottom of Fig. 6.3).

The spectra of Fig. 6.3 are strongly modified when detuning L_z from the exact Bragg condition ($L_z = 240$ nm). For example, sharp dips appear close to the reflection maximum at 1.7 eV for nanowire separations of $L_z = 220$ nm and $L_z = 260$ nm in panel (b). These reflection minima show a dispersive behavior in dependence on L_z. A further increase of the spacer layer thickness ($L_z > 260$ nm) induces a red-shift of the reflection dip. Simultaneously, a spectral broadening of the minimum can be observed. Decreasing the nanowire separation ($L_z < 220$ nm), on the other hand, leads to an opposite shift. The sharp reflection dip is now spectrally broadened while shifting to higher energies. We have to remark that the appearing reflection dips are directly related to strong peaks in the absorption spectra of Fig. 6.3 (c). Generally, they show similar tendencies as the corresponding reflection minima. The absorption peaks are getting broader and less pronounced while shifting towards higher (lower) energies for decreased

---

[1]For simplicity reasons, the penetration of the electromagnetic fields into the metal wires is neglected. The nanowires are therefore treated in a point dipole approximation.

(increased) nanowire separations. Finally, the absorption peaks disappear for bilayer structures with spacer layer thicknesses above $L_z = 420$ nm and below $L_z = 100$ nm. In contrast to pronounced minima (maxima) in the reflection (absorption) spectra, only cusp-like anomalies can be found in the corresponding extinction spectra. In some respects, their spectral signature resembles the specific shape of so-called diffractive anomalies, which have been observed in case of planar grating structures [201].

Further on, the second order Bragg condition ($m=2$) is fulfilled when the vertical nanowire separation equals approximately $L_z = 480$ nm. Similar to the first Bragg order ($m=1$), sharp minima can be observed close to the reflection maximum at 1.7 eV for slight detunings of L_z [see panel (b) of Fig. 6.3]. The arising reflection minima as well as the related absorption maxima are again strongly pronounced. Their dispersive character is clearly visible in the displayed spectra. Starting from $L_z = 480$ nm, the observed absorption maximum (reflection minimum) is shifting to higher energies when decreasing the nanowire separation. Simultaneously, the absorption maximum is broadened until disappearing for spacer layer thicknesses below approximately $L_z = 240$ nm.

In addition to the described dispersive features, the clear signature of the higher order plasmon resonance can be found in all calculated spectra of the silver bilayer structures in Fig. 6.3. In contrast to the spectral region in close vicinity to the dipolar plasmon resonance at 1.7 eV, the higher order resonance at approximately 2.9 eV is more or less weakly affected when changing the nanowire separation. The resonance appears as a pronounced peak in the absorption spectra. Only for nearly touching nanowires with $L_z \leq 40$ nm, a clear splitting of the resonance can be observed in the displayed absorption spectra.

The explicit spacer layer dependence of the observed spectral features is again summarized in Fig. 6.4. Particularly, the positions of the extinction and absorption maxima are depicted in dependence on the spacer layer thickness L_z. All plotted data points have been extracted from the numerically obtained spectra in Fig. 6.3. The dispersion of the reflection minima is not included.

Before proceeding with a detailed discussions of the observed coupling phenomena, we will compare the calculated spectra of Fig. 6.3 with results for a similar grating-film design. For example, it is intriguing to analyze how the optical properties change when the second nanowire layer (lower grating in Fig. 6.1) is replaced by a thin metal mirror. As has been shown in the last chapter, the individual nanowires of a metal grating interact with the induced mirror dipoles
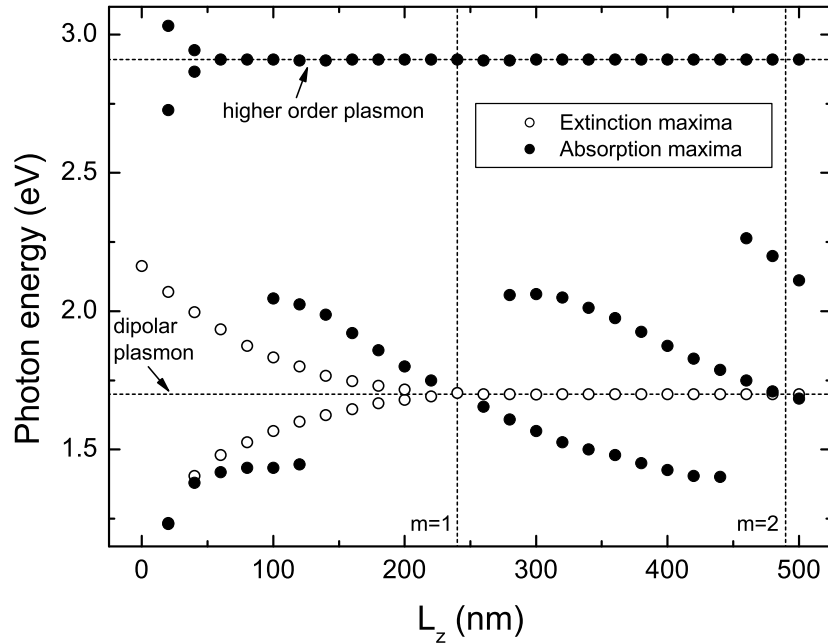
Figure 6.4:   Calculated energies of the extinction and absorption spectra maxima for interacting silver nanowire arrays. The dependencies on L_z are displayed for normal light incidence and TM polarization, respectively. The horizontal dotted lines denote the position of the particle plasmon resonances of a single layer structure. The Bragg orders ($m = 1, 2$) are marked by vertical lines.

in a closely spaced metal film. The numerical results for a silver nanowire array in front of a 20-nm-thick silver film are depicted in Fig. 6.5. In contrast to the assumed sample design in Chap. 5, the silver nanowires in front of the metal film are now embedded between two quartz half spaces ($\varepsilon_c = \varepsilon_{sp} = \varepsilon_{quartz} = 2.13$). Again, the calculated extinction (a), reflection (b), and absorption (c) spectra of the structure are displayed for normal light incidence and TM polarization. From top to bottom, the spacer layer thickness L_z is decreased from 210 nm to 0 nm in steps of 10 nm. Additionally, the calculated spectra of a single nanowire layer (i.e., without the nearby silver film) are displayed as a reference (dotted lines at the bottom) in all three panels.

As expected, the calculated spectra of the grating-film structure (solid lines in Fig. 6.5) show some remarkable differences in comparison to the double layer geometry (solid lines in Fig. 6.3). For example, the extinction spectra of the grating-film structure (solid lines) in Fig. 6.5 (a) are indeed characterized by a strong extinction peak at 1.7 eV (marked by a vertical dotted line in all three
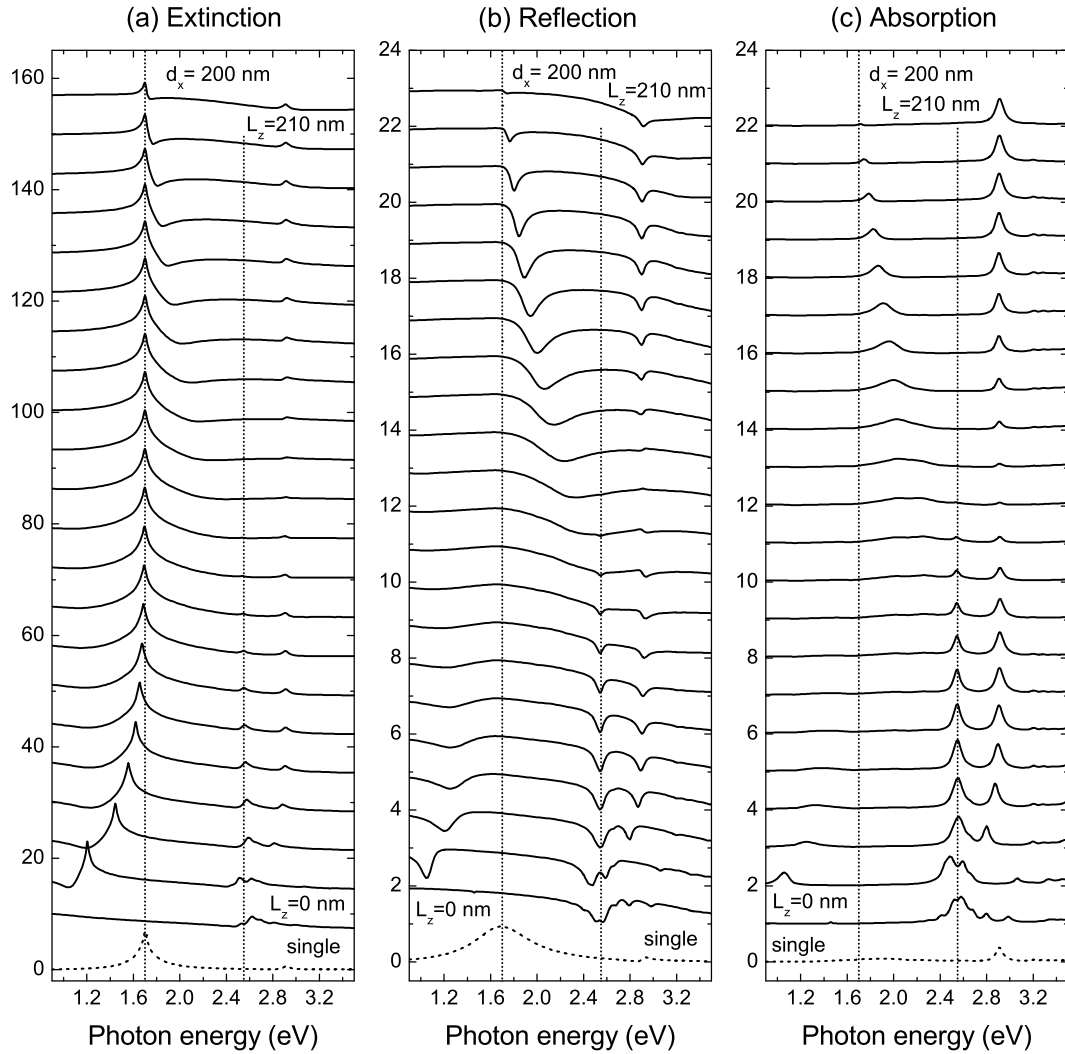
Figure 6.5:   Calculated extinction (a), reflection (b), and absorption (c) spectra of a silver grating in front of a 20-nm-thick silver film (normal incidence and TM polarization). Spectra for nanowire arrays (wire cross-section 100×10 nm^2) with a period of 200 nm are shown. From top to bottom, the spacer layer thickness L_z is decreased from 210 nm to 0 nm in steps of 10 nm (solid lines). The individual spectra are shifted upwards for clarity in each panel. The calculated spectra of a single grating structure without adjacent silver layer are displayed as a reference (dotted lines at the bottom) in all three panels. The vertical dotted lines denote the spectral positions of the dipolar nanowire plasmon of the single layer structure (1.7 eV) and the position of the short range surface plasmon mode (2.54 eV).

panels). But in contrast to the bilayer nanowire structures, no splitting phenomena can be observed when decreasing the nanowire-film separation in Fig. 6.5. However, the single extinction maximum at 1.7 eV is continuously red-shifted in

all spectra for structures with $L_z < 70$ nm. The shifted extinction maxima are related to reflection minima and absorption maxima, respectively. Note that the correlated reflection and absorption features are slightly red-shifted in comparison to the extinction maxima. Furthermore, no splitting is found for the higher order plasmon mode centered at approximately 2.9 eV. Similar to the extinction maximum at 1.7 eV, the absorption maximum at 2.9 eV is shifting to lower energies when decreasing the spacer layer thickness. Starting from the case where the Bragg condition is fulfilled ($L_z \approx 210$ nm), the reflection spectra in panel (b) are characterized by an additional sharp minimum at approximately 1.7 eV. While shifting to higher energies, the observed minimum and the related absorption maximum are spectrally broadened when decreasing the nanowire-film separation. Their spectral signatures finally disappear for nanowire structures with $L_z < 100$ nm.

In contrast to the double layer grating design of Fig. 6.3, the coupled grating-film geometry supports surface plasmon polariton modes. This important fact can be clearly observed in the calculated spectra of Fig. 6.5. The absorption peak at approximately 2.54 eV is caused by the excitation of the short-range surface plasmon mode (antisymmetric plasmon mode) at the homogeneous silver layer. The exact position of the surface plasmon resonance (2.54 eV) is marked by a vertical dotted line in all three panels of Fig. 6.5. While the resonance is only weakly pronounced in the extinction spectra, the surface plasmon appears as a pronounced dip (peak) in the corresponding reflection (absorption) spectra. The surface plasmon signatures finally disappear for structures with $L_z > 100$ nm due to the L_z-dependent excitation efficiency. Note that the spectral position of the surface plasmon resonance is only weakly affected when increasing the spacer layer thickness. As expected, the surface plasmon mode shows a dispersive behavior when changing the nanowire period d_x (not shown).

The presented theoretical spectra reveal a very complex optical behavior. Generally, the detailed discussion of the spacer layer dependent optical response has to account for both near- (quasistatic dipole-dipole coupling) as well as far-field (dynamic dipole-dipole coupling) interaction effects. Although a strict separation of both mechanism might be very difficult (e.g., especially for intermediate spacer layer thicknesses), distinct spectral modifications can be clearly attributed to the particular interaction mechanism. While far-field interaction might be interpreted in terms of cavity-polariton formation, additional shifts of the particle plasmon resonances have to be considered in the near-field regime. The related optical phenomena will be addressed in more details in the following two sections.
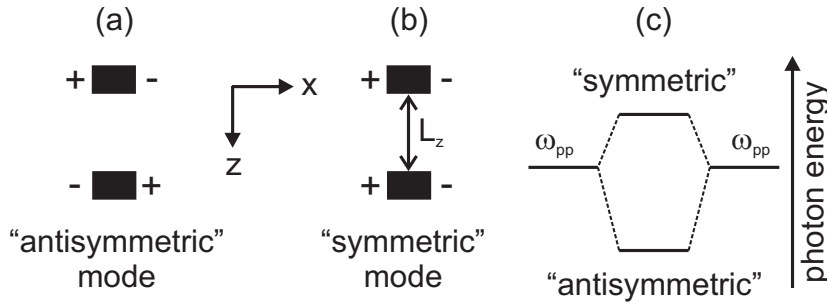
Figure 6.6:   Schematic illustration of the polarization charge distributions corresponding to the two normal modes of the coupled nanowire system: Antisymmetric (a) and symmetric (b) modes are displayed. The cross-sections of the silver nanowires are denoted by the solid rectangles. Additionally, the plasmon hybridization principle is drawn in panel (c).

6.3.2   Near-field regime

The optical properties of coupled nanowire pairs differ drastically from the properties of their uncoupled counterparts. As already addressed in the introduction of this chapter, near-field interaction between closely spaced metal particles leads to the formation of so-called collective plasmon modes. This important fact is clearly illustrated by the theoretical spectra in Fig. 6.3. When the vertical distance between the two stacked nanowire arrays is decreased ($L_z \rightarrow 0$), the particle plasmons of adjacent nanowires interact via their resonant near-fields. Additional resonances appear in the spectra of the coupled wire system as a result of the continuously increased quasistatic dipole-dipole interaction. The theoretically investigated nanowire pair structures show a clear splitting of their plasmon resonances when decreasing the vertical nanowire separation below $L_z = 200$ nm. More precisely, the dipolar particle plasmon resonance at 1.7 eV [e.g., see extinction spectra in panel (a) of Fig. 6.3] as well as the higher order plasmon mode at 2.9 eV [e.g., see absorption spectra in panel (c) of Fig. 6.3] are split and evolve into two distinct resonances, respectively. In contrast to uncoupled nanowire pairs with a single doubly degenerated plasmon resonance, the appearing resonances can be related to collective plasmon modes of opposite symmetry [109].

Generally, the observed near-field interaction between the vertically stacked silver nanowires in Fig. 6.3 resembles the behavior of two coupled classical oscillators. It is well-known that a coupling between N identical oscillators leads to the formation of N normal modes. These normal modes differ in their resonance frequencies as well as in their symmetry. In case of two oscillators, the corresponding normal
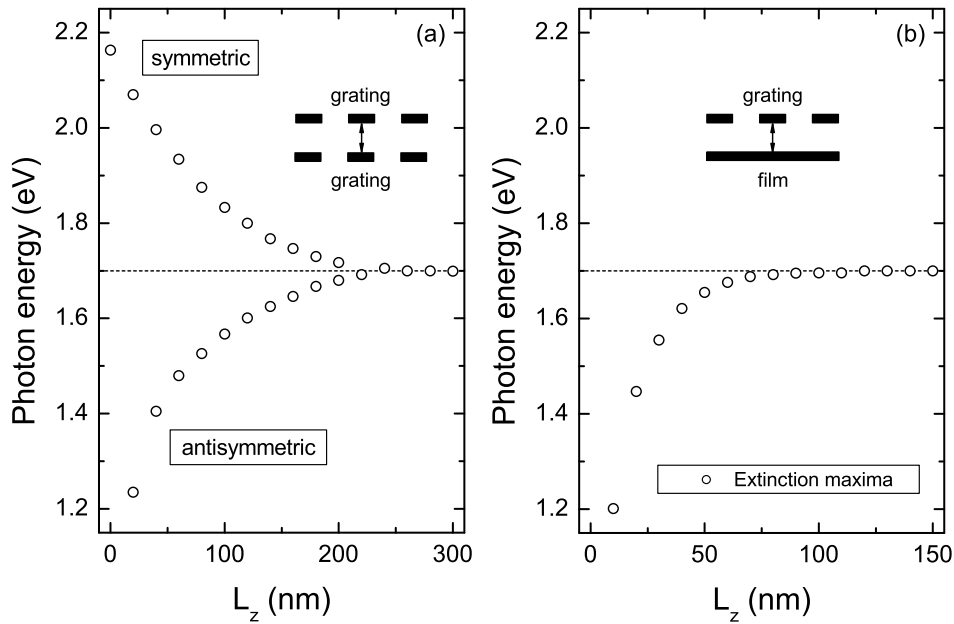
Figure 6.7:   Calculated energies of the extinction spectra maxima for coupled silver nanowire arrays. Results for grating-grating and grating-film interaction are shown. The dependencies on L_z are displayed for normal light incidence and TM polarization, respectively.

modes can be classified into a symmetric and an antisymmetric solution. While the symmetric mode corresponds to an in-phase oscillation of both oscillators, the anti-symmetric mode on the other hand is related to an out-of-phase oscillation of the coupled oscillators (see, e.g., standard textbooks on classical mechanics). A nearly identical behavior can be found for the considered silver nanowire pair geometry. Two collective plasmon modes of opposite symmetry can be excited when the two nanowires are brought into close proximity. In case of interaction between dipolar plasmon resonances, the incident electromagnetic field (normal incidence, TM polarization) sets up a coherent oscillation of the conduction band electrons in the silver nanowires (oscillation along the x-axis). The symmetric normal mode corresponds to the excitation of parallel currents in the two coupled nanowires. The antisymmetric mode, on the other hand, is related to antiparallel currents in both adjacent nanowires. Exemplarily, a schematic view of the resulting polarization charge distributions for the two normal modes is displayed in Fig. 6.6. The shown static situation corresponds to the specific moment of time at which the induced currents change their sign (when the corresponding surface polarizations reach their maximum value).

In a simple qualitative picture, the near-field induced spectral splitting can be directly related to the specific symmetry of the two polariton modes. Generally, the plasmon oscillation frequency is determined by the strength of the arising linear restoring forces. These forces appear as a result of the surface polarization due to the induced electron displacement. In contrast to the single nanowire case, an antisymmetric polarization charge distribution [see panel (a) in Fig. 6.6] leads to a lowering of the resonance frequency (red-shift) in case of double layer structures. The restoring forces are effectively reduced due to the arising attractive forces between the negative and positive surface charges of the closely spaced nanowires. The situation is inverted in case of a symmetric polarization charge distribution [see panel (b) in Fig. 6.6]. Now the appearing restoring forces are enhanced in both nanowires due to repulsive forces between the arising identical charges, thus increasing the resonance frequency. The coupling strength between the two nanowire plasmons, which is in turn proportional to the spectral splitting of the appearing collective polariton modes, is directly controlled by adjusting the vertical distance between the nanowires[2]. Exemplarily, the dispersion of the normal modes is shown in panel (a) of Fig. 6.7 on the basis of the extinction spectra. The spectral positions of the extinction maxima, extracted from panel (a) of Fig. 6.3, are displayed in this figure in dependence on the vertical nanowire separation L_z. Note that the considered extinction maxima only reveal the approximate position of the coupled plasmon modes. Due to the Fano-type nature of the resonances, especially the exact position of the lower antisymmetric plasmon mode can slightly deviate from the position of the extinction maximum. As displayed in panel (a) of the figure, the lower polariton branch is associated with the antisymmetric normal mode of the coupled nanowire system. The spectral position of the mode is strongly red-shifted when decreasing the nanowire separation. The upper extinction maxima, on the other hand, are related to the symmetric normal mode of the collective nanowire system. This mode is characterized by a blue-shift of the related extinction maxima.

In addition to the spectral response of the nanowire pair structures in Fig. 6.3, the optical properties of a similar grating-film design (silver nanowires in front of a thin silver film) have been calculated. The dependence of the extinction maximum on the nanowire-film separation L_z is shown by the spectra in Fig. 6.5. The

---

[2]Note that the energy splitting (i.e., plasmon hybridization) can be alternatively understood when taking into account the forces between the induced electric dipoles. The arising attractive forces between two antiparallel dipoles generally result in a bonding state. Its energy is lowered by the spacer layer dependent binding energy. The antibonding state is characterized by repulsive forces between the parallel dipoles, thus increasing the energy of the coupled state.

appearing near-field effects differ from the results of the bilayer grating structures. Especially none of the near-field induced splitting phenomena can be observed in the corresponding extinction spectra [see panel (a) of Fig. 6.5]. Both the dipolar (1.7 eV) as well as the higher order plasmon mode (2.9 eV) are shifted towards lower energies. The dispersion of the appearing lower plasmon mode is plotted in panel (b) of Fig. 6.7, thus allowing a direct comparison of the plasmon dispersions for both nanowire structures. The depicted positions of the extinction maxima have been extracted from panel (a) of Fig. 6.5. Although the extinction maxima can be considered as a good approximation, the Fano-type nature of the resonances has to be taken into account for a more exact determination of the plasmon resonance position (e.g., see the discussion in Chap. 5).

In spite of all observed spectral differences, the underlying coupling mechanisms show some striking similarities. For example, the plasmon dispersion in Fig. 6.7 (b) shows an identical behavior as the antisymmetric branch in panel (a) of the same figure (red-shift for decreasing spacer layer thickness). Instead of near-field interaction between closely spaced nanowires, the nanowire plasmon in front of the silver film is coupled to its own image dipole in the metal layer (see Chap. 5). Note that the upper symmetric branch of the coupled plasmon polariton mode does not exist in case of the grating-film geometry. The induced oscillations of the mirror dipole are always phase-shifted by 180 degree. Thus, the coupling between a single wire and its own image dipole resembles the situation of excitation of an antisymmetric plasmon polariton mode in the stacked nanowire structures.

In order to extend the spectral analysis of Fig. 6.3 and to support our qualitative discussion, it is very instructive to take a closer look at the calculated near-field distributions of the coupled nanowire pairs. The following discussion will be limited to the double layer structures with a vertical nanowire separation of $L_z = 20$ nm to highlight the main features of the complex near-field distributions. Additionally, only the field distributions for characteristic photon energies will be shown. The extinction and absorption spectra of the considered nanowire geometry are again displayed in Fig. 6.8 for normal light incidence and TM polarization (magnified view of the spectra shown in Fig. 6.3). Silver nanowire arrays ($d_x = 200$ nm) with an individual nanowire cross-section of 100×10 nm^2 and a spacer layer thickness of $L_z = 20$ nm have been considered for the calculation of the depicted spectra. As already described in the previous section, the spectra can be characterized by four main features. The two distinct extinction maxima a and b arise due to a spectral splitting of the degenerated dipolar plasmon
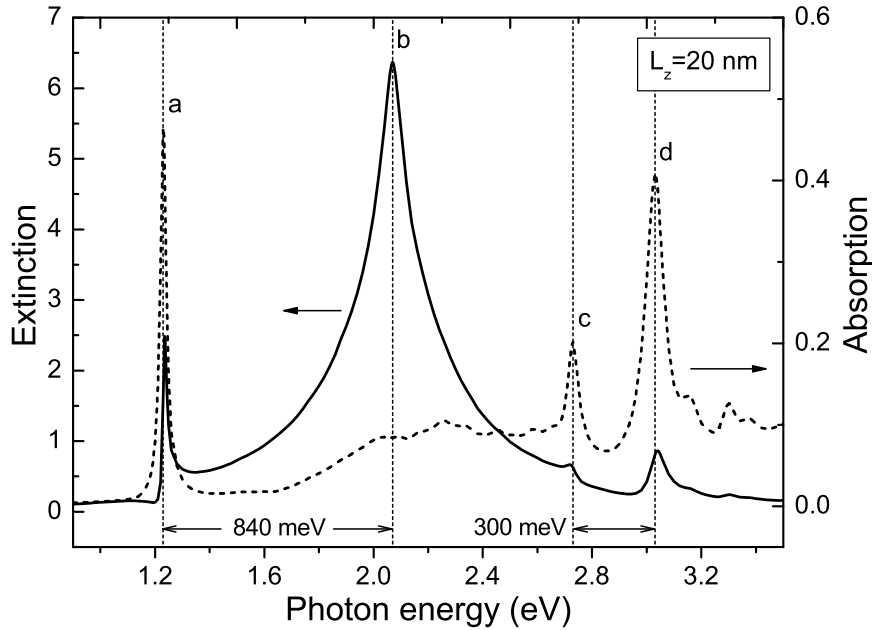
Figure 6.8: Calculated extinction (solid line) and absorption (dashed line) spectra for a system of two interacting silver nanowire arrays (normal light incidence and TM polarization). The nanowire gratings ($d_x = 200$ nm) are spatially separated by a quartz spacer layer of thickness $L_z = 20$ nm. The spectral positions of the collective plasmon resonances are marked by dotted vertical lines (a-d).

resonances of the uncoupled nanowires. Note that the near-field coupling results in a remarkable splitting of nearly 840 meV. In a similar way, the upper maxima c and d emerge due to the near-field induced splitting of the higher-order particle plasmon modes. A smaller peak separation of 300 meV is found for these higher-order modes. The spectral position of the new plasmon polariton modes are marked by dotted vertical lines in Fig. 6.8.

We will start with a detailed study of the two lower nanowire plasmon resonances of Fig. 6.8. The field distributions at the position of the lower antisymmetric mode (peak a, 1.23 eV) and at the upper symmetric mode (peak b, 2.07 eV) are displayed in Fig. 6.9 and Fig. 6.10, respectively. The electric (a) and magnetic (b) field vectors are shown as a two-dimensional array of colored cones in the figures. The length of the cones is proportional to the field strength at the central point of each cone, and the orientation of the cones specifies the respective field direction. However, these field distributions are oscillating with time and their dynamics cannot be displayed in a static picture. Thus, the near-field distributions are shown at the most characteristic moments of time, when the spatially integrated intensity of the corresponding fields reaches its maximum value (see below). The

schematic cross-section of the nanowire pairs is displayed by solid lines in each figure. Note that the incoming light field propagates from the top to the bottom of the figure in all calculations (propagation along the z direction).

To understand the basis of the coupling phenomena, all fields are depicted in Fig. 6.9 and Fig. 6.10 at the moments of time t (measured in units of the light period $T = 2\pi/\omega$ and shown in the title of each panel) when the field intensities integrated over the displayed cross sections $\int_A \mathbf{E}^2 dA$ and $\int_A \mathbf{H}^2 dA$ reach maxima. Additional important information is provided by the calculated quantities t/T and $E_{\max}$ (H_{max} for magnetic fields), shown in each panel, allowing an improved interpretation of the static illustration of the oscillating fields.

The parameter t/T enables a direct derivation of temporal information. For example, the electric field is $\mathbf{E}(\mathbf{r}, t) = \mathrm{Re}\left[\vec{\mathcal{E}}(\mathbf{r})\exp(-i\omega t)\right]$, where $\vec{\mathcal{E}}(\mathbf{r}) = \vec{\mathcal{R}}(\mathbf{r}) + i\vec{\mathcal{I}}(\mathbf{r})$. Then the electric field intensity integrated over the displayed area A is

$$W_E(t) = \int_A \mathbf{E}^2(\mathbf{r}, t)dA \qquad (6.2)$$
$$= \overline{R_E^2}\cos^2(\omega t) + \overline{I_E^2}\sin^2(\omega t) + 2\overline{R_E I_E}\sin(\omega t)\cos(\omega t),$$

where

$$\overline{R_E^2} = \int_A \vec{\mathcal{R}}^2(\mathbf{r})dA, \qquad (6.3)$$
$$\overline{I_E^2} = \int_A \vec{\mathcal{I}}^2(\mathbf{r})dA,$$
$$\overline{R_E I_E} = \int_A \vec{\mathcal{R}}(\mathbf{r})\vec{\mathcal{I}}(\mathbf{r})dA.$$

Thus, $W_E(t)$ oscillates with frequency 2ω as

$$W_E(t) = \frac{1}{2}\left(\overline{R_E^2} + \overline{I_E^2}\right) \qquad (6.4)$$
$$+ \frac{1}{2}\left[\left(\overline{R_E^2} - \overline{I_E^2}\right)^2 + 4\overline{R_E I_E}^2\right]^{1/2}\cos(2\omega t - \beta_E),$$
$$\beta_E = \arctan\frac{2\overline{R_E I_E}}{\overline{R_E^2} - \overline{I_E^2}}, \qquad (6.5)$$

reaching its maximum value at $\omega t = \beta_E/2$ or $t/T = \beta_E/4\pi$, where $T = 2\pi/\omega$ is the light period. For the magnetic field, the maximum of $W_H(t)$ is reached at $t/T = \beta_H/4\pi$, with respective changes in Eqs. (6.2)-(6.5). Note that the minima of W_E and W_H are reached a time span $T/4$ later. The correspondingly calculated values of t/T are shown for each panel.

By comparing the values of t/T for electric and magnetic fields, the character of the light propagation (standing or propagating wave) at a particular frequency can be estimated. In the case of purely running character, and without averaging over the spatial area, both maxima are reached simultaneously. In the case of a purely standing wave, there should be a $T/4$ delay between the appearance of both maxima, as the light energy oscillates between the electric and magnetic fields.

Note that the fields of Fig. 6.9 and Fig. 6.10 are scaled by different coefficients. In order to compare the absolute magnitudes of the fields, the maximum absolute value of each field, $E_{\max}$ and $H_{\max}$, measured in units of the incoming field amplitudes is shown in each panel. Additionally, the largest cones in panel (a) of Fig. 6.9 (for the strongest electric fields near the silver nanowire edges) are shown in red and scaled by a factor 0.5 in order to emphasize the regions of the largest field enhancement. Again, it is important to note that the averaged characteristics of the near-field distributions t/T, $E_{\max}$, and $H_{\max}$ fluctuate with the mesh and cross-section A which is chosen to display the near-fields. However, they provide an instructive qualitative information on the near-field distributions.

The calculated spatial near-field distributions of the appearing normal modes differ strongly (resonances a and b in Fig. 6.8), when assuming a vertical nanowire separation of $L_z = 20$ nm. The displayed electric (a) and magnetic (b) field distributions in Fig. 6.9 and Fig. 6.10 clearly reveal the characteristic symmetry of the corresponding polariton modes. In case of the lower antisymmetric plasmon mode at 1.23 eV (resonance a in Fig. 6.8), the depicted electric field in panel (a) of Fig. 6.9 is nearly homogeneous inside both nanowires. However, due to the antisymmetric character, both fields point into opposite directions. Note that the displayed static field distribution resembles the moment of time when the induced currents are nearly zero in both nanowires (i.e., the induced polarization reaches its maximum). A very important additional observation is related to the arising polarization charges. The observable strong electric fields directly indicate the appearing positive and negative surface charges, which are localized at the right and left edges of the adjacent nanowires. Due to the antisymmetric charge distribution, the strong fields between the wires are orientated in opposite directions. Note that the electric field is almost zero at the center of the coupled nanowire pair system. In contrast to the electric field, the corresponding magnetic field in panel (b) of Fig. 6.9 is characterized by a strong field enhancement within the small gap between the closely spaced wires. The field is more or less homogeneous within the gap and changes its direction inside the nanowires, respectively.

(a) Electric field

$\hbar\omega$=1.230 eV, t/T=0.026, η=212.1, E_{max}=29.4

(b) Magnetic field

$\hbar\omega$=1.230 eV, t/T=0.269, η=95.5, H_{max}=15.1
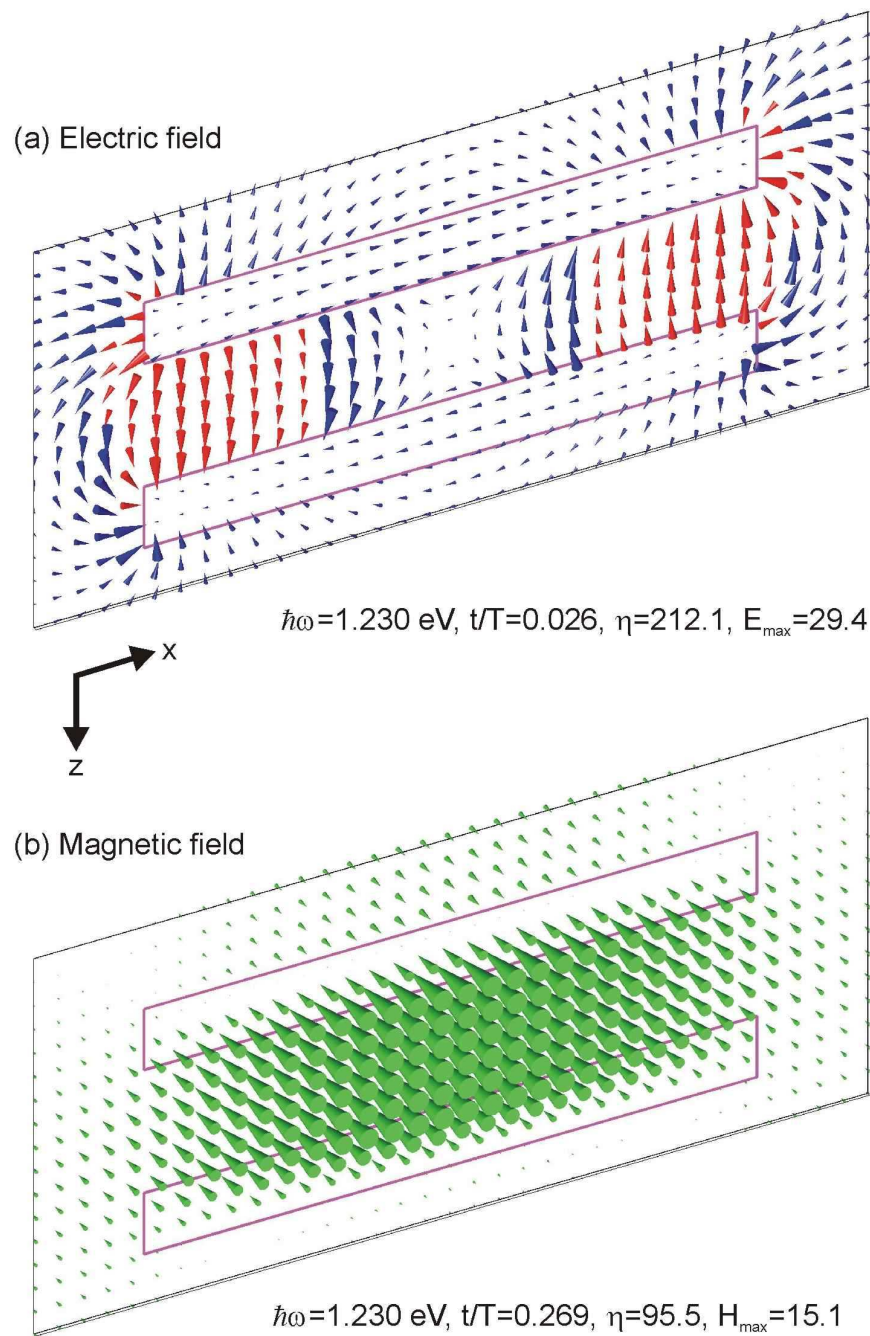
Figure 6.9:   Calculated spatial distribution of the electric (a) and magnetic (b) fields in a silver nanowire bilayer structure for normal light incidence ($\vartheta = \varphi = 0°$) and TM-polarization. The fields are shown for a photon energy of $\hbar\omega = 1.23$ eV and a nanowire separation of $L_z = 20$ nm. Solid magenta lines denote the cross-section (100×10 nm^2) of the individual silver nanowires. Red cones in panel (a) are scaled by a factor of 0.5.
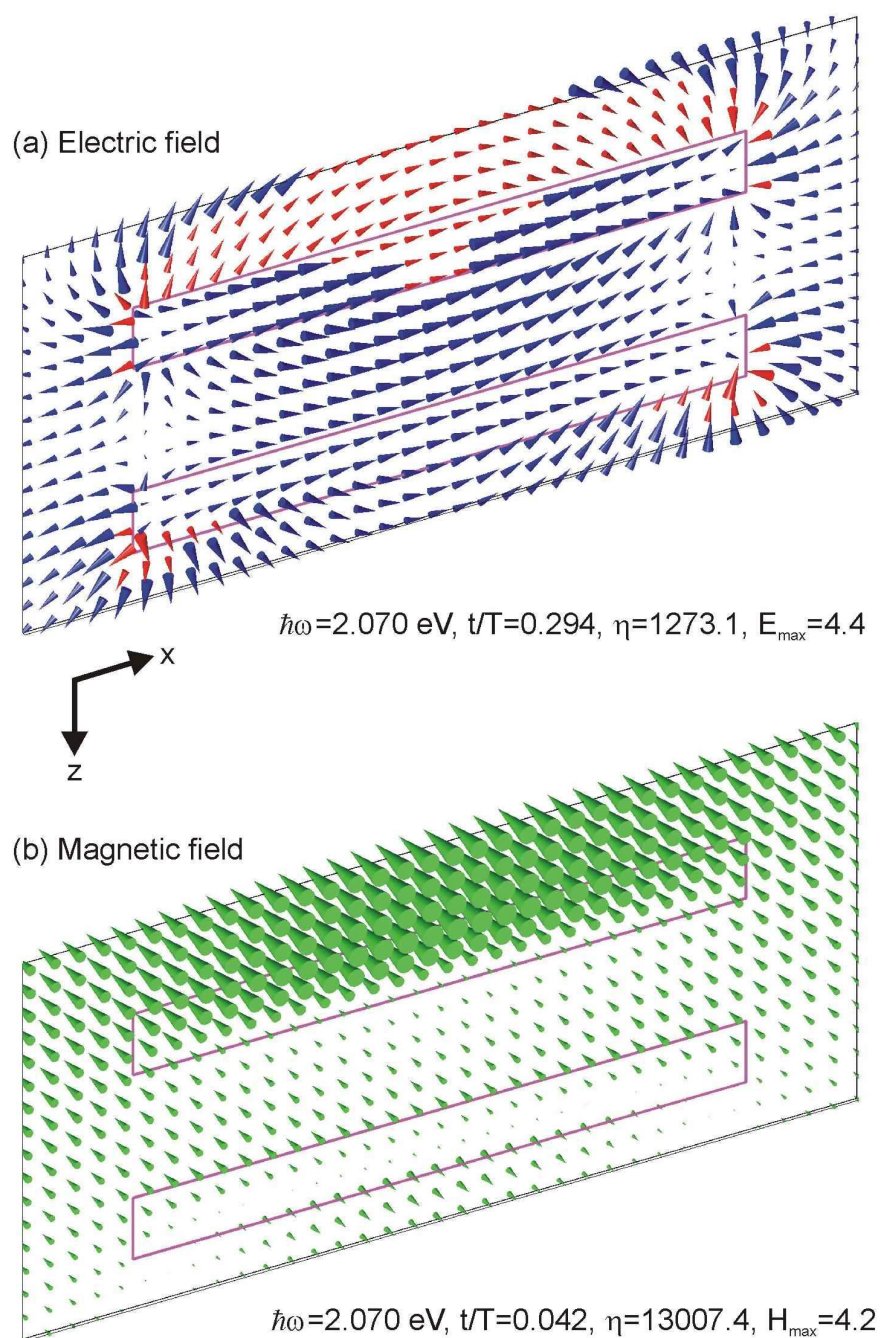
Figure 6.10: Calculated spatial distribution of the electric (a) and magnetic (b) fields in a silver nanowire bilayer structure for normal light incidence ($\vartheta = \varphi = 0°$) and TM-polarization. The fields are shown for a photon energy of $\hbar\omega = 2.07$ eV and a nanowire separation of $L_z = 20$ nm. Solid magenta lines denote the cross-section (100×10 nm^2) of the individual silver nanowires. Red cones in panel (a) are scaled by a factor of 0.5 in order to exclude overlapping cones.

Note that the averaged magnetic field reaches its maximum approximately 1/4 of the period later than the corresponding electric field, indicating the nonradiative character of the displayed field components.

The calculated electric and magnetic field distributions of the symmetric plasmon polariton mode can be found in panels (a) and (b) of Fig. 6.10. The fields are shown for a photon energy of 2.07 eV, which corresponds to the spectral position of resonance b in Fig. 6.8. In contrast to the antisymmetric polariton mode at 1.23 eV, the electric fields inside the two nanowires are now oriented parallel to each other and point in the same direction. A strong electric field amplitude is found above the nanowires, as marked by the red cones in panel (a) of Fig. 6.10. Due to the symmetric distribution of the surface charges, the facing charges on the adjacent nanowires repel each other. As a result, the electric fields are rather weak between the wires on both edges of the pair structure. Similar to the corresponding electric field distribution, also the magnetic field in panel (b) is characterized by a strong field enhancement above the two nanowires. Only weak fields can be found close to the lower second nanowire. Again, due to the nonradiative character of the depicted near-field, the averaged electric and magnetic field maxima are not reached simultaneously. Thus, as indicated by the parameters t/T in Fig. 6.10, the magnetic field is displayed approximately 1/4 of the period earlier than the electric field.

The displayed field distributions in Fig. 6.9 and Fig. 6.10 reveal the orthogonality of the arising normal modes of the coupled nanowire pair structure. While the lower mode a in Fig. 6.8 arises as a result of an antiparallel orientation of the induced dipole moments, the upper mode b, on the other hand, is characterized by a parallel alignment of the individual nanowire dipole moments. However, it is further important to point out that the normal mode coupling (i.e., quasistatic dipole-dipole interaction) does not only result in a lifting of the degeneracy of the bare particle plasmon modes but also affects the lifetimes of the arising normal modes. For example, the lifetime modifications can be directly observed in Fig. 6.8. The antisymmetric mode is characterized by a very narrow spectral linewidth (i.e., absorption peak), indicating the prolonged plasmon dephasing times. The lifetime of the upper symmetric mode is shortened in comparison to the bare particle plasmon mode, leading to a spectrally broadened resonance. Similar to the energy splitting of the normal modes, also their lifetimes reveal a strong dependence on the exact nanowire spacing as can be extracted from the displayed dependencies in Fig. 6.3. The shortened lifetime of the upper symmetric normal mode can be simply understood in terms of a stimulated decay

processes and is closely analogous to a superradiant behavior [225]. The decay rate is strongly enhanced due to constructive interference of the radiation fields of both nanoantennas (i.e., in-phase oscillation of the two closely spaced dipoles). In contrast to the symmetric mode, the lower antisymmetric normal mode becomes more and more subradiant in character. The induced antiparallel oscillation of the electric dipoles tend to cancel each other. Radiative decay is therefore determined by destructive interference of the radiation fields which directly results in a strongly absorptive character of the resonance. Thus, the antisymmetric plasmon mode a in Fig. 6.8 shows up as a pronounced maximum in the depicted absorption spectrum.

So far, a very fundamental consequence of the orthogonality of the arising normal modes has not been considered within the previous discussions. Especially the antisymmetric plasmon mode of the closely spaced wires shows some interesting properties which justify a more detailed study. As initially addressed theoretically in Refs. [226, 227], the electromagnetic excitation of two closely spaced (i.e., near-field coupled) metal nanowires might lead to a strong magnetic response of the composite structure

It is important to remark that such artificial materials with a strong magnetic resonance are currently the subject of extensive research activities. Such materials are believed to show negative permeability μ in a certain frequency range near to their magnetic resonance. Generally, a negative permeability is one of the requirements for implementation of negative-index materials. As initially suggested by Veselago in 1968 [228], a medium which simultaneously exhibits negative dielectric permittivity ε and magnetic permeability μ can be described as having a negative refractive index. Such materials, sometimes called metamaterials, give rise to a variety of interesting optical phenomena like the predicted counterintuitive negative refraction of electromagnetic waves [229]. One way of achieving negative refraction is based on a composite material consisting of split ring resonators (providing magnetic response) and conducting wires (providing electric response) as building blocks [230]. Using this approach, negative refraction has been demonstrated experimentally at microwave frequencies [231]. However, a demonstration in the optical regime is still missing up to now. A promising approach to achieve negative refraction at higher frequencies might be the downscaling of the structure sizes. The recent demonstration of split-ring resonators with a magnetic response at infrared wavelengths (3-μm) can be considered as a first step towards its realization [97]. Especially the fabrication of such nanostructures seems to be very challenging due to the required small
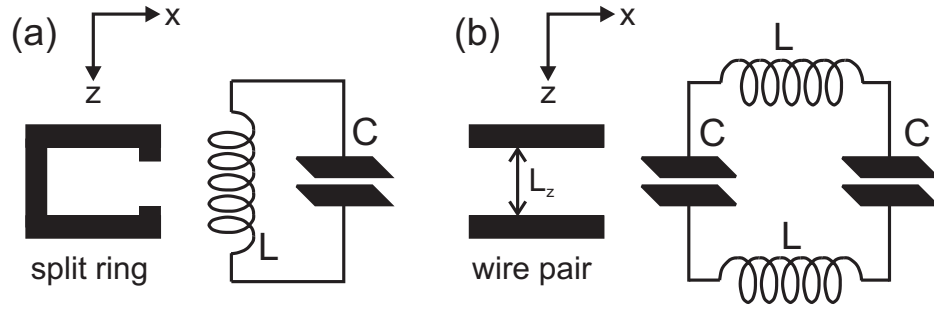
Figure 6.11:   Schematic illustration of split ring (a) and nanowire pair (b) resonators. The equivalent circuit diagrams are shown, respectively. The electronic circuits consist of inductances L and capacitances C.

structure sizes. Another material system that is expected to allow the realization of negative refraction are the proposed metal nanowire composites. As theoretically predicted, these structures provide one of the fundamental requirements for obtaining negative index materials, namely negative magnetic permeability at optical wavelengths [226, 227, 232].

Generally, a magnetic response (i.e., magnetic moment) can be established if local currents can be induced to circulate in closed loops. A very prominent realization are the so-called metallic split ring resonators. As schematically shown in panel (a) of Fig. 6.11, a single split ring resonator is a close analogue of a conventional LC circuit. While the metal ring can be considered as being a single loop of a magnetic coil with inductance L, its open ends act as a capacitor with capacitance C. At resonance, the eigenfrequency of the oscillator is thus simply obtained from the relation $\omega_{LC} = 1/\sqrt{LC}$. It has been shown theoretically that an external electromagnetic field can couple to the LC (split ring) resonance of the properly designed resonator in two different ways [233]. So far, only an excitation by the electric field component (electric field has to be oriented parallel to the z-axis) has been demonstrated experimentally in the optical regime [97]. However, the strongly desired negative permeability can only be achieved by a coupling of the magnetic field component. When the split ring resonator is oriented such that the magnetic field is oriented perpendicular to the plane of the split ring, circular currents are induced. Such currents may result in a magnetic field that counteracts the driving external field, thus leading to a strong magnetic response of the structure. Nevertheless, an experimental verification of the predicted negative permeability in the optical regime is still missing.

Alternatively, also the studied closely spaced metal nanowire pairs represent a

possible design for the realization of a magnetic response. As already shown in panel (b) of Fig. 6.9, the excitation of the lower antisymmetric plasmon resonance is accompanied by a large enhancement of the magnetic fields which is a clear indication of the oscillating antiparallel currents in the wires (along the x-axis). The schematic view in panel (b) of Fig. 6.11 illustrates the equivalent circuit diagram. The two closely spaced nanowires mimic two coupled split ring resonators. In particular, the theoretically assumed nanowire pairs resemble a conducting loop that exhibits two gaps (capacitance) which in turn give rise to a resonance and a related magnetic moment. Note that the current loop is closed by the displacement currents between the facing edges of the nanowires. In contrast to the symmetric plasmon mode, the lower antisymmetric mode might be interpreted as "magnetic" resonance of the nanowire ensemble under certain conditions.

Although the related fundamental phenomena will not be addressed in more details within this thesis, it is important to mention that the predicted magnetic properties should exhibit a very strong dependence on the exact spacer layer thickness L_z. While the induced electric dipole moment tends to zero when the separation between the two nanowires is reduced, the magnetic dipole moment, on the other hand, is simultaneously increased. Due to the fact that both electric and magnetic field components couple to the antisymmetric plasmon resonance of the wire pair structure (coupling of the electric field component will lead to a modification of the effective permeability), it is especially necessary to clarify the exact spacer layer thickness which ensures an effective negative permeability of the composite material. In a same way, also the possible influence of the nanowire pair density (periodicity) has to be included in a more detailed study. The huge absorption losses are another problem which has to be addressed. For example, the antisymmetric plasmon resonance a in Fig. 6.8 is strongly absorptive due to its subradiant character (destructive interference of the radiation fields). However, it is generally questionable whether the considered nanowire-based structure can be treated within the metamaterial limit. While the concept of designing composite materials with effective optical properties works quite well in the microwave region (e.g., utilization of split ring resonators), the equivalent implementation of similar materials in the optical regime requires special caution. The structure size should be much smaller than the resonance wavelength which might not be fulfilled in case of the nanowire composites.

In addition to our studies on coupling phenomena in stacked nanowire structures [e.g., panel (a) of Fig. 6.12], it might be interesting to compare the obtained results with similar calculations for a slightly changed nanowire structure. The
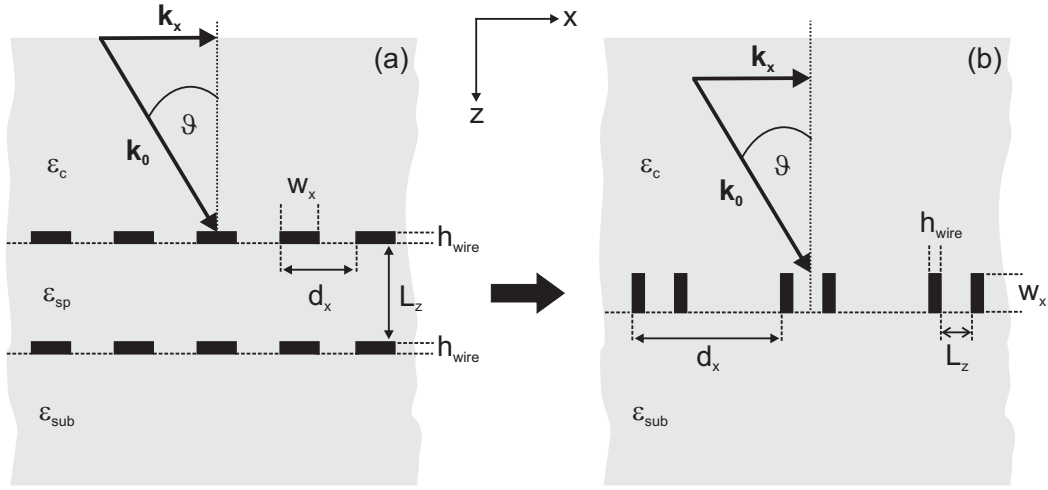
Figure 6.12: Schematic view of two different nanowire pair structures. In addition to the studied stacked geometry (a), also planar structures might be of potential interest (b). The individual nanowires of panel (b) are rotated by 90 degree. Structure (b) can be considered as a superlattice composed of a nanowire pair on each lattice site.

modified grating design is displayed in panel (b) of Fig. 6.12. The sample structure can be considered as a realization of a nanowire superlattice in some respects. While the nanowire cross-section and the nanowire separation L_z are unchanged in comparison to the stacked structures [panel (a) of Fig. 6.12], each nanowire pair is rotated by 90 degrees. Further calculations have to prove whether the so-called magnetic resonance of the modified pair structure can still be excited by an incident electromagnetic radiation field (normal incidence and TM polarization).

Only the fields of the lower dipolar plasmon resonances have been investigated up to now (maxima a and b in Fig. 6.8). Thus, before resuming with the detailed discussion of far-field induced interaction phenomena in the next section, the field distributions of the two remaining plasmon resonances (maxima c and d in Fig. 6.8) will be presented for the sake of completeness. Similar to the discussed normal modes due to coupling of the dipolar nanowire plasmons, the additional resonances are caused by the direct near-field coupling between higher order plasmon modes of the adjacent nanowires. The field distributions for photon energies of 2.73 eV (peak c in Fig. 6.8) and 3.03 eV (peak d in Fig. 6.8) are displayed in Fig. 6.13 and Fig. 6.14, respectively. Both electric (a) as well as magnetic (b) fields are shown.

Obviously, the depicted near-field distributions in both figures exhibit a more complex structure than the dipolar fields of the two lower plasmon polariton

(a) Electric field

$\hbar\omega$=2.730 eV, t/T=0.036, η=9.7, E_{max}=6.1

(b) Magnetic field

$\hbar\omega$=2.730 eV, t/T=0.120, η=2.2, H_{max}=2.9
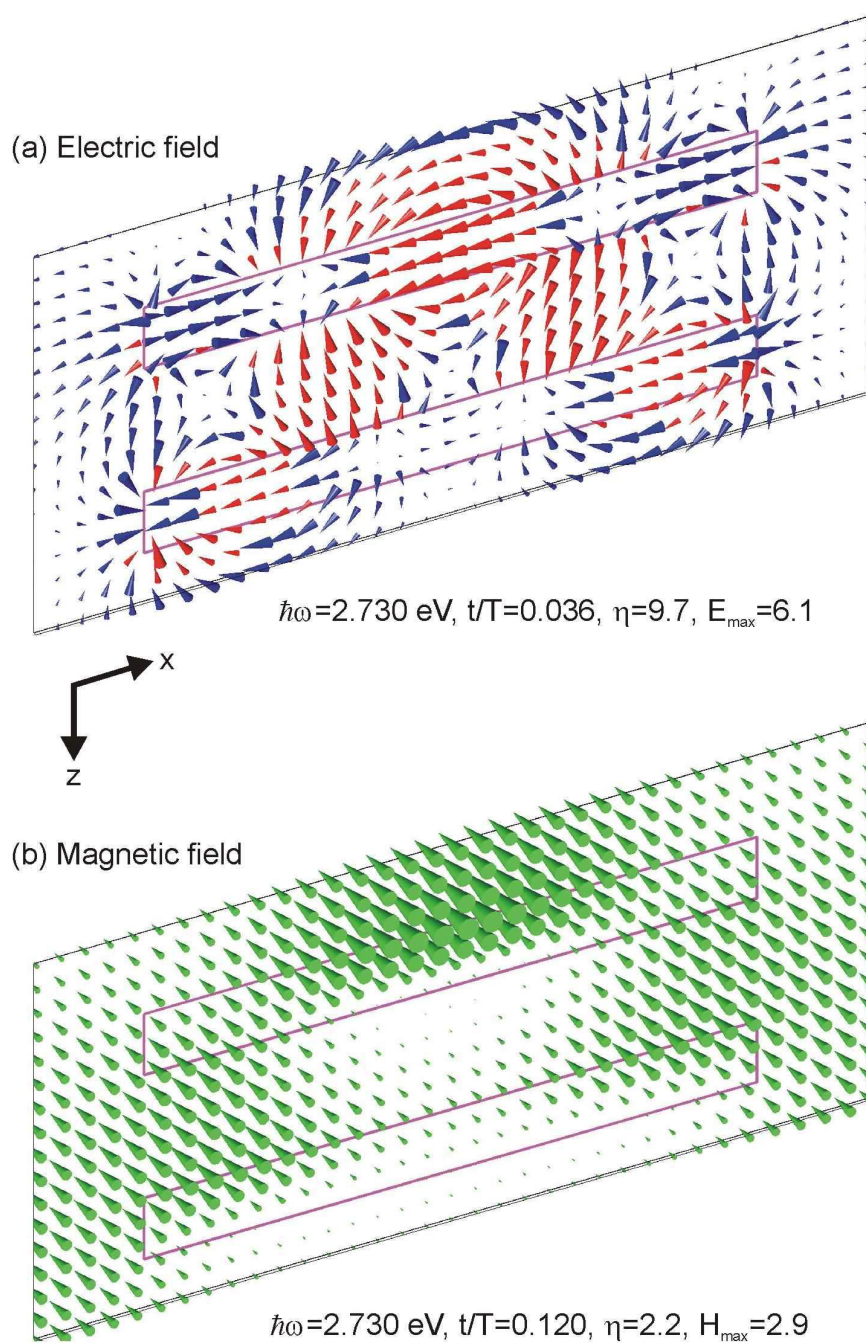
Figure 6.13: Calculated spatial distribution of the electric (a) and magnetic (b) fields in a silver nanowire structure for normal light incidence ($\vartheta = \varphi = 0°$) and TM-polarization. The fields are shown for a photon energy of $\hbar\omega = 2.73$ eV and a nanowire separation of $L_z = 20$ nm. Solid magenta lines denote the cross-section (100×10 nm^2) of the individual silver nanowires. Red cones in panel (a) are scaled by a multiplier of 0.5 in order to exclude an overlap of the cones.

(a) Electric field

$\hbar\omega$=3.030 eV, t/T=0.248, η=12.0, E_{max}=8.6

(b) Magnetic field

$\hbar\omega$=3.030 eV, t/T=0.036, η=11.4, H_{max}=3.5

Figure 6.14: Calculated spatial distribution of the electric (a) and magnetic (b) fields in a silver nanowire structure for normal light incidence ($\vartheta = \varphi = 0°$) and TM-polarization. The fields are shown for a photon energy of $\hbar\omega = 3.03$ eV and a nanowire separation of $L_z = 20$ nm. Solid magenta lines denote the cross-section (100×10 nm^2) of the individual silver nanowires. Red cones in panel (a) are scaled by a multiplier of 0.5 in order to exclude an overlap of the cones.

resonances (maxima *a* and *b* in Fig. 6.8). For example, instead of homogeneous electric fields inside the wires, pronounced field minima can be found along the *x*-axis of the nanowires. Regardless of these differences, the considered polariton modes are again characterized by the specific symmetry of the appearing near-fields. The plasmon mode in Fig. 6.13 shows a clear antisymmet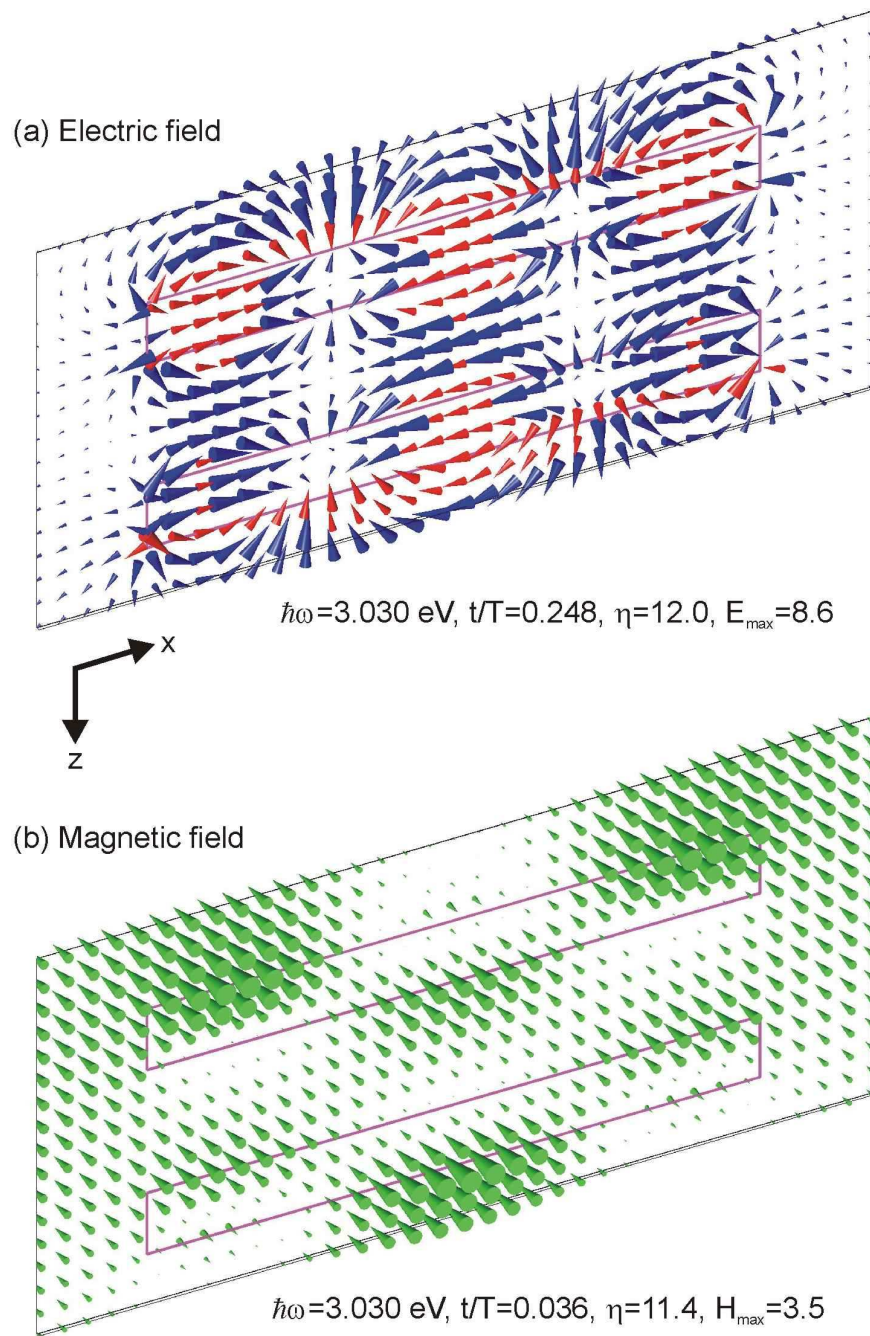ric behavior. The electric fields within the upper nanowire point into the opposite direction as compared with the corresponding fields along the second wire [see panel (a)]. The situation is inverted for the upper polariton mode, which is displayed in Fig. 6.14. Now the symmetric character of the mode can be clearly deduced from the depicted electric field distribution. The fields within the adjacent nanowires are orientated parallel to each other.

6.3.3 Far-field regime

The direct (i.e., quasistatic) dipole-dipole interaction is generally restricted to closely spaced wire pairs and decreases gradually with the spacer layer thickness. However, as the nanowire separation increases and the coupling exceeds the near-field regime, strong modifications of the optical response can be observed. In particular, the calculated spectra in Fig. 6.3 give clear evidence for the appearance of far-field coupling effects. The nanowires can interact through their common radiation field which might be interpreted in terms of a dynamic dipole-dipole interaction. Although the optical response of the proposed nanowire pair structure can be easily calculated by using numerical methods, the theoretical spectra in Fig. 6.3 generally do not provide a deeper physical insight into the underlying light-matter interaction phenomena. In order to achieve a more detailed qualitative understanding of the far-field effects, it might be very instructive to take a closer look at an analog semiconductor-based system. In semiconductor physics, similar coupling phenomena have been studied extensively. For example, the investigations on multiple-quantum-well structures have already pointed out the importance of interwell coupling via dynamic dipole-dipole interaction [110, 205, 219, 234].

A multiple-quantum-well structure is a periodic multilayer system built of two semiconductor materials (e.g., GaAs and $Al_xGa_{1-x}As$). Electrons and holes are confined in thin layers of a material with a smaller band gap (quantum wells) which are separated from each other by wide layers of a semiconductor with a larger band gap (barrier layers). In these systems, the role of dipolar excitation is assigned to the excitons confined in the individual semiconductor quantum wells of the stacked structure. It has been shown that the radiative interaction

between excitons (i.e., coupling via the exchange of photons) critically depends on the number N of stacked quantum wells as well as on their spatial separation. Some of the most interesting radiative coupling effects have been observed in case of Bragg-periodic structures, i.e., when the quantum well spacing is equal to an integer multiple of half the wavelength of light at the exciton frequency. In these multiple-quantum-well Bragg structures, the collective response of the radiatively coupled quantum wells results in an enhanced radiative decay of the coherent optical polarization. For example, the coupling can been interpreted in terms of a superradiant-like behavior in the small N limit [110]. Generally, the radiative interaction leads to the formation of N normal modes. Only one mode is superradiant in character (so-called bright mode), while all other $N-1$ modes are optically inactive, i.e., they can be considered as subradiant or dark modes [235]. Furthermore, it has been shown that the optical response of a set of N Bragg-coupled quantum wells is therefore equivalent to a single quantum well with an N times amplified radiative coupling coefficient (i.e., N times broadening of the radiative linewidth). In particular, the decay time of this superradiant response inversely scales with the quantum well number N. The reflection from Bragg-periodic structures is characterized by a Lorentzian line (under idealized conditions) which grows in peak reflectivity and linewidth with increasing N. The reflection and transmission coefficients of such structures can be analytically obtained by the simple relations [110]

$$r_N(kd = \pi) = \frac{-iN\Gamma_0}{\omega_0 - \omega - i(\Gamma + N\Gamma_0)}, \qquad (6.6)$$

$$t_N(kd = \pi) = (-1)^N \frac{\omega_0 - \omega - i\Gamma}{\omega_0 - \omega - i(\Gamma + N\Gamma_0)}, \qquad (6.7)$$

where $k = (\omega/c_0)n_{sp}$ is the wavevector in the sample, n_{sp} is the refractive index of the barrier material (spacer layer), and d is the periodicity of the quantum wells. The frequency ω_0 specifies the exciton resonance frequency, while Γ and Γ_0 are the nonradiative and radiative damping rates of a single quantum well (half width at half maximum of the nonradiative and radiative line widths). Thus, the total damping rate can be obtained by the relation $\gamma = \Gamma + N\Gamma_0$. The optical response becomes more complex when the considered multiple-quantum-well structures are detuned from the exact Bragg condition. Away from Bragg resonance, all of the previously subradiant modes $(N-1)$ become optically active to some extent and couple to the external radiation field. Especially anti-Bragg structures have been investigated. In particular, a splitting into two distinct

modes should be observable in case of double layer structures [205]. However, it is important to remark that the interpretation of the optical response in terms of a superradiant decay may be misleading for long-period (i.e, high-N) quantum well structures. In the limit of large N, the reflectivity reaches unity and a square profile characteristic for the reflection of a photonic band gap is formed.

Generally, the optical response of the proposed metal nanowire pair structures should show similar far-field interaction effects as were previously discussed for the case of multiple-quantum-well-based structures. Especially superradiant phenomena, i.e., a doubling of the radiative decay rates should occur under Bragg condition. Due to the complexity of the theoretically obtained spectra in Fig. 6.3, far-field interaction in nanowire pair structures will only be analyzed for two specific spacer layer thicknesses. More precisely, the focus of the following considerations will be on Bragg and anti-Bragg spaced pair structures.

(i) Bragg spacing

In case of Bragg spacing (i.e., $L_z = 240$ nm), the optical response of the coupled nanowire-based double layer structure might be interpreted in terms of a superradiant decay process. Consequently, superradiance implies the formation of two degenerate modes. Taking into account the results of the discussed semiconductor analog (multiple-quantum-well structures), one emerging mode should be superradiant in character which means that its radiative damping rate Γ_0 should be doubled in comparison to the single layer case. Simultaneously, a subradiant mode should be supported by the structure. The signature of the subradiant mode should vanish in the spectra due to the fact that the mode is optically inactive and does not couple to the incident radiation fields. Although the underlying effects tend to be more complicated, as will be discussed later on, the evidence of a superradiant-like behavior can be found in Fig. 6.3. In particular, the spectral width of the reflection spectrum of the nanowire pair structure under Bragg condition is strongly broadened in comparison to the single layer structure (lowest spectra in Fig. 6.3). A more significant spectral feature is the vanishing of the second degenerate mode of the coupled system. For slight detunings from the exact Bragg condition, the degeneracy is lifted and the mode becomes optically active to some degree. For example, while being optically inactive under Bragg spacing, the mode shows up as a sharp dip (peak) in the reflection (absorption) spectra for structures with a spacer layer thickness of $L_z = 260$ nm and $L_z = 220$ nm. However, the exact interpretation on the basis of the displayed theoretical spectra is somewhat difficult due to the fact that the considered small-

period grating structures ($d_x = 200$ nm) possess a large background reflectivity. Even the spectra of the single layer structure are characterized by slightly asymmetric non-Lorentzian, i.e., Fano-like line shapes. Alternatively, it might be very instructive to take a closer look at the calculated spatial field distribution for two characteristic energies in the next step.

First, the calculated field distribution is analyzed for the specific case of Bragg spacing. The calculated spatial distribution of the electric and magnetic fields are therefore depicted in Fig. 6.15 and Fig. 6.16, respectively. All fields are displayed for a photon energy of $\hbar\omega = 1.704$ eV which corresponds to the spectral position of the related reflection maximum. The electric (a) and magnetic (b) field vectors are again shown as a two-dimensional array of colored cones in both figures. The length of the cones is proportional to the field strength at the central point of each cone. The field direction is specified by the orientation of the cones. In particular, the field distributions are depicted at the most characteristic moments of time, i.e., when the integrated intensity of the corresponding fields reaches its maximum value. The schematic cross-section of the nanowire pairs is displayed by solid lines in each figure. Note that the incoming light field propagates from the top to the bottom of the figure in all calculations [3]. Further on, the fields of Fig. 6.15 and Fig. 6.16 are scaled by different coefficients. In order to compare the absolute magnitudes of the fields, the maximum absolute value of each field, $E_{\max}$ and $H_{\max}$, measured in units of the incoming field amplitudes is specified in each panel.

The displayed electric and magnetic field distributions show several interesting features. In Fig. 6.15, for example, plasmon excitation is clearly observable due to the related field enhancement. In particular, it is visible that the collective charge oscillations causes a large resonant enhancement of the local field inside and near the nanowires. The oscillations of the conduction band electrons along the x-axis of the wires directly lead to the expected typical dipolar near-field distribution. A very important additional point is the correlation between the plasmon oscillations in both nanowires. A superradiant decay implies a constructive interference of the radiation fields from the adjacent nanowires, i.e., a certain phase coherence is necessary. Thus, the respective charge oscillations in the facing nanowires should be characterized by a phase shift of π in case of Bragg spacing. This antisymmetric nature of the superradiant mode can be clearly deduced from Fig. 6.15. In particular, the dipolar near-fields close to the individual wires of the

---

[3]See Sec. 6.3.2 for a more detailed discussion of the introduced parameters.

1.704 eV, t/T=0.266, η=25.9, E$_{max}$=4.7

(a) Electric field

Figure 6.15:   Calculated spatial distribution of the electric field in a silver nanowire structure for normal light incidence ($\vartheta = \varphi = 0°$) and TM-polarization. The fields are shown for a photon energy of $\hbar\omega = 1.704$ eV and a nanowire separation of $L_z = 240$ nm. Solid magenta lines denote the cross-section of the individual silver nanowires.

1.704 eV, t/T=0.02, η=57.6, H$_{max}$=4.0
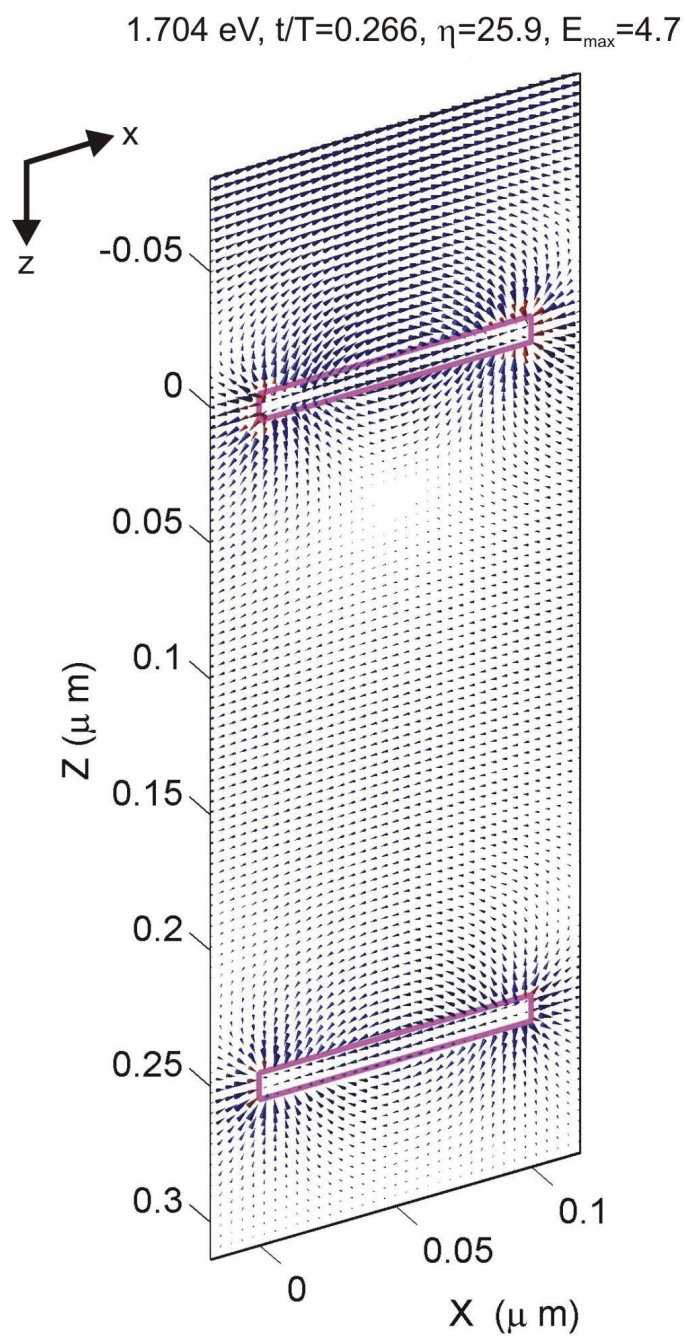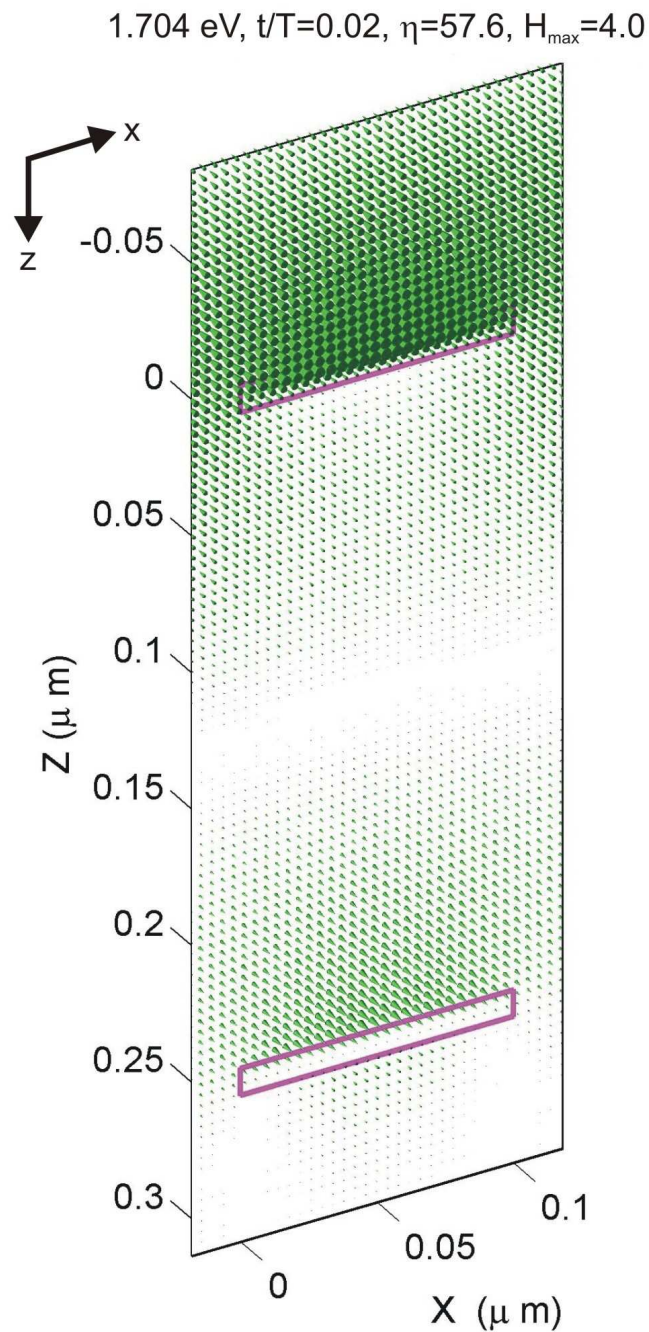
(b) Magnetic field

Figure 6.16:   Calculated spatial distribution of the magnetic field in a silver nanowire structure for normal light incidence ($\vartheta = \varphi = 0°$) and TM-polarization. The fields are shown for a photon energy of $\hbar\omega = 1.704$ eV and a nanowire separation of $L_z = 240$ nm. Solid magenta lines denote the cross-section of the individual silver nanowires.

radiatively coupled system are oriented in opposite directions (i.e., antiparallel oscillations). As a result, the observed phase shift should be approximately on the order of π. Another important information can be deduced from the depicted parameters t/T. The electric field in Fig. 6.15 is displayed approximately 1/4 of the period earlier than the magnetic field in Fig. 6.16, indicating the standing wave character of the fields.

The field distributions of a second characteristic situation will be discussed in the following. Further insight can especially be gained when considering a slightly detuned Bragg structure. To support our qualitative discussion, the numerically obtained electric and magnetic field distributions for a structure with $L_z = 260$ nm are displayed in Fig. 6.17 and Fig. 6.18, respectively. The fields are shown for a photon energy of $\hbar\omega_s = 1.652$ eV (i.e., at the position of the narrow absorption line in Fig. 6.3), assuming normal light incidence and TM polarization. Similarly to the previous plots, the field vectors are shown as a two-dimensional array of colored cones. While the orientation of the cones specifies the respective field direction, their length is proportional to the field strength at the central point of each cone. Again, the field distributions are shown for the very moments in time when the spatially integrated intensity of the corresponding fields reaches its maximum value. The fields in Fig. 6.17 and Fig. 6.18 are again scaled by different coefficients. In order to compare the absolute magnitudes of the fields, the maximum absolute values of each field, E_{max} and H_{max}, measured in units of the incoming field amplitudes are shown in each panel.

The considered photon energy corresponds to the spectral position of the second normal mode which becomes subradiant in case of Bragg spacing. However, the mode can be excited, i.e., becomes optically active when detuning from the exact Bragg condition. Again, the displayed electric field distribution in Fig. 6.17 reveals the dipolar nature of the near-fields close to the individual nanowires. This specific field distribution is a clear sign of the collective electron oscillations within the displayed nanowires. In contrast to the superradiant mode, the subradiant mode is characterized by its symmetric nature. The induced plasmon oscillations of the individual wires are in phase, i.e, the resulting dipolar near-fields are now characterized by an identical orientation. As an important result of the symmetric nature, the radiation fields of both metal wires interfere destructively. Thus, while the excitation of this mode is generally forbidden under Bragg conditions, a slight detunig results in a long living plasmon mode which is predominantly nonradiative in nature. In other words, the decay of this mode is determined by absorption. This important fact can be clearly deduced from the corresponding spectra in

(a) Electric field

Figure 6.17:   Calculated spatial distribution of the electric field in a silver nanowire structure for normal light incidence ($\vartheta = \varphi = 0°$) and TM-polarization. The fields are shown for a photon energy of $\hbar\omega = 1.652$ eV and a nanowire separation of $L_z = 260$ nm. Solid magenta lines denote the cross-section of the individual silver nanowires.

1.652 eV, t/T=0.225, η=12.4, H$_{max}$=9.5
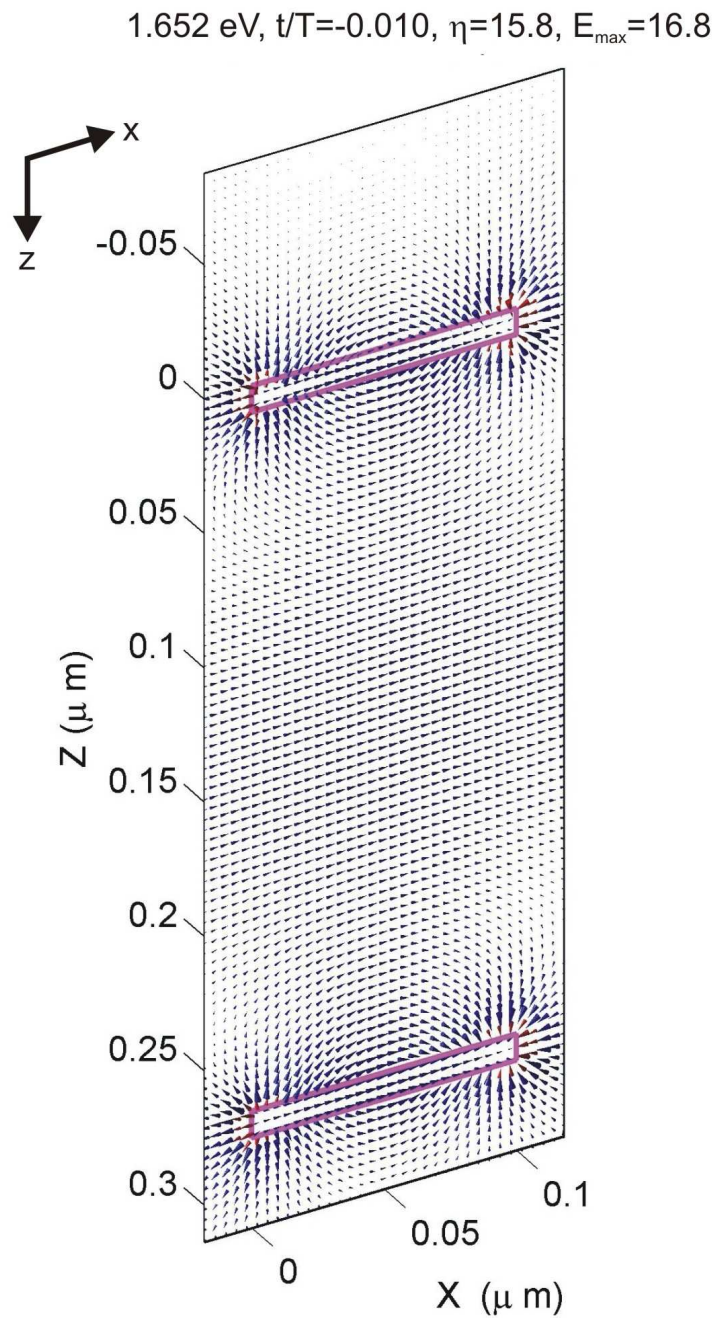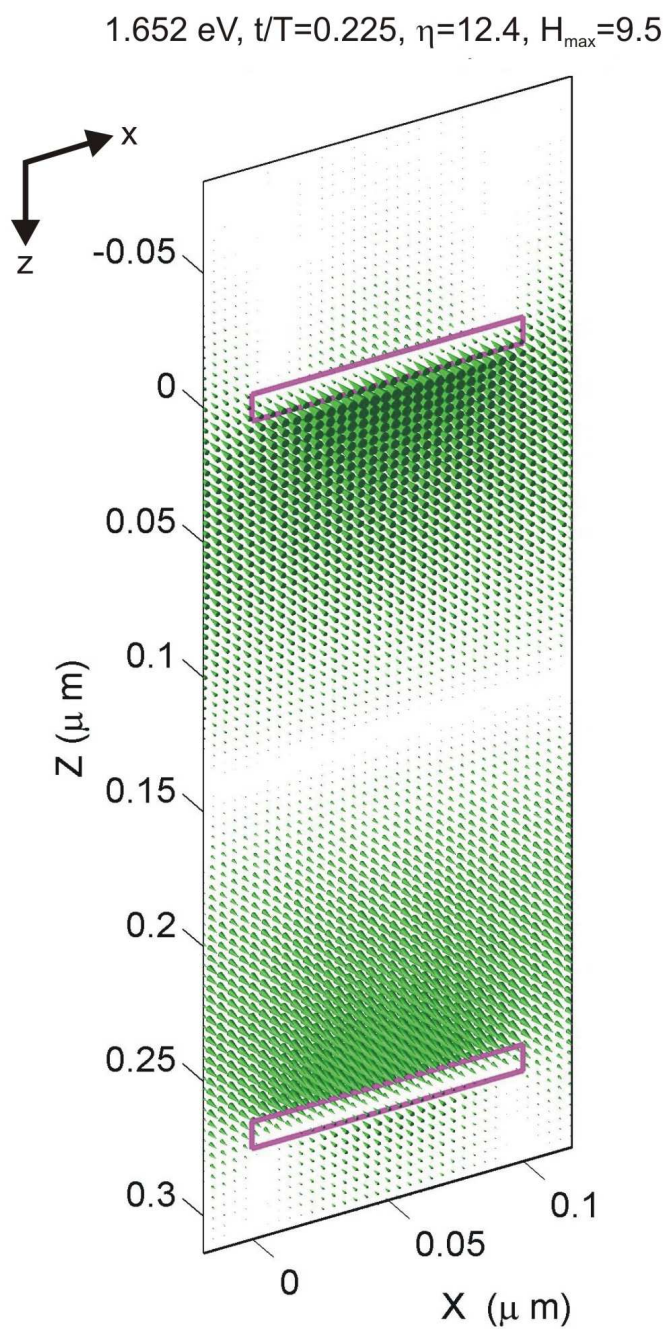
(b) Magnetic field

Figure 6.18:   Calculated spatial distribution of the magnetic field in a silver nanowire structure for normal light incidence ($\vartheta = \varphi = 0°$) and TM-polarization. The fields are shown for a photon energy of $\hbar\omega = 1.652$ eV and a nanowire separation of $L_z = 260$ nm. Solid magenta lines denote the cross-section of the individual silver nanowires.

Fig. 6.3 where the mode shows up as a pronounced absorption peak. Additionally, it is important to point out that the considered mode is connected to a standing wave, i.e., the two grating layers act as active cavity mirrors. The cavity-mode-like standing wave is indicated by the strong magnetic fields in Fig. 6.18. The node of the related magnetic field is located at the center between both grating layers, while the maximum field intensities are reached in close proximity to the facing nanowires.

A very important geometrical parameter of the proposed nanowire pair structures has not been addressed so far. Additional insight can be gained by analyzing the influence of the in-plane nanowire period d_x. As already demonstrated for the case of single layer structures (e.g., see first part of the chapter), near-field interaction between closely spaced nanowires affects the spectral bandwidth and the position of the plasmon resonances. Obviously, these two effects have to be taken into account for a more detailed study of the optical response. All previous discussions of the double layer geometry have been restricted to structures with a periodicity of $d_x = 200$ nm. Although the underlying physical effects will not be discussed in much details, important period-dependent results will be shortly reviewed to highlight some of the related phenomena.

Exemplarily, calculated reflection spectra of single and double layer grating structures are displayed in Fig. 6.19. In case of the double layer design, the spacer layer thickness has been chosen such that the Bragg condition ($L_z = 240$ nm) is approximately fulfilled. The period-dependent spectra are shown for normal light incidence and TM polarization. Results for structures with nanowire periods of $d_x = 150$ nm, $d_x = 200$ nm, and $d_x = 350$ nm are included, respectively. The depicted spectra clearly reveal the strong influence of the nanowire period. For example, the spectra in panel (a) again demonstrate the induced redshift and a significant broadening of the plasmon resonances in case of single layer structures. It is further interesting to remark that only the structure with a nanowire period of $d_x = 350$ nm is characterized by an almost Lorentzian reflection line. Strictly speaking, the observed reflection lines are also Fano resonances. However, the characteristic Fano profile is much stronger pronounced in case of structures with a smaller grating period. This fact is simply related to the background reflectivity which is strongly enhanced due to the larger metal coverage. As expected, the near-field induced phenomena directly affect the spectra of the double layer structure in a similar fashion. More precisely, a continuous line broadening can be observed in panel (b) when increasing the nanowire period. In addition to the linewidth, especially the specific shape of the reflection lines is further modified.
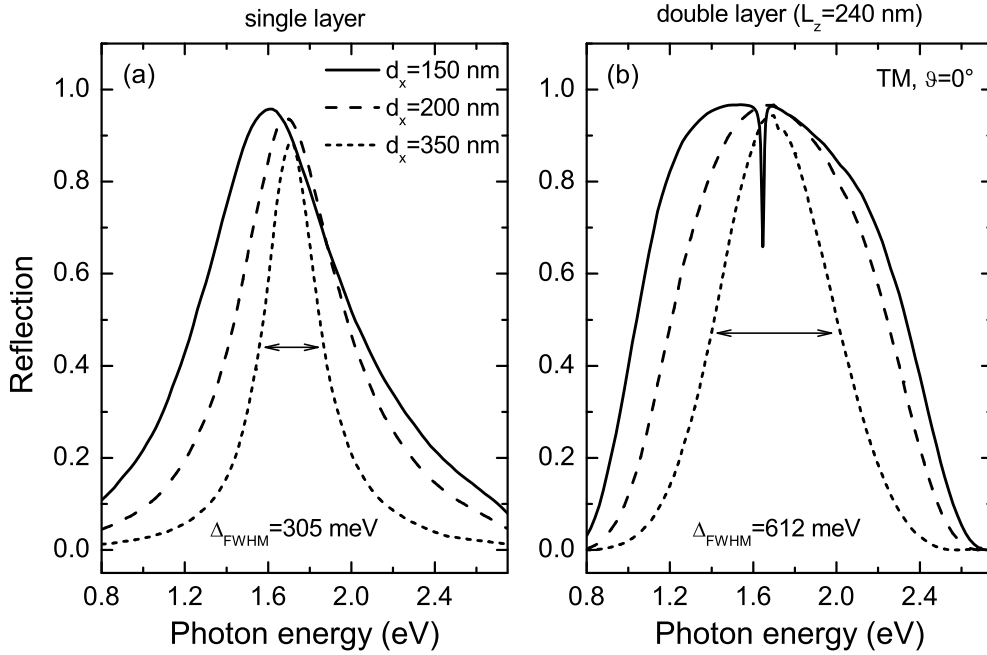
Figure 6.19:   Calculated reflection spectra of single (a) and double layer (b) grating structures in dependence of the silver nanowire period. The individual silver nanowires have a cross-section of 100×10 nm^2. The spectra are shown for normal light incidence and TM polarization. A spacer layer thickness of $L_z = 240$ nm has been used for the calculations in panel (b). Results for $d_x = 150$ nm (dotted line), $d_x = 200$ nm (dashed line), and $d_x = 350$ nm (solid line) are displayed, respectively.

For example, the nearly Lorentzian reflection peak ($d_x = 350$ nm) is transferred into a more or less rectangular shaped maximum. Generally, the reflection saturates and resembles to a so-called Reststrahlbande [236]. Another important feature of panel (b) is the sharp dip in the reflection spectrum of the double layer structure with the smallest period of $d_x = 150$ nm. Due to the near-field induced plasmon shifts which are illustrated in panel (a) of the figure, the Bragg condition becomes period-dependent. Strictly speaking, the exact Bragg condition is only fulfilled for structures with a lateral period of 200 nm. A smaller grating period, i.e., a slight detuning from the Bragg condition results in the appearance of an additional mode. As already discussed, the central subradiant mode becomes optically active and emerges as a sharp minimum close to the center of the broad reflection maximum.

Furthermore, it is important to show that the spacer layer dependent optical response is generally not fundamentally changed in character when the nanowire
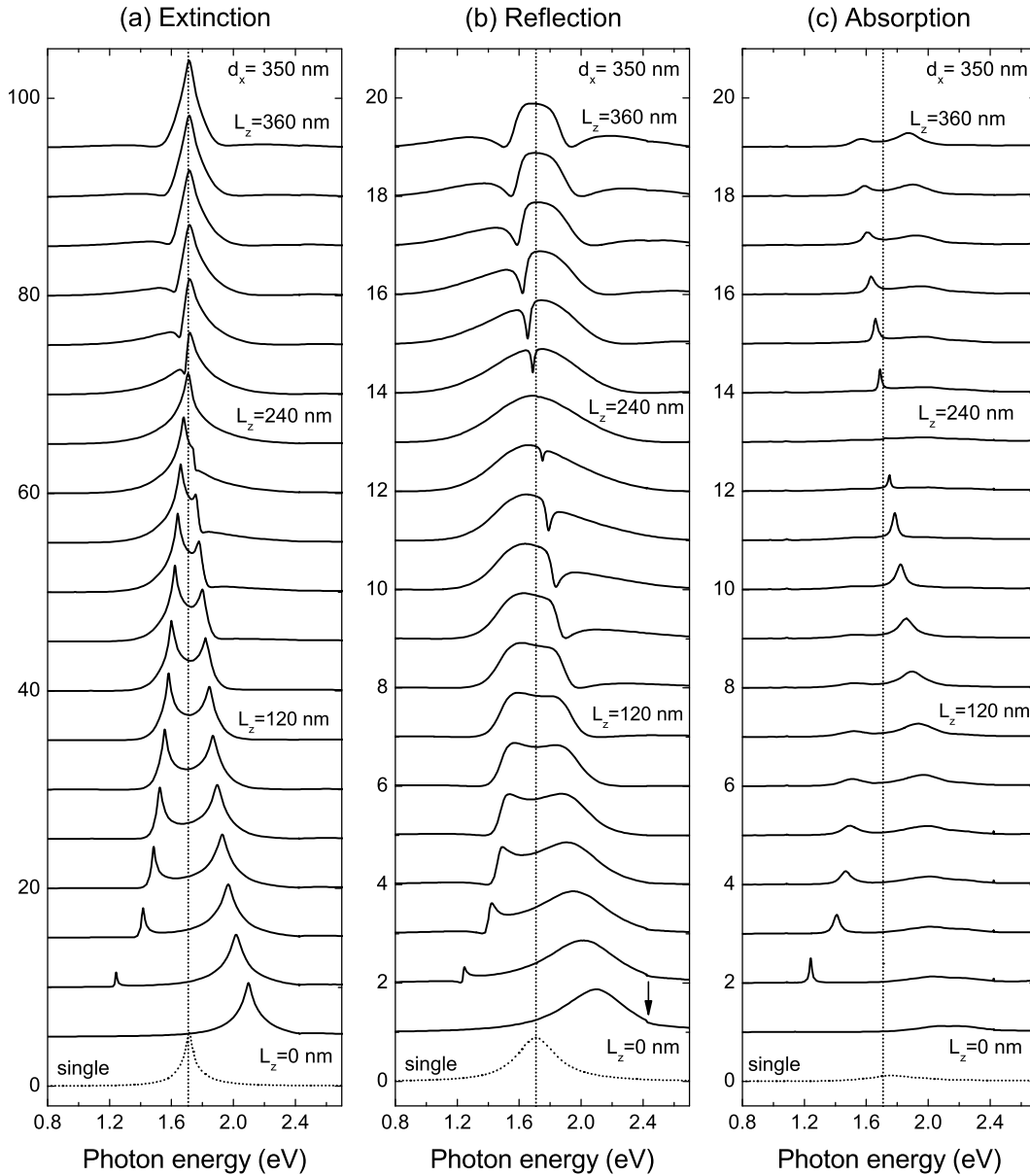
Figure 6.20: Calculated extinction (a), reflection (b), and absorption (c) spectra of two coupled silver grating layers at normal incidence ($\vartheta = 0°$) and TM polarization. Spectra for nanowire arrays with a period of 350 nm are shown. From top to bottom, the spacer layer thickness L_z is decreased from 360 nm to 0 nm in steps of 20 nm. The individual spectra are shifted upwards for clarity in each panel. The calculated spectra of a single grating layer are displayed as a reference (dotted lines at the bottom) in all three panels. The dotted vertical lines mark the position of the dipolar particle plasmon resonance of the single layer structure. The arrow in panel (b) marks the position of the Rayleigh anomaly.

period is increased. Thus, the numerical calculations displayed in Fig. 6.3 have been repeated assuming an identical double layer structure, taking into account a larger in-plane period of $d_x = 350$ nm. The obtained extinction (a), reflection (b), and absorption (c) spectra of the modified double layer grating structure are depicted in Fig. 6.20 for the sake of completeness. From top to bottom, the spacer layer thickness L_z is decreased from 360 nm to 0 nm in steps of 20 nm. The calculated spectra of a single grating layer are again displayed as a reference. Apart form small spectral shifts, the general dependencies are not altered in comparison to Fig. 6.3. For example, the clear splitting of the plasmon resonance can be observed for closely spaced wire pairs. However, some of the spectral features become more pronounced due to the reduced plasmon linewidth. As will be discussed later on, especially the reflection spectra in case of anti-Bragg spacing show a more significant line shape. Note that the increased periodicity of the system leads to the appearance of a Rayleigh anomaly which is caused by the opening of diffraction channels. As marked by the arrow in panel (b), a cusp-like feature can be observed on the high energy tail of the blue shifted plasmon mode.

Due to the nearly Lorentzian line shape of the single layer plasmon resonance for structures with a nanowire period of $d_x = 350$ nm, it might further be possible to check the validity of the superradiant picture by applying relation 6.6. In a first approximation, neglecting the influence of the background reflectivity, the reflection spectrum of the single layer structure can be modeled with an acceptable accuracy. Exemplarily, the obtained results of the fitting procedure are displayed in panel (a) of Fig. 6.21. A plasmon resonance energy of $\hbar\omega_0 = 1.708$ eV has been used for the modeling of the single layer reflection spectrum ($N = 1$). Furthermore, the use of radiative and nonradiative damping rates of $\Gamma_0 = 144.5$ meV and $\Gamma = 8$ meV leads to satisfactory results. The chosen set of parameters leads to a total damping rate of $\gamma = 152.5$ meV, i.e., a spectral linewidth of $2\gamma = 305$ meV. This value directly corresponds to the spectral width (FWHM) extracted from the scattering-matrix based calculations. The more important results of the double layer structure are shown in panel (b) of Fig. 6.21. As already mentioned, the numerically obtained reflection spectrum of the considered Bragg structure is clearly broadened. Again, the spectrum has been fitted by applying the analytical model. While the values of all other parameters have been kept constant (similar to the fit of the single layer structure), the double layer geometry is taken into account by using $N = 2$. A comparison with the analytical model shows that the calculated reflection spectrum of the Bragg structure definitely deviates from the ideal Lorentzian lineshape. While the widths of the reflection lines are more or
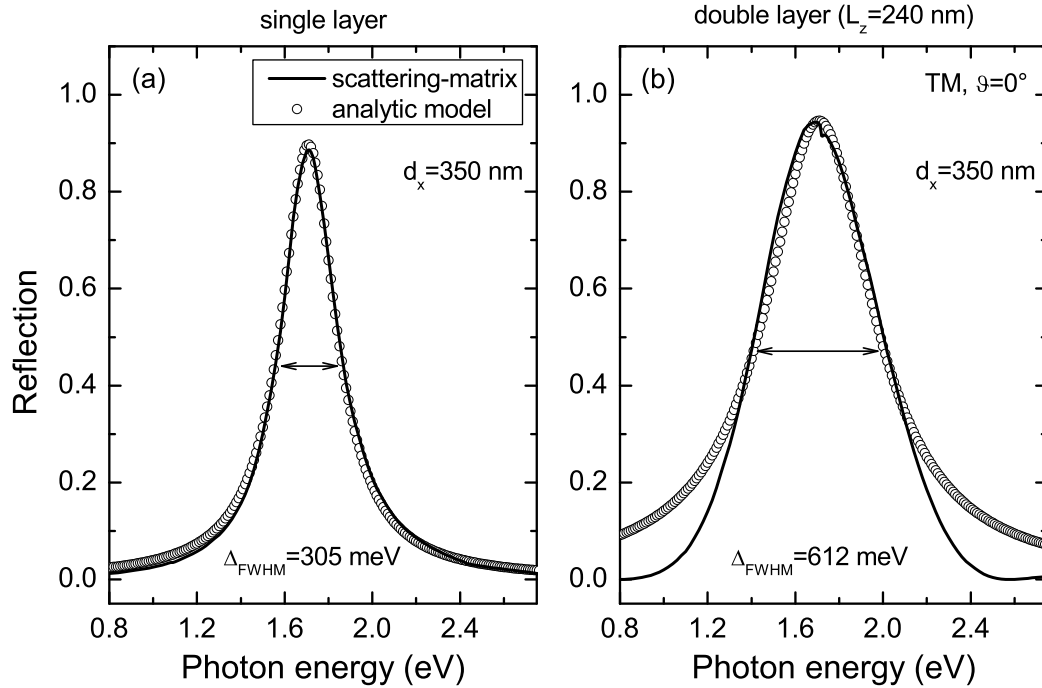
Figure 6.21:   Calculated reflection spectra of single (a) and double layer (b) grating structures are displayed for normal incidence ($\vartheta = 0°$) and TM polarization. Spectra for nanowire arrays with a period of 350 nm are shown. A spacer layer thickness of $L_z = 240$ nm has been used for the calculations in panel (b). The scattering-matrix-based spectra (solid line) are compared with results of the analytic model (circles).

less identical, it seems that the high and low energy tails of the Lorentzian line are suppressed in the results of the numerical calculations. The analytical model predicts a spectral bandwidth of $\Delta_{FWHM} = 594$ meV which is slightly smaller as the width of $\Delta_{FWHM} = 612$ meV extracted from the numerically obtained spectrum.

Although the superradiant picture might be reasonable, further studies of the metal nanowire-based system have to clarify two major points. For example, the background reflectivity is generally neglected in most studies on multiple-quantum-well-based structures [221, 222]. Thus, the barrier and the quantum well material are assumed to have an identical background dielectric constant. Although this approximation might be possible in case of semiconductor systems, the effect has to be included in more detailed studies of the metallic structures. The optical properties are usually determined by an interplay between interface reflection and resonant light-plasmon interaction. For example, the Fano

nature and the resulting strongly asymmetric lineshapes complicate the interpretation of the linear optical response. Another directly related phenomenon is well known from the semiconductor-based systems. Especially the finite thickness of the cladding layers (i.e., reflection from the semiconductor-air interface) has to be taken into account [204, 207]. Although this effect has been excluded in the presented scattering-matrix based calculations due to the specific sample geometry (infinite thickness of the cladding layers), it should not be ignored in future experimental studies. However, a very important further discrepancy between the metallic and the semiconductor-based realization arises from the strong difference of the characteristic decay times of the involved dipolar excitations. Superradiant coupling and the enhanced radiative decay is a coherent process, i.e., possible retardation effects have to be taken into account. While retardation effects can be nearly neglected in studies of quantum-well structures in the small N limit, they may become relevant for metal nanowire-based Bragg structures even in the considered double layer geometry. Especially the short plasmon lifetimes of only a few fs are a very critical and limiting parameter. For example, a homogeneous linewidth of 305 meV has been extracted from the numerically obtained reflection spectrum of the silver nanowire grating with a period of $d_x = 350$ nm. This theoretically determined value corresponds to plasmon decay time $T_2 = 2\hbar/\Gamma_{hom} = \hbar/\gamma$ of approximately 4.3 fs. Thus, the characteristic coherence length approaches 1.3 μm which is already very close to the considered spacer layer thicknesses.

(ii) Anti-Bragg spacing

In addition to the discussed Bragg structures, so-called anti-Bragg structures (i.e., the quantum well spacing is equal to a quarter of the wavelength of light at the exciton frequency) have been investigated both theoretically [218] and experimentally [186, 219] in the semiconductor case. Contrarily to Bragg spacing, all N coupled modes of the multiple-quantum-well system are optically active under these specific conditions. Thus, two distinct modes can be observed in case of a quantum-well pair structure [205]. In a classical picture, when considering the coupling between two harmonic oscillators, the splitting might be interpreted in terms of normal mode formation (i.e., the coupled oscillator system can be described by its symmetric and antisymmetric normal modes).

A similar behavior, i.e., a distinct splitting into two normal modes should also be observable in case of anti-Bragg spaced nanowire pair structures. The anti-Bragg condition requires a spacer layer thickness close to $L_z = 120$ nm. To
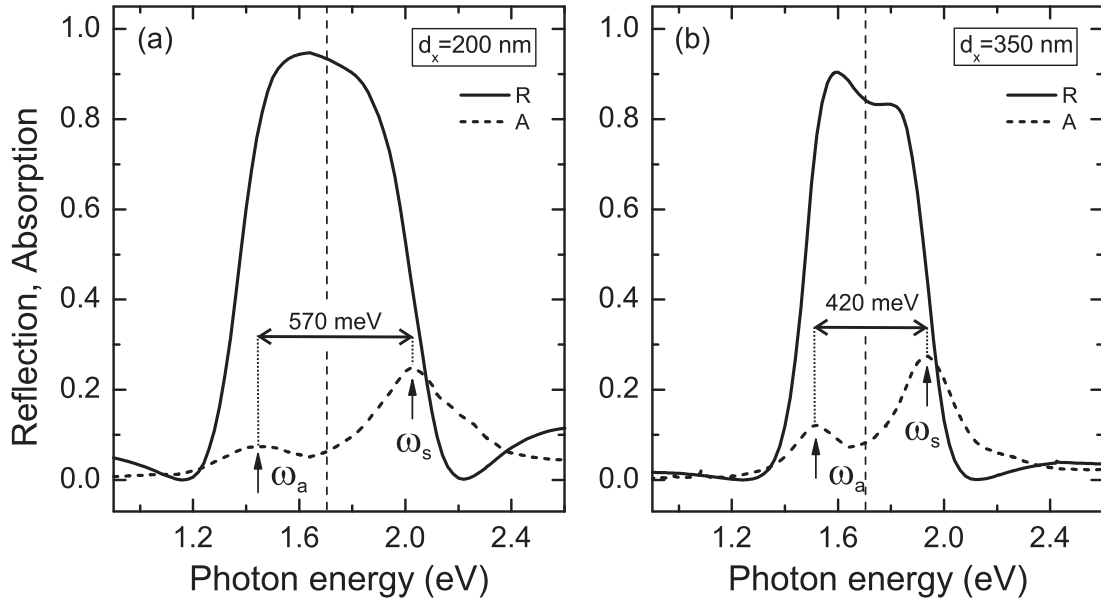
Figure 6.22:   Calculated reflection (R) and absorption (A) spectra of nanowire pair structures are displayed for normal light incidence and TM polarization. The chosen spacer layer thickness of 120 nm corresponds to an anti-Bragg spacing of the nanowires. Spectra for periods of $d_x = 200$ nm (a) and $d_x = 350$ nm (b) are shown.

highlight the main phenomena, the numerically obtained reflection and absorption spectra of the anti-Bragg structures [4] are displayed in Fig. 6.22 for two different nanowire periods. In particular, the panels allow a direct comparison of the spectra for structures with a nanowire period of $d_x = 200$ nm and $d_x = 350$ nm. Note that the displayed spectra have been extracted form Fig. 6.3 and Fig. 6.20, respectively. In contrast to structures with Bragg-spaced grating layers, distinct absorption maxima can now be found. For example, both absorption spectra of Fig. 6.22 are characterized by two pronounced maxima which is in turn a direct indication of the expected mode splitting. Due to the fact that the upper mode ω_s emerges from the subradiant mode (e.g., see Figs. 6.3 and 6.20), the mode is symmetric in nature, i.e., the nanowires of the individual layers are characterized by an in-phase oscillation of their conduction band electrons. On the other hand, the superradiant mode is transferred into the lower second mode ω_a. The mode is antisymmetric which means that the plasmon oscillations of the facing wires show a phase shift of π. As already discussed in Ref. [205] for the semiconductor-based systems, the splitting of the modes should be directly

---

[4]We will refer to this structrese as anti-Bragg structures although the spacer layer thickness may slightly deviate from the exact condition.

proportional to the nonradiative decay rate Γ_0. A similar behavior can be deduced form Fig. 6.22. While a splitting of 420 meV can be extracted from the calculated spectrum in panel (b), the value is increased to 570 meV in case of the short-period structures due the shortened radiative decay times. Simultaneously, a clear broadening of the absorption maxima can be observed in panel (a). This additional phenomenon is also directly related to the enhanced radiative width of the single layer plasmon resonances. It is further important to remark that also the shape of the reflectivity stop band is significantly modified. Instead of a single broad maximum in panel (a), two reflection peaks are clearly resolvable for structures with a period of $d_x = 350$ nm. The observed reflection bands are formed from two closely spaced reflection maxima which are related to the normal modes of opposite symmetry. As displayed in panel (a) of Fig. 6.22, the mode splitting cannot be resolved in the reflection spectra due to the enhanced spectral width of the individual resonances. Only in panel (b), two distinct maxima can be observed as a result of the line narrowing.

Further detailed studies have to clarify to which extend near-field interaction already influences the spectra in case of anti-Bragg spaced wire pair structures. While the discussed splitting phenomena can be explained in terms of radiative coupling in a first approximation (similar to multi-quantum-well-based structures), arising near-field effects have to be taken into account. For example, starting from a nanowire separation of $L_z \approx 100$ nm, quasistatic dipole-dipole interaction has to be considered as the dominate coupling mechanism.

6.3.4   Further investigations

An interesting extension to the spectral studies of coupling in closely spaced metal nanowire pairs might be the investigation of their light emitting capabilities. Generally, the emission of light from metal-insulator-metal (MIM) tunnel junctions was first reported by Lambe and McCarthy in 1976 [237]. It was shown that the fabricated Ag-Al_2O_3-Al multilayer structures emit light under appropriate bias voltage in the visible range. Scattering of surface plasmon polaritons at the roughened top metal electrode has been identified as the main mechanism. More precisely, the emission of light is caused by the radiative decay of surface plasmons excited by electrons tunneling through the insulating barrier that separates the two metal electrodes. Typically, 10^{-5} photons per tunnel-injected electron were observed. Since the first observations, different structures have been investigated. In addition of the usage of rough metal electrodes (e.g., see Ref [238]),
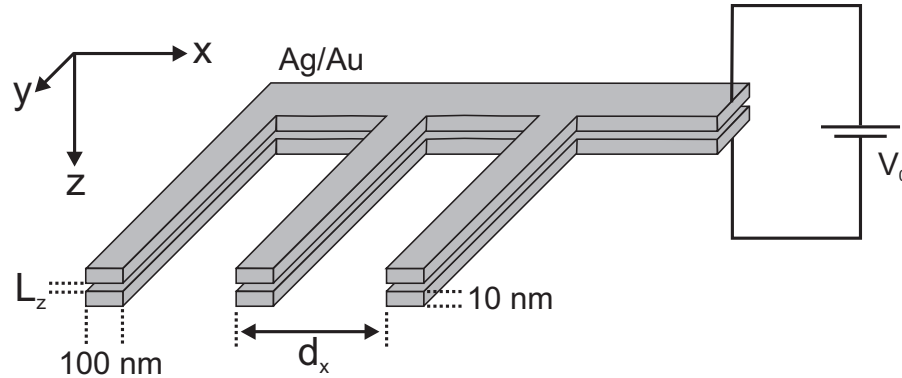
Figure 6.23: Schematic view of the proposed metal-oxide-metal tunnel junction. The two identical nanowire arrays are separated from each other by a thin oxide layer of thickness L_z. V_0 denotes the externally applied junction bias voltage.

also the influence of surface gratings [239] and small metal particles have been investigated [240].

The proposed design of the metal-insulator-metal tunnel junction is displayed schematically in Fig. 6.23. Two metal nanowire gratings are separated from each other by an insulating spacer layer. The dielectric spacer layer has to ensure a high electron tunnelling probability, which implies a layer thickness of approximately $L_z = 5$ nm. In these structures light is supposed to couple out from the localized plasmon modes of the bilayer nanowire system.

6.4   Plasmonic Bragg structures

As discussed in the previous section, the optical response of interacting silver nanowire pairs shows a strong dependence on the chosen nanowire-nanowire spacing L_z. The clear signature of both near- as well as far-field induced coupling effects can be found in the theoretically obtained spectra of the metallo-dielectric composite structures. Additional remarkable optical phenomena can be studied when extending the analysis to multilayer structures which incorporate more than two individual nanowire layers. Fundamental light-matter interaction effects can be highlighted when assuming a stacked multilayer structure based on Bragg-spaced nanowire arrays. Such a periodic metal nanowire structure can be described as an optically active or resonant photonic crystal design. Especially the strong frequency dispersion of the dielectric constants due to particle plasmon excitation might be useful to extend common band gap engineering possibilities.

However, before resuming with the discussion of the proposed resonant photonic crystal geometry, the optical properties of more common metallo-dielectric band gap structures are shortly reviewed for the sake of completeness.

6.4.1 One-dimensional metallic photonic crystals

The simplest possible photonic crystal design is a one-dimensional periodic multilayer geometry [2]. The stack structure generally consists of alternating layers of materials with different dielectric permittivity (i.e., alternating high and low index materials form a quarter-wave stack). Such structures, also known as dielectric Bragg mirrors, are characterized by large frequency gaps. Light propagation is not possible within these stopbands, thus, leading to an enhanced and nearly complete reflection over a certain frequency range. A very interesting extension of these purely dielectric photonic crystals are the recently proposed one-dimensional metallo-dielectric band gap structures. Alternatively, the layered periodic structures are now composed of thin metal films which are separated from each other by dielectric spacer layers. The optical properties of these structures reveal several important phenomena. For example, it has been shown that the reflectivity of metallic structures can be enhanced with respect to bulk if the metal is arranged to form a periodic structure. Theoretically, the reflection of bulk aluminum can be enhanced from 95% to approximately 98% over a narrow frequency range [241]. Other works reveal that metallic multilayer stacks can be made nearly transparent in the visible region [223, 224], even if the total metal thickness is increased to several tens of skin-depths. Similar to periodic structures built from thin metal wires [242], it has been further proposed that one-dimensional metallo-dielectric photonic crystals might be interpreted in terms of an effective metallic medium with a well-defined effective plasma frequency [243].

Exemplarily, scattering-matrix-based transmission and reflection spectra of a metallic multilayer structure are displayed in Fig. 6.24 to highlight some of the fundamental optical phenomena. As shown by the schematic drawing in the right panel of the figure, the considered structure consists of ten stacked silver layers. The individual silver films exhibit a thickness of 10 nm and are separated from each other by a SiO_2 spacer layer. From top to bottom, the spacer layer thickness L_z is reduced from 320 nm to 0 nm in both panels. The lowest spectra of the 100-nm-thick metal layer might be considered as a reference. All spectra are shown for normal light incidence. As expected, the transmission and reflection spectra are strongly modified when increasing the spacer layer thickness. The
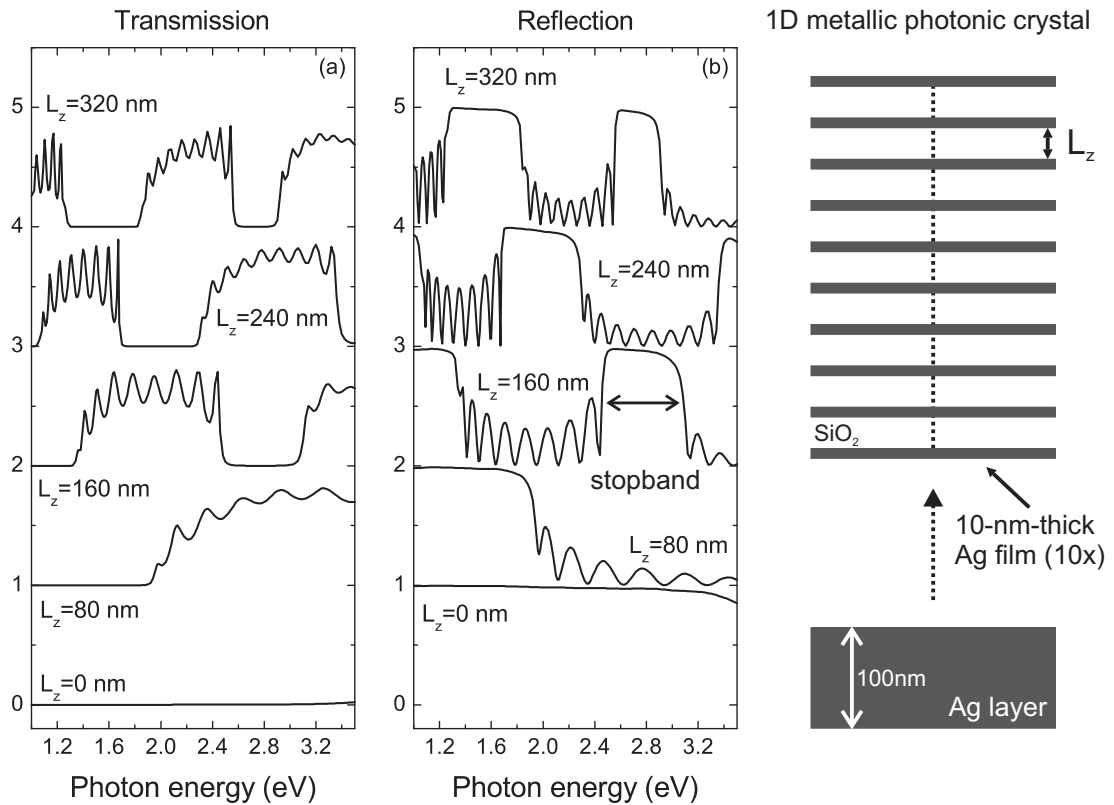
Figure 6.24:   Calculated transmission (a) and reflection (b) spectra of a one-dimensional metallic photonic crystal are displayed. As schematically shown, the multilayer structure consists of ten stacked silver films (right panel). The individual silver films exhibit a thickness of 10 nm. From top to bottom, the dielectric (SiO_2) spacer layer thickness L_z is reduced from 320 nm to 0 nm. All spectra are shown for normal light incidence. The arrow in panel (b) indicates the stopband width of approximately 620 meV.

spectra for the sturture with vanishing spacer layer resemble the characteristic properties of bulk silver. The 100-nm-thick silver layer is nearly opaque and almost full reflection of an incident radiation field can be achieved over the displayed spectral region. The optical response changes drastically when switching to the multilayer design. While the sandwiched structures maintain their reflectivity properties for low-frequency radiation, transparency regions appear over a tunable range of frequencies. In dependence on the spacer layer thickness, high transmission for ultraviolet or optical frequencies can be achieved. The transparency regions, which allow light to propagation almost unattenuated, are interrupted by large photonic stopbands. For example, the lowest stopband for structures with a spacer layer thickness of $L_z = 160$ nm exhibits a bandwidth of

approximately 620 meV [indicated by an arrow in panel (b) of Fig. 6.24]. The appearing stopbands as well as the onset of the lowest pass band show a strong spacer layer dependence. Increasing (decreasing) the thickness of the dielectric material cause a shift of the band structure towards longer (shorter) wavelengths.

In order to provide some physical insight, it might be very reasonable considering a metallic Fabry-Perot cavity in a first step. Assuming a system of only two metallic layers which are separated by a dielectric spacer of thickness L_z, the cavity modes can be simply derived as

$$\omega_m = m \frac{\pi c}{n_{sp}(L_z + 2\delta)}, \tag{6.8}$$

where δ is the penetration depth of the electromagnetic fields into the metallic layers and n_{sp} is the refractive index of the spacer layer material. The parameter m specifies the order of the cavity mode ($m = 1, 2, 3, ...$). The individual cavity modes generally induce dips in the reflection spectrum due to resonantly enhanced transmission. Light which is directly transmitted through the structure interferes constructively with the scattered radiation fields. The cavity roundtrip generally implies a phase shift equal to an integral multiple of 2π which results in a lowest order mode with a single electric field maximum (antinode) between both metal mirrors. However, the distinct transparency regions can be stepwise increased by adding further metal layers. Thus, multiple scattering directly results in additional resonances (i.e. transmission eigenmodes) which show up in the spectra of the structure. Only in the limit of an infinitely extended multi-layer stack, the closely spaced resonances form so-called pass bands which are spectrally separated from each other by the arising stopbands. Now it becomes more convenient to interpret the optical response in terms of a one-dimensional band structure. Note that the theoretical spectra in Fig. 6.24 clearly indicate the finite height of the considered multilayer stack. Although the stopbands are already strongly pronounced, especially the transparency regions are characterized by distinct modulations. The observed oscillatory behavior of the transmissivity (reflectivity) directly reflects the finite number of supported modes.

Further important properties can be extracted from the displayed reflection spectra. The shape of the arising stopbands shows a clear asymmetry. The reflectivity on the low energy side of the individual stopbands is enhanced, leading to a more square-like shape of the lower band edge. The observable asymmetric shape of the stopbands can be easily explained when considering the specific wave function of the band edge states. Generally, reflection from a photonic crystal stopband produces a phase change between π and zero [244]. The photon wave functions of
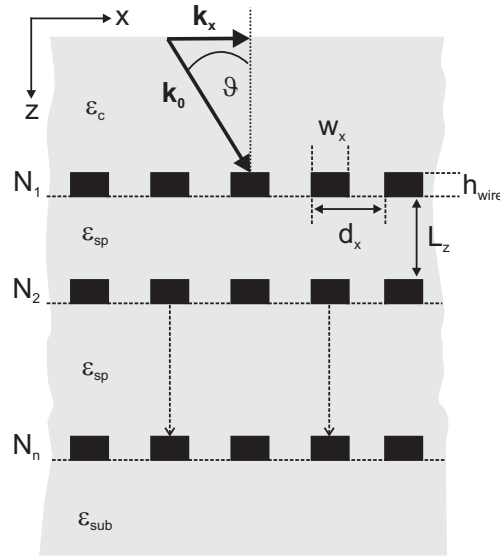
Figure 6.25:   Schematic view of the proposed one-dimensional plasmonic Bragg structure. Periodic metal nanowire arrays are separated from each other by dielectric spacer layers. The dependence on the spacer layer thickness L_z as well as the influence of the number of grating layers $(N_1,...,N_n)$ have been investigated theoretically.

the two band edge states are standing waves, respectively. At the bottom of the stopband, the nodes of the standing wave (electric field) are localized at the metal planes (i.e., π phase change on reflection). This means that the overlap between the metal layers and the electric field is minimized and the absorption is small. As a result, the reflectivity is correspondingly high. The situation is inverted at the upper band edge. Now the nodes of the wave lie between the metal layers (i.e., zero phase change on reflection). The maximized overlap between metal and electric field results in large absorption and a correspondingly reduced reflectivity. Note that the addressed electric field mode profiles directly indicate the origin of the photonic stopbands. As discussed, there are two ways to center a standing wave within the multilayer stack without violating symmetry. Therefore, the frequency difference of the band edge states and the opening of the related stopband can be understood when taking into account the differences in field energy concentration. In other words, the frequency of the wave depends on how many field energy is located within the metallic parts of the stacked structure.

6.4.2   Plasmonic bandgap

The optical properties of the proposed resonant metallo-dielectric photonic crystal structure will be studied in the following section. In contrast to the discussed multilayer geometry in Sec. 6.4.1 (i.e., multilayer structure built of stacked homogeneous metal films), the grating-based structures provide an alternative approach to the design of a one-dimensional photonic crystal. The resonant (i.e., dipole active) structure is a very important geometry due to the fact that its optical properties are not only determined by the refractive index contrast of the constituent materials. Generally, an interplay between interface scattering and resonant light-plasmon interaction has to be taken into account in case of active structures (e.g., see Ref. [222]). In some respects, the plasmonic crystal structure can be considered as a direct analog of a so-called optical lattice. An optical lattice usually constitutes a specific form of matter in which atoms are located at periodic sites separated on the scale of the optical wavelength [245]. However, especially the semiconductor-based realization of optical lattices has attracted remarkable interest in recent years. Instead of using single atoms as an elementary building block, excitonic resonances are utilized. For example, the optical properties of the well-known multiple-quantum-well structures are determined by radiative coupling between quantum confined excitons [110, 234].

The proposed resonant sample design is schematically displayed in Fig. 6.25. The one-dimensional resonant photonic crystal consists of regular metal nanowire arrays with a lateral period of $d_x = 200$ nm, which are separated by a dielectric spacer layer of thickness L_z, respectively. In contrast to Fig. 6.1, the numerical calculations are now expanded to grating stacks with up to 10 individual nanowire layers. The investigations will be focused on Bragg periodic structures, i.e., the silver nanowires exhibit a vertical center to center distance that corresponds to the half wavelength of light at the plasmon resonance frequency. Similar to the previous calculations, silver nanowires with a cross-sections of 100×10 nm^2 have been taken into account. Quartz with a constant permittivity of $\varepsilon_{quartz} = 2.13$ is chosen as substrate (ε_{sub}), spacer (ε_{sp}), and cap layer material (ε_c).

The linear optical response of the Bragg-coupled silver nanowire arrays ($L_z = 240$ nm) is highlighted in Fig. 6.26 in dependence on the number of stacked grating layers. The calculated transmission (a), reflection (b), and absorption (c) spectra are displayed for normal light incidence ($\vartheta = 0°$) and TM polarization, respectively. Starting from the single layer structure (lowest spectra in Fig. 6.26), the number of grating layers (N_n) is increased stepwise until the maximum stack-
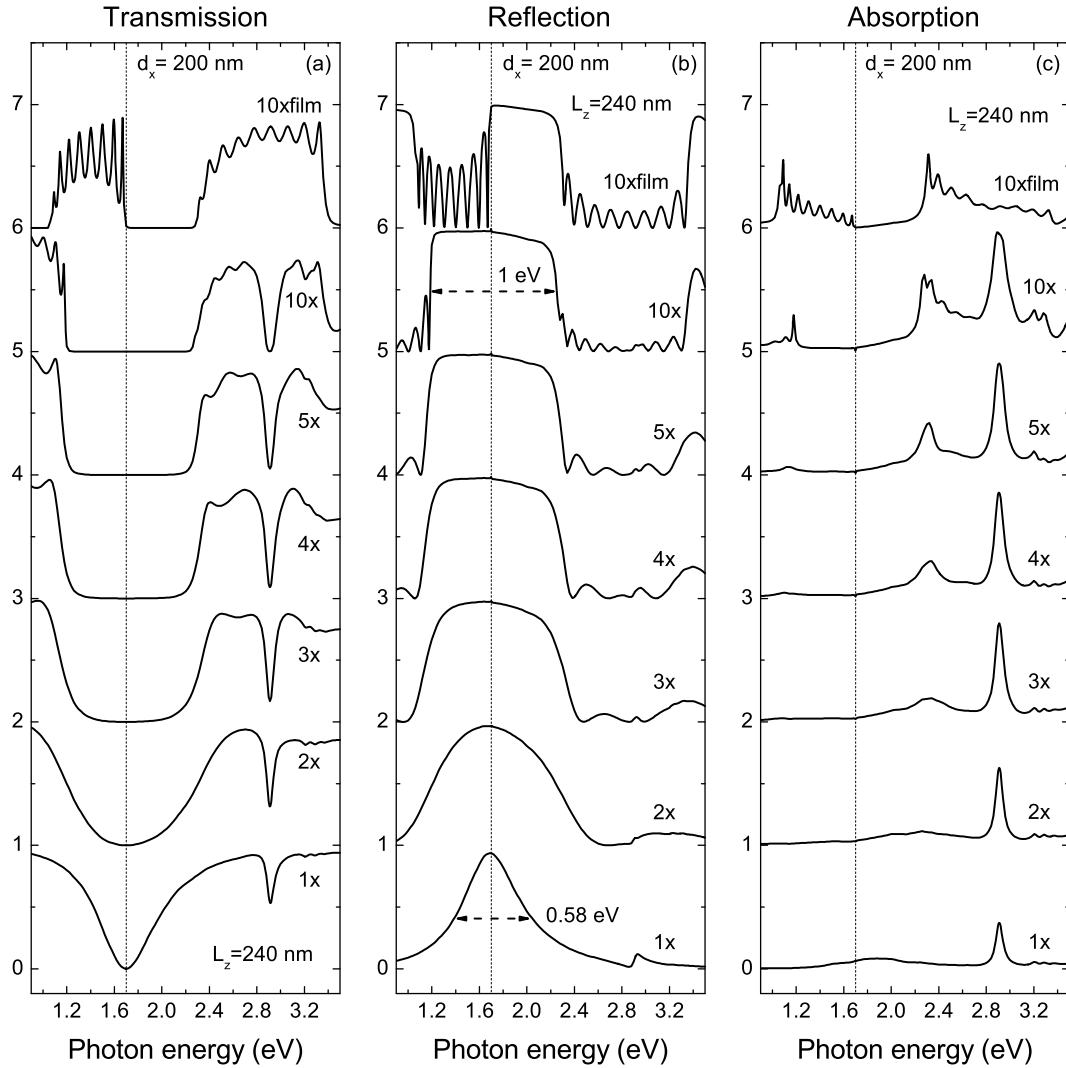
Figure 6.26: Calculated transmission (a), reflection (b), and absorption (c) spectra of Bragg coupled sivler nanowire arrays at normal incidence ($\vartheta = 0°$) and TM polarization. From bottom to top, the number N_n of grating layers is increased stepwise. The individual nanowire arrays exhibit a period of $d_x = 200$ nm and are separated by a quartz spacer layer of thickness $L_z = 240$ nm. Additionally, also the calculated spectra of a one-dimensional stack of silver films with an identical spacing of 240 nm are displayed as a reference (last spectrum in each panel, 10xfilm). The individual spectra are shifted upwards for clarity in each panel. The position of the particle plasmon resonance for uncoupled silver nanowires is marked by a dotted vertical line in all three panels (1.7 eV).

ing height of 10 layers is reached. In addition to the results of the resonant Bragg structures (periodic arrangement of nanowire arrays), the spectra of an identical

silver film structure are shown as a reference (upper spectra in Fig. 6.26). Instead of using regular nanowires arrays, homogeneous silver films with a vertical separation of 240 nm have been assumed for these calculations. The spectra of a ten-layer structure with an individual silver film thickness of 10 nm are displayed in each panel of Fig. 6.26 (labeled as 10xfilm).

The depicted spectra of the resonant photonic crystals in Fig. 6.26 reveal a clear dependence on the number of grating layers N_n. For example, the spectral bandwidth of the broad reflection maxima centered at 1.7 eV is further increased by adding additional nanowire layers. As marked by the arrows in panel (b), the full width at half maximum (FWHM) of the reflection peak at 1.7 eV raises from 0.58 eV (single layer structure, 1x) to approximately 1 eV (ten layer structure, 10x). Simultaneously, the spectral shape of the reflection peak is strongly modified. The Lorentzian-like line shape of the reflection peak changes to a more or less rectangular-shaped stopband in case of the ten layer geometry. The formation of the stopband is accompanied by distinct modifications of the related absorption spectra in panel (c). The absorption spectrum of the single layer structure shows one distinct peak at approximately 2.9 eV in addition to the less pronounced absorption of the nanowire plasmons. While the amplitude and the width of the upper resonance are slightly increased by adding additional grating layers, the lower second absorption maximum is simultaneously transferred into the arising band edge states. Generally, two more or less pronounced sidebands appear at the edges of the stopband. For example, the absorption spectrum exhibits one weaker maximum at 1.17 eV and a stronger second peak at 2.27 eV in case of the ten layer geometry (x10). A very important phenomenon can be extracted when the spectra of the grating structure are compared with the corresponding results of the silver film-based Bragg structure. Obviously, the calculated stopband of the film geometry exhibits a much smaller spectral bandwidth of approximately 0.6 eV. It is further noticeable that the lower band edge of the rectangular stopband directly matches the spectral position of the nanowire reflection maximum in the single layer case (marked by the vertical dotted lines in Fig. 6.26).

In order to get a qualitative understanding of the physical mechanism, it might be very instructive to compare the displayed linear spectra with equivalent results of a semiconductor-based system. As already mentioned, the direct analog to the considered plasmonic Bragg structures are the well explored multiple-quantum-well structures. In these prominent structures, the role of dipolar excitation is assigned to the quantum well excitons. Thus, instead of far-field interaction between nanowire plasmons, radiative coupling between excitons confined to the

respective quantum well layers has to be considered as the main interaction mechanism. The coupling is particularly important in case of Bragg spacing, i.e., when the quantum well spacing is equal to an integer multiple of half the wavelength of light at the exciton frequency. In these structures, the radiative interaction between excitons critically depends on the number N of the stacked quantum wells. For example, coupling has been interpreted in terms of a superradiant-like behavior in the small N limit [110]. It has been shown that the optical response of a set of N Bragg-coupled quantum wells is equivalent to a single quantum well with a N times amplified radiative coupling coefficient (i.e., N times broadening of the radiative linewidth). Only one normal mode is superradiant in character (bright mode), while all other $N-1$ modes are optically inactive, i.e., they can be considered as subradiant or dark modes [235]. However, the picture is no longer valid in case of long-period structures. The superradiant mode is transferred into a broad polaritonic stopband when the number of coupled quantum wells is continuously increased [219, 220, 246, 247]. Simultaneously, the reflectance and transmission line shapes clearly change from Lorentzian to Bragg-reflector-like. In the superlattice limit (i.e., infinitely long periodic structure), radiative interaction gives rise to a photonic band structure with a large polaritonic stopband in the vicinity of the bare exciton frequency. Light propagation in these structures is thus determined by exciton polariton formation [234]. Theoretically, it has been shown that the width of the arising one-dimensional band gap approaches

$$\Delta E_{gap} = 2\sqrt{2\hbar\omega_0\Gamma_0/\pi} \tag{6.9}$$

in the limit of a Bragg periodic superlattice ($N \to \infty$) [246, 248].

Although a more detailed analysis of the plasmonic Bragg structures might be necessary, their theoretical spectra in Fig. 6.26 generally correspond to similar results for the quantum well-based Bragg structures. The formation of a polaritonic band gap indicates that the light propagation in these plasmonic crystals has to be interpreted in terms of superlattice plasmon polaritons. For example, a clear broadening of the nanowire plasmon resonance at 1.7 eV can be observed in the calculated reflection and transmission spectra when increasing the number of grating layers. Simultaneously, more or less pronounced absorption peaks arise at both edges of the reflection band. Already a stacking of five (5x) identical grating arrays leads to the formation of a broad one-dimensional stopband in case of Bragg spacing, i.e., the reflectivity spectrum evolves into a silk-hat shape which is typical for a photonic band gap. This is a striking difference to quantum well-based Bragg structures, where a stacking of approximately 100 individual layers
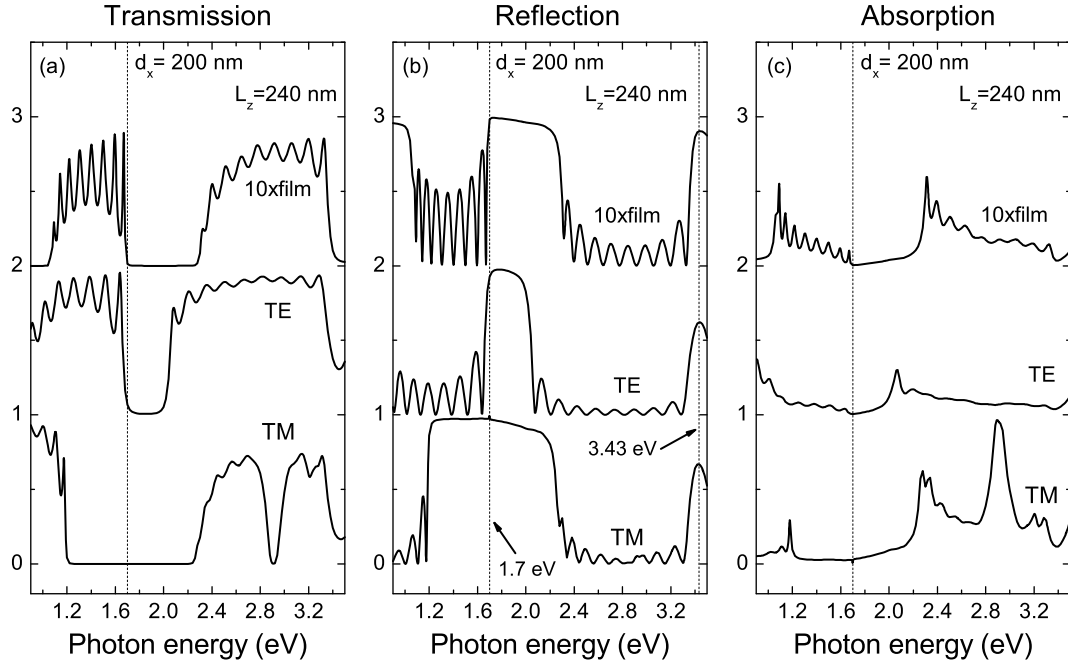
Figure 6.27: Calculated transmission (a), reflection (b), and absorption (c) spectra of Bragg coupled silver nanowire arrays are shown for TE and TM polarization ($\vartheta = 0°$). The individual nanowire arrays exhibit a period of $d_x = 200$ nm and are separated by a quartz spacer layer of thickness $L_z = 240$ nm. Additionally, also the calculated spectra of a one-dimensional stack of silver films with an identical spacing of 240 nm are displayed as a reference (10xfilm). The individual spectra are shifted upwards for clarity in each panel. The approximate position of the particle plasmon resonance for uncoupled silver nanowires is marked by a dotted vertical line in all three panels (1.7 eV).

is necessary to exceed the superradiant regime and to observe similar saturation effects. On the other hand, the nanowire-based Bragg structures already show a non-Lorentzian line shape in the reflection spectra of the double layer structure. Strictly speaking, although a superradiant-like broadening can be observed for the double layer structure, the N dependence of the radiative decay times is not fulfilled in case of the considered high density (i.e., short-period) multilayer nanowire arrays. Further studies have to clarify to which extend retardation effects and the large background reflectivity of the wire gratings influence the observed interaction phenomena.

Exemplarily, the strong background reflectivity of the grating layers can be visualized in case of TE polarization. Due to the one-dimensional design of the used dipole active layers (i.e., silver nanowires), plasmon excitation can be pre-

vented by simply turning the light polarization. The obtained theoretical results are highlighted in Fig. 6.27. The figure displays calculated transmission (a), reflection (b), and absorption (c) spectra of Bragg coupled silver nanowire arrays for TE and TM polarization. The individual nanowire arrays of the ten-layer structure are again arranged with a period of 200 nm. The calculated spectra of a one-dimensional stack of silver films with an identical spacing of 240 nm are displayed as a reference. Although any plasmonic effects are switched off in TE polarization, a small stopband can be observed in case of the considered grating structures. Similar to the displayed film structures, interface scattering generally leads to the formation of a one-dimensional band structure. Due to the fact that the lower band edge mode is a standing wave with nodes at the grating layers, its spectral position is not changed in comparison to the film-based structure. Only the upper band edge is lowered in energy as a result of the modified overlap between the electric field and the metallic parts of the structure. In particular, the optical response in TE polarization can be easily interpreted in terms of an effective medium approach. The individual metal layers can be replaced by homogeneous films with an adapted effective permittivity. Note that also the lower band edge of the second order stopband can be clearly observed in all displayed reflection spectra of Fig. 6.27. Due to the fact that no plasmon resonances are involved in the gap formation, its lower band edge energy does neither depend on the specific design of the considered metallic layer (i.e., grating or homogeneous film) nor on the chosen light polarization. The onset of the second stopband is indicated by a dotted vertical line at 3.43 eV.

A further fundamental phenomenon is directly related to the nanowire period of the multilayer Bragg structure. In contrast to quantum well-based Bragg structures, this important parameter provides an additional degree of freedom. For example, the spatial density of dipole oscillators can be artificially controlled by changing the lateral nanowire spacing d_x. The strong influence of the nanowire period on the spectral response is theoretically demonstrated in Fig. 6.28. Calculated transmission (a), reflection (b), and absorption (c) spectra of coupled silver nanowire arrays are displayed for two different nanowire periods. Results for a ten-layer grating structure are shown for periods of $d_x = 200$ nm and $d_x = 350$ nm, respectively. Identical nanowire cross-sections of 100×10 nm^2 have been assumed. It is clearly observable that the nanowire density directly affects the width of the induced stopband. In particular, its bandwidth is reduced by 200 meV when increasing the period from 200 nm to 350 nm. Simultaneously, as can be seen from the insets in panel (c), also the shape of the reflection band is
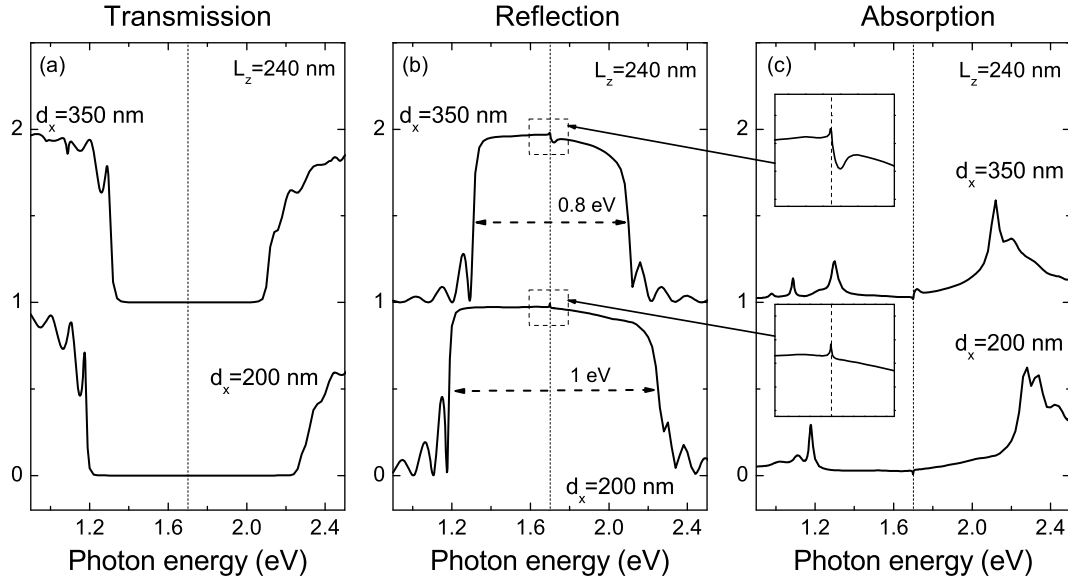
Figure 6.28: Calculated transmission (a), reflection (b), and absorption (c) spectra of coupled silver nanowire arrays in TM polarization ($\vartheta = 0°$). Results for a ten-layer grating structure are shown for periods of $d_x = 200$ nm and $d_x = 350$ nm, respectively. The individual nanowire arrays are separated by a quartz spacer layer of thickness $L_z = 240$ nm. The individual spectra are shifted upwards for clarity in each panel. The approximate position of the particle plasmon resonance for uncoupled silver nanowires is marked by a dotted vertical line in all three panels (1.7 eV). The two insets in panel (c) allow a magnified view on the center of the reflection band.

slightly modified close to its center. A small dip (peak) appears near the center of the reflection (absorption) spectrum for structures with a grating period of $d_x = 350$ nm.

The observed stopband shrinking might be directly related to the period dependent radiative decay rate of the particle plasmons. In case of single layer structures, the arising dipole-dipole interaction between the adjacent silver nanowires leads to a spectral broadening of the plasmon resonances when reducing the nanowire period d_x. This effect directly modifies the spectral width of the stopband in case of stacked Bragg structures with an increased nanowire density. When the influence of the background reflectivity is neglected in a first approximation, the width of the stopband can be estimated by applying relation 6.9. For example, our previous studies (e.g., see discussion of the double layer Bragg structures) have shown that a nanowire period of 350 nm leads to a radiative decay rate of approximately $\Gamma_0 = 144.5$ meV in case of single layer grating struc-

tures. Using relation 6.9 and a plasmon energy of $\hbar\omega_0 = 1.74$ eV, a stopband with a spectral width of $\Delta E_{gap} = 790$ meV should built up in the superlattice limit. Surprisingly, this result is very close to the value of 800 meV extracted from the scattering-matrix-based calculations.

Additionally, as already presented in Sec. 6.3, the near-filed interaction between closely spaced nanowires induces spectral shifts of the plasmon resonances. This important effect results in a period (d_x) dependent Bragg condition. For example, while the exact Bragg condition is fulfilled in case of $d_x = 200$ nm, the effect of a slight detuning can be clearly observed for the structure with an increased nanowire period of $d_x = 350$ nm. As displayed by the upper inset of Fig. 6.28, the formerly subradiant polariton modes show up as a weakly pronounced dip close to the center of the reflection band when increasing the nanowire periodicity.

6.4.3   Influence of the spacer layer thickness

Furthermore, additional calculations for slightly detuned Bragg structures have been performed to probe the influence of the vertical nanowire spacing L_z in case of multilayer structures. The calculated transmission (a), reflection (b), and absorption (c) spectra for a five-layer nanowire geometry are displayed in Fig. 6.29. All spectra are shown for normal light incidence ($\vartheta = 0°$) and TM polarization, respectively. From top to bottom, the vertical separation between the individual grating layers is decreased from $L_z = 300$ nm to $L_z = 160$ nm in steps of 20 nm.

Fig. 6.29 clearly demonstrates that only the calculated reflection and transmission spectra of the Bragg structures ($L_z = 240$ nm) exhibit the characteristic stopband signature. For slight detunings, additional features appear in the shown spectra. For example, the reflection spectra are characterized by sharp minima, which arise close to the center of the stopband (1.7 eV). These minima shift to higher (lower) energies when decreasing (increasing) the vertical nanowire separation. Simultaneously, the spectral features are broadened until distinct reflection minima can be resolved. The calculated reflection minima are directly related to peaks in the corresponding transmission and absorption spectra, respectively. Note that also the upper and lower boundaries of the stopband are slightly shifted in dependence of the spacer layer thickness.

The depicted spectral behavior again resembles the known spacer layer dependent optical response of multiple-quantum-well Bragg structures [219, 220, 246, 249].
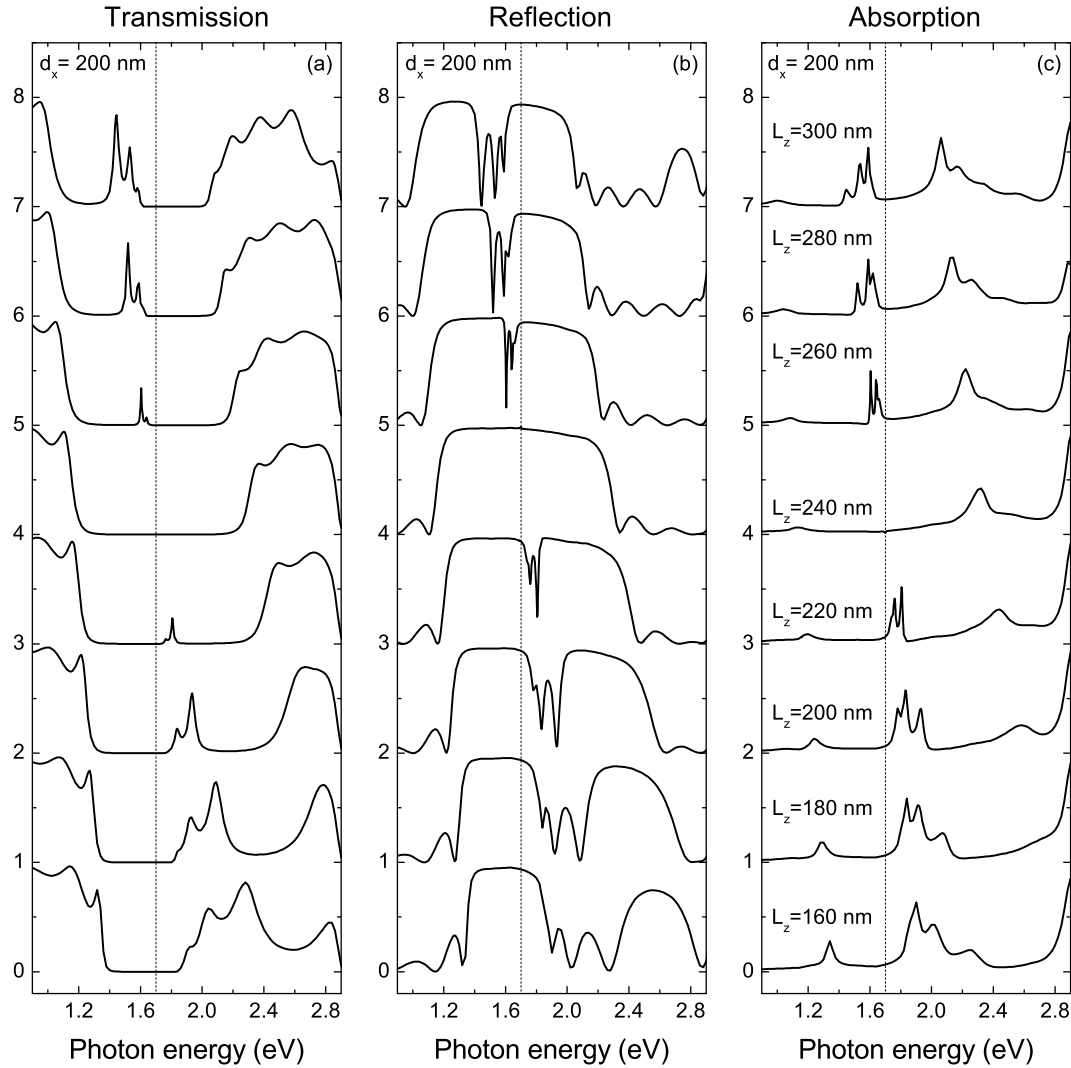
Figure 6.29: Calculated transmission (a), reflection (b), and absorption (c) spectra of a structure with five coupled silver nanowire arrays at normal incidence ($\vartheta = 0°$) and TM polarization. The individual nanowire arrays exhibit a period of $d_x = 200$ nm. From top to bottom, the distance between the grating layers is decreased from $L_z = 300$ nm to $L_z = 160$ nm in steps of 20 nm. The individual spectra are shifted upwards for clarity. The position of the particle plasmon resonance for uncoupled silver nanowires is marked by a dotted vertical line in all three panels (1.7 eV).

When the system of stacked dipole active layers is detuned from the Bragg resonance, a transparency window appears within the band gap. While in case of Bragg spacing only the photonic band gap modes are seen, all other modes become optically active for slight detunings from the exact Bragg condition.

6.5   Conclusions

In conclusion, we have shown theoretically that the optical response of inter-
acting silver nanowire ensembles strongly differs from the single nanowire case.
More precisely, the presented scattering-matrix-based calculations reveal the ex-
istence of coupled plasmon modes which give rise to several interesting effects.
The light-matter interaction in such systems depends on the specific geometry of
the structures and can be controllably modified. The analysis shows that espe-
cially the considered silver nanowire pair structures represent a very fundamental
model system. Both the influence of near- as well as far-field interaction phe-
nomena have been studied in dependence on the vertical nanowire separation.
In contrast to planar nanowire structures, the orthogonal normal modes can be
excited as a result of the interaction with a retarded electromagnetic field. For
example, the near-field interaction between closely spaced nanowires leads to a
remarkable splitting of the degenerated plasmon resonances. Two plasmon po-
lariton modes of different symmetry can be observed in the spectra for closely
spaced silver nanowires. Calculations of the spatial near-field distribution show
that the appearing upper plasmon polariton mode corresponds to in-phase os-
cillations of the conduction band electrons in the adjacent nanowires (parallel
currents). The lower polariton mode on the other hand is related to out-of-phase
oscillations (anti-parallel currents). The spectral splitting between the plasmon
modes, i.e., the coupling efficiency depends on the spacer layer thickness. In par-
ticular, a nanowire separation of $L_z = 20$ nm results in a normal mode splitting
of nearly 840 meV. For larger vertical nanowire separations, i.e, when exceeding
the near-field regime, the optical response is dominated by far-field effects. In
the special case of Bragg spacing, radiative coupling leads to superradiant-like
phenomena. The plasmon decay time of the coupled nanowire pairs is shortened
in comparison to the single wire case. Additionally, cavity-polariton-like modes
can be observed. The spectral position as well as the linewidth of these modes
show a strong depependence on the specific spacer layer thickness. In addition
to silver nanowire pair structures, also stacked multilayer structures have been
investigated in the last section. The optical response of a nanowire ensemble is
strongly modified when the number of grating layers is increased. Sample struc-
tures with a stacking height of up to ten layers have been analyzed theoretically.
The numerical calculations give clear evidence for the formation of a broad polari-
tonic stopband in case of Bragg spaced nanowire arrays. Remarkably, a spectral
bandwidth of approximately 1 eV can be observed in case of a ten layer geom-

etry. In contrast to photonic crystals which are build from dielectric materials with frequency independent permittivities, light-plasmon interaction has to be taken into account.

Chapter 7

Conclusion

This chapter summarizes the work presented in this thesis and gives a short
outlook on possible future research activities.

7.1 Summary

The linear optical properties of metallic photonic crystal structures are analyzed
both theoretically and experimentally. In contrast to investigations on purely
passive structures, all presented studies focus on so-called resonant or active pho-
tonic crystals. In these prominent structures the periodic modulation of the
dielectric constant is accompanied by the presence of an additional internal elec-
tronic excitation. The detailed studies show that especially metal nanowire-based
photonic crystals represent well-defined model systems which allow the investi-
gation of fundamental light-matter interaction phenomena. The metal nanowires
are generally characterized by their ability to support localized particle plasmon
resonances at optical frequencies. These resonances are related to collective os-
cillations of the conduction band electrons which can be excited by an external
radiation field. It is well-known that the lifetime and the spectral position of the
particle plasmon resonances are directly determined by the geometry of the indi-
vidual metal wires (e.g., their cross-section). However, the appearance of various
coupling phenomena has to be taken into account when considering a photonic
crystal geometry, i.e., a periodic nanowire ensemble. Depending on the chosen
geometry, the arising near- as well as far-field interaction effects induce strong
modifications of the optical response in comparison to the single nanowire case.
In particular, three different nanowire-based geometries are studied to highlight

the extraordinary optical properties of such metallo-dielectric structures.

Metal nanowire-based photonic crystal slab structures are discussed in the first part of this thesis. The investigation of such planar designs is very favorable due to the utilization of common nanofabrication techniques. Standard electron-beam lithography is used for fabrication of metal nanowire gratings on top of thin dielectric slab layers with a high spatial resolution. Experimentally, the characterization of the structures is accomplished by probing the optical properties with linear spectroscopic methods. It turns out that especially the slab thickness is a very important geometrical parameter which determines the coupling effects. Metal nanowire arrays deposited on top of thin dielectric slab layers (15-nm-thick ITO films) show strong modifications of the supported particle plasmon resonances due to the opening of diffraction channels into the quartz substrate. As a result, so-called Rayleigh anomalies appear as cusp-like features within the plasmon resonances. Depending on the exact nanowire period, the diffractive anomalies induce strong lineshape modifications in comparison to the bare particle plasmon resonances. More dramatic changes are observed when increasing the slab layer thickness. Metal nanowire arrays on top of waveguiding layers (140-nm-thick ITO layers) act as grating coupler an allow the excitation of quasiguided slab modes. When the bare particle plasmon and the supported waveguide mode are tuned to resonance, strong coupling phenomena are induced. The strong coupling results in the formation of waveguide-plasmon polariton modes which are characterized by a polaritonic mode splitting of almost 250 meV. It is further shown that the observed interaction effects can be controlled by varying the nanowire period, the angle of incidence, or by introducing an additional dielectric spacer layer. In addition to the use of simply periodic structures, possible modifications due to the realization of a superlattice are discussed. By changing the nanowire arrangement, it is shown that the specific design of the individual supercells can be treated as an artificial form factor. Especially the nanowire periodicity is a very crucial parameter, which is further demonstrated by analyzing structures with distinct disorder. The introduction of structural disorder (i.e., spatial variation of the nanowire positions) results in a weakening of the observed coupling phenomena. The experimental analysis of the photonic crystal slab structures is generally supported by extensive theoretical studies. Scattering-matrix based numerical calculations show an excellent agrement with the measured optical response. The theoretical results are very impressive especially because the theory works without any fitting parameters. Only the exact geometrical parameters and the dielectric permittivity of the used materials are considered within the

numerical approach.

Due to the growing research efforts in the field of surface plasmon optics (sometimes referred to a plasmonics), it seems very promising to transfer the waveguide-plasmon polariton concept to a purely metallic photonic crystal slab structure. Instead of using a dielectric waveguide slab as substrate material, the metal nanowire arrays are therefore deposited in front of a thin metal film. This modified design makes use of surface plasmon polariton modes at the metal layer which replace the waveguide resonances. The thickness of the homogeneous metal film is chosen such that short- and long-range surface plasmon modes are supported. The experimental and theoretical studies in the second part of the thesis clearly reveal that the expected interaction phenomena and thus the optical response critically depend on the exact grating-film separation. In particular, the distance between the grating array and the underlying metal film has to be controlled by introducing a dielectric spacer layer during sample fabrication. Furthermore, the detailed investigation shows that three fundamental interaction phenomena have to be taken into account when interpreting the optical response of the proposed multilayer structure. First, a quasistatic dipole-dipole interaction between the individual nanowire plasmons and their images in the metal layer is observed. The near-field effect shows a strong dependence on the grating-film separation and induces a redshift of the particle plasmon resonances. Second, drastic modifications due to radiative coupling are found. Far-field interaction leads to modifications of the particle plasmon dephasing rates and induces pronounced frequency shifts. The dispersion of the particle plasmon related resonances might be interpreted in terms of cavity-polariton formation. Third, similar to the formation of waveguide-plasmon polaritons, coupling between the supported surface plasmon and particle plasmon related resonances can be observed. The related anticrossing behavior of the normal modes can be interpreted in terms of polariton formation. Although the coupling phenomena are mainly discussed on the basis of numerically obtained spectra, first experimental work is presented to highlight the capacity of the used theoretical approach.

The third part of the thesis resumes purely theoretical studies of a further modified multilayer structure. The proposed design incorporates two identical metal nanowire gratings which are separated by a thin dielectric spacer layer. Obviously, the structure can be considered as being a direct extension of the grating-film geometry. However, instead of an interaction between the particle plasmons and their own imagages, direct plasmon-plasmon interaction can be observed. The chosen nanowire pair design induces very fundamental optical effects which

may open up interesting further applications. More precisely, it is shown theoretically that both near- as well as far-field interaction effects lead to strong modifications of the optical response in comparison to the single layer grating structures. The near-field interaction, i.e., the quasistatic dipole-dipole interaction between the adjacent nanowires results in a splitting of the degenerated particle plasmon modes when using very thin spacer layers. Two normal modes of opposite symmetry can be observed in the calculated spectra. Especially the arising antisymmetric normal mode is of certain interest. The individual nanowire pairs resemble a so-called split-ring resonantor which leads to the formation of a magnetic resonance in the optical regime. The expected negative magnetic permeability in the vicinity of the antisymmetric mode is a very exciting phenomenon which might be very useful for the realization of future optomagnetic composite media. In addition to the important near-field effects, also possible far-field interaction phenomena are discussed. Spacer layer dependent calculations show that the radiative coupling results in a superradiant-like behavior. Additionally, multiple-grating structures incorporating more than two periodic nanowire layers are shortly addressed. Especially structures with a Bragg-spacing of the individual grating layers show some remarkable optical properties. The considered structure represents a specific realization of a one-dimensional resonant photonic crystal. Radiative interaction between the nanowire plasmons in these structures cause the formation of large optical stopbands with a bandwidth of approximately 1 eV. Similar to the exciton polariton modes in multiple-quantum-well structures, light propagation has to be described in terms of so-called superlattice plasmon polaritons in these plasmonic crystals.

7.2   Outlook

The general goal in starting this research was to develop a more detailed understanding of the linear optical properties of metallic photonic crystal structures. One of the fundamental questions, in broad terms, was how the optical response would change in dependence of the chosen geometrical parameters. Shortly after starting the investigations of metallic nanostructures, it turned out that especially nanowire-based metal structures are a very suitable and powerful model system. From both an experimental and theoretical point of view, their one-dimensional nature facilitates the study of resonant light-matter interaction phenomena. Three different nanowire-based metal structures have been analyzed and the importance of plasmon-plasmon coupling has been explicitly pointed

out. However, due to the complexity of the considered systems, some phenomena are only shortly reviewed within this work. For example, the qualitative discussion of far-field (radiative) interaction in stacked structures has to be extended. Especially a comparison between periodic and non-periodic structures might be helpful in a next step of the research project. A further point is directly related to the challenging fabrication processes. Experimental results are available for the presented planar geometries, while they are still missing in case of stacked grating structures. It has to be clarified to which extent a fabrication of the proposed multilayer grating structures might be possible.

It might be very interesting to address some of the following fundamental questions in further studies on metal-based composite materials:

- All presented discussions are restricted to metallo-dielectric photonic crystal structures within this work. However, first preliminary experimental studies (not presented within this thesis) have shown that the introduction of additional dipole-active material might be of certain interest. For example, lower-dimensional semiconductor structures are excellent candidates. The coupling between plasmons and quantum dots or quantum wells might be a very promising research direction. Metal nanostructures such as dots or wires might act as nanoantennas or nanocavities to enhance the light emission processes.

- The investigation of so-called metamaterials is currently a very active field of research. The predicted optical properties of artificial materials with a negative refractive index have stimulated many interesting developments. In particular, further studies have to clarify to with extent metallic nanostructures can be applied for the realization of a magnetic resonance in the optical regime. As theoretically discussed in Chap. 6, especially nanowire pair structures can be used to generated strong and spatially concentrated magnetic fields in the visible wavelength range. The detailed analysis of related interaction effects might be very important from a fundamental as well as from an applied point of view, although a negative index of refraction might be out of reach at all.

- An alternative research direction might be the detailed investigation of possible disorder effects. Both fluctuations of the period as well as of the cross-section of the considered metallic scatterers have to be considered. While such effects are well explored in case of solid state crystals (e.g.,

x-ray scattering), similar extensive studies for photonic crystal structures are still missing. Especially more detailed theoretical studies should be accomplished to describe the influence of structural disorder on the discussed light-matter interaction phenomena. These effects should include both 1-D and 2-D disorder, as well as near-field, far-field, and correlated disorder.

- Only the linear optical properties of the proposed metal-based photonic crystal structures have been studied so far. However, the utilization of the large field enhancement due to particle plasmon excitation might also lead to interesting applications in the non-linear regime. For example, the investigation of light-induced transport phenomena in metallic photonic crystals might be a promising research direction. Another interesting topic might be the use of metal nanostructures to enhance optical bistability in more complex composite materials, for example by using highly nonlinear substrates such as $LiNbO_3$.

Appendix A

Sample preparation and experimental setup

A.1 Sample preparation

All of the investigated planar metallo-dielectric photonic crystal slab structures have been fabricated by using electron beam lithography (e.g., see Ref. [99]). Generally, electron beam lithography is a widely spread tool for lateral structuring below the resolution limit of standard photolithography. Compared to other nanostructuring methods, it combines high resolution with excellent flexibility and reasonable patterning speed.

The schematic view of the required fabrication steps is depicted in panel (a) of Fig.A.1. The implemented metallo-dielectric sample structures are based on planar indium-tin-oxide (ITO, In_2O_3:SnO_2) slab layers which are sputtered onto a 2 mm thick fused silica substrate (commercially offered by Laseroptik GmbH, Garbsen, Germany). After a first cleaning step (rinsing with ultrasound and acetone) in order to improve the adhesion, two electron beam resist layers are spin coated onto the ITO layer in the second step. Note that the two resist layers differ in their electron sensitivity which facilitates the fabrication of so-called *undercut* structures. Polymethylmethacrylate (PMMA) is used as positive electron beam resist material. The first layer (molecular weight 200 K, 3.5 % in chlorobenzene) is more sensitive to electrons then the second layer (molecular weight 950 K, 1.5 % in chlorobenzene). Note that the sample is softbaked for one hour at approximately 150°C after spin coating of the individual layers, respectively.

As third step, electron beam exposure is utilized to pattern the resist layers (e.g.,
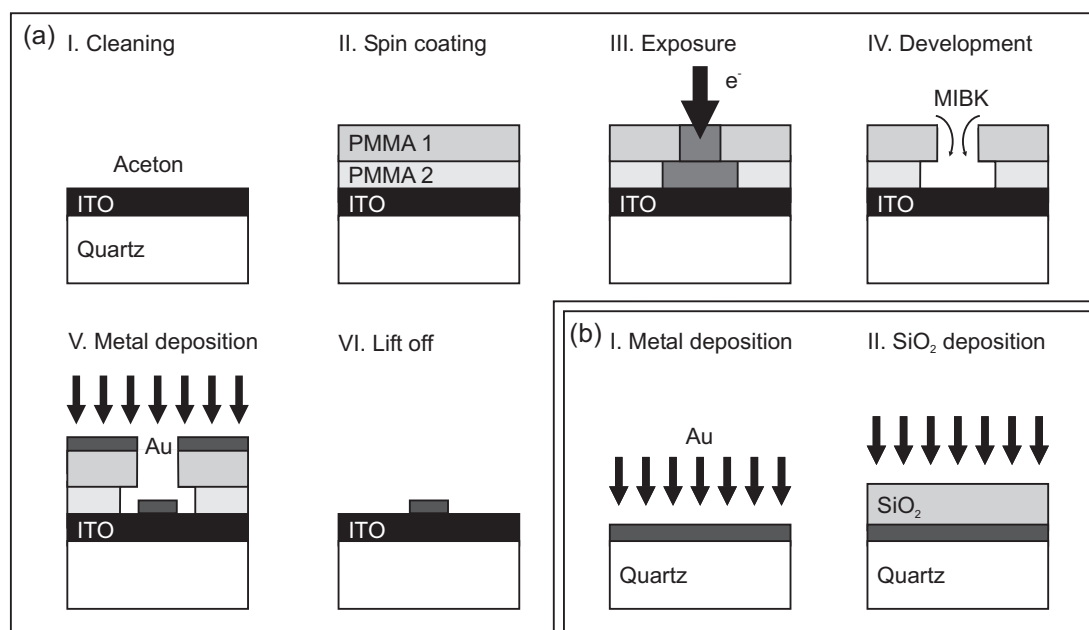
Figure A.1: Schematic view of the electron beam lithography fabrication process. Panel (a) displays the necessary steps for the fabrication of the gold nanowire arrays. The additional steps for preparation of the coated metal films are illustrated in panel (b).

nanowire arrays). The exposure process is accomplished by the use of a modified scanning electron microscope (Hitachi 2300) which is equipped with an additional electron beam control unit (Sietec Nanobeam). The overall size of the exposed area is approximately 100×100 μm^2. The spatial extension is limited by the field of view of the electron microscope at the magnification used for the beam writing. Note that the underlying thin ITO layer is very important during the electron beam exposure. In addition to the later use as waveguiding layer, especially the finite conductivity is very beneficial. The ITO layer generally minimizes unwanted charging effects during the writing process.

The electron beam resist pattern is then developed in a fourth step. A dilution of methylisobutylketon (MIBK) and propanol (1:3 ratio) is used as developer. After immersion into the MIBK mixture for 90 seconds (ultrasonic bath), the sample structure is immediately transferred to a propanol bath (stop bath). After development of the electron beam resist layers, the sample structure is blown dry with nitrogen. In an additional step, oxygen plasma ashing is used to remove the remaining polymeric material within the patterned undercut regions.

Subsequently, the whole sample structure is coated with a thin metal film by
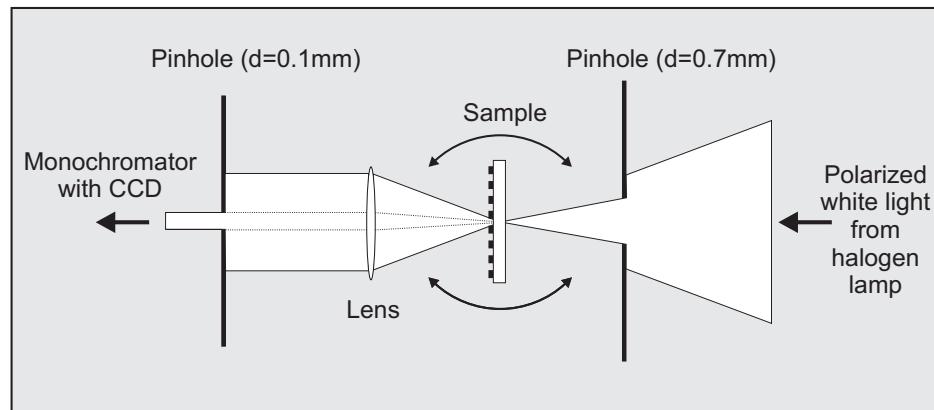
Figure A.2: Schematic view of the used experimental setup. Two pinholes have been introduced to reduce the numerical aperture of the white light beam.

thermal evaporation. Metal structures (i.e., wires or clusters) with a height of up to 60 nm can be realized with the used multilayer resist design (overall resist thickness of approximately 200 nm). Finally, the patterns are lifted off by dissolving the photoresist in a remover bath (AR 300-70, ALLRESIST), leaving the gold nanowires in the previously exposed undercut areas.

Fig.A.1 (b) displays the required additional fabrication steps for the preparation of the metal film based photonic crystal structures. Instead of using ITO-coated substrates, a cleaned fused silica substrate is covered by a thin metal layer in a first step (thickness of approximately 20 nm). In the following step, a thin SiO_2 layer is deposited on top of the homogeneous metal film. The SiO_2 layer is used as a spacer which controls the grating-film separation in the experimental studies. All subsequent fabrication steps (i.e., deposition of the nanowire grating) are similar to the described preparation process of the ITO-based metallo-dielectric photonic crystal structures.

A.2   Experimental setup

Standard transmission spectroscopy has been used to determine the linear optical properties of the investigated photonic crystal slab structures. Thus, a conventional transmission setup including a halogen lamp was used for recording all presented extinction spectra. The schematic view of the experimental setup is shown in Fig.A.2. A collimated homogeneous white light beam from a halogen lamp is focused by a microscope objective (magnification 10x, numerical aperture

0.3). The sample itself is mounted on a rotating stage so that angle dependent transmission measurements are possible. Generally, the transmitted and recollimated light fields are spectrally resolved by a monochromator (Roper Scientific, SpectraPro 500i, gratings with 150 or 300 lines/mm) and detected with an attached CCD camera (CCD: charge-coupled device). It is further important to note that the aperture angle of the transmitted white light beam is artificially reduced below 0.2° by using two narrow pinholes (diameter $d = 0.7$ mm and $d = 0.1$ mm). Especially the second pinhole is essential to secure the required angular resolution. Without the pinhole, the angular resolution is lowered due to the simultaneous detection of light fields that cross the sample under different angles. An alternative approach might be the replacement of the microscope objective by a lens with a longer focal distance and lower numerical aperture.

Note that the used setup has been slightly modified for the angle-dependent measurement depicted in Fig. 3.12. Instead of rotating the sample stepwise (original procedure), the displayed contour plot was deduced from a single measurement. The angular information was simply extracted from the transmitted beam by removing the second pinhole and replacing the spherical lens in front of the monochromator by a cylindrical one.

Bibliography

[1] K. Sakoda, *Optical Properties of Photonic Crystals* (Springer-Verlag Berlin Heidelberg New York, 2001).

[2] J. D. Joannopoulos, R. D. Meade, and J. N. Winn, *Photonic Crystals: Molding the Flow of Light* (Princeton Univ. Press, Princeton, NJ, 1995).

[3] E. Yablonovitch, *Inhibited Spontaneous Emission in Solid-State Physics and Electronics*, Phys. Rev. Lett. **58**(20), 2059 (1987).

[4] S. John, *Strong localization of photons in certain disordered dielectric superlattices*, Phys. Rev. Lett. **58**(23), 2486 (1987).

[5] R. Zengerle, *Lichtausbreitung in ebenen periodischen Wellenleitern*, PhD Thesis, Universität Stuttgart (1979).

[6] Y. Akahane, T. Asano, B. S. Song, and S. Noda, *High-Q photonic nanocavity in a two-dimensional photonic crystal*, Nature **425**, 944 (2003).

[7] O. Painter, R. K. Lee, A. Scherer, A. Yariv, J. D. O'Brien, P. D. Dapkus, and I. Kim, *Two-dimensional photonic band-gap defect mode laser*, Science **284**, 1819 (1999).

[8] T. Yoshie, A. Scherer, J. Hendrickson, G. Khitrova, H. M. Gibbs, G. Rupper, C. Ell, O. B. Shchekin, and D. G. Deppe, *Vacuum Rabi splitting with a single quantum dot in a photonic crystal nanocavity*, Nature **432**, 200 (2005).

[9] B. S. Song, S. Noda, T. Asano, and Y. Akahane, *Ultra-high-Q photonic double-heterostructure nanocavity*, Nature Materials **4**, 207 (2005).

[10] W. L. Barnes, A. Dereux, and T. W. Ebbesen, *Surface plasmon subwavelength optics*, Nature (London) **424**, 824 (2003).

[11] H. Raether, *Excitation of Plasmons and Interband Transitions by Electrons* (Springer-Verlag, Berlin, 1980).

[12] H. Raether, *Surface Plasmons on Smooth and Rough Surfaces and on Gratings* (Springer-Verlag, Berlin, 1988).

[13] U. Fano, *The Theory of Anomalous Diffraction Gratings and of Quasi-Stationary Waves on Metallic Surfaces (Sommerfeld´s Waves)*, J. Opt. Soc. Am. **31**, 213 (1941).

[14] R. H. Ritchie, *Plasma Losses by Fast Electrons in Thin Films*, Phys. Rev. **106**(5), 874 (1957).

[15] E. A. Stern and R. A. Ferrell, *Surface Plasma Oscillations of a Degenerate Electron Gas*, Phys. Rev. **120**(1), 130 (1960).

[16] C. J. Powell and J. B. Swan, *Origin of the Characteristic Electron Energy Losses in Aluminum*, Phys. Rev. **115**, 869 (1959).

[17] R. W. Wood, *On a remarkable case of uneven distribution of light in a diffraction grating spectrum*, Phil. Mag. **4**, 396 (1902).

[18] D. Sarid, *Long-Range Surface-Plasma Waves on Very Thin Metal Films*, Phys. Rev. Lett. **47**, 1927 (1981).

[19] J. Homola, S. S. Yee, and G. Gauglitz, *Surface plasmon resonance sensors: review*, Sensors Actuat. **54**, 3 (1999).

[20] M. Moskivits, *Surface-enhanced spectroscopy*, Rev. Mod. Phys. **57**, 783 (1985).

[21] J. C. Quail, J. G. Rako, H. J. Simon, and R. T. Deck, *Optical Second-Harmonic Generation with Long-Range Surface Plasmons*, Phys. Rev. Lett. **50**, 1987 (1984).

[22] T. Y. F. Tsang, *Surface-plasmon-enhanced third-harmonic generation in thin silver films*, Opt. Lett. **21**, 245 (1996).

[23] R. K. Hickernell and D. Sarid, *Optical bistability using prism-coupled, long-range surface plasmons*, J. Opt. Soc. Am. B **3**, 1059 (1986).

[24] I. I. Smolyaninov, *Quantum Fluctuations of the Refractive Index near the Interface between a Metal and a Nonlinear Dielectric*, Phys. Rev. Lett. **94**, 057403 (2005).

[25] W. L. Barnes, *Fluorescence near interfaces: the role of photonic mode density*, J. mod. Optics **445**, 661 (1998).

[26] R. R. Chance, A. Prock, and R. Silbey, *Molecular Fluorescence and Energy Transfer near Interfaces*, Adv. chem. Phys. **37**, 1 (1978).

[27] I. Gontijo, M. Boroditsky, E. Yablonovitch, S. Keller, U. K. Mishra, and S. P. DenBaars, *Coupling of InGaN quantum-well photoluminescence to silver surface plasmons*, Phys. Rev. B **60**, 11564 (1999).

[28] A. Neogi, C. W. Lee, H. O. Everitt, T. Kuroda, A. Tackeuchi, and E. Yablonovitch, *Enhancement of spontaneous recombination rate in a quantum well by resonant surface plasmon coupling*, Phys. Rev. B **66**, 153305 (2002).

[29] A. Neogi, H. Morkoc, T. Kuroda, and A. Tackeuchi, *Coupling of spontaneous emission from GaN-AlN quantum dots into silver surface plasmons*, Opt. Lett. **30**, 93 (2005).

[30] W. L. Barnes, *Turning the tables on surface plasmons*, Nature Mater. **3**, 588 (2004).

[31] P. A. Hobson, S. Wedge, J. A. Wasey, I. Sage, and W. L. Barnes, *Surface Plasmon Mediated Emission from Organic Light-Emitting Diodes*, Adv. Mater. **14**, 1393 (2002).

[32] K. Okamoto, I. Niki, A. Shvartser, Y. Narukawa, T. Mukai, and A. Scherer, *Surface-plasmon-enhanced light emitters based on InGaN quantum wells*, Nature Materials **3**, 601 (2004).

[33] R. W. Gruhlke, W. R. Holland, and D. G. Hall, *Surface-Plasmon Cross Coupling in Molecular Fluorescence near a Corrugated Thin Metal Film*, Phys. Rev. Lett. **56**, 2823 (1986).

[34] P. Andrew and W. L. Barnes, *Energy Transfer Across a Metal Film Mediated by Surface Plasmon Polaritons*, Science **306**, 1002 (2004).

[35] F. D. Stefani, K. Vasilev, N. Bocchio, N. Stoyanova, and M. Kreiter, *Surface-Plasmon-Mediated Single-Molecule Fluorescence Through a Thin Metallic Film*, Phys. Rev. Lett. **94**, 23005 (2005).

[36] U. Kreibig and M. Vollmer, *Optical Properties of Metal Clusters* (Springer-Verlag, Berlin, 1995).

[37] G. Mie, *Beiträge zur Optik trüber Medien, speziell kolloidaler Metalllösungen*, Ann. d. Phys. **25**, 377 (1908).

[38] U. Kreibig and P. Zacharias, *Surface Plasma Resonances in Small Spherical Silver and Gold Particles*, Z. Phys. **231**, 128 (1970).

[39] M. C. Daniel and D. Astruc, *Gold nanoparticles: Assembly, supramolecular chemistry, quantum-size-related properties, and applications toward biology, catalysis, and nanotechnology*, Chem. Rev. **104**, 293 (2004).

[40] K. Baba and M. Miyagi, *Optical Polarizer using Anisotropic Metallic Island Films with a Large Aperture and a High Extinction Ratio*, Opt. Lett. **16**(12), 954 (1991).

[41] S. D. Stookey and R. J. Araujo, *Selective Polarization of Light due to Absorption by Small Elongated Silver Particles in Glass*, Appl. Opt. **7**(5), 777 (1968).

[42] K. Kneipp, H. Kneipp, I. Itzkan, R. R. Dasari, and M. S. Feld, *Surface-enhanced Raman scattering and biophysics*, J. Phys. C. **14**, R597 (2002).

[43] K. Kneipp, Y. Wang, H. Kneipp, L. T. Perelman, I. Itzkan, R. R. Dasari, and M. S. Feld, *Single molecule detection using surface-enhanced Raman scattering (SERS)*, Phys. Rev. Lett. **78**(9), 1667 (1997).

[44] M. Quinten, A. Leitner, J. R. Krenn, and F. R. Aussenegg, *Electromagnetic energy transport via linear chains of silver nanoparticles*, Opt. Lett. **23**, 1331 (1998).

[45] M. L. Brongersma, J. W. Hartman, and H. A. Atwater, *Electromagnetic energy transfer and switching in nanoparticle chain arrays below the diffraction limit*, Phys. Rev. B **62**(24), R16356 (2000).

[46] S. A. Maier, P. G. Kik, H. A. Atwater, S. Meltzer, E. Harel, B. E. Koel, and A. A. G. Requicha, *Local detection of electromagnetic energy transport below the diffraction limit in metal nanoparticle plasmon waveguides*, Nature Materials **2**, 229 (2003).

[47] A. R. McGurn and A. A. Maradudin, *Polariton effects in multiple-quantum-well structures of $CdTe/Cd_{1-x}Zn_xTe$*, Phys. Rev. B **48**, 17576 (1993).

[48] E. R. Brown and O. B. McMahon, *Large electromagnetic stop bands in metallodielectric photonic crystals*, Appl. Phys. Lett. **67**(15), 2138 (1995).

[49] D. F. Sievenpiper, E. Yablonovitch, J. N. Winn, S. Fan, P. R. Villeneuve, and J. D. Joannopoulos, *3D Metallo-Dielectric Photonic Crystals with Strong Capacitive Coupling between Metallic Islands*, Phys. Rev. Lett. **80**, 2829 (1998).

[50] A. Moroz, *Three-Dimensional Complete Photonic-Band-gap Structures in the Visible*, Phys. Rev. Lett. **83**, 5274 (2002).

[51] J. G. Fleming, S. Y. Lin, I. El-Kady, R. Biswas, and K. M. Ho, *All-metallic three-dimensional photonic crystals with a large infrared bandgap*, Nature (London) **417**, 52 (2002).

[52] E. Özbay, B. Temelkuran, M. Sigalas, G. Tuttle, C. M. Soukoulis, and K. M. Ho, *Defect structures in metallic photonic crystals*, Appl. Phys. Lett. **69**, 3797 (1996).

[53] F. Gadot, A. de Lustrac, J. M. Lourtioz, T. Brillat, A. Ammouche, and E. Akmansoy, *High-transmission defect modes in two-dimensional metallic photonic crystals*, J. Appl. Phys. **85**, 8499 (1999).

[54] E. Cubukcu, K. Aydin, E. Ozbay, S. Foteinopoulou, and C. M. Soukoulis, *Negative refraction by photonic crystals*, Nature (London) **423**, 605 (2003).

[55] S. C. Kitson, W. L. Barnes, and J. R. Sambles, *Full Photonic Band Gap for Surface Modes in the Visible*, Phys. Rev. Lett. **277**(13), 2670 (1996).

[56] W. L. Barnes, T. W. Preist, S. C. Kitson, and J. R. Sambles, *Physical origin of photonic energy gaps in the propagation of surface plasmons on gratings*, Phys. Rev. B **54**, 6227 (1996).

[57] W. L. Barnes, S. C. Kitson, T. W. Preist, and J. R. Sambles, *Photonic surfaces for surface-plasmon polaritons*, J. Opt. Soc. Am. A **14**, 1654 (1997).

[58] U. Schröter and D. Heitmann, *Grating couplers for surface plasmons excited on thin metal films in the Kretschmann-Raether configuration*, Phys. Rev. B **60**, 4992 (1999).

[59] S. I. Bozhevolnyi, J. Erland, K. Leosson, P. M. W. Skovgaard, and J. M. Hvam, *Waveguiding in Surface Plasmon Polariton Band Gap Structures*, Phys. Rev. Lett. **86**(14), 3008 (2001).

[60] H. Ditlbacher, J. R. Krenn, G. Schider, A. Leitner, and F. R. Aussenegg, *Two-dimensional optics with surface plasmon polaritons*, Appl. Phys. Lett. **81**, 1622 (1962).

[61] D. K. Gifford and D. G. Hall, *Extraordinary transmission of organic photoluminescence through an otherwise opaque metal layer via surface plasmon cross coupling*, Appl. Phys. Lett. **80**, 3679 (2002).

[62] D. K. Gifford and D. G. Hall, *Emission through one of two metal electrodes of an organic light-emitting diode via surface-plasmon cross coupling*, Appl. Phys. Lett. **81**, 4315 (2002).

[63] S. Wedge and W. L. Barnes, *Surface plasmon-polariton mediated light emission through thin metal films*, Opt. Express **12**, 3673 (2004).

[64] A. Köck, W. Beinstingl, K. Berthold, and E. Gornik, *Surface plasmon polariton enhanced light emission from Schottky diodes*, Appl. Phys. Lett. **52**, 1164 (1988).

[65] A. Köck, E. Gornik, M. Hauser, and W. Beinstingl, *Strongly directional emission from AlGaAs/GaAs light-emitting diodes*, Appl. Phys. Lett. **57**, 2327 (1990).

[66] N. E. Hecker, R. A. Höpfel, N. Sawaki, T. Maier, and G. Strasser, *Surface plasmon enhanced photoluminescence from a single quantum well*, Appl. Phys. Lett. **75**, 1577 (1999).

[67] T. Ishihara, *Optical response of semiconductor and metal-embedded photonic crystal slabs*, Phys. stat. sol (a) **201**, 398 (2004).

[68] S. C. Kitson, W. L. Barnes, and J. R. Sambles, *Photonic band gaps in metallic microcavities*, J. Appl. Phys. **84**, 2399 (1998).

[69] M. G. Salt and W. L. Barnes, *Flat photonic bands in guided modes of textured metallic microcavities*, Phys. Rev. B **61**, 11125 (2000).

[70] J. Vuckovic, M. Loncar, and A. Scherer, *Surface plasmon enhanced light-emitting diode*, IEEE. J. Quant. Elec. **QE 36**, 1131 (2000).

[71] T. W. Ebbesen, H. J. Lezec, H. F. Ghaemi, T. Thio, and P. A. Wolff, *Extraordinary optical transmission through sub-wavelength hole arrays*, Nature (London) **391**, 667 (1998).

[72] H. F. Ghaemi, Tineke Thio, D. E. Grupp, T. W. Ebbesen, and H. J. Lezec, *Surface plasmons enhance optical transmission through subwavelength holes*, Phys. Rev. B **58**, 6779 (1998).

[73] J. A. Porto, F. J. García-Vidal, and J. B. Pendry, *Transmission Resonances on Metallic Gratings with Very Narrow Slits*, Phys. Rev. Lett. **83**, 2845 (1999).

[74] S. Astilean, Ph. Lalanne, and M. Palamaru, *Light transmission through metallic channels much smaller than the wavelength*, Opt. Commun. **175**, 265 (2000).

[75] L. Martín-Moreno, F. J. García-Vidal, H. J. Lezec, K. M. Pellerin, T. Thio, J. B. Pendry, and T. W. Ebbesen, *Theory of Extraordinary Optical Transmission through Subwavelength Hole Arrays*, Phys. Rev. Lett. **86**, 1114 (2001).

[76] Y. Takakura, *Optical Resonance in a Narrow Slit in a Thick Metallic Screen*, Phys. Rev. Lett. **86**, 05601 (2001).

[77] Q. Cao and P. Lalanne, *Negative Role of Surface Plasmons in the Transmission of Metallic Gratings with Very Narrow Slits*, Phys. Rev. Lett. **88**, 057403 (2002).

[78] F. J. García-Vidal and L. Martín-Moreno, *Transmission and focusing of light in one-dimensional periodically nanostructured metals*, Phys. Rev. B **66**, 155412 (2002).

[79] J. A. Porto, L. Martin-Moreno, and F. J. Garcia-Vidal, *Optical bistability in subwavelength slit apertures containing nonlinear media*, Phys. Rev. B **70**, 081402 (2004).

[80] I. I. Smolyaninov, A. V. Zayats, A. Stanishevsky, and C. C. Davis, *Optical control of photon tunneling through an array of nanometer-scale cylindrical channels*, Phys. Rev. B **66**, 205414 (2002).

[81] J. Dintinger, S. Klein, F. Bustos, W. L. Barnes, and T. W. Ebbesen, *Strong coupling between surface plasmon-polaritons and organic molecules in subwavelength hole arrays*, Phys. Rev. Lett. **71**, 035424 (2005).

[82] C. Ropers, D. J. Park, G. Stibenz, G. Steinmeyer, J. Kim, D. S. Kim, and C. Lienau, *Surface-Plasmon Resonance Effect in Grating Diffraction*, Phys. Rev. Lett. **94**, 113901 (2005).

[83] H. J. Lezec, A. Degiron, E. Devaux, R. A. Linke, L. Martin-Moreno, F. J. Garcia-Vidal, and T. W. Ebbesen, *Beaming light from a subwavelength aperture*, Science **297**, 820 (2002).

[84] F. J. García-Vidal, L. Martín-Moreno, H. J. Lezec, and T. W. Ebbesen, *Focusing light with a single subwavelength aperture flanked by surface corrugations*, Appl. Phys. Lett. **83**, 4500 (2002).

[85] E. Altewischer, M. P. van Exter, and J. P. Woerdman, *Plasmon-assisted transmission of entangled photons*, Nature **418**, 304 (2002).

[86] S. Fasel, F. Robin, E. Moreno, D. Erni, N. Gisin, and H. Zbinden, *Energy-Time Entanglement Preservation in Plasmon-Assisted Light Transmission*, Phys. Rev. Lett. **94**, 110501 (2005).

[87] W. Fan, S. Zhang, B. Minhas, K. J. Malloy, and S. R. J. Brueck*, *Enhanced Infrared Transmission through Subwavelength Coaxial Metallic Arrays*, Phys. Rev. Lett. **94**, 033902 (2005).

[88] A. Papakostas, A. Potts, D.M. Bagnall, S. L. Prosvirnin, H. J. Coles, and N. I. Zheludev, *Optical Manifestations of Planar Chirality*, Phys. Rev. Lett. **90**, 107404 (2003).

[89] B. Lamprecht, G. Schider, R. T. Lechner, H. Ditlbacher, J. R. Krenn, A. Leitner, and F. R. Aussenegg, *Metal Nanoparticle Gratings: Influence of Dipolar Particle Interaction on the Plasmon Resonance*, Phys. Rev. Lett. **84**(20), 4721 (2000).

[90] S. Linden, J. Kuhl, and H. Giessen, *Controlling the Interaction between Light and Gold Nanoparticle: Selective Supression of Extinction*, Phys. Rev. Lett. **86**(20), 4688 (2001).

[91] S. Linden, A.Christ, J. Kuhl, and H. Giessen, *Selective supression of extinction within the plasmon resonance of gold nanoparticles*, Appl. Phys. B **73**, 311 (2001).

[92] B. Lamprecht, A.Leitner, and F.R.Aussenegg, *Femtosecond decay time measurement of electron plasma oscillation in nanolithographically designed silver particles*, Appl. Phys. B **64**, 269 (1997).

[93] B. K. Canfield, S. Kujala, K. Jefimovs, J. Turunen, and M. Kauranen, *Linear and nonlinear optical responses influenced by broken symmetry in an array of gold nanoparticles*, Opt. Express **22**, 5418 (2004).

[94] N. Félidj, J. Aubard, G. Lévi, J. R. Krenn, M. Salerno, G. Schider, B. Lamprecht, A. Leitner, and F. R. Aussenegg, *Controlling the optical response of regular arrays of gold particles for surface-enhanced Raman scattering*, Phys. Rev. B **65**, 75419 (2002).

[95] T. Zentgraf, A. Christ, J. Kuhl, and H. Giessen, *Tailoring the Ultrafast Dephasing of Quasiparticles in Metallic Photonic Crystals*, Phys. Rev. Lett. **93**, 243901 (2004).

[96] J. Stehr, J. Crewett, F. Schindler, R. Sperling, G. von Plessen, U. Lemmer, J. M. Lupton, T. A. Klar, J. Feldmann, A. W. Holleitner, M. Forster, and U. Scherf, *A low threshold polymer laser based on metallic nanoparticle gratings*, Adv. Mat. **15**, 1726 (2003).

[97] S. Linden, C. Enrich, M. Wegener, J. Zhou, T. Koschny, and C. M. Soukoulis, *Magnetic Response of Metamaterials at 100 Terahertz*, Science **306**, 1351 (2004).

[98] M. Quinten and U. Kreibig, *Optical Properties of Aggregates of Small Metal Particles*, Surf. Sci. **172**, 557 (1988).

[99] H. G. Craighead and G. A. Niklasson, *Characterization and optical properties of arrays of small gold particles*, Appl. Phys. Lett. **44**, 1134 (1984).

[100] G. Schider, J. R. Krenn, W. Gotschy, B. Lamprecht, H. Ditlbacher, A. Leitner, and F. R. Aussenegg, *Optical properties of Ag and Au nanowire gratings*, J. Appl. Phys. **90**(8), 3825 (2001).

[101] W. Rechberger, A. Hohenau, A. Leitner, J. R. Krenn, B. Lamprecht, and F. R. Aussenegg, *Optical properties of two interacting gold nanoparticles*, Opt. Commun. **220**, 137 (2003).

[102] S. A. Maier, M. L. Brongersma, P. G. Kik, and H. A. Atwater, *Observation of near-field coupling in metal nanoparticle chains using far-field polarization spectroscopy*, Phys. Rev. B **65**(19), 193408 (2002).

[103] M. Meier, A. Wokaun, and P. F. Liao, *Enhanced fields on rough surfaces: dipolar interactions among particles of sizes exceeding the Rayleigh limit*, J. Opt. Soc. Am. B **2**, 931 (1985).

[104] H. R. Stuart and D. G. Hall, *Enhanced Dipole-Dipole Interaction between Elementary Radiators Near a Surface*, Phys. Rev. Lett. **80**(25), 5663 (1998).

[105] P. Nordlander and E. Prodan, *Plasmon Hybridization in Nanoparticles near Metal Surfaces*, Nano Lett. **4**, 2209 (2004).

[106] W. R. Holland and D. G. Hall, *Surface-plasmon dispersion relation: Shifts induced by the interaction with localized plasma resonances*, Phys. Rev. B **27**(12), 7765 (1983).

[107] W. R. Holland and D. G. Hall, *Frequency Shifts of an Electric-Dipole Resonance near a Conducting Surface*, Phys. Rev. Lett. **52**(12), 1041 (1984).

[108] A. Pinchuk, A. Hilger, G. von Plessen, and U. Kreibib, *Substrate effect on the optical response of silver nanoparticles*, Nanotechnology **15**, 1890 (2004).

[109] P. Nordlander, C. Oubre, E. Prodan, K. Li, and M. I. Stockman, *Plasmon Hybridization in Nanoparticle Dimers*, Nano Lett. **4**, 899 (2004).

[110] E. L. Ivchenko, A.N. Nesvizhskii, and S. Jorda, *Bragg reflection of light from quantum-well structures*, Phys. Solid State **36**, 1156 (1994).

[111] C. Kittel, *Introduction to Solid State Physics* (John Wiley & Sons, New York, 1996).

[112] P. B. Johnson and R. W. Christy, *Optical Constants of the Noble Metals*, Phys. Rev. B **6**(12) (1972).

[113] M. Born and E. Wolf, *Principles of Optics* (Pergamon Press, 1980).

[114] C. F. Bohren and D. R. Hufman, *Absorption and Scattering of Light by Small Particles* (John Wiley & Sons, New York, 1983).

[115] F. Bassani and G. P. Parravicini, *Electronic States and Optical Transitions in Solids* (Pergamon, London, 1975).

[116] H. Ehrenreich and H. R. Philipp, *Optical Properties of Ag and Cu*, Phys. Rev. **128**(4), 1622 (1962).

[117] M. Schlüter, *Die optischen Eigenschaften von Gold, Silber und Gold-Silber-Legierungen zwischen 2 und 40 eV aus Energieverlustmessungen*, Z. Physik **250**, 87 (1972).

[118] R. H. Ritchie, *Surface Plasmons in Solids*, Surf. Sci. **34**, 1 (1973).

[119] J. J. Burke, G. I. Stegeman, and T. Tamir, *Surface-polariton-like waves guided by thin, lossy metal films*, Phys. Rev. B **33**(8), 5186 (1986).

[120] M. K. Barnoski, *Introduction to Integrated Optics*, chapter 3, 53–72 (Univ. of Calif., Santa Barbara, 1973).

[121] Fuzi Yang, J. R. Sambles, and G. W. Bradberry, *Long-range surface modes supported by thin films*, Phys. Rev. B **44**(11), 5855 (1991).

[122] J. C. Weeber, A. Dereux, C. Girard, J. R. Krenn, and J. P. Goudonnet, *Plasmon polaritons of metallic nanowires for controlling submicron propagation of light*, Phys. Rev. B **60**, 9061 (1999).

[123] P. Berini, *Plasmon-polariton waves guided by thin lossy metal films of finite width: Bound modes of symmetric structures*, Phys. Rev. B **61**, 10484 (2000).

[124] P. Berini, *Plasmon-polariton waves guided by thin lossy metal films of finite width: Bound modes of asymmetric structures*, Phys. Rev. B **63**, 125417 (2001).

[125] S. J. Al-Bader, *Optical Transmission on Metallic Wires: Fundamental Modes*, IEEE J. Quantum Electron. **QE 40**(3), 325 (2004).

[126] A. Otto, *Excitation of nonradiative surface plasma waves in silver by method of frustrated total reflection*, Z. Phys. **216**, 398 (1968).

[127] E. Kretschmann, *Determination of optical constants of metals by excitation of surface plasmons*, Z. Phys. **241**, 313 (1971).

[128] C. D. Ager and H. P. Hughes, *Optical properties of stratified systems including lamellar gratings*, Phys. Rev. B **44**(24), 13453 (1991).

[129] D. M. Whittaker and I. S. Culshaw, *Scattering-matrix treatment of patterned multilayer photonic structures*, Phys. Rev. B **60**(15), 2610 (1999).

[130] S. G. Tikhodeev, A. L. Yablonskii, E. A. Muljarov, N. A. Gippius, and T. Ishihara, *Quasi-guided modes and optical properties of photonic crystal slabs*, Phys. Rev. B **66**, 045102 (2002).

[131] G. I. Stegeman, R. F. Wallis, and A. A. Maradudin, *Excitation of surface polaritons by end-fire coupling*, Opt. Lett. **8**, 386 (1983).

[132] J. D. Jackson, *Classical Electrodynamics* (Wiley, 1975).

[133] R. G. Freeman, K. C. Grabar, K. J. Allison, R. M. Bright, J. A. Davis, A. P. Guthrie, M. B. Hommer, M. A. Jackson, P. C. Smith, D. G. Walter, and M. J. Natan, *Self-Assembled metal colloid monolayers: An approach to SERS substrates*, Science **267**, 1629 (1995).

[134] A. Wokaun, J. G. Bergman, J. O. Heritage, A. M. Glass, P. F. Liao, and D. H. Olson, *Surface second-harmonic generation from metal island films and microlithographic structures*, Phys. Rev. B **24**, 849 (1981).

[135] T. Götz, M. Buck, C. Dressler, F. Eisert, and F. Träger, *Optical second-harmonic generation by supported metal clusters: Size and shape effects*, Appl. Phys. A **60**, 607 (1995).

[136] M. Faraday, *Experimental relations of gold and other metals to light*, Phil. Trans. Roayal Soc. **147**, 145 (1857).

[137] J. C. Maxwell Garnett, *Colours in Metal Glasses and in Metallic Films*, Phil. Trans. **203**, 385 (1904).

[138] F. Kirchner and R. Zsigmondy, *Über die Ursache der Farbänderung von Gold-Gelantinepräparaten*, Ann. Phys. **15**, 573 (1904).

[139] H. C. van de Hulst, *Light Scattering by Small Particles* (Dover Publications, 1981).

[140] B. Lamprecht, J. R. Krenn, G. Schider, H. Ditlbacher, M. Salerno, N. Felidj, A.Leitner, F.R.Aussenegg, and J. C. Weeber, *Surface plasmon propagation in microscale metal stripes*, Appl. Phys. Lett. **79**, 51 (2001).

[141] E. J. Heilweil and R. M. Hochstrasser, *Nonlinear spectroscopy and picosecond transient grating study of colloidal gold*, J. Chem. Phys. **82**, 4762 (1985).

[142] T. Klar, M. Perner, S. Grosse, G. von Plessen, W. Spirkl, and J. Feldmann, *Surface-Plasmon Resonances in Single Metallic Nanoparticles*, Phys. Rev. Lett. **80**(19), 4249 (1998).

[143] C. Sönnichsen, T. Franzl, T. Wilk, G. von Plessen, J. Feldmann, O. Wilson, and P. Mulvaney, *Drastic Reduction of Plasmon Damping in Gold Nanorods*, Phys. Rev. Lett. **88**(7), 077402/1 (2002).

[144] F. Stietz, J. Bosbach, T. Wenzel, T. Vartanyan, A. Goldmann, and F. Träger, *Decay Times of Surface Plasmon Excitation in Metal Nanoparticles by Persistent Spectral Hole Burning*, Phys. Rev. Lett. **84**(24), 5644 (2000).

[145] B. Lamprecht, J. R. Krenn, A. Leitner, and F. R. Aussenegg, *Particle-plasmon decay-time determination by measuring the optical near-field's autocorrelation: influence of inhomogeneous broadening*, Appl. Phys. B **69**, 223 (1999).

[146] B. Lamprecht, J. R. Krenn, A. Leitner, and F. R. Aussenegg, *Resonant and Off-Resonant Light-Driven Plasmons in Metal Nanoparticles Studied by Femtosecond-Resolution*, Phys. Rev. Lett. **83**(21), 4421 (1999).

[147] M. W. Klein, T. Tritschler, M. Wegener, and S. Linden, *Lineshape of harmonic generation on metal nanoparticles and metallic Photonic Crystal slabs*, to be published (2005).

[148] K. J. Vahala, *Optical microcavities*, Nature **424**, 839 (2003).

[149] P. Lodahl, A. F. van Driel, I. S. Nikolaev, A. Irman, K. Overgaag, D. Vanmaekelbergh, and W. L. Vos, *Controlling the dynamics of spontaneous emission from quantum dots by photonic crystals*, Nature **430**, 654 (2004).

[150] R. Zengerle, *Light-propagation in singly and doubly periodic planar waveguides*, J. mod. Optics **34**, 1589 (1987).

[151] S. J. McNab, N. Moll, and Y. A. Vlasov, *Ultra-low loss photonic integrated circuit with membrane-type photonic crystal waveguides*, Opt. Express **11**, 2927 (2003).

[152] S. Fan and J. D. Joannopoulos, *Analysis of guided resonances in photonic crystal slabs*, Phys. Rev. B **65**, 235112 (2002).

[153] J. W. S. Rayleigh, *On the Remarkable Case of Diffraction Spectra Described by Prof. Wood*, Philos. Mag. **14**, 60 (1907).

[154] A. Hessel and A. A. Oliner, *A New Theory of Woods Anomalies on Optical Gratings*, Appl. Opt. **4**(10), 1275 (1965).

[155] M. Nevière, *The homogeneous problem*, R. Petit, editor, *Electromagnetic theory of gratings*, chapter 5, 123–157 (Springer-Verlag, Berlin, 1980).

[156] K. Kawano and T. Kitoh, *Introduction to Optical Waveguide Analysis* (John Wiley & Sons, New York, 2001).

[157] A. Christ, S. G. Tikhodeev, N. A. Gippius, J. Kuhl, and H. Giessen, *Waveguide-plasmon polaritons: Strong coupling of photonic and electronic resonances in a metallic photonic crystal slab*, Phys. Rev. Lett. **91**(18), 183901 (2003).

[158] U. Fano, *Effects of Configuration Interaction on Intensities and Phase Shifts*, Phys. Rev. **124**, 1866 (1961).

[159] S. Fan, W. Suh, and J. D. Joannopoulos, *Temporal coupled-mode theory for the Fano resonance in optical resonators*, J. Opt. Soc. Am. A **20**, 569 (2003).

[160] R. R. Boye and R. K. Kostuk, *Investigation of the effect of finite grating size on the performance of guided-mode resonance filters*, Appl. Opt. **39**, 3649 (2000).

[161] J. M. Bendickson, E. N. Glytsis, T. K. Gaylord, and D. L. Brundrett, *Guided-mode resonant subwavelength gratings: effects of finite beams and finite gratings*, J. Opt. Soc. Am. A **18**(8), 1912 (2001).

[162] N. A. Gippius, S. G. Tikhodeev, and T. Ishihara, *Optical properties of photonic crystal slabs with asymmetric unit cell*, Phys. Rev. B **72**, 045138 (2005).

[163] P. Vincent and M. Nevière, *Corrugated Dielectric Waveguides: A Numerical Study of the Second-Order Stop Bands*, App. Phys. **20**, 345 (1979).

[164] A. Yariv and M. Nakamura, *Periodic Structures for Integrated Optics*, IEEE. J. Quant. Elec. **QE 13**(4), 233 (1977).

[165] G. A. Golubenko, A. S. Svakhin, V. A. Sychugov, and A. V. Tischenko, *The total light-reflection from a corrugated surface of a dielectric wave-guide*, Soviet J. quant. Electron. **12**, 1334 (1985).

[166] E. Popov, L. Mashev, and D. Maystre, *Theoretical study of the anomalies of coated dielectric gratings*, Optica Acta **33**, 607 (1986).

[167] I. A. Avrutsky and V. A. Sychugov, *Reflection of a beam of finite size from a corrugated waveguide*, J. mod. Optics **36**, 1527 (1989).

[168] R. Magnusson and S. S. Wang, *New principle for optical filters*, Appl. Phys. Lett. **61**, 1022 (1992).

[169] S. S. Wang and R. Magnusson, *Theory and application of guided-mode resonance filters*, Appl. Opt. **32**(14), 2606 (1993).

[170] D. Rosenblatt, A. Sharon, and A. A. Friesem, *Resonant Grating Waveguide Structures*, IEEE. J. Quant. Elec. **QE 33**, 2038 (1997).

[171] Z. S. Liu, S. Tibuleac, D. Shin, P. P. Young, and R. Magnusson, *High-efficiency guided-mode resonance filter*, Opt. Lett. **23**(19), 1556 (1998).

[172] P. S. Priambodo, T. A. Maldonado, and R. Magnusson, *Fabrication and characterization of high-quality waveguide-mode resonant optical filters*, Appl. Phys. Lett. **83**, 3248 (2003).

[173] A. Sharon, G. Glasberg, D. Rosenblatt, and A. A. Friesem, *Metal-based resonant grating waveguide structures*, J. Opt. Soc. Am. A **14**(3), 588 (1997).

[174] A. Sharon, D. Rosenblatt, and A. A. Friesem, *Narrow spectral bandwidths with grating waveguide structures*, Appl. Phys. Lett. **69**(27), 4154 (1996).

[175] V. N. Astratov, D. M. Whittaker, I. S. Culshaw, R. M. Stevenson, M. S. Skolnick, T. F. Krauss, and R. M. De La Rue, *Photonic band-structure effects in the reflectivity of periodically patterned waveguides*, Phys. Rev. B **60**(24), R16255 (1999).

[176] P. Paddon and J. F. Young, *Two-dimensional vector-coupled-mode theory for textured planar waveguides*, Phys. Rev. B **61**(3), 2090 (2000).

[177] C. H. Henry, R. F. Kazarinov, R. A. Logan, and R. Yen, *Observation of Destructive Interference in the Dadiation Loss of Second-Order Distributed Feedback Lasers*, IEEE J. Quantum Electron. **QE 21**(2), 151 (1985).

[178] T. Fujita, T. Kitabayashi, A. Seki, M. Hirasawa, and T. Ishihara, *Optical properties of asymmetric photonic crystals*, Physica E **7**, 681 (2000).

[179] D. Nau, A. Christ, S. Linden, J. Kuhl, and H. Giessen, *The influence of disorder in metallic photonic crystal slabs*, CLEO/IQEC and PhAST Technical Digest on CDROM (The Optical Society of America, Washington, DC, 2004), IThB6 (2004).

[180] S. T. Peng, *Rigorous analysis of guided waves in doubly periodic structures*, J. Opt. Soc. Am. A **7**, 1448 (1990).

[181] F. Lemarchand, A. Sentenac, and H. Giovannini, *Increasing the angular tolerance of resonant grating filters with doubly periodic structures*, Opt. Lett. **23**(15), 1149 (1998).

[182] F. Lemarchand, A. Sentenac, E. Cambril, and H. Giovannini, *Study of the resonant behavior of waveguide gratings: increasing the angular tolerance of guided-mode filters*, J. Opt. A: Pure Appl. Opt. **1**, 545 (1999).

[183] R. Sapienza, P. Costantino, and D. Wiersma, *Optical Analogue of Electronic Bloch Oscillations*, Phys. Rev. Lett. **91**(26), 263902 (2003).

[184] J. D. Joannopoulos, R. D. Meade, and J. N. Winn, *Photonic Crystals* (Princeton University Press, Princeton, NJ, 1995).

[185] V. P. Kochereshko, G. R. Pozina, E. L. Ivchenko, D. R. Yakovlev, A. Waag, W. Ossau, G. Landwehr, R. Hellmann, and E. O. Göbel, *Giant exciton resonance reflectance in Bragg MQW structures*, Superlattices Microstruct. **15**, 471 (1994).

[186] M. Hübner, J. Kuhl, T. Stroucken, A. Knorr, S.W. Koch, R. Hey, and K. Ploog, *Collective Effects of Excitons in Multiple-Quantum-Well Bragg and Anti-Bragg Structures*, Phys. Rev. Lett. **76**(22), 4199 (1996).

[187] L. Pilozzi, A. D'Andrea, and R. Del Sole, *Electromagnetic properties of a dielectric grating.II. Quantum wells excited by surface waves*, Phys. Rev. B **54**(15), 10763 (1996).

[188] T. Fujita, Y. Sato, T. Kuitani, and T. Ishihara, *Tunable polariton absorption of distributed feedback microcavities at room temperature*, Phys. Rev. B **57**(19), 12428 (1998).

[189] R. H. Ritchie, E. T. Arakawa, J. J. Cowan, and R. N. Hamm, *Surface-Plasmon Resonance Effect in Grating Diffraction*, Phys. Rev. Lett. **21**(22), 1530 (1968).

[190] P. Lalanne and G. M. Morris, *Highly improved convergence of the coupled-wave method for TM polarization*, J. Opt. Soc. Am. A **13**, 779 (1996).

[191] C. L. Haynes, A. D. McFarland, L. Zhao, R. P. Van Duyne, G. C. Schatz, L. Gunnarsson, J. Prikulis, B. Kaesemo, and M. Käll, *Nanoparticle Optics: The Importance of radiative Dipole Coupling in Two-Dimensional Nanoparticle Arrays*, J. Phys. Chem. B **107**, 7337 (2003).

[192] R. Shimada, A. L. Yablonskii, S. G. Tikhodeev, and T. Ishihara, *Transmission properties of a two-dimensional photonic crystal slab with an excitonic resonance*, IEEE J. Quantum Electron. **QE 38**(7), 872 (2002).

[193] A. L. Yablonskii, E. A. Muljarov, N. A. Gippius, S. G. Tikhodeev, T. Fujita, and T. Ishihara, *Polariton effect in distributed feedback microcavities*, J. Phys. Soc. Jpn **70**(4), 1137 (2001).

[194] C. Weisbuch, M. Nishioka, A. Ishikawa, and Y. Arakawa, *Observation of the coupled exciton-photon mode splitting in a semiconductor quantum microcavity*, Phys. Rev. Lett. **69**(23), 3314 (1992).

[195] U. Neuberth, N. Rau, M. Wegener, S. Linden, S. Pereira, K. Busch, A. Christ, and J. Kuhl, *One-dimensional metallic photonic crystal slabs: Near-field optical spectroscopy*, International Symposium on Photonic and Electromagnetic Crystal Structures V, Tu-P6, Kyoto, Japan (2004).

[196] E. Fermi, *Quantum Theory of Radiation*, Rev. Mod. Phys. **4**, 87 (1932).

[197] E. M. Purcell, *Spontaneous Emission Probabilities at Radio Frequencies*, Phys. Rev. **69**, 681 (1946).

[198] R. R. Chance, A. Prock, and R. Silbey, *Frequency shifts of an electric-dipole transition near a partially reflecting surface*, Phys. Rev. A **12**, 1448 (1975).

[199] N. E. Hecker, R. A. Höpfel, and N. Sawaki, *Enhanced light emission from a single quantum well located near a metal coated surface*, Physica E **2**, 98 (1998).

[200] S. C. Kitson, W. L. Barnes, and J. R. Sambles, *Surface-plasmon energy gaps and photoluminescence*, Phys. Rev. B **52**, 11441 (1995).

[201] A. Christ, T. Zentgraf, J. Kuhl, S. G. Tikhodeev, N. A. Gippius, and H. Giessen, *Optical properties of planar metallic photonic crystal structures: Experiment and theory*, Phys. Rev. B **70**, 125113 (2004).

[202] K. H. Su, Q. H. Wei, X. Zhang, J. J. Mock, D. R. Smith, and S. Schultz, *Interparticle Coupling Effects on Plasmon Resonances of Nanogold Particles*, Nano. Lett. **3**(8), 1087 (2003).

[203] J. Bravo-Abad, L. Martín-Moreno, and F. J. García-Vidal, *Transmission properties of a single metallic slit: From the subwavelength regime to the geometrical-optics limit*, Phys. Rev. E **69**, 026601 (2004).

[204] D. Ammerlahn, B. Grote, S. W. Koch, J. Kuhl, M. Hübner, R. Hey, and K. Ploog, *Influence of the dielectric enviroment on the radiative lifetime of quantum-well excitons*, Phys. Rev. B **61**, 4801 (2000).

[205] Y. Merle d'Aubigne, A. Wasiela, H. Mariette, and T. Dietl, *Polariton effects in multiple-quantum-well structures of $CdTe/Cd_{1-x}Zn_xTe$*, Phys. Rev. B **54**(19), 14003 (1996).

[206] S. Haas, T. Stroucken, M. Hübner, J. Kuhl, B. Grote, A. Knorr, F. Jahnke, S. W. Koch, R. Hey, and K. Ploog, *Intensity dependence of superradiant emission from radiatively coupled excitons in multiple-quantum-well Bragg structures*, Phys. Rev. B **57**, 14 860 (1998).

[207] X. L. Zheng, D. Heiman, B. Lax, and F. A. Chambers, *Reflectance line shapes from $GaAs/Ga_{1-x}Al_xAs$ quantum well structures*, Appl. Phys. Lett. **52**, 287 (1988).

[208] G. Khitrova, H. M. Gibbs, F. Jahnke, M. Kira, and S.W. Koch, *Nonlinear optics of normal-mode-coupling semiconductor microcavities*, Rev. Mod. Phys. **71**, 1591 (1999).

[209] S. Nie and S. R. Emory, *Probing Single Molecules and Single Nanoparticles by Surface-Enhanced Raman Scattering*, Science **275**, 1102 (1997).

[210] R. Ruppin, *Surface modes of two spheres*, Phys. Rev. B **26**, 3440 (1982).

[211] J. P. Kottmann and O. J. F. Martin, *Retardation-induced plasmon resonances in coupled nanoparticles*, Opt. Lett. **26**, 1096 (2001).

[212] C. Rockstuhl, M. G. Salt, and H. P. Herzig, *Application of the boundary-element method to the interaction of ligth with single and coupled metallic nanoparticles*, J. Opt. Soc. Am. A **20**, 1969 (2003).

[213] H. Tamaru, H. Kuwata, H. T. Miyazaki, and K. Miyano, *Resonant light scattering from individual Ag nanoparticles and particle pairs*, Appl. Phys. Lett. **80**, 1826 (2002).

[214] T. Atay, J. H. Song, and A. V. Nurmikko, *Strongly interacting plasmon nanoparticle pairs: From dipole-dipole interaction to conductively coupled regime*, Nano. Lett. **4**(9), 1627 (2004).

[215] S. A. Maier, P. G. Kik, and H. A. Atwater, *Optical pulse propagation in metal nanoparticle chain waveguides*, Phys. Rev. B **67**, 205402 (2003).

[216] D. S. Citrin, *Coherent Excitation Transport in Metal-Nanoparticle Chains*, Nano. Lett. **4**(9), 1561 (2004).

[217] J. R. Krenn, A. Dereux, J. C. Weeber, E. Bourillot, Y. Lacroute, J. P. Goudonnet, G. Schider, W. Gotschy, A. Leitner, F. R. Aussenegg, and C. Girard, *Squeezing the Optical Near-Field Zone by Plasmon Coupling of Metallic Nanoparticles*, Phys. Rev. Lett. **82**, 2590 (1999).

[218] T. Stroucken, A. Knorr, P. Thomas, and S. W. Koch, *Coherent dynamics of radiatively coupled quantum-well excitons*, Phys. Rev. B **53**(4), 2026 (1996).

[219] J. P. Prineas, C. Ell, E. S. Lee, G. Khitrova, H. M. Gibbs, and S. W. Koch, *Exciton-polariton eigenmodes in light-coupled $In_{0.04}Ga_{0.96}As/GaAs$ semiconductor multiple-quantum-well periodic structures*, Phys. Rev. B **61**(20), 13863 (2000).

[220] M. Hübner, J. P. Prineas, C. Ell, P. Brick, E. S. Lee, G. Khitrova, H. M. Gibbs, and S.W. Koch, *Optical Lattices Achieved by Excitons in Periodic Quantum Well Structures*, Phys. Rev. Lett. **83**(14), 2841 (1999).

[221] E. L. Ivchenko, M. M. Voronov, M. V. Erementchouk, L. I. Deych, and A. A. Lisyansky, *Multiple-quantum-well-based photonic crystals with simple and compound elementary supercells*, Phys. Rev. B **70**, 195106 (2004).

[222] M. V. Erementchouk, L. I. Deych, and A. A. Lisyansky, *Optical properties of one-dimensional photonic crystals based on multiple-quantum-well structures*, Phys. Rev. B **71**, 235335 (2005).

[223] M. J. Bloemer and M. Scalora, *Transmissive properties of Ag/MgF_2 photonic band gaps*, Appl. Phys. Lett. **72**, 1676 (1998).

[224] M. Scalora, M. J. Bloemer, A. S. Pethel, J. P. Dowling, C. M. Bowden, and A. S. Manka, *Transparent, metallo-dielectric, one-dimensional, photonic band-gap structures*, J. Appl. Phys. **83**(5), 2377 (1998).

[225] L. Allen and J. H. Eberly, *Optical Resonace and Two-level Atoms* (John Wiley & Sons, New York, 1975).

[226] L. V. Panina, A. N. Grigorenko, and D. P. Makhnovskiy, *Optomagnetic composite medium with conducting nanoelements*, Phys. Rev. B **66**, 155411 (2002).

[227] V.A. Podolskiy, A.K. Sarychev, E.E. Narimanov, and V.M. Shalaev, *Resonant light interaction with plasmonic nanowire systems*, J. Optics A **7**, S32 (2005).

[228] V. G. Veselago, *The electrodynamics of substances with simultaneously negative values of ε and μ*, Sov. Phys. Usp. **10**, 509 (1968).

[229] S. A. Ramakrishna, *Physics of negative refractive index materials*, Rep. Prog. Phys. **68**, 449 (2005).

[230] J. B. Pendry, A. J. Holden, D. J. Robbins, and W. J. Stewart, *Magnetism from conductors and enhanced nonlinear phenomena*, IEEE. Trans. Microwave Theory Tech. **47**, 2057 (1999).

[231] R. A. Shelby, D. R. Smith, and S. Schultz, *Experimental verification of a negative index of refraction*, Science **292**, 77 (2001).

[232] V.A. Podolskiy, A.K. Sarychev, and V.M. Shalaev, *Plasmon modes and negative refraction in metal nanowire composites*, Opt. Express **11**, 735 (2003).

[233] N. Katsarakis, T. Koschny, M. Kafesaki, E. N. Economou, and C. M. Soukoulis, *Electric coupling to the magnetic resonance of split ring resonators*, Appl. Phys. Lett. **84**(15), 2943 (2004).

[234] L. C. Andreani, *Polaritons in Multiple Quantum Wells*, phys. stat. sol. (b) **188**, 29 (1995).

[235] G. Björk, S. Pau, J. M. Jacobsen, H. Cao, and Y. Yamamoto, *Excitonic superradiance to exciton-polariton crossover and the pole approximations*, Phys. Rev. B **52**, 17310 (1995).

[236] C. F. Klingshirn, *Semiconductor Optics* (Springer-Verlag, Berlin, 1997).

[237] J. Lambe and S. L. McCarthy, *Light Emission from Inelastic Electron Tunneling*, Phys. Rev. Lett. **37**(14), 923 (1976).

[238] M. Hänisch and A. Otto, *Light emission from rough tunnel junctions in UHV*, J. Phys.: Condens. Matter **6**, 9659 (1994).

[239] J. Kirtley, T. N. Theis, and J. C. Tsang, *Light emission from tunnel junctions on gratings*, Phys. Rev. B **24**(10), 5650 (1981).

[240] P. K. Hansma and H. P. Broida, *Light emission from gold particles excited by electron tunneling*, Appl. Phys. Lett. **32**, 545 (1978).

[241] A. J. Ward, J. B. Pendry, and W. J. Stewart, *Photonic dispersion surfaces*, J. Phys.: Condens. Matter **7**, 2217 (1995).

[242] J. B. Pendry, A. J. Holden, W. J. Stewart, and I. Youngs, *Extremely Low Frequency Plasmons in Metallic Mesostructures*, Phys. Rev. Lett. **76**, 4773 (1996).

[243] X. Xu, Y. Xi, D. Han, X. Liu, J. Zi, and Z. Zhu, *Effective plasma frequency in one-dimensional metallic-dielectric photonic crystals*, Appl. Phys. Lett. **86**, 091112 (2005).

[244] E. Istrate and E. H. Sargent, *Measurement of the phase shift upon reflection from photonic crystals*, Appl. Phys. Lett. **86**, 151112 (2005).

[245] I. H. Deutsch, R. J. C. Spreeuw, S. L. Rolston, and W. D. Phillips, *Photonic band gaps in optical lattices*, Phys. Rev. A **52**, 1394 (1995).

[246] L. I. Deych and A. A. Lisyansky, *Polariton dispersion law in periodic-Bragg and near-Bragg multiple quantum well structures*, Phys. Rev. B **62**, 4242 (2000).

[247] L. Pilozzi, A. D'Andrea, and K. Cho, *Spatial dispersion effects on the optical properties of a resonant Bragg reflector*, Phys. Rev. B **69**, 205311 (2004).

[248] T. Ilawa and K. Cho, *Fate of the superradient mode in a resonant Bragg reflector*, Phys. Rev. B **66**, 085338 (2002).

[249] A. V. Mintsev, L. V. Butov, C. Ell, S. Mosor, G. Khitrova, and H. M. Gibbs, *Polariton Dispersion of Periodic Quantum Well Structures*, JETP Letters **76**, 637 (2002).

Acknowledgments

I would like to thank . . .

- Prof. Dr. W. W. Rühle for taking me on as external student and therefore giving me an opportunity to prepare this thesis at the Max-Planck-Institut für Festkörperforschung in Stuttgart.

- Prof. Dr. H. W. Giessen for mentorship, for his endless enthusiasm, and for many stimulating scientific discussions.

- Dr. J. Kuhl for giving me the opportunity to work in his group and for his constant interest in forthcoming of this thesis.

- Prof. Dr. S. G. Tikhodeev and Dr. N. A. Gippius for many contributions to this work. Especially for providing outstanding theoretical support (scattering-matrix formalism) and many rewarding scientific discussions.

- Prof. Dr. G. von Plessen for fruitful discussions.

- Prof. Dr. T. Ishihara for inviting me as JSPS fellow.

- Ulrike Waizmann, Monika Riek, and Thomas Reindl for introducing me to optical and electron beam lithography and all of their invaluable help concerning sample preparation.

- Peter Andler, Wolfgang König, and Armin Schulz for constant help and technical support.

- Yvonne Manz for constant help concerning the quantum-dot studies.

- my colleagues Stefan Linden, Nils C. Nielsen, Kai Schubert, Tilman Höner zu Siderdissen, and Thomas Zentgraf for warm working atmosphere, many beneficial work, and private discussions.

- my friends for their strong support.

- my parents for continuous encouragement.

- last but not least Elena Tchernychova for mental support and standing by me throughout these times.

Lebenslauf

Persönliche Daten

André Christ
Rosenbergstr. 95
70193 Stuttgart

Tel.: (07 11) 5 05 49 10
e-mail: a.christ@fkf.mpg.de

Geb. am 27. 05. 1975 in Marburg
Ledig, deutsch

Schulbildung

1981–1994	Grundschule und Gymnasium der Freiherr-vom-Stein Schule in Gladenbach (Leistungskurse Mathematik und Physik)

Wehrdienst

1994–1995	Heeresfliegerregiment 36 in Fritzlar

Studium

1995–2000	Physikstudium an der Philipps-Universität Marburg (Nebenfach Informatik)
9/1997	Vordiplom Physik
9/2000	Diplom Physik; Diplomarbeit in der Arbeitsruppe Rühle: *Ladungsträgerdynamik in gestapelten InP Quantenpunktstrukturen* Abschluss mit Note sehr gut

Promotion

seit 01/2001	Max-Planck-Institut für Festkörperforschung Stuttgart Wissenschaftlicher Mitarbeiter in der Abteilung Spektroskopie; Promotion mit dem Titel: *Optical properties of metallic photonic crystal structures*

Stipendien

01/05–04/05	Exciton Engineering Laboratory (RIKEN), Wako, Japan JSPS Fellowship (short term)

Praktika

| 8/94–9/94 | Zimmermann Formenbau GmbH, Gladenbach |
| | Praktikum in Metallbearbeitung und Formenbau |

2/98–4/98	Ascom Systec AG, Mägenwil, Schweiz
	Auslandspraktikum: Realisierung numerischer Optimierungsmethoden
	(Simulated Annealing)

3/99–5/99	Hitachi Europe Ltd., Cavendish Laboratory,
	Cambridge University, United Kingdom
	Auslandspraktikum: Aufbau eines Femtosekunden-Pulsmodulators

| 10/00–12/00 | Arthur Andersen, Frankfurt am Main |
| | Praktikum: Financial and Commodity Risk Consulting |

Semestertätigkeiten

6/98–12/98	Fachbereich Chemie, Philipps-Universität Marburg
	Studentische Hilfskraft: Optische Untersuchungen zur Homogenität
	von Bacteriorhodopsin-Filmen

1/99–4/99	Fachbereich Wirtschaftswissenschaften,
	Philipps-Universität Marburg
	Studentische Hilfskraft: Analyse der Produktivität deutscher Banken
	mit Hilfe der Data Envelopment Analysis (DEA)

| 10/99–2/00 | Fachbereich Physik, Philipps-Universität Marburg |
| | Studentische Hilfskraft: Betreuung von Studenten im Fortgeschrittenen-Praktikum |

| 1997–1999 | Fachbereich Physik, Philipps-Universität Marburg |
| | Laborpraktikant: Untersuchung der Eigenschaften von photo-refraktiven Materialen (Infrarotsensitive Polymere) |